DGK Ausschuss Geodäsie (DGK)
der Bayerischen Akademie der Wissenschaften

Reihe C | Dissertationen | Heft Nr. 979

Patrick Alexander Schreiner

On the potential of co-location in space for reference frame and gravity field determination

München 2026

Verlag der Bayerischen Akademie der Wissenschaften, München

ISSN 0065-5325 ISBN 978-3-7696-5391-5

DGK Ausschuss Geodäsie (DGK)
der Bayerischen Akademie der Wissenschaften

Reihe C Dissertationen Heft Nr. 979

On the potential of co-location in space for reference frame and gravity field determination

An der Fakultät VI - Planen Bauen Umwelt
der Technischen Universität Berlin
zur Erlangung des akademischen Grades
Doktor der Ingenieurwissenschaften
- Dr.-Ing. -
genehmigte Dissertation

vorgelegt von

Patrick Alexander Schreiner, M. Sc.

München 2026

Verlag der Bayerischen Akademie der Wissenschaften, München

ISSN 0065-5325 ISBN 978-3-7696-5378-6

Adresse des Ausschusses Geodäsie (DGK)
der Bayerischen Akademie der Wissenschaften:

Ausschuss Geodäsie (DGK) der Bayerischen Akademie der Wissenschaften
Alfons-Goppel-Straße 11 ● D – 80 539 München
Telefon +49 – 89 – 23 031 1113 ● Telefax +49 – 89 – 23 031 - 1283 / - 1100
e-mail post@dgk.badw.de ● http://www.dgk.badw.de

Promotionsausschuss:
Vorsitzender: Prof. Dr. Frank Neitzel (TU Berlin)
Gutachter: Prof. Dr. Frank Flechtner (GFZ & TU Berlin)
Prof. Dr. Dr. h.c. Harald Schuh (GFZ & TU Berlin)
Prof. Dr. Markus Rothacher (ETH Zürich)
Dr. Alexandre Couhert (CNES)

Tag der wissenschaftlichen Aussprache: 18. Februar 2026

Diese Dissertation ist auf dem Server des Ausschusses Geodäsie (DGK)
der Bayerischen Akademie der Wissenschaften, München unter <http://dgk.badw.de/>
sowie auf dem Server der TU Berlin unter < https://doi.org/10.14279/depositonce-26218>,
Berlin 2026, elektronisch publiziert

© 2026 Ausschuss Geodäsie (DGK) der Bayerischen Akademie der Wissenschaften, München

Alle Rechte vorbehalten. Ohne Genehmigung der Herausgeber ist es auch nicht gestattet,
die Veröffentlichung oder Teile daraus zu vervielfältigen.

ISSN 0065-5325 ISBN 978-3-7696-5391-5

Publication note

This dissertation was accepted by Technische Universität Berlin in 2026 and first published as:

Schreiner PA (2026) On the potential of co-location in space for reference frame and gravity field determination. Doctoral thesis. Berlin: Technische Universität Berlin. DOI: 10.14279/depositonce-26218.

The academic content of this dissertation is also published as:

Schreiner PA (2026) On the potential of co-location in space for reference frame and gravity field determination. Munich: Ausschuss Geodäsie der Bayerischen Akademie der Wissenschaften, Reihe C, No. 979, ISBN: 978-3-7696-5391-5, www.dgk.badw.de.

Schreiner PA (2026) On the potential of co-location in space for reference frame and gravity field determination. Scientific Technical Report STR; 26/02. Potsdam: GFZ Helmholtz Centre for Geosciences. DOI: 10.48440/GFZ.b103-2602.

Licence information

© 2026 Patrick Alexander Schreiner

Unless otherwise stated, this work is licensed under a Creative Commons Attribution 4.0 International License (CC BY 4.0).

Third-party material, including figures, photographs, maps, and graphics reproduced or adapted from external sources, is excluded from this licence unless explicitly stated otherwise. Such material remains subject to the rights of the respective rights holders and is identified by the corresponding source references in the captions and bibliography.

Licence: https://creativecommons.org/licenses/by/4.0/

Abstract

Global geodynamic processes show that the Earth is a dynamic system. To observe these changes with high precision, geodesy determines the Earth's geometry, the orientation of its rotation axis in space, and its gravity field. These three quantities are commonly referred to as the three pillars of geodesy. Satellite-based observations make it possible to obtain global and homogeneous observations within short time spans. The United Nations emphasised the importance of reliable spatial information for achieving the Sustainable Development Goals in Resolution A/RES/69/266 in 2015. Geodetic reference frames are fundamental to this endeavour and indispensable for positioning and Earth system monitoring. In this context, the International Association of Geodesy (IAG) established the Global Geodetic Observing System (GGOS) in 2003 as a major project, defining target accuracies of 1 mm in position and 1 mm per decade in long-term stability for the parameters defining the reference frame.

Today, the space geodetic techniques Doppler Orbitography and Radiopositioning Integrated by Satellite (DORIS), Global Navigation Satellite Systems (GNSS), Satellite Laser Ranging (SLR) and Very Long Baseline Interferometry (VLBI) are the main contributors to reference frame determination. Since each technique has different strengths in different parameter groups, they are combined in order to exploit their complementary characteristics and to provide a more complete description of the Earth system. So far, this has been achieved by using common parameters, such as Earth Rotation Parameters (ERPs) or atmospheric parameters, and by surveying Local Ties (LTs) between technique-specific reference points at co-location sites on the Earth's surface.

This thesis investigates the potential of co-locating the space geodetic techniques DORIS, Global Positioning System (GPS) and SLR on a single satellite. On such a 'space-tie satellite', multiple observation techniques are integrated on a single platform, thereby enabling co-location of the techniques in space. For this purpose, a simulation environment was developed that is capable of simulating realistic observations for the three observation techniques. Real data were evaluated and subsequently re-simulated to obtain information for the subsequent simulations of the space-tie satellite and to represent the existing ground and space segments. Together, these reference simulations provide the basis for investigating the improvement potential of the space-tie satellite scenarios. Using the information obtained from real data, observations of the three techniques were simulated for six different space-tie satellite scenarios. The scenarios comprise the previously proposed NASA GRASP and ESA E-GRASP/Eratosthenes mission concepts, a modified E-GRASP scenario with a lower numerical eccentricity, and three circular scenarios at an altitude of 7'000 km with inclinations of 30, 60, and 89 degrees.

The potential for improvement arising from a space-tie satellite was first analysed separately for each technique, with emphasis on the technique-specific impact on the reference frame and the ERPs. Selected mismodelling effects were then imposed in the simulations to assess the robustness of the scenarios and to quantify their impact on the reference frame and ERPs. In this way, it is possible to evaluate the risk that the space-tie satellite mission might not achieve its full potential due to systematic modelling errors.

The techniques were then combined in a simulation with observations free of systematic errors. To isolate the contribution of the Space Tie (ST), a combination using only Global Ties (GTs) was first carried out. These parameters include the ERPs and, in the case of

gravity field estimation, the spherical harmonic coefficients of the gravity field. Subsequently, the space-tie satellite orbits from the individual single-technique solutions were combined, thereby introducing the ST.

To take the third pillar of geodesy, the Earth's gravity field, into account, the potential of the space-tie satellites was investigated in terms of their ability to estimate the gravity field using the three techniques. This was examined for each technique individually and in combination with GTs, with the spherical harmonic coefficients of the estimated gravity field being combined. Subsequently, the solutions were also combined with the ST in order to assess the potential of the ST for gravity field determination.

The results demonstrate that a central benefit of a space-tie satellite lies in strengthening the combined reference frame solution, in particular by enabling the geodetic datum realised by GPS to be transferred to DORIS and SLR at the millimetre level through the ST combination. In the simulation, the joint use of GTs and the ST enabled the recovery of distances between technique-specific reference points at co-location sites with an accuracy of about one millimetre. This provides a promising basis for the global validation of LTs determined by local surveys, especially for reference points that are difficult or impossible to access directly. In this way, inter-technique consistency can be improved and systematic discrepancies can be revealed.

Improvements in the ERPs are mainly achieved through the combination with GTs, while the additional contribution of the ST is small. The gravity field analysis indicates that the space-tie satellite solutions based on GPS observations provide the lowest errors among the techniques investigated and is the dominating technique in the combination. In the overall assessment of the gravity field results, the additional ST combination does not show a clear systematic improvement, although improvements may occur for individual coefficients.

The scenario assessment shows that, among the orbit configurations investigated, the near-polar circular scenario with an inclination of 89 degrees yields the best overall performance for reference frame determination and datum transfer via the ST. The circular scenario with an inclination of 60 degrees and the eccentric E-GRASP-like scenario represent the strongest alternatives, whereas the modified E-GRASP scenario, the circular scenario with an inclination of 30 degrees, and the GRASP-like scenario are less advantageous in the overall assessment.

Although the GRASP-like scenario shows considerable potential for reference frame improvement and provides the highest sensitivity to the gravity field owing to its lower orbital altitude, its overall performance is limited by its vulnerability to systematic modelling errors. The mismodelling analyses therefore demonstrate that the maximum achievable potential alone is not sufficient for selecting an orbit, since beneficial geometric properties can be accompanied by increased vulnerability to systematic modelling errors.

Overall, the results provide a basis for recommendations on the orbit design of future co-location-in-space missions, emphasising the need to optimise the orbit configuration with respect to reference frame realisation, mission-specific gravity field sensitivity, robustness against mismodelling, and inter-technique consistency.

Kurzfassung

Globale geodynamische Prozesse zeigen, dass die Erde kontinuierlich dynamischen Veränderungen unterliegt. Für die hochpräzise Beobachtung dieser Vorgänge beschäftigt sich die Geodäsie mit Messungen der Geometrie der Erde, der Orientierung ihrer Rotationsachse im Raum und ihres Schwerefeldes. Diese drei Zielgrößen werden als die drei Grundpfeiler der Geodäsie bezeichnet. Mithilfe satellitengestützter Beobachtungen ist es heutzutage möglich, innerhalb kürzester Zeit homogene globale Beobachtungen zu erhalten. Die Bedeutung dessen wurde im Jahr 2015 von den Vereinten Nationen in der Resolution A/RES/69/266 bekräftigt, in der die Wichtigkeit verlässlicher raumbezogener Informationen für das Ziel einer nachhaltigen Entwicklung (engl. Sustainable Development Goals) festgehalten ist. Geodätische Referenzrahmen sind hierfür ein fundamentales Produkt, das für Positionierungsaufgaben sowie die Beobachtungen des Systems Erde unabdingbar ist. In diesem Rahmen hat die International Association of Geodesy (IAG) im Jahr 2003 das Global Geodetic Observing System (GGOS) als Projekt initiiert, in dessen Zusammenhang eine Genauigkeit von 1 mm in der Position und 1 mm pro Dekade Langzeitstabilität für die den Referenzrahmen definierenden Parameter als Ziel festgehalten wurde.

Für die Referenzrahmenbestimmung leisten die weltraumgeodätischen Techniken Doppler Orbitography and Radiopositioning Integrated by Satellite (DORIS), Global Navigation Satellite Systems (GNSS), Satellite Laser Ranging (SLR) und Very Long Baseline Interferometry (VLBI) heute den Hauptbeitrag. Da jede dieser Techniken ihre Vorteile in unterschiedlichen Parametergruppen hat, werden sie kombiniert, um die Stärken zu vereinen und das System Erde mit allen Parametern allumfassend beschreiben zu können. Bisher erfolgt diese Kombination durch gemeinsame Parameter, wie z. B. über die Erdrotationsparameter (ERPs) oder Atmosphärenparameter, sowie durch die lokale Vermessung von Inter-Technik-Distanzen zwischen technikspezifischen Referenzpunkten an Kolokationsstationen auf der Erdoberfläche, den sogenannten Local Ties (LTs).

In der vorliegenden Arbeit wird das Potenzial der Ko-Lokation der weltraumgeodätischen Techniken DORIS, GPS und SLR durch einen Satelliten im Weltraum untersucht. Auf einem solchen „Space-tie Satelliten“ sind mehrere Techniken auf einer gemeinsamen Plattform vereint, wodurch die Ko-Lokation der Techniken ermöglicht wird. Für die Untersuchungen in dieser Arbeit wurde eine Simulationsumgebung implementiert, mit der realistische Beobachtungen der drei Techniken simuliert werden können. Als Grundlage für die Simulation wurden Echtdaten ausgewertet und anschließend nachsimuliert, um einerseits Informationen für die anschließenden Simulationen des Space-tie Satelliten zu sammeln und andererseits das existierende Boden- und Raumsegment zu simulieren. In Bezug auf diese Referenzlösungen kann das Verbesserungspotenzial der Space-tie Satelliten untersucht werden. Unter Verwendung der aus den Echtdaten gewonnenen Informationen wurden Beobachtungen der drei oben genannten Techniken zu sechs unterschiedlichen Space-Tie-Satellitenszenarien simuliert. Die untersuchten Szenarien umfassen die Orbits der ehemals von der NASA vorgeschlagenen Satellitenmission GRASP, der von der ESA vorgeschlagenen Satellitenmission E-GRASP/Eratosthenes sowie einer modifizierten Version mit niedrigerer numerischer Exzentrizität. Darüber hinaus wurden drei zirkuläre Szenarien mit einer Flughöhe von 7’000 km und Inklinationen von 30, 60 und 89 Grad simuliert.

Das Verbesserungspotenzial durch den Space-tie Satelliten wurde für jede Technik einzeln analysiert und der Einfluss auf den Referenzrahmen sowie die mit der jeweiligen

Technik bestimmten Erdrotationsparameter (ERPs) untersucht. Darüber hinaus wurde der Einfluss verschiedener Modellierungsfehler untersucht, um festzustellen, welche Auswirkungen diese auf den Referenzrahmen und die ERPs haben. So kann das Risiko beurteilt werden, inwieweit die Space-tie Satellitenmission durch in der Realität auftretende Mismodellierungseinflüsse ihr Verbesserungspotenzial nicht voll entfalten kann.

Die Kombination der Techniken wurde anschließend für den Fall einer Simulation mit Beobachtungen frei von systematischen Fehlern vollzogen. Um das Potenzial der Ko-Lokation anhand der Space Tie (ST) zu beurteilen, wurde zunächst eine Kombination der Techniken mit globalen Verknüpfungsparametern (engl. – Global Ties – GTs) durchgeführt. Dabei handelt es sich um die Erdrotationsparameter und im Fall der Schwerefeldschätzung auch um die sphärisch harmonischen Koeffizienten des Schwerefeldes. Anschließend wurde zudem der Orbit des Space-tie Satelliten der Einzeltechniklösungen kombiniert, um den Effekt der ST-Kombination zu isolieren.

Um auch den dritten Pfeiler der Geodäsie, das Schwerefeld der Erde, zu berücksichtigen, wurde untersucht, inwiefern es möglich ist, das Schwerefeld mit den Space-tie Satelliten und den drei Beobachtungstechniken zu bestimmen. Dies wurde für jede Technik einzeln untersucht sowie in Kombination mit GTs, wobei an dieser Stelle die Schwerefeldkoeffizienten (engl. Spherical Harmonics) kombiniert wurden. Anschließend wurde auch hier zusätzlich mit der ST kombiniert, um beurteilen zu können, wie sich die Verwendung der ST auf die Schwerefeldbestimmung auswirkt.

Die Ergebnisse zeigen, dass ein zentraler Nutzen eines Space-tie Satelliten in der Stärkung der kombinierten Referenzrahmenlösung liegt. Dies zeigt sich insbesondere darin, dass sich das durch Global Positioning System (GPS) realisierte geodätische Datum durch die Kombination mit der ST mit Millimetergenauigkeit auf DORIS und SLR übertragen lässt. In der Simulation war es unter Verwendung von GTs und ST möglich, zwischentechnische Distanzen an Ko-Lokationsstationen mit einer Genauigkeit von etwa einem Millimeter zu bestimmen. Dies ist ein vielversprechendes Ergebnis, um global intertechnische LTs zu validieren, die mit lokalen Vermessungen zu teils unzugänglichen Referenzpunkten bestimmt werden. Dadurch können die Konsistenz zwischen den Techniken verbessert sowie systematische Abweichungen aufgedeckt werden.

Verbesserungen der ERPs werden vor allem durch die Kombination mit GTs erzielt, während der zusätzliche Beitrag der ST gering bleibt. Die Schwerefeldanalyse zeigt, dass unter den untersuchten Techniken die auf GPS Beobachtungen basierenden Space-Tie-Satellitenlösungen die geringsten Fehler aufweisen und die kombinierte Lösung maßgeblich bestimmen. In der Gesamtbewertung der Schwerefeldergebnisse lässt die zusätzliche Kombination mit der ST keine eindeutige systematische Verbesserung erkennen, auch wenn für einzelne Koeffizienten Verbesserungen auftreten können.

Die Szenariobewertung zeigt, dass unter den untersuchten Bahnkonfigurationen das nahezu polare zirkuläre Szenario mit einer Inklination von 89 Grad die beste Gesamtleistung für die Referenzrahmenbestimmung und den Datumstransfer über die ST aufweist. Das zirkuläre Szenario mit einer Inklination von 60 Grad und das exzentrische E-GRASP ähnliche Szenario erweisen sich als stärkste Alternativen. Das modifizierte E-GRASP Szenario, das zirkuläre Szenario mit einer Inklination von 30 Grad und das GRASP ähnliche Szenario schneiden in der Gesamtbewertung dagegen weniger vorteilhaft ab.

Obwohl das GRASP ähnliche Szenario ein nicht unwesentliches Potenzial zur Verbesserung des Referenzrahmens zeigt und aufgrund seiner geringeren Bahnhöhe die höchste Sensitivität gegenüber dem Erdschwerefeld aufweist, wird seine Gesamtbewertung durch die erhöhte Anfälligkeit gegenüber systematischen Modellierungsfehlern begrenzt. Die Un-

tersuchungen zu Mismodellierungseffekten zeigen daher, dass das maximal erreichbare Verbesserungspotenzial allein nicht ausreicht, um eine Umlaufbahn auszuwählen, da vorteilhafte geometrische Eigenschaften zugleich mit einer erhöhten Sensitivität gegenüber Mismodellierungen einhergehen können.

Insgesamt bilden die Ergebnisse eine Grundlage für Empfehlungen zur Auslegung der Umlaufbahn zukünftiger Missionen zur Ko-Lokation im Weltraum. Sie verdeutlichen, dass die Wahl der Umlaufbahn im Hinblick auf die Referenzrahmenrealisierung, die missionsspezifische Sensitivität gegenüber dem Erdschwerefeld, die Robustheit gegenüber Mismodellierungseffekten und die Konsistenz zwischen den Techniken optimiert werden muss.

Acknowledgements

This dissertation deals with reference frames in a scientific sense. In a more personal sense, its completion was also shaped by a number of reference points: people who provided guidance, trust, critical discussion, and support over many years.

I would like to begin by expressing my sincere gratitude to my doctoral advisor, Prof. Dr. Frank Flechtner, for his trust, long-standing support, and the scientific opportunities he provided. The scientific and institutional framework he established enabled me to develop within the field of satellite geodesy, contribute to challenging research projects, and gain visibility through scientific exchange.

My particular gratitude goes to Dr. Rolf König for his dedicated supervision and scientific guidance throughout this work. His expertise in satellite geodesy, scientific data analysis, and the translation of complex geodetic methods into practical analysis strategies strongly influenced my approach to scientific problems. I greatly appreciated our many discussions, his critical questions, and his practical advice. His supervision further strengthened my methodological precision, my ability to critically assess results, and my focus on the broader scientific objective. I am also very grateful for the trust he placed in me, the scientific freedom he granted me, and his support as I progressed towards handling demanding scientific tasks independently.

Prof. Dr. Dr. h.c. Harald Schuh and Prof. Dr. Susanne Glaser were closely involved in the scientific project in which this dissertation was embedded. Their advice, critical questions, and constructive suggestions helped to sharpen the scientific focus of this work, place it within the broader context of space-geodetic reference-frame research, and increase the visibility of its results within the scientific community. I am also grateful to Prof. Schuh for his careful assessment as a reviewer of this dissertation.

My sincere thanks also go to Prof. Dr. Markus Rothacher and Dr. Alexandre Couhert for serving as reviewers of this dissertation and for their valuable scientific input. Their careful assessment and complementary perspectives within satellite geodesy contributed significantly to the final form of this work.

The scientific, mathematical, and technical exchange with Dr. Karl Hans Neumayer was highly valuable throughout this work. I greatly appreciated his advice on software and analysis questions and his precise and constructive engagement with challenging methodological ideas. Our discussions provided an excellent basis for testing and refining complex ideas and technical concepts.

I am also very grateful to Margarita Vei for her continuous encouragement and support as she accompanied me on my path at GFZ from its early stages. My thanks go to my colleagues at GFZ in Oberpfaffenhofen for the productive and collegial working environment, the scientific discussions, and the technical exchanges that supported this work.

Finally, I would like to thank my family and friends for their encouragement and support. I am especially grateful to my wife for her patience, understanding, and steady support during the years in which I wrote this dissertation.

Patrick Schreiner
Munich, June 2026

Abbreviations

AC	Analysis Center
AAC	Associate Analysis Centers
ANTEX	Antenna Exchange Format
AU	Astronomical Unit
A/M	Area-to-Mass ratio
BIH	Bureau International de l'Heure
BIPM	Bureau International des Poids et Mesures
CC	Combination Center
CCRS	Conventional Celestial Reference System
CDDIS	Crustal Dynamics Data Information System
CEP	Celestial Ephemeris Pole
CHAMP	CHAllenging Minisatellite Payload
CIP	Celestial Intermediate Pole
CIS	Conventional Inertial System
CoM	Center of Mass
CTRF	Conventional Terrestrial Reference Frame
CTP	Conventional Terrestrial Pole
CTS	Conventional Terrestrial System
CNES	Centre National d'Études Spatiales
CPV	Code Phase Variations
DD	Double Differences
DFG	German Research Foundation — German: Deutsche Forschungsgemeinschaft
DHF	Data Handling File
DoF	Degree of Freedom
DORIS	Doppler Orbitography and Radiopositioning Integrated by Satellite
DTM	Drag Temperature Model
EGM	Earth Gravitational Model
E-GRASP	E-GRASP/Eratosthenes
ET	Ephemeris Time
ETH	Eidgenössische Technische Hochschule Zürich
ENVISAT	ENVironmental SATellite
EOP	Earth Orientation Parameter
EPOS	Earth Parameter and Orbit System
EPOS-CS	Earth Parameter and Orbit System - Combination and Solution
EPOS-OC	Earth Parameter and Orbit System - Orbit Computation
ERP	Earth Rotation Parameter
ESA	European Space Agency
EWH	Equivalent Water Height
GAST	Greenwich Apparent Sidereal Time
GFZ	GFZ Helmholtz Centre for Geosciences
GGOS	Global Geodetic Observing System
GLONASS	Global'naya Navigatsionnaya Sputnikovaya Sistema

GMF Global Mapping Function

GMST Greenwich Mean Sidereal Time

GNSS Global Navigation Satellite Systems

GPS Global Positioning System

GPST GPS Time

GRACE Gravity Recovery and Climate Experiment

GRACE-FO GRACE Follow-On

GRASP Geodetic Reference Antenna in Space

GRGS Groupe de Recherche de Géodésie Spatiale

GT Global Tie

IAG International Association of Geodesy

IAU International Astronomical Union

ICRS International Celestial Reference System

IDS International DORIS Service

IERS International Earth Rotation and Reference Systems Service

IGN Institut National de l'information Géographique et Forestière

IGS International GNSS Service

ILRS International Laser Ranging Service

IR InfraRed radiation

ITRF International Terrestrial Reference Frame

ITRS International Terrestrial Reference System

IUGG International Union for Geodesy and Geophysics

IVS International VLBI Service

JD Julian Date

LAST Local Apparent Sidereal Time

LAGEOS LAser GEOdynamics Satellite

LEO Low Earth Orbit

LIP Loss of Improvement Potential

LLR Lunar Laser Ranging

LNA Low Noise Amplifier

LOD Length Of Day

LT Local Tie

MCS Master Control Stations

NASA National Aeronautics and Space Administration

NAVSTAR NAVigational Satellite Timing And Ranging

NRT Near Real-Time

NNR No-Net-Rotation

NNS No-Net-Scale

NNT No-Net-Translation

NP Normal Point

O-C Observed minus Computed

OCS Operational Control System

OSI Observation Scaled Improvement

PCO Phase Center Offset

PCV Phase Center Variation

POD Precise Orbit Determination

PRN PseudoRandom Noise

PSD post-seismic deformation

PSO Precise Science Orbit

QZSS Quasi-Zenith Satellite System

RINEX	Receiver INdependent EXchange format
RMS	Root Mean Square
RSO	Rapid Science Orbit
SAA	South Atlantic Anomaly
SBAS	Satellite-Based Augmentation Systems
SH	Spherical Harmonic
SI	Système international d'unités
SISRE	Signal-in-Space Range Error
SLR	Satellite Laser Ranging
SNR	Signal-to-Noise Ratio
SOD	Site Occupation Designator
SRP	Solar Radiation Pressure
SSALTO	Multi-Mission Altimetry, Orbitography and Precise Positioning Ground Segment — French: Segment Sol multi missions ALTimétrie, Orbitographie et localisation précise
SST	Satellite-to-Satellite Tracking
ST	Space Tie
SV	Satellite Vehicle
TCB	Barycentric Coordinate Time
TDB	Barycentric Dynamical Time
TCG	Geocentric Coordinate Time
TAI	International Atomic Time — French: Temps Atomique International
TDT	Terrestrial Dynamical Time
TT	Terrestrial Time
TRF	Terrestrial Reference Frame
TRS	Terrestrial Reference System
TUB	Technische Universität Berlin
TOPEX	TOPography EXperiment/Poseidon
T2L2	Time Transfer by Laser Link
UPS	Uninterruptible Power Supply
USDOD	United States Department of Defense
USO	Ultra Stable Oscillator
UT	Universal Time
UTC	Coordinated Universal Time
VLBI	Very Long Baseline Interferometry
VMF	Vienna Mapping Function

Contents

Title page

Abstract **i**

Kurzfassung **iii**

Acknowledgements **vii**

Abbreviations **ix**

List of Figures **xix**

List of Tables **xxv**

1 Introduction and objectives **1**

2 Theory **5**
2.1 Earth orientation 5
2.1.1 Precession and nutation 6
2.1.2 Earth rotation angle 6
2.1.3 Polar motion 7
2.2 Time systems 7
2.2.1 Universal time 8
2.2.2 Atomic time 9
2.2.2.1 UTC 10
2.2.2.2 GPS time 10
2.2.3 Inertial time 10
2.3 Coordinate systems 11
2.3.1 Conventional Inertial Reference System 11
2.3.2 Conventional Terrestrial Reference System 11
2.3.3 IERS Terrestrial Reference Frame (ITRF) 11
2.4 Orbit determination 12
2.4.1 Osculating orbital elements 12
2.4.2 Equation of motion 13
2.4.3 Perturbation forces 13
2.4.3.1 Gravity field of the Earth 15
2.4.3.2 Third body 16
2.4.3.3 Tidal forces 17
2.4.3.4 Radiation pressure 19
2.4.3.5 Atmospheric drag 21
2.4.3.6 Corrections due to relativistic effects 22
2.5 The EPOS software 23
2.6 Orbit and parameter determination with EPOS-OC 25
2.6.1 Solution of the equation of motion 25

2.6.2 Adjustment and parameter determination . . . 25
2.6.2.1 Differential orbit improvement process . . . 28
2.6.2.2 Outer parameter determination process . . . 28
2.7 Combination strategies . . . 28
2.7.1 Accumulation of normal equations . . . 30
2.7.2 Normal equation parameter reduction . . . 31
2.7.3 Parameter constraints . . . 32
2.7.4 Network datum constraints . . . 32
2.7.5 Combination with global parameters - global tie . . . 33
2.7.6 Combination with co-location on ground - local tie . . . 33
2.7.7 Combination with co-location in space - space tie . . . 34

3 Space geodetic techniques 35
3.1 Doppler Orbitography and Radiopositioning Integrated by Satellite . . . 35
3.1.1 System components . . . 36
3.1.1.1 Ground segment . . . 36
3.1.1.2 Space segment . . . 38
3.1.1.3 Onboard receiver . . . 38
3.1.2 International DORIS Service . . . 38
3.1.3 Measurement principle . . . 39
3.1.4 DORIS observation in EPOS-OC . . . 40
3.1.5 Technique-specific obstacles . . . 42
3.1.5.1 South Atlantic Anomaly . . . 42
3.1.5.2 DORIS time-bias . . . 43
3.1.6 Open potential for reference frame determination . . . 43
3.2 Satellite Laser Ranging . . . 43
3.2.1 System components . . . 44
3.2.1.1 Ground segment . . . 44
3.2.1.2 Space segment . . . 44
3.2.2 International Laser Ranging Service . . . 45
3.2.3 Measurement principle . . . 45
3.2.4 SLR observation in EPOS-OC . . . 46
3.2.5 Technique-specific obstacles . . . 47
3.2.5.1 Range bias . . . 47
3.2.5.2 Time bias . . . 48
3.3 Global Navigation Satellite Systems . . . 48
3.3.1 System components . . . 48
3.3.1.1 Space segment . . . 48
3.3.1.2 Control segment . . . 48
3.3.1.3 User segment . . . 49
3.3.1.4 Ground segment . . . 49
3.3.2 International GNSS Service . . . 49
3.3.3 Measurement principle . . . 49
3.3.4 GNSS observation in EPOS-OC . . . 51
3.3.5 Technique-specific obstacles . . . 52
3.3.5.1 Availability of satellite-specific information . . . 52
3.3.5.2 Clock biases . . . 52

4 Simulation scenarios and simulator methodology **55**
4.1 Co-location in space satellite orbit scenarios . . . 55
4.2 Technique-wise feasibility assessment of the orbits . . . 56
4.3 Simulation procedure . . . 59
4.4 Simulation setup . . . 62
4.4.1 Model definition . . . 62
4.4.2 Space-tie satellite configuration . . . 62
4.4.3 GPS satellite configuration . . . 64
4.5 Steps included in the simulation . . . 64
4.5.1 Simulation run . . . 64
4.5.2 Recovery run . . . 65
4.5.3 Normal equation run . . . 66
4.6 Mismodelling scenarios . . . 67
4.6.1 Centre of mass mismodelling . . . 67
4.6.2 Atmospheric drag . . . 68
4.6.3 Solar radiation pressure . . . 68
4.6.4 Frequency bias . . . 68
4.6.5 Earth gravity field mismodelling . . . 69

5 Real data analysis and ensuing simulations **71**
5.1 DORIS . . . 71
5.1.1 Ground antenna types . . . 71
5.1.2 Ground station elevation cut-off angle . . . 72
5.1.3 Observation sampling rate . . . 73
5.1.4 Further observation characteristics . . . 73
5.1.5 Global observation coverage . . . 74
5.1.6 Station availability . . . 76
5.1.7 Overall orbital fit . . . 77
5.1.8 Conclusion DORIS . . . 79
5.2 SLR . . . 81
5.2.1 Ground station elevation cut-off angle . . . 81
5.2.2 Observation sampling rate . . . 81
5.2.3 Global observation coverage . . . 83
5.2.4 Station availability . . . 84
5.2.5 Station pass and observation yield . . . 85
5.2.6 Overall orbital fit . . . 86
5.2.7 Conclusion SLR . . . 87
5.3 GPS . . . 89
5.3.1 Elevation cut-off angle . . . 90
5.3.2 Observation sampling rate . . . 91
5.3.3 Station availability . . . 91
5.3.4 GPS satellite availability . . . 91
5.3.5 GPS satellite block configuration . . . 92
5.3.6 Code and phase residuals . . . 93
5.3.7 Receiver channel limitation . . . 95
5.3.8 Global observation coverage . . . 96
5.3.9 Conclusion GPS . . . 97

6 Technique-wise simulation analysis **99**
6.1 DORIS . . . 101
6.1.1 Reference solution . . . 101
6.1.1.1 Orbital fit . . . 102
6.1.1.2 Orbit recovery . . . 102
6.1.1.3 Reference frame . . . 103
6.1.1.4 ERP analysis . . . 106
6.1.2 DORIS space-tie satellite results . . . 106
6.1.2.1 Case free of systematic errors . . . 106
6.1.2.2 Influence of center-of-mass displacements . . . 122
6.1.2.3 Influence of atmospheric drag mismodelling . . . 130
6.1.2.4 Influence of solar radiation pressure mismodelling . . . 136
6.1.2.5 Influence of ground beacon frequency bias mismodelling . . . 142
6.1.2.6 Influence of Earth gravity field mismodelling . . . 149
6.1.3 Single-technique conclusion for DORIS . . . 166
6.2 SLR . . . 167
6.2.1 Reference solution . . . 167
6.2.1.1 Orbital fit . . . 167
6.2.1.2 Orbit recovery . . . 167
6.2.1.3 Reference frame . . . 168
6.2.1.4 ERP analysis . . . 171
6.2.2 SLR space-tie satellite results . . . 171
6.2.2.1 Case free of systematic errors . . . 172
6.2.2.2 Influence of center-of-mass displacements . . . 182
6.2.2.3 Influence of atmospheric drag mismodelling . . . 192
6.2.2.4 Influence of solar radiation pressure mismodelling . . . 198
6.2.2.5 Influence of Earth gravity field mismodelling . . . 203
6.2.3 Single-technique conclusion for SLR . . . 217
6.3 GPS . . . 218
6.3.1 Reference solution . . . 218
6.3.1.1 Orbital fit . . . 218
6.3.1.2 Orbit recovery . . . 219
6.3.1.3 Reference frame . . . 221
6.3.1.4 ERP analysis . . . 224
6.3.2 GPS space-tie satellite results . . . 224
6.3.2.1 Case free of systematic errors . . . 224
6.3.2.2 Influence of solar radiation pressure mismodelling . . . 240
6.3.2.3 Influence of Earth gravity field mismodelling . . . 248
6.3.3 Single-technique conclusion for GPS . . . 263

7 Co-location in space combination and analysis **265**
7.1 Inter-technique orbit comparison . . . 265
7.2 Inter-technique TRF comparison . . . 266
7.3 Inter-technique ERP comparison . . . 266
7.4 Inter-technique comparison of estimated Earth gravity field . . . 267
7.5 Combination with co-location in space . . . 268
7.5.1 Reference frame evaluation . . . 268
7.5.1.1 Helmert parameters . . . 268

7.5.1.2 Formal errors 271
7.5.2 ERP analysis 273
7.5.3 Earth gravity field determination in combination 274
7.6 Conclusion - Co-location in space 276

8 Conclusion and outlook **279**
8.1 Potential for reference frame determination 279
8.2 Potential for gravity field determination 282
8.3 Outlook 283

Bibliography **285**

A GPS ambiguity handling at normal equation level with EPOS **297**

B Zero mean condition for random noise sequences **299**

C Influence of EPOS-OC time granularity on DORIS simulations **301**

D Statistical evaluation of changes in formal errors **303**

E Evaluation of formal errors **305**

F Compilation of assessment statistics **307**

G Supplementary illustrations of the analysis **371**

List of Figures

2.1 Transition from the inertial to the Earth-fixed system 5
2.2 CIP corrections according to EOP20C04 data 7
2.3 Pole coordinates according to EOP20C04 data 8
2.4 Overview of different time systems 9
2.5 Orbital elements 13
2.6 Magnitudes of individual perturbation forces for GPS satellites and different space-tie orbit scenarios 15
2.7 Overview of the EPOS software structure 24
2.8 Concept of co-location in space illustrated by a space-tie satellite 34

3.1 Overview of the IAG Services and the path to the ITRF 36
3.2 Map of DORIS station network 37
3.3 Picture of a DORIS ground beacon 38
3.4 Picture of a DORIS antenna 38
3.5 Visualisation of the SAA region 43
3.6 DORIS time bias over time for TOPEX/Poseidon 43
3.7 Map of ILRS station network 44
3.8 Picture of Potsdam SLR station 46
3.9 Compilation of geodetic satellites 46
3.10 Map of IGS station network 49

4.1 Ground tracks of the investigated space-tie satellite scenarios 57
4.2 Three-dimensional representation of the E-GRASP-like orbit 58
4.3 Flowchart of the simulation procedure for DORIS and SLR 60
4.4 Example of the output of the real data parser 61
4.5 Visualisation of the macro-model used for the space-tie satellite simulation . 64
4.6 Flowchart of the simulation process with EPOS-OC 65

5.1 Active DORIS antennas by type over time 72
5.2 Sampling rate analysis of DORIS real data 74
5.3 Comparison of real and simulated DORIS observations 75
5.4 Comparison of real and simulated global DORIS observation coverage . . . 76
5.5 Three-dimensional DORIS observation geometry by receiver type 77
5.6 Analysis of accepted DORIS observations per arc and satellite 78
5.7 Orbital fit for real and simulated data of ENVISAT, Jason-1, and Jason-2 . . . 80
5.8 SLR elevation cut-off angle derived from real data for LAGEOS-1 82
5.9 Distribution of sampling rate for SLR real data 83
5.10 Geographic distribution of real and simulated SLR observations 84
5.11 Analysis of number of SLR observations per arc and satellite 85
5.12 Ratio of maximum possible to actual LAGEOS-1 passes per station 86
5.13 Ratio of maximum possible to actual LAGEOS-1 observations per station . . 87
5.14 Orbital fit over time for the real and simulated LAGEOS-1 data 88
5.15 Conceptual illustration of the integrated approach for GPS processing 89
5.16 Number of GPS stations used for GPS real data solution and simulation . . . 92

5.17 Number of simulated GPS satellites over time 92
5.18 GPS orbital fit of the real data evaluation and simulation 94
5.19 Comparison of real and simulated GPS PRNs received in parallel at Ny Ålesund station 96
5.20 Comparison of real and simulated GPS PRNs received in parallel on the Sentinel-3A satellite 96
5.21 Global coverage of GPS observations based on real data for Sentinel-3A . . 97

6.1 Simulated arcs over time for DORIS reference solution 101
6.2 Global distribution of the mean standard deviation of simulated DORIS observations for the reference solution 102
6.3 Global mean orbit differences of the simulated DORIS reference solution . . 104
6.4 DORIS station network of the simulation 105
6.5 DORIS orbital fit for simulated scenarios sys. error-free 108
6.6 Global observation coverage of simulated DORIS observations for the space-tie satellite scenarios 110
6.7 Global distribution of the mean standard deviation of simulated DORIS observations for the space-tie satellite scenarios 111
6.8 DORIS orbit comparison of the space-tie satellite sys. error-free 112
6.9 DORIS global orbit differences for the simulated space-tie satellites sys. error-free 113
6.10 DORIS Helmert parameters for the space-tie satellite sys. error-free 114
6.11 DORIS space-tie formal errors systematic error-free case in Cartesian coordinates 118
6.12 DORIS space-tie formal errors systematic error-free case in geographic coordinates 119
6.13 DORIS formal error peak improvement analysis sys. error-free 120
6.14 Global difference in DORIS observation residuals 10 mm CoM mismodelling 123
6.15 DORIS orbit comparison of the space-tie satellite scenarios CoM mismodelling 125
6.16 DORIS global orbit differences for 10 mm CoM mismodelling 126
6.17 DORIS Helmert parameters for CoM mismodelling 128
6.18 Difference in total acceleration due to atmospheric drag mismodelling 131
6.19 Global difference in DORIS observation residuals due to atmospheric drag mismodelling 133
6.20 DORIS orbit comparison of the space-tie satellite scenarios in the atmospheric drag mismodelling case 134
6.21 DORIS global orbit differences for atmospheric drag mismodelling 135
6.22 Difference in total acceleration due to SRP mismodelling 138
6.23 Global difference in DORIS observation residuals due to SRP mismodelling . 139
6.24 DORIS orbit comparison of the space-tie satellite scenarios in the SRP mismodelling case 140
6.25 DORIS global orbit differences for the SRP mismodelling case 141
6.26 Global difference in DORIS observation residuals due to frequency bias mismodelling 144
6.27 DORIS orbit comparison of the space-tie satellite scenario in the frequency bias mismodelling case 145
6.28 DORIS global orbit differences for the frequency bias mismodelling case . . 146

6.29 Percentage loss of maximum improvement for DORIS for frequency bias mismodelling . . . 148
6.30 Difference in total acceleration due to EGM mismodelling . . . 150
6.31 Global difference in DORIS observation residuals due to EGM mismodelling 151
6.32 DORIS orbit comparison of the space-tie satellite scenario in the EGM mismodelling case . . . 152
6.33 DORIS global orbit differences for EGM mismodelling . . . 153
6.34 DORIS Helmert parameters for EGM mismodelling . . . 154
6.35 Percentage loss of maximum improvement for DORIS for EGM mismodelling 155
6.36 Percentage loss of maximum improvement for DORIS for EGM mismodelling with SH co-estimated . . . 157
6.37 Analytical Earth gravity field sensitivity analysis of the space-tie satellite scenarios . . . 159
6.38 SH triangular plots for the space-tie satellite scenarios with DORIS . . . 161
6.39 SH degree amplitudes for the space-tie satellite scenarios with DORIS . . . 162
6.40 Cumulative error of estimated gravity field for the space-tie satellite scenarios with DORIS . . . 163
6.41 Global distribution of the mean standard deviation of simulated SLR observations for the reference solution . . . 168
6.42 Global mean orbit differences of the simulated SLR reference solution . . . 169
6.43 SLR station network of simulation . . . 170
6.44 ERP amplitude spectrum of the SLR reference solution . . . 171
6.45 Global observation coverage of simulated SLR observations for the space-tie satellite scenarios . . . 173
6.46 Global distribution of mean standard deviation of simulated SLR observations for the space-tie scenarios . . . 174
6.47 SLR global orbit differences for the simulated space-tie satellites sys. error-free 175
6.48 SLR Helmert parameters for the space-tie satellite sys. error-free . . . 176
6.49 SLR space-tie formal errors systematic error-free case in Cartesian coordinates 178
6.50 SLR space-tie formal errors systematic error-free case in geographic coordinates 179
6.51 SLR formal error peak improvement analysis sys. error-free . . . 180
6.52 SLR orbit comparison of the space-tie satellite scenarios with CoM mismodelling 184
6.53 Global difference in SLR observation residuals for 10 mm CoM mismodelling 185
6.54 SLR global orbit differences for 10 mm CoM mismodelling . . . 186
6.55 SLR Helmert parameters for CoM mismodelling . . . 188
6.56 Percentage loss of maximum improvement for SLR for 5 mm CoM displacement 189
6.57 Percentage loss of maximum improvement for SLR for 10 mm CoM displacement 190
6.58 Global difference in SLR observation residuals due to atmospheric drag mismodelling . . . 193
6.59 SLR orbit comparison of the space-tie satellite scenarios due to atmospheric drag mismodelling . . . 194
6.60 SLR global orbit differences for atmospheric drag mismodelling . . . 195
6.61 Percentage loss of maximum improvement for SLR for atmospheric drag mismodelling . . . 196
6.62 Global difference in SLR observation residuals due to SRP mismodelling . . . 199
6.63 SLR orbit comparison of the space-tie satellite scenarios with SRP mismodelling 200
6.64 SLR global orbit differences for SRP mismodelling . . . 201
6.65 Percentage loss of maximum improvement for SLR for SRP mismodelling . . . 202

6.66 Global difference in SLR observation residuals due to EGM mismodelling . . 205
6.67 SLR orbit comparison of the space-tie satellite scenarios for EGM mismodelling 206
6.68 SLR global orbit differences for EGM mismodelling 207
6.69 SLR Helmert parameters for EGM mismodelling 208
6.70 Percentage loss of maximum improvement for SLR for EGM mismodelling . 209
6.71 Percentage loss of maximum improvement for SLR for EGM mismodelling with SH co-estimated 210
6.72 SH triangular plots for the space-tie satellite scenarios with SLR 212
6.73 SH degree amplitudes for the space-tie satellite scenarios with SLR 213
6.74 Cumulative error of estimated gravity field for the space-tie satellite scenarios with SLR 214
6.75 Global distribution of simulated GPS code observations for all PRNs, total, median and standard deviation of code and phase 220
6.76 Global mean orbit differences for the simulated GPS constellation sys. error-free 221
6.77 Clock difference for a GPS satellite sys. error-free 221
6.78 GPS station network of the simulation 223
6.79 GPS orbit fit of phase observations for the space-tie satellite scenarios . . . 226
6.80 Number of visible and tracked PRNs per epoch for the space-tie satellite scenarios 227
6.81 Number of GPS observations over the elevation for the space-tie satellite scenarios 228
6.82 Skyplot of tracked GPS observations for space-tie satellite scenarios 229
6.83 Global observation coverage of simulated GPS observations 230
6.84 GPS orbit comparison of the space-tie satellite sys. error-free 231
6.85 GPS global orbit differences for the simulated space-tie satellites sys. error-free 232
6.86 GPS constellation clock differences with space-tie satellite systematic error-free 234
6.87 GPS Helmert parameters for the space-tie satellite sys. error-free 235
6.88 GPS formal errors systematic error-free case in Cartesian coordinates . . . 237
6.89 GPS formal errors systematic error-free case in geographic coordinates . . . 238
6.90 Difference in total acceleration of a GPS satellite due to SRP mismodelling . 240
6.91 Comparison of GPS space-tie satellite orbits in the case of GPS satellite SRP mismodelling 241
6.92 Median orbit differences of the GPS constellation in the SRP mismodelling case 243
6.93 Clock difference for a GPS satellite due to SRP mismodelling 244
6.94 GPS Helmert parameters for EGM mismodelling 245
6.95 GPS formal errors in the case of SRP mismodelling 246
6.96 ERP amplitude spectrum of the GPS constellation for the SRP mismodelling case 247
6.97 Difference in total acceleration of a GPS satellite due to EGM mismodelling . 248
6.98 Global difference in the LEO GPS phase observation residuals in the EGM mismodelling case 249
6.99 GPS orbit comparison of the space-tie satellite scenarios for the EGM mismodelling case 250
6.100 GPS space-tie satellite orbit differences in the EGM mismodelling case . . . 251
6.101 Median orbit differences of the GPS constellation in the EGM mismodelling case 252
6.102 Clock difference for a GPS satellite due to EGM mismodelling 253
6.103 GPS Helmert parameters for the EGM mismodelling case 254
6.104 GPS Helmert parameters for EGM mismodelling and SHs estimated 255

6.105 Sensitivity analysis and analysis of estimated SHs for the GPS constellation 257
6.106 SH triangular plots for the space-tie satellite scenarios with GPS 258
6.107 SH degree amplitudes for the space-tie satellite scenarios with GPS 259
6.108 Cumulative error of estimated gravity field for the space-tie satellite scenarios with GPS 260

7.1 Helmert parameters of the multi-technique combination 269
7.2 Differences in formal errors for GPS through ST combination 272
7.3 Differences in formal errors for SLR through ST combination 273
7.4 SH triangular plots of the differences for the space-tie satellite scenarios with and without ST combination 275

C.1 Influence of EPOS-OC time granularity on simulated DORIS epochs 301

D.1 Analysis of formal error distributions 303

G.1 ERP amplitude spectrum of the DORIS reference solution 371
G.2 ERP amplitude spectrum of the DORIS sys. error-free GRASP-like solution . 372
G.3 ERP amplitude spectrum of the DORIS sys. error-free E-GRASP-mod solution 372
G.4 ERP amplitude spectrum of the DORIS sys. error-free E-GRASP-like solution 373
G.5 ERP amplitude spectrum of the DORIS sys. error-free Circular 30° solution . 373
G.6 ERP amplitude spectrum of the DORIS sys. error-free Circular 60° solution . 374
G.7 ERP amplitude spectrum of the DORIS sys. error-free Circular 89° solution . 374
G.8 ERP amplitude spectrum of the DORIS GRASP-like atmospheric drag mismodelling case 375
G.9 ERP amplitude spectrum of the DORIS E-GRASP-like atmospheric drag mismodelling case 376
G.10 Differences of the percentage improvements compared to the sys. error-free case for DORIS 377
G.11 SLR space-tie orbital fit in the systematic error-free case 378
G.12 SLR space-tie satellite orbit comparison in the systematic error-free case . . 379
G.13 ERP amplitude spectrum for the SLR sys. error-free GRASP-like solution . . 379
G.14 ERP amplitude spectrum for the SLR sys. error-free E-GRASP-mod solution 380
G.15 ERP amplitude spectrum for the SLR sys. error-free E-GRASP-like solution . 380
G.16 ERP amplitude spectrum for the SLR sys. error-free Circular 30° solution . . 381
G.17 ERP amplitude spectrum for the SLR sys. error-free Circular 60° solution . . 381
G.18 ERP amplitude spectrum for the SLR sys. error-free Circular 89° solution . . 382
G.19 SLR ERP amplitude spectrum - GRASP-like scenario 10 mm CoM displacement 383
G.20 SLR ERP amplitude spectrum - E-GRASP-mod scenario 10 mm CoM displacement 384
G.21 SLR ERP amplitude spectrum - E-GRASP-like scenario 10 mm CoM displacement 384
G.22 SLR ERP amplitude spectrum - Circular 30° scenario 10 mm CoM displacement 385
G.23 SLR ERP amplitude spectrum - Circular 60° scenario 10 mm CoM displacement 385
G.24 SLR ERP amplitude spectrum - Circular 89° scenario 10 mm CoM displacement 386
G.25 SLR ERP amplitude spectrum - GRASP-like scenario atmospheric drag mismodelling 387
G.26 SLR ERP amplitude spectrum - E-GRASP-like scenario atmospheric drag mismodelling 388

G.27 GPS constellation orbit differences with space-tie satellite systematic error-free 389
G.28 GPS space-tie satellite orbit differences in the SRP mismodelling case . . . 390
G.29 GPS constellation orbit differences with space-tie satellite in the SRP mismodelling case . . . 391
G.30 GPS constellation clock differences with space-tie satellite in the SRP mismodelling case . . . 392
G.31 GPS constellation orbit differences with space-tie satellite in the EGM mismodelling case . . . 393
G.32 GPS constellation clock differences with space-tie satellite in the EGM mismodelling case . . . 394
G.33 Formal error improvements for DORIS in multi-technique combination with GTs 395
G.34 Formal error improvements for GPS in multi-technique combination with GTs and ST . . . 396
G.35 Formal error improvements for SLR in multi-technique combination with GTs and ST . . . 397
G.36 ERP amplitude spectrum of the combined multi-technique solution for the sys. error-free GRASP-like scenario . . . 398
G.37 ERP amplitude spectrum of the combined multi-technique solution for the sys. error-free E-GRASP-mod scenario . . . 398
G.38 ERP amplitude spectrum of the combined multi-technique solution for the sys. error-free E-GRASP-like scenario . . . 399
G.39 ERP amplitude spectrum of the combined multi-technique solution for the sys. error-free Circular 30° scenario . . . 399
G.40 ERP amplitude spectrum of the combined multi-technique solution for the sys. error-free Circular 60° scenario . . . 400
G.41 ERP amplitude spectrum of the combined multi-technique solution for the sys. error-free Circular 89° scenario . . . 400
G.42 SH triangular plots for the space-tie satellite scenarios in the combination with GTs . . . 401
G.43 SH triangular plots for the space-tie satellite scenarios in the combination with GTs and ST . . . 402
G.44 SH degree amplitudes for the space-tie satellite scenarios in the combination with GTs . . . 403
G.45 SH degree amplitudes for the space-tie satellite scenarios in the combination with GTs and ST . . . 404
G.46 Cumulative error of estimated gravity field for the space-tie satellite scenarios in the combination with GTs . . . 405
G.47 Cumulative error of estimated gravity field for the space-tie satellite scenarios in the combination with GTs and ST . . . 406

List of Tables

3.1 Overview of capabilities and contributions of space geodetic techniques for TRF determination . . . 36
3.2 Overview of DORIS master and time beacons . . . 37
3.3 Overview of different DORIS receivers . . . 39

4.1 Orbital elements of the simulation scenarios for the satellites at launch . . . 55
4.2 Orbital periods of the investigated space-tie satellite scenarios . . . 56
4.3 Overview of the models used in the POD . . . 63
4.4 Parameterisation of the case without systematic errors . . . 66
4.5 Performed simulation mismodelling cases . . . 67
4.6 Frequency bias values used for DORIS simulations . . . 69

5.1 Satellites used for DORIS real data evaluation . . . 72
5.2 Post-fit residuals and number of observations for DORIS real data evaluation 79
5.3 Analysed geodetic satellites and their orbital elements . . . 81
5.4 SLR normal point bin size and real data observation sampling rate . . . 83
5.5 SLR orbital fit statistics for real and simulated data . . . 87
5.6 Orbital elements of evaluated LEO satellite missions for GPS . . . 90
5.7 GPS satellite PCO values of the simulation . . . 93
5.8 Characteristics of the GPS satellite box-wing model of the simulation . . . 93
5.9 GPS ground station scaling factors of the simulation . . . 95

6.1 Parameterisation for the DORIS real data evaluation . . . 102
6.2 DORIS mean orbit differences of the simulated reference solution . . . 103
6.3 DORIS datum stations . . . 105
6.4 DORIS Helmert parameters of the reference solution . . . 106
6.5 DORIS parameterisation in the systematic error-free case . . . 107
6.6 DORIS post fit statistics for the space-tie satellite scenarios . . . 109
6.7 Summary of DORIS space-tie satellite potential in the sys. error-free case . 122
6.8 Estimated CoM coordinates with DORIS . . . 127
6.9 Summary DORIS space-tie satellite vulnerability to CoM mismodelling . . . 130
6.10 Dynamic parameterisation used for DORIS in the atmospheric drag mismodelling case . . . 132
6.11 Summary DORIS space-tie satellite vulnerability to atmospheric drag mismodelling . . . 136
6.12 Modified space-tie satellite macro-model for SRP mismodelling . . . 137
6.13 Dynamic parameterisation used for DORIS in the SRP mismodelling case . . 137
6.14 Summary DORIS space-tie satellite vulnerability to SRP mismodelling . . . 142
6.15 Dynamic parameterisation used for DORIS in the frequency bias mismodelling case . . . 143
6.16 Summary DORIS space-tie satellite vulnerability to frequency bias mismodelling 148
6.17 Dynamic parameterisation used for DORIS in the EGM mismodelling case . 149
6.18 Summary DORIS space-tie satellite vulnerability to EGM mismodelling . . . 165
6.19 Summary DORIS space-tie satellite potential for gravity field estimation . . . 165

6.20 Summary of maximum space-tie satellite potential and vulnerability for DORIS 166
6.21 SLR mean orbit differences of the simulated reference solution 168
6.22 SLR datum stations 169
6.23 SLR Helmert parameters of the reference solution 170
6.24 SLR parameterisation in the systematic error-free case 172
6.25 SLR post fit statistics for the space-tie satellite scenarios 173
6.26 Summary of SLR space-tie satellite potential in the sys. error-free case . . . 182
6.27 Estimated CoM coordinates with SLR 187
6.28 Summary SLR space-tie satellite vulnerability to CoM mismodelling 192
6.29 Dynamic parameterisation used for SLR in the atmospheric drag mismodelling case 192
6.30 Summary SLR space-tie satellite vulnerability to atmospheric drag mismodelling 197
6.31 Dynamic parameterisation used for SLR in the SRP mismodelling case . . . 198
6.32 Summary SLR space-tie satellite vulnerability to SRP mismodelling 203
6.33 Dynamic parameterisation used for SLR in the EGM mismodelling case . . . 203
6.34 Summary SLR space-tie satellite vulnerability to EGM mismodelling 216
6.35 Summary SLR space-tie satellite potential for gravity field estimation 216
6.36 Summary of maximum space-tie satellite potential and vulnerability for SLR . 217
6.37 GPS constellation parameterisation in the systematic error-free case 219
6.38 Statistics of the recovered orbit and clocks in the systematic error-free case for the GPS constellation 220
6.39 GPS datum stations 222
6.40 GPS Helmert parameters of the reference solution 223
6.41 GPS parameterisation in the systematic error-free case 225
6.42 GPS orbit fit statistics for the space-tie satellite scenarios 225
6.43 Statistics of the recovered orbit and clocks of the GPS constellation systematic error-free 233
6.44 Summary of GPS space-tie satellite potential in the sys. error-free case . . . 240
6.45 Statistics of recovered orbit and clocks of the GPS constellation in the SRP mismodelling case 242
6.46 Summary GPS space-tie satellite vulnerability to SRP mismodelling 248
6.47 Statistics of recovered orbit and clocks of the GPS constellation in the EGM mismodelling case 252
6.48 Summary GPS space-tie satellite potential for gravity field estimation 262
6.49 Summary GPS space-tie satellite vulnerability to EGM mismodelling 262
6.50 Summary of maximum space-tie satellite potential and vulnerability for GPS 263

7.1 RMS of LTs in the combination with GTs and ST 270
7.2 Summary potential of the co-location in space 277
7.3 Summary potential for gravity field estimation in the multi-technique combination 278

8.1 Multi-technique summary of space-tie satellite potential 281
8.2 Summary of overall potential for gravity field determination for the space-tie satellite scenarios 282

F.1 DORIS Helmert parameters systematic error-free case 308
F.2 DORIS formal errors systematic error-free case 309
F.3 DORIS ERP statistics error-free case 310
F.4 DORIS Helmert parameters 5 mm CoM displacement case 311

F.5 DORIS Helmert parameters 10 mm CoM displacement case 312
F.6 DORIS formal errors 5 mm CoM displacement case, coordinates fixed 313
F.7 DORIS formal errors 10 mm CoM displacement case, coordinates fixed . . . 314
F.8 DORIS formal errors 5 mm CoM displacement case, coordinates estimated . 315
F.9 DORIS formal errors 10 mm CoM displacement case, coordinates estimated 316
F.10 DORIS ERP statistics CoM displacement case 317
F.11 DORIS Helmert parameters atmospheric drag mismodelling case 318
F.12 DORIS formal errors atmospheric drag mismodelling case 319
F.13 DORIS ERP statistics atmospheric drag mismodelling case 320
F.14 DORIS Helmert parameters SRP mismodelling case 321
F.15 DORIS formal errors SRP mismodelling case 322
F.16 DORIS ERP statistics SRP mismodelling case 323
F.17 DORIS Helmert parameters frequency bias mismodelling case 324
F.18 DORIS formal errors frequency bias mismodelling case 325
F.19 DORIS ERP statistics frequency bias mismodelling case 326
F.20 DORIS Helmert parameters EGM mismodelling case 327
F.21 DORIS formal errors EGM mismodelling case 328
F.22 DORIS formal errors EGM mismodelling case, SHs estimated 329
F.23 DORIS ERP statistics EGM mismodelling case 330
F.24 SLR Helmert parameters systematic error-free case 331
F.25 SLR formal errors systematic error-free case 332
F.26 SLR ERP statistics error-free case 333
F.27 SLR Helmert parameters 5 mm CoM displacement case 334
F.28 SLR Helmert parameters 10 mm CoM displacement case 335
F.29 SLR formal errors 5 mm CoM displacement, coordinates fixed 336
F.30 SLR formal errors 10 mm CoM displacement, coordinates fixed 337
F.31 SLR formal errors 5 mm CoM displacement, coordinates estimated 338
F.32 SLR formal errors 10 mm CoM displacement, coordinates estimated 339
F.33 SLR ERP statistics CoM displacement case 340
F.34 SLR Helmert parameters atmospheric drag mismodelling case 341
F.35 SLR formal errors atmospheric drag mismodelling case 342
F.36 SLR ERP statistics atmospheric drag mismodelling case 343
F.37 SLR Helmert parameters SRP mismodelling case 344
F.38 SLR formal errors SRP mismodelling case 345
F.39 SLR ERP statistics SRP mismodelling case 346
F.40 SLR Helmert parameters EGM mismodelling case 347
F.41 SLR formal errors EGM mismodelling case 348
F.42 SLR formal errors EGM mismodelling case, SHs estimated 349
F.43 SLR ERP statistics EGM mismodelling case 350
F.44 GPS Helmert parameters systematic error-free case 351
F.45 GPS formal errors systematic error-free case 352
F.46 GPS ERP statistics error-free case 353
F.47 GPS Helmert parameters SRP mismodelling case 354
F.48 GPS formal errors SRP mismodelling case 355
F.49 GPS ERP statistics SRP mismodelling case 356
F.50 GPS Helmert parameters EGM mismodelling case 357
F.51 GPS formal errors EGM mismodelling case 358
F.52 GPS formal errors EGM mismodelling case, SHs estimated 359

F.53 GPS ERP statistics EGM mismodelling case 360
F.54 Helmert parameters for DORIS in the multi-technique combination 361
F.55 Helmert parameters for GPS in the multi-technique combination 362
F.56 Helmert parameters for SLR in the multi-technique combination 363
F.57 DORIS formal errors in the systematic error-free combination without ST . . 364
F.58 DORIS formal errors in the systematic error-free combination with ST 365
F.59 GPS formal errors in the systematic error-free combination without ST 366
F.60 GPS formal errors in the systematic error-free combination with ST 367
F.61 SLR formal errors in the systematic error-free combination without ST 368
F.62 SLR formal errors in the systematic error-free combination with ST 369
F.63 Multi-technique ERP statistics error-free case 370

1 Introduction and objectives

In the context of global warming and its consequences, society is increasingly confronted with geodynamic processes, such as sea-level rise and natural hazards. Other phenomena, including extreme weather, changes in ocean circulation and ice mass loss, further demonstrate that the Earth is continuously subject to highly dynamic processes. Since these interactions directly affect our living environment, there is a strong interest in observing and monitoring them, understanding their causes and consequences, as well as controlling their impact. In this context, geodesy provides the basis for these tasks by dealing with the measurement of the geometry of the Earth, the orientation of its rotation axis in space and its gravity field, commonly referred to as the three pillars of geodesy. Today, high-precision measurement data from satellites orbiting the Earth provide an essential contribution, as they enable homogeneous global observations within a very short time. This importance was further emphasised by the United Nations in 2015 with the adoption of UN Resolution A/RES/69/266, entitled 'A global geodetic reference frame for sustainable development', which endorses the relevance of reliable geospatial information for the goals of sustainable development. For a uniform reference of spatial measurement data, global geodetic reference frames are fundamental products that are indispensable for all positioning tasks. As part of the Global Geodetic Observing System (GGOS) (Gross et al., 2009), initiated in 2003 by the International Association of Geodesy (IAG) as its observing system, the accuracy requirements for an International Terrestrial Reference Frame (ITRF) are set at 1 mm in position and 1 mm per decade in long-term stability, which have not yet been achieved.

To determine a Terrestrial Reference Frame (TRF), the four main space geodetic techniques Doppler Orbitography and Radiopositioning Integrated by Satellite (DORIS), Global Navigation Satellite Systems (GNSS), Satellite Laser Ranging (SLR) and Very Long Baseline Interferometry (VLBI) are used in combination. DORIS and SLR rely on active stations on the Earth's surface. In the case of DORIS, ground beacons transmit signals that are received by satellites, whereas SLR stations emit laser pulses that are reflected by retroreflectors on satellites. In the case of GNSS, signals are emitted by the GNSS satellites and received by passive (no bidirectional communication) receivers on the ground or on Low Earth Orbit (LEO) satellites. So far, only observations from ground stations are typically used to determine precise orbits and clocks of the GNSS satellites. With VLBI, active galactic nuclei, such as quasars, are observed, enabling the unique determination of the Earth's orientation in inertial space. The link between the techniques is achieved by using so-called Local Ties (LTs) and Global Ties (GTs). LTs can be eccentricities between the ground stations of different techniques at co-location sites, precisely measured by local surveying. Co-location sites are sites where at least two of the techniques are located in close proximity. GTs are global parameters that can be determined by more than one technique, such as the Earth Orientation Parameters (EOPs). The current realisation of the ITRF, the ITRF2020 (Altamimi et al., 2023), attains an accuracy of 5 mm with a long-term stability of 0.5 mm per year in the origin of the frame. Accordingly, an improvement by a factor of five is necessary to achieve the GGOS goals. The full potential of the techniques can only be achieved if systematic errors in the techniques, which prevent an optimal combination of the space segment of the techniques, are unveiled and resolved.

A concept to achieve this is the co-location of the techniques in space, known as Space Ties (STs). Here, one or more satellites are placed in orbit around the Earth with at least two of the techniques on board. Thereby, the link between the techniques should be strengthened, systematic measurement errors revealed, and their influence reduced. Previously proposed co-location-in-space missions, such as the Geodetic Reference Antenna in Space (GRASP) (National Aeronautics and Space Administration (NASA)/USA) (Bar-Sever et al., 2009) or the European mission E-GRASP/Eratosthenes (E-GRASP) (European Space Agency (ESA)) (Biancale et al., 2017), envisaged such scenarios and indicated their potential to contribute to the GGOS accuracy requirements. So far, none of these missions has been realised. One of the reasons for this was the unclear optimal mission orbit, as well as the doubts and uncertainties regarding a satellite-based VLBI transmitter, as VLBI observations of transmitters on satellites are a novelty. On 23 November 2022, the Genesis mission (Delva et al., 2023), carrying all four techniques on board, was approved and funded by ESA. The plan is to launch this mission in 2028, although the final orbit characteristics and shape of the satellite have not yet been decided.

In fact, various applications based on the co-location-in-space concept have already been studied. Zhu et al. (2004) investigated the integrated adjustment of LEO satellites carrying a Global Positioning System (GPS) receiver together with the GPS satellites and the GPS ground network. It has been shown that LEO satellites provide additional information, especially on the geocentre, which is beneficial to the global network adjustment.

Männel (2016) confirmed this and achieved a 20% improvement in geocentre formal errors by integrating one LEO satellite into a GNSS constellation. This improvement was eight times larger than the improvement expected from the increase in the Degree of Freedom (DoF) alone. Furthermore, Männel explored the potential for using VLBI to observe GNSS satellites, successfully achieving an accuracy of approximately 1 cm in estimated station coordinates. In the context of GNSS co-location with VLBI and also SLR, Herrera Pinzón (2023) investigated strategies to identify and reduce systematic errors and inaccuracies in inter-technique LT distances. By analysing short baselines, technique-specific biases could be identified and minimised using innovative methods. Notably, a double-difference SLR method was introduced, which avoids the need to estimate SLR range biases. Furthermore, a combination of clock parameters was performed between two VLBI telescopes, thereby achieving millimetre-level agreement with the measured LT distances. Moreover, a rigorous combination of GNSS and VLBI at the observation level was performed, using LTs in the form of inter-technique distances and troposphere parameters. As a result, significant improvements were achieved in the station coordinates, particularly the height components, and all EOPs.

Since some of the GNSS satellites have meanwhile been equipped with SLR retro-reflectors, SLR and GNSS can be co-located in space using GNSS satellites. Thaller et al. (2011) investigated this option and carried out a co-location of the two techniques using GPS and the Global'naya Navigatsionnaya Sputnikovaya Sistema (GLONASS) satellites as a ST. It was found that the scale could be transferred from SLR to GNSS, despite the estimation of the GNSS transmitter antennas' eccentricities (Phase Center Offsets (PCOs)), which are correlated with the scale and the estimated clock offsets. Solar Radiation Pressure (SRP) modelling for GNSS satellites weakened the determination of the geocentre, and it is recommended that geodetic satellites, such as LAser GEOdynamics Satellite (LAGEOS), be included in the analysis. Bruni et al. (2017) extended this approach by including geodetic satellites such as LAGEOS, but could not verify advantages for the scale and origin transfer

through the ST. Moreover, an optimistic simulation of SLR observations to GNSS satellites was conducted, assuming a perfectly homogeneous SLR station network and optimal observation tracking for every pass. These results further emphasised this finding, revealing that the GNSS and SLR station networks coexist with their own independent frame realisation. Bury et al. (2021) conducted a similar study, investigating the optimal approach to combine SLR and GNSS, using GNSS satellites as the ST. The most favourable results were attained when both No-Net-Rotation (NNR) and No-Net-Translation (NNT) conditions were applied to the SLR and GNSS networks. However, the rotation and translation datum could not be reliably transferred from GNSS to SLR in this study either. Nevertheless, an improvement in the determined Length Of Day (LOD) was identified, and eccentricities for ground co-location sites derived from the solution were consistent with LTs at the millimetre level. Some LEO satellites, such as Sentinel-3 and -6, are also equipped with multiple observation techniques and already provide co-location in space of DORIS, GNSS and SLR, which can be used as a ST. Haines et al. (2024) made use of these and performed a first combination of SLR and GPS with STs at the observation level. The GPS and LEO satellites were used as the STs, while VLBI observations of extragalactic radio sources were used to establish the link to the celestial frame. The derived TRF demonstrated comparable accuracy to the current ITRF realisation (ITRF2020), despite the considerably shorter processing period, and thus highlighted the potential of co-location on satellites.

The German Research Foundation — German: Deutsche Forschungsgemeinschaft (DFG) project GGOS-SIM (Schuh et al., 2015), realised by GFZ Helmholtz Centre for Geosciences (GFZ) in cooperation with the Technische Universität Berlin (TUB), performed simulations of the techniques GPS, SLR, and VLBI to investigate, inter alia, the influence of improvements in the station network (e.g. adding new stations) and differences in combination using LTs and GTs. Investigations on the influence of different observation accuracies on the TRF and the EOPs for VLBI were performed by Glaser et al. (2016). Thereafter, the transfer of the geodetic datum was examined using LTs and GTs (Glaser et al., 2017). It was demonstrated that the rotation around the Z-axis could not be adequately transferred from VLBI to SLR with these ties. Subsequently, Glaser et al. (2018) investigated the influence of the weight of LTs in a combination of GPS, SLR and VLBI, and how systematic errors in the LTs affect the derived TRF. For SLR, Glaser et al. (2019) demonstrated the refinement of single- and multi-technique TRF due to the addition of future SLR stations.

The DFG project GGOS-SIM-2 is a follow-up to this project (again realised by GFZ in cooperation with the TUB) and is dedicated to the topic of co-location in space and investigating possibilities to achieve the mentioned GGOS goals by simulation. This thesis focuses on the simulation results for the techniques DORIS, GNSS, and SLR. The VLBI part of the project in combination with the SLR part elaborated in this thesis was the topic of the PhD thesis by Mammadaliyev (2024).

The objective of this thesis is to provide answers to the following research questions:

Q1 To what extent can a possible space-tie satellite contribute to TRF solutions — technique-specific and in combination?

Q2 To what extent does mismodelling of the space-tie satellite affect the single-technique TRF determination?

Q3 Which orbit scenarios are most beneficial for contributing to the GGOS goals?

Q4 To what extent can a possible space-tie mission contribute to gravity field recovery, and what is the effect of the spacetie?

This thesis begins with an introduction to relevant theoretical aspects in Chap. 2 and information about the observation techniques used in Chap. 3. Thereafter, six different space-tie satellite orbit scenarios are investigated. The adopted orbit scenarios comprise the GRASP and E-GRASP missions, a modified version of the E-GRASP scenario with lower numerical eccentricity, and three circular scenarios at an altitude of 7'000 km with three different inclinations of 30, 60, and 89 degrees. To achieve highly realistic simulations, a simulation environment has been developed that is trained using real data. The methodology of this simulation environment is described in Chap. 4. Subsequently, real data from a wide variety of satellite missions with the observation techniques DORIS, GPS, and SLR were evaluated and analysed, ranging from LAGEOS for SLR and TOPography EXperiment/Poseidon (TOPEX) for DORIS to recent missions such as Sentinel-6A Michael Freilich. As part of the training for the simulation environment, existing satellites currently used by the techniques to determine the TRF were also simulated and form the technique-wise reference solutions, which are to be improved. The results thereof are presented in Chap. 5. In the following, scenarios of observations to the space-tiesatellite were simulated over a period of seven years for the three techniques, and the potential to improve the single-technique TRF has been analysed. At this point, cases of systematic mismodelling have also been examined to assess the extent to which the TRF is affected, and to identify the orbit scenario posing the least risk to achieving the mission objective. This step also involved estimating the Earth gravity field for each technique individually, to take the third pillar of geodesy into account. These results are presented for each technique in Chap. 6. Subsequently, the scenariosthat are free from systematic error influences are combined using the ST, and the potential for TRF improvement is assessed. The details on this are provided in Chap. 7. The results obtained are summarised in Chap. 8 and the outlined research questions are answered. The results will help identify the best trade-off for a satellite that co-locates all four techniques in space and supports progress towards GGOS-compliant TRFs and Earth rotation parameters.

2 Theory

In this chapter, relevant theoretical aspects are introduced that are used in the subsequent analyses. Starting with theoretical aspects of Earth orientation (Sec. 2.1), time systems (Sec. 2.2) and coordinate systems (Sec. 2.3), the method of dynamic orbit determination is introduced in Sec. 2.4. Sec. 2.5 provides insight into the functionality of the Earth Parameter and Orbit System (EPOS) software, which is used in this work. Sec. 2.6 then describes in detail how orbit determination is carried out using the Earth Parameter and Orbit System - Orbit Computation (EPOS-OC) module. Finally, Sec. 2.7 demonstrates relevant normal equation operations used for the processing and determination of reference frame solutions, and introduces the method used for combining the techniques with a ST.

Spacegeodetic observations as used in the following are carried out by DORIS, GNSS and SLR. VLBI is not used in this work. Positions of sites located on the Earth's surface are conveniently described by coordinates in an Earth-fixed system rotating with the Earth. The satellite being observed is in orbit around the Earth, and its dynamic motion is best described in an inertial system in which no apparent forces have to be introduced. To transform between the Earth-fixed system and the inertial system in order to analyse observations from the ground to the satellite, rotations involving the EOPs need to be taken into account. According to Seitz & Schuh (2010), the transition from an inertial to an Earth-fixed reference system can be described by precession (P), nutation (N), sidereal rotation (G) and polar motion (M) as described in Fig. 2.1 and discussed in detail in Secs. 2.1, 2.2 and 2.3 below.

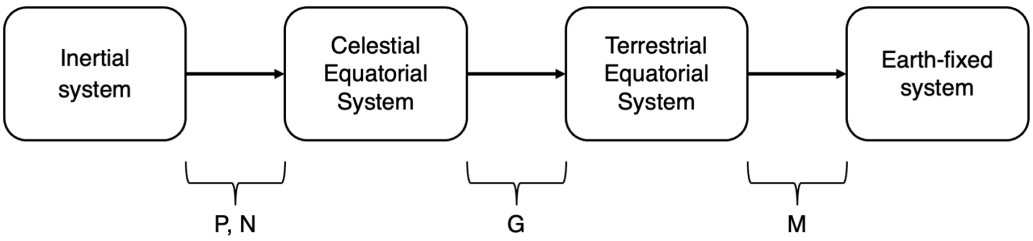

Figure 2.1: Transition from the inertial to the Earth-fixed system.

The orbit of a satellite is subject to several perturbations. The theoretical background of orbit determination and perturbation modelling is described in Sec. 2.4. Information on the EPOS software used in this thesis is given in Sec. 2.5. Sec. 2.6 provides a more detailed description of parameter estimation with the module EPOS-OC. After the orbit determination process, normal equations are set up, accumulated, combined and solved. These steps are described in detail in Sec. 2.7, where the relation to the combination of space geodetic techniques and the concept of co-location in space is described.

2.1 Earth orientation

The term EOPs is used to describe the orientation and the variation of an Earth-fixed reference system with respect to an inertial system. The rotations from an Earth-fixed reference system to an inertial system can be described by the following rotations:

$$R_{EOP}(t) = \underbrace{P_{(t)}}_{Precession} \quad \underbrace{N_{(t)}}_{Nutation} \quad \underbrace{G_{(t)}}_{GAST} \quad \underbrace{M_{(t)}}_{Polarmotion} \tag{2.1}$$

P, N, G and M are rotation matrices containing the EOPs, G and M the Earth Rotation Parameters (ERPs). These are as an approximation described with models in conventions for reference frame realisations, such as the International Earth Rotation and Reference Systems Service (IERS) conventions (Petit & Luzum, 2010). These models for precession, nutation, GAST and polar motion only describe the long-term components that can be well modelled. Absolute values and deviations from the model are published by the IERS as EOPs on a continuous basis. The ERPs are an essential part of the analyses presented in Chap. 5, 6 and 7.

2.1.1 Precession and nutation

An International Celestial Reference System (ICRS), according to the International Astronomical Union (IAU) conventions, is nowadays defined in such a way that the X-axis of a three-dimensional Cartesian coordinate system points to a reference direction close to the true equinox at epoch J2000.0 = 0 based on observations to extragalactical radio sources. The Y-axis is situated orthogonal in the equatorial plane, while the Z-axis completes the right-hand rectangular coordinate system. The position and gravitational force of the Sun and Moon in relation to the plane of the Earth's equator result in a constant motion of the Earth's axis of rotation.

As a consequence, this force gives rise to the precession of the Earth's axis around the ecliptic pole, which has an angle of approximately 23.5 degrees. Therefore, the vernal equinox moves clockwise along the ecliptic with a period of approximately 25'800 years, which defines a Platonic year.

Nutation can be defined as an oscillation superimposed on precession, with significantly shorter periods (Mathews et al., 2002). The most significant component of nutation can be attributed to the inclination of the moon's orbital plane. This is at an inclination of 5 degrees to the ecliptic, with the node of the orbital plane exhibiting a period of 18.6 years as it drifts along the ecliptic. This results in a torque being exerted on the Earth with the same period, the strength of which is dependent on the position of the moon's orbital node in relation to the vernal equinox. In comparison to precession, nutation has a significantly smaller opening angle of approximately 10 arc seconds (Seitz & Müller, 2016).

A rotation around the combined effect of precession and nutation allows the transition from the inertial system to the celestial equatorial system, where the pole is defined as the Celestial Intermediate Pole (CIP) (McCarthy & Petit, 2004) and the X-axis points towards the true equinox. Using accurate ephemerides, precession and nutation can be calculated according to a model such as that given in Petit & Luzum (2010). The IERS publishes the deviations from this calculated pole as celestial pole offsets in the X and Y components, ΔX-CIP and ΔY-CIP, as its motion cannot be accurately enough be described by models (see Fig. 2.2). These offsets are determined from VLBI observations to extragalactic radio sources.

2.1.2 Earth rotation angle

For the transition from the celestial to the terrestrial equatorial system, it is necessary to rotate around the CIP. This establishes the relationship between the true equinox and the zero meridian. This is expressed by GAST, which is then linked to the difference between

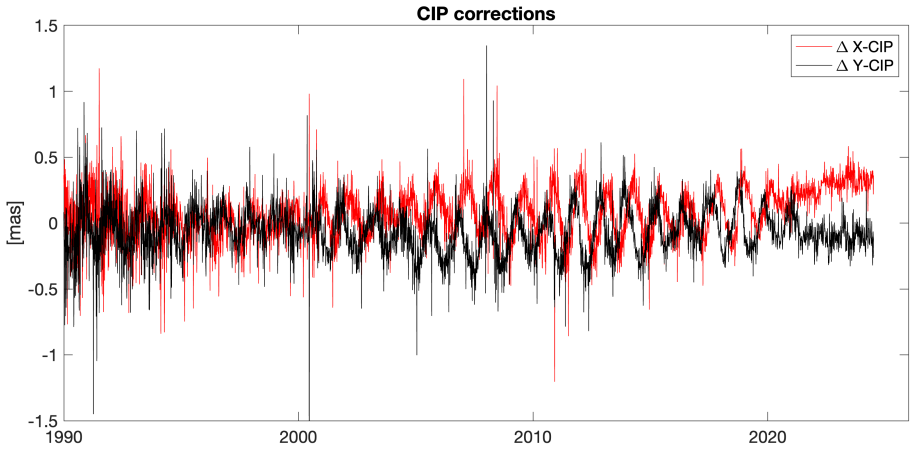

Figure 2.2: Time line of the corrections to CIP according to EOP20C04 data.

the astronomical time Universal Time (UT), which is determined by recurring astronomical events, and Coordinated Universal Time (UTC), which is defined by atomic time.

The discrepancy between the mean solar day and the mean sidereal day can be expressed as $\Delta UT = UT1 - UTC$, which illustrates the relationship between the atomic time measure and the orientation of the Earth in the inertial frame. These values are published by the IERS as part of the EOPs. The central observation technique used to determine UT1 is VLBI, as it is the only technique that observes space-fixed targets (Schmid, 2009). Furthermore, it can be expressed as the variation of LOD, with the relation: $LOD - 86400s = \Delta LOD = -\frac{d}{dt}\Delta UT \cdot 86400s$ (Moritz & Mueller, 1988). Further detailed information on time systems can be found in Sec. 2.2. The absolute rotation angle of the Earth can only be determined with VLBI. Variations in LOD are also accessible from satellite observations.

2.1.3 Polar motion

In the Earth-fixed system, the Z-axis of the ITRF is defined as the Conventional Terrestrial Pole (CTP). For the transition from the terrestrial equatorial system to the Earth-fixed system two rotations around the X- and Y-axis are necessary (Seitz & Müller, 2016). These two rotations are the Earth pole coordinates, which describe the difference from the instantaneous rotation axis of the Earth's crust to the CTP (Mueller, 1989). For the latest EOP20C04 dataset, they are shown in Fig. 2.3.

2.2 Time systems

In satellite geodesy, the analysis of observations from space geodetic techniques and the calculation of parameters such as satellite orbits and the orientation of the Earth involves different time systems. The subject of time systems is inherently complex, and therefore only those time systems that are necessary for the applications in this thesis will be discussed in more detail here. These are illustrated in Fig. 2.4 and can be classified, according to, for example, Seeber (2003), into three categories of time measurement: UT, atomic time, and inertial time. Further information on time systems can be found in, for example, Seidelmann (1992). Each of these time scales is based on the measurement of astronomical

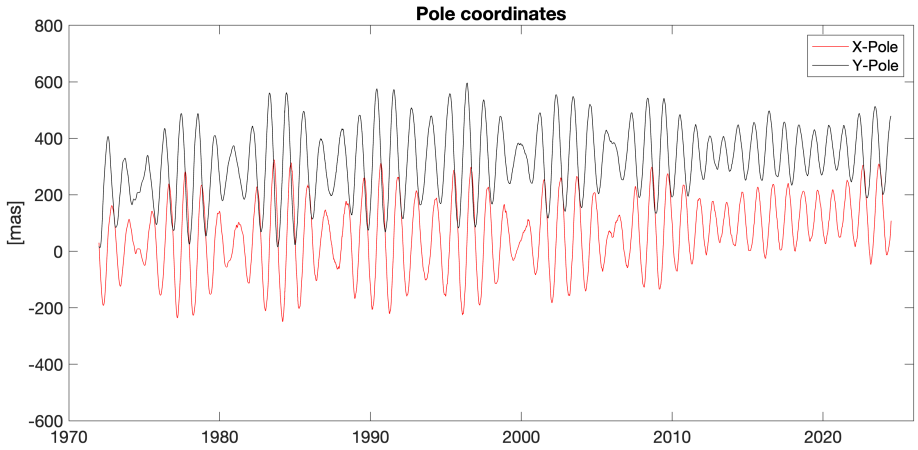

Figure 2.3: Time line of the pole coordinates according to EOP20C04 data.

or physical events:

UT is the time system, which is based on astronomical events, specifically the Earth rotation and the mean solar day at the Greenwich meridian. It provides a reference from the Earth-fixed reference system, in which, for example, ground stations are located and the rotation of the Earth in inertial space. It depends on the rotational speed of the Earth, contains its irregularities and therefore varies over time.

Atomic times, such as the International Atomic Time — French: Temps Atomique International (TAI), which uses the Système international d'unités (SI) second, are used as a highly precise uniform time system. This is essential for space geodetic measurements, including time of flight measurements in terms of SLR and time tagging of observation epochs.

Inertial time systems are uniform time systems that are free of effects of general relativity, and are used to describe the motion of satellites or planets in inertial space. It is our understanding that inertial time systems are, at least in theory, free from relativistic effects in relation to the reference system in which they are defined. This time system can then be used in the equation of motion.

2.2.1 Universal time

The UT time system is a time system based on astronomical events and used in conjunction with the Earth's rotation. In order to define this time system and relate it to the Earth's rotation, it is first necessary to introduce the concept of sidereal time systems. The term 'sidereal time' is defined in relation to the meridian and its position in relation to the vernal equinox. This is defined in a uniform manner with respect to the Greenwich meridian, referred to as the Greenwich Apparent Sidereal Time (GAST). For any given longitude, the East longitude angle can be extended to yield the Local Apparent Sidereal Time (LAST).

This orientation of the Earth in the inertial frame can be determined from astronomical observations. As a consequence of the Earth's polar motion and the associated temporal variation in the position of the equator relative to the ecliptic, this time measurement is subject to periodic variations.

Once the effect of nutation has been accounted for, a mean vernal equinox can be defined that is subject only to the effects of precession. In the context of the Greenwich

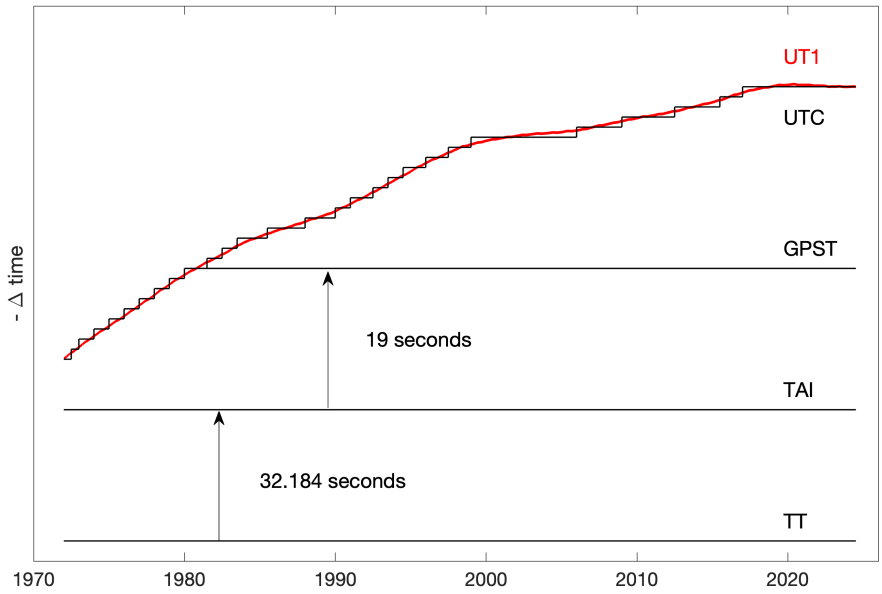

Figure 2.4: Overview of the different time systems and their differences to each other. UT1 data according to EOP20C04 data.

meridian, this is referred to as Greenwich Mean Sidereal Time (GMST). The mean sidereal day is thus defined as the interval between two consecutive passages of the upper meridian. As a consequence of the residual effect of precession, the mean sidereal day exhibits a deviation of approximately 0.0084 seconds from a full rotation of the Earth.

If the aforementioned time measurement is not based on the mean vernal equinox, but rather on a calculated mean position of the Sun, the mean solar day can be defined. The hour angle of the Greenwich meridian with respect to the mean position of the Sun is referred to as UT. As a consequence of the Earth's movement around the Sun, the mean solar day defined in this way differs from a mean sidereal day by 3 minutes and 55.909 seconds. After correction for the effects of polar motion and with respect to the CTP, the time system UT1 can be defined, which is linearly proportional to the Earth's rotation angle in accordance with McCarthy & Petit (2004).

2.2.2 Atomic time

Atomic time is founded upon the observation of periodic physical phenomena, thereby providing a consistent and uniform measure of time. It's unit is the SI second, set forth in the BIPM standards (BIPM, 1960; BIPM, 1967; BIPM, 2018). It was selected to align as closely as possible to the preceding ephemeris second, which was defined on the basis of the mean rotation of the Earth between 1900 and 1905. Given the inherent variability in the performance of individual atomic clocks, it is essential to develop a unified solution based on a set of high-precision atomic clocks distributed globally to establish TAI. It is anticipated that this combined solution will exhibit superior accuracy and minimal residual error. On 1 January 1958, TAI corresponded to the epoch of UT1.

2.2.2.1 UTC

The two time systems, TAI and UT1, show increasing discrepancies over time due to secular variations in UT1. In certain applications, a uniform time system closely aligned to UT1 is required. To address this need, the time system UTC was defined as a kind of approximative step function to UT1. The steps are referred to as leap seconds and, if necessary, are introduced at the beginning or middle of the year. This allows the discrepancy between UTC and UT1 to be maintained below 0.9 seconds. Consequently, there is a constant offset between UTC and TAI, which has been 37 seconds since 1 January 2017.

2.2.2.2 GPS time

The GPS Time (GPST) is a time system defined by the GPS control segment. It is derived from a set of ground station clocks and GPS onboard clocks. At the 00:00 UTC epoch on 6 January 1980, GPS time was identical to UTC. The GPS time differs from TAI by a constant offset of 19 seconds. Furthermore, due to the use of different atomic clocks in formulating the time system, there may be slight differences in the time systems that are kept below the microsecond level.

2.2.3 Inertial time

Inertial time systems have their historical origins in the theory of the dynamics of planetary bodies and are, in principle, the closest approximation to an absolutely uniform time system over long time periods.

Ephemeris Time (ET) was an inertial time system based on the tropical year 1900, which at that time coincided with UT1. Due to discrepancies between ET and the Earth rotation and the atomic time, it diverged from TAI over time.

The concepts of special and general relativity were first articulated by Einstein (1905) and Einstein (1916). It posits that a clock in a gravitational field (general relativity) and due to relative movement (special relativity) undergoes time dilation. To define a time system based on atomic time which also indirectly incorporates relativistic influences, the dynamic time system Barycentric Dynamical Time (TDB) and Terrestrial Dynamical Time (TDT) were introduced at 00:00:00 TAI on 1 January 1977 (Müller, 1977) and the SI second defined as the time measure. TDT was equated with ET at this epoch, resulting in an offset of 32,184 seconds compared to TAI. Relativistic effect were not explicitly stated, they were incorporated through the definition of the SI second.

As the precision of atomic clocks advanced, phenomena of general relativity became increasingly significant, reaching a point where they were comparable to the definition of the atomic second. Accordingly, the 1991 IAU Resolution explicitly incorporated the full influence of general relativity into the definition of the space-time reference frame. Barycentric Coordinate Time (TCB) and Geocentric Coordinate Time (TCG) were defined, incorporating full effect of general relativity. The term ‘dynamic’ was removed from the designation TDT, and the definition of Terrestrial Time (TT) was precised as being a scaled version of TCG. Therefore TCG differs from TT by a relativistic scaling factor (Thomas et al., 1994), after which TCG differs from TT by 21.98 milliseconds over 365 days Seeber (2003).

EPOS-OC uses TT for the calculation of near-Earth satellite orbits, which are subject to the same relativistic effects as the Earth around the Sun.

2.3 Coordinate systems

As previously stated at the outset of Sec. 2.1, two reference systems are of paramount importance for the applications addressed in this thesis: an inertial and a terrestrial one. In the inertial reference system, the equation of motion of the satellites is expressed, given that Newton's axioms are applicable and no apparent forces are present. In the terrestrial reference system, the specifications include station coordinates, observations and models such as the gravitational field. In EPOS-OC, the mean equatorial reference system is used as the inertial reference system and the CTS as the terrestrial reference system.

2.3.1 Conventional Inertial Reference System

The Conventional Inertial System (CIS) is a quasi-intertial space-fixed geocentric frame. The origin is situated at the centre of mass of the Earth, and it is characterised as a three-dimensional Cartesian coordinate system. The Z-axis coincides with the mean equatorial frame, which is defined by the mean celestial pole. The X-axis coincides with the mean vernal equinox at the origin epoch, which is epoch 0 in the J2000.0, starting at 0:00 on 1 January 2000. The inertial frame employed in EPOS-OC is the mean equatorial reference system at epoch J2000.0 = 0, which is a well adapted Earth centred quasi-inertial reference system in the sense of general relativity (Reigber, 1989).

2.3.2 Conventional Terrestrial Reference System

The definition of the Conventional Terrestrial System (CTS) is in accordance with the IERS conventions set forth in Petit & Luzum (2010). In accordance with these conventions, the origin is situated at the centre of mass of the Earth, the SI metre is used as the length measure, and the time scale being TCG. As an Earth-fixed reference system, it should retain its orientation with respect to the Earth's crust.

2.3.3 IERS Terrestrial Reference Frame (ITRF)

A conventional reference system is defined in accordance with the relevant conventions. The realisation of such a reference system is what is referred to as a reference frame. In the case of a terrestrial realisation, this is the TRF. In accordance with Resolution 2 of the IUGG, the IERS has been entrusted with the realisation and dissemination of the International Terrestrial Reference System (ITRS). The CTS realisation is the ITRF, which is currently available in the ITRF2020 realisation (Altamimi et al., 2023). It comprises the positions and temporal variations of globally distributed stations that are geographically fixed to the crust of the Earth with respect to a reference epoch, as well as a combined solution of the EOPs. Prior to this, the temporal variation included the velocities of the stations and was described by a linear function (Altamimi et al., 2016). Since the ITRF2014, post-seismic deformation (PSD) represents a distinct category of data, providing a description of the non-linear positional movement of stations in the aftermath of seismic events. From ITRF2020 onward, these temporal variations also encompass seasonal and geocentric variations. The four main space geodetic techniques, namely DORIS, GNSS, SLR and VLBI, are currently employed in combination for the realisation of the ITRF. As concluded, the accuracy of the ITRF2020 in the scale is 5 mm in position and 0.5 mm/year long-term stability. Following the application of a filter to the SLR and VLBI solutions, selected epochs demonstrate a scale agreement of 1 mm at the equator with respect to the reference epoch, exhibiting no significant drift. In accordance with the GGOS requirements for the precision of a TRF realisation, i.e. 1 mm and 0.1 mm/a in the reference frame defining parameters, it is indicated

that this objective has not yet been attained and that an enhancement of at least a factor of five is imperative.

2.4 Orbit determination

The problem of orbit and gravity field determination and it's numerical solution was demonstrated by (Kaula, 1966). The motion of a satellite subjected to a force $\mathbf{F}$ can, in accordance with Newton for the two-body problem in a non-rotating geocentric reference system be expressed by the following differential equation:

$$\ddot{\mathbf{r}} = \frac{\mathbf{F}(t, \mathbf{r}, \dot{\mathbf{r}})}{m} = -\frac{GM}{r^3}\mathbf{r} \tag{2.2}$$

with:

- $\ddot{\mathbf{r}}$ - geocentric acceleration vector of the satellite
- $\mathbf{F}$ - Force
- t - Epoch
- $\mathbf{r}$ - Satellite geocentric position vector
- $\dot{\mathbf{r}}$ - Satellite velocity vector
- m - Mass of the satellite
- G - Gravity constant
- M - Mass of the Earth
- r - Satellite orbital radius
- $-\frac{GM}{r^3}\mathbf{r}$ - Central gravity term

2.4.1 Osculating orbital elements

Assuming that there are no perturbing forces acting on a satellite, the satellite's orbit can be described by six constant orbital elements. EPOS-OC uses the orbital elements $a, e, i, \omega, \Omega, M$ (see Fig. 2.5). These are congruent with the six element state vector containing position $\mathbf{r}$ and velocity $\dot{\mathbf{r}}$ of the satellite. For the case where there are no perturbing forces, a set of orbital elements can be calculated from the state vector at time $\mathbf{t}$ for a future epoch $\mathbf{t} + \Delta\mathbf{t}$. Since, contrary to the above assumption, perturbative forces act on a satellite, its orbit deviates from a Keplerian ellipse, and the orbital elements thus become functions of time and are called osculating orbital elements.

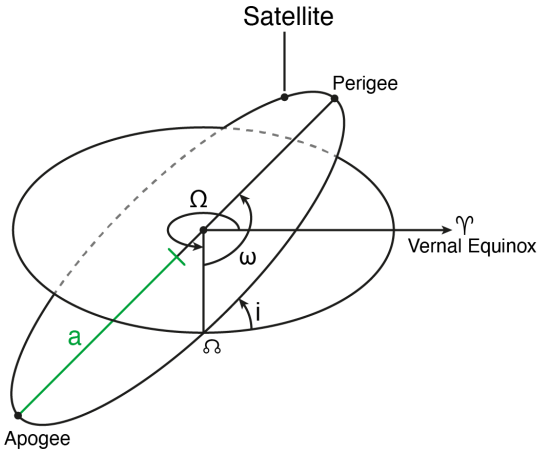

Figure 2.5: Orbital elements

- a - Semi-major axis
- e - Eccentricity
- i - Inclination
- ω - Argument of perigee
- Ω - Right ascension of the ascending node
- M - Mean anomaly

2.4.2 Equation of motion

In a geocentric, quasi-inertial reference system, the equation of motion of a satellite can be represented by extending the Kepler term $\frac{GM}{r^3}\mathbf{r}$ of the two-body problem to include perturbation accelerations $\ddot{r}_{pert}$ (Beutler, 2005).

$$\ddot{\mathbf{r}} = -\frac{GM}{r^3}\mathbf{r} + \ddot{r}_{pert} \tag{2.3}$$

2.4.3 Perturbation forces

The dominant part of the forces acting on an orbiting satellite is the conservative force due to the Earth's gravity. The remaining much smaller forces are several disturbance forces, which can be divided into other **conservative forces** and **non-conservative forces**. Non-conservative forces are often referred to as surface forces because they act directly on the satellite and are therefore a function of the satellite's size, mass and orientation. The main surface forces acting on a low-orbiting satellite are radiation pressure and drag from the upper atmosphere. Each of the perturbation forces can be expressed as an acceleration, taking into account the mass of the satellite. In the following, the perturbation acceleration term from formula 2.3 is split into individual components and their implementation in EPOS-OC is explained in detail.

Fig. 2.6 shows the individual perturbation forces and their minimum and maximum magnitudes for a GPS satellite and the individual space-tie satellite scenarios considered

in this thesis (for information on the orbital characteristics of the scenarios, see Sec. 4.1). It can be seen that the dominant force is due to the Kepler term and the oblateness of the Earth's gravitational field. The next largest forces are about 4 orders of magnitude smaller.

- **conservative forces**:
  - Earth gravitational field
  - Third body effect
    - Gravitational field of the Moon
    - Gravitational field of the Sun and planets
  - Tides
    - Earth tides
    - Ocean tides
- **Non-conservative forces**:
  - Radiation pressure
    - Solar radiation pressure
    - Earth radiation pressure
  - Atmospheric drag
- **Corrections due to relativistic effects**
  - Schwarzschild
  - Lense-Thirring
  - DeSitter

The perturbation forces, which are summarised in Equation (2.3) to $\ddot{\mathbf{r}}_{\mathbf{pert}}$, can now be defined individually as follows (Beutler, 2005):

$$\ddot{\mathbf{r}}_{\mathbf{pert}} = \ddot{\mathbf{r}}_g + \ddot{\mathbf{r}}_b + \ddot{\mathbf{r}}_e + \ddot{\mathbf{r}}_o + \ddot{\mathbf{r}}_s + \ddot{\mathbf{r}}_a + \ddot{\mathbf{r}}_d + \ddot{\mathbf{r}}_{rel} + ... \tag{2.4}$$

with:

- $\ddot{\mathbf{r}}_g$ - Gravitational acceleration due to the deviation of the Earth from a spherical shape and a radially symmetric mass distribution. Sec. 2.4.3.1
- $\ddot{\mathbf{r}}_b$ - Acceleration due to third bodies. Sec. 2.4.3.2
- $\ddot{\mathbf{r}}_e$, $\ddot{\mathbf{r}}_o$ - Acceleration due to Earth's and ocean tidal potential. Sec. 2.4.3.3
- $\ddot{\mathbf{r}}_s$, $\ddot{\mathbf{r}}_a$ - Direct and indirect solar radiation pressure acceleration. Sec. 2.4.3.4
- $\ddot{\mathbf{r}}_d$ - Acceleration due to atmospheric drag. Sec. 2.4.3.5
- $\ddot{\mathbf{r}}_{rel}$ - Relativistic corrections. Sec. 2.4.3.6

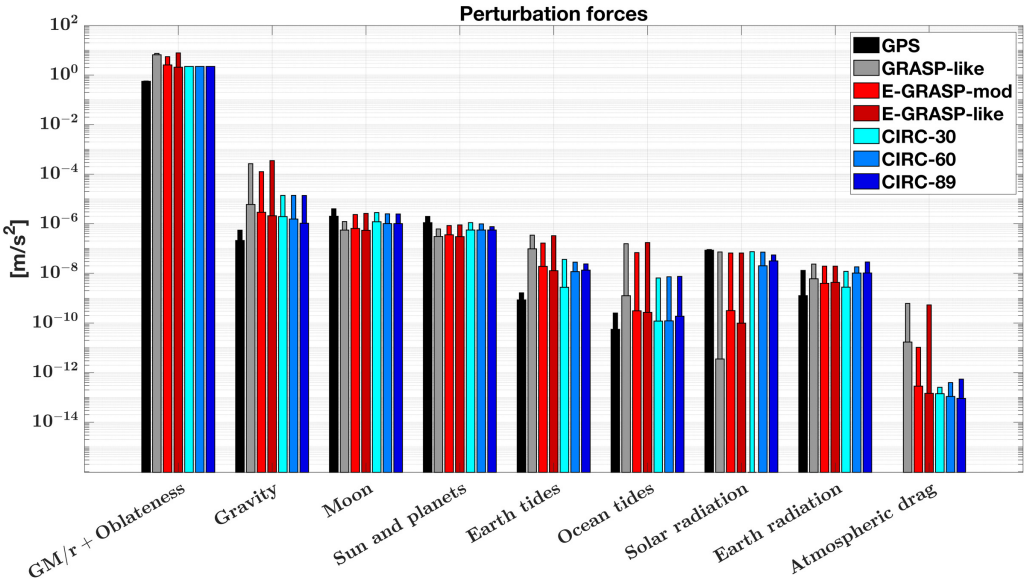

Figure 2.6: Minimum and maximum values of the acceleration of each perturbing force for GPS satellites and each space-tie satellite scenario. (For satellites passing through the Earth's shadow, the minimum radiation pressure value would be zero.)

In order to ascertain the true acceleration acting on a satellite, it is imperative to determine these perturbation forces with a high degree of accuracy. Therefore, they will be discussed in greater detail. In the subsequent simulations (Chap. 6), the impact of inaccuracies on specific perturbation forces is investigated. For the introduction of systematic error effects in Chap. 6, certain parameters for the computation of the perturbation accelerations are modified, which will be outlined in the following.

2.4.3.1 Gravity field of the Earth

The largest perturbation force acting on a satellite is induced by the variations in the Earth's gravity field. The resulting accelerations can be expressed by the gradient ∇ of the gravity potential $\mathbf{V}$.

$$\ddot{\mathbf{r}}_{\mathbf{g}} = \nabla V(\mathbf{r}) \tag{2.5}$$

where the vector of the position $\mathbf{r}$ is expressed in spherical coordinates:

$$\mathbf{r} = \begin{pmatrix} r\cos(\phi)\cos(\lambda) \\ r\cos(\phi)\sin(\lambda) \\ r\sin(\phi) \end{pmatrix} \tag{2.6}$$

where:

- λ, ϕ - geocentric longitude and latitude of the satellite

So the gravitational potential, represented by the function $V = V(r, \lambda, \phi)$, is expressed by Spherical Harmonics (SHs) as a spherical harmonic expansion:

$$V(r,\lambda,\phi) = \frac{GM}{r}\sum_{n=o}^{\infty}\left(\frac{R_0}{r}\right)^n \sum_{m=0}^{n} P_{nm}(\sin(\phi))[C_{nm}cos(m\lambda) + S_{nm}sin(m\lambda)] \tag{2.7}$$

whereby:

- R_0 - mean radius of the Earth at the equator
- n, m - degree and order of the geopotential
- P_{nm} - normalized Legendre function of degree n and order m
- C_{nm}, S_{nm} - SH geopotential coefficient of degree n and order m

The geopotential coefficients describe the density distribution of the mass inside the Earth. These can be differentiated into zonal (m=0), sectorial (m=n) and tesseral (0<m<n) coefficients. Terms of order m=0 are in the English-speaking world denoted as $J_n = -C_{n0}$. The harmonic coefficients up to degree 2 have particular meanings:

- C_{00} - The physical scale of the Earth according to the two-body problem, by definition set to 1
- C_{10}, C_{11}, S_{11} - The translation of the center of mass to the origin of the reference frame on the x, y and z axis, per definition set to 0
- C_{20} - The oblateness of the Earth, the largest influence on the perturbation forces
- C_{21}, S_{21} - The deviation of the principle inertia tensor axes from the reference frame axes in the inertial system

As part of the investigation of systematic errors below in Chap. 6, the SH coefficients of the Earth Gravitational Model (EGM) are modified, resulting in a discrepancy between the simulated and recovered gravitational forces. In the case of estimating the gravity field, the SH coefficients of the EGM are set up as solved-for parameters.

2.4.3.2 Third body

An additional significant influencing factor is the perturbation, which arises from the gravitational attraction of the Sun, the Moon and the planets. These perturbation forces can be calculated by approximating the gravitational attraction with a point mass, as outlined in e.g. Beutler (2005):

$$\ddot{\mathbf{r}}_b = -\sum_j GM_j\left(\frac{\mathbf{r}-\mathbf{r}_j}{|\mathbf{r}-\mathbf{r}_j|^3} + \frac{\mathbf{r}_j}{|\mathbf{r}_j|^3}\right) \tag{2.8}$$

with:

- $\mathbf{r}_j, M_j$ - Geocentric position vector and mass of the point mass element j

Thus a third body perturbation force for every attracting body can be computed. The formula employs the position vectors of the respective body, for which ephemerides, generated for instance by NASA's Jet Propulsion Laboratory (JPL) for the celestial bodies within our solar system, can be utilised. JPL's DE421 ephemerides (Folkner et al., 2009) are employed in this thesis. Prior to processing with EPOS-OC, they are preprocessed into a time series within the inertial Earth-centred reference frame of the orbit computation, comprising the position and its first and second derivatives. During processing, this information is interpolated to encompass the specified time period. For greatest accuracy, a gravitational field can also be included in the computation of the third body perturbation of the Moon in EPOS-OC, such as that by Ferrari (1977).

2.4.3.3 Tidal forces

The gravitational force of the Sun and Moon exerts a permanent deformation on the shape of the Earth, which in turn gives rise to changes in the gravitational potential and thus to accelerations of the satellite. These can be classified according to their prominence, with the most notable effects being the Earth and Ocean tidal effects.

Earth tides

In EPOS-OC the modulation of Earth tides is conducted in accordance with the recommendations set forth by the IERS conventions 2010 (Petit & Luzum, 2010). These comprise the tidal model in accordance with the recommendations set forth by Wahr (1981) and the elastic Earth model 1066A, as proposed by Gilbert & Dziewonski (1975). This model is dependent on the position of the Sun and Moon, and thus introduces a change to the gravity model of the rigid Earth, making it time-dependent. In EPOS-OC, this influence is calculated as a difference in the geopotential coefficients. As a first approximation, the variation for degree two, ΔV, on the Earth's surface can be expressed as quasi frequency-independent as follows:

$$\Delta V = K_2 R_0^2 \sum_{j=S,M} \frac{GM_j}{r_j^3} P_{20}(cos\Psi_j) \tag{2.9}$$

and for a satellite orbiting in free space outside the Earth's surface:

$$\Delta V = K_2 \frac{R_0^5}{r^3} \sum_{j=S,M} \frac{GM_j}{r_j^3} P_{20}(cos\Psi_j) \tag{2.10}$$

with:

- K_2 - Love number
- GM_j - Gravitational constant time mass of j=M, the Moon, and j=S, the Sun
- r_j - Geocentric position vector of j=M, the Moon, and j=S, the Sun
- Ψ_j - Geocentric angular separation of j=M, the Moon, and j=S, the Sun
- $P_{n0}(\cos\Psi)$ - Assigned Legendre-function of degree n

The required alterations to the geopotential coefficients can be obtained by incorporating the factor $GM_E R_{eq}^2$ into the equation, where R_{eq} represents the equatorial radius of the Earth. For the normalised zonal degree two coefficient it follows:

$$\Delta\overline{C_{20}} = \frac{1}{\sqrt{5}} K_2(0) \frac{R_0^5}{GM_E R_{eq}^2} \sum_{j=S,M} \frac{GM_j}{r_j^3} P_{20}(sin\phi_j) \tag{2.11}$$

with:

- λ_j, ϕ_j - geocentric longitude and latitude in the Earth-fixed frame

with the resulting expression for the changes in normalized spherical harmonic coefficients:

$$\Delta\overline{C_{nm}} - i\Delta\overline{S_{nm}} = A_m \sum_{S(n,m)} \Delta K_S H_S \begin{pmatrix} 1 \\ -i \end{pmatrix}_{n+m\ \ odd}^{n+m\ \ even} e^{i\theta_s} \tag{2.12}$$

whereby A_M holds:

$$A_M = \frac{(-1)^m}{R_0 \sqrt{4\pi(2-\delta_{om})}} \tag{2.13}$$

and:

- δ_{om} - $\begin{cases} 1, & m = 0 \\ 0, & m \neq 0 \end{cases}$
- θ_s - Doodson arguments
- ΔK_s - Difference of the frequency-dependent Love number $K_2^s(1)$ and the nominal one $K_2(1)$
- H_s - Amplitude of tidal generating potential

Ocean tides

The oceans demonstrate a response to tidal-driven potential change. These variations in the ocean mass distribution can be described as a set of tidal height components with frequencies, amplitudes, and phase information. For use with EPOS-OC, these are expanded to changes in SH coefficients. The tidal height components ζ_s can be described for any point on the ocean surface (λ, ϕ) and the Doodson argument (θ) as follows:

$$\zeta_s = \sum_{n=0}^{\infty} \sum_{m=o}^{n} \sum_{+}^{-} (C_{snm}^{\pm} cos(m\lambda \pm \theta_s) \pm S_{snm}^{\pm} sin(m\lambda \pm \theta_s)) P_{nm}(sin\phi) \tag{2.14}$$

- $C_{snm}^{\pm}, S_{snm}^{\pm}$ - Coefficient of the ocean tide constituent s

Once the SH coefficients and the Doodsen arguments have been calculated, the dynamic effect on a satellite can be expressed as a variation of the normalised geopotential coefficients.

$$\Delta\overline{C}_{nm} = F_{nm} \sum_{s(n,m)} ((C^{+}_{snm} + C^{-}_{snm})cos(\theta_s) + (S^{+}_{snm} + S^{-}_{snm})sin(\theta_s)) \quad (2.15)$$

$$\Delta\overline{S}_{nm} = F_{nm} \sum_{s(n,m)} ((S^{+}_{snm} + S^{-}_{snm})cos(\theta_s) - (C^{+}_{snm} + C^{-}_{snm})sin(\theta_s)) \quad (2.16)$$

whereby:

$$F_{nm} = \frac{4\pi G\rho_w}{\frac{GM}{R_0^2}} [\frac{(n+m)!}{(n-m)!(2n+1)(2-\delta_{om})}]^{\frac{1}{2}} \frac{1+K'_n}{2n+1} \quad (2.17)$$

with:

- $\frac{4\pi G\rho_w}{\frac{GM}{R_0^2}}$ =$+8.752 * 10^{-8}$
- K'_n - Load Love number

For this computation, the $C^{\pm}_{snm}$ and $S^{\pm}_{snm}$ coefficients of the respective tidal component s are passed to EPOS-OC, along with the associated Doodsen argument θ_s.

2.4.3.4 Radiation pressure

The radiation pressure experienced by a satellite can be divided into two distinct components. The direct component represents the force exerted by direct radiation from the Sun, commonly referred to as SRP. Conversely, the indirect component describes the radiation coming from the Earth, mainly in the optical and infrared spectrum, and is hence referred to as Earth radiation pressure, also known as albedo.

Solar Radiation Pressure
The direct radiation results in an acceleration, which can be described as follows:

$$\ddot{\mathbf{r}}_{\mathbf{R}} = -\gamma\kappa[\frac{l}{R}]^2 C_R \frac{1}{m} \sum_i s_i[(1-\rho_i)\mathbf{u_s} + 2(\frac{\delta_i}{3} + \rho_i(\mathbf{u_s}\cdot\mathbf{n_i}))\mathbf{n_i}]A_i(\mathbf{u_s}\cdot\mathbf{n_i}) \quad (2.18)$$

whereby:

- γ - A shadow factor that holds:
  - $\gamma = 0$ The satellite is in the shadow of the Earth (Umbra), or the Moon
  - $0 < \gamma < 1$ The satellite is in half-shade (Penumbra)
  - $\gamma = 1$ The satellite is situated in an area of direct irradiation.
- κ - Bolometric solar constant in Newton/m^2
- l - Astronomical unit in metres

- $\mathbf{R}$ - Difference between the geocentric position vectors of the Sun and the satellite $\mathbf{r_{sun}} - \mathbf{r_{satellite}}$
- C_R - Scaling factor which can be adjusted
- s_i - Shadow factor of the surface element i $\begin{cases} 1, & \mathbf{u_s} \cdot \mathbf{n_i} > 0 \\ 0, & \mathbf{u_s} \cdot \mathbf{n_i} \leq 0 \end{cases}$
- m - The mass of the satellite
- $\mathbf{u_s}$ - Unit vector from the satellite to the Sun $\frac{R}{|R|}$
- A_i - Area of the satellite surface element i
- $\mathbf{n_i}$ - Normal vector of the satellite surface element i
- $\rho_i, \delta_i, \alpha_i$ - Fraction of the incident sunlight that is reflected, diffused or absorbed, whereby $\rho_i + \delta_i + \alpha_i = 1$

Two of the optical properties coefficients are required by EPOS-OC, the third is computed internally. Nevertheless, some difficulties emerge when considering the solar constant determined by Johnson (1954). For example, the variation of the solar constant was measured over approximately 30 years by the Observatory of the Smithsonian Institute, which indicated a variation of the solar constant by approximately 0.1% (Hoyt, 1979). However, it should be noted that these measurements are defined for a distance of 1 AU and an absorption value of α=1, which does not align with the conditions experienced by satellites. Moreover, it is challenging to develop a precise model for the shadow transition and the factor γ. In many cases, data pertaining to surface properties are only available in a limited manner. However, the creation of macro-models based on these data for Precise Orbit Determination (POD) inevitably results in some degree of inaccuracy. This is due to the fact that an exact spectral measurement is not always available for every material used. Furthermore, surfaces are typically composed of multiple materials, resulting in a heterogeneous mixture of surface properties.

For the calculation of radiation pressure in EPOS-OC the following variables are passed: the bolometric solar constant, two surface optical property coefficients, the area and orientation of the surface elements in the satellite-fixed reference frame, the mass of the satellite, and scaling factors, which can also be estimated. In the analysis of systematic errors in radiation pressure force presented in Chap. 6, the surface properties $\rho_i, \delta_i, \alpha_i$ were perturbed for the LEO satellite. For the GPS transmitter satellites, the size of the partial surfaces was modified.

Earth Radiation Pressure

The force resulting from radiation reflected by the Earth from incident solar radiation and the thermal radiation of long wavelengths can be collectively described as Earth radiation (albedo). This force can be expressed, starting from an area of the Earth, E_j, for an area element of a satellite, A_i, as follows:

$$\begin{aligned} \mathbf{F_{ij}} &= s_i C_R \kappa \left[\frac{l}{R}\right]^2 (s_j a_j cos(\Theta_{sj}) + \frac{e_j}{4}) \frac{dE_j cos(\tau_j)}{\pi r_j^2} \\ &\quad \left[(1-\rho_i) \cdot \mathbf{u_j} + 2(\frac{\delta_i}{3} + \rho_i cos(\beta_{ij}) \cdot \mathbf{n_i})\right] A_i cos(\beta_{ij}) \end{aligned} \tag{2.19}$$

The nomenclature of the variables $\kappa, l, R, A_i, \mathbf{n_i}, \rho_i, \delta_i, \mathbf{u_s}, C_R$ is identical to that used for solar radiation pressure. Additionally, we define:

- s_i - $\begin{cases} 1, & cos\beta_{ij} > 0 \\ 0, & cos\beta_{ij} \leq 0 \end{cases}$
- s_j - $\begin{cases} 1, & cos\beta_{sj} > 0 \\ 0, & cos\beta_{sj} \leq 0 \end{cases}$
- a_j - Albedo value of j-th Earth's surface element dE_j
- Θ_{sj} - Angle between $\mathbf{n_j}$ and $\mathbf{u_s}$
- e_j - Thermal radiation of j-th Earth's surface element dE_j
- dE_j - Surface element of the Earth
- τ_j - Angle between $\mathbf{n_j}$ and $-\mathbf{u_j}$
- $\mathbf{r_j}$ - Vector from the j-th Earth's surface element center to the satellite
- $\mathbf{u_j}$ - $-\frac{\mathbf{r_j}}{r_j}$
- β_{ij} - Angle between $\mathbf{n_i}$ and $\mathbf{u_j}$
- $\mathbf{n_j}$ - Normal vector for dE_j

A global albedo value is passed to EPOS-OC, which is then used to calculate the albedo and thermal radiation values at the satellite position according to an internal analytical model. The specified satellite macro-model is then used to calculate the orientation of the surface elements to the Earth. The total acceleration is therefore the sum of the acceleration of all sub-areas of the satellite and all sub-areas of the Earth radiation model:

$$\ddot{\mathbf{r}}_\mathbf{a} = \frac{1}{m} \sum_i \sum_j \mathbf{F_{ij}} \tag{2.20}$$

2.4.3.5 Atmospheric drag

As satellites pass through the atmosphere, they are subject to atmospheric drag and lift. These forces can be described as follows:

Atmospheric drag:

$$\ddot{r}_d = -\frac{1}{2} C_D \rho \frac{v_{rel}^2}{m} \left[\sum_i A_i cos(\nu_i) K_D^i \right] \cdot \mathbf{u}_D \tag{2.21}$$

Atmospheric lift:

$$\ddot{r}_l = +\frac{1}{2} C_L \rho \frac{v_{rel}^2}{m} \left[\sum_i A_i cos(\nu_i) K_L^i \cdot \mathbf{u}_L^i \right] \tag{2.22}$$

whereby:

$$\mathbf{u}_D = \frac{\dot{\mathbf{r}} - \omega \times \mathbf{r}}{|\dot{\mathbf{r}} - \omega \times \mathbf{r}|} \tag{2.23}$$

$$\mathbf{u}_L^i = \frac{\mathbf{u}_D \times (\mathbf{u}_D \times \mathbf{n}_i)}{sin(\nu_i)} \tag{2.24}$$

with:

- $C_{D,L}$ - Scaling factors (can be adjusted in EPOS-OC)
- ρ - Density of the atmosphere
- v_{rel} - Velocity of the satellite relative to the atmosphere
- m - Mass of the satellite
- A_i - Area of the satellite surface element i
- ν_i - Angle between the velocity vector $\dot{\mathbf{r}}$ relative to the atmosphere and the normal of the surface element $\mathbf{n}_i$
- $K_{D,L}$ - Coefficient, describing the surface interaction with the atmosphere
- $\mathbf{r}, \dot{\mathbf{r}}$ - Geocentric position and velocity of the satellite in the integration reference system
- ω - Angular velocity of the Earth in the integration reference system
- $\mathbf{n}_i$ - Unit vector of the surface element i

The normal vectors of the satellite surfaces are expressed in the satellite-fixed reference frame. Subsequently, these are transformed into the reference system of the integration utilising a rotation matrix, depending on the attitude control system. The calculation of the atmospheric drag presents two significant challenges. The initial challenge is to ascertain an appropriate value for the atmospheric density ρ at the location of the satellite. The second challenge pertains to the determination of suitable coefficients K_D^i for the surface materials. The values for the density of the atmosphere are derived from atmospheric models. The resistance coefficients are provided by the satellite manufacturer if available.

In the investigation of the influence of atmospheric resistance (see Sec. 4.6.2), the atmospheric model is replaced, resulting in a change of the parameter ρ at this point. Subsequently, the parameter C_D is estimated to minimize the introduced disturbance. Atmospheric lift is not taken into account in this thesis.

2.4.3.6 Corrections due to relativistic effects

In order to accommodate Newton's law of gravity within a relativistic spacetime, it is necessary to make certain corrections. In the context of a geocentric reference system (as in EPOS-OC), relativistic corrections to acceleration and observations are due to the Schwarzschild effect, the Lense-Thirring effect, and the de Sitter effect.

Of the three relativistic corrections mentioned here, the acceleration due to the Schwarzschild effect is the most significant. This effect results in a deviation from the constant ellipse described in Newton's gravitation law for the orbit of a mass around a central mass. Instead, the perigee drifts in the direction of the velocity vector of the orbit (Schwarzschild, 1916). The size of the effect is approximately $10^{-8} m/s^2$ at an altitude of 1'000 km and diminishes with increasing altitude.

The Lense–Thirring effect describes the twisting of space-time around a rotating mass in the local inertial system (Lense & Thirring, 1918). The rotating mass exerts a force on the surrounding space-time, analogous to the viscosity of a viscous liquid. For a satellite in Earth orbit, this results in a drift of the ascending node and perigee. The effect is approximately two orders of magnitude weaker than the Schwarzschild effect (i.e. $10^{-10} m/s^2$ at an altitude of 1'000 km) and also diminishes with increasing altitude (Ciufolini & Pavlis, 2004).

The de Sitter effect, named after its discoverer Willem de Sitter (de Sitter, 1916; de Sitter, 1917), describes a relativistic phenomenon occurring along the axis of rotation of a rotating body within the gravitational field of a central body. In the case of a satellite orbiting the Earth, this results in a precession of the orbital plane of the satellite, given that it is not in the plane of rotation of the Sun, which results in a drift of the ascending node and perigee. The strength of the effect varies less with the altitude of the satellite than with the current position of the satellite, Earth, and Sun constellation, and is approximately at the level of $3 \cdot 10^{-11} m/s^2$ for LEO satellites.

2.5 The EPOS software

The software employed at GFZ for the estimation of Earth system parameters and satellite orbits is the Earth Parameter and Orbit System (EPOS) (Neumayer et al., 2024). EPOS is a suite of modules that augment the core module OC (Orbit Computation). The OA module (Orbit Analyses) enables the comparison and geographic analysis of orbits, among other capabilities. The CS (Combination and Solution) module is used to analyse normal equations, in particular, to accumulate them, to impose weak or stringent constraints, reduce or fix parameters, and to solve them. Collectively, the modules facilitate data preparation, orbit integration, orbit and Earth parameter adjustment, orbit prediction, orbit analysis, linear algebra applications with normal equations, and the simulation of observations (see Fig. 2.7).

An example of the operational use of EPOS is POD (e.g. Schreiner et al. (2022c)) and gravity field determination for the satellite mission GRACE Follow-On (GRACE-FO) (Landerer et al., 2020). For this purpose, several measurement techniques such as DORIS, SLR, GNSS and VLBI can be processed with EPOS-OC. Fig. 2.7 shows the programme flow of EPOS-OC. The process starts with reading the input data, such as the observation data. After that, different modes can be executed, depending on the user's choice. The modes theoretically build on each other, so if mode 3 is used, the steps of mode 0, 1, 20, 2 and 3 will be gone through. As an example, the simulation of observations takes place in mode 1. After the calculation of the theoretical observation, the module stops there and does not proceed with mode 20, 2 and 3, going directly to the next step, the simulation of the observations and the output. For POD, mode 3, the parameter adjustment, is used. This process goes through several iterations until the convergence criterion is reached and then the output files are generated. In this thesis, mode 0 is used for the orbit design of the space-tie satellites, mode 1 for the simulation of the observations, mode 3 for POD and mode 2 for the generation of normal equations to solve for dedicated parameters.

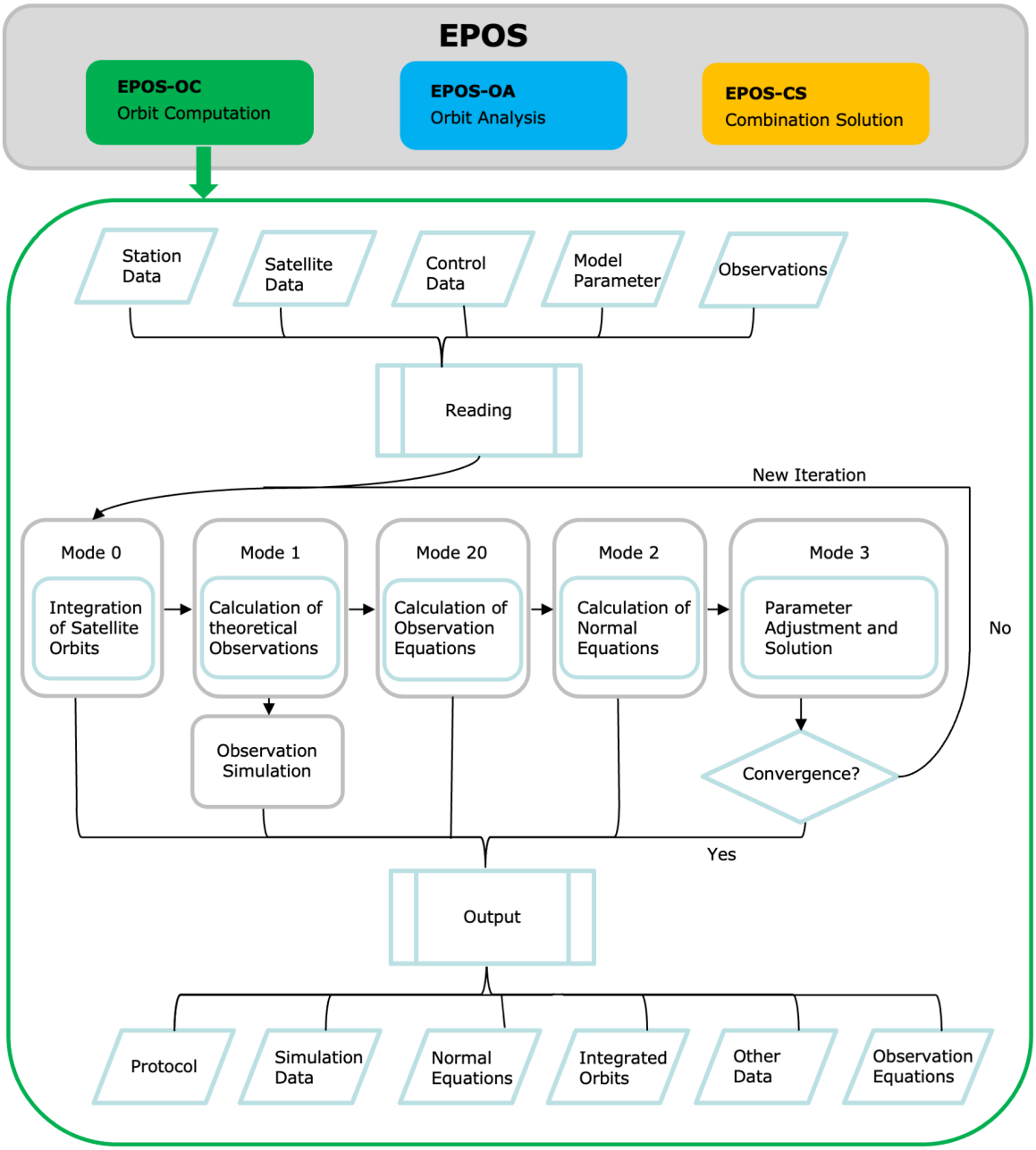

Figure 2.7: Diagram of the EPOS software with its individual packages for orbit computation (OC), orbit analysis (OA), and handling of normal equations (CS) with the schematic flow chart of the OC module.

2.6 Orbit and parameter determination with EPOS-OC

The equations of motion described in Sec. 2.4.2, are typically formulated in an inertial reference system. For orbit modelling of satellite orbits close to the Earth, EPOS-OC uses the mean equatorial reference system at epoch J2000.0 = 0, which is a well adapted Earth centred approximation for an inertial reference system in the sense of general relativity (Reigber, 1989). The mean equatorial system differs from the CIS due to the effect of precession. This is taken into account for numerical purposes in the form of an approximation based on IAU models. The differential equations describing the motion of the satellite are extended to include the relevant perturbations in Sec. 2.4.3. Since a direct analytical solution of these equations is not feasible, EPOS-OC uses a numerical solution procedure to solve the equation of motion.

2.6.1 Solution of the equation of motion

In the numerical solution procedure, the complete perturbation model is incorporated into the equation of motion, therefore we speak of the dynamical approach. Subsequently, the differential equations are integrated numerically for the position and velocity vector. The integrator of EPOS-OC employs a symmetric, double totalised Cowell method (Brouwer & Clemence, 1961; Borderies, 1977) with adaptation in accordance with Kulikov (1963). In this method, the equation of motion and all perturbation forces are solved in a Cartesian coordinate system within an inertial reference frame, step by step, until a certain epoch is reached. The acceleration vector is given by equation (2.4) and the equation of motion is expressed as (2.3). Here, the individual components can be written as:

$$\mathbf{r} = \begin{pmatrix} x \\ y \\ z \end{pmatrix}, \quad \dot{\mathbf{r}} = \begin{pmatrix} \dot{r}_x \\ \dot{r}_y \\ \dot{r}_z \end{pmatrix}, \quad \ddot{\mathbf{r}}_{\mathbf{pert}} = \begin{pmatrix} \ddot{r}_{pert,x} \\ \ddot{r}_{pert,y} \\ \ddot{r}_{pert,z} \end{pmatrix} \tag{2.25}$$

To compute the position and velocity of a satellite at a specific time t, it is necessary to integrate the six equations for $\mathbf{r}$ and $\dot{\mathbf{r}}$. In order to achieve this, the initial position and velocity are required. However, there are inherent limitations to this approach, namely rounding errors and the accumulation of discretisation errors. These can be mitigated by reducing the step size of the integrator or increasing the order height of the integrator, thereby enhancing the accuracy of the solution. In this regard, EPOS-OC is well-optimised in terms of the absolute accuracy of the integrator, as evidenced by adjustments such as those proposed by Kulikov (1963) and results of internal studies.

2.6.2 Adjustment and parameter determination

The application of the dynamic method for the determination of satellite orbits and geodetic parameters relies on observations such as ranges from the Earth surface to the satellite and many other possibilities to track a satellite. In the case of GNSS, however, it is the GNSS satellites that transmit and the ground stations or LEO satellites that receive. For ground-to-satellite observations, the observation can generally be expressed as follows:

$$q = q(t, P) = \bar{q}(t, X_S(P), X_T(P), P) \tag{2.26}$$

So the observation q is a function of time t and the set of parameters P. More precisely, X_S represents the position vector of the observed satellite given in the CIS and being dependent

on the parameters we want to solve, and X_T denotes the position vector of the observing station, and given in the CTS and being also dependent on the parameters. The position vector of the satellite (X_S) is derived from the theoretical formulation of satellite orbit motion. The station vector (X_T) is derived from the theoretical modelling of the motion of a topocenter on the dynamic Earth and its motion in space. These formulations are based on the use of models, for which the following information is necessary:

- The geocentric position of the observing station in the CTS at a reference epoch T_0. Here the ITRF2014 (Altamimi et al., 2016) is used .
- The motion of Earth's crust at the position of the observing station (station velocities, tidal deformation, ocean loading).
- The irregular motion of the CIP and its relation to the CTP, consequently celestial pole offsets, UT1 variations and polar motion.

The geocentric position vector of the satellite, X_S, in the inertial reference system is derived from the integration of the equation of motion, which is based upon the mechanics of Newton.

$$m\ddot{\bar{x}}_S = \sum_i \bar{F}_i \tag{2.27}$$

The right side of this formula describes all gravitational and non-gravitational forces that act on the satellite, as well as those that arise due to the rotation of the integration system in relation to a truely inertial system S. In order to describe the position of the satellite with reasonable accuracy, information about the aforementioned perturbation forces (for further details, please refer to Sec. 2.4.3) and some initial knowledge of the parameters is needed. So an actual observation q_{obs} at time t will not coincide with the theoretical observation q_{theo} based on the initial parameters P_R.

$$q_{theo} = q(t, P_R) \tag{2.28}$$

The objective is to minimise the distance between q_{obs} and q_{theo} by employing a differential parameter improvement of P. To this end, the observation equation is expanded into a Taylor series around P_R. The distance

$$q_{obs} - q_{theo} = q_{obs} - q(t, P_R) = q_{obs} - \left(q(t, P_R) + \sum_i \frac{\partial q}{\partial P_i} \Delta P_i \right) \tag{2.29}$$

with $\Delta P = P - P_R$.

If the approximation P_R is close enough to P, terms of order greater than one can be neglected in the Taylor series and we obtain:

$$q(t, P) = q(t, P_R) + \sum_i \frac{\partial q}{\partial P_i} \Delta P_i \tag{2.30}$$

The set of parameters can be divided as follows:

$$q(t, P) = \bar{q}(t, X_S(X_S^0, \beta, \epsilon), X_T(S_T, \beta, \omega)) \tag{2.31}$$

with:

X_S^0 = $(\mathbf{r}(t_0), \mathbf{v}(t_0))$ initial state vector of the satellite in the CIS

S_T = $(x_T^1, x_T^2, x_T^3)^T$ position of the observing station in the CTS

β = $(\beta_1, ..., \beta_n)^T$ set of parameters of the geopotential

ϵ = $(\epsilon_1, ..., \epsilon_n)^T$ set of parameters of the surface force models of the disturbance forces

ω = $(x_p, y_p, UT1)$ set of EOPs for the rotation between the terrestrial and the inertial frame

With formula 2.31, 2.30 can now be written as:

$$\Delta q = q(t, P) - q(t, P_R) = \begin{pmatrix} \frac{\partial q}{\partial X_S} & \frac{\partial q}{\partial X_T} \end{pmatrix} \sum_i \begin{pmatrix} \frac{\partial X_S}{\partial P_i} \\ \frac{\partial X_T}{\partial P_i} \end{pmatrix} \Delta P_i \tag{2.32}$$

or in matrix notation

$$\Delta q = [\mathbf{SETRG}] \begin{bmatrix} \Delta P_S \\ \Delta P_\epsilon \\ \Delta P_T \\ \Delta P_\omega \\ \Delta P_\beta \end{bmatrix} \tag{2.33}$$

with the following arc-dependent parameters (inner parameters)

- P_S - Initial state vector of the satellite
- P_ϵ - Empirical accelerations and force model parameters

the following arc-independent parameters (outer parameters)

- P_T - Coordinates of the observing station
- P_ω - Earth rotation parameters
- P_β - Earth's gravitation parameters

and $\mathbf{SETRG}$ the block matrix containing the respective partial derivatives of the parameters. In Equation 2.33, Δq describes the deviation of the calculated from the true value of q. The vectors $\mathbf{S}$ to $\mathbf{G}$ describe the partial derivatives of the observations with respect to the inner and outer parameters. For a sufficient number of observations of a single arc, a system of observation equations can be established to solve for the inner parameters. In order to solve for the outer parameters, the process is divided into two steps:

- The differential orbit improvement process, where only the inner parameters are determined from observation data for each arc.
- Estimation of geodetic parameters, where the outer parameters are determined from observational data from multiple arcs and satellites.

2.6.2.1 Differential orbit improvement process

In this process, only the inner parameters are considered. It is assumed that all other parameters are known, which reduces the system of observation equations to:

$$\Delta q_i = \left[\mathbf{SE}\right]_i \begin{bmatrix} \Delta P_S \\ \Delta P_\epsilon \end{bmatrix} \tag{2.34}$$

The necessity of linearity is fundamental to the least squares method. Therefore, the approximation parameters in this highly non-linear problem must be sufficiently close to the true values, which is achieved by differential parameter improvement. Therefore, once appropriate weights have been applied, the equation is solved using the least squares method to determine the arc-dependent parameters $\Delta\bar{P}_S$ and $\Delta\bar{P}_\epsilon$. The improvements are then incorporated into the reference value, and the resulting parameters establish a new system. This process is repeated until the weighted square sum of the residuals Δq_i^n converges to a minimum.

2.6.2.2 Outer parameter determination process

Once the initial step of parameter determination has been completed and the inner parameters have been estimated, the outer parameters can be estimated. In order to achieve this, the normal equation of the system of equations is set up in a further step, as in the converged state before, but extended by the external parameters, such as gravity field coefficients. The normal equations generated in this way over a certain time period are accumulated and eventually inverted using Cholesky decomposition.

For instance, a period of at least 2.5 years is recommended for estimating station velocities (Blewitt & Lavallée, 2002), while a month is typically used for the estimation of the $C_{2,0}$ SH coefficient with SLR, and several decades for long-term trend estimation (Cheng & Tapley, 2004; Cheng et al., 2013). With Gravity Recovery and Climate Experiment (GRACE) and GRACE-FO, monthly gravity fields of SH coefficients are usually estimated and also used for combinations (Meyer et al., 2023), but daily solutions are also possible and provide insightful information, for example on high-frequency water flux information (Eicker et al., 2020).

2.7 Combination strategies

The combination of single and multiple space geodetic techniques can be achieved in three different ways. This is exemplified by the use of the space-tie satellite in the context of this thesis. The combination can be made at the observation level (Gauß, 1809; Gauß, 1887), normal equation level (Gauß, 1823) or parameter level (Gauß, 1828). In the following, only the combination on normal equation level will be used. To illustrate the differences between the combination methods, the basic formulation of the Gauss-Markov least squares adjustment will be examined, which requires linearity (compare above) ('Linear') and provides the most accurate ('Best'), unbiased ('Unbiased') estimator ('Estimator'), say BLUE (Aitken, 1936).

The least squares method for the linear model is described as follows:

$$\tilde{l} = A\tilde{x} \tag{2.35}$$

where $\tilde{l}$ is the vector of true observations, $\tilde{x}$ is the vector of true unknowns, and A is the Jacobi matrix. Since we do not have the true values, we must use the actual observations l to determine the estimated values $\hat{x}$. The functional model is only consistent if we add a vector of residuals v to the observations.

$$l + v = A\hat{x} \tag{2.36}$$

Because the issues related to orbit and gravity field determination are inherently nonlinear, the functional relationship between the observations and the unknowns $\tilde{x}$, must be expressed as follows:

$$l + v = f(\hat{x}) = f(x_0) + A\Delta x \tag{2.37}$$

with the parameter correction vector Δx. The stochastic model for this is given by the covariance matrix K_{ll} for a given vector of observations l, one can combine the variance factor σ_0^2 with the cofactor matrix Q_{ll}.

$$K_{ll} = \sigma_0^2 Q_{ll} \tag{2.38}$$

The inverse of this matrix is the weight matrix, denoted P_{ll}, which is used in the following.

$$P_{ll} = K_{ll}^{-1} \tag{2.39}$$

Furthermore, by rearranging formula (2.37) in accordance with

$$\hat{x} = x_0 + \Delta\hat{x} \tag{2.40}$$

and the aforementioned residuals, we obtain:

$$v = f(\hat{x}) - l = f(x_0 + \Delta\hat{x}) - l \tag{2.41}$$

Where x_0 is an approximate value. This can be linearised using a Taylor series which can be terminated after the first order.

$$v = f(x_0) + \frac{\partial f(x_0)}{\partial x_0} + ... - l \tag{2.42}$$

Now we introduce the Jacobi matrix as the partial derivative of the nonlinear functional relations according to the approximate value

$$A = \frac{\partial f(x_0)}{\partial x_0} \tag{2.43}$$

and the reduced observation vector w

$$w = l - f(x_0) \tag{2.44}$$

the equation of the residuals can in first approximation with $Ax_0 = f(x_0)$ be written as:

$$v = A\Delta\hat{x} - w \tag{2.45}$$

The combination of techniques at this point would be classified as an **observation-level combination**, with $v = \begin{pmatrix} v_{DORIS} \\ v_{GPS} \\ v_{SLR} \end{pmatrix}$

The method of least squares minimises the sum of the weighted squares of these residuals. In order to achieve the objective function $v^T P_{ll} v \rightarrow min$, it is necessary to determine the extreme, which is a minimum of the objective function. Derivation and rearrangement according to the estimated values gives the system of normal equations:

$$(A^T P_{ll} A)\Delta\hat{x} = A^T P_{ll} w \tag{2.46}$$

The solution of this system of normal equations can be written as:

$$\Delta\hat{x} = (A^T P_{ll} A)^{-1} A^T P_{ll} w \tag{2.47}$$

in which the normal equation matrix is referred to:

$$N = A^T P_{ll} A \tag{2.48}$$

and the vector of the right-hand side of the normal equation system:

$$y = A^T P_{ll} w \tag{2.49}$$

A combination at this point would be a **combination on normal equation level** with $N_{combined} = N_{DORIS} + N_{GPS} + N_{SLR}$.

The rank of the matrices N and A is equal and of full rank if the rank is equal to the number of unknown parameters. If this is not the case, the matrices are singular and indicate a configuration or datum defect. To care for the datum, certain conditions can be introduced. The estimated parameters are eventually calculated according to 2.47 and 2.40 as:

$$\hat{x} = x_0 + (A^T P_{ll} A)^{-1} A^T P_{ll} w = x_0 + N^{-1} y \tag{2.50}$$

With the redundancy (or DoF) $r = n - u$ as the difference between the number of observations n and the number of unknowns u, we can estimate the a posteriori variance factor from the residuals:

$$\sigma_v^2 = \frac{v^T P_{ll} v}{r} \tag{2.51}$$

and the variance-covariance matrix of the estimated unknowns as:

$$K_{\hat{x}\hat{x}} = \sigma_v^2 N^{-1} \tag{2.52}$$

A combination at this point would be a **combination at parameter level**. If more than one solution is available, they can be combined using different methods, such as averaging or normal equation accumulation.

2.7.1 Accumulation of normal equations

In order to combine several normal equations over a longer analysis period or from several satellites, for instance to determine external parameters, normal equations from several solution systems are accumulated, thus combining the information on common parameters. Assuming that there are no correlations between the systems, EPOS-OC stores for each solution system the normal equation $N_i = A_i^T P_{ll_i} A_i^T$ and the vector of the right-hand

side $y_i = A_i^T P_{ll_i} w_i$. With Δx denoting the set of all parameters of the individual normal equations, the accumulation is written as:

$$\sum_i N_i \Delta x = \sum_i y_i \tag{2.53}$$

2.7.2 Normal equation parameter reduction

The reduction of parameters from the normal equation is used intensively in the following, especially in the GPS processing in Sec. 5.3 and 6.3. This allows to reduce parameters not of further interest so that they no longer appear explicitly. However, the information content of the estimate is transferred to the remaining equation system, so parameter reduction must be strictly distinguished from parameter fixing. For example, EPOS-OC uses reduction for the epoch clock parameters during GNSS processing to reduce the dimension of the normal equations and significantly speed up the processing time.

Besides the normal equation and the vector of the right hand side, EPOS-OC also returns the value of the objective function $q = v^T P_{ll} v$ at the point $x = x_0$ with $v = l - Ax_0$, as well as the initial value x_0. To reduce the system of equations, the components are partitioned into the parameters Δx_1 to be kept and the parameters Δx_2 to be reduced, with $\Delta x = x - x_0$. Accordingly, we can write:

$$N = \begin{pmatrix} N_{11} N_{12} \\ N_{12}^T N_{22} \end{pmatrix}, \Delta x = \begin{pmatrix} \Delta x_1 \\ \Delta x_2 \end{pmatrix}, y = \begin{pmatrix} y_1 \\ y_2 \end{pmatrix} \tag{2.54}$$

The solution of $N\Delta x = y$ is equivalent to the solution of the optimisation:

$$\min_q \left\{ \Delta x^T N \Delta x - 2y^T \Delta x + q \right\} \tag{2.55}$$

The reduction is done by finding the optimum of the objective function for the partial vector Δx_2 and inserting it into the initital objective function, which yields:

$$\min_{\tilde{q}} \left\{ \Delta x_1^T \tilde{N} \Delta x_1 - 2\tilde{y}^T \Delta x_1 + \tilde{q} \right\} \tag{2.56}$$

The new normal equation now reads:

$$\tilde{N} \Delta x_1 = \tilde{y} \tag{2.57}$$

with

$$\tilde{N} = N_{11} - N_{12} N_{22}^{-1} N_{12}^T \tag{2.58}$$

$$\tilde{y} = y_1 - N_{12} N_{22}^{-1} y_2 \tag{2.59}$$

and the objective function

$$\tilde{q} = q - y_2^T N_{22}^{-1} y_2 \tag{2.60}$$

The original system of equations has thus been reduced by the parameter group Δx_2.

2.7.3 Parameter constraints

Parameter constraints may be necessary to stabilise singular normal equation systems so that they can be inverted. In the context of this thesis, parameter constraints are primarily used to introduce the geodetic datum. Constraints can be applied to parameters in several ways, such as by applying a conditional adjustment or, as is the case here, by introducing pseudo-observations. The observation equation of the pseudo-observations can be written for x_c, a subgroup of x, in the same way as for real observations as $v_c = A_c \Delta x_c - w_c$. With the observation equation of the constrained Eq. 2.62, a system of normal equations is generated for the pseudo-observation in the same way as for real data. The normal equation system of the pseudo-observations is then added to the actual normal equation system (Eq. 2.62), as described above in Sec. 2.7.1. Hereby, the variance of the pseudo-observation determines the weight of the condition. In the case of a small weight, this corresponds to loose constraints, in the case of a large weight, it is equivalent to a condition.

$$l_c + v_c = A_c \hat{x}_c \tag{2.61}$$

$$(N + N_c)\hat{x} = (A^T P l + A_c^T P_c l_c) \tag{2.62}$$

2.7.4 Network datum constraints

Network conditions allow that a network that has to be estimated, gets aligned to a specific reference frame defined by coordinates. If the rank defect of the normal equation is solely corrected by a condition of the same rank as the datum defect, this corresponds to the minimum constraint approach.

The pseudo-observations of the commonly used No-Net-Scale (NNS), NNR and NNT conditions (Boucher & Altamimi, 1993) are derived from the Helmert transformation:

$$\begin{bmatrix} X_D \\ Y_D \\ Z_D \end{bmatrix} = (1 + sc) \begin{bmatrix} 1 & -R_3 & R_2 \\ R_3 & 1 & -R_1 \\ -R_2 & R_1 & 1 \end{bmatrix} * \begin{bmatrix} X_S \\ Y_S \\ Z_S \end{bmatrix} + \begin{bmatrix} T_1 \\ T_2 \\ T_3 \end{bmatrix} \tag{2.63}$$

where X_S, Y_S and Z_S are the source coordinates and X_D, Y_D and Z_D are the destination coordinates. The transformation parameters are the rotation angles R_i, the scale sc, and the translation values T_i. With l_H the pseudo-observation of the Helmert constraint, the observation equation and the design matrix can be written as:

$$l_H + v_H = A_H \hat{x}_H \tag{2.64}$$

$$\Delta x_H = [sc, R, T] \tag{2.65}$$

$$A_H = \begin{bmatrix} 1 & 0 & 0 & 0 & Z_{apri} & -Y_{apri} & X_{apri} \\ 0 & 1 & 0 & -Z_{apri} & 0 & X_{apri} & Y_{apri} \\ 0 & 0 & 1 & Y_{apri} & -X_{apri} & 0 & Z_{apri} \end{bmatrix} \tag{2.66}$$

The Helmert parameters $\mathbf{x_H}$ can be determined by a least squares adjustment:

$$N_H \Delta x_H = A_H^T P_H w_H \tag{2.67}$$

$$\hat{x}_H = x_{0_H} + \Delta x_H \tag{2.68}$$

In order to obtain a more compact form of the Helmert constraint normal equation that can be added directly to the original normal equation, a parameter change can be made to the estimated Helmert parameters, $\hat{x}_H$, and the pseudo-observations, l_H. The normal equation of the Helmert constraint can therefore be written as:

$$N_H \hat{x}_H = A_H^T P_H l_H \tag{2.69}$$

and the overall least squares solution is obtained by adding the constraint normal equation to the original normal equation system. With N as the notation for the original and N_H for the constraint normal equation $A^T P A$ results in:

$$(N + N_H)\hat{x} = A^T P l + A_H^T P_H l_H \tag{2.70}$$

Here, P_H is the weighting matrix of the transformation parameters. In the case of hard constraints, the value of σ_H in the weighting $\frac{1}{\sigma_H^2}$ of P_H, is chosen to be near zero. Thereby the network is constrained to the a priori network, and the vector l_J becomes 0. Forcing the rotation parameters R_i to zero expresses a NNR condition, the translation parameters T_i a NNT condition and the scale parameter sc a NNS condition.

2.7.5 Combination with global parameters - global tie

The concept of global ties is understood to represent global parameters, which can also be described as external parameters in the context of the adjustment theory (see also Sec. 2.6.2). In this thesis, global ties are the ERPs, and if applicable, also the spherical harmonic coefficients of the gravity field. Global tie parameters are combined by merging the parameters from different solutions into one set of parameters when adding several normal equations, as described in Sec. 2.7.1. The information content for these parameters is thus combined.

2.7.6 Combination with co-location on ground - local tie

Local ties are defined as locations on ground where multiple space geodetic techniques are situated in close proximity to one another. Consequently, the discrepancies between the techniques can be quantified with great accuracy through a local survey. A challenge thus arises in determining the reference point of the measurement station. In the case of SLR or VLBI, this is not a straightforward process, as the reference points in question are not accessible due to their location within the instrument or construction. For DORIS and GNSS the antenna mounting points are measured to which a calibrated PCO is added to give the absolute reference point for the combination. These phase centre patterns may pose similar problems for the GNSS and DORIS analysis as the reference points of large telescopes do.

The eccentricities between the techniques can be incorporated into the normal equation system as a relative constraint between a pair of coordinates. As outlined by f.i. Thaller (2008), the observation equation for the measured eccentricity, denoted by $\mathbf{l}_{LT}$, between two positions, $\mathbf{X}_1$ and $\mathbf{X}_2$, with a displacement of $\mathbf{X}_1 - \mathbf{X}_2 = \mathbf{l}_{LT}$, can be expressed as:

$$\mathbf{l}_{LT} + \mathbf{v}_{LT} = \mathbf{A}_{LT}\mathbf{x}_{LT} = \begin{bmatrix} -1 & 1 \end{bmatrix} \cdot \begin{bmatrix} \mathbf{X_1} \\ \mathbf{X_2} \end{bmatrix} \tag{2.71}$$

$$\mathbf{N}_{LT}\hat{\mathbf{x}}_{LT} = \mathbf{A}_{LT}^T \mathbf{P}_{LT} \mathbf{l}_{LT} \tag{2.72}$$

The strength of the local tie is considered by the weight matrix $\mathbf{P}_{LT}$. The resulting normal equation of the local tie $\mathbf{N}_{LT}$ can be applied, by adding it to the original normal equation system. In this thesis, local ties are not utilised, they are presented here for the sake of comprehensiveness and as a precursor to co-location in space.

$$(\mathbf{N} + \mathbf{N}_{LT})\hat{\mathbf{x}} = \mathbf{A}^T\mathbf{P}\mathbf{l} + \mathbf{A}_{LT}^T\mathbf{P}_{LT}\mathbf{l}_{LT} \tag{2.73}$$

2.7.7 Combination with co-location in space - space tie

A space tie is comparable to a local tie in that it involves the co-location of several techniques. However, in this case, the co-location occurs on a satellite that is in orbit around the Earth. Ideally, the eccentricities between the techniques should be determined with great precision prior to launch. The satellite can thus serve as a high-precision connection point for the techniques in space. Figure 2.8 illustrates a theoretical representation of a space-tie satellite, which incorporates the four main space geodetic techniques. As with local ties, a space tie can also be introduced at the normal equation level with relative constraints (see Sec. 2.7.6). Another method for the combination of several techniques by means of a space tie is achieved by the addition of common parameters at the normal equation level, which is used in this thesis. The common parameters are the dynamic parameters of the satellite orbit in each arc. Additionally, estimated empirical parameters used in the integrated POD of the space-tie satellite and the GPS constellation to achieve a more stable processing, are reduced prior to combination. This results in the transfer of information content to the orbital elements, which are then used for combination.

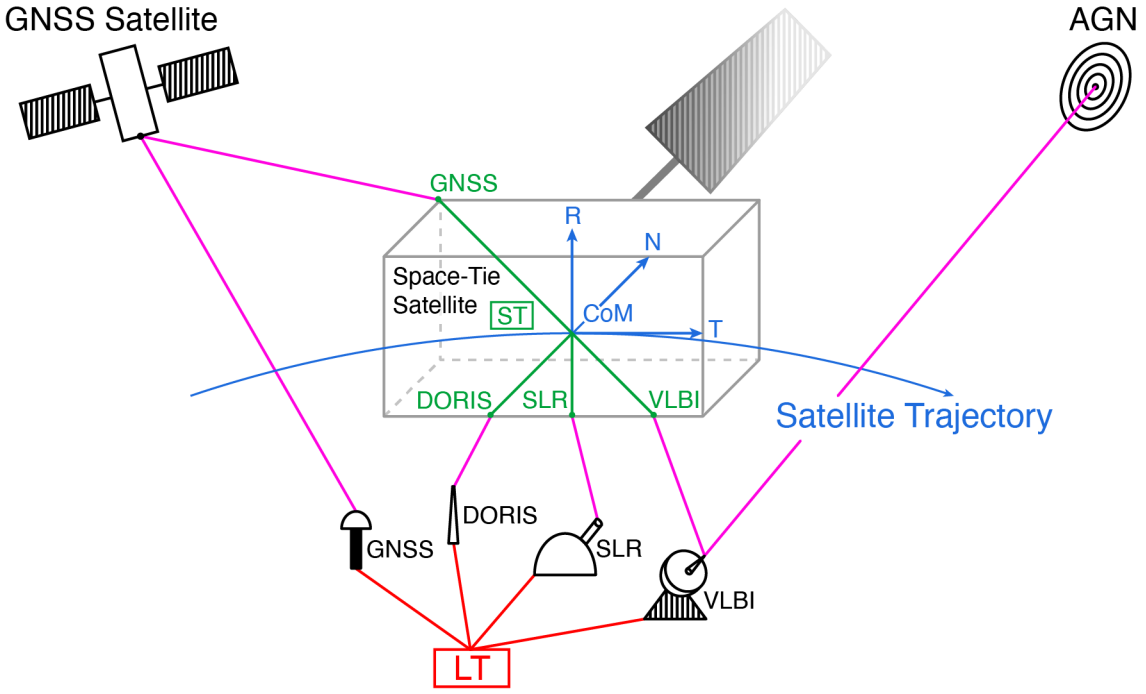

Figure 2.8: Theoretical sketch of a space-tie satellite and co-location in space.

3 Space geodetic techniques

Four main space geodetic techniques are currently used for determining the ITRF: DORIS, GNSS, SLR and VLBI. For each of these techniques, a dedicated service is operated by the IAG. These are the International DORIS Service (IDS), the International GNSS Service (IGS), the International Laser Ranging Service (ILRS) and the International VLBI Service (IVS). Fig. 3.1 shows an illustration of the structure of the IAG services contributing to the realisation of the ITRF. Each of the individual services generates a combined contribution for the respective technique from the contributions of its international Analysis Centers (ACs). These are then delivered to the ITRS combination centres for ITRF determination via the IERS Central Office. Each of these techniques has its own distinctive advantages and strengths. With regard to the determination of reference frames, the relevant techniques are listed in Tab. 3.1. Given that no single technique can address all aspects, a combination of the techniques is essential for a comprehensive realisation of the ITRS. The ITRS combination centres are responsible for carrying out this combination based on the input data sets, resulting in the generation of a TRF. The official ITRF product is generated by the ITRS Product Centre. As indicated by the green ticks in brackets in Tab. 3.1, the contribution of the corresponding technique to the parameter in question has not been included in the realisation of the respective parameter of the ITRF. This demonstrates that the full potential of the techniques and their combination is not yet being fully exploited, as there are residual systematic uncertainties in these parameters that preclude the combination. It is anticipated that the combination by means of co-location on a satellite in space will make a significant contribution to the resolution of this issue. The focus of this thesis is on the simulation analyses of DORIS, SLR and GPS for co-location in space. The aforementioned techniques are discussed in greater detail in Secs. 3.1, 3.2 and 3.3, respectively. The order is based on that of the individual single-technique analyses. As the GPS analysis differs slightly from the other two techniques, it is listed last. For the VLBI technique, the reader is referred to Mammadaliyev (2024), in which a simulation and analysis of VLBI for co-location on a satellite in space, in line with the present work, is investigated.

3.1 Doppler Orbitography and Radiopositioning Integrated by Satellite

The observation technique Doppler Orbitography and Radiopositioning Integrated by Satellite (DORIS) was developed by a joint venture between Centre National d'Études Spatiales (CNES), Institut National de l'information Géographique et Forestière (IGN), and Groupe de Recherche de Géodésie Spatiale (GRGS), in the 1990s as part of the TOPEX satellite mission with the objective of determining the orbit of satellites with high accuracy. As DORIS was originally developed for POD of scientific altimetry missions, it also became one of the four main space geodetic techniques, offering the potential to determine not only the satellite orbit, but also station positions, tectonics, polar motion and the Earth's gravity field. One of the technique's principal advantages is the homogeneous and dense distribution of ground stations, which is conducive to the determination of a TRF and allows comprehensive global observation coverage, including for satellites in lower orbits. The measurement technique permits highly precise orbit determination, particularly in the radial direction, which is of considerable interest for applications such as altimetry.

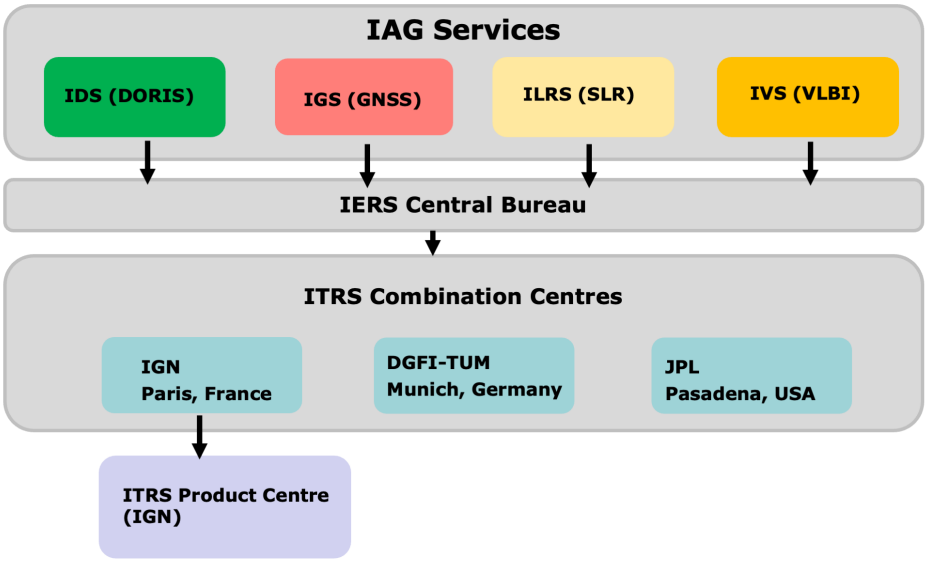

Figure 3.1: Overview of the IAG Services and the path to the ITRF (adapted from Seitz et al. (2015)).

Table 3.1: Overview of different capabilities of space geodetic techniques and their contribution to the ITRF2020 realisation. Information in brackets indicates that this contribution was not used for the realisation of the respective parameter. (Adapted from Rothacher (2003) and Altamimi et al. (2023)).

	DORIS	GNSS	SLR	VLBI
Radio source coordinates	×	×	×	✓
Nutation offsets	×	×	×	✓
Nutation rates	(✓)	(✓)	(✓)	×
Terrestrial pole	✓	✓	✓	✓
UT1-UTC	×	×	×	✓
LOD	(✓)	(✓)	(✓)	×
Station coordinates	✓	✓	✓	✓
Origin	(✓)	(✓)	✓	×
Scale	(✓)	(✓)	✓	✓

3.1.1 System components

3.1.1.1 Ground segment

The DORIS ground segment comprises approximately 60 ground stations distributed globally in a homogeneous manner (see Fig. 3.2). Each ground station is equipped with a transmitter, designated as the beacon (see Fig. 3.3), which emits on two frequencies, 400 MHz and 2 GHz. Furthermore, the stations are equipped with an Ultra Stable Oscillator (USO), an omnidirectional antenna, Uninterruptible Power Supply (UPS) and a package of measurement instruments for the recording of meteorological data. The initial generation of antennas was the Alcatel, the last of which was deactivated in 2008. The Starec antennas represent a more modern iteration of the antenna technology. They are utilised in versions B, C and D (D being the latest one) (see Fig. 3.4). As the signal is generated by the beacon, the ground

stations are also directly referred to as beacons. Ground beacons may be classified as Orbitography Beacons, Customer Beacons, or Location Beacons, as well as IDS Beacons, Time Beacons and Master Beacons (see Tab. 3.2). Orbitography beacons are mounted on geodetic points. In this configuration, a dedicated foundation ensures that the position of the antenna remains stable. Customer or Location beacons provide an accurate location for the customer, but do not disseminate data or coordinates as part of the IDS. Time beacons are orbitographic beacons, which exhibit a high degree of stability in terms of their frequency and time parameters. The stability of these stations is ensured by the precise control of their clocks in relation to the TAI atomic time standard, which is monitored by Multi-Mission Altimetry, Orbitography and Precise Positioning Ground Segment — French: Segment Sol multi missions ALTimétrie, Orbitographie et localisation précise (SSALTO). Mostly these beacons are linked to an external atomic clock. The highest level is represented by the master beacons, which, in addition to the time beacons, have a direct connection to the SSALTO. Through them, the current time information from all master and time beacons and the geographic positions of all beacons are uploaded to the satellites, which are necessary for the accurate functionality of the onboard receiver.

Table 3.2: Overview of DORIS master and time beacons

	Station code	Beacontype
Hartebeesthoek	HBMB	Master Beacon
Kourou	KRWB	Master Beacon
Papeete	PAUB	Master Beacon
Terre Adelie	ADGB	Time Beacon
Toulouse	TLSB	Master Beacon

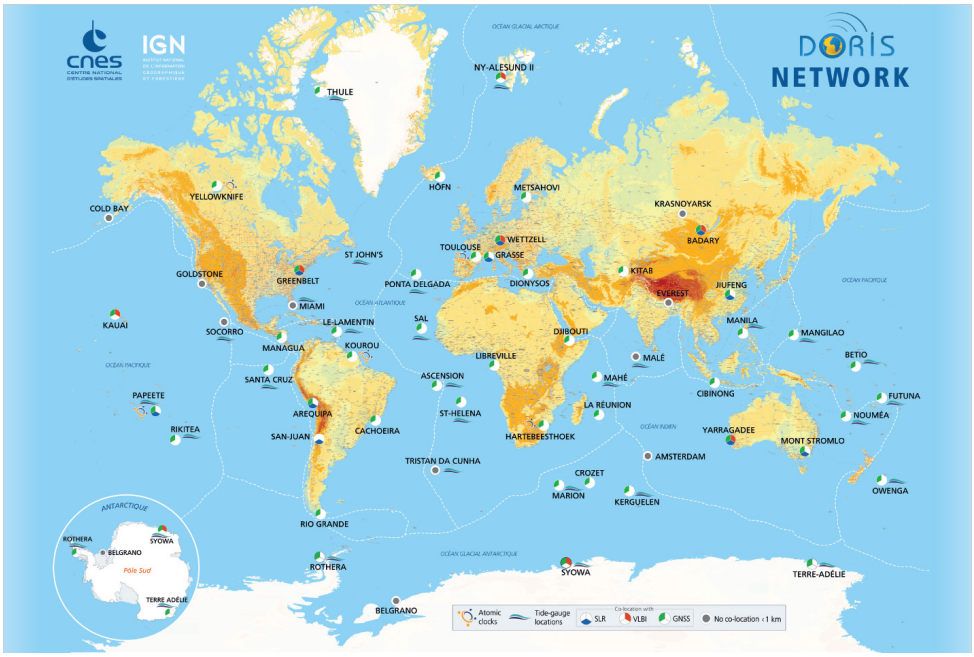

Figure 3.2: Map of the DORIS station network as of November 2020. Image citation. Cited from: CNES-CLS (2024).

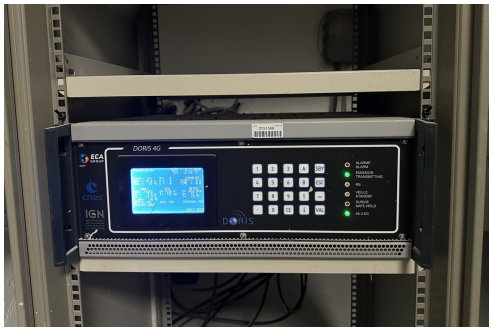

Figure 3.3: Picture of a DORIS ground beacon in Dionysos. Photograph by the author.



Figure 3.4: Picture of the Starec antenna in Terre Adélie. Image citation. Cited from: CNES (2024a).

3.1.1.2 Space segment

The space segment of DORIS is theoretically not limited in terms of the number of satellites that can be operated, given that it is a quasi-passive system. The ground stations only transmit the signal and are not necessarily in a two-way communication with the receivers. Nevertheless, communication links do also exist for the purpose of synchronising the onboard clock or receiving information from the satellite for the purpose of controlling the ground network in relation to the received signals. In this context, receiving satellites can be divided into those which only receive the signal and use it for their own purposes, and those which are contributing satellites. These also provide downstream data on the received DORIS data to the SSALTO ground segment for system analysis and monitoring.

3.1.1.3 Onboard receiver

To receive DORIS signals on a satellite, it is necessary to have a special receiver and an antenna orientated towards the Earth. The first generation of receivers was capable of tracking a single channel at a time and had a weight of 18 kg. Over time, these receivers have undergone significant technological advancement. Present-day receivers, such as the DGXX-S, are capable of simultaneously receiving up to seven channels and are equipped with a redundant unit that automatically switches to redundant in the case of a malfunction. The reduction in weight, which has decreased to approximately 1 kg, represents a significant enhancement, as it diminishes the payload mass (see Tab. 3.3 for further details).

3.1.2 International DORIS Service

The IDS was established in 2003 during the International Union for Geodesy and Geophysics (IUGG) General Assembly with the objective of fostering international collaboration in the domain of DORIS data analysis and the generation of scientific geodetic products based

Table 3.3: Overview of the development of DORIS receivers (CNES, 2024b)

	Year	Weight [kg]	Channels
1st Generation	1992-2013	18	1
2nd Generation	2002-2012	5.5	2
2nd Generation miniaturised	2001-2015	3	2
Intermediate DGXX	not oper. used	3	2
Full DGXX and DGXX-S generation	2008-utd	1.15	2x7 (redundant)

on the DORIS technique, within the framework of the IERS. The IDS generates scientific products that contribute to GGOS under the guidance of the IAG, functioning as an IAG service (Willis et al., 2010). In 2024, six ACs and four Associate Analysis Centerss (AACs) have been active within the IDS. The contributions of the IDS ACs are combined by the IDS Combination Center (CC), which is responsible for generating the IDS's contribution to the generation of the ITRF. Further details regarding the generation and combination of the IDS contribution can be found in Willis et al. (2015b). Moreover, the IDS CC generates and provides a special adaptation of the ITRF for DORIS, known as the DPOD (DORIS extension of the ITRF for Precise Orbit Determination) (Moreaux et al., 2023a).

3.1.3 Measurement principle

The principle of the observation of DORIS is based on the Doppler effect. Ground beacons, which are distributed globally, emit a constant frequency electromagnetic signal. DORIS-equipped satellites orbiting the Earth pass the ground station, receive the signal, and track the pseudorange and phase of the signal. As the satellites pass the horizon of the ground station, the distance of the transmitted signal changes, resulting in a Doppler shift of the radio frequency. The Doppler shift in the received signal onboard the satellite can be expressed in terms of the wavelength as:

$$\lambda_{received} = \lambda_{ground} - v_{satellite} \cdot \Delta t \tag{3.1}$$

with

- λ_{ground} – Wavelength of the beacon on ground
- $\lambda_{received}$ – Received wavelength onboard the satellite
- $v_{satellite}$ – Velocity of the satellite in the direction of the ground station
- Δt – Doppler integration interval

The receiver generates measurements every 3 and 10 seconds (0s, 3s, 10s, 13s, 20s, 23s, etc.). Noteworthy, EPOS-OC uses only those observations taken at the 10-second interval, which aligns with the Doppler integration interval of the formerly used Doppler range rate observations given in the DORIS data exchange format (CNES, 2008). The typical level of precision for a common Doppler range rate observation over an integration interval of 10 seconds is approximately 0.3 mm/s, which corresponds approximately to 3 mm of phase observation.

3.1.4 DORIS observation in EPOS-OC

The initial format for the provision of real DORIS observation data was the DORIS data exchange format for range rate observations. This format provides measurements of range rate, the count interval, and information regarding the application of corrections, such as the tropospheric correction. Following the launch of the Jason-2 satellite, this format was superseded by the Receiver INdependent EXchange format (RINEX) format, which remains in use today. The RINEX format differs from the previous one in that it provides direct pseudorange and carrier phase measurements at the two DORIS frequencies, rather than the range rate, which can be calculated from the phase observations.

As EPOS-OC is not yet capable of directly processing DORIS pseudorange and phase observations, this thesis makes use of Doppler range rate measurements. Accordingly, the phase measurements provided in the DORIS RINEX observation files are subject to a preprocessing procedure that consists of the following steps. The explanations and values presented herein are based on the current state-of-the-art in DORIS equipment, which refers to the Starec ground antennas. The following implementations and their underlying mathematical principles are originally published in Schreiner et al. (2023), to which reference is made here.

The two frequencies used within DORIS are $f_1 = 2036.25$ MHz and $f_2 = 401.25$ MHz. Prior to any other considerations, the frequency shift of the DORIS beacons is taken into account. The use of shifted frequencies for beacons serves to avoid Doppler collisions. As a result, the nominal frequency of the emitted signals of a station is shifted by a small amount. This allows modern DORIS receivers to correctly distinguish signals from multiple ground stations. The station frequency shift factor, denoted by the variable k, is specific to each station and is stated in the RINEX observation files. The fundamental frequencies that have been shifted are given by:

$$\begin{aligned} f_1 &= 543 \cdot F_0(\frac{3}{4}) + (\frac{87 \cdot k}{5 \cdot 2^{26}}) \\ f_2 &= 107 \cdot F_0 \cdot (\frac{3}{4}) + (\frac{87 \cdot k}{5 \cdot 2^{26}}) \end{aligned} \tag{3.2}$$

with:

- k – Integer station frequency shift factor between -90 and +90
- F_0 – $5 \cdot 10^6 Hz \pm 0.21$ USO frequency of the beacon

with these we can form the frequency relation (γ) for the ionosphere-free linear combination, which is independent of the k-factor:

$$\gamma = \frac{f_2^2}{f_1^2} = 25.75325356 \tag{3.3}$$

and the ionosphere-free linear combination for the measurement points i and $i+1$ of the 2 GHz signal:

$$\begin{aligned} L_{1,i,iono-free,2GHz} &= L_{1,i} + \frac{L_{1,i} - \sqrt{\gamma} \cdot L_{2,i}}{\gamma - 1} \\ L_{1,i+1,iono-free,2GHz} &= L_{1,i+1} + \frac{L_{1,i+1} - \sqrt{\gamma} \cdot L_{2,i+1}}{\gamma - 1} \end{aligned} \tag{3.4}$$

with

L_1 – Phase measurement at 2036.25 MHz

L_2 – Phase measurement at 401.25 MHz

i – Epoch

From these two ionosphere-free measurements the difference between the two data points can be calculated. This gives the integrated Doppler count N_{DOP} for the time period Δ_t:

$$N_{DOP} = -(L_{i,i+1,iono-free,2GHz} - L_{1,i,iono-free,2GHz}) \tag{3.5}$$

Given that the formation of an ionosphere-free linear combination of phase measurements was undertaken with the purpose of determining the integrated Doppler count, it follows that the ionosphere-free reference points must be used for both the ground and satellite antennas. Accordingly, this can be express as:

$$PCO_{iono-free} = \frac{f_1^2}{(f_1^2 - f_2^2)} \cdot PCO_{f_1} - \frac{f_2^2}{(f_1^2 - f_2^2)} \cdot PCO_{f_2} \tag{3.6}$$

Based on the integrated Doppler, the Doppler range rate can be calculated:

$$DRR = c \cdot (1 + \Delta_{fbeac}) \cdot \frac{1}{f_{beac}} \cdot \frac{-N_{DOP}}{\Delta_t} \tag{3.7}$$

with:

DRR – DORIS range rate measurement

c – Speed of light

$\Delta_{f_{beac}}$ – Ground beacon frequency bias in Hz

f_{beac} – Ground beacon frequency (2.036250 GHz)

N_{DOP} – Integrated Doppler count

Δt – Doppler count interval duration

The calculated range rate measurements are those provided in the DORIS data exchange format. This allows the same observation input to be used in EPOS-OC as for conventional range rate measurements. However, EPOS-OC makes use of the actual Doppler count itself as the theoretical measurement to be measured. Therefore, this range rate measurement is converted to the integrated Doppler count value according to the following equation:

$$zmes = \Delta t \cdot (f_{beac} \cdot (1 - \frac{DRR}{c}) - f_{sat}) \tag{3.8}$$

with:

$zmes$ – Measured integrated Doppler count measurement

f_{sat} – Actual satellite frequency (nominal: 2.036125 GHz)

The theoretical measurement in EPOS-OC is described by:

$$ztheo = \frac{Dist_{t_1} - Dist_{t_2}}{\lambda} - \Delta_t \cdot \Delta_{f_{beac}} + \Delta_{Tropo} + \Delta_{Relat} - \Delta_{Phase} \tag{3.9}$$

with:

$ztheo$ – Theoretical measurement as integrated Doppler count

$Dist_{t_1}$ – Euclidean distance between station and satellite at Doppler count start interval t_1

$Dist_{t_2}$ – Euclidean distance between station and satellite at Doppler count end interval t_2

λ – Carrier wavelength

In this formula, the first term of the sum represents the theoretical value of the Doppler count resulting from the satellite's movement towards the ground station. The remaining terms of the sum pertain to the influence of the ground station's frequency bias, tropospheric effects, relativistic effects, and the phase variation of the signal.

3.1.5 Technique-specific obstacles

Significant technical obstacles for DORIS include the influence of the South Atlantic Anomaly (SAA) on the USO of the satellites and the time synchronisation of the system, both of which will be explained in more detail below. Another drawback is the noise in the DORIS code observations, which prevents the phase ambiguities from being resolved using the same strategy as for GNSS.

3.1.5.1 South Atlantic Anomaly

The SAA is a region in the southern Atlantic that moves slowly over South America. It is characterised by a higher proton flux compared to the rest of the world, which can be attributed to anomalies in the inner Van Allen radiation belt (Ginisty et al., 2024). This in turn affects the quartz USO, which is used on board the satellite, given that it is highly sensitive to radiations. Moreover, anomalous frequency glitches and irregular clock behaviours can be observed, resulting in distortion of the phase measurement. This results in inaccuracies in the determination of station positions within the SAA, for example. One common method of addressing this issue is to downweight or even exclude these stations from the POD process, or to adjust parameters empirically to mitigate this effect. For example, this could involve accounting for frequency drift over the SAA region during each pass. Another option for satellites with a GNSS receiver on board and connected to the same USO is to transfer the GNSS clock estimates to the DORIS measurement. However, this is only possible if the two techniques utilise the same USO. Fig. 3.5 shows the region where a higher dose exposure can be detected.

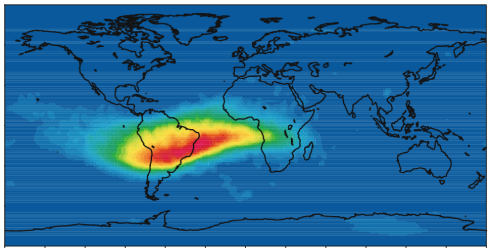

Figure 3.5: Visualisation of the higher dose exposure over the SAA region for an altitude of 1'300 km. Colour scale from low exposure in blue to high exposure in red. Image citation, adapted. Cited from: Lemoine & Capdeville (2006).

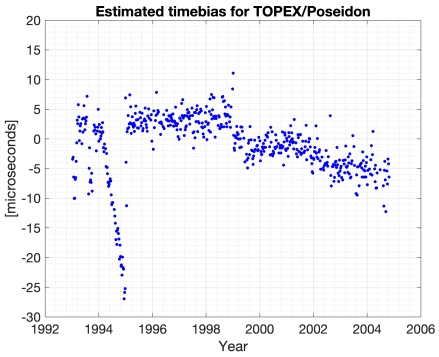

Figure 3.6: DORIS time bias for TOPEX relative to SLR, calculated at GFZ.

3.1.5.2 DORIS time-bias

DORIS observations are received and generated on board the satellite and given a timestamp whose time information comes from the USO on board. The satellite's clock must be synchronised to a reference time. This is done using a time transfer at time beacons which, for the on-board USO, provide a correspondence to International Atomic Time (TAI) with an accuracy of about 1 microsecond today. Remaining differences in the time stamping procedure can be resolved, e.g., with the Time Transfer by Laser Link (T2L2) system (Belli et al., 2020), which was so far only put onboard the Jason-2 satellite, or with a common onboard USO for the DORIS and GNSS receivers, if applicable. This allows the behaviour of the on-board clock to be evaluated directly via GNSS. If the satellite carries other tracking techniques, any inter-technique time bias can be solved for in a POD process, e.g. by fixing the DORIS-only orbit. Fig. 3.6 shows the DORIS time bias for TOPEX relative to SLR derived using this approach.

3.1.6 Open potential for reference frame determination

Currently, DORIS does not contribute to the origin and scale of the ITRF (Altamimi et al., 2023). Since the processing of DORIS-based reference frames began in the 1990s, starting with the TOPEX mission, the derived scale shows unclear artefacts such as an offset or drift in comparison to SLR and VLBI, which define the scale of the ITRF-2020. The calibration of the scale between different DORIS satellite missions, and the exclusion of missions for this reason, is also an issue that has not been finally resolved (Moreaux et al., 2023b). Because of these issues, the DORIS ground segment antennas, Alcatel and Starec, were used in a calibration campaign for high-precision chamber calibration. This was also a key factor in providing more precise information on the absolute phase centre position of the antennas (Tourain et al., 2016). However, this scale uncertainty has not yet been fully resolved.

3.2 Satellite Laser Ranging

Since the development of the laser (around 1960), SLR has been used to measure geometric distances to various satellites in orbit. It is the only measurement principle that uses the optical spectrum of electromagnetic waves, and therefore is not capable of penetrating, for instance, clouds. The only requirement for the satellites is the installation of a passive reflector element. Measurements can be made to either purely passive satellites (geodetic

satellites) or to other satellites that have been equipped with reflectors to use SLR for backup orbit determination, orbit quality control and calibration. The first satellite to be equipped with reflectors was BEACON Explorer B, which was launched on 9 Nov. 1964 as part of the American Explorer programme (Seeber, 2003). The first successful SLR measurement followed shortly afterwards in 1965, achieving an accuracy of a few metres. Since then, the accuracy has steadily improved over the years and is now within a few millimetres (McGarry et al., 2018).

3.2.1 System components

3.2.1.1 Ground segment

The SLR ground segment consists of approximately 40 stations distributed across the globe (see Fig. 3.7). In comparison to other techniques, the number of stations is not as high due to the significant financial investment required for each station. Furthermore, the distribution is less homogeneous than in the case of DORIS, for example, because possible locations of the stations are restricted by external conditions such as cloud coverage, rainy seasons, snow, dust or connection to civilisation. Figure 3.8 shows the Potsdam SLR station during a night measurement, serving as an illustrative example of a station within the global ground segment.

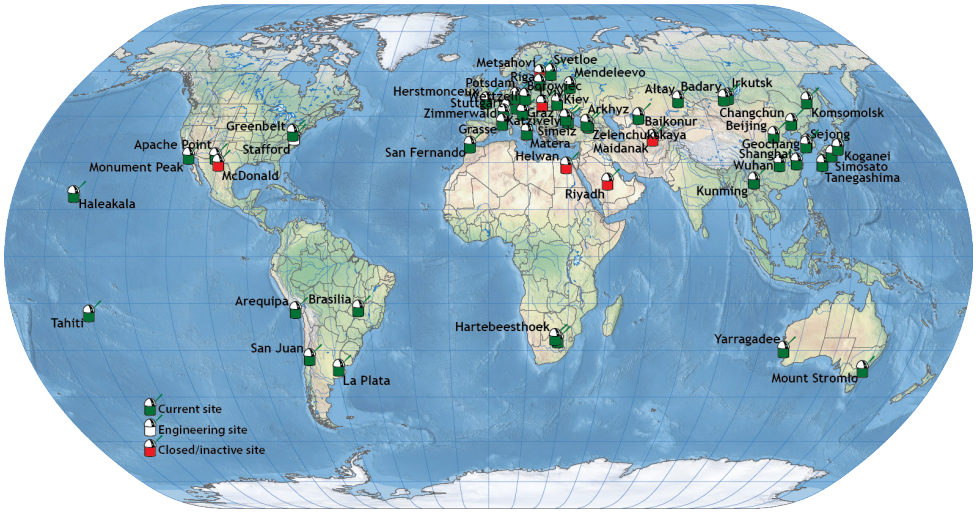

Figure 3.7: SLR station network. Image citation. Cited from: NASA (2024).

3.2.1.2 Space segment

The SLR space segment used within the ILRS for the determination of Earth system parameters are geodetic satellites, which are satellites designed and constructed with the specific intention of being observed with SLR. These satellites are designed as spheres with reflectors on the outside and are usually made of very dense material to achieve a low area-to-mass ratio. This reduces the sensitivity of the satellite's motion to perturbations such as atmospheric drag or solar radiation pressure. Fig. 3.9 illustrates a selection of prominent geodetic satellites, including LAGEOS (fifth from the left), which plays the most significant role in the determination of an SLR-based reference frame.

3.2.2 International Laser Ranging Service

The ILRS is a geodetic service operating under the umbrella of the IAG. It was established in September 1998 with the objective of supporting geophysical research and participating in the definition of the ITRF (Pearlman et al., 2002). Today the ILRS additionally supports the activities of GGOS. The ILRS collects, archives, analyses and provides observations from over 40 observing stations. The SLR observations are analysed by the ILRS ACs and subsequent solutions are combined by the ILRS CC. The ILRS contribution to the ITRF2020 was formed by a combination of seven ACs, as documented in Pavlis & Luceri (2022). The ITRF adaptation of the ILRS is called the SLRF and provides station coordinates and velocities and the Data Handling File (DHF) (Rodríguez et al., 2019).

3.2.3 Measurement principle

The measurement principle is based on the travel time of light from the ground station to the satellite and back. The SLR station transmits a laser pulse to the satellite, which is reflected by a retroreflector on the satellite, and the reflected pulse is received back at the station. While the pulse repetition rate was in the low double-digit range in the early days, it is now in the kilohertz range, and megahertz lasers are already in development at some stations.

The basic observation data product for SLR analysis consists of Normal Points (NPs). The formation of NPs reduces the noise in the observations and reduces the amount and number of observations, which are usually highly correlated, so that no valuable information is lost (Kucharski et al., 2015). Full-rate data on the other hand can be used for special applications, such as determining the spin of a satellite (Kucharski et al., 2012). NPs are processed over a given interval of time, known as the bin size.

The observation equation for two-way ranging is written as follows:

$$\Delta t = \frac{2}{c}(d_{gr}^{S} + \delta_{tro}) + \frac{1}{c}\delta_{sys} + \epsilon \tag{3.10}$$

with:

- Δt – Observed time interval between the emission of the laser pulse and the detection of the reflected pulse
- d_{gr}^{S} – One way distance between observation station and satellite
- c – Speed of light
- δ_{tro} – Delay of the signal due to the troposphere
- δ_{sys} – Correction due to the signal delay in the system
- ϵ – Time interval measurement error

The precision with which a time interval can be measured currently reaches several picoseconds. It is possible to further divide a measured time interval into two parts: an interval Δt_1 describing the path of a pulse from the observing station (denoted by $\mathbf{r}_{gr}$) to a satellite (denoted by $\mathbf{r}^{S}$), and another interval Δt_2 describing the subsequent path from the satellite to the measuring station. The time measurement can thus be written as follows:

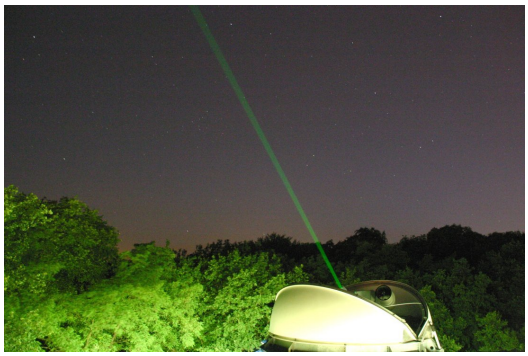

Figure 3.8: SLR station in Potsdam. Image citation. Cited from: GFZ (2026).

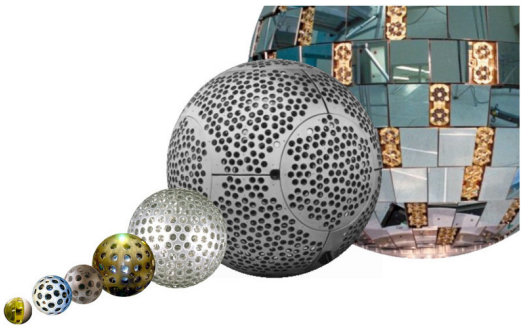

Figure 3.9: Compilation of well-known geodetic satellites. LAGEOS, the most important for reference frame determination, is shown fifth from left. Image citation. Cited from: NERC (2024).

$$\Delta t_{gr}^{S} = \Delta t_1 + \Delta t_2 = \frac{1}{c}(|\mathbf{r}^S(t^S) - \mathbf{r}_{gr}(t^S - \Delta t_1)| + |\mathbf{r}^S(t^S) - \mathbf{r}_{gr}(t^S + \Delta t_2)|) \tag{3.11}$$

The two position vectors of the SLR observation station, $\mathbf{r}_{gr}$, at time epochs $(t^S - \Delta t_1)$ and $(t^S + \Delta t_2)$, can be approximated by neglecting the higher-order terms of a Taylor series expansion:

$$\mathbf{r}_{gr}(t^S - \Delta t_1) \approx \mathbf{r}_{gr}(t^S - \frac{1}{2}\Delta t_{gr}^{S}), \mathbf{r}_{gr}(t^S + \Delta t_2) \approx \mathbf{r}_{gr}(t^S + \frac{1}{2}\Delta t_{gr}^{S}) \tag{3.12}$$

In this manner, the interrelationship between the time measurement vectors and the position vectors can be expressed as follows:

$$\Delta t_{gr}^{S} = \frac{2}{c}|\mathbf{r}^S(t^S) - \mathbf{r}_{gr}(t^S))| \tag{3.13}$$

3.2.4 SLR observation in EPOS-OC

In EPOS-OC, the extended observation equation of an SLR measurement holds for the range between ground station and satellite, with the corrections to be applied:

$$d(t^S) = \frac{1}{2}c\Delta t + \delta_{rel} + \delta_{rot} + \delta_{gr} + \delta_{RB} + \delta_{CoM} + \delta_Z m_f + \epsilon \tag{3.14}$$

whereby:

- $d(t^S)$ – One way distance from the observation station to the satellite at time t^S.
- t^S – Epoch of the observation
- c – Speed of light
- Δt – Measured runtime
- δ_{rel} – Relativistic correction

δ_{rot} – Corrections due to the rotation of the Earth and satellite motion in the inertial system

δ_{gr} – Corrections of the measuring point to the reference point of the observation station

δ_{RB} – Range bias (RB) of the observing station

δ_{CoM} – Center of Mass correction of the satellite

$\delta_{Z}m_{f}$ – Correction of the troposphere delay at zenith mapped to slant range

ϵ – Random errors

The correction of the SLR measurement point to the reference point of the observing telescope describes the process of aligning the point where the return pulse is detected to the intersection of the telescope axes. Range bias corrections are the result of errors in the measurement electronics or faulty calibrations. The ILRS provides recommendations for range or time bias corrections to be applied over longer time intervals, which are provided in the DHF. The estimation of a range bias results in a reduction in the DoF, and a range bias estimate is highly correlated with the height component of the station. The term Center of Mass (CoM) correction describes a distance that is added to the range, as the measured range refers to the distance to a reflector on the satellite. However, the dynamic orbit determination models the motion of the centre of mass of the satellite. Corrections due to the delay in the travel time of the laser pulse as it passes through the atmosphere, specifically the troposphere in the case of visible light, are described by a model that includes a correction to the signal at zenith and a mapping function from which a correction can be calculated for the particular elevation angle (Mendes & Pavlis, 2004). The distortion of the signal by the ionosphere is below 0.1 μm for the wavelengths employed in SLR, and thus can be considered negligible (Seeber, 2003).

3.2.5 Technique-specific obstacles

In SLR, there are several obstacles that hamper optimal data. These include network-related effects such as the non-optimal global distribution of ground stations. However, as purely technical effects, the two most significant influences, range and time bias are discussed below.

3.2.5.1 Range bias

Range biases are one of the most significant factors limiting the accuracy of SLR-derived geodetic products (Appleby et al., 2016). These biases can be caused by time walk effects, range calibration errors, temporal system delays, refraction correction errors resulting from inaccurate barometric measurements, and amplitude variations in the event timer system (McGarry et al., 2018), to name just a few causes. Range biases are dependent on the station, satellite and time. Empirically determined range bias values can be used for correction in the POD, which are published by the ILRS in the DHF. However, these biases can only be used for other satellites to a limited extent. Rodríguez et al. (2019) states that the station-dependent bias is assumed to be accurate to about 2 mm, but satellite-specific biases may remain. Therefore, it is common practice to estimate range biases in the POD for satellites that are not provided with range biases in the DHF. However, this leads to a reduction in the DoF, and the biases are highly correlated with the height component of the

station position (Coulot et al., 2009). Estimated biases can also absorb systematic offsets in the orbit, e.g. in the case of SLR orbit validation (Arnold et al., 2018), or in the on-board SLR reference point (Otsubo & Appleby, 2003).

3.2.5.2 Time bias

SLR time biases affect the time epoch of the measurement. These can be caused by instabilities in the timekeeper, calibration errors or thermal effects, for example. Most time biases for SLR stations were found to be very small (Luceri et al., 2019). However, Exertier et al. (2017) showed, through the T2L2 project (Samain et al., 2008), that time biases of several microseconds can be found for individual stations. The influence on estimated station coordinates was found to be most significant in the East-West component, at several millimetres. The ILRS also provides recommendations for applying time bias corrections in the DHF.

3.3 Global Navigation Satellite Systems

GNSS began with the NAVigational Satellite Timing And Ranging (NAVSTAR) GPS developed by the United States Department of Defense (USDOD) in the 1970s. In the subsequent years, further satellite navigation systems followed, in chronological order of development: the Russian GLONASS, the Chinese Beidou, and the European Galileo. In addition to GNSS, there are also some regional navigation systems, called Satellite-Based Augmentation Systems (SBAS), such as the Japanese Quasi-Zenith Satellite System (QZSS). These satellites are used in addition to, for instance, GPS observations to achieve a more precise positioning.

3.3.1 System components

Each of the aforementioned satellite systems can be divided into several segments. Here, we divide them into four subgroups, each of which is described in greater detail with respect to GPS, as it is the system used exclusively in the following.

3.3.1.1 Space segment

The space segment is comprised of up to 32 satellites, though not all are typically active or in operation simultaneously. The satellites are distributed across six orbital planes at an altitude of approximately 20’200 km, with an inclination of approximately 55 degrees and an orbital plane separation of 60 degrees. A single revolution of a GPS satellite lasts for about 11 hours and 58 minutes. The constellation has a repeat cycle of two revolutions, meaning that a fixed point on Earth will see the exact same constellation of GPS satellites after 23 hours and 56 minutes.

3.3.1.2 Control segment

The Operational Control System (OCS) for GPS is comprised of the Master Control Stations (MCS), monitor stations, and ground antennas. The MCS bears responsibility for the monitoring, control and general operation of the system. The monitor stations are dedicated ground observation stations, which transfer their data to the MCS, thereby enabling the latter to conduct comprehensive global control of the transmitted signals. The ground antennas are employed for communication with the satellites and transmit data, including the broadcast messages, to the satellites.

3.3.1.3 User segment

The user segment includes all GPS receivers. These can be either ground stations, such as those in the IGS, or receivers in mobile phones, cars, aircraft or on satellites.

3.3.1.4 Ground segment

In addition to the three official system components, the ground segment can also be defined as a system component. There are several networks of receivers that are used for specific types of service. This includes, for instance, the global network of receivers associated with the IGS. This network, which in 2024 consisted of more than 500 ground stations distributed across the globe, is used for the operational generation of IGS products, including orbit and clock products. Furthermore, it serves as the basis for the determination of ERPs and station coordinates in the context of the IGS, thus contributing to the ITRF. Figure 3.10 illustrates the network of IGS ground stations. In comparison to other techniques, the large number and global distribution of receivers is remarkable (NCO, 2022).

3.3.2 International GNSS Service

The IGS was established in August 1993 by the IAG and commenced its operations in 1994 (Johnston et al., 2017). The IGS has set itself a number of objectives, one of which is the public dissemination of GNSS data, including that from the IGS network, as well as products such as orbits and clock solutions (Dow et al., 2005). Moreover, the IGS contributes to the ITRF and is committed to providing the scientific community with continuous Earth monitoring. The IGS currently comprises over two hundred international research institutes, national agencies and the like. The IGS contribution to the ITRF2020 (Rebischung et al., 2024) was formed by contributions from 10 ACs and generated by a combination carried out by the IGS CC, which also generates the IGS adaptation of the ITRF2020, consisting of station coordinates, as well as PCO and Phase Center Variation (PCV) calibration values for ground receivers and transmitting satellites.

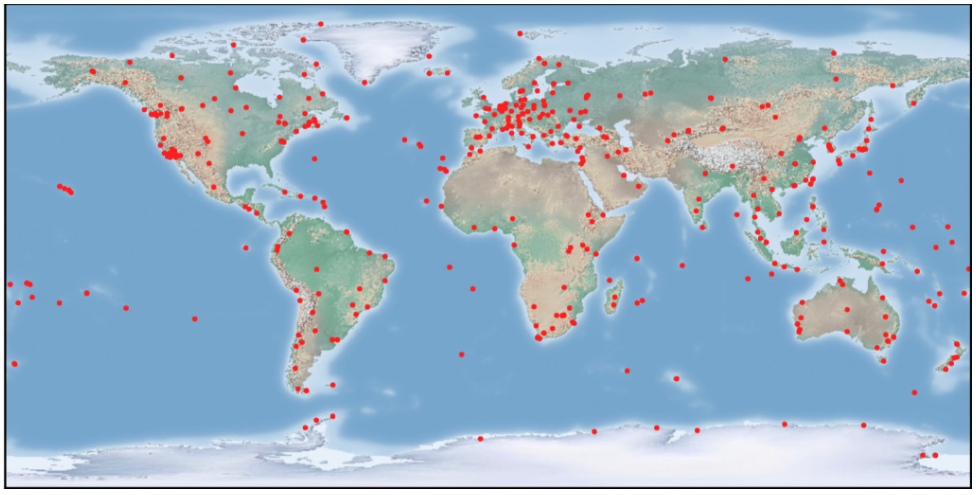

Figure 3.10: Map of the IGS GNSS station network. Image citation. Cited from: International GNSS Service (IGS) (2022).

3.3.3 Measurement principle

The principle of GPS is based on radio frequency signals emitted by the GPS satellites and received by the receiver. The transmitting satellites emit different signals with a frequency

of a few GHz in the so-called L-band. This has the advantage that this waveband of the microwave spectrum can effectively penetrate the atmosphere and is more resistant to ionospheric effects, thus ensuring the robustness of the signal. The signals transmitted are all derived from the fundamental frequency generated by the atomic clock on board the satellite. For GPS, this fundamental frequency is 10.23 MHz. Current GPS satellites transmit on three different ground frequencies. While older satellites only transmit on L1 and L2, newer satellites, such as Block III satellites, also transmit on L5. These signals have a different frequency, which differs from the fundamental frequency by a multiplication factor. This factor is 154 for L1, 120 for L2 and 115 for L5, resulting in frequencies of 1575.42 MHz, 1227.60 MHz and 1176.45 MHz, respectively. A code is modulated on these ground frequencies using phase modulation. The observation equation for pseudorange (code) measurements can be written as:

$$P_r^s = r_r^s + c\delta t_r - c\delta t^s + T_r^s + \frac{f_{ref}^2}{f_n^2} I_r^s + \epsilon^P \tag{3.15}$$

whereby:

- P_r^s – Measured pseudo distance
- r_r^s – Geometric distance between receiver and sender
- $\delta t_r, \delta t^s$ – Receiver and sender clock correction to GPS time
- T_r^s,I_r^s – Delays due to troposphere and ionosphere
- $\frac{f_{ref}^2}{f_n^2}$ – Fractional scaling of the ionosphere for frequency n with respect to the reference frequency
- ϵ^P – Pseudorange random errors

And the observation equation for phase measurements as:

$$L_r^s = r_r^s + c\delta t_r - c\delta t^s + T_r^s - \frac{f_{ref}^2}{f_n^2} I_r^s + \lambda N_r^s + \epsilon^L \tag{3.16}$$

whereby:

- λN_r^s – Ambiguity of the phase
- ϵ^L – Phase random errors

Note that the ionosphere effect on the phases causes an advance rather than a delay as with the code. In addition, when observing phases, there is also the part of phase ambiguities. Apart from the random errors, all other quantities in the code and phase equations are equal due to the coherent signals. The noise levels of the code and phase observations in the ionospheric-free linear combination are approximately 50 cm and 5 mm, respectively.

3.3.4 GNSS observation in EPOS-OC

The processing of GPS observations in EPOS-OC is based on the ionosphere-free linear combination of two code and two phase observations, respectively. The ionosphere-free code observation results in:

$$C_{Iono-free} = \frac{f_1^2}{(f_1^2 - f_2^2)} \cdot C_1 - \frac{f_2^2}{(f_1^2 - f_2^2)} \cdot C_2 \tag{3.17}$$

and the corresponding ionosphere-free phase observation:

$$L_{Iono-free} = \frac{f_1^2}{(f_1^2 - f_2^2)} \cdot L_1 - \frac{f_2^2}{(f_1^2 - f_2^2)} \cdot L_2 \tag{3.18}$$

whereby:

- f_1 – 1.57542 GHz
- f_2 – 1.22760 GHz
- C_i – Pseudorange observation on frequency channel i
- L_i – Carrier phase observation on frequency channel i

These observations are subsequently processed in EPOS-OC as zero-difference observations. The observation equation for zero-difference Satellite-to-Satellite Tracking (SST) observations of a receiver on a satellite can be written as follows:

$$L_{Iono-free,t} = |r^{sender}(t - \rho/c) - r_{receiver}(t)| + c(\delta t_{receiver}(t) - \delta t^{sender}(t - \rho/c)) + \delta_{rel} + \epsilon \tag{3.19}$$

with:

- $r^{sender}(t)$ – Geocentric position vector of the sender
- $r_{receiver}(t)$ – Geocentric position vector of the receiver
- $\delta t^{sender}(t)$ – Clock error of the sender
- $\delta t_{receiver}(t)$ – Clock error of the receiver
- δ_{rel} – Relativistic corrections
- ρ/c – Light travel time from the GPS satellite to the receiver for the distance ρ between the satellite and the receiver
- ϵ – Random errors

Since the ionosphere-free linear combination is used here as an observation, this also refers to the associated ionosphere-free phase centre reference points of the receiver and transmitter antennas (the so-called PCO), which are calculated accordingly:

$$L_{Iono-free,PCO} = \frac{f_1^2}{(f_1^2 - f_2^2)} \cdot L_{1,PCO} - \frac{f_2^2}{(f_1^2 - f_2^2)} \cdot L_{2,PCO} \tag{3.20}$$

3.3.5 Technique-specific obstacles

The processing of GNSS data is hindered by a variety of obstacles. These can include signal distortions in the troposphere and ionosphere, as well as multipath, ambiguities, and cycle slips, to name just a few. Technical obstacles that significantly influence POD in GPS do include the limitied availability of satellite-specific information and the need to resolve epoch-specific clock parameters. These will be discussed in more detail below.

3.3.5.1 Availability of satellite-specific information

GPS satellite specifications, such as absolute attitude information, satellite design and transmitter antenna characteristics, are not made publicly available.

Kouba (2008) demonstrates the importance of highly accurate attitude information from GPS satellites, which is essential in POD for the computation of the orientation of the antenna, the associated calculation of the centre of mass, the determination of disturbance forces and phase wind-up corrections. Various models have been developed and optimised for attitude modelling, especially in shadow passages (Bar-Sever, 1996; Kouba, 2008), which arise from the necessity that deviations from the nominal orientation of the satellite are not known. As part of the IGS, attitude information is published by the ACs, which is derived from the attitude models implemented in the different software packages. Yang et al. (2021) investigates their use for precise point positioning ambiguity fixing and underlines their effectiveness and importance.

Another point is the exact design of the satellites and materials used. This makes the construction of box-wing models, which can be used within POD for calculating radiation pressure, significantly more difficult (Steigenberger et al., 2020). For the modelling of radiation pressure, various box-wing models for GPS satellites were generated (Rodriguez-Solano et al., 2012; Steigenberger et al., 2020), as well as analytical models such as ROCK (Fliegel et al., 1992) and empirical modelling approaches such as the widely used ECOM (Springer et al., 1999; Arnold et al., 2015).

Furthermore, transmitter antenna characteristics such as PCOs and transmitt power are not publicly known from manufacturer's calibration. PCO values can be estimated over longer periods of time in GNSS processing with chamber-calibrated ground stations (e.g. Schmid et al., 2007). For Galileo, where the manufacturer's values have been published, deviations in the decimetre range were found between estimated values (Steigenberger et al., 2016) and manufacturer's values (EUSPA, 2023). The inclusion of LEO satellites with chamber-calibrated PCOs and PCVs has proven helpful in this regard (Haines et al., 2015; Huang et al., 2020). Another method is to transfer the scale of Galileo with manufacturer values for PCO and PCVs to other GNSS (Villiger et al., 2020).

The radiation characteristics of satellites can be measured using high-gain antennas (Steigenberger et al., 2024) and subsequently taken into account in POD.

3.3.5.2 Clock biases

The need to estimate epoch clock parameters in GNSS processing is an obstacle, which can also be considered technical due to its origin. Due to various influences, GNSS satellites' clocks are subject to high-frequency disturbances that cannot be predicted with sufficient accuracy (Hauschild & Montenbruck, 2008).

For many kinematic positioning tasks high-resolution GNSS orbit and clock solutions are necessary. Computing these high-resolution clocks requires a considerable amount of

processing due to the large number of parameters involved. Approaches such as carrier phase clock interpolation can offer an efficient solution to this problem (Hesselbarth & Wanninger, 2008).

It is also common practice for ground stations to estimate epoch clock offsets. However, these are highly correlated with the height component of the stations, among other things. For ground stations with less stable clocks, this is unavoidable, however for stations with highly stable masers, approaches such as stochastic clock modelling can be highly effective in improving positioning (Wang & Rothacher, 2013; Weinbach, 2013).

For future GNSS constellations, optical clocks (Boldbaatar et al., 2023) or new observation types, such as inter-satellite range links, inter-satellite clock synchronisation (Giorgi et al., 2019; Glaser et al., 2020; Kur et al., 2020; Trainotti et al., 2023) and accelerometers (Schreiner et al., 2024a) offer promising results for improved POD and positioning.

4 Simulation scenarios and simulator methodology

This chapter outlines the satellite scenarios, the simulation environment, and the processing steps that are used in subsequent analyses. Sec. 4.1 introduces and compares the orbit scenarios of the space-tie satellites in more detail. Sec. 4.2 examines the feasibility of these orbit scenarios and whether obstacles that could hinder successful tracking with the different observation techniques can be identified. Subsequently, the implemented simulation environment is described in Sec. 4.3, the setup used for the simulation in Sec. 4.4.1 and the steps from the simulation to the generation of the normal equations in Sec. 4.5. Lastly, Sec. 4.6 describes the mismodelling scenarios investigated.

4.1 Co-location in space satellite orbit scenarios

The six orbit scenarios for the simulation studies (see Tab. 4.1) include the orbit characteristics of the formerly proposed NASA mission 'GRASP' (Bar-Sever et al., 2009), which stands for Geodetic Reference Antenna in Space, and the European equivalent E-GRASP/Eratosthenes mission (ESA) (Biancale et al., 2017), denoted GRASP-like and E-GRASP-like in the following [1].

Table 4.1: Orbital elements[2] of the simulation scenarios for the satellites at launch

	$\mathbf{a}[\mathbf{km}]$	$\mathbf{e}$	$\mathbf{i}[\mathbf{deg.}]$	$\omega[\mathbf{deg.}]$	peri. h. [km]	apo. h. [km]
GRASP-like	7540.67	0.0325	100.2162	79.7583	919.69	1410.51
E-GRASP-like	10495.07	0.3197	63.3981	179.9933	763.83	7474.91
E-GRASP-mod	10493.93	0.1904	63.4225	179.8667	2120.16	6115.84
Circular 30°	13378.16	0.0003	29.9984	88.9886	6993.05	7000.43
Circular 60°	13378.15	0.0006	60.0002	89.2790	6992.69	7007.36
Circular 89°	13378.14	0.0006	89.0018	89.5241	6993.93	7009.38

Another scenario is a modified version of the E-GRASP-like orbit scenario, designated E-GRASP-mod (modified), which exhibits a lower numerical eccentricity. This results in a more circular orbit, with a higher perigee and a lower apogee. In the context of the E-GRASP-like and E-GRASP-mod scenarios, a particular inclination stands out, with a numerical value of approximately 63.4 degrees. This value describes the critical inclination, indicating that these orbits have zero apogee drift. Given that the apogee is always situated at the same point in the orbital plane, in this case at the equator with ω = 180 degrees, stations located in close proximity to the equator will consistently observe the perigee and apogee of the orbit, whereas stations further North and South will consistently observe passes of medium altitude. The remaining three scenarios are circular orbits with an altitude of approximately

[1] The two orbit scenarios, designated as 'GRASP-like' and 'E-GRASP-like', are referred to in this study as 'like' to clarify that the orbit characteristics are similar, but that the studies, including simulations, are independent of the particular mission proposal.

[2] $\mathbf{a}$ = semimajor axis, $\mathbf{e}$ = numerical eccentricity, $\mathbf{i}$ = inclination, ω = argument of perigee, peri. h. = height of the perigee, apo. h. = height of the apogee

7'000 km and inclinations of 30, 60 and 89 degrees. These three scenarios were selected on the basis that a higher orbit would allow a larger number of VLBI observations the scheduled, in order to assess the potential of VLBI observations for LEO satellites. Therefore, the line of orbit scenarios comprises the GRASP-like, representing the lowest orbiting scenario, E-GRASP-like and E-GRASP-mod, which cover the mid-range up to near 7'000 km in apogee, and three higher-orbiting circular scenarios. The corresponding VLBI simulation of this project and its analysis are presented in the thesis Mammadaliyev (2024).
The ground tracks of the six orbital scenarios are shown in Fig. 4.1 for a period of one week. It can be seen that the GRASP-like and the three circular scenarios have a homogeneous spatial resolution across the range of their inclinations. The E-GRASP-like and E-GRASP-mod scenarios have a less dense ground track coverage and show higher orbital passes, which are always in ascending arcs with their apogee at the equator. Fig. 4.2 illustrates a three-dimensional representation of the E-GRASP-like orbit in the inertial frame. The impact of the critical inclination on the orbit is evident, with the positions of perigee and apogee remaining stable.

From the integrated orbits of the scenarios, the periods listed in Tab. 4.2 are computed. These include the sidereal period of revolution, the main and first sub-periods of the beta angle, and the draconitic period. Due to the orbit geometry, these periods can cause resonance effects in the ERPs, which are relevant for the spectral analyses in Chap. 6 and 7. For all scenarios, either the main beta-angle period or the first beta-angle sub-period is close to the corresponding period of the GPS constellation. Furthermore, only for the GRASP-like and E-GRASP-mod scenarios is the nodal period close to the annual period.

Table 4.2: Orbital periods: Period of revolution, main beta angle period and first sub period, and draconitic period.

	Sidereaal [min]	β angle [days]	draconitic [days]	nodal [days]
GRASP-like	114	longer than 7 years	18340.1	372.7
E-GRASP-like	154	197, 357	197.2	428.8
E-GRASP-mod	178	184, 362	184.3	372.0
Circular 30°	257	220, 365	220.4	556.1
Circular 60°	257	265, 361	264.9	963.8
Circular 89°	257	360	360.4	26921.7
GPS satellites	718	346-353	349.7-351.5	8215.9-9330.4

4.2 Technique-wise feasibility assessment of the orbits

It can be assumed that each of the techniques has different requirements in terms of the orbit scenario in order to achieve an optimal result.

In the case of DORIS, it is important to consider the altitude at which the satellite is orbiting. Conventional satellites equipped with a DORIS receiver typically orbit at altitudes ranging from a few hundred kilometres to approximately one and a half thousand kilometres (for example, ~1350 km for Sentinel-6 Michael Freilich). In all orbital scenarios in this simulation, with the exception of the GRASP-like scenario, the question arises as to whether DORIS observations at altitudes beyond these altitudes are indeed feasible. The atmo-

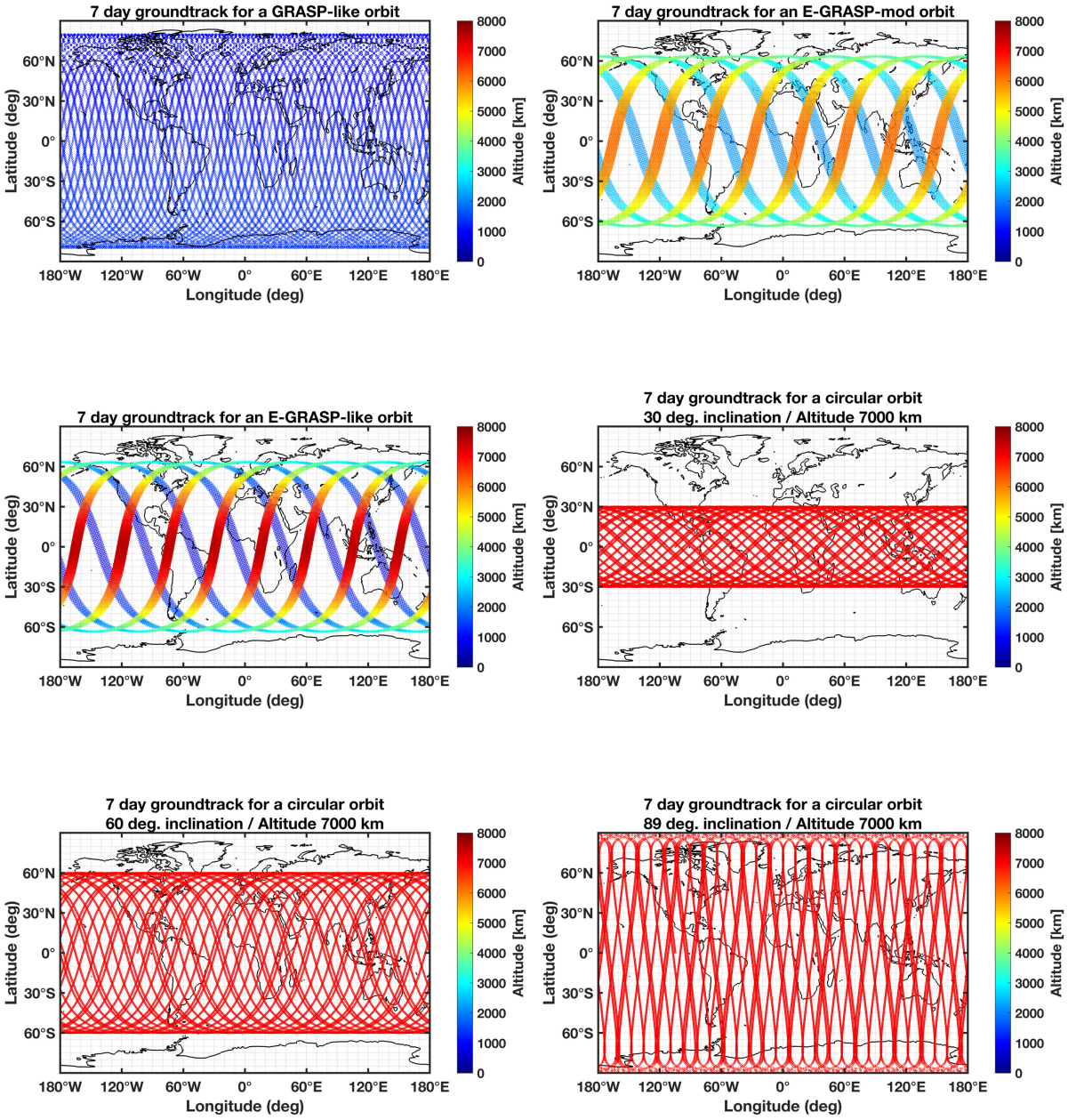

Figure 4.1: Seven-day ground track for each mission scenario, giving a sense of the global coverage achievable in time. Satellite altitude is indicated by the colour bar.

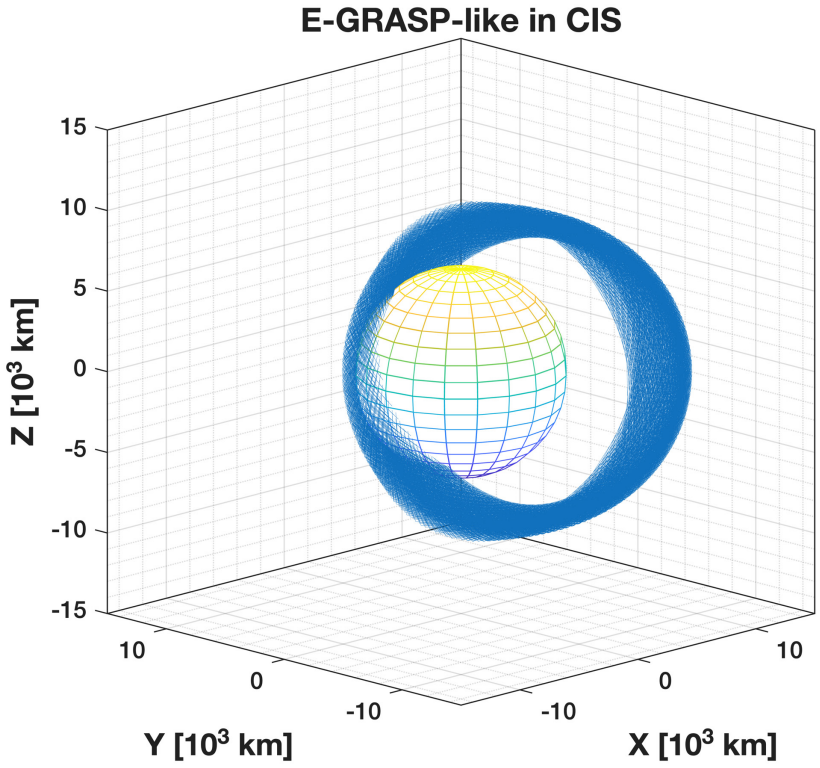

Figure 4.2: Three-dimensional representation of the E-GRASP-like mission over a 90-day period in the intertial frame

spheric opacity for radio waves in the 0.4–2 GHz frequency spectrum employed by DORIS is close to zero, as these frequencies are within the radio window. Consequently, there are no significant atmospheric obstacles to signal transmission or Signal-to-Noise Ratio (SNR). However, it should be noted that signal power decreases quadratically with height. This results in a signal that is approximately 27 times weaker at an altitude of 7'000 km than at the Jason satellites' altitude of around 1340 km. It is recommended that any increase in transmit power that may be required should be used with caution, at least at co-location sites, due to the potential impact on S-band reception by VLBI and the sensitivity of the Low Noise Amplifiers (LNAs) used within VLBI stations. With increasing altitude, the number of DORIS stations simultaneously visible to the satellite increases, so that the receiver reaches the maximum number of stations that can be tracked simultaneously. Another issue is that of Doppler collisions, where the signals from multiple ground stations are received by the on-board receiver at a similar frequency and frequency rate, making it practically impossible to distinguish between them. Doppler collisions can be remedied by shifting the frequency of the ground beacons. This has already been successfully done for Jason-3 (Jayles et al., 2021).

For SLR, there appears to be a lower risk of complications. SLR measurements to higher orbiting targets, such as the two geodetic satellites ETALON-1 and ETALON-2, or GNSS satellites at altitudes in the range of 20-25'000 km, are today a standard task for SLR stations. In consideration of the maximum altitude of the simulated space-tie satellite's orbit scenarios, which is approximately 7,000 km, it is improbable that SLR will impose any restrictions. At very low altitudes, tracking becomes increasingly difficult as satellite predictions deteriorate,

making target acquisition significantly more problematic. This was noticeable, for example, at the end of the GFZ-1 mission at an altitude of 350 km.

In the context of GNSS, particularly GPS, receivers at ground stations and on LEO satellites at altitudes reaching several thousand kilometres are standard. Therefore, the orbital scenarios investigated here, with an altitude of up to 7'000 km, are slightly higher than those of operational LEO missions carrying GNSS receivers. Experimental missions such as Equator-S have demonstrated that it is feasible to receive and track a sufficient number of GNSS signals for orbit determination even in significantly higher orbits (Balbach et al., 1998). Furthermore, it is also possible to use GNSS signals for positioning in altitudes beyond the GNSS constellation, such as in geostationary orbits. This can be achieved through the use of specialised GNSS receivers, including the NAVIGATOR GPS receiver (Winternitz et al., 2009). At an altitude of approximately 10'000 km, Capuano et al. (2013) found that a single-satellite receiver should be able to track a -134.2 dBm signal, while a dual satellite system receiver (e.g. GPS and Galileo) would need to track a -120.8 dBm signal. Moreover, the simulation results from the aforementioned study indicate that with increasing altitude, substantial performance enhancements can be achieved through the utilisation of a multi-satellite system receiver. Montenbruck et al. (2023) address the topic of GNSS characteristics at an altitude of 6'000 km and different receiver orientations on the satellite, with a particular focus on the upcoming Genesis mission (Delva et al., 2023). The study concludes that at higher altitudes, the sidelobes of the GPS signal play an important role in satellite visibility. It is therefore strongly recommended that calibrated PCV values of GNSS satellites be published for higher off-boresight angles in order to achieve optimal positioning performance. The simulations of GNSS observations for ground stations and SST on the space-tie satellite in this thesis are based on GPS only. Furthermore, it is assumed that calibrated PCV values for GNSS satellites will be available for higher off-boresight angles. With regard to signal strength, only GPS is used and no loss in receiver performance is assumed. Consequently, in the simulation, this at least partly counteracts the recommendation of a multi-GNSS receiver for higher flight altitudes and the improved geometry that a second nadir antenna would provide.

4.3 Simulation procedure

The simulations are based on evaluations of real data. Therefore, a variety of real data-based information about accuracy, precision, availability, and visibility of each technique and station are obtained in a POD process. The simulation process for GPS is based on fixed assumptions regarding noise, availability, performance and ambiguity behaviour, due to the large number of observations and the consistently high and continuous availability of the receivers. For both DORIS and SLR, a specific simulation approach has been developed and implemented, as shown in Fig. 4.3. The method employs the storage of real data-based information in matrices, designated as simulation configuration matrices. These matrices regulate the operation of various simulation programs, which can then apply the stored information to simulations of existing or fictitious satellites and stations. This process involves a preliminary 'learning' step for existing satellites, followed by the application of the stored information to a simulation of existing satellites for validation purposes. After successfully passing a quality check, the stored information is then applied to fictional scenarios.

In the initial phase, EPOS-OC is used for POD of real data. The real data observations are then evaluated with regard to their fundamental characteristics. These characteristics in-

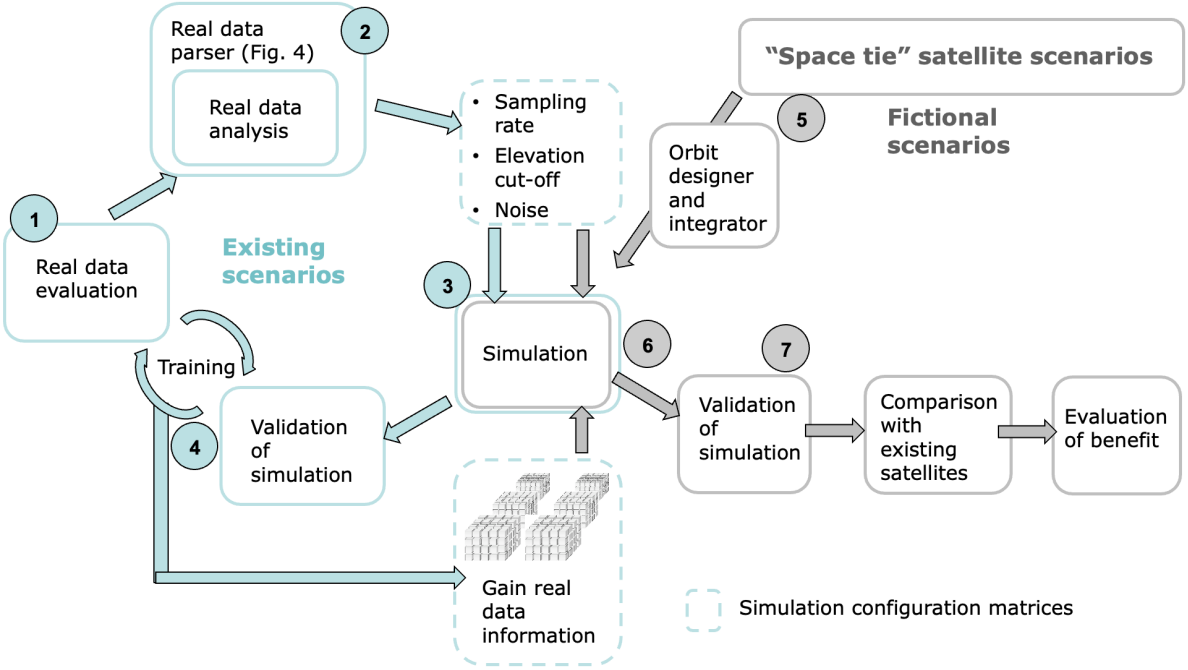

Figure 4.3: Flowchart of the simulation procedure for DORIS and SLR. The numbers indicate the order of the steps.

clude the NP bin size and sampling rate for SLR, the Doppler count integration sampling rate for DORIS and the sampling rate for GNSS. In addition to these, the azimuth and elevation angles for ground stations and temporal variations are also considered. Fig. 4.4 provides an illustrative example of the real data parser's output, which analyses characteristics such as the sampling rate and coherences with the length of the observed arc.

In the second step of the process, the real data observations are searched for the lowest possible elevation angle per station and stored as a global parameter per station in the simulation configuration matrix. For DORIS the minimum elevation angle is set to 10 degrees, for GPS ground stations 20 degrees and for GPS SST observations 10 degrees. These values represent the lower limits used in the real data processing, so there may be real observations below these values, but as they were not used in real data processing, they are not simulated. Higher elevation cut-off angles were not identified in these cases.

In the third step EPOS-OC is used to simulate all possible observations based on the basic simulation characteristics. These are the sampling rate, the maximum number of receiver channels (DORIS and GPS), the elevation cut-off angle (all techniques), the number of ambiguities and cycle slips (GPS) and the PseudoRandom Noise (PRN) yield factor (GPS). The PRN yield factor is a value that determines how many satellites a receiver should track in comparison to the potential number of satellites that could be tracked. This value is calculated by employing simulations to determine the actual maximum number of satellites that could have been tracked and comparing the result to the outcomes of real data processing. It thus indirectly replicates the receiver software that decides when to observe which satellite. In the case of both DORIS and SLR, the simulated observations are all those that would be feasible due to geometry and are free of errors in this step. For GPS, EPOS-OC also simulates a realistic number of satellites tracked. This is achieved by adjusting the aforementioned PRN yield factor. Furthermore, the noise on the code and

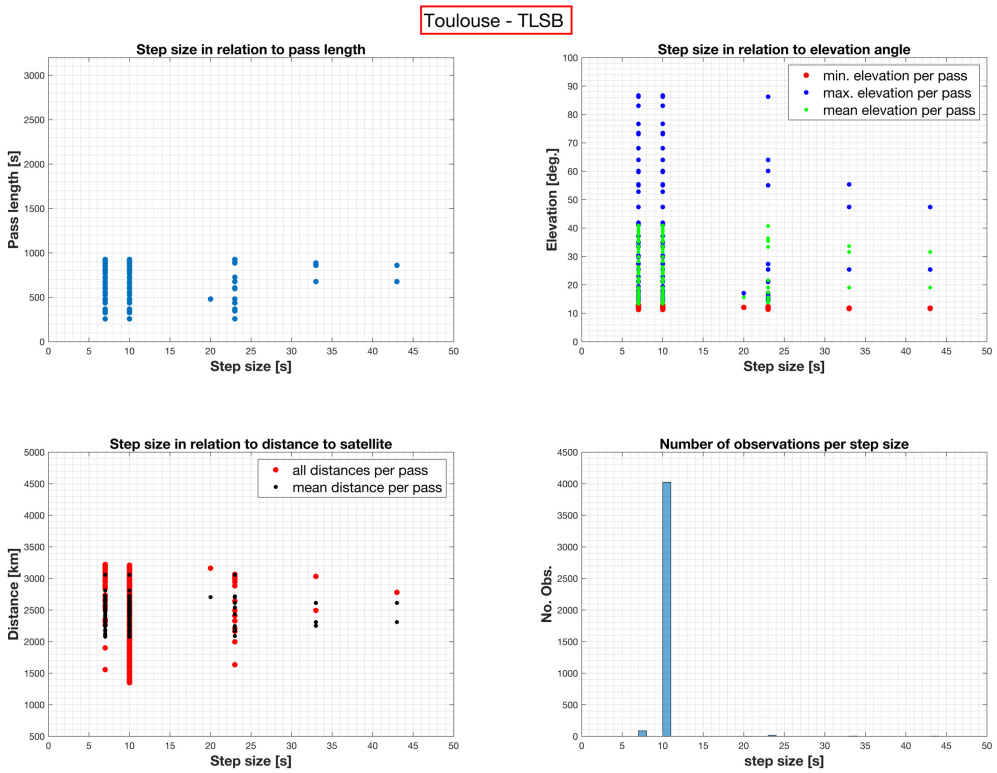

Figure 4.4: Output of the real data parser, analysing several observation characteristics such as the sampling rate of the observations in relation to the length of the observed pass. As an example, the output for the observations of the TLSB DORIS station in Toulouse received by Jason-1 over one week in 2010 is shown.

phase observations, as well as ambiguities and cycle slips, are simulated based on the given settings. Upon completion of this step, the simulated GPS observations are ready for use, and subsequent steps are only performed for DORIS and SLR.

In the fourth step, the training is conducted with the objective of obtaining the information necessary to configure the simulation. Firstly, the number of passes in the simulated observations is quantified. This number is then compared with the number of passes observed in reality, and the resulting factor, defined as the pass yield factor, is stored for each station in the simulation configuration matrices at a weekly time resolution. The number of passes is thereafter reduced in accordance with the aforementioned pass yield factor, with the passes to be removed being selected at random. The pass-scaled simulated observations are employed once more within a POD in EPOS-OC for the purpose of evaluating the efficiency of the pass scaling and determining the remaining number of observations per station. Given that the number of passes is now consistent with the real data, the remaining number of observations is compared. The resulting observation yield factor is also stored for each station in the simulation configuration matrices with a weekly temporal resolution. Subsequently, observations are removed from the pass-scaled simulated observation file based on the respective yield factor, with the selection of which observation to remove determined by a random generator. Thereafter, the simulated observations are once again used within a

POD in EPOS-OC to validate the final number of observations and passes.

Following this final verification step, the observation noise of the real data POD is incorporated into the simulation configuration matrices for each station with a weekly time resolution. The noise values are obtained in the context of the POD for the real data set, with the noise expressed in terms of post-fit standard deviations of the Observed minus Computed (O-C) residuals. The values according to the data set of the noise configuration matrices are then applied to the simulated observations. In the configuration used, the Gaussian noise generator generates noise that is both station and time-related and has a loose zero mean condition. Further information regarding the rationale behind the zero mean condition and its applications can be found in App. B.

4.4 Simulation setup

4.4.1 Model definition

In the simulations, the method of dynamic orbit determination is employed. This requires certain models, which are listed in detail in Tab. 4.3. In the case of real data evaluations, it is desirable to use models that are as close to reality as possible, thereby minimising the number of empirically estimated parameters that absorb the residual non-modelled forces. However, for the purpose of a simulation, the extent of the perturbations introduced by the models used must be quantified once systematic mismodelling comes into play.

4.4.2 Space-tie satellite configuration

To simulate a fictitious satellite mission, a number of assumptions must be made about the satellite itself. These include the shape, the mass and CoM of the satellite, the attitude law and the technique reference point eccentricities onboard, as well as reference point variations, such as PCVs. In this case, the space-tie satellite was assumed to be like the CHAllenging Minisatellite Payload (CHAMP) satellite (Reigber et al., 2006). CHAMP was launched into a near-polar orbit at an altitude of approximately 460 km. Launched in 2000 with a planned mission duration of five years, the mission was successfully operated for a total of ten years.

The shape of the space-tie satellite body was based on that of the CHAMP satellite. The satellite body comprises a body and a 4-metre-long boom, to which a magnetometer was mounted. The lateral and upper surfaces of the satellite are equipped with solar panels. The macro-model of the satellite is the essential basis for the calculation of disturbance forces for the simulation and recovery as part of the dynamic POD. This model, depicted in Fig. 4.5, comprises a total of 14 individual surfaces.

The mass of the space-tie satellite was chosen to be 522.63 kg, which is identical to the launch mass of CHAMP. This mass was assumed to remain constant over the seven-year duration of the simulated mission. The centre of mass of the satellite was positioned at the origin of the satellite-fixed reference frame.

The phase centre reference points of the DORIS and GPS antennas, as well as the optical phase centre of the SLR retroreflector, were placed in the origin of the satellite reference frame. In reality, such geometries are not possible. However, for the purposes of the simulation, this assumption can be made, providing a simplified means of investig-

Table 4.3: Models used for dynamic POD and for simulating and recovering DORIS, SLR and GPS.

	DORIS & SLR	**GPS**	**Reference**
General			
Software	EPOS-OC (v6.74)	idem	(Neumayer et al., 2024)
Arc-length	7 days (00:00-00:00 UTC)	24h (00:00-00:00 UTC)	
Simulation time span	7 years	idem	
Dynamic model			
Gravity field	EIGEN-6C 60x60	idem	(Shako et al., 2013)
	time variable 60x60	idem	
Atmospheric tide	BB2003	idem	(Biancale & Bode, 2006)
Earth tide	Wahr model	idem	(Wahr, 1981)
	IERS Conventions 2010	idem	(Petit & Luzum, 2010)
Ocean pole tide	Desai 30x30	idem	(Desai, 2002)
Ocean tide model	FES2014 30x30	idem	(Lyard et al., 2021)
Ephemeris	DE421	idem	(Folkner et al., 2014)
Moon	FERRARI77	idem	(Ferrari, 1977)
Albedo with IR	Internal implementation	idem	
Atmosphere	NRL-MSIS-E-00	idem	(Hedin, 1991)
Geometric model			
Earth Orientation Parameters	IERS C04 08	idem	(Bizouard et al., 2018)
Mean pole	Linear mean pole	idem	(Ries, 2017)
Station coordinates	DPOD 2008		(Willis et al., 2015a)
	SLRF 2008		(Pavlis et al., 2008)
		IGS 2008	(Rebischung et al., 2011)
Satellite configuration			
Attitude	Attitude law	idem	
Centre of mass	no variation over time	idem	
Satellite mass	no variation over time	idem	
Satellite model	LEO: Macro-model	LEO: Macro-model	
		Sender: Macro-model	(Steigenberger et al., 2020)
Observations			
Observation	DORIS: integrated Doppler count	Code and Phase	
	SLR: range	on L_1 and L_2	
Elevation angle cut-off	DORIS: 10 deg.	LEO: 10 deg.	
	SLR: station-specific	Ground: 20 deg.	
Downweighting law	DORIS/SLR: none	GPS: none	
Observation correction models			
Frequency bias and drift	DORIS: zero		
Optical phase map	SLR: zero		
Antenna phase pattern		Sender: modified igs14	(Rebischung et al., 2016)
		Ground receiver: igs08	
		Satellite receiver: zero	
Antenna code pattern		zero	
Carrier phase wind-up		applied	
Range bias	SLR: zero		
Time bias	DORIS/SLR: zero	GPS: zero	
Troposphere model	DORIS: VMF-1	GPS (ground): GMF	(Boehm et al., 2006)
	SLR: MP 2004		(Mendes & Pavlis, 2004)

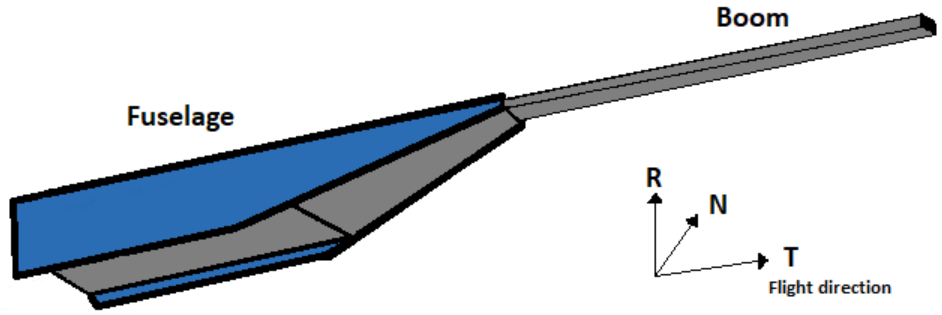

Figure 4.5: Visualisation of the implemented macro-model for the space-tie satellite.

ating systematic errors. In the case of GPS, the PCO was set to zero, thereby equating to the antenna mounting point. No azimuth- or elevation-dependent PCV or Code Phase Variations (CPV) has been introduced.

The attitude of the satellite is controlled using a nominal attitude law, which stipulates that the satellite always flies straightforward, with its radial axis aligned to the radial position vector, starting from the centre of mass of the Earth. The normal direction is defined as the norm of the radial position vector and the velocity vector, and the transversal direction completes the right-hand system.

4.4.3 GPS satellite configuration

As part of the integrated processing of the space-tie LEO satellite together with a GPS constellation, it is necessary to simulate this GPS constellation as well. For this purpose, it was assumed that a future GPS satellite constellation would consist primarily of the current Block III satellites. Accordingly, the entire constellation was defined as Block III satellites. The PCO and PCV characteristics have been derived from the values published in igs14 (Rebischung et al., 2016). A macro-model of the GPS III satellites was constructed for the simulation of radiation pressure and albedo radiation with InfraRed radiation (IR), in accordance with the specifications outlined in Steigenberger et al. (2020). A set of five reduced ECOM-1 parameters (D0B1) (Arnold et al., 2015) was also estimated for this model in the POD run, which corresponds to a hybrid approach to radiation pressure modelling. With no systematic error influences, the use of the macro-model of the simulation in the recovery would result in the same perturbation forces as those simulated. Any remaining variations can be attributed to the influence of noise of the observations and correlations between the estimated parameters.

4.5 Steps included in the simulation

The simulation process with EPOS-OC is comprised of a series of steps, which are executed until the normal equation of the scenario can be established. These steps are described in greater detail in the following sections, from 4.5.1 to 4.5.3, and are illustrated as a flowchart in Fig. 4.6.

4.5.1 Simulation run

The simulation generates both the orbit of the satellite and the observations. This is achieved by integrating the orbit over the entire time horizon of the simulation, utilising the

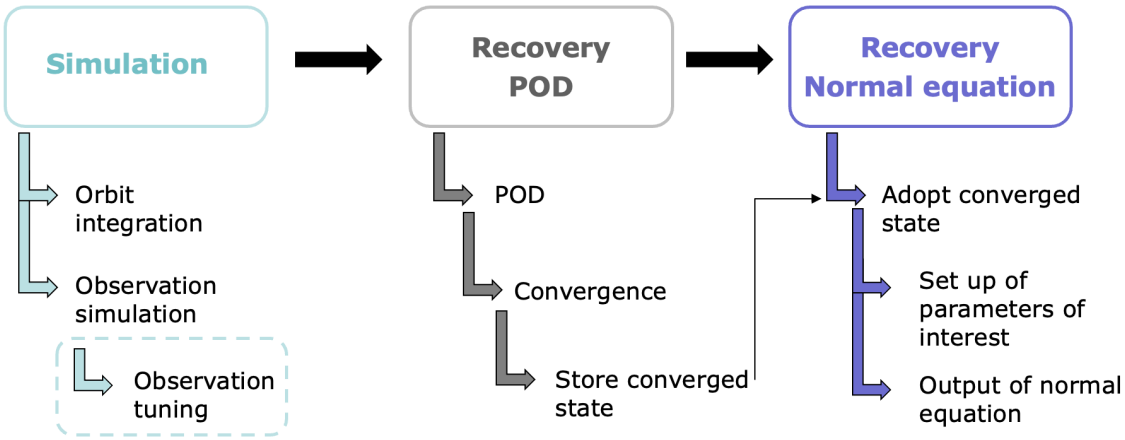

Figure 4.6: Flowchart of the simulation process with EPOS-OC

models delineated in Sec. 4.4.1. Subsequently, the integrated orbit is examined for stability and consistency with the desired orbit characteristics. Thereafter, the orbit is divided into smaller time segments, which are used for observation simulation and further recovery steps. Following this, observations are simulated for these segments in accordance with the procedures described in Sec. 4.3. To enhance the realism of the simulated observations, the programs of the simulation environment, as described in Sec. 4.3, are used to edit the observations in a separate step outside of EPOS-OC.

4.5.2 Recovery run

In the recovery run, previously simulated observations are used in a POD process. In this way, what has been simulated is recovered, hence the name recovery. In the absence of systematic perturbations and sufficiently dense and uniform observations across the arc, this step should yield the same orbit as the integration of the simulation. The step is slightly different for the DORIS and SLR techniques compared to GPS, and as such, these techniques are explained separately. Tab. 4.4 gives an overview of the parameterisation of each technique described below for the scenarios free of systematic errors.

As part of the adjustment of the orbit determination, several parameters can be estimated. Since the systematic error-free simulation for DORIS and SLR does not contain any error influences other than the noise of the observations, only the initial state elements of the satellite are estimated in this step. The following adjustment process is iterated until convergence is reached. This converged state is then stored in order to be used as initial information for the following normal equation step. In this example for DORIS and SLR, the stored information consists only of the estimated initial state elements.

The procedure for GPS is slightly different at this point. In principle, the entire GPS constellation is always solved in a network adjustment. For cases involving a space-tie satellite, the LEO satellite is integrated into the network adjustment and the whole system is solved again, i.e. the ground station coordinates and the GPS and LEO orbits. Since the simulated GPS observations contain not only noise on code and phase observations, but also ambiguities and cycle slips, the parameterisation is slightly different from that for DORIS and SLR. In real data processing of GPS constellations, station coordinates are typically estimated during the network adjustment, so they are also estimated in the POD

recovery run of the simulation. To align the station coordinates to the a priori network, no-net constraints on scale, rotation and translation are applied. Thus, the station coordinates have only a residual freedom to vary within the noise level of the simulated observations.

Since cycle slips and ambiguities are simulated, ambiguities are initially co-estimated as float values. The iterative cycle slip detection of EPOS-OC is used to detect further ambiguities during POD, tropospheric scaling factors are also estimated. For the transmitter satellites of the GPS constellation, the initial state elements and empirical coefficients as well as the radiation pressure parameters are estimated using the reduced ECOM-1 parameter set (as also employed in Steigenberger et al. (2020)). The parameterisation of the LEO satellite, integrated into the GPS constellation, is comparable (compare Tab. 4.4). For the LEO, the empirical coefficients are setup more densely in time and no radiation pressure parameters are estimated. The POD process is first iterated until convergence is reached. This is followed by an ambiguity fixing process where the estimated float values are fixed to integer values using double differences. In the case of the integrated LEO satellite, its ambiguities are also fixed in this way. Fixing is achieved by introducing side constraints on the ambiguities of the converged arc and continuing the iterative process from there until convergence is reached again. The final state of convergence is now saved to allow the use of the normal equation mode of EPOS-OC from this converged state onwards. Further information on the handling of ambiguities at normal equation level with EPOS-OC can be found in App. A.

Table 4.4: Parameterisation for the cases without systematic errors. T = transversal, N = normal, DD = double differences

	DORIS	SLR	GPS constellation	GPS LEO
Initial state	estimated	idem	idem	idem
Atmospheric drag	fixed	idem	idem	estimated every 6h
Albedo with IR	fixed	idem	idem	idem
Solar radiation	fixed	idem	reduced ECOM-1	fixed
Empirical acc.	fixed	idem	constant and 1/rev cos, sin every 24h in T direction	1/rev cos, sin every 75' in N and T direction with piecewise linear amplitude modelling
Troposphere			estimated	
Ambiguities			estimated - DD fixed	estimated - DD fixed

4.5.3 Normal equation run

In the final step EPOS-OC is used in normal equation mode. The previously described stored final state of the converged arc is read, used as the initial condition, and the normal equation is set up according to the set of parameters to be estimated. In this step, all parameters of interest can be activated, which has the advantage that station coordinates and velocities, ERPs and gravity field coefficients can be set up for estimation without the necessity of a priori information or constraints and without further iteration of the solution. In order to obtain a reasonable solution for the station velocities and the gravity field, the

normal equations need to be accumulated over a longer period of time (at least 2.5 years for the velocities according to Blewitt & Lavallée (2002)).

At this point, the processing with EPOS-OC is complete. The Earth Parameter and Orbit System - Combination and Solution (EPOS-CS) software package is then used for further processing of normal equations. EPOS-CS is part of EPOS (see Sec. 2.5) and has been developed to handle normal equations. In this case, the normal equations are first accumulated over the entire time period to obtain one set of parameters for station positions and velocities and, if applicable, gravity field coefficients. After adding the geodetic datum, this normal equation is then inverted and evaluated.

4.6 Mismodelling scenarios

In order to evaluate the impact of different mismodelling on orbit and reference frame realisations, the scenarios presented in Tab. 4.5 were selected. The simulations start with a systematic error-free scenario for all techniques. This is done with the intention of generating observations that imitate a perfect world with only noise on the observations. Only technically necessary conditions are applied to the simulated observations. This includes white noise in any case, and for GPS, it also includes cycle slips and ambiguities. This decision was made on the basis that cycle slips and ambiguities are a technical fact that cannot be avoided even in a perfect scenario. On the other hand, DORIS frequency biases could be eliminated if all beacons were connected to high-precision clocks as frequency transmitters. (So far this is not the case). With regard to SLR, it was decided not to estimate or simulate range biases, since the effect is comparable to CoM biases, which are also treated in the following.

Table 4.5: Performed simulation mismodelling cases

	DORIS Sec. 6.1	SLR Sec. 6.2	GPS Sec. 6.3
Systematic error-free	yes	yes	yes
5 [mm] CoM bias fixed	yes	yes	
5 [mm] CoM bias estimated	yes	yes	
10 [mm] CoM bias fixed	yes	yes	
10 [mm] CoM bias estimated	yes	yes	
Atmosphere mismodelling	yes	yes	
Solar and Earth radiation pressure mism.	yes	yes	for the constellation
Frequency bias	yes		
Earth gravity field mismodelling	yes	yes	yes

4.6.1 Centre of mass mismodelling

The issue of the reference point (antenna for DORIS, reflector for SLR) mismodelling is investigated for DORIS and SLR. To introduce an error of the vector from the CoM to the reference point of the observation technique, either the antenna and reflector reference points can be modified or the location of the CoM of the satellite. In this case, the displacement of the CoM was chosen. A similar investigation was not conducted for GPS, as the calibration and influence of PCO values of GPS transmitter satellites and the integration of LEOs to a GPS constellation are extensive topics in their own right. Several authors have published on these subjects, providing valuable insights (e.g. Huang (2022)).

The CoM displacement is examined for two different values. The vector to the reference point is altered by 3 mm and 6 mm in all three directions, resulting in an Euclidean distance of approximately 5 mm and 10 mm, respectively. Subsequently, the value is either kept fixed and the influence is investigated, or estimated in order to assess the extent to which it can be calibrated in orbit.

4.6.2 Atmospheric drag

The influence of atmospheric drag mismodelling is investigated for DORIS and SLR only. For the mismodelling, the atmosphere model employed in the simulation, namely NRL-MSIS-E-00, is substituted by the DTM 78 model (Barlier et al., 1978). This results in a change of the composition of the upper atmosphere, which is derived from the models and is used to calculate the satellite's drag disturbance force.

4.6.3 Solar radiation pressure

The impact of radiation pressure modelling inaccuracies is investigated for the LEO space-tie satellite scenarios for DORIS and SLR. In the case of GPS, the LEO is not subjected to mismodelling, but the GPS transmitter satellites are, in order to determine the extent to which the integration of a LEO satellite into the constellation could help. The impact of incident radiation on satellites can be modelled in EPOS-OC using macro-models of the satellites. Radiation pressure modelling includes the direct radiation pressure of the radiation emitted by the Sun and the radiation reflected by the Earth (albedo). In the method used here, radiation includes solar radiation and albedo of the visible and infrared light spectrum. The total force is calculated based on the areas and surface properties of the macro-model of the satellite. However, the aforementioned macro-model is also used for the computation of the atmospheric drag disturbance force. The drag influence of the upper atmosphere on satellites varies depending on their flight altitude. Consequently, modifications to the satellite macro-model, for example in terms of area or structure, would also result in variations of the influence of the upper atmosphere. Therefore, only the visible and infrared absorption properties of the solar panels were modified and increased by 5%. This modification affects the radiation pressure forces, but leaves the atmospheric drag computation unchanged.

The GPS transmitter satellites are not subject to drag from the upper atmosphere due to their altitude of more than 20'200 km. Accordingly, this force has not been simulated for these satellites. This has the advantage that the radiation pressure can be perturbed, for example by varying the area of the box-wing model, without any additional influence on the drag force. Consequently, all areas of the box-wing model of the GPS transmitter satellites were increased by 5%. It should be noted that this mismodelling also affects the albedo (including infrared radiation).

4.6.4 Frequency bias

The frequency bias represents a specific effect unique to DORIS. This bias is a consequence of the fact that the transmission frequency of the ground beacons does not perfectly align with the nominal frequency of the signal. As not all beacons are connected to atomic clocks, discrepancies in the frequency of the transmitted signal occur for stations relying on a free USO.
A comparable phenomenon is observed in relation to the satellite's onboard frequency. Over time, the onboard frequency of the satellite's USO undergoes a drift, which must be rectified during the processing. On the one hand, this is done by an onboard software of the satellite, that estimates the current onboard frequency deviation in relation to the nominal frequency.

On the other hand, this can be achieved during the processing by correcting the satellite's onboard frequency in accordance with the estimated frequency bias of the master beacons. As previously outlined in Sec. 3.1.1.1, these beacons are connected to atomic clocks, which ensures that the frequency bias of these stations is approximately zero. Therefore, the mean deviation of the estimated frequency bias of these stations from zero reflects the difference between the onboard USO frequency and the nominal frequency. Given that current satellites, such as Sentinel-3A/-3B or -6A (MF), carry an USO, which is connected to the DORIS and also to the GPS/GNSS receiver, it is possible to calibrate the onboard frequency using GPS satellite clock estimates. For the mismodelling of the frequency bias performed here, the ground beacons are perturbed only, but not the on-board frequency of the USO. To model the frequency bias, the average values of the estimated frequency biases derived from the Jason-2 real data evaluation are employed. These values are provided in Tab. 4.6 and are applied to the simulated observations as constant values over the entire simulation time span. As the onboard USO drift was not corrected in this analysis, most of the frequency biases are positive.

Table 4.6: Frequency bias values used for DORIS frequency bias modelling

Station	Bias in Hz	Station	Bias in Hz	Station	Bias in Hz
ADEB	76	HBMB	85	PATB	49
AMUB	68	HEMB	63	PDMB	88
ARFB	111	JIUB	-4	REUB	132
ASDB	36	KETB	72	REZB	137
BADB	105	KIUB	113	RIDA	50
BEMB	130	KOLB	41	RIKB	26
BETB	188	KRBB	104	RIPB	139
CADB	122	KRWB	88	ROUB	13
CHAB	110	LAOB	92	SAKB	49
CICB	61	LICB	107	SALB	76
COBB	136	MAHB	75	SANB	114
CRPB	44	MALB	68	SCRB	0
DIOB	83	MANB	107	SODB	94
DJIB	135	MATB	102	SPJB	72
EASB	82	METB	33	STJB	118
EVEB	171	MIAB	97	SYPB	-106
FAIB	-4	MOOB	96	THUB	133
FUTB	67	MORB	46	TLSB	85
GAVB	-125	MSPB	110	TRIB	158
GR3B	106	NOWB	50	YASB	-42
GREB	38	OWEC	173	YEMB	82

4.6.5 Earth gravity field mismodelling

To ascertain the sensitivity of each orbit scenario to the gravity field of the Earth, the EGM used for the recovery is modified. The EGM used in the simulation is the EIGEN-6C up to degree and order 60. Time-variable gravity information is represented by linear drift terms up to degree and order 60 in this model. In the modified EGM, the static part of this

model is replaced by the static part of the GGM05S model (Tapley et al., 2013), while the drift terms remain unchanged.

The gravitational mismodelling resulting from this allows the evaluation of the impact on the orbits and the TRF. In a subsequent step, the static part of the gravity field is estimated to the maximum degree and order of the expansion, and the generated normal equations are accumulated over the full simulation time span. Thereafter, the determined SHs are compared to those of the simulation. This allows errors in the estimated SHs to be identified, where they occur, and to what extent a satellite mission utilising each observation technique can contribute to the determination of the gravity field.

5 Real data analysis and ensuing simulations

In order to make the simulations in this thesis as realistic as possible, the simulator uses information derived from real observations, as described in Chap. 4. This approach ensures that the characteristics of the simulated observations are as close as possible to those of real observations. For each observation technique, POD was performed for well-known satellites in order to analyse the real observation data. The results are presented for DORIS in Sec. 5.1, for SLR in Sec. 5.2, and for GPS in Sec. 5.3.

5.1 DORIS

For the DORIS real data evaluation, the satellites listed in Tab. 5.1 were considered. Not all satellites overlap with the time window of the simulations (2008 to 2014). Nevertheless, an evaluation of all the aforementioned satellites was conducted in order to obtain the DORIS technique, ground station, and satellite-specific characteristics. These include the temporal availability of the ground stations, pass yield, observation yield, elevation cut-off angle, achievable orbital fit in terms of Root Mean Square (RMS), mean and standard deviation values, observation sampling rate and the maximum number of signals tracked in parallel. In addition to being the source of data for subsequent simulations, the ENVironmental SATellite (ENVISAT), Jason-1 and Jason-2 satellites themselves were also simulated. The simulation of these three satellites provides the reference solution for the DORIS observation technique. The simulations of the DORIS observations of the space-tie satellites are based on the characteristics analysed in greater detail below. In the simulator, the satellites were prioritised in descending order: Jason-2, Jason-1 and ENVISAT. As soon as the information from Jason-2 is not available, for instance due to data gaps, Jason-1 is employed, followed by ENVISAT. For Jason-1 the SAA-corrected date according to Capdeville et al. (2016) was used. Consequently, at the outset of the simulation period prior to the launch of Jason-2, the simulation relies on the information obtained from Jason-1 and ENVISAT. This, however, does not affect the configuration of the receiver used in the simulation, which was chosen to emulate a DGXX/DGXX-S receiver with seven parallel channels.

5.1.1 Ground antenna types

Over the past few decades, the antennas used at DORIS ground stations for signal transmission have undergone a series of evolutionary changes. The initial generation of antennas used, were the Alcatel. Subsequently, these were replaced over the years by their successor, the Starec-B antenna. Since 2014, the latest antenna models, Starec-C and Starec-D, have been installed. As the Starec-C and Starec-D models are very similar and the phase centre measurements do not differ, the Starec-D models are not explicitly identified in the station code and are assigned the same ‘C’ designation as the Starec-C antennas. They are henceforth referred to as Starec-C, and are not explicitly distinguished. Fig. 5.1 illustrates the evolution of the antennas employed over time. The number of ground stations has remained at approximately 60 since the end of the 1990s. The simulation is based on antenna availability between 2008 and 2014. During this period, the Starec-B antenna was the primary opertional choice. In the context of the simulation, the antenna

Table 5.1: Used satellites, sorted by launch date. Satellites marked with a * overlap with the simulation time span from 2008 to 2014. Orbital elements taken from the real data analysis prepared for this work.

		Perigee	Inclination	Ecc.	Receiver	Launch	EOL
	TOPEX	1336 km	66.1 °	0.0006	1G	10-Aug-1992	18-Jan-2006
*	Jason-1	1324 km	66.0 °	0.0006	2GM	07-Dec-2001	01-Jul-2013
*	ENVISAT	758 km	98.5°	0.0014	2G	01-Mar-2002	08-Apr-2012
*	Jason-2	1310 km	66.0°	0.0006	DGXX	20-Jun-2008	09-Oct-2019
	Jason-3	1336 km	65.9°	0.0006	DGXX-S	17-Jan-2016	
	Sentinel-3A	794 km	98.7°	0.0014	DGXX-S	16-Feb-2016	
	Sentinel-3B	794 km	98.7°	0.0014	DGXX-S	25-Apr-2018	
	Sentinel-6A (MF)	1336 km	65.9°	0.0006	DGXX-S	21-Nov-2020	

type is only of relevance if one wishes to analyse antenna-type specific effects, such as the PCV. Furthermore, the characteristics of the observations, including the noise, pass yield and observation yield, are dependent on the station setup, specifically the antenna and beacon used. A simulation based on real data information obtained with Starec-B and Starec-C antenna characteristics and a network of approximately 60 stations is realistic for near-future missions. The station network of the simulation is therefore composed of Starec-B and Starec-C stations. The PCV of the stations is assumed to be error-free for the purposes of the simulation.

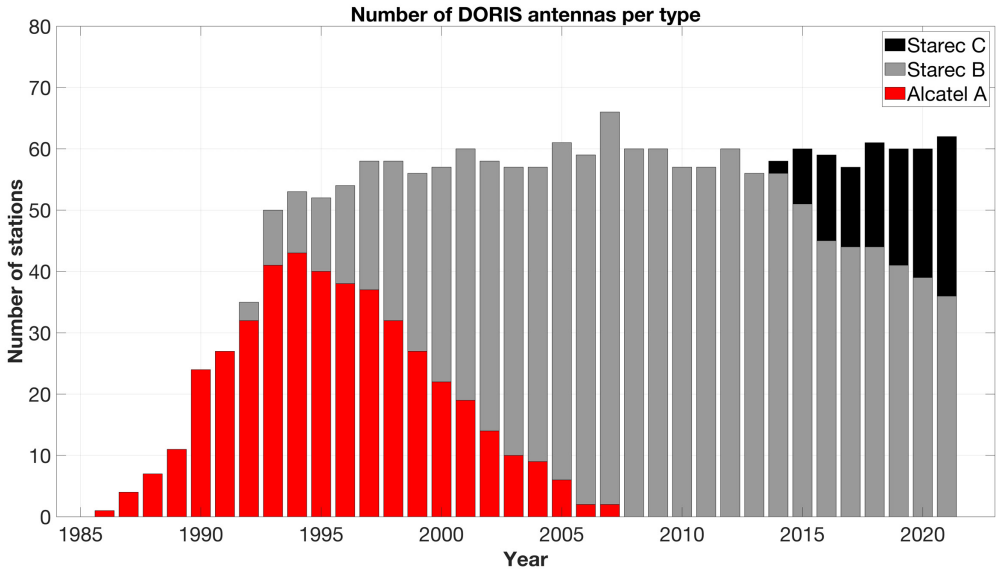

Figure 5.1: Total number of active DORIS antennas and their type over the years. Starec-C also includes Starec-D antennas.

5.1.2 Ground station elevation cut-off angle

In the evaluation of the real data, the elevation cut-off angle employed is 10 degrees, as no downweighting law for lower elevations is applied. To ascertain whether specific stations exhibit higher cut-off angles, potentially due to obstructions in the line of sight, the real data

of ENVISAT, Jason-1 and Jason-2 were examined for their minimum elevation angle for the period between 2008 and 2014. In this analysis, azimuth-dependent variations were not considered. No station was identified that exhibited a cut-off angle exceeding 10 degrees. Therefore, the minimum cut-off angle is represented by the POD value of 10 degrees, which was applied to all DORIS simulations for all ground stations.

5.1.3 Observation sampling rate

DORIS observations are generated on-board the satellite. The USO gives the time interval after which observations are formed and assigned with a time stamp. Starting with the old DORIS data exchange format, observations were formed at intervals of either seven or ten seconds. Two distinct types of Doppler integration intervals have been employed. In the event that the integration was chained to a preceding one, the interval is ten seconds, and these observations are designated as chained. If the aforementioned interval was not connected to a preceding one, the integration interval of the observation was set to seven seconds, resulting in the observations being designated as unchained. Today, DORIS observations are provided in the RINEX format, wherein the code and phase observations underlying the Doppler range rate measurement are given. These are provided every 7- and 10-second interval, resulting in observations at 0, 7, 10, 17, 20, and 27 seconds, and so forth. The preprocessing used to process RINEX phase observations with EPOS-OC employes a 10-second integration interval to generate range-rate observations. This approach is analogous to the chained mode of the previous data format. The time difference between consecutive accepted observations serves as a fundamental basis for the simulations. Fig. 5.2 illustrates the sampling rate between two consecutive accepted observations in the performed POD with real data for ENVISAT (ENVISAT observations are provided in the DORIS data exchange format). The majority of observations exhibit a sampling rate of 7 or 10 seconds, significantly fewer have a sampling rate of 14 seconds. This occurs when multiple seven-second observations come in line and an intermediate one is excluded during the POD, or when no valid observation is generated for other reasons (e.g., zero phase). Other notable peaks in the sampling rates are observed in the histogram at 20 and 24 seconds. These are attributed to disparate combinations of the various integration intervals and the absence or acceptance of a few observations in between. In the simulation, observations are initially simulated at 10-second intervals. These are subsequently processed by the ensuing steps of the simulator, where some of the observations are eliminated, also resulting in larger sampling rates between observations.

5.1.4 Further observation characteristics

Other characteristics of the DORIS real data that are analysed for the simulations are the number of ground stations received in parallel, the noise of the observations, and the global distribution of azimuth and elevation of the observations at the ground stations. Fig. 5.3 illustrates the analysis of the simulated observations using ENVISAT as an example. The results for the real observations are displayed on the left, while the results for the simulated observations after completion of the full sequence of the simulator environment (as described in Chap. 4) are shown on the right. The figures illustrate, from top to bottom, the number of ground stations received in parallel and the distribution of the residual RMS of the POD. The figures underneath present the distribution of observations for all stations over the azimuth angle and the distribution over the elevation angle. The maximum number of stations that can be received in parallel is two for ENVISAT, given that it is equipped with a 2G receiver, the upper limit of which is two channels. The simulation for ENVISAT is able to reproduce this

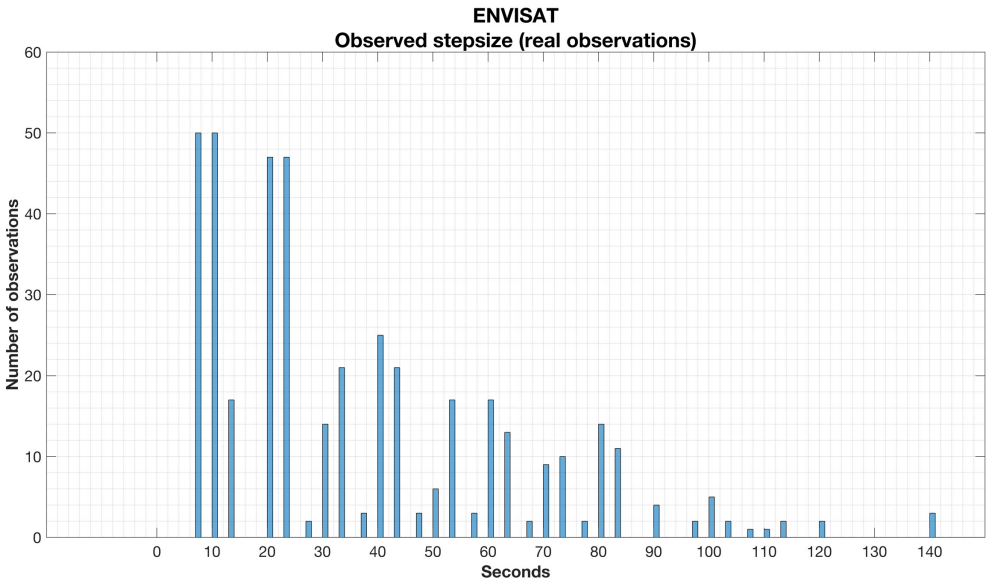

Figure 5.2: Analyses of the sampling rate of accepted DORIS observations of a POD using real data for ENVISAT. Most observations show a sampling rate of 7 and 10 seconds to each other.

structure with a high degree of accuracy. The distribution of the residuals shows a Gaussian distribution for both the real data and the simulated observations, with a mean value close to zero. The observations are almost evenly distributed across the azimuth angles for all ground stations. Minor maxima are observed at approximately 180 and 360 degrees. This can be attributed to the fact that near-polar stations have only a direct line of sight to the satellite, for instance, to the South or to the North. The distribution of observations over the elevation angle decreases uniformly with increasing angle. This can be attributed to the fact that the time a satellite flies over a station in the direct or near zenith is the shortest, while further on the horizon it becomes longer and longer at almost the same elevation angle, resulting in a greater number of observations. A comparison between the real observations and the simulated ones reveals that the simulation is capable of reproducing the behaviour over the elevation angle as well as the fine structures in the azimuth.

5.1.5 Global observation coverage

To ensure that all parts of the satellite's orbit are covered with observations, it is important to have an optimal global distribution of the ground stations. This is needed to ensure the most accurate state determination of the satellite at any given time and location. Fig. 5.4 illustrates the global observation coverage and distribution for the real and simulated observations. It is evident that ENVISAT exhibits a greater number of observation gaps in comparison to the two Jason satellites, which can be attributed to its lower altitude. Jason-1 and 2 do not show observations in the near polar regions due to their lower inclination. In comparison, Jason-2 exhibits a markedly higher number of observations. This is due to the DGXX receiver on board, which is capable of tracking up to seven signals from ground stations in parallel, in contrast to the two signals that can be tracked by ENVISAT and Jason-1. At the altitude of the Jason satellites, DORIS achieves an almost perfect global observation coverage. It is observed that, for all missions, there are minor gaps in the observation coverage in the North-Eastern and South-Western regions. The global observation coverage of the simulated observations is shown for each of the three satellites

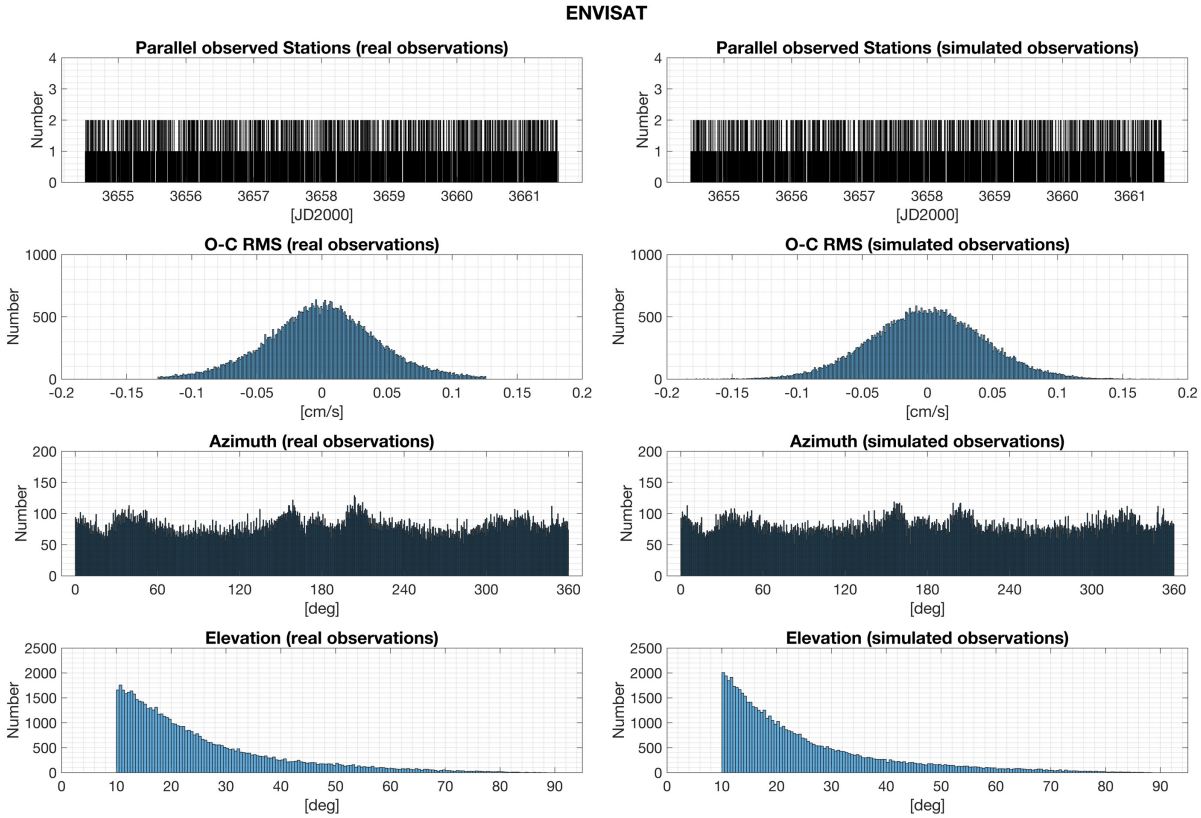

Figure 5.3: Analyses of observations for the maximum number of ground stations tracked in parallel, histogram of residual RMS, and azimuth and elevation dependent distribution of observations for one week. The left figures show the analysis for real observations, the right figures for simulated observations. Since the simulator is trained with real data, and real data are also required for quality control, ENVISAT is used as an example.

on the right-hand side of Fig. 5.4. Slight discrepancies can be noticed between the real data and the simulated data in the case of ENVISAT. In the regions of overlap between ground station visibility, the number of observations in the simulation is slightly higher than in the real world. This can be attributed to the onboard software that schedules the real observations. To verify this assertion, three-dimensional plots of ENVISAT's observation vectors during a short arc are presented in Fig. 5.5 a) and b). In the closer view on the right figure b) it can be seen, how the receiver, with its two channels, switches between the possible signals of the ground stations in order to achieve an optimal observation distribution. Here short observation gaps become obvious e.g. at the observations shown in light red. In contrast, in the simulation, the signal switch occurs instantaneously, resulting in a slight increase in observations in overlapping areas. However, this phenomenon is only discernible for ENVISAT, the higher orbiting Jason-1 satellite exhibits minimal indication of this effect, and Jason-2 not at all, which is capable of tracking up to seven signals in parallel. Fig. 5.5 c) and d) illustrate the difference between two and seven receive channels, examplified by Jason-1 and Jason-2, situated in approximately the same geographical position along the arc. The greater number of channels leads to a considerable increase in the number of observations, even for stations located at greater distances. For the simulation of the space-tie satellite scenarios, the characteristics of the most advanced type of DORIS receivers is chosen (i.e. DGXX/DGXX-S), capable of tracking up to seven signals in parallel.

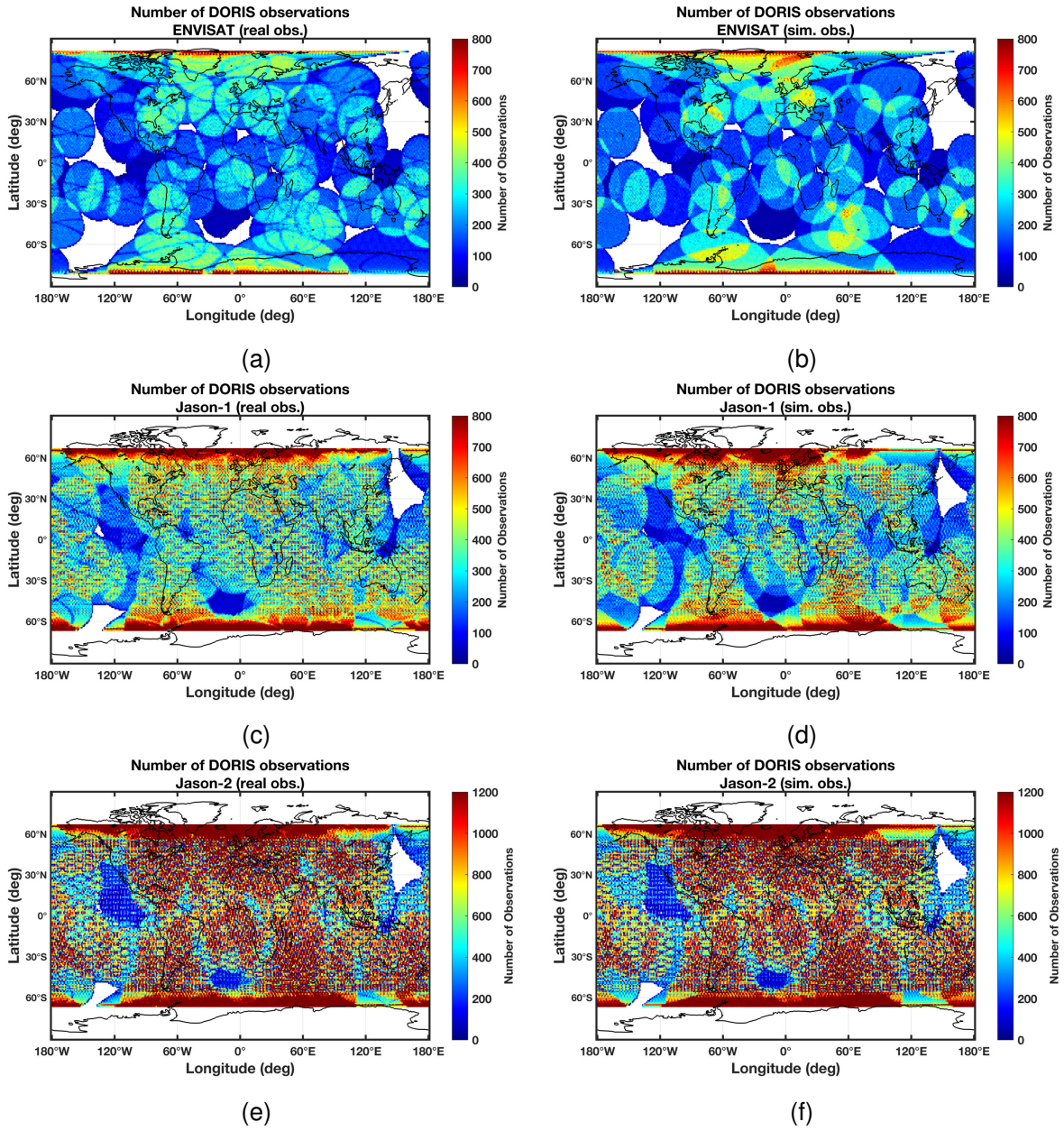

Figure 5.4: The figures on the left (a,c,e) show the global observation coverage with real observation data for the satellites ENVISAT, Jason-1 and Jason-2. The figures on the right (b,d,f) show the global observation coverage with the simulated observation data for the respective satellite.

5.1.6 Station availability

The availability of DORIS ground stations can be interrupted, e.g. due to maintenance, technical issues or equipment upgrades. This behaviour has to be reproduced for a realistic simulation. To this end, the station availability per station and arc was analysed for the three satellites. Fig. 5.6 shows for each satellite the number of accepted observations for each station and arc. Stations situated closer to the poles have a greater number of observations than others, depending on the inclination of the satellite. The station availability is reproduced directly in the simulation as an on/off switch.

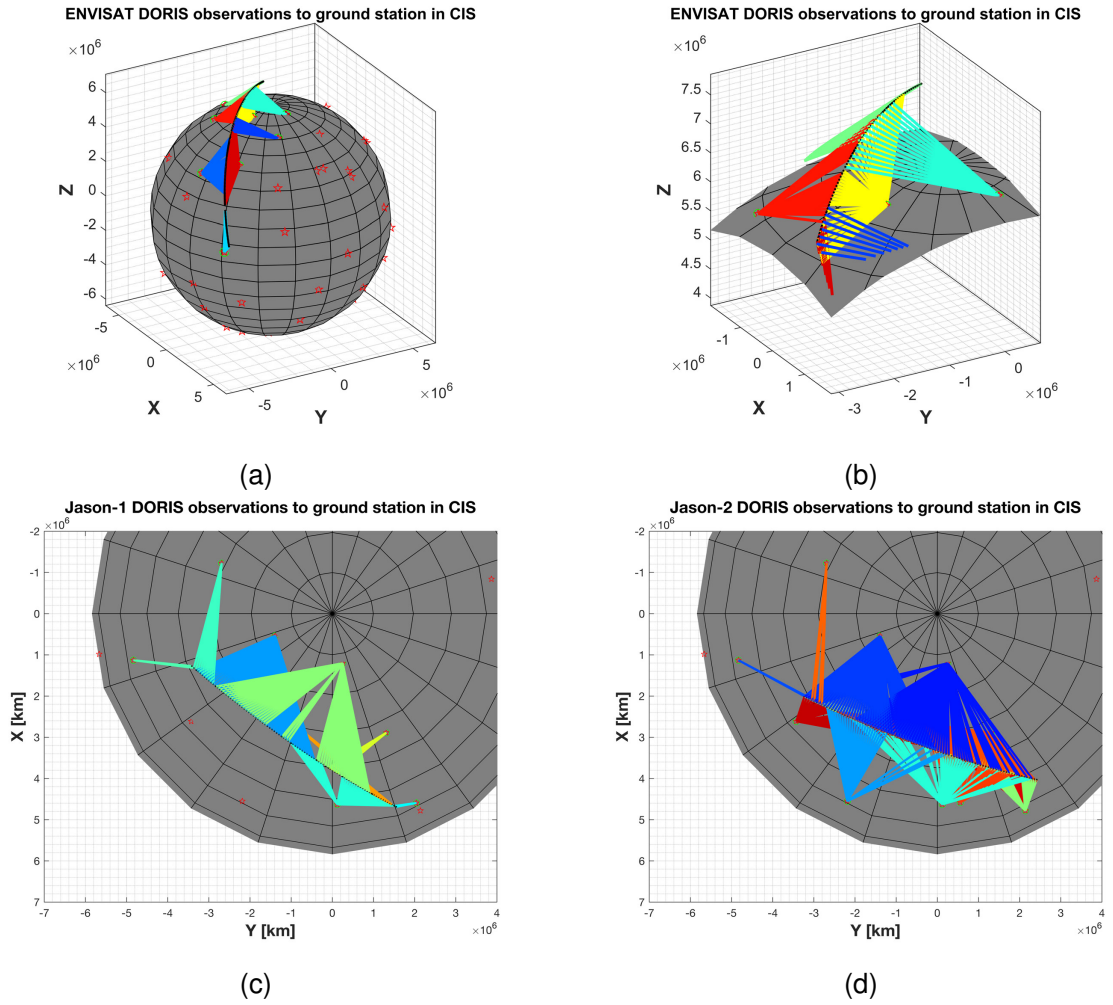

Figure 5.5: Three-dimensional view of the geometry of the DORIS observations. The stars mark the ground stations, the position of the satellite is marked in black and the coloured vectors show the observations, with each colour representing the observations from a ground station. Figure a) shows the vectors of the observations received by the ENVISAT 2G receiver. Figure b) shows a closer view of this pass. Figures c) and d) show a comparison of Jason-1 and Jason-2, highlighting the difference between the 2-channel 2GM receiver and the 7-channel DGXX receiver.

5.1.7 Overall orbital fit

The obtained orbital fit of the POD provides the basis for the measurement noise of the simulated observations. The statistical values of the POD, i.e. RMS, mean, standard deviation and the number of accepted observations and passes per arc, are presented for the three satellites in Fig. 5.7 a), c) and e). Additionally, the global RMS values are provided in Tab. 5.2. The global mean RMS values for DORIS are 0.35 mm/s for Jason-1 and Jason-2, with ENVISAT exhibiting slightly higher RMS values of 0.42 mm/s. The SLR observations were first used in the real data analysis to calculate and correct the DORIS time bias, and subsequently downweighted for quality control of the orbits. The RMS values of the SLR observations are approximately 1 cm for all three missions. This confirms the accuracy of the orbits and the setup of the DORIS orbit determination. The missions show an average of approximately 60 thousand accepted observations per weekly arc for ENVISAT, 80 thousand for Jason-1, and 116 thousand for Jason-2. A comparison of the capabilities of

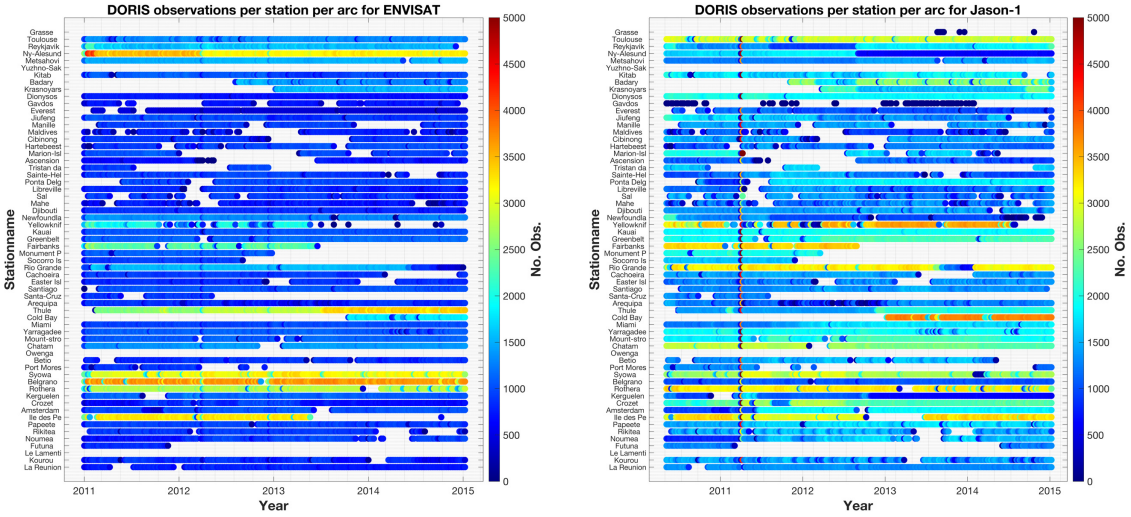

(a) ENVISAT real observations

(b) Jason-1 real observations

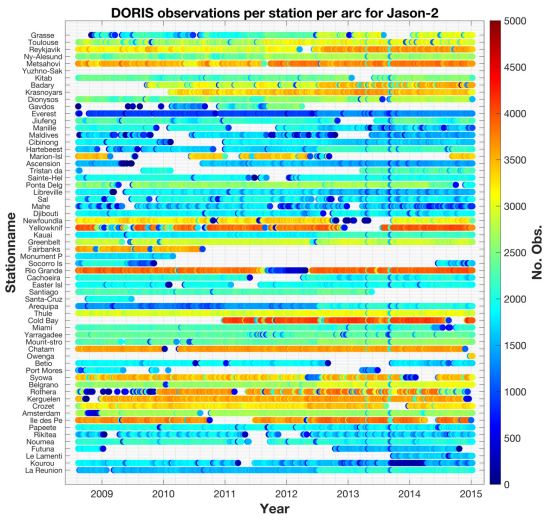

(c) Jason-2 real observations

Figure 5.6: Number of accepted observations per station per arc for a) ENVISAT, b) Jason-1 and c) Jason-2

the Jason-1 and Jason-2 reveales the benefit of the additional observation channels, which leads to approximately 45% more observations. Fig. 5.7 b), d) and f) and Tab. 5.2 show the results of the POD evaluation with the simulated observations. These results demonstrate a high degree of fidelity to the characteristics of the real data. The simulation of DORIS observations for the space-tie satellite scenario makes use of information from all three real satellites analysed. A DGXX-S receiver with seven channels is simulated, with the statistical characteristics of the stations employed in descending order of priority from Jason-2, Jason-1 and ENVISAT. Consequently, if no information is available from real data from Jason-2 at any stage during the simulation of the space-tie satellite, Jason-1 is utilised, and if that is also unavailable, ENVISAT is employed.

Table 5.2: Post-fit residuals and number of observations for the three satellites (SLR down-weighted in the real data case for orbit quality control). The time span is the full mission duration between the project period from the beginning of 2008 to the end of 2014.

	DORIS [mm/s]			SLR [cm]		
	RMS	Mean	No. Obs.	RMS	Mean	No. Obs.
ENVISAT (real data)	0.42	0	12'352'695	1.23	0	324'570
ENVISAT (simulated data)	0.42	0	12'346'603	-	-	-
Jason-1 (real data)	0.35	0	19'384'620	1.00	0	692'203
Jason-1 (simulated data)	0.35	0	19'249'774	-	-	-
Jason-2 (real data)	0.35	0	38'722'235	1.04	0	1'155'866
Jason-2 (simulated data)	0.35	0	38'712'550	-	-	-

5.1.8 Conclusion DORIS

The real data from the ENVISAT, Jason-1 and Jason-2 satellites were evaluated for the DORIS simulation of the existing space and ground segment. Based on the results of the POD, the simulation was trained for these three satellites. The aforementioned satellites were subsequently simulated themselves, whereby the combination of these three forms the simulated reference solution for DORIS. The training data gives the basis for the simulation of DORIS observations of the space-tie satellite scenarios, which are employed in descending order of Jason-2, Jason-1 or ENVISAT, depending on availability. The DORIS receiver of the space-tie satellite is simulated as a DGXX-S receiver, with the capability to track up to seven signals in parallel.

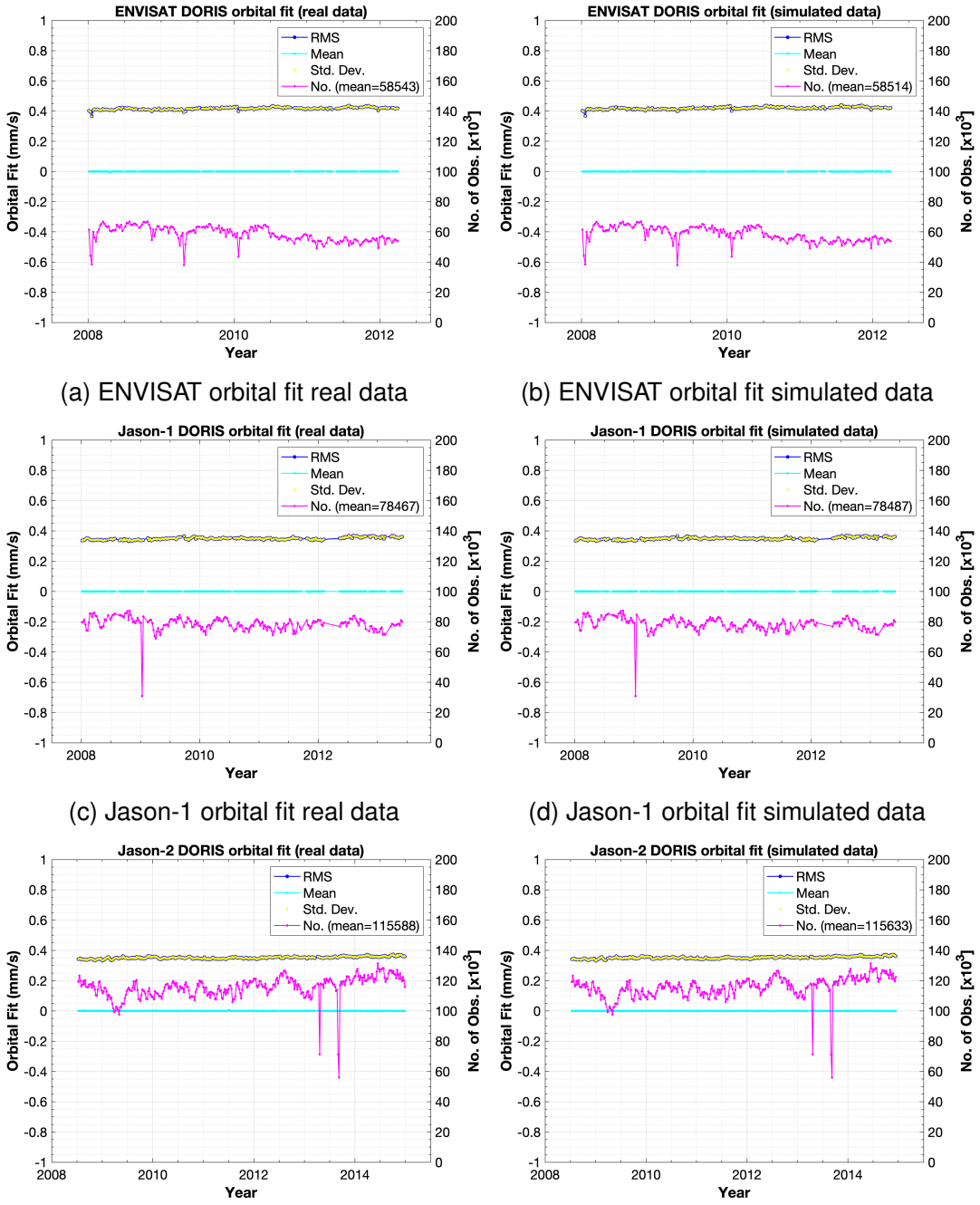

(a) ENVISAT orbital fit real data

(b) ENVISAT orbital fit simulated data

(c) Jason-1 orbital fit real data

(d) Jason-1 orbital fit simulated data

(e) Jason-2 orbital fit real data

(f) Jason-2 orbital fit simulated data

Figure 5.7: Orbital fit obtained for the three satellites used as direct basis for the simulations. The figures on the left (a,c,e) refer to the real data, the figures on the right (b,d,f) to the simulated data. The peaks in the number of observations represent arcs where either observation gaps occur or a higher number of observations are eliminated due to, for example, manoeuvres. This was included in the simulation in order to simulate these scenarios in a realistic manner.

5.2 SLR

The existing space segment currently used within the ILRS for reference frame determination with SLR has, over the past few decades, consisted of the two geodetic satellites LAGEOS 1 and 2 and the two Etalon satellites. For the real data evaluation with SLR, in addition to the two LAGEOS satellites, a number of well-known geodetic satellites are also taken into account, which are listed in Tab. 5.3. These are used at GFZ, for the determination of the C_{20} time series (König et al., 2019) and other low-degree SHs in the context of GRACE/GRACE-FO missions' gravity fields (Dahle & Murböck, 2020). The two Etalon satellites are not included, as they are not used at GFZ for the purpose of gravity field modelling. In order to evaluate the characteristic properties of the SLR technique, the real data is analysed for the elevation cut-off angle, station availability, pass yield, observation yield, and the sampling rate of the observations. Additionally, the measurement noise of the observations is taken into account, specifically in terms of the achievable orbital fit. The process by which these simulations are created, which forms the basis for the SLR simulations of the space-tie satellites, is described in detail in the following section. The procedure and results for LAGEOS-1 are presented in greater detail as an illustrative example, as LAGEOS-1 provides the primary basis for control information for the SLR space-tie satellite simulation. The procedure and results for LAGEOS-2 are identical.

Table 5.3: Geodetic satellites that have been analysed and evaluated. Orbital elements taken from the real data analysis prepared for this work.

	Per. h. [km]	Apo. h. [km]	Inclination	Ecc.	A/M [cm^2/kg]	Launch
Ajisai	1480.19	1496.18	50.0°	0.0009	53.0	12-Aug-1986
LAGEOS-1	5844.45	5942.49	109.9°	0.0040	6.9	04-May-1976
LAGEOS-2	5610.16	5956.58	52.6°	0.0142	7.0	22-Oct-1992
LARES	1441.37	1449.92	69.4°	0.0007	2.7	13-Feb-2012
Starlette	799.77	1110.76	49.9°	0.0211	9.5	06-Feb-1975
Stella	788.49	813.48	98.4°	0.0018	9.4	26-Sep-1993

5.2.1 Ground station elevation cut-off angle

In the default POD setup for the SLR real data evaluation, an elevation cut-off angle of 10 degrees is used. However, not every SLR station is capable of observing down to 10 degrees or below, due to the limitations of its construction or its surrounding environment. In order to ascertain the individual angle of each station and thereby enable station-by-station control in the simulation, the accepted observations of the performed POD of the satellites from Tab. 5.3 are analysed for their lowest elevation angle. Fig. 5.8 illustrates the results for LAGEOS-1, ordered by descending angle. The mean angle for all stations is approximately 18 degrees, with only a few stations capable of observing down to the predefined minimum angle of 10 degrees. These station values are used as constant values for the minimum elevation of the simulation of SLR observations for all scenarios.

5.2.2 Observation sampling rate

The term 'bin size' refers to the time interval used to generate NPs from full-rate SLR observations. This value is specific to each satellite and depends on the altitude of the satellite. A bin size recommendation is given by the ILRS (NASA, 2024). In the case of LAGEOS-1, this value is 120 seconds. In the simulation, the sampling rate of the observations

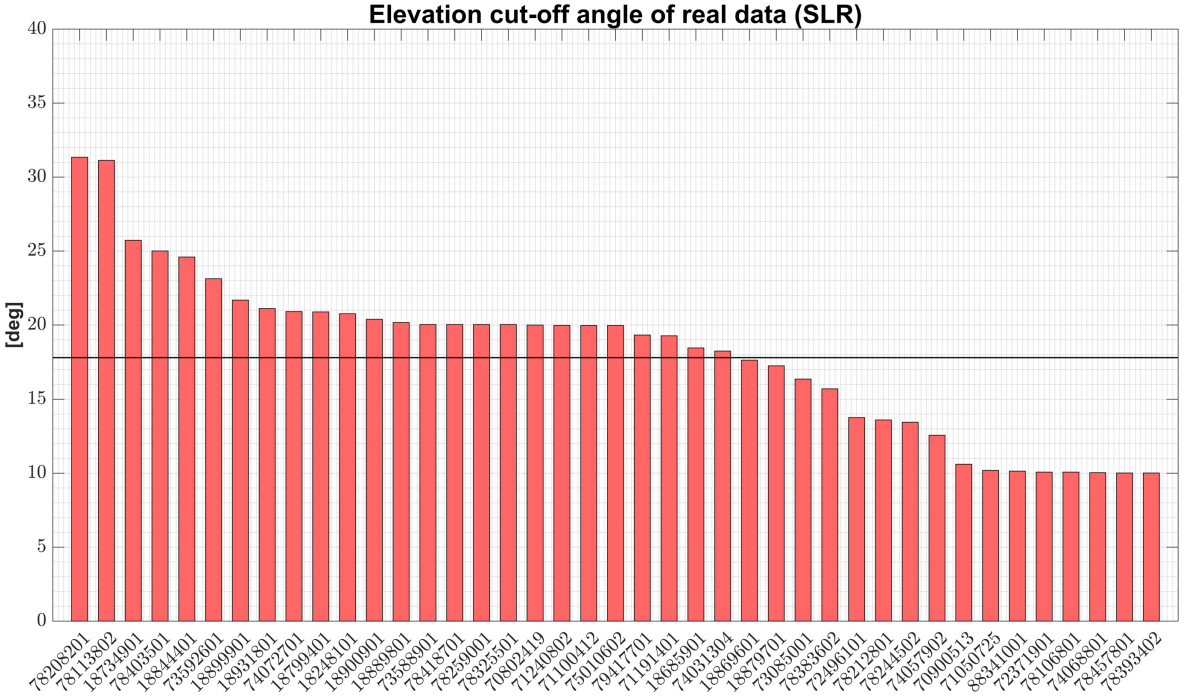

Figure 5.8: Elevation cut-off angle derived from real data for LAGEOS-1 (threshold in POD processing 10 degrees, therefore no analysed observations below this value). The black line symbolises the mean cut-off angle of 18.1 degrees for all stations.

is defined, which, in this context, can also be understood as the bin size. Nevertheless, it is necessary to ascertain whether the sampling rate of the accepted observations in a POD is approximately equivalent to the recommended bin size when utilising real data. Fig. 5.9 shows the sampling rate of the accepted observations of the POD with real observations for LAGEOS-1. Tab. 5.4 lists the mean values of the fitted Gaussian distribution for the evaluated missions. The sampling rates for LAGEOS-1 exhibit a fairly good Gaussian distribution around the mean value of 111 seconds. As can be seen in the histogram, the sampling rate between two observations can also be considerably smaller than the bin size. This phenomenon can be attributed to the manner in which the filter program assigns the NP epoch (e.g., mean or median) and the distribution of observations within the NP. To illustrate, if the full-rate observations are generated over a time interval of 20 seconds and this period is at the end of a bin, i.e. 100 to 120 seconds from T0, then a NP filter program would assign this NP the middle epoch of the full-rate observations, for example, which in this example would be T0+110 seconds. Consequently, the subsequent bin epoch would span from T0+120 seconds to T0+240 seconds. In the event that the 20-second full-rate observations being observed at the beginning of the subsequent bin rather than at the end, the time interval between the initial and subsequent NP is 20 seconds, still with a bin size of 120 seconds. If the initial observation were to be made at the beginning of the first bin and the subsequent observation at the end of the second bin, this would result in a lengthening of the sampling rate. The elimination of observations during the POD process, as well as the slewing of the SLR station from one satellite to another in order to generate observations for other satellites as well (segmented observations), mean that the sampling rate can also vary significantly.
In the simulation of the space-tie satellite scenarios, the sampling rate is adjusted iteratively

following an initial simulation to ensure that the average number of observations across the entire simulation period is approximately equivalent to that observed for LAGEOS-1. Consequently, all scenarios of the space-tie simulation possess a comparable number of SLR observations.

Table 5.4: Bin size according to NASA (2024) and analysed sampling rate of the accepted observation. All values in seconds.

		Sampling rate	
	Bin size	real data	simulation
Ajisai	30	28 ± 11	-
LAGEOS-1	120	111 ± 43	120
LAGEOS-2	120	111 ± 43	120
LARES	30	31 ± 14	-
Starlette	30	28 ± 11	-
Stella	30	28 ± 11	-

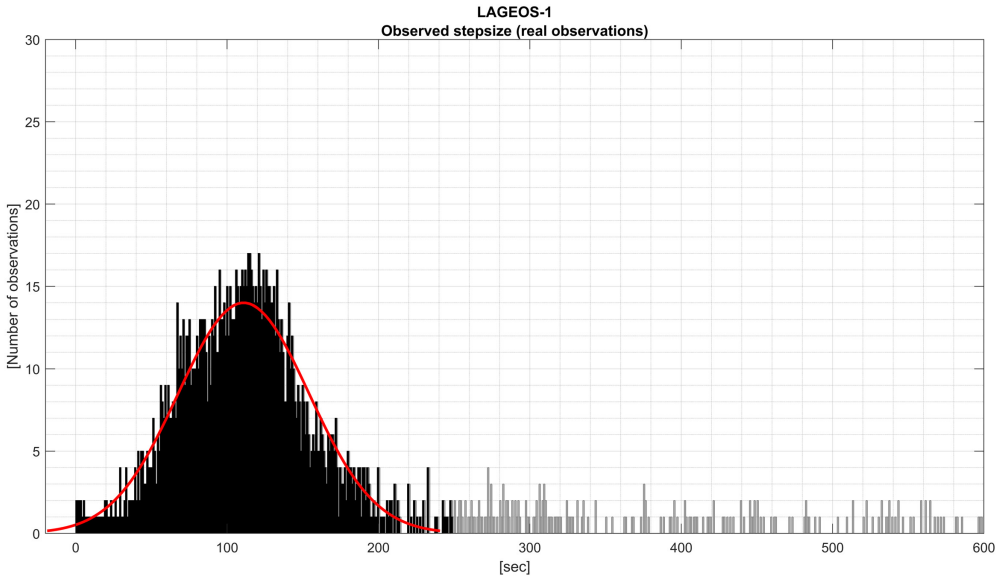

Figure 5.9: Distribution of the sampling rate of accepted SLR observations in a POD. The grey bars show all data, the black ones the data used to fit the Gaussian distribution shown in red.

5.2.3 Global observation coverage

The geographical distribution of the SLR observations for LAGEOS-1 and 2 is illustrated in Fig. 5.10 a) and c). The global coverage of SLR varies significantly with the altitude of the satellite, due to the fact that there are considerably fewer ground stations compared to DORIS, for instance. As a result, as the altitude of the satellite decreases, the observation patterns become increasingly spot-like in proximity to the stations and in regions where observations are not possible. The effect is less pronounced for the two LAGEOS satellites, due to their altitude of approximatly 6'000 km. The right figures b) and d) in Fig. 5.10 show

the geographical distribution of the simulated observations. The simulated observations demonstrate a high degree of agreement with the real data. Some minor differences can be seen in the observation gaps near the equator at 30 degrees West and 60 degrees East, which are slightly smaller in the simulation. Furthermore, the observations in the region extending from Central Europe to North Africa and South Australia are slightly more evenly distributed in the simulation. The geographical observation maps of the simulated SLR observations for the space-tie scenarios can be found in Sec. 6.2, where they are subject to detailed analysis.

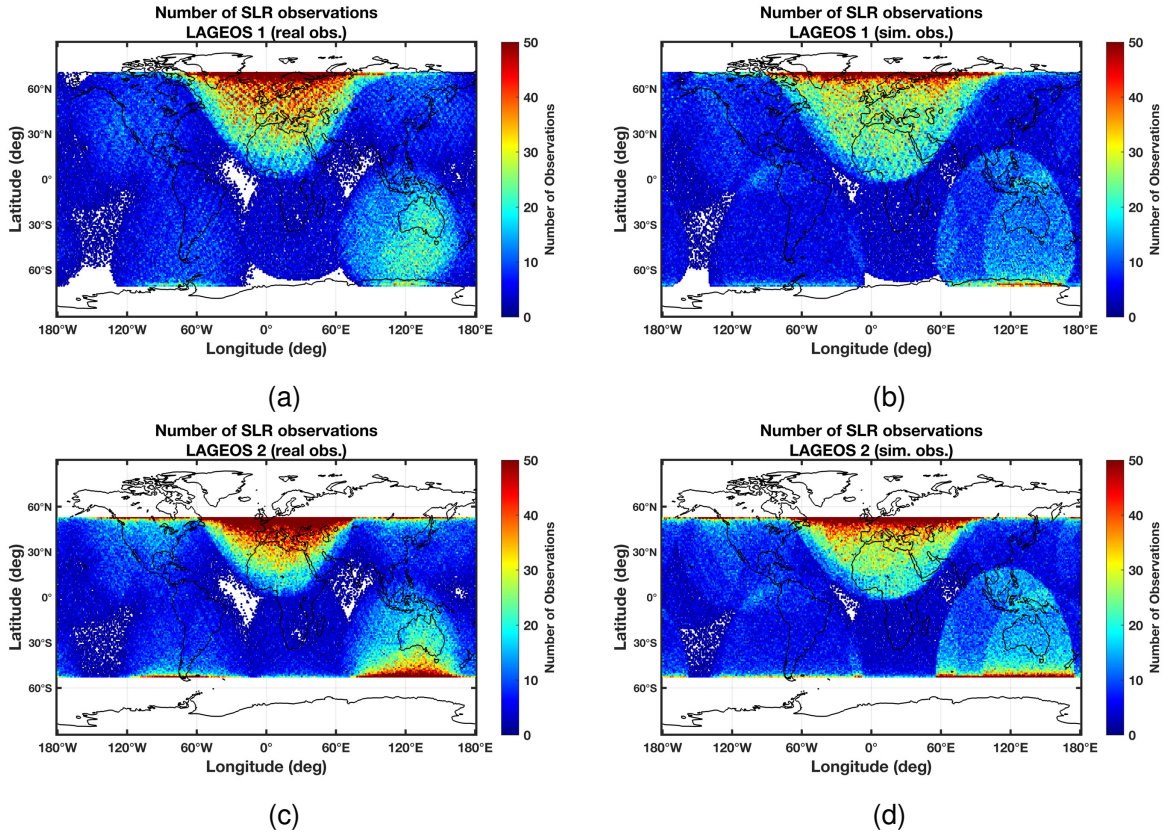

(a) (b)

(c) (d)

Figure 5.10: Maps showing the geographical distribution of SLR observations to LAGEOS-1 and LAGEOS-2 for the real observations in the figures on the left, and for the simulated observations in the figures on the right.

5.2.4 Station availability

The SLR ground stations are not in continuous autonomous operation. Despite the growing automation of processes such as the tracking process itself, external factors such as weather remain a significant limiting factor. Therefore, there are intervals during which the station is unable to observe satellites. For the simulation, it is important to reproduce these periods as accurately as possible. For this purpose, all stations were analysed for their availability during the simulation period, based on real data. This information is then used in the simulation to control the number of observations to be generated. The evaluation of LAGEOS-1 is illustrated in Fig. 5.11. After that, stations that have been observing with more than one Site Occupation Designator (SOD) number within the specified time period are summarised for the simulation as a single station with one SOD (for example, Haleakala 71191401 and 71191402). This is done because station velocities are to be estimated, and this requires observations over several years (see also Sec. 4.5.3). In a real data analysis,

these two time spans, where the same station has observed with different SOD numbers, would be connected, for example by local ties (see also Sec. 2.7.6).

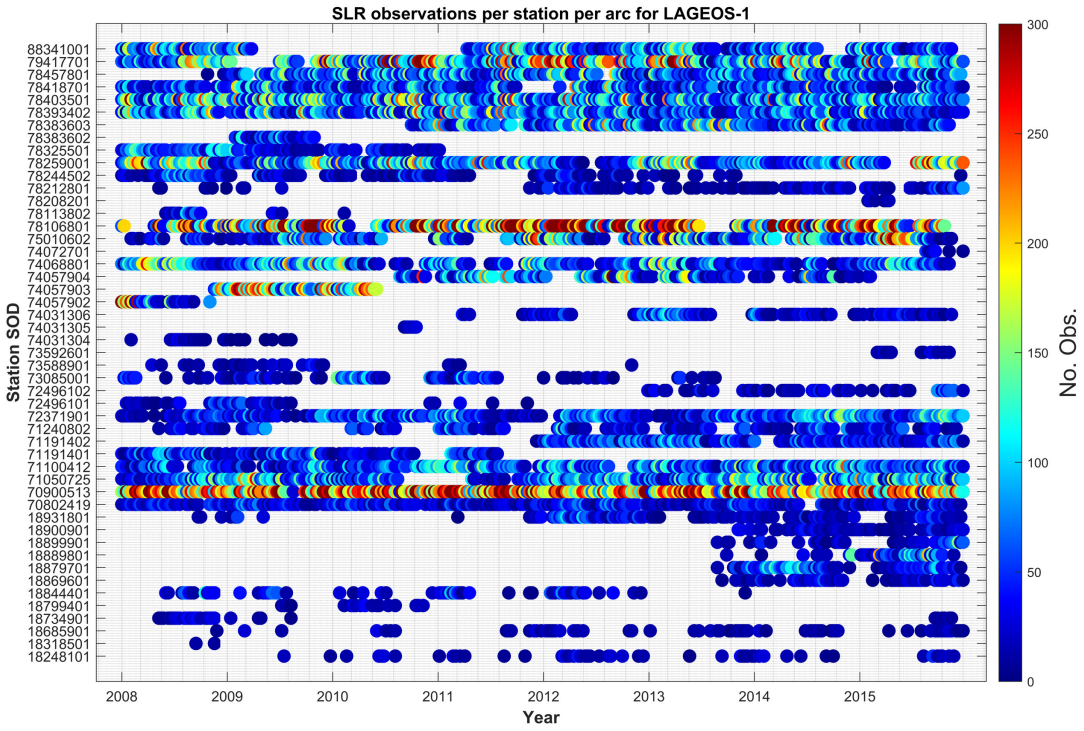

Figure 5.11: Number of accepted observations per station per arc after POD with real data for LAGEOS-1.

5.2.5 Station pass and observation yield

The term 'pass yield factor' can be defined as the ratio of the number of passes actually observed and the number of passes possible at most. In order to achieve this, a simulation is conducted in which all possible observations and all possible passes are considered. Only the sampling rate and the station specific elevation cut-off angles are used as control conditions for the simulator. The number of simulated passes is related to the number of accepted passes from the real data to obtain the pass yield factor. The average factor for LAGEOS-1 is approximately 10 (Pass yield factor = $N_{sim.\ passes}/N_{real\ passes}$). This indicates that each ground station observes only about every tenth possible pass of the satellite (see Fig. 5.12). If one wants to interpret this factor not only as a control parameter of the simulation, but also with respect to the real data, it should be noted that the simulation at this point does not take into account any limiting factors, such as weather conditions at a given time. The number of simulated passes is now adjusted to align with the number of passes obtained using the aforementioned pass yield factor. A comparison with the real data reveales an average deviation of -0.6% between the simulation and the real data in terms of the number of passes (negative values indicate a lower number of passes in the simulation).

Once the number of passes has been scaled, the theoretical maximum number of possible observations in the remaining passes can be compared to the number of accepted observations in the real data in the same way. This comparison demonstrates that, on average, approximately 3.5 times as many observations would be possible within the passes

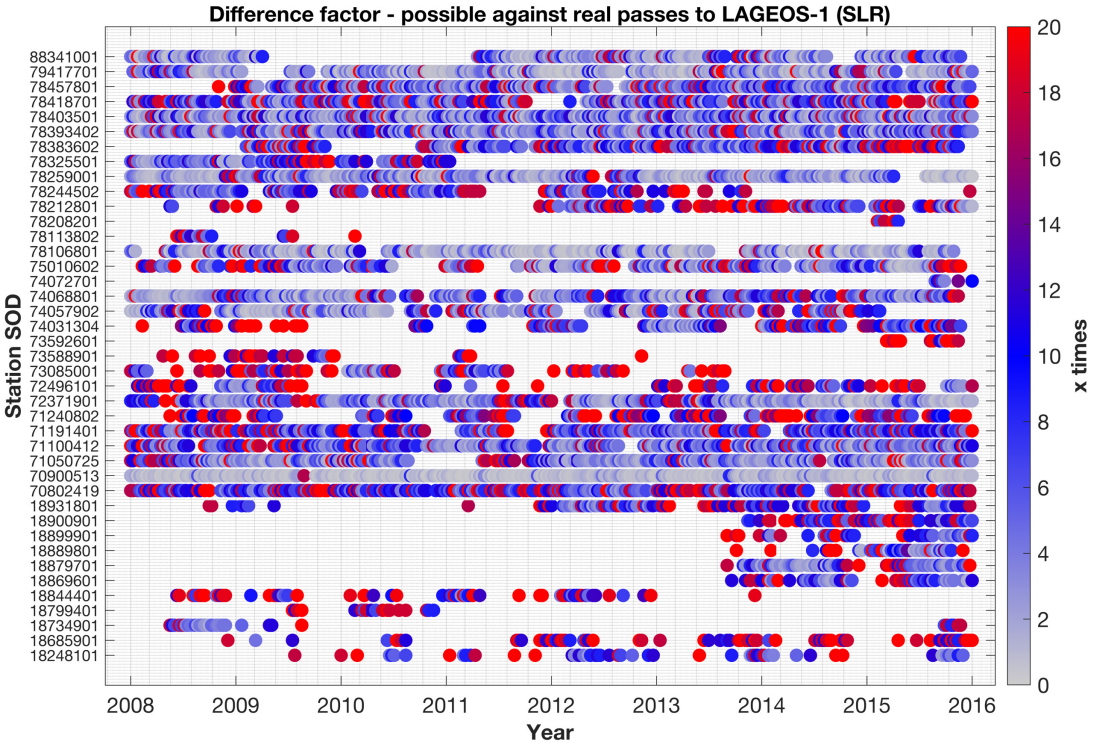

Figure 5.12: Factor showing the maximum possible number of passes per station to LAGEOS-1 compared to the actual number of passes observed. Light grey indicates that the station is operating close to its maximum. Blue shows the average of 10 and indicates that about 10 times more passes were theoretically possible. Red indicates that more than twice the average number of passes would have been possible.

observed in reality for LAGEOS-1 (see Fig. 5.13). One potential explanation for this discrepancy is the duration of a pass of a higher-orbiting satellite like LAGEOS-1, which can last several minutes. During this time, the station does not use its full capacity exclusively for observations of a single satellite. Instead, it also performs slews to other visible satellites, allowing these to be observed as well. Additionally, local conditions, such as weather, may prevent observations from being conducted. Subsequently, the observation yield factor is used to edit the number of observations within the remaining passes. Once more, a comparison is made between the simulation and the real data, resulting in a discrepancy of approximately 2% in the number of observations (a positive value indicates that the simulation yields a higher number of observations). The aforementioned deviations in passes and observations allow for the calculation of a performance factor for the simulator, defined as 100% minus the absolute value of the deviation. The factor is 99.4% for the number of passes and 98.0% for the number of observations. Both values can be accepted as a nearly perfect simulation.

5.2.6 Overall orbital fit

The standard deviation of the orbital fit obtained in the POD with real data is used as the basis for the measurement noise of the SLR observation simulations. For the POD the same setup is used as at the GFZ ILRS AC. The calculated global RMS values in Tab. 5.5 refer to the project period from 2008 to 2014. The values for LAGEOS-1 for this period are shown in

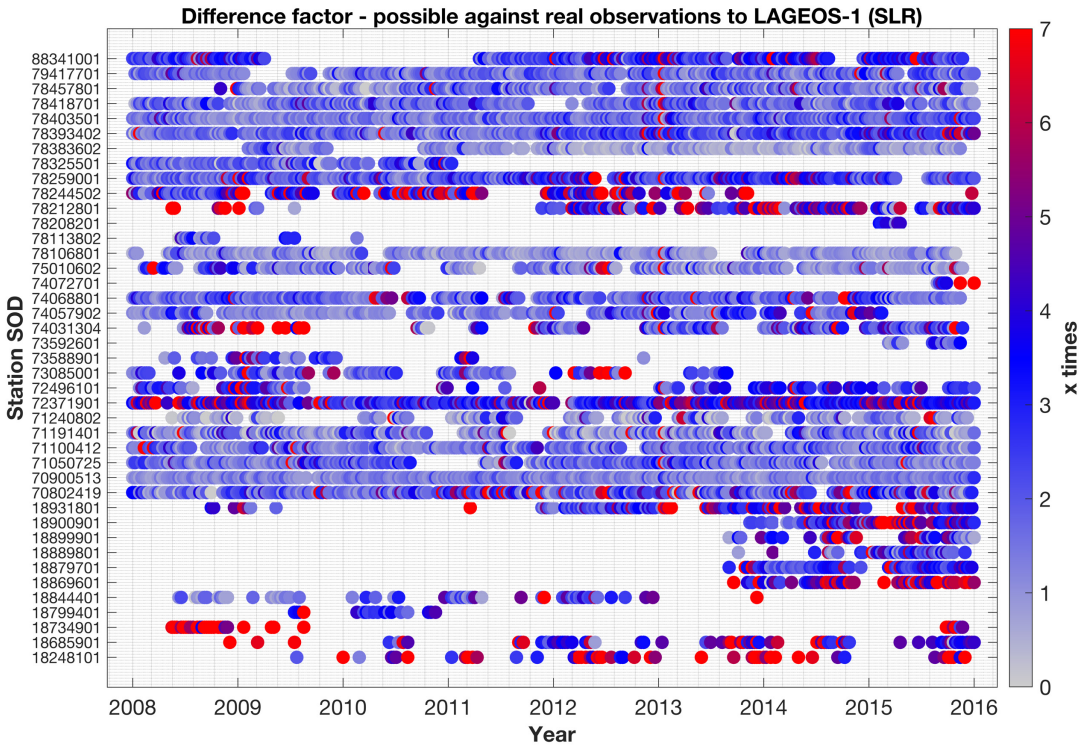

Figure 5.13: Factor indicating the maximum possible number of observations per station for LAGEOS-1 within the scaled passes. Light grey indicates that the station is close to its maximum, blue indicates a possible increase near the mean of about 3.5 times more observations, and red indicates a possible increase of more than twice the mean.

Fig. 5.14. These values are employed as control parameters for the white noise applied to the simulated observations, together with a zero mean condition, as described in Sec. 4.3. A comparison of the calculated standard deviations of the real and simulated data in the POD shows an agreement of 98.4%. Therefore, the mean of the generated noise is ~1.6% lower than that of the real data, indicating a very good agreement of the simulation with reality.

Table 5.5: Post-fit residuals and number of observations for the existing satellites, evaluated and simulated. The time span is the full analysis time period from the beginning of 2008 to the end of 2014.

	Real data			Simulation		
	RMS [cm]	Mean [cm]	No. Obs.	RMS [cm]	Mean [cm]	No. Obs.
LAGEOS-1	0.88	0.03	528’688	0.87	0.01	523’981
LAGEOS-2	0.91	0.03	468’834	0.90	0.01	464’880

5.2.7 Conclusion SLR

The simulated reference solution for SLR is formed by the combination of the two satellites LAGEOS-1 and 2. For the simulation of these two satellites, real data was evaluated and the simulator was trained. The accuracy of the simulation achieved in terms of the number of passes and observations, as well as the noise level, is over 98% for both satellites. The

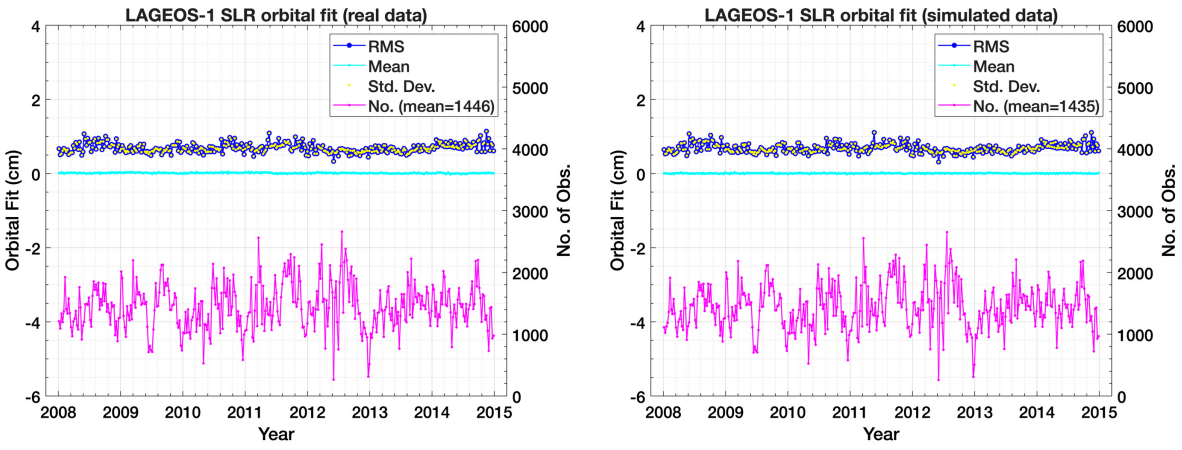

(a) (b)

Figure 5.14: The two figures show the achieved orbital fit for LAGEOS-1. Figure a) shows the values for the real data, figure b) for the simulated data. The mean number of observations per weekly arc is 1446 for the real data and 1435 for the simulation.

training data from LAGEOS-1 serves as the basis for the simulation of the SLR observations of the space-tie satellite scenarios.

5.3 GPS

In comparison to DORIS and SLR, the processing of GPS data typically comprises two distinct steps, referred to as the two-step approach (see Fig. 5.15). The first step involves the utilisation of a ground network of globally distributed receivers, which receive the signals transmitted by the GPS satellites. These observations can be used in a network adjustment to determine ERPs, ground station coordinates and the orbits and clocks of the GPS constellation. The second step then concerns only the satellites carrying a GPS receiver (here we consider only LEO satellites). The positions of the GPS satellites and their clocks are fixed in order to calculate the orbit and the clock parameters of the LEO satellite.

The LEO satellites observe the GPS satellites, but so far they are not commonly used to determine the orbits and clocks of the GPS constellation. An integrated approach, whereby ground station and LEO observations are processed in one single step, has been introduced by Zhu et al. (2004). Here, the LEO satellites are included in the adjustment of the GPS constellation. In this way, they contribute to the determination of the orbits and clocks of the transmitting satellites and thus indirectly also to the determination of the position and velocity of the ground stations and the ERPs. Fig. 5.15 illustrates this concept.

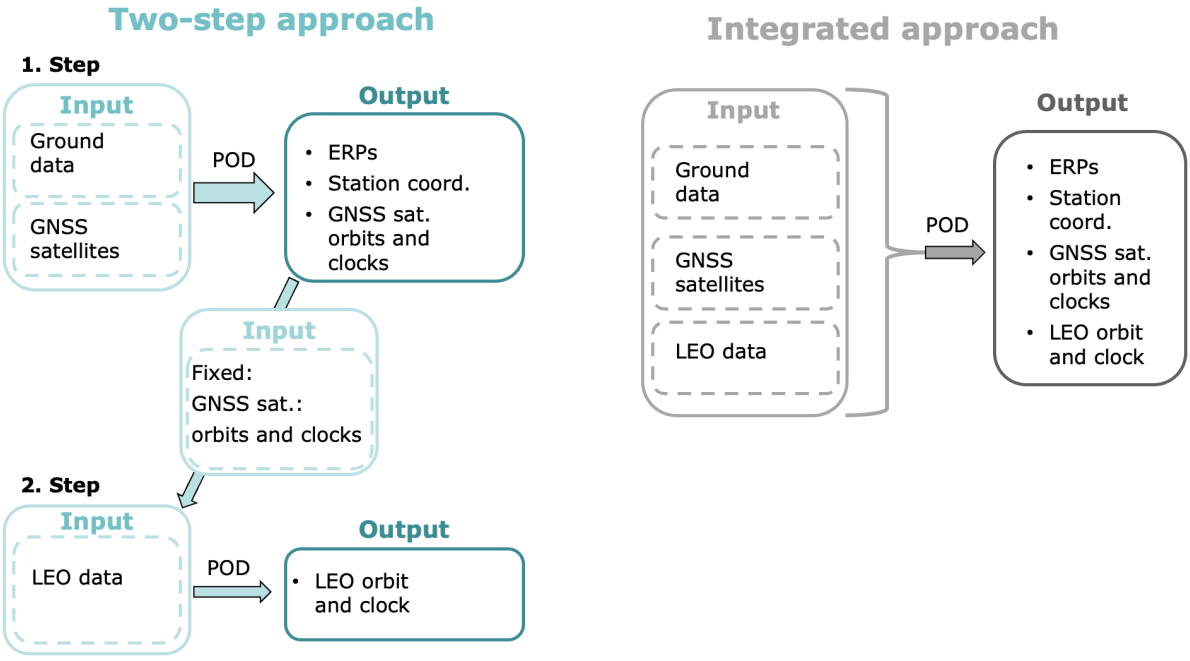

Figure 5.15: Conceptual illustration of the integrated approach compared to the conventional two-step approach.

For the GPS technique, the simulations are once more based on real data processing, albeit with a somewhat different approach in comparison to that of DORIS and SLR. As the integrated processing of LEOs together with a GPS constellation is not yet common practice, the conventional two-step approach has been employed for the preparation of the real data. Nevertheless, it is expected that the post-fit noise level will be on an equal level for the integrated approach. For the ground stations and the GPS satellites, the results of the Rapid Science Orbit (RSO) (Schreiner et al., 2022a) and Precise Science Orbit (PSO) GPS constellation solutions or specially prepared ones are used. These differ in terms of the number of stations employed, the length of the arc and the delay in the calculation. The basis for the LEO GPS information is the GFZ RSO solutions (Schreiner et al., 2022c), or

specially prepared orbits of the satellites listed in Tab. 5.6. The main focus is laid on the Sentinel-3A and Sentinel-3B satellites.

Table 5.6: Evaluated LEO satellite missions with GPS receiver and their orbital elements taken from the analysis prepared for this work.

	Perigee	Inclination	Ecc.	Launch	Evaluation reference
GRACE	449 km	89.0°	0.0029	16-Mar-2002	(König et al., 2022a)
					(König et al., 2022b)
GRACE-FO	478 km	89.0°	0.0021	22-May-2018	(Schreiner et al., 2022a)
					(Schreiner et al., 2022b)
Jason-2	1336 km	66.1°	0.0006	20-Jun-2008	specially generated
Jason-3	1336 km	66.1°	0.0006	17-Jan-2016	specially generated
Sentinel-3A	794 km	98.6°	0.0014	16-Feb-2016	specially generated
Sentinel-3B	794 km	98.6°	0.0014	4-May-1976	specially generated
Sentinel-6A (MF)	1336 km	66.2°	0.0006	21-Nov-2020	specially generated
SWARM-A	425 km	87.3°	0.0017	22-Nov-2013	specially generated
SWARM-B	492 km	87.8°	0.0016	22-Nov-2013	specially generated
SWARM-C	425 km	87.3°	0.0017	22-Nov-2013	specially generated
TanDEM-X	499 km	97.5°	0.0016	21-Jun-2010	(Schreiner et al., 2022e)
TerraSAR-X	499 km	97.5°	0.0015	15-Jun-2007	(Schreiner et al., 2022d)

5.3.1 Elevation cut-off angle

In the operational processing of the GFZ RSO and PSO constellation, the elevation cut-off angle employed for ground stations is 20 degrees. In the context of diverse projects, such as the Copernicus Sentinel satellites, alternative special constellation solutions are also generated, based on the utilisation of specific models for the purpose of ensuring consistent model processing. Some of these special solutions employ lower elevation cut-off angles. Nevertheless, the improvements in orbit and clock solutions resulting from the additional observations and improved geometry are modest, while the processing time rises considerably due to the markedly higher number of observations. Furthermore, the noise associated with the observations increases considerably when the elevation is below 20 degrees. To address this issue, a weighting function is typically used to assign reduced weight to observations with low elevation. In the case of the processing of the operational RSO constellation with EPOS-OC, no elevation-dependent weighting is employed with an elevation cut-off angle of 20 degrees. For the simulation here, given the time span of 7 years and the selected size of the station network, it was decided to adopt the same approach and simulate only observations down to a minimum elevation of 20 degrees, without elevation-dependent noise and without a weighting model.

In the processing of real GPS data from LEO satellites, no minimum elevation restriction is employed. However, it was found that the receiver for Sentinel-3A and Sentinel-3B is configured to not generate observations below 10 degrees. Therefore, the minimum elevation for the simulation of LEO GPS observations was set to 10 degrees.

5.3.2 Observation sampling rate

The current observation sampling rate for GPS ground receivers in the IGS network is 30 seconds for hourly or daily observation files. Nevertheless, an increasing number of stations are providing high-rate data, with observations taken every second. Here, for the processing of the GPS constellations, the hourly and daily observations are used (International GNSS Service (IGS), 1992a), as available at Crustal Dynamics Data Information System (CDDIS) (Noll, 2010). This configuration is followed in the simulation and an observation sampling rate of 30 seconds is simulated.

The observation sampling rate for LEO satellites is dependent upon the specific mission. Some receivers, such as those on Sentinel-3A and Sentinel-3B, are capable of providing continuous observations at one-second intervals for all signals. Other receivers, such as that on GRACE-FO, also provide observations at one-second intervals, but only a complete set of observations is available every ten seconds for all signals. In the case of the real data POD, a 30-second sampling rate is typically used in the Sentinel orbit determination configuration at GFZ, given that the constellation clock solutions are also generated in 30 second intervals, and thus no interpolation is required. The interpolation of clock solutions, depending on the sampling rate of the data set to be interpolated, can result in interpolation errors due to the non-linear behaviour of clocks. This leads to an increase in noise in the phase observations, which can have a detrimental impact on the accuracy of the orbit determination. Consequently, the sampling rate of the simulation of the LEO observations was chosen to align with that of the ground stations, which is 30 seconds.

5.3.3 Station availability

GPS receivers are nowadays ubiquitous and have been developed to a high standard by a wide range of manufacturers. Such devices are capable of functioning with a high degree of reliability over extended periods of time. Interruptions may occur due to a number of factors, including construction work, power outages, technical maintenance, replacement of antennas, and so forth. However, such interruptions are often of short duration. Therefore, an alternative method has been used to assess the availability of ground station receivers for GPS. To calculate the GFZ PSO GPS constellation solution, an average of 130-145 globally well-distributed GPS receiving stations are selected, for the GFZ RSO GPS solution about 80. The number of stations processed per arc over the years is shown in Fig. 5.16 for the PSO solution. For the simulation, a station network was created containing 128 stations[1], which are well-distributed globally. In each simulation arc, a random generator removes 5% of the stations (equivalent to 7 stations) from the network. This results in 121 stations (11^2) remaining for simulation and recovery.

5.3.4 GPS satellite availability

The GPS constellation comprises up to 32 satellites. Ideally, 32 satellites are active, utilising unique PRN codes. It is possible that a satellite may be temporarily unavailable, or that a particular PRN code may not be actively used by a satellite vehicle for an extended period of time. Such occurrences can be attributed to a number of factors, including satellite manoeuvres undertaken to maintain the orbital configuration of the satellites, cases of deactivation, the removal of satellites and the launch of new satellites. In the simulation, the information regarding the availability of each satellite is based on the IGS combined orbit solutions (International GNSS Service (IGS), 1992b). These are employed to extract

[1]The number 128 was chosen because it corresponds to 2^7 and therefore allows for easy subdivision into subgroups.

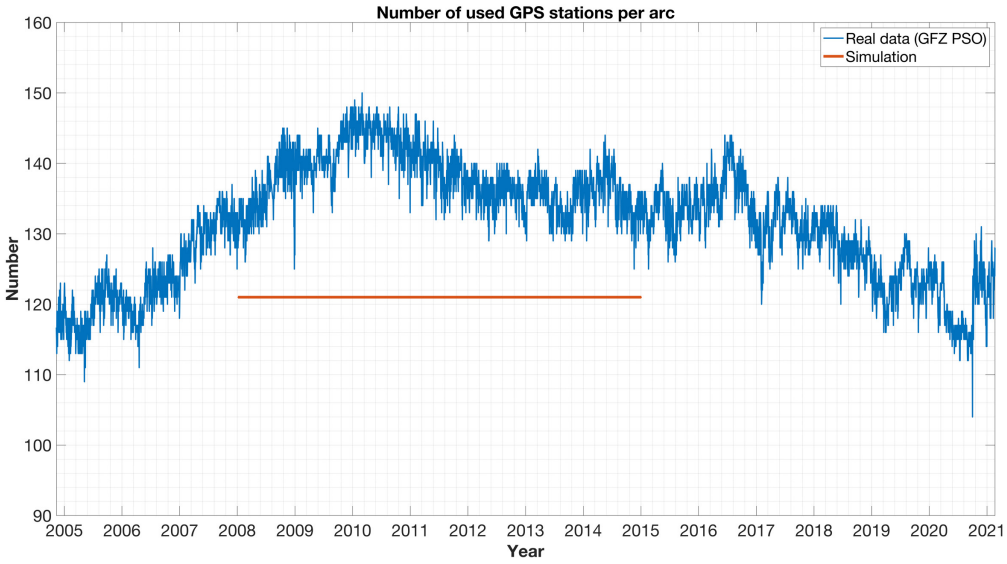

Figure 5.16: Number of stations used for the GFZ PSO GPS solution per day and for the simulation.

information regarding the initial elements of each satellite. If a particular PRN is not listed there, it is assumed to have experienced an outage and is also disabled in the simulation for that day. The number of PRNs subsequently used for the simulation is illustrated in Fig. 5.17.

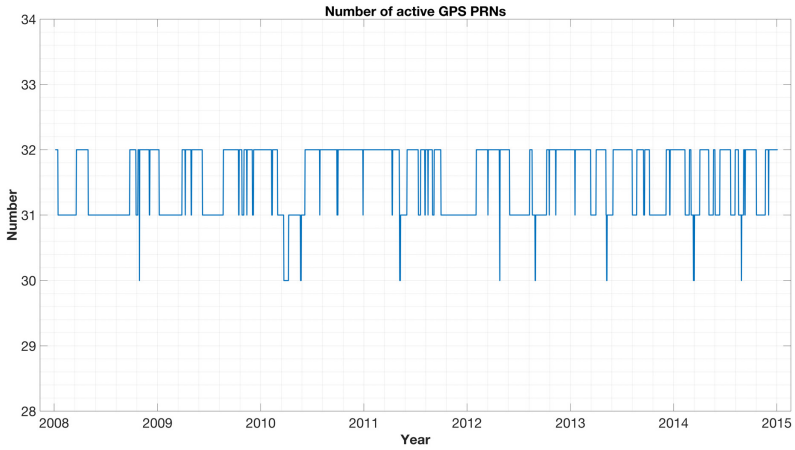

Figure 5.17: Number of simulated GPS satellites per day

5.3.5 GPS satellite block configuration

Over the years, various so-called GPS block types have been developed, with each iteration incorporating a number of innovative features. The actual GPS constellation for the period covered by the simulation (2008-2014) comprises a combination of older Block IIA to newer Block IIF satellites. The most recent block type is currently Block III. As the simulations describe a space-tie satellite in a future scenario, it was decided that the GPS constellation should be as up-to-date as possible. It was therefore assumed that all older block types would be superseded over the next few years by newer Block III satellites, which

have a projected operational lifespan of 15 years (NCO, 2022). Accordingly, the simulated constellation comprises solely Block III satellites. The PCO values listed in Tab. 5.7 and PCV characteristics were taken from the IGS14 Antenna Exchange Format (ANTEX) file (Johnston et al., 2017) of a Block III satellite and used for all. The shape of the satellite was configured using a box-wing model whose parameters were taken from Steigenberger et al., 2020 and further adapted based on images of the satellite body published by, for example, Lockheed Martin Corporation (2024). The final configuration of the box-wing model is listed in Tab. 5.8. These geometric and diffuse reflection coefficients for visible and IR wavelengths serve as the input for the calculation of the radiation pressure forces, as described in Sec. 2.4.3.4.

Table 5.7: PCO values used for all GPS satellites in millimetres. Axes orientation according to IGS conventions.

	X	Y	Z
L1	4.88	-21.04	1992.74
L2	4.88	-21.04	1992.74

Table 5.8: Used box-wing model for Block III satellites. Geometric reflection coefficient ρ and diffuse reflection coefficient δ. The axes follow the IGS conventions. Z radial, X direction to the Sun, Y direction to the solar panel rotation axis.

		Front				Back			
		visible		IR		visible		IR	
	Area [m^2]	ρ	δ	ρ	δ	ρ	δ	ρ	δ
X	3.96	0.01	0.46	0.00	0.46	0.00	0.46	0.00	0.46
Y	9.24	0.00	0.06	0.00	0.06	0.00	0.06	0.00	0.06
Z	7.56	0.10	0.46	0.10	0.46	0.10	0.46	0.10	0.46
Solar array	28.20	0.08	0.00	0.08	0.00	0.08	0.00	0.08	0.00

5.3.6 Code and phase residuals

The processing of real GPS data and the simulation with EPOS-OC uses code and phase observations at two frequencies. These are here the L1 and L2 frequencies. Furthermore, Block III satellites also transmit on the newer L5 frequency. However, given that the measurement in EPOS-OC refers to the ionosphere-free linear combination of two frequencies and that no mismodelling, such as that of the ionosphere, or bit errors are taken into account, the choice of frequency bands is not a critical factor. In order to create a realistic simulation, white noise is added to the simulated data. In the following, the terms 'code' and 'phase' are used to refer to the values of the ionosphere-free linear combination of pseudoranges and carrier phases. The noise values of the observations are based on the orbital fit values obtained from the processing of the real data. For this purpose the aforementioned constellations processed with EPOS-OC at GFZ were utilised. For POD with real data Fig. 5.18 a) and c) show the orbital fit values of the accepted code and phase observations, each globally for all stations per arc. The values of the code observations are about two orders of magnitude larger than those of the phase observations. The globally

obtained RMS values of the code observations are approximately 60 cm, while for the phase observations, they are approximately 4 millimetres.

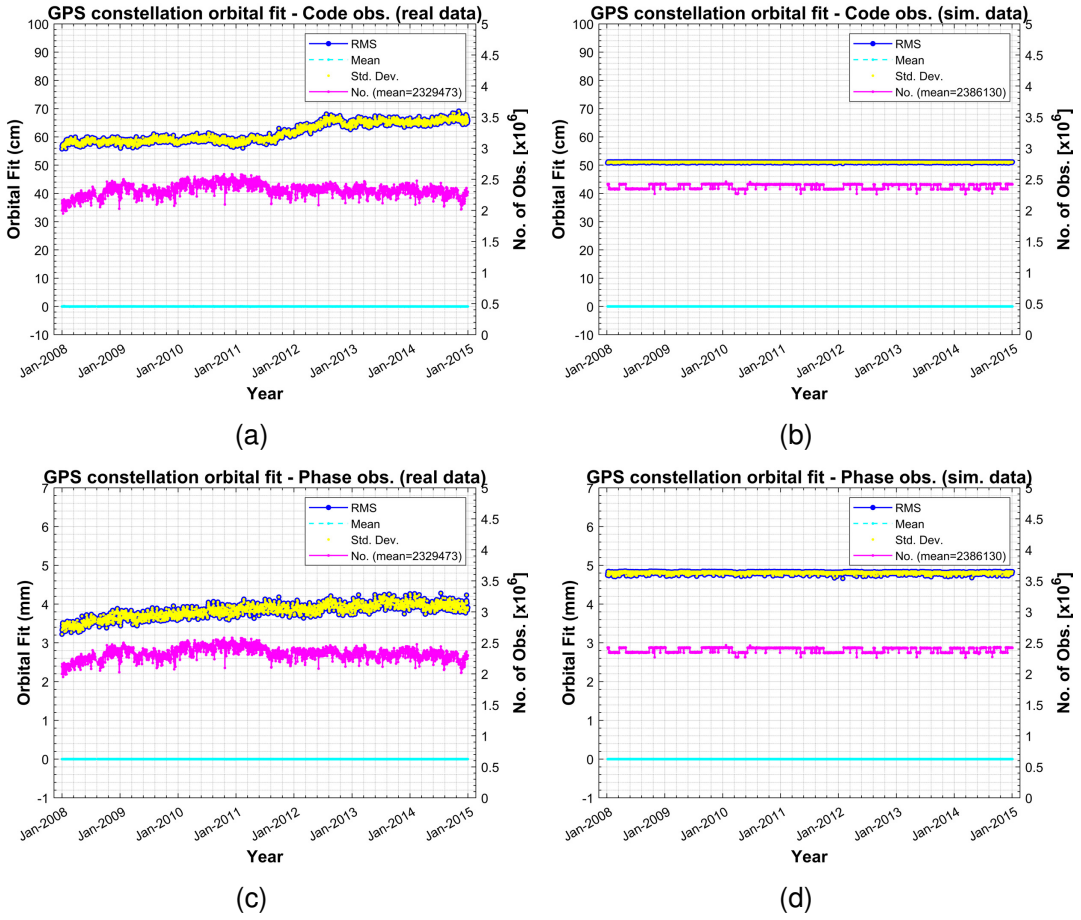

Figure 5.18: Global orbital fit of GPS code and phase observations for the real data based GFZ GPS PSO in the left subfigures and for the simulated observations in the right subfigures.

In the simulation, the aforementioned values have not been directly adopted for the noise. In order to achieve a ratio of weighting for code and phase observations of 1 to 100, the mean of the obtained code and phase RMS values in accordance with the desired weight ratio were used, which for the code can be calculated as $(Code_{RMS} + Phase_{RMS} \cdot 100)/2 = 50\,\mathrm{cm}$. The resulting noise value for the code is therefore 50 cm, while the phase value was set at 5 millimetres. Furthermore, the ground stations were categorised into two distinct groups. The majority of stations, i.e. 122, are assigned the above mentioned values for the observation noise. An increased phase noise of 10 mm and code noise of 70 cm is applied to another group of six ground stations. These values roughly correspond to the highest post-fit RMS of ground stations in the GFZ PSO. The orbit fit achieved in terms of RMS values for the current BLOCK III satellites is not significantly different from that of other block types. This was done in order to ensure that stations in the daily station subnetwork exhibit slightly lower performance following the random selection of stations from the total station network. Six ground stations were selected, so that, after the random generator has selected the total of 121 stations per arc, a maximum of about 5% (6/121) of the ground stations have these lower specifications. The post-fit values for the simulation are presented in Fig. 5.18 b) and d).

For the noise of the SST GPS observations of the receiver mounted on the space-tie LEO satellite, primarily the residuals achieved post-fit for the two satellites Sentinel-3A and Sentinel-3B are utilised. The mean residuals for the code observations are 38.9 cm and 37.5 cm, while the phase observations yield 3.1 mm and 3.2 mm, respectively (Schreiner et al., 2023). Accordingly, the noise for the LEO GPS receiver was set to 38 cm for the code and 3.1 mm for the phase observations.

5.3.7 Receiver channel limitation

The number of receiving channels of GPS receivers can be a limiting factor, particularly for those situated in LEO satellites. It can happen that the number of visible GPS satellites exceeds the number of channels available for parallel observations. This makes it impossible for a receiver to observe all theoretically possible satellites. In order to reproduce this effect for the GPS ground receivers of the simulation, general internal scaling factors have been employed which omit certain passes within a simulation arc. This consequently results in a reduction in the number of parallel observations. To ascertain an appropriate scaling value, the real data were evaluated with respect to the number of parallel received signals and compared with the simulations. The scaling factor for all stations was adjusted so that the average number of passes and the number of satellites received in parallel were identical for all stations. The scaling factor subsequently employed is 97% for the general network of stations and 85% for a subnetwork of five stations, as listed in Tab. 5.9 in order to include stations with lower performance. Fig. 5.19 shows for the GPS receiver in Ny Ålesund the number of satellites tracked in parallel for the real data evaluation and the simulated data, achieved with the respective scaling factor, the difference is insignificant.

Table 5.9: Scaling factors for the GPS ground stations in the simulation.

Site	City	Location	Scaling
TIDB	Tidbinbilla	Australia	85%
NKLG	Libreville	Gabon	85%
KIT3	Kitab	Uzbekistan	85%
KERG	Port-aux-Français	Kerguelen Islands	85%
REUN	Le Tampon	La Réunion	85%
all other			97%

The characteristics of the GPS receiver on the LEO satellite in terms of the number of available channels are based on a rigorous analysis of real data from the Sentinel-3A and Sentinel-3B satellites. The two satellites are constructed in an identical manner and are equipped with the same receiver. The receiver is capable of tracking up to eight satellites in parallel with full dual-frequency observations. Fig. 5.20 illustrates the number of parallel tracked PRNs for a 28-hour arc of real data processing from Sentinel-3A. The maximum number of parallel receive channels is therefore limited to eight for the GPS receiver of the simulated LEO satellite. This is achieved by simulating all possible observations initially. Subsequently, a post-processing step identifies the sessions of each PRN and the maximum number of PRNs tracked in parallel per epoch. Finally, a random generator eliminates several channels until the maximum condition of eight is met.

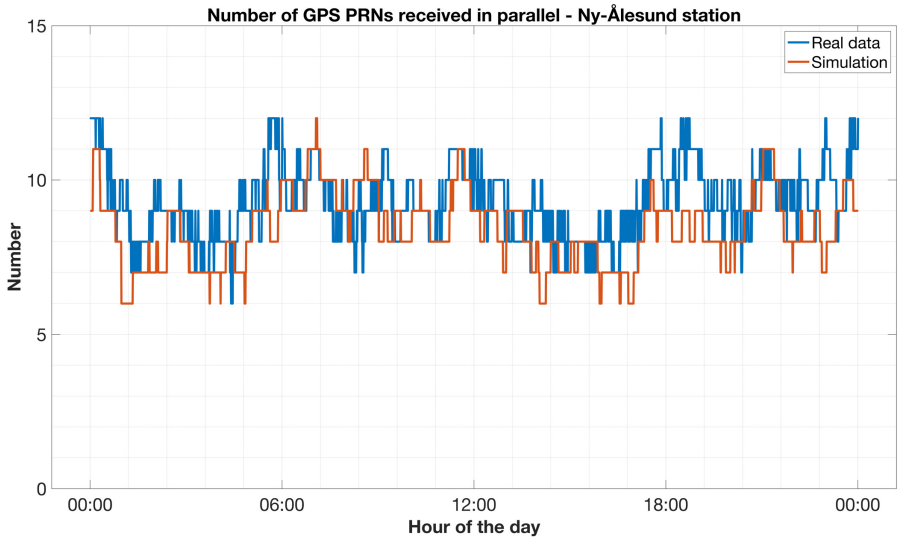

Figure 5.19: Number of GPS PRNs received in parallel for the ground receiver at the IGS station in Ny Ålesund. The real data are shown in blue, with an average of 9.2 PRNs, and the simulated observations are shown in red, with an average of 8.4 PRNs.

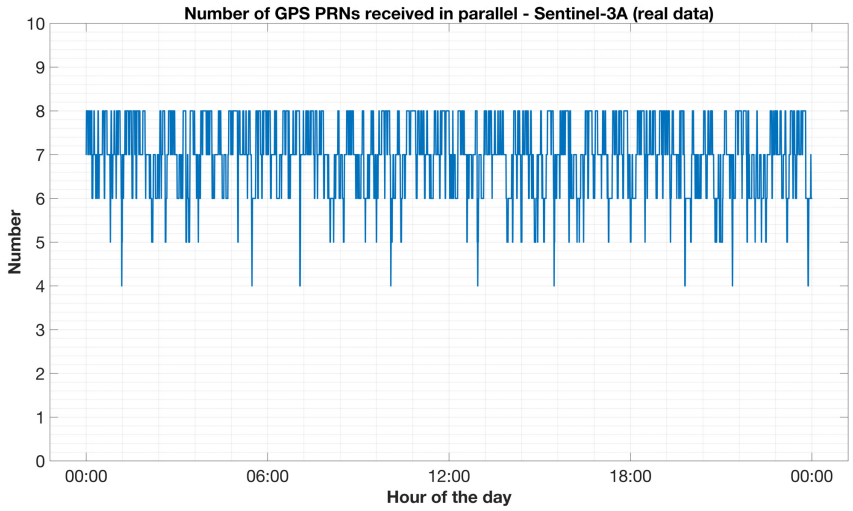

Figure 5.20: Number of PRNs received in parallel one the Sentinel-3A satellite, based on real data analysis.

5.3.8 Global observation coverage

The global coverage of observations of GPS signals by ground stations is highly dependent on the choice of the ground network. The majority of receivers in the IGS network is on continents, with a smaller number situated on islands. In general, the density of receivers is lower over the oceans. A notable number of receivers are distributed across Europe. Depending on which receivers are selected for processing, there is a different structure of global observation coverage. For the GPS processing with EPOS-OC, an optimisation is performed to obtain a globally homogeneous observation distribution. The ground station network used for the simulations is based on the same principle.
For LEO satellites with GPS receivers, the situation is slightly different. In contrast to fixed receivers on Earth, both LEO and GPS satellites are subject to orbital motion. The global

distribution of observations is shown in Fig. 5.21 for Sentinel-3A, evaluating all observations in 2021. The distribution of observations is notably homogeneous, although a band of approximately 60 degrees in longitude exhibits a markedly higher density of observations, the reason for this phenomenon is the sun-synchronous orbit of Sentinel-3A.

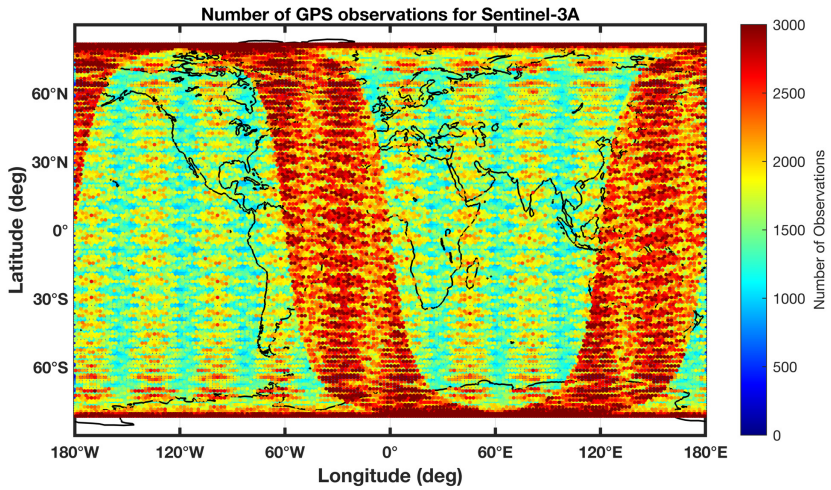

Figure 5.21: Global GPS coverage for Sentinel-3A in 2021 using real observations.

5.3.9 Conclusion GPS

The simulation of GPS observations is based on the analysis of real data used to provide realistic global settings. For the generation of the simulated reference solution for GPS, a GPS constellation and ground network was simulated, into which the simulated space-tie satellite can be integrated according to the integrated approach presented above. For the simulation of the GPS observations of the space-tie satellite, the characteristics are derived from Sentinel-3A and Sentinel-3B, and the GPS receiver of the space-tie satellite is chosen to be an 8-channel receiver.

6 Technique-wise simulation analysis

This chapter presents the results of technique-wise simulations conducted for a co-location in space on a satellite (space tie) in various orbital scenarios, utilising the techniques DORIS (Sec. 6.1), SLR (Sec. 6.2) and GPS (Sec. 6.3). The potential for improvements in the determination of the TRF and ERPs is evaluated by incorporating the space-tie satellite scenario into a technique-specific reference solution. For DORIS and SLR, this is done by adding the normal equation of the space-tie satellite scenario to the reference solution. Subsequently, the impact on the formal errors associated with the station coordinates, station velocities, and ERPs is examined.

The simulated reference solution for DORIS is a combined solution of ENVISAT, Jason-1 and Jason-2 (see Sec. 5.1), and for SLR, it is a combined solution of LAGEOS-1 and -2 (see Sec. 5.2).

In the case of GPS, the reference solution is constituted by the GPS constellation and the ground network, as described in Sec. 5.3. The potential of a space-tie satellite equipped with a GPS receiver is in this case assessed by using an integrated adjustment approach, as described in Sec. 5.3. The process involves solving for the ground network, the GPS constellation, and one space-tie satellite scenario at a time within one common POD adjustment run.

In order to identify the effects on the TRF, the influence of each scenario on the reference solution is examined in a systematic error-free case and with systematic mismodelling. This is accomplished by examining the parameters that define the reference frame, namely translation, rotation, and scale, and the estimated ERPs. The potential for improvement can be identified through the change in formal errors. Systematic effects on the ERPs are revealed by comparing the a posteriori parameters using linear regression, hypothesis testing and spectral analyses. The potential with regard to the retrieval of the Earth gravity field is assessed for each space-tie scenario and each technique individually, without a respective combination with a reference solution. Only in the case of GPS is the estimation of the gravity field carried out together with the GPS constellation due to the integrated approach. For the evaluation, an analytical sensitivity analysis is used, as well as difference plots of the SH coefficients and degree amplitudes.

The methods of evaluation and interpretation are described in greater detail in the first section (Sec. 6.1), which addresses DORIS. For the subsequent analyses, reference is made to the description given there.

To investigate the influence of different mismodelling effects on the scenarios and techniques, the following influences are considered for the DORIS and SLR techniques: CoM coordinate displacement, atmospheric drag mismodelling and SRP mismodelling. Furthermore, the impact of ground beacon frequency offsets on DORIS is examined. In the case of GPS, in addition to the systematic error-free case and the gravity field investigations, only the influence of SRP mismodelling of the GPS satellites is considered in conjunction with one of the space-tie satellites. Investigations for the space-tie satellite regarding CoM displacement and atmospheric drag have been omitted for GPS due to the considerable computational effort required and the extensive scope (i.e. CoM and PCO), which remains a topic of ongoing discussions.

Following the examinations of the systematic error-free cases, a subjective quality assessment on a scale from one to three is made, where a lower number is always better.

This assessment is intended to demonstrate which scenario offers the greatest potential for achieving the desired objectives. Furthermore, this assessment is conducted in a consistent manner for each case of mismodelling, with the objective of evaluating the vulnerability of each scenario to various mismodelling effects. In this context, vulnerability refers to the susceptibility of a scenario to losing its theoretically achievable improvement potential in the presence of mismodelling effects, rather than to an actual deterioration of the reference solution itself. Finally, the assessment of vulnerability to mismodelling is incorporated into the overall assessment as a risk factor.

6.1 DORIS

For reference frame determination with DORIS, the ACs of the IDS use a variety of satellites equipped with a DORIS receiver. These are mostly altimetry or radar satellites. The three satellites chosen here to form the reference solution are ENVISAT, Jason-1 and Jason-2, which overlap with the simulation period. Other satellites, such as the SPOT satellite, were not taken into account, as no radar satellite orbits were processed at GFZ at that time.

The real data of the three satellites were processed according to the models listed in Tab. 4.3 in Sec. 4.4.1 and the parameterisation described in Tab. 6.1. Further information on the real data evaluation can be found in Chap. 5.1. These three satellites were subsequently simulated following the simulation steps described in detail in Chap. 4, the results of which are used as the basis for the following simulations. The simulated weekly arcs per satellite are shown in Fig. 6.1. The simulated single-satellite solutions are subsequently used to estimate station coordinates, station velocities and ERPs. The resulting normal equations are accumulated over the full time span for each satellite and the resulting single-satellite normal equations are combined to form the reference solution. This solution is free of systematic errors, and the combined parameters are station coordinates, station velocities and ERPs.

For the evaluation of the space-tie satellite scenarios for DORIS, the single-satellite normal equation of the respective space-tie satellite scenario is combined with the DORIS reference solution to evaluate the improvement of the scenario relative to the reference solution. In the following, the maximum potential of the individual space-tie satellite scenarios is first analysed in a systematic error-free case in Sec. 6.1.2.1. This is followed by an analysis of the influence of CoM deviations (Sec. 6.1.2.2), atmospheric drag (Sec. 6.1.2.3), SRP (Sec. 6.1.2.4), ground beacon frequency offsets (Sec. 6.1.2.5) and the influence and potential of gravity field estimation (Sec. 6.1.2.6).

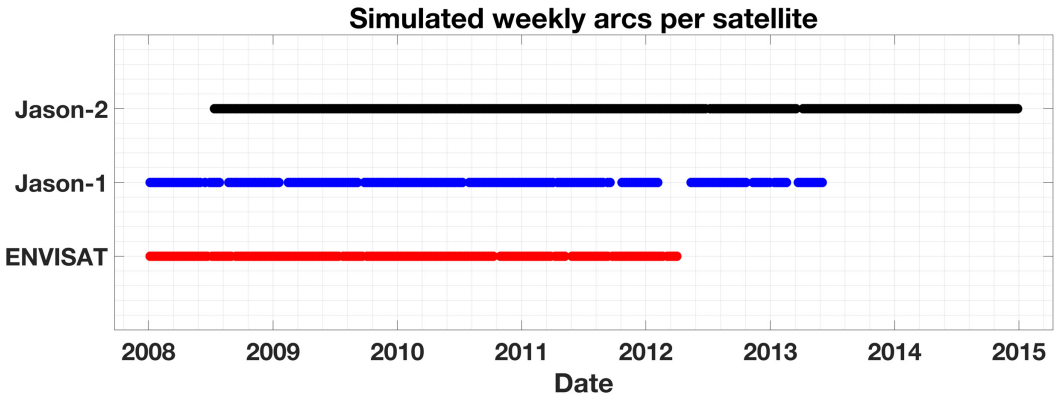

Figure 6.1: Simulated weekly arcs over time for the DORIS reference solution.

6.1.1 Reference solution

In the reference solution only white noise is added to the simulated observations. Apart from that the simulation is free of systematic errors. In the POD, to achieve the maximum potential, only initial state elements are solved for, as there are no unmodelled perturbations, which should be handled by additional parameters. In doing so, just the direct effect of the noise of the observations on the orbit, derived TRF and ERPs can be obtained.

Table 6.1: Parameterisation for the DORIS real data evaluation. T = transversal, N = normal.

	DORIS
Initial state	Estimated
Atmospheric drag	Piecewise linear scaling factors every 3h
Albedo with IR	One linear scaling factor
Solar radiation	One linear scaling factor
Empirical acc.	1/rev cos, sin every 12h in N and T direction
Frequency bias	Once per station and pass estimated
Troposphere bias	Once per station and pass estimated
Time bias	Estimated per arc

6.1.1.1 Orbital fit

The orbital fit of the scenarios and its comparison to the real data evaluation are presented in Sec. 5.1.7. The global distribution of the residuals is illustrated in Fig. 6.2 as the mean of the standard deviation of the residuals. A geographic pattern is evident for all satellites, particularly in the SAA region, where the standard deviation is slightly larger. This can be attributed to the fact that the simulator is replicating the real observations, which demonstrate increased orbital fit values in this region.

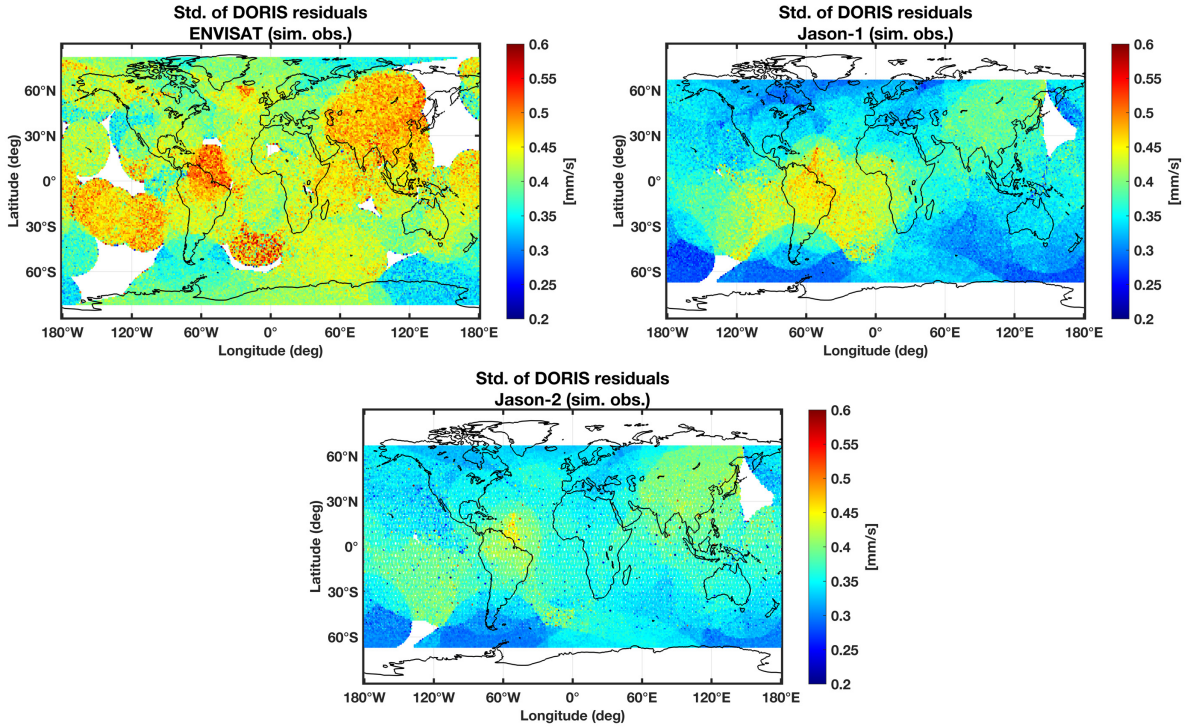

Figure 6.2: Global distribution of the mean standard deviation of the simulated DORIS observations for the three satellites of the reference solution.

6.1.1.2 Orbit recovery

The orbit comparison of the true orbit of the simulation with the recovered orbit gives the statistical values given in Tab. 6.2. The clear strength of the DORIS observation technique

shows up in radial direction, where the mean RMS values for all three satellites are in the submillimeter range. Values in cross-track and along-track direction are higher with RMS values of 2 to 3 mm. A bias in the mean can be observed for all orbit scenarios with values of about 2 mm in along-track direction. This can be attributed to a so far unavoidable discrepancy within EPOS-OC for calculating simulated DORIS time epochs. At the present time, this has to be accepted. The interested reader is referred to appendix C for further details.

The geographic distributions of the mean orbit differences are shown in Fig. 6.3. In the radial direction, no systematics can be detected for any of the satellites, the mean differences are globally uniform near zero. In cross-track direction the geographic differences are slightly larger and show a very slight stripe pattern along the longitudes for ENVISAT with an amplitude of 0.3 mm. Both Jason satellites show a North-South distribution with an amplitude of approximately 0.5 mm for Jason-1 and 0.3 mm for Jason-2. The two satellites have similar orbits, but the amplitude is probably smaller due to the higher number of receiver channels of the on-board receiver of Jason-2. In the along-track direction, the aforementioned mean deviation caused by the simulation software has been removed for the orbit comparison. Furthermore, no additional geographic patterns are evident in the along-track direction. No correlation with the geographic distribution of the residuals can be identified.

Table 6.2: Mean orbit differences of the simulated and recovered orbits.

	RMS [cm]	Mean [cm]	Max [cm]
ENVISAT			
Radial	+0.025	+0.000	+0.037
Cross-track	+0.199	+0.000	+0.323
Along-track	+0.257	-0.232	+0.442
Jason-1			
Radial	+0.029	+0.000	+0.042
Cross-track	+0.231	-0.000	+0.359
Along-track	+0.229	-0.198	+0.413
Jason-2			
Radial	+0.026	-0.000	+0.038
Cross-track	+0.185	+0.000	+0.288
Along-track	+0.208	-0.180	+0.375

6.1.1.3 Reference frame

From the converged arcs of the POD, the normal equation mode of EPOS-OC is used to set up weekly normal equations. In this mode it is possible to take the converged state of the POD with all parameters and in a single further iteration estimate parameters of interest and incorporate them into the normal equation (see also Sec. 2.6.2.2). Here, the estimation of station positions, velocities and ERPs is activated without any constraints. This results in weekly normal equations per satellite, which are then accumulated over the entire simulation period, resulting in one set of station coordinates and velocities per station for the whole timespan and ERPs with daily resolution. These accumulated normal equations for

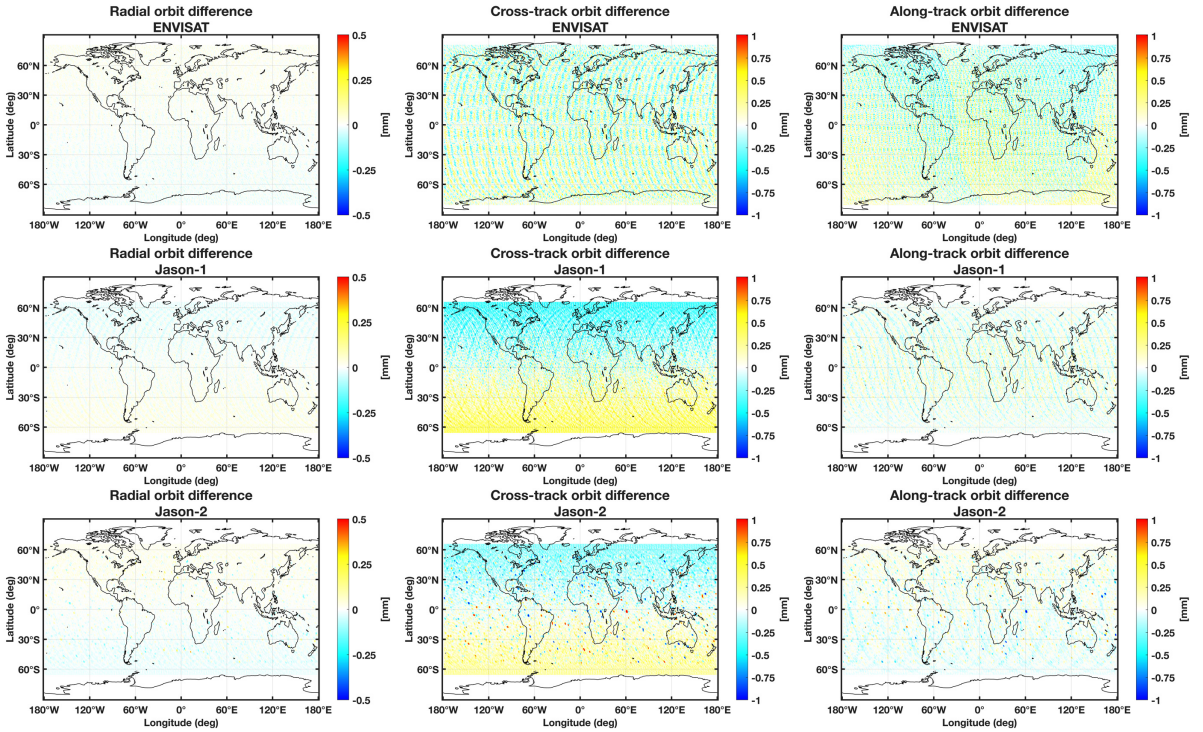

Figure 6.3: Mean orbit differences of the true simulated and recovered orbit over the full simulation time span. From the top to the bottom, ENVISAT, Jason-1, and Jason-2. From left to right in radial, cross-track, and along-track direction. In along-track direction the values are corrected by the mean along-track bias of the scenario.

each satellite are now also accumulated, resulting in the normal equation of the reference solution — an equally-weighted combination of ENVISAT, Jason-1 and Jason-2. For the introduction of the geodetic datum, a total of 11 DORIS stations according to Tab. 6.3 were selected. The DORIS station network of the simulation and the datum stations are shown in Fig. 6.4. Stations were chosen as datum stations, which observe over the entire period of the simulation at most gapless (compare Fig. 5.6 in Sec. 5.1.6) and the totality of the datum stations is as evenly distributed globally as possible. Thus, a NNR condition is imposed as a free network constraint (see Sec. 2.7.4) on these stations. The strength of the condition is chosen as 1 mm for station coordinates and 0.1 mm/a for station velocities according to the recommendation of Altamimi (2003). The two stations OWEC and LAOB were reduced before inverting the normal equation because they show larger differences to the a priori station coordinates and velocities, which negatively affects the overall results. This can be attributed to the fact that only Jason-2 received these two stations and the observation period is only a few weeks for OWEC and about one and a half years for LAOB. This is not sufficient especially for the station velocities, whereby larger deviations arise.

Helmert parameters The normal equation of the reference solution is subsequently inverted and analysed with respect to the parameters defining the reference frame, namely the origin, orientation and scale. For this purpose two 7 parameter Helmert transformation are used. The parameters of the Helmert transformation (Tab. 6.4) demonstrate discrepancies of less than 0.3 mm and 0.02 mm/a compared to the a priori station network for the datum stations and for the totality of all stations. The largest discrepancies are found in the station positions, where minor Z-translations and rotations in X and Z can be observed, with

Table 6.3: DORIS datum stations and stations which have been reduced.

Datum stations		Reduced stations	
Station code	Name	Station code	Name
SPJB	Ny-Alesund	OWEC	Owenga
TLSB	Toulouse	LAOB	Le Lamentin
HBMB	Hartebeesthoek		
SYPB	Syowa		
JIUB	Jiufeng		
STJB	Newfoundland		
YASB	Yarragadee		
MSPB	Mount-stromlo		
GREB	Greenbelt		
PATB	Papeete		

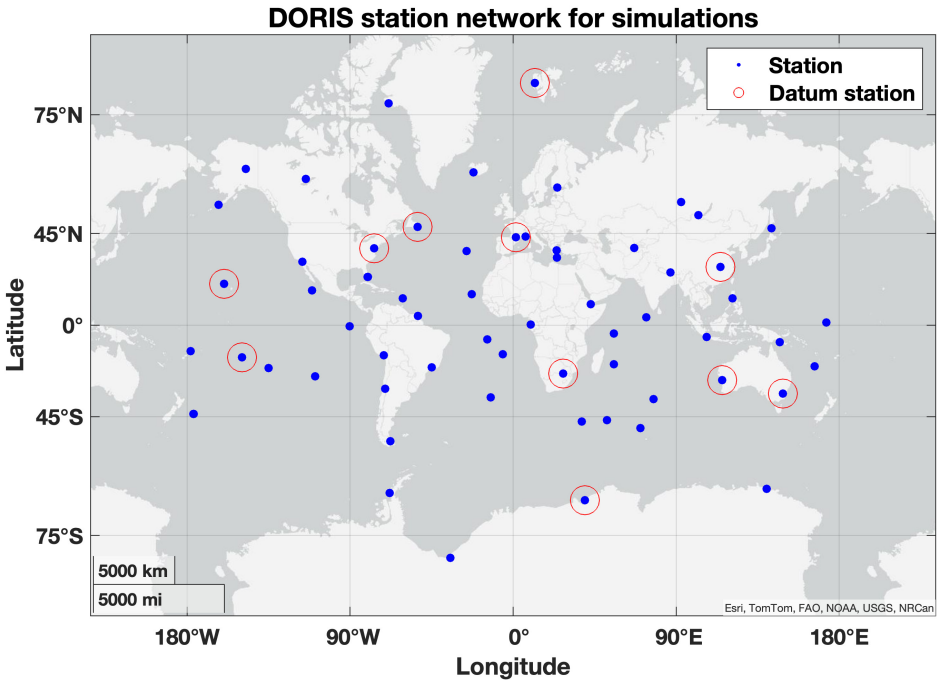

Figure 6.4: The DORIS station network of the simulation. All stations used are shown in blue, datum stations are additionally encircled in red.

maximum absolute values of 0.27 mm. This is well below the strength of the applied NNR condition.

Formal errors The median formal errors of the estimated station coordinates, velocities, and ERPs are used as another criterion (Tab. F.2 in App. F.1). These are in the sub-millimeter range for the station coordinates. Especially the formal errors in X-direction are noticeable smaller, with values even below one hundredth of a millimeter. The formal errors of the station velocities are at a similar level for all three axes, ranging from 0.21 to 0.24 mm/decade. The pole coordinates show values for formal errors of about 1.6 mm for the X-pole and Y-pole in both cases, and 0.38 μm for LOD. [1]

6.1.1.4 ERP analysis

The differences in the estimated ERPs compared to a priori show a scatter of 1.7 mm, 1.9 mm and 0.9 μm for X-pole, Y-pole and LOD respectively (Tab. F.3). The fewer satellites are involved in the combined solution, the higher is the noise in the ERP differences (compare Fig. 6.1 and G.1). A significant bias can only be detected in the Y-pole, which is in the range of 0.2 mm, significant trends cannot be detected (see Tab. F.3). The spectral analysis of the ERPs does not reveal any significant frequencies beyond 0.1 mm.

Table 6.4: Helmert parameters and their standard deviation to a priori for station positions and velocities of the DORIS reference solution.

	T_x [mm] $T_{\dot{x}}$ [mm/s]	T_y [mm] $T_{\dot{y}}$ [mm/s]	T_z [mm] $T_{\dot{z}}$ [mm/s]	R_x [mm] $R_{\dot{x}}$ [mm/s]	R_y [mm] $R_{\dot{y}}$ [mm/s]	R_z [mm] $R_{\dot{z}}$ [mm/s]	sc [mm] $\dot{sc}$ [mm/s]	s_0 s_0
Combined reference								
datum stations	0.01 $\pm$ 0.04	0.05 $\pm$ 0.04	0.22 $\pm$ 0.04	0.08 $\pm$ 0.05	0.03 $\pm$ 0.05	-0.15 $\pm$ 0.06	0.06 $\pm$ 0.04	0.14
	0.00 $\pm$ 0.00	0.00 $\pm$ 0.00	0.02 $\pm$ 0.00	0.00 $\pm$ 0.01	0.00 $\pm$ 0.00	-0.01 $\pm$ 0.01	0.01 $\pm$ 0.00	0.01
all stations	0.05 $\pm$ 0.03	0.05 $\pm$ 0.03	0.27 $\pm$ 0.03	0.16 $\pm$ 0.04	0.02 $\pm$ 0.04	-0.15 $\pm$ 0.04	-0.03 $\pm$ 0.03	0.25
	0.01 $\pm$ 0.01	0.00 $\pm$ 0.01	0.02 $\pm$ 0.01	0.00 $\pm$ 0.01	0.00 $\pm$ 0.01	0.00 $\pm$ 0.01	-0.02 $\pm$ 0.01	0.07

6.1.2 DORIS space-tie satellite results

The single-technique solutions for the different space-tie scenarios are created in the same way as described for the reference solution. To investigate the influence of the space-tie satellite scenarios, the normal equation of one of the simulated space-tie satellite scenarios at a time is added to the simulated DORIS reference solution and evaluated. Subsequently, the changes due to the inclusion of this scenario in the reference solution are assessed. After the systematic error-free case, which is intended to reflect the maximum achievable potential of each scenario, various mismodelling cases are investigated. It is analysed how much of the full potential could be lost, in which parameters losses occur, how the TRFs and ERPs change and where systematics appear.

6.1.2.1 Case free of systematic errors

In the case of systematic error-free simulations, only white noise is added to the simulated DORIS observations. As the simulated DORIS beacon frequency is identical to the nominal

[1] Values of the pole coordinates are converted to millimeters, and LOD to μm for easier comparison. For pole coordinates, this results in $pole_{mm} = pole_{arcseconds} \cdot \frac{2\pi R}{60 \cdot 60 \cdot 360} \cdot 10^6$, and for LOD in $LOD_{\mu m} = LOD_{sec} \cdot \frac{2\pi R}{60 \cdot 60 \cdot 24} \cdot 10^9$, where $R = 6378\,\mathrm{km}$ is the radius of the Earth.

frequency, no frequency bias or drift is estimated for ground stations in this case. The estimated parameters are listed in Tab. 6.5. This configuration may be regarded as optimistic, but would be feasible if all ground beacons were connected to, for example, a maser for high-precision frequency monitoring. However, the influence of frequency biases and their estimation is examined in greater detail in Sec. 6.1.2.5. Further details on the simulation can be found in Chap. 4.

Table 6.5: Estimated parameters and dynamic parameterisation used in the systematic error-free case.

Parameterisation for systematic error-free case	
All scenarios	
Arc length	7 days
Initial state parameters	estimated

Orbital fit For each simulation scenario, the orbital fit values are provided in Tab. 6.6 and the variation over time is shown in Fig. 6.5. The global RMS of the simulated DORIS observations is observed to be approximately 0.35 mm/s on a consistent basis. In comparison, the GRASP-like scenario demonstrates a markedly reduced number of observations with an average of approximately 100'000 observations per week. More observations are achievable for all other scenarios. For the E-GRASP-mod and E-GRASP-like scenario this is about 3 times higher, for the cirular scenarios more than 4 times. The variation in the number of observations is similar over the simulation period for all scenarios. Especially at the beginning of the period until the launch of Jason-2 in mid-2008, the number of observations is in each case about 25% lower. This is due to the fact that the simulation in this period is based on the real data results of ENVISAT and Jason-1. This effect is also noticeable a few times in 2012 and 2013, where the simulation falls back on the information of ENVISAT, or Jason-1, because Jason-2 is not available in the real data evaluation, e.g. due to bad POD results or observation data gaps. This variation in the number of observations can be assumed realistic. At the beginning of satellite missions often certain settings are checked and tested before the maximum functionality of the instruments is reached. Temporary reductions in the number of observations, as seen in 2012 and 2013, can be caused by e.g. on-board receiver changes, reboots, software updates, or switches to redundant receiver unit.

Global observation coverage The global distribution of simulated DORIS observations is shown in Fig. 6.6 for each of the space-tie satellite scenarios. The colour bar is scaled 5 times smaller for the GRASP-like scenario, which has the lowest number of observations, due to its much lower altitude. Compared to the E-GRASP-mod scenario, the E-GRASP-like scenario provides more observations over Europe and North Africa due to the higher apogee and density of DORIS stations in these areas. A similar distribution of observations is obtained with the circular scenario at 60 degrees inclination, whereby even more observations are possible over Europe and North Africa, as well as in the south-eastern regions near South Africa and Australia. When the inclination is reduced to 30 degrees (Circular 30° scenario), the observations cluster around the area defined by the inclination, showing significantly more observations over Africa and around the 30 degree North and South latitude boundaries. A

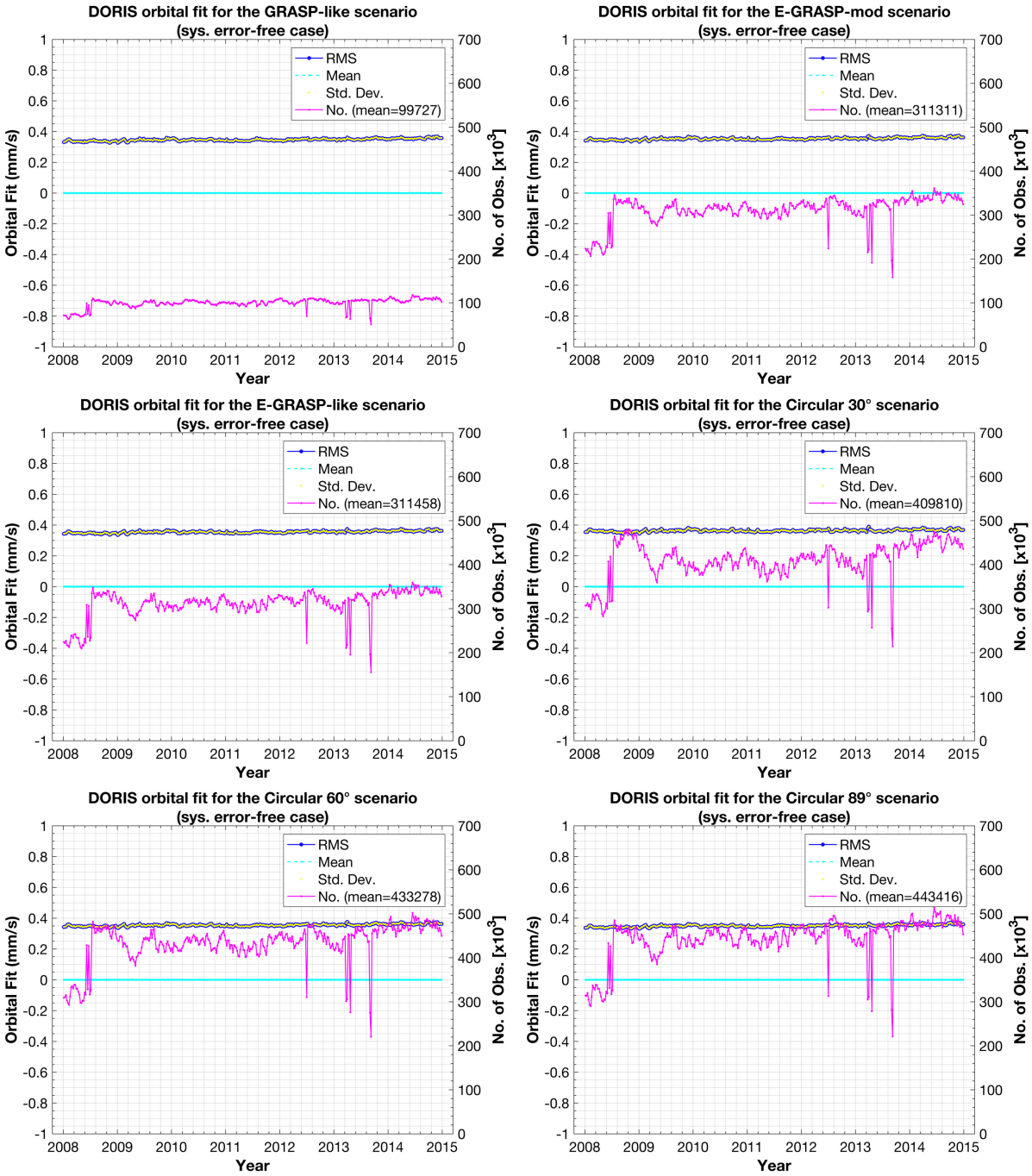

Figure 6.5: Orbital fits for the simulation scenarios in the systematic error-free case.

Table 6.6: DORIS post fit statistics, total number of observations and passes for the simulated space-tie satellite scenarios. Full simulation time span from beginning of 2008 to end of 2014.

	DORIS						
	[mm/s]					Number	
	Min.	Max.	RMS	Mean	Std.	Observations	Passes
GRASP-like	-2.18	2.41	0.35	0.00	0.35	36'400'560	636'060
E-GRASP-mod	-2.36	2.27	0.35	0.00	0.35	113'628'736	589'979
E-GRASP-like	-2.32	2.38	0.36	0.00	0.36	113'682'183	538'398
Circular 30°	-2.27	2.41	0.36	0.00	0.36	149'580'663	417'089
Circular 60°	-2.41	2.42	0.36	0.00	0.36	158'146'731	464'841
Circular 89°	-2.51	2.42	0.35	0.00	0.35	161'847'129	518'320

larger inclination of 89 degrees (Circular 89°) results in a more homogeneous distribution of observation, where more observations are visible over Europe to Greenland as well as the Antarctic Ocean. The E-GRASP-like, E-GRASP-mod and Circular 89° scenarios show the most globally homogeneous distribution of observations.

Fig. 6.7 shows the global distribution of the mean standard deviation of the simulated observations for each scenario. The residuals of the observations are collected over the entire simulation period and analysed in a bin of 1 degree latitude and 1 degree longitude. For the low-orbiting GRASP-like scenario, slightly increased values are seen near the SAA and West of South America, as well as over Southeast and East Asia. This is due to the fact that the simulated observations are based on the post-fit residuals of the real data analyses, which therefore include effects such as the SAA that lead to a regional increase of the RMS. However, the mean values of the observations do not show any global structure, just a higher scatter. The regional effects decrease with increasing altitude, and the lowest standard deviation values are in general observed near the polar regions, whereby the GRASP-like scenario shows slightly lower values than the Circular 89° scenario.

Orbit recovery To assess the maximum accuracy of the POD in each scenario, the recovered orbit is compared with the orbit of the simulation, which describes the true orbit. The maximum potential is reflected when just initial state elements are estimated. Subsequently, the mean of the RMS values and mean values in the radial, cross-track, and along-track directions are calculated, as well as the mean 3D RMS. The results of these calculations are shown in Fig. 6.8. Here, too, the mean along-track bias of the DORIS simulation is evident for all scenarios, which was already mentioned in Sec. C. A comparison of the directions reveals that the radial direction is the most precise for all scenarios, with RMS values below or close to 1 mm. Significantly higher RMS values are found in the cross-track and along-track directions, with the cross-track direction being the weakest. Comparing the scenarios among each other shows significantly better accuracy of the orbit for the GRASP-like scenario. This is most likely due to the lower orbit of the satellite and better observation geometry. The two eccentric scenarios, E-GRASP-mod and E-GRASP-like, which in the perigee show similar flight altitudes as the GRASP-like scenario, exhibit lower RMS values as the circular orbits. The lower perigee of these scenarios shows a positive effect on the overall accuracy of the orbit in cross-track and along-track direction, with RMS

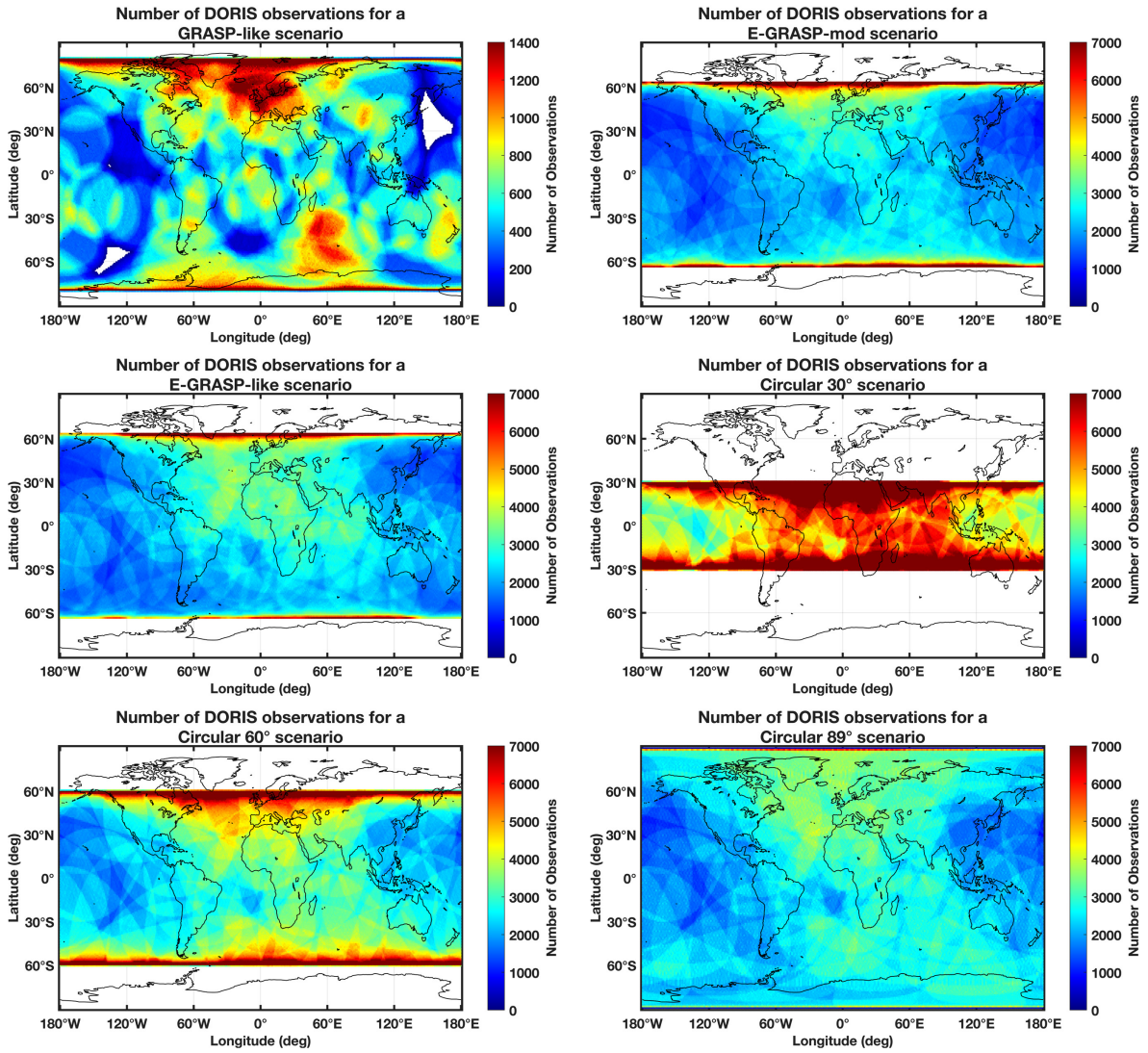

Figure 6.6: Global observation coverage of simulated DORIS observations for the space-tie satellite scenarios. Please note the different color bar limits for the GRASP-like scenario.

values in along-track direction that are comparable to those of the GRASP-like scenario. The different eccentricity of the E-GRASP-mod and E-GRASP-like scenario does not appear to have a major effect on the orbital fit, the results are almost identical.

The geographical distribution of mean orbit differences is shown for each scenario in radial, cross-track, and along-track directions in Fig. 6.9. The distribution of differences is most homogeneous for the GRASP-like scenario, where no regional effects are visible. The two eccentric orbit scenarios, E-GRASP-mod and E-GRASP-like, exhibit a stripe pattern in radial direction as well as in cross-track direction and a slight North-South asymmetry, that is inverted between the two scenarios. The most pronounced regional variations are observed in the cross-track direction, where eight stripes are visible. It is assumed, that this is an effect of the critical inclination, where perigee and apogee of the orbit show no drift within the orbital plane (apsidal precession). The ground tracks with the flight altitude, as shown in Fig. 4.1 in Sec. 4.1, show for these scenarios a pattern, whereby the apogee is consistently reached with ascending arcs and always at the equator. This pattern of the flight altitude is strongly correlated with the deviations in the recovered orbit, which show up in cross-track direction and are significantly higher at the apogee. The decrease in the

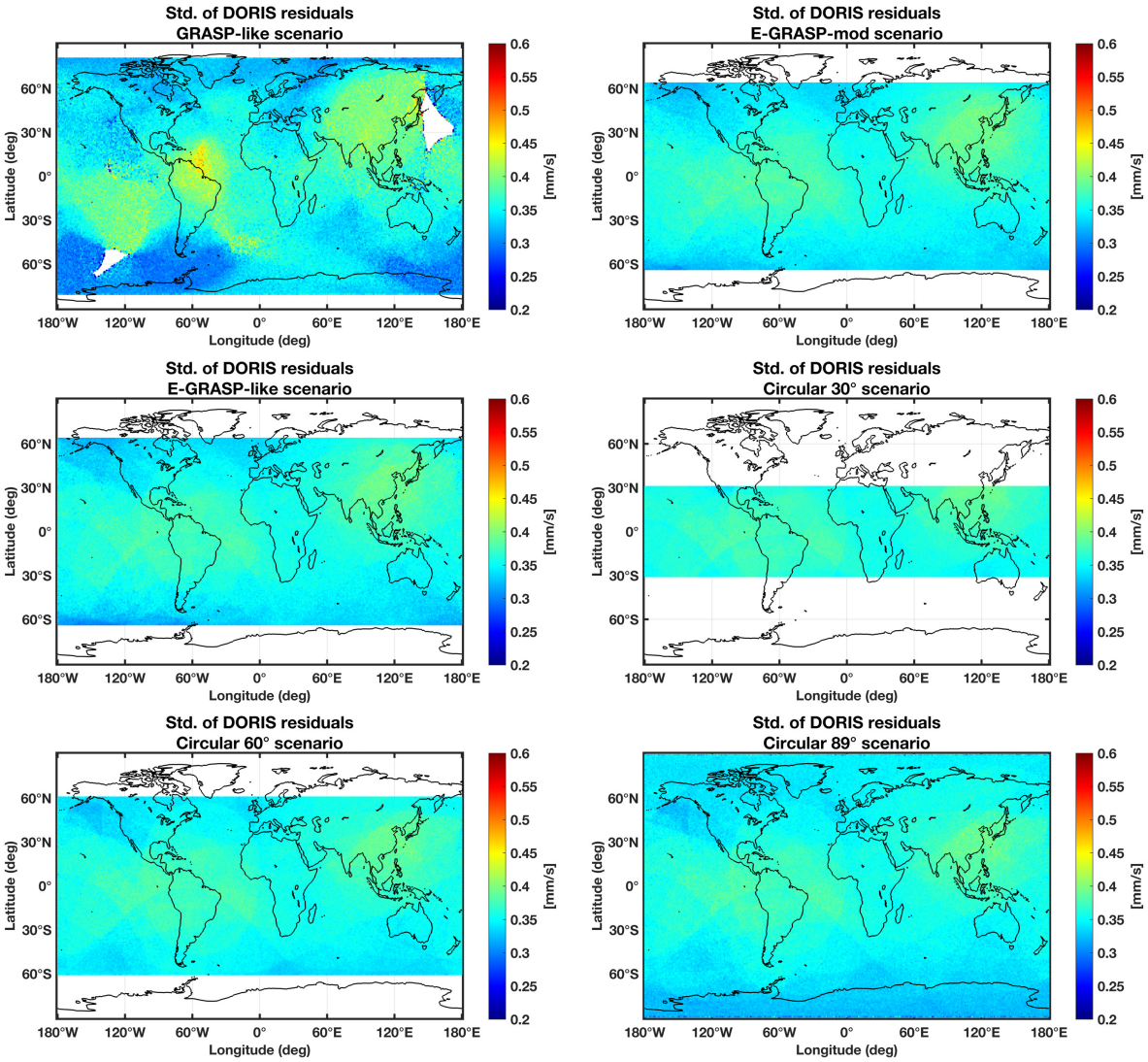

Figure 6.7: Global distribution of the mean standard deviation of the simulated DORIS observations for the space-tie satellite scenarios in the systematic error-free case.

strength to determine the cross-track component with increasing altitude has already been noticed for the circular scenarios (compare Fig. 6.8). Given that the node of the orbit drifts even at a critical inclination, this appears to be an effect related to the angle of the orbital plane to the Sun (beta angle) or a geographic effect. However, with regard to the orbital repeat cycle, which is approximately one month, no correlation with the beta angle could be identified. Consequently, it is assumed that this is a geographic effect. In the along-track direction, a slight regional pattern is visible for the E-GRASP-like scenario, where negative orbital differences towards the poles and positive ones near the equator appear. In contrast, the circular orbit scenarios show overall nearly no significant regional patterns, with only minor patterns appearing in the North-South direction.

Whether eccentric orbits in general, or only in connection with the choice of the critical inclination, lead to higher deviations and systematic patterns in the cross-track direction, which is desirable to avoid, cannot be concluded from the scenarios analysed here. The higher orbiting scenarios all show significantly increased RMS values in the cross-track and along-track direction, indicating that the accuracy of DORIS position determination in these directions decreases with increasing altitude. The accuracy of the position determination

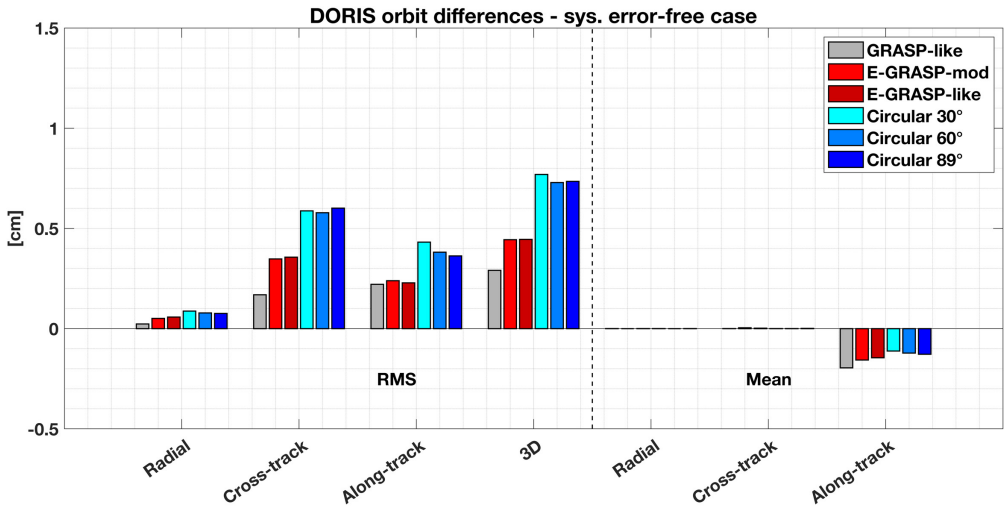

Figure 6.8: Mean RMS value of the orbit comparison in radial, cross-track, along track and 3D directions, as well as the mean orbit deviation. True orbit of the simulation compared to the orbit recovered in the systematic error-free case.

in radial direction is less affected by altitude or eccentricity, with RMS values in the radial direction being significantly smaller and close to or below 1 mm for each scenario.

Based on the results of the orbit recovery, an orbit with a low numerical eccentricity seems to be the best to avoid regional patterns in the POD, lower altitudes improve the accuracy.

Reference frame evaluation As stated at the beginning of this section, the potential of a space-tie satellite scenario to improve a DORIS based TRF is determined by adding the normal equation of the appropriate scenario to the DORIS reference solution. A TRF is determined from the resulting normal equation using the same procedure as for the reference solution in Sec. 6.1.1. Subsequently, two 7 parameter Helmert transformations of the positions and velocities with respect to the a priori reference frame are first calculated to monitor possible systematic effects. The potential for improvement is then determined based on the changes in the median of the formal errors of station coordinates, velocities and ERPs. This is done first in the Cartesian X, Y, Z coordinate system, and then in a geographic coordinate system to better understand local geometric effects. To assess the significance, the p-value of the hypothesis test against the reference is given. This is considered significant if, based on a two-sigma criterion, equivalent to 5%, the p-value is less than 0.05. For more information on the distribution of formal errors and the hypothesis tests used, see App. D, which deals with robust hypothesis testing of the median for non-normally distributed data.

Formal error evaluation In order to quantify improvements in formal errors, the following terms are introduced:
Expected improvement is defined as the improvement that is expected to result from a change in the DoF, mainly due to additional observations.
Scaled improvement is defined as the change of two formal errors expressed in percentage, for instance, the relation of the reference to the test scenario. In this case, negative values represent a reduction in formal errors by that percentage, thus indicating an improvement.
Observation scaled improvement is a percentage value representing the improvement

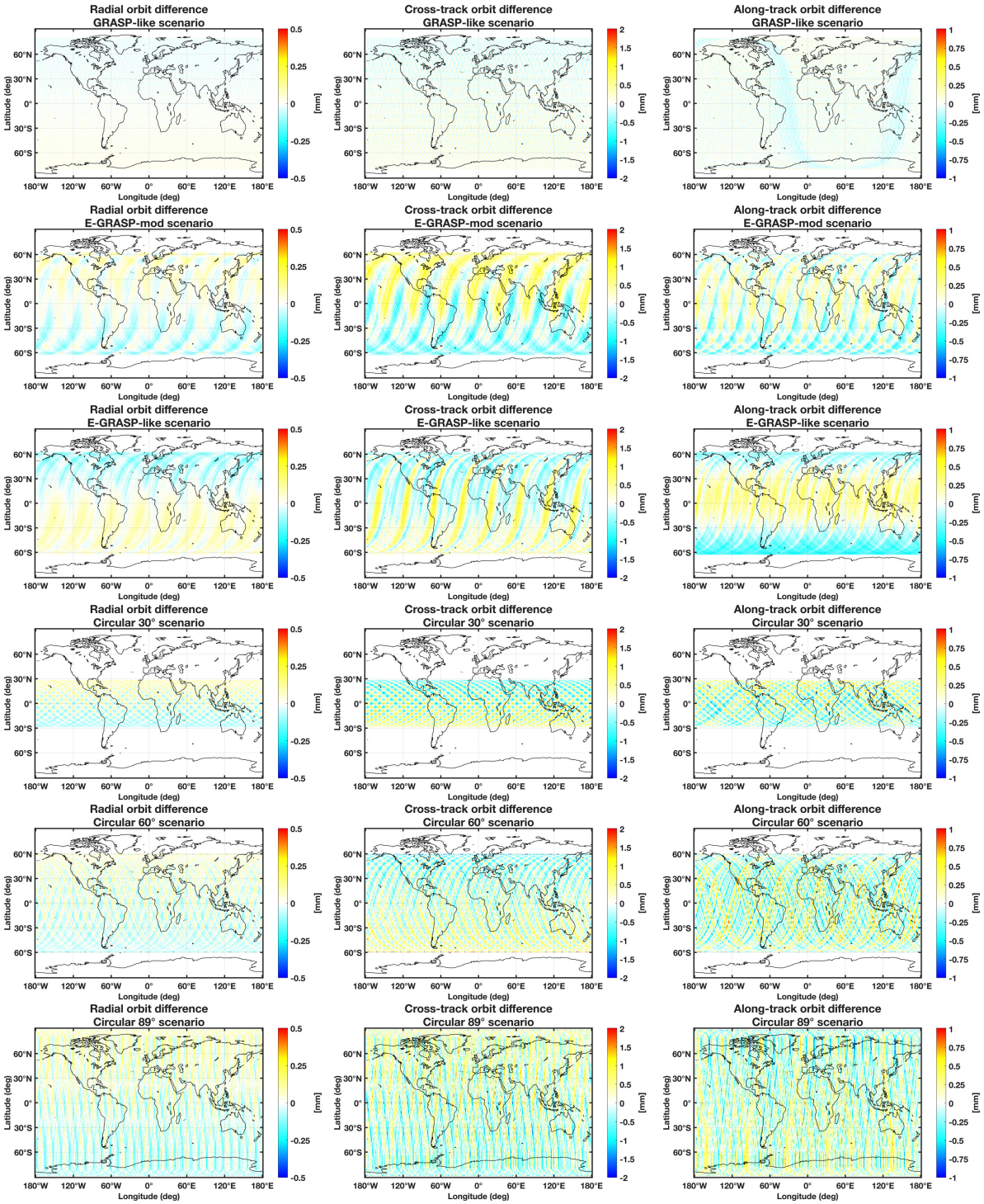

Figure 6.9: Mean orbit differences of the true simulated and recovered orbit over the full simulation time span of 7 years for DORIS in the systematic error-free case. From the top to the bottom, GRASP-like, E-GRASP-mod, E-GRASP-like, Circular 30°, Circular 60°, Circular 89° scenario. From left to right in radial, cross-track, and along-track direction. In along-track direction the values are corrected by the along-track bias of the scenario.

adjusted to the expected improvement. In the case of negative values, this indicates an improvement that is greater than the expected value, thus indicating a geometric added value.

Loss of Improvement Potential (LIP) describes the loss of a scaled improvement, in relation to the maximum potential of improvement achieved. For example, if a scenario achieves an improvement of a reduction of the formal error of a parameter to 50% of the value of the reference solution in the systematically error-free case, this is defined as the maximum improvement to be achieved. Should the formal error values of the scenario now increase to 75% of the value of the reference due to systematic mismodelling, this would represent a loss of 50% of the potential for improvement. A 100% LIP would indicate that the formal error of the parameter has returned to the value of the reference. This is done to assess the risk of a scenario to achieve its maximum potential for improvement.
Further details on this topic, including its mathematical representation, can be found in App. E.

Helmert parameters The values of the Helmert parameters for each of the scenarios are illustrated in Fig. 6.10 and listed in Tab. F.1 in App. F.1. Deviations in the Z-translation and in the X- and Z-rotations of the positions and velocities are slightly more pronounced in the reference scenario. These can be reduced by the inclusion of any of the space-tie satellite scenarios. All Helmert parameters are below 2/10 mm and 0.025 mm/a, respectively. The variance factors of the transformation demonstrate a similar reduction of 70-80% for all scenarios, with the exception of GRASP-like, which is at the level of the reference.

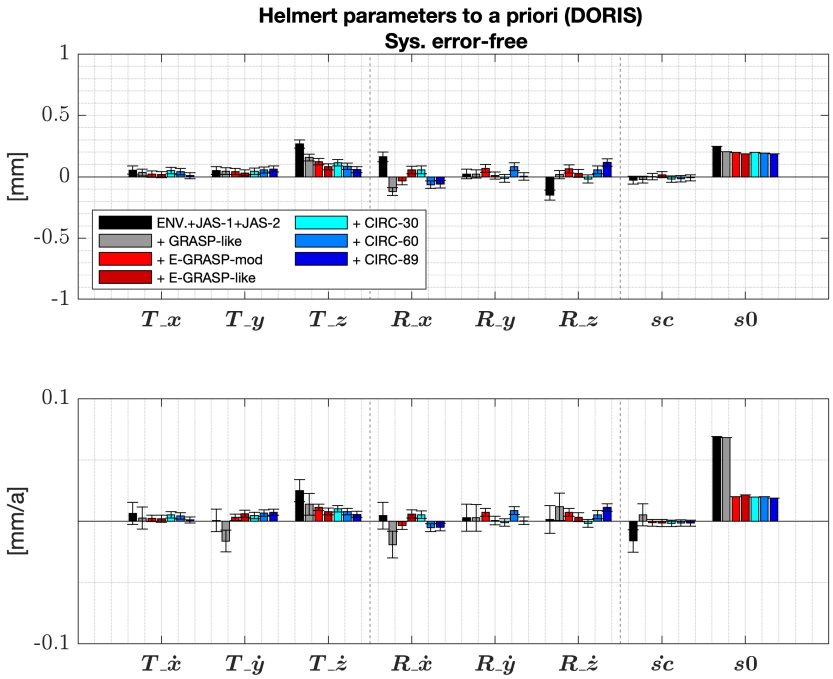

Figure 6.10: The upper figure shows the Helmert parameters of all station positions for the systematic error-free case compared to a priori. The lower figure shows the values for the velocities.

Formal errors The formal error results for each scenario are presented for coordinates in X, Y, and Z in Fig. 6.11 and for latitude, longitude, and height in Fig. 6.12 (absolute values for all scenarios can be found in App. F. Further details on the test methods to identify significant changes can be found in App. D). The values for the ERPs are identical in both figures and for the pole coordinates converted to cm and for LOD to μm equivalent on the Earth's surface. The expected improvement for the GRASP-like scenario is about 19%, that of the other scenarios between 38 and 45% (compare Tab. F.2 in App. F.1).

Formal errors of station coordinates It is noticeable that the formal errors in a systematically error-free case reach very low values. These values are clearly below 1 mm for station position and LOD, below 1 mm per decade for station velocities and about 1.5 mm for the pole coordinates. This demonstrates the theoretically very high potential of DORIS for TRF and ERP determination. In a real data evaluation of a combined solution of Sentinel-3A, -3B and -6A (MF) (Schreiner et al., 2023), the achieved values for station coordinates were in the range of 5-10 mm for station coordinates, where however, station coordinates were solved per weekly arc and no station velocities were estimated. Worth mentioning are also the formal errors of the station coordinates in X-direction, which are below 1 micrometre. This is a consequence of the good global distribution of the DORIS station network. If the Cartesian coordinates are converted into geographic coordinates, local geometric effects of the stations can be identified. Formal errors of the station coordinates are for the reference solution along latitude (North-South) 0.07 mm , in longitude direction (West-East) 0.01 mm and for the height component at 0.04 mm. Results of real data evaluation with EPOS-OC at GFZ (Schreiner et al., 2023), as well as the combination of the IDS CC (Moreaux et al., 2023b), show that the residuals of the position deviations in the West-East direction and the height component are generally on a similar level and higher than in the North-South direction. One potential explanation for these different results is that these solutions are based on weekly arcs or shorter, and various existing modelling errors may have a stronger influence on the West-East and height components than on the North-South component.
The scaled improvements provide a more accurate representation of the change in relation to the reference solution. These are evident in both the X- and Y-directions, with a reduction in formal errors between 20 and 30% with the circular 30° scenario demonstrates the least improvement. The Observation Scaled Improvements (OSIs) results indicate that only the GRASP-like scenario shows a minor geometric added value. For station coordinates in the Z-direction, the situation is different. Here, all scenarios show a scaled improvement of 50-60%, with the exception of the GRASP-like scenario, which exhibits an improvement of only 20%. A geometric added value in terms of OSI is observed for all scenarios in the Z-direction, the largest being for the circular scenario with an inclination of 89 degree and the E-GRASP-like scenario with up to 14%. This is due to the fact that the clustering of observations around the equator is highly beneficial for the determination of station positions in this region. Therefore, stations such as Papeete (S: -17 ° 34', W: 149° 36'), Rikitea (S: 23° 8', W: 134° 57') and Socorro (N: 18° 44', W: 110 ° 57') benefit from the many additional observations. These stations have fewer observations in the reference, which is, in general, weaker in the reference solution in the North- and Southeast Pacific region. The geographic values exhibit a similar pattern. The improvements for all scenarios except the GRASP-like scenario are of a comparable magnitude, at approximately 50%, 25% and 55% for the North-South, West-East and height components respectively. The 30 degree inclined circular scenario shows an improvement of about 10% less in the West-East direction than all other scenarios. Due to the smaller number of observations, the improvements for the GRASP-like

scenario are lower, and in the range of 25-30% for all three components. A geometric added value can be found for all scenarios in the North-South direction of 5-15% and in the height component below 10%. Exclusively for the GRASP-like scenario there is also an added value of 5% in the West-East component, where the circular scenario with an inclination of 30 degrees is the least favourable.

Formal errors of station velocities With regard to the station velocities, all scenarios demonstrate comparable improvements of approximately 16-30% in the Cartesian and geographic coordinate analysis. The circular scenario with an inclination of 30 degrees is once again less favourable, in terms of station velocities in the Z-direction, respectively in the North-South and height component. Only the GRASP-like scenario slightly exceeds its expected improvement in all three components, and shows a geometric added value in the low single-digit percentage range, particularly in the Z-direction. The OSI in geographic coordinates indicates that this geometric added value is present in both the horizontal component and, to a slightly greater extent, in the height component.

Methodology peak improvement analysis As stated at the beginning of this section, the median is used for the overall evaluation of changes in formal errors. In App. D this is discussed in more detail, and it is shown that the formal errors of individual stations can exhibit considerable variation compared to the majority of stations. In order to identify instances where strong improvements are found for individual stations, the arithmetic mean value of the formal error distribution is used. To this end, the mean of the formal errors of a given parameter is calculated and the percentage difference in comparison to the mean formal errors of the reference is determined. Should this value differ significantly from the percentage change based on the median, this would indicate an improvement in outliers. Negative values would indicate a more pronounced improvement in strongly deviating values, resulting in a notable shift in the mean. Conversely, a positive value would indicate that the mean improvement is less than the median, suggesting that no further improvement is evident for these stations.

Peak improvement analysis for station coordinates and velocities The results of the difference analysis of the mean and median are presented in Fig. 6.13. In the case of station coordinate positions, sudden improvements of a similar magnitude can be observed, particularly in the higher orbiting scenarios (i.e., E-GRASP-mod and the circular scenarios) in the X and Y directions. In particular, the circular scenario with an inclination of 30 degrees exhibits notable improvements, which can be attributed to the low inclination of the scenario and the consequent dense clustering of observations around the equator. The geographical coordinates indicate that the West-East and height components are particularly affected.

In the case of station velocities, peaks in improvement can be seen almost exclusively in the Y-direction and for the constantly higher orbiting scenarios (i.e. E-GRASP-mod and the circular scenarios). The geographic coordinates indicate that these improvements are primarily evident in the height component, to a lesser extent also in the West-East direction. It therefore seems that stations situated in close proximity to the geometric Y-direction experience significant improvement in the height component for position and velocity. The observation coverage of the reference solution shows less observations at 90 degrees West and in the direction to the North Pacific. Indeed, the highest improvement in the Y-component of the velocities can be observed for the Santa Cruz station, whose location corresponds exactly to the aforementioned assumptions (Latitude: 0° 45', Longitude: 269°

42'). It can be seen that long observation passes from a satellite orbiting at a higher altitude are advantageous in this context. However, a comparison of the E-GRASP-mod and E-GRASP-like scenarios shows that the highly eccentric orbit of the latter does not achieve this advantage. It can therefore be concluded that the orbit should have a constant higher altitude.

It is important to note that peak improvements also depend on the reference solution. The inclusion of further satellites to the reference could improve the regional observation coverage, thus improving the values and stability of the formal errors observed for stations in the aforementioned regions in the geometrical Y-direction. In this case, the peak improvement would be different and perhaps less distinct. However, the majority of the DORIS satellites fly on comparable orbits to those utilised for the reference. Based on the aforementioned results, it can be assumed that the space-tie satellite scenarios, which demonstrate a peak improvement, enhance the stability of the station position estimates for these regions and make them less dependent on the reference solution. Consequently, the precision of the positioning can be assured even if individual satellites in conventional DORIS orbits fall out of the reference.

Formal errors of ERPs The improvements are more modest for the pole coordinates, with the majority of scenarios exhibiting a reduction of less than 15%. The sole scenario that exhibits a reduction of approximately 25% is the GRASP-like scenario, which also demonstrates a geometric added value. In terms of LOD, all scenarios demonstrate substantial improvements, with a range of 30-45%. This aligns closely with the expected improvement, and only in the case of the GRASP-like scenario, a slight geometric added value in the low single-digit percentage range is notable. When comparing the three circular scenarios, it appears that a lower inclination, in this case 30 degrees, may offer a slightly less benefit.

A comparison of the two eccentric scenarios with the circular 60° scenario, which has a similar inclination, demonstrates that an eccentric orbit is marginally better to improve the ERPs, but there is almost no difference between the E-GRASP-mod and E-GRASP-like scenario. The lower orbiting GRASP-like scenario achieves the most substantial improvements for ERPs overall. Additionally, peak improvements can be observed in LOD. This holds for all scenarios and can be attributed to the additional observations that help to avoid outliers caused by e.g. the transition in the number of satellites in the combined reference.

A posteriori ERP analysis Furthermore, the impact of incorporating the space-tie scenario into the reference solution on the a posteriori ERP values is evaluated.

For this purpose, the mean, standard deviation and linear regression values of the ERP differences to the a priori are analysed. The significance of each standard deviation of differences is determined by means of a Brown-Forsythe test (Brown & Forsythe, 1974). In order to ascertain the significance of the linear regression parameters, a two-sided t-test (Student, 1908) is employed. In the tables of the statistics of the ERPs, as f.i. Tab. F.3 in App. F.1, the 5% significance level is expressed as a p-value. A significant change exists when the p-value is less than 0.05. Similarly, for the linear regression, a significant offset or trend can be detected when the p-value is less than 0.05.

The statistics pertaining to the ERPs are presented in Tab. F.3. It is possible to reduce the standard deviation of the ERPs to a significant extent in all scenarios. With regard to the pole coordinates, the 30 degree inclined circular scenario exhibits the most modest reduction, in the range of 8 to 11%. In contrast, the GRASP-like scenario demonstrates the most substantial reduction, in the range of 23 to 28%. The remaining scenarios demonstrate

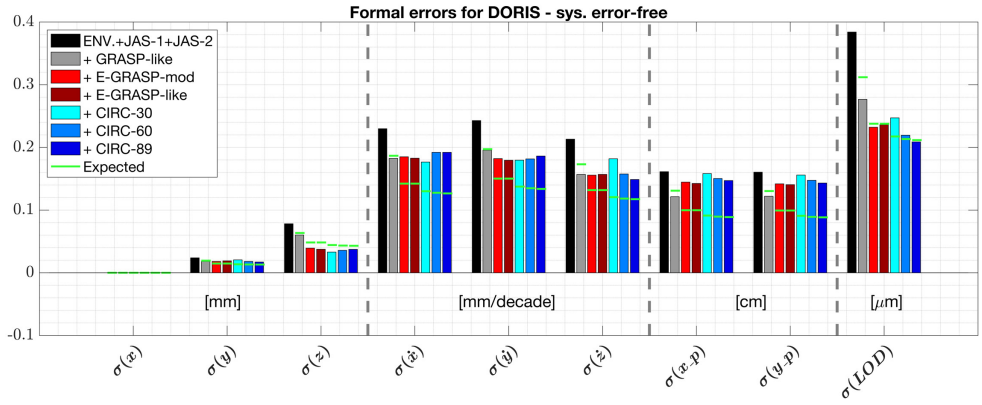

(a) Absolute values of the median of formal errors. The green bars indicate the expected improvement.

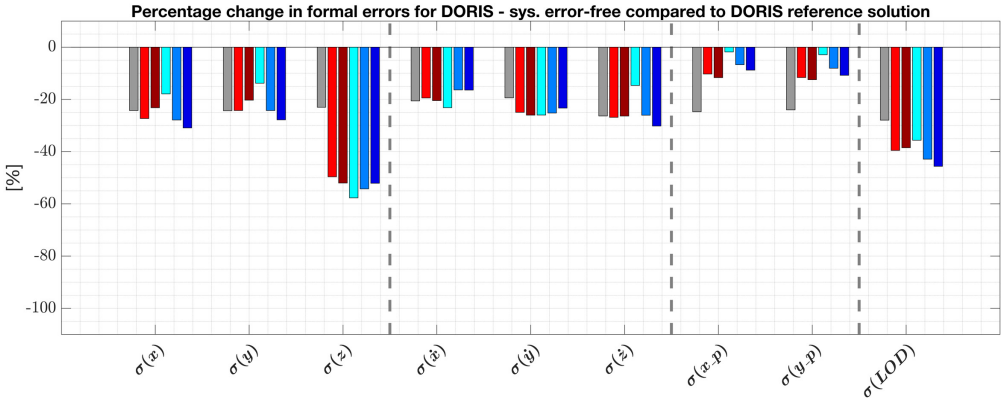

(b) Scaled improvement

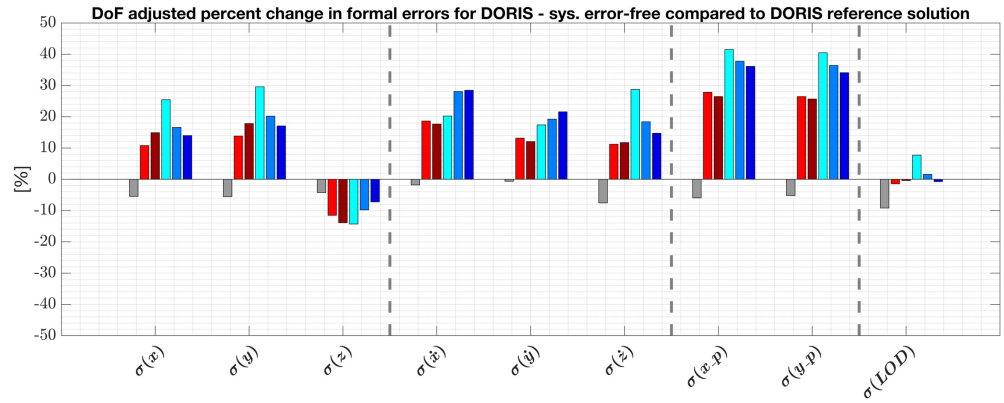

(c) Observation scaled improvement

Figure 6.11: Fig. a) shows the absolute values of the median of the formal errors in X, Y, and Z for the reference scenario and each of the space-tie satellite scenarios. Fig. b) shows the scaled improvement, Fig. c) shows the observation scaled improvement.

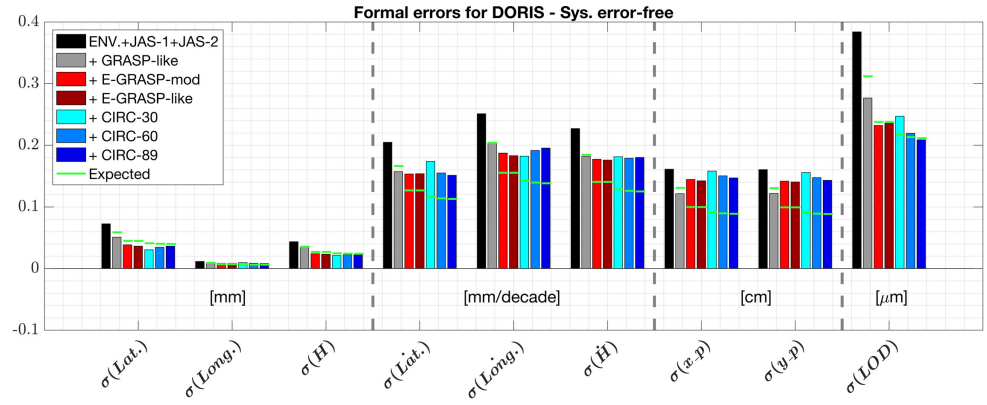

(a) Absolute values of the median of formal errors. The green bars indicate the expected improvement.

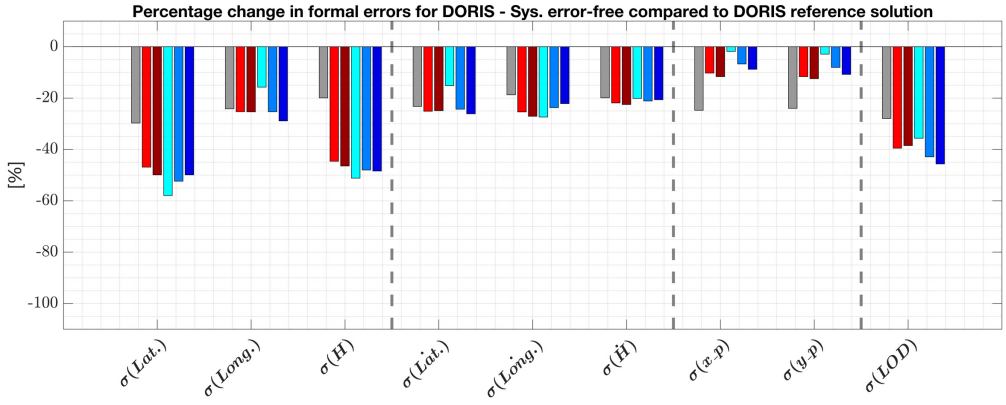

(b) Scaled improvement

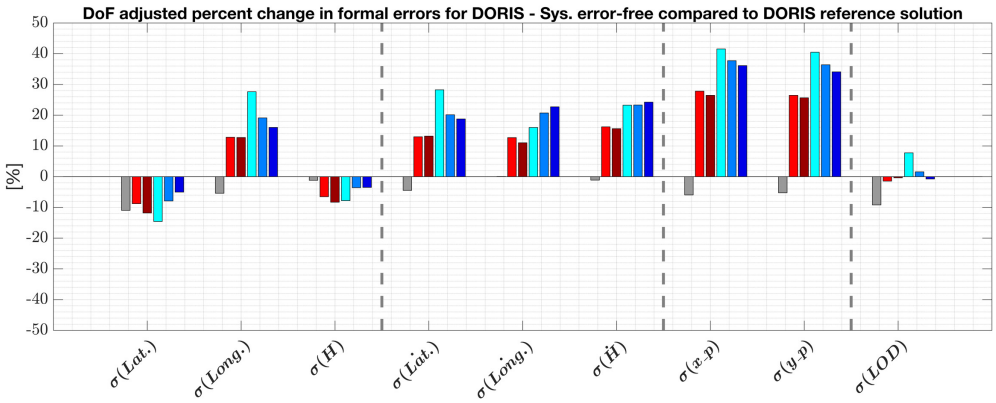

(c) Observation scaled improvement

Figure 6.12: Fig. a) shows the absolute values of the median of the formal errors in latitude, longitude, and height for the reference scenario and each of the space-tie satellite scenarios. Fig. b) shows the scaled improvement, Fig. c) shows the observation scaled improvement.

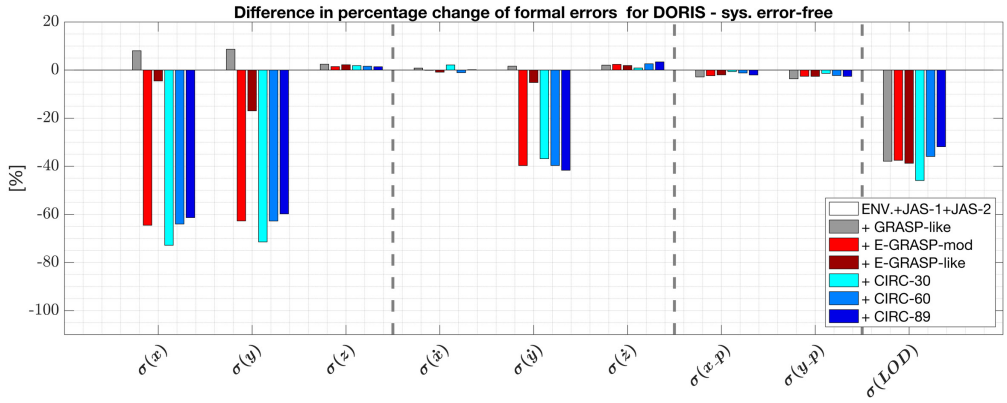

(a) Difference in improvement in Cartesian coordinates

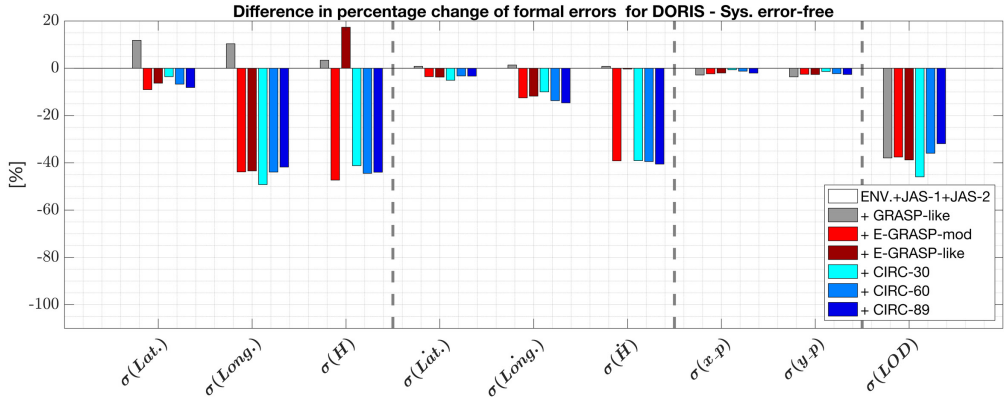

(b) Difference in improvement in geographic coordinates

Figure 6.13: Fig. a) and b) show the difference in scaled improvements based on the mean and median of the formal errors. Large negative values indicate a peak improvement for outlier values.

comparable reductions, ranging from 11 to 20%. In contrast, the greatest reduction for LOD is observed for the three higher orbiting circular scenarios, with values ranging from 65 to 69%. Comparable values can be achieved by the E-GRASP-mod and the E-GRASP-like scenarios, while the GRASP-like scenario shows the least reduction, with a value of 45%.

The linear regression reveals notable offsets in the ERPs for a number of scenarios. Nevertheless, these are in the order of 1/10 mm in the pole coordinates. In the Y-pole, the reference solution already exhibits a slight offset of 0.2 mm, which is reduced by the inclusion of any of the scenarios. In LOD, there are also some significant offsets, however, compared to the GGOS goals, these are well below the millimetre level aimed for. Furthermore, the trend analysis shows that there is no significant detectable trend in the ERPs for any of the scenarios.

ERP spectral analysis The objective of the spectral analysis of the scenarios is to ascertain whether the incorporation of a scenario results in a reduction of specific periods identified within the ERPs, or possibly also induces new periods. The inclusion of the space-tie satellites does not lead to signals being amplified above 0.1 mm in any of the scenarios. A reduction in signals can be observed in all scenarios, but the variations compared to the reference scenario are in the micrometre range. For the sake of completeness, the ERP

differences to a priori, and the respective Lomb-Scargale periodograms are presented for all scenarios in Fig. G.2 to G.7.

Conclusion - systematic error-free The simulations of the systematic error-free case of the scenarios for DORIS demonstrate a globally homogeneous observation coverage, even in low-orbiting scenarios. Scenarios with higher altitudes achieve a significantly higher number of observations, due to the fact that more ground stations are continuously visible, which leads to a continuously higher utilisation of the DORIS receiver.

The highest orbit accuracy can be achieved in a low-orbiting scenario, such as the GRASP-like scenario. As the altitude of the scenario increases, the orbit accuracy deteriorates. It appear that the eccentricity plays a less important role than the apogee height. Systematic geographical differences in the determined orbits can be determined primarily for the eccentric orbits, where these reach a maximum amplitude of 1 mm.

The capacity to improve formal errors in station positions and velocities is particularly evident in the GRASP-like scenario, which is the sole scenario exhibiting a persistent geometric added value. The remaining scenarios are not much inferior, but particularly in regard to station velocities, they are unable to achieve the anticipated degree of expected improvement due to the additional observations. Continuously higher orbiting scenarios, such as the E-GRASP-mod and the circular scenarios, can enhance global observation coverage, thereby leading to a notable improvement in the stability of position and velocity, particularly in regions where conventional DORIS satellites offer less observations.

The potential to reduce formal errors in the pole coordinates is found to be smaller, where only the low-orbiting GRASP-like scenario demonstrates a geometric added value. Same holds for the reduction of noise in the a posteriori pole coordinate, which can be most effectively reduced with the GRASP-like scenario. All other scenarios are less effective in this regard. The periodic signals in the ERPs can be reduced, especially with the GRASP-like, E-GRASP-like, and the circular scenario with an inclination of 89 degrees. However, the E-GRASP-like scenario is less effective in reducing higher frequency signals.

The formal errors of LOD can be improved by a similar amount with each scenario, although only to the level of expectation due to additional observations. All scenarios except the GRASP-like achieve the lowest noise of the a posteriori values for LOD, the GRASP-like is slightly less effective. Each of the investigated scenarios can reduce periodic signals, however, variations are below 0.1 mm.

With regard to the improvement in the accuracy of the TRF and ERPs, the rating is given in Tab. 6.7. The GRASP-like scenario is the most suitable. The E-GRASP-mod, E-GRASP-like, and the circular scenarios with 60 and 89 degrees inclination demonstrate slight differences in the advantages they offer, but on average, they exhibit a similar level of benefit. Continuously higher orbiting scenarios, specifically the E-GRASP-mod and all circular scenarios, were identified as particularly effective in enhancing the independence of the reference solution for station coordinate estimates. Conversely, the circular scenario with 30 degree inclination appears to offer the least benefit.

Table 6.7: Maximum potential of the satellite scenarios for DORIS to improve the TRF and ERPs in the case free of systematic errors. The lower the stated value, the better the rating. The summary represents the unweighted mean value. The abbreviations are G-like for GRASP-like, E-G-mod for E-GRASP-mod, E-G-like for E-GRASP-like, f.e. for formal error.

	G-like	E-G-mod	E-G-like	Circ. 30°	Circ. 60°	Circ. 89°
Obs. cov.	②	①	①	②	①	①
Orbit	①	②	②	②	②	②
Helmert	①	①	①	①	①	①
Station pos. f.e.	①	②	②	③	②	②
Station veloc. f.e.	①	②	②	③	③	③
Stat. stab. f.e.	③	①	③	②	①	①
Pole coord. f.e.	①	②	②	③	③	③
Pole coord. est.	①	②	②	③	②	②
LOD f.e.	①	②	②	③	②	②
LOD est.	②	①	①	①	①	①
ERP stab. f.e.	①	①	①	①	①	①
Summary	1.4	1.5	1.7	2.2	1.7	1.7

6.1.2.2 Influence of center-of-mass displacements

A crucial aspect of a space-tie satellite is the necessity for precision in determining the eccentricities of the reference points of the measurement techniques, both prior to the launch of the satellite and in orbit. This section will investigate how errors in the reference point affect the orbit and, subsequently the reference frame determination. In reality, the CoM of the satellite and the eccentricity of the reference points of the measurement techniques are determined prior to the launch. The eccentricities of the measurement techniques depend on their position on the satellite. In turn, the position of the CoM of the satellite depends on its geometry and the distribution of masses within it.

In the context of the simulations, in the absence of any systematic errors, both the CoM and all reference points of the measurement techniques are, for the sake of simplicity, situated at the origin. In order to introduce a systematic displacement of the measurement techniques, the CoM correction is shifted in the recovery. Post-launch DORIS reference point estimates for altimetry satellites calibrated by dynamic POD (Cerri et al., 2021), or CoM deviations (Montenbruck et al., 2017), are in the millimeter to centimeter range in comparison to the manufacturer's values. Two scenarios are thus established, the first of which entails a shift of the reference point by 3 mm in all three axes, and the second by 6 mm. This results in a 5 mm and 10 mm displacement in three dimensions, respectively. Given the selected attitude control of the simulated satellite, these axes directly correspond to the radial, cross-track, and along-track components. The dynamic modelling remains unchanged thorughout this process.

Orbital fit The orbital fits (minimum, maximum, RMS, mean, standard deviation) demonstrate no deviation from the values of the systematic error-free case for any of the satellite scenarios for both 5 mm and 10 mm systematic displacement. Therefore, the solved for paramters absorb the introduced mismodelling and it is not reflected in the orbital fit. The

geographical distribution of the residuals demonstrates a discernible systematic influence, particularly in the case of the GRASP-like scenario. The extremes of the differences in mean values are concentrated in intermediate regions between ground stations (see Fig. 6.14). This effect is less pronounced in the E-GRASP-mod and E-GRASP-like scenarios, and in the circular scenarios the influence is almost undetectable.

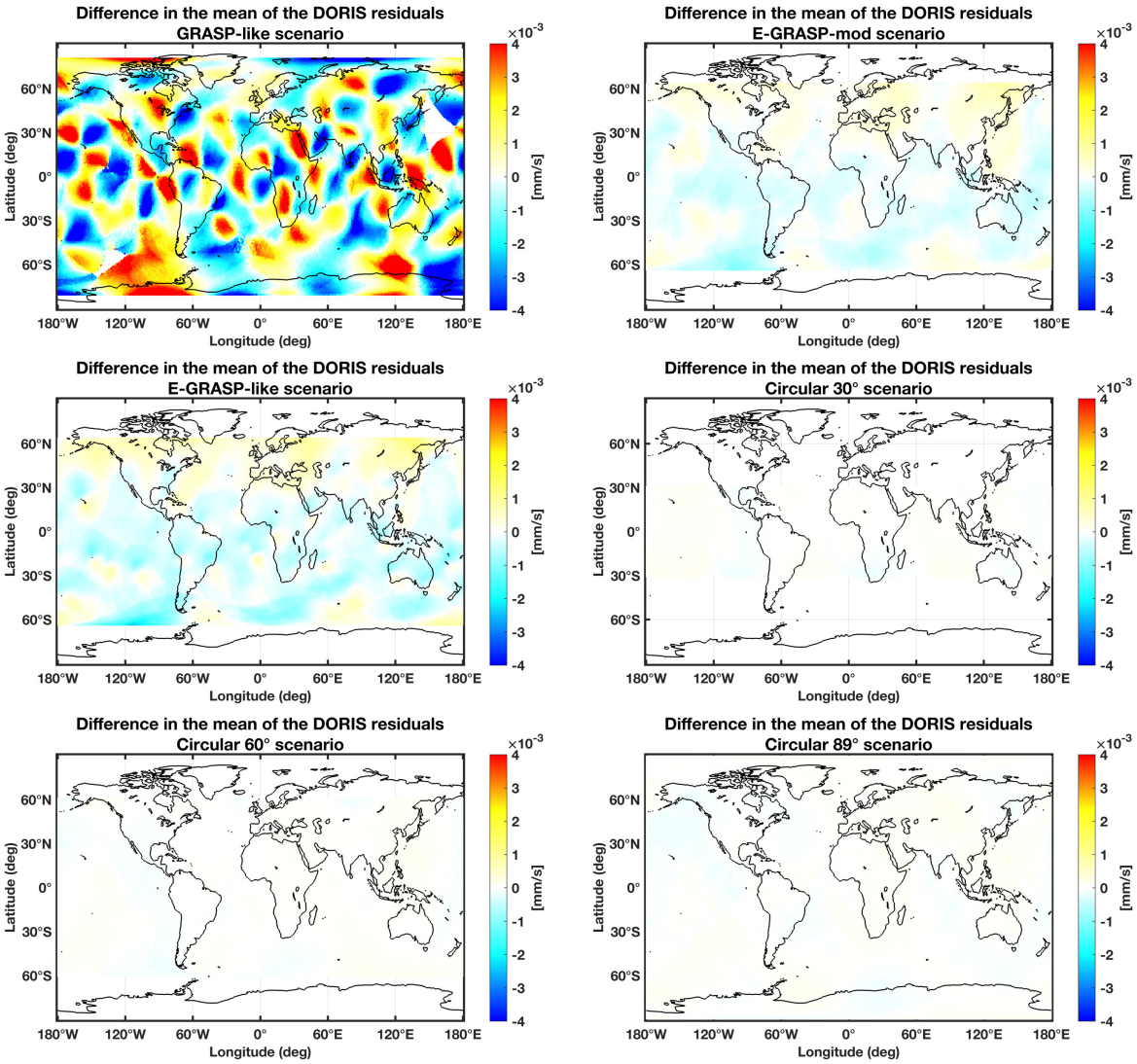

Figure 6.14: Global distribution of the difference in the mean of the observation residuals for the 3D 10 mm CoM mismodelling scenario compared to systematic error-free.

Orbital recovery The results of the orbit comparisons, as illustrated in Fig. 6.15, indicate that a systematic shift of the CoM affects the orbit to a different extent depending on the specific orbit configurations. In the radial direction, almost no increase in the RMS or mean deviation across all scenarios. Only the eccentric orbit scenarios exhibit a slight increase in the RMS, with the E-GRASP-like scenario being slightly more affected. Moreover, in the cross-track direction, all scenarios except the two eccentric ones (E-GRASP-mod and E-GRASP-like) demonstrate no impact on the RMS and mean. The effect on the RMS is discernible for the E-GRASP-like and E-GRASP-mod scenarios, exhibiting a deterioration of 20% and 10%, respectively, in comparison to the systematic error-free case. Furthermore,

both scenarios exhibit a systematic deviation, which, represents approximately 50% of the introduced displacement in the E-GRASP-like scenario and 20% in the E-GRASP-mod scenario. In the along-track direction, each scenario reflects 100% of the introduced shift and the RMS values increase the most for the lower orbiting GRASP-like and the two eccentric E-GRASP-like and E-GRASP-mod scenarios.

A geographically systematic influence on the orbit is evident, particularly for the E-GRASP-like scenario and to a lesser extent for the E-GRASP-mod scenario (see Fig. 6.16). In the case of 10 mm CoM displacement, a systematic North-South distribution is observed in the radial component, with an amplitude of 1.7 mm for the E-GRASP-like scenario and 1 mm for the E-GRASP-mod scenario. In the cross-track direction, a systematic increase in orbit differences around the equator is observed, with an amplitude of up to 7 mm for the E-GRASP-like scenario and 2.7 mm for the E-GRASP-mod scenario. In the along-track direction, the geographical patterns are less pronounced and show an amplitude of up to 1 mm around the systematic bias and are correlated with the radial component. The other scenarios, namely GRASP-like and all circular scenarios, are much less affected and demonstrate geographical patterns only in the sub-millimetre range.

The results demonstrate that the DORIS observation technique is particularly effective in the radial direction, which is also an essential characteristic for one of its primary applications, i.e. orbit determination for altimetry satellites. No systematic effects are observed in the radial and cross-track directions, independent of inclination or altitude, for circular orbits. The performance of eccentric scenarios is inferior, with the influence increasing with greater numerical eccentricity. In the along-track direction, all scenarios reflect the full displacement introduced.

DORIS reference point estimation A common approach is to estimate the CoM coordinates and the reference point of the observation technique in orbit within the dynamic POD. In this case, considerable discrepancies are frequently observed. As demonstrated by the findings presented in Montenbruck et al. (2017), an error of 10 mm in the CoM coordinates for the Sentinel-3A satellite was identified. This approach was also adopted for the scenarios presented here, with the CoM coordinates estimated for each arc. Subsequently, the weekly normal equations were accumulated over the entire time span to obtain one set of CoM coordinates. The results of this process are presented in Tab. 6.8. The expected values of the differences of the estimated parameters to the simulation are zero, so that the estimated CoM coordinates would be identical to those in the simulation.

It can be observed that in all scenarios it is possible to determine the CoM coordinates with an accuracy below 1 mm in the radial and normal directions, whereby the higher orbiting circular scenarios show the highest inaccuracy. Only the circular scenarios with an inclination of 30 and 60 degrees exhibit slightly larger deviations, with a maximum of 1.5 mm, in comparison to the scenario with an inclination of 89 degrees. The greatest inaccuracy is observed in the transversal direction, where discrepancies size up to multiple centimetres, and a respective standard deviation of up to 156 cm. The best values in transversal direction are achieved by the E-GRASP-mod and E-GRASP-like scenario, exhibiting differences in the millimetre and sub-millimetre range. The GRASP-like performs worse with deviations in the centimetre range, while the higher orbiting circular scenarios deviate significantly, with deviations in the decimetre to metre range.

The increase of the displacement from 3 mm per axis to 6 mm shows no major influence on the estimated values across the various scenarios. In light of the introduced systematic shift and the considerably larger deviation of the estimated values, it can be concluded that

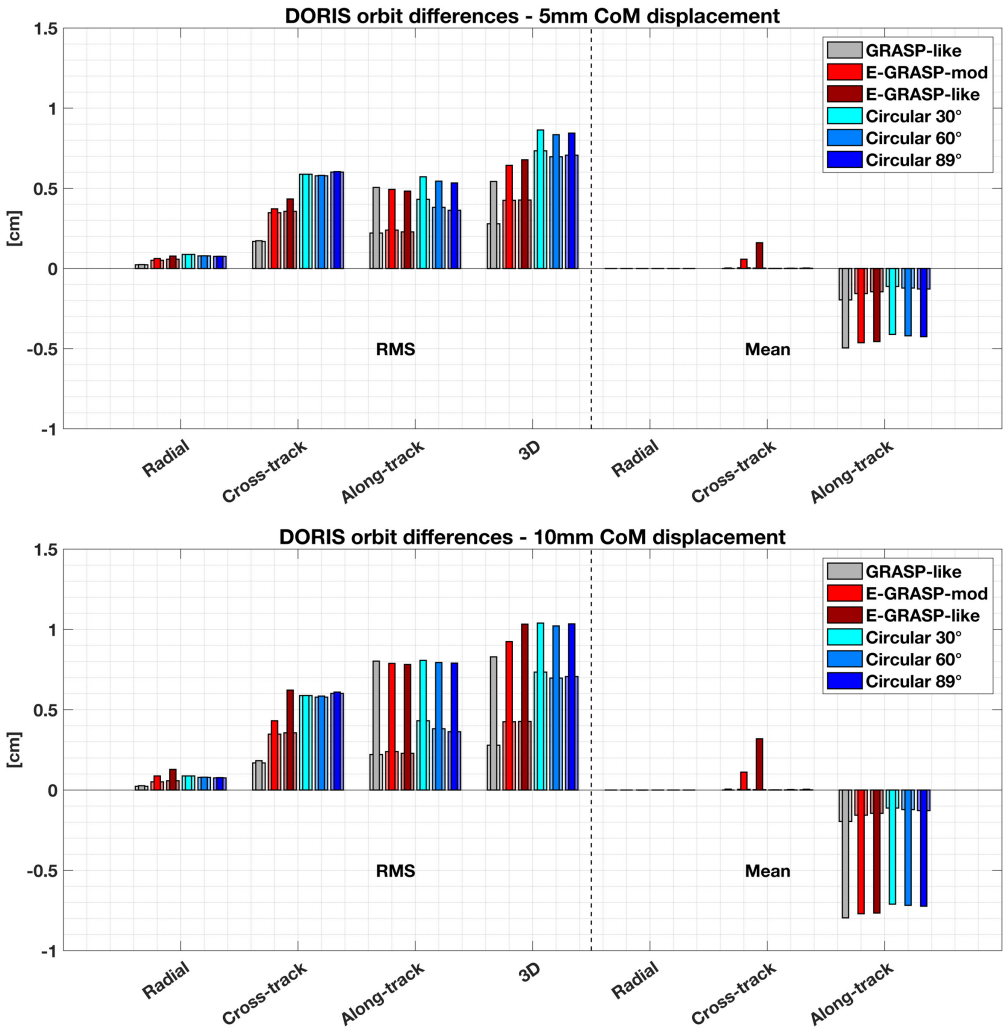

Figure 6.15: Mean RMS and mean values of the orbit comparison of the simulated and recovered orbit with 5 mm and 10 mm systematic displacement, respectively. The thinner bars show the results of the test scenarios with the systematic displacement, the thicker bars in the background show the values achieved in the systematic error-free case.

it is not possible to derive a meaningful estimate of the reference point in the transversal direction in the GRASP-like and all circular scenarios. In the E-GRASP-like and E-GRASP-mod scenarios, it is possible to a certain level, however, a bias at the millimetre level remains in the E-GRASP-mod scenario. In reality, correlated effects such as a possible DORIS time bias would prevent the separation of a time tagging bias and a reference point bias in the transversal direction.

Reference frame

Helmert parameters A systematic effect on the TRF can be seen, particularly in the case of the low-orbiting GRASP-like scenario. In this scenario, larger translations occur in the Z direction for both station positions and velocities (see Fig. 6.17 and Tab. F.4 and F.5 in App. F.1). These are 0.3 mm in the Z direction, which is approximately 1/10th of the one-dimensional displacement introduced (3 mm). Additionally, a rotation around X is observed, less strong also around Z, for the station positions and velocities. An influence on

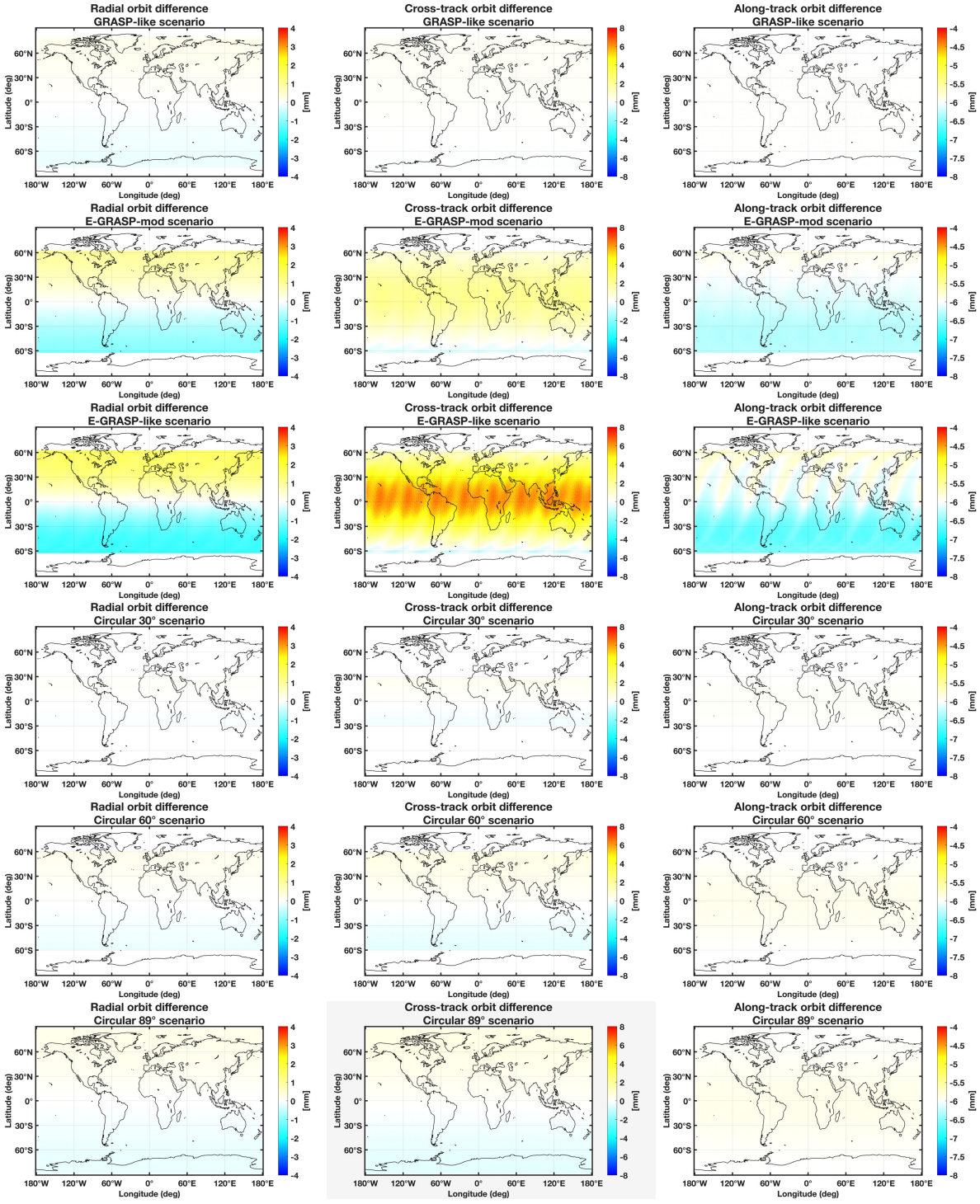

Figure 6.16: Mean orbit differences of the systematic error-free scenario and the recovered orbit for the 3D 10 mm CoM mismodelling scenario. From left to right in radial, cross-track, and along-track direction. From the top to the bottom, GRASP-like, E-GRASP-mod, E-GRASP-like, Circular 30°, Circular 60°, Circular 89°.

Table 6.8: Difference of estimated CoM coordinates to the simulation. All values in millimetre with the corresponding standard deviation of the estimate. Introduced CoM coordinates displacement of 3 and 6 mm all three components.

	3 mm per component introduced			6 mm per component introduced		
	Radial	**Transversal**	**Normal**	**Radial**	**Transversal**	**Normal**
GRASP-like	-0.21 $\pm$ 0.10	-13.33 $\pm$ 8.75	-0.03 $\pm$ 0.09	-0.21 $\pm$ 0.10	-13.30 $\pm$ 8.75	-0.03 $\pm$ 0.09
E-GRASP-mod	0.01 $\pm$ 0.25	3.47 $\pm$ 3.21	0.13 $\pm$ 0.31	0.01 $\pm$ 0.25	3.47 $\pm$ 3.21	0.13 $\pm$ 0.31
E-GRASP-like	0.00 $\pm$ 0.16	0.81 $\pm$ 1.60	0.06 $\pm$ 0.25	0.00 $\pm$ 0.16	0.81 $\pm$ 1.60	0.06 $\pm$ 0.25
Circular 30	-0.64 $\pm$ 0.92	-1407.02 $\pm$ 1565.00	-1.54 $\pm$ 0.96	-0.64 $\pm$ 0.92	-1425.25 $\pm$ 1575.00	-1.54 $\pm$ 0.96
Circular 60	-0.59 $\pm$ 0.81	-290.33 $\pm$ 602.50	-1.01 $\pm$ 0.77	-0.59 $\pm$ 0.81	-290.56 $\pm$ 602.50	-1.01 $\pm$ 0.77
Circular 89	-0.29 $\pm$ 0.73	648.64 $\pm$ 484.50	-0.22 $\pm$ 0.69	-0.29 $\pm$ 0.73	648.20 $\pm$ 484.20	-0.22 $\pm$ 0.69

the scale can also be noted, which again is reflected with the factor of 1/10 of the introduced displacement.

In the case of the two E-GRASP-like and E-GRASP-mod scenarios, there is significantly less effect on the translations. Furthermore, the impact on the rotations is evidently less pronounced than in the GRASP-like scenario, exhibiting only discernible rotations around the X-axis. However, these rotations represent approximately a 1/30 ratio of the introduced one-dimensional displacement. This effect is slightly stronger for the more eccentric E-GRASP-like scenario. The two eccentric scenarios also show an influence on the scale and its velocity, albeit to a considerably lesser extent than in the GRASP-like scenario.

All circular scenarios demonstrate a negligible impact on the Helmert parameters pertaining to station positions and velocities, where the translations are all close to zero and rotations can only be noted around X and Z, but are very small with values below 1/10 mm. Same holds for the scale, where the maximum discrepancies appear to be below 1/10 mm and 1/100 mm/a, respectively.

The Helmert parameters for the case of co-estimating the CoM coordinates show no significant difference from the a priori station network across all scenarios. All previously observed effects on the station network can be rectified. It is also noteworthy that the very poorly determinable transversal CoM coordinates of the circular scenarios are not reflected in the station coordinates.

Formal errors The impact of the fixed CoM displacement on the formal errors of the station coordinates, velocities and ERPs is vanishing small for all scenarios, with a change of less than 2/100% (see Tab. F.6 and F.7 in App. F.1). The co-estimation of the CoM coordinates of the space-tie satellite result in a slight increase in the formal errors associated with the station velocities (see Tab. F.8 and F.9 in App. F.1). This effect is most pronounced in the GRASP-like scenario. The two eccentric scenarios, E-GRASP-mod and E-GRASP-like, exhibit a slightly stronger increase than the circular scenarios, but most are on a similar level with LIP below 1%. The maximum LIP of approximately 3% can be observed for the station velocities in the Z-direction for the GRASP-like scenario.

ERP analysis The statistical parameters for the analysis of the impact on the ERPs are listed in tab. F.10. It can be observed that the standard deviation of the estimated ERPs is not affected in all scenarios. A major significant effect on the ERPs can only solely be seen for the GRASP-like, E-GRASP-mod, and E-GRASP-like scenarios. In these scenarios, the primary effect is observed in the Y-pole, with a 10 mm 3D CoM displacement resulting in an offset of up to approximately 1.4 mm and a trend of 0.127 mm/a. The other scenarios are

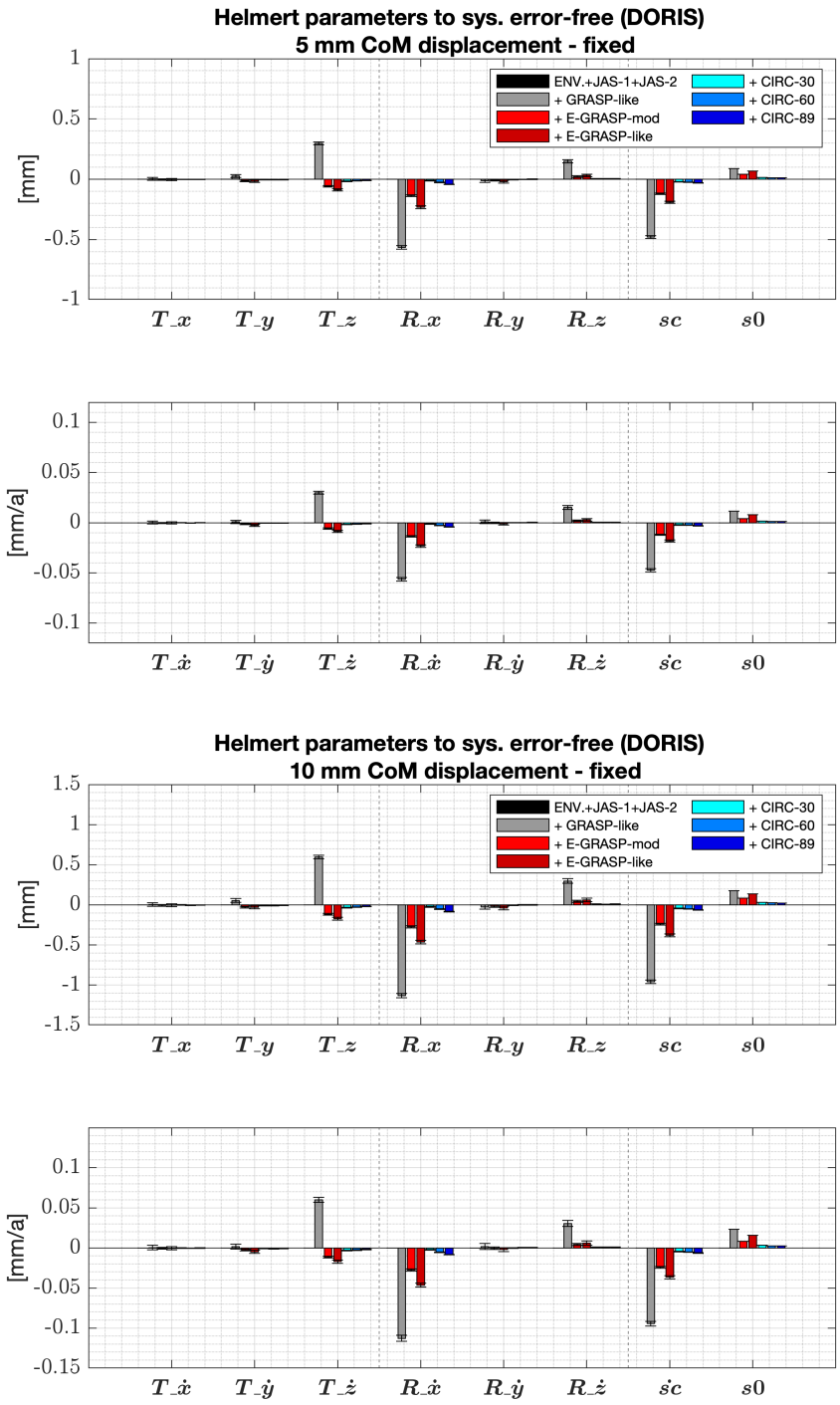

Figure 6.17: Helmert parameters for all stations for 5 mm (top figure) and 10 mm (bottom figure) CoM displacement compared to the a posteriori coordinates of the respective systematic error-free reference solution. The respective upper figures show the values of the station positions, the lower ones those of the velocities.

effected less. By co-estimating the CoM coordinates, it is possible to eliminate or reduce the aforementioned effects in the Y-pole to an insignificant level or below 0.1 mm.

The spectral analysis of the ERPs shows no changes for a displacement of 5 mm. From a displacement of 10 mm, slight variations begin to appear, but these are in the micrometre range and are limited to the pole coordinates. In all cases of CoM coordinate estimation, no changes can be detected compared to the systematically error-free case. It is noteworthy that the poorly estimated CoM corrections, for example for the circular scenario with 30 degree inclination of about 140 cm in the transversal direction, are not reflected in the ERPs. This is most likely absorbed by the initial state elements.

Conclusion - systematic center-of-mass displacement The coordinates of the CoM have been shifted by 3 and 6 mm in all three axes, which corresponds to approximately 5 and 10 mm, respectively, in 3D.

It has been shown that the accuracy of the orbit is most impacted in the along-track component, where the full displacement is reflected.With increasing eccentricity of the orbit, the cross-track component also partly reflects the introduced displacement, which is at the level of 20% of the introduced displacement for the E-GRASP-like scenario and 50% for the E-GRASP-mod scenario. Systematic geographic influences on the orbit are only evident in the E-GRASP-mod and E-GRASP-like scenarios.

The effect on the formal errors of station coordinates and ERPs was shown to be negligible.

Systematic errors in the TRF are observed exclusevily in the GRASP-like, E-GRASP-mod, and E-GRASP-like scenarios and appear as translations in the Z direction, rotations around X, and scale errors. These are strongest for the GRASP-like scenario and reflect approximately one tenth of the introduced CoM shift. Circular higher orbiting satellites show almost no effect on the TRF and in the ERPs due to displacement.

The estimation of the reference point with DORIS is possible in each of the examined scenarios in both the radial and normal directions. However, in the along-track direction, it is clearly worse and for the GRASP-like and all higher orbiting circular orbits not possible at all. The co-estimation of the reference point coordinates indicates a slight deterioration in the formal errors of the station coordinates and ERPs, which, however, is at most 3% LIP. It is noteworthy that the considerable and erroneous estimated along-track CoM coordinates of the higher orbiting circular scenarios exhibit minimal impact on the TRF and ERPs.

This indicates that higher orbits exhibit a greater margin of error for less precisely calibrated reference points in the DORIS measurement technique. Therefore these scenarios are suitable to reduce the risk of achieving the mission's objective, due to CoM and DORIS reference point calibration inaccuracies.

The rating of the DORIS CoM mismodelling is listed in Tab. 6.9.

Table 6.9: Vulnerability of the satellite scenarios for DORIS for systematic CoM mismodelling.

	G-like	E-G-mod	E-G-like	Circ. 30°	Circ. 60°	Circ. 89°
Orbit	②	③	③	①	①	①
CoM est.	②	①	①	②	②	②
Helmert CoM fixed	③	②	②	①	①	①
Helmert CoM est.	①	①	①	①	①	①
Station pos. form. err.	①	①	①	①	①	①
Station veloc. form. err.	①	①	①	①	①	①
Pole coord. form. err.	①	①	①	①	①	①
LOD form. err.	①	①	①	①	①	①
ERPs est. CoM fixed	②	②	②	①	①	①
ERPs est. CoM est.	①	①	①	①	①	①
Summary	1.5	1.4	1.4	1.1	1.1	1.1

6.1.2.3 Influence of atmospheric drag mismodelling

Atmospheric drag mismodelling will be used to demonstrate the degree to which a satellite is susceptible to drag effects that have not been modelled, across the different orbital scenarios. The discrepancy between the model used for the simulation, which represents the truth, and the one used in recovery is intended to reflect the inaccuracy of atmospheric drag modelling on a satellite. The model representing the truth for the simulation is the NRL-MSIS-E-00 atmosphere model (Picone et al., 2002), which is replaced for the recovery by the Drag Temperature Model (DTM) '78 by Barlier (Barlier et al., 1978). The macro-model of the satellite remains unchanged, further information regarding the macro-model can be found in Sec. 4.4.2. The mismodelling of drag results in a temporal variation in the perturbation forces acting on the satellite. This variation is illustrated for the different scenarios over a seven-day period in Fig. 6.18. Shown are the differences between the sums of all accelerations (i.e. atmospheric drag, Albedo and infrared radiation of the Earth, SRP, empirical accelerations, Earth and Ocean tides and gravitational forces and attraction of the Earth, the Sun and planets) for the truth and the mismodelling case.

No significant change in accelerations is seen for the circular orbit scenarios. This is due to the altitude of the scenarios, which makes the influence of the high atmosphere vanishingly small. In contrast, the situation is distinct for the GRASP-like, E-GRASP-mod, and E-GRASP-like scenarios. The GRASP-like scenario is continuously exposed to mismodelling due to its consistent altitude of below 1'000km. This is demonstrated by the growing discrepancy in acceleration in the radial direction. As a consequence of the continuous different drag acceleration, the integrated orbit undergoes a significant change over time. This is also evidenced by the increasing discrepancy in the accelerations in the transversal direction over time. The E-GRASP-mod and E-GRASP-like scenarios show a different behaviour. As a consequence of the eccentricity of the orbit, the perturbation increases markedly with each entry into the atmosphere and then decreases rapidly as the satellite approaches its apogee. In the E-GRASP-mod scenario, this effect is notably less pronounced due to the higher perigee compared to the E-GRASP-like scenario. For the E-GRASP-like scenario, this perturbation factor increases so much over one week that it is eventually exceeding

that of the GRASP-like scenario. To address the mismodelling introduced, the parameters outlined in Tab. 6.10 are set up in the POD.

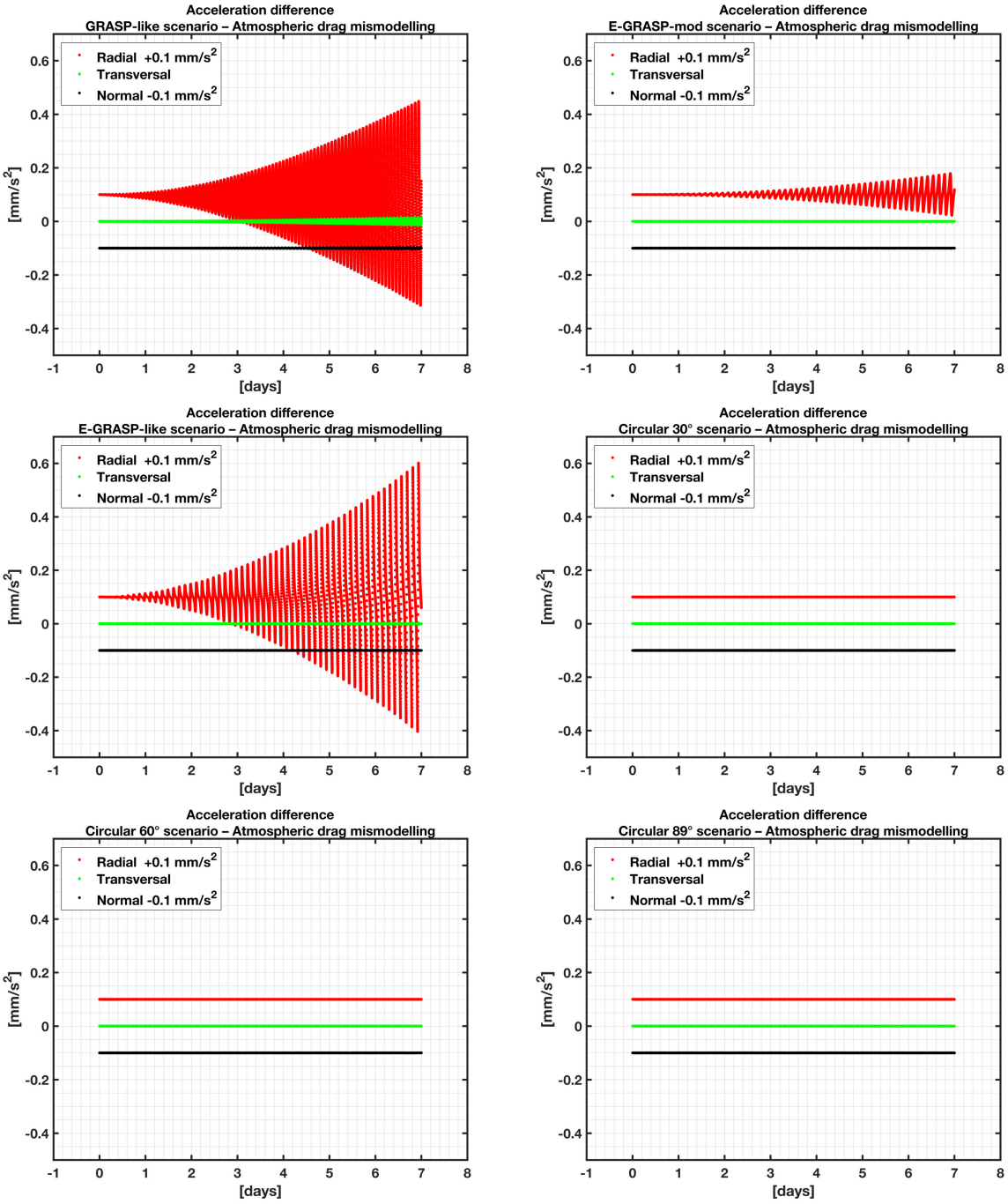

Figure 6.18: Difference in the sum of all accelerations acting on the satellite over 7 days with mismodelled atmospheric drag.

It is important to note that the results of addressing an introduced mismodelling with a dynamic parameterisation depend on the specific set of parameters being estimated. The objective here is not to find the best possible parameterisation, but rather to find a parameterisation that is sufficient to demonstrate the impact of introduced errors on the TRF and ERPs. It is possible that alternative parameterisations may yield better results, however, it is reasonable to expect that the fundamental aspect where these errors show up will be

similar. Parameters are selected with the intention of absorbing unmodelled disturbance forces while preserving the signal of interest.

Table 6.10: Used dynamic parameterisation and estimated parameters for the atmospheric drag mismodelling case.

Parameterisation for atmospheric drag mismodelling case	
All scenarios	
Arc length	7 days
Initial state parameters	estimated
Atmospheric drag parameters	one global scaling factor per arc and scaling factors every 12h set up as piecewise linear polygon

Orbital fit The introduced atmospheric drag mismodelling does not result in any differences in the orbital fits (minimum, maximum, RMS, mean, standard deviation) compared to the systematically error-free case for any of the satellite scenarios. The global distribution of the residuals (see Fig. 6.19) reveales a discernible geographic pattern only for the GRASP-like scenario, in which a West-East pattern can be noted. This is markedly less pronounced in the E-GRASP-like scenario and is not noticeable for the other scenarios at all.

Orbit recovery Fig. 6.20 illustrates the orbit comparisons of the true and the recovered orbits for the case of atmospheric drag mismodelling. Initially, none of the scenarios shows a systematic mean offset in comparison to the values obtained in the systematically error-free case.
In the comparison of the RMS values of the orbit differences, especially the GRASP-like scenario demonstrates a pronounced influence. Increased differences can be noted in both the radial and along-track directions. The E-GRASP-like scenario is the next one to be significantly impacted, where the differences are mainly reflected in increased RMS values in the along-track direction. It appears, that the frequently stronger influence of the acceleration difference for the E-GRASP-like scenario can be better absorbed, in comparison to the GRASP-like scenario. The remaining scenarios are significantly less affected. In the cross-track direction none of them shows increased orbital differences.
The GRASP-like and E-GRASP-like scenarios are also the two that primarily show a systematic difference in the radial and along-track directions in the geographic distribution of the orbit differences (see Fig. 6.21). In both cases, a West-East pattern is observed for both directions, although it is noteworthy that this is the other way around for the two scenarios, which can be attributed to the prograde and retrograde inclination. Additionally, the E-GRASP-like scenario exhibits a North-South pattern in the along-track direction.

Reference frame

Helmert parameters The impact on the TRF is shown by the Helmert parameters presented in Tab. F.11. The most significant effect can be seen for the GRASP-like scenario. In this case, the predominant effect is a significant translation of -1.67 mm and -0.17 mm/year in the Z-direction of the station positions and velocities, respectively. Smaller translations and

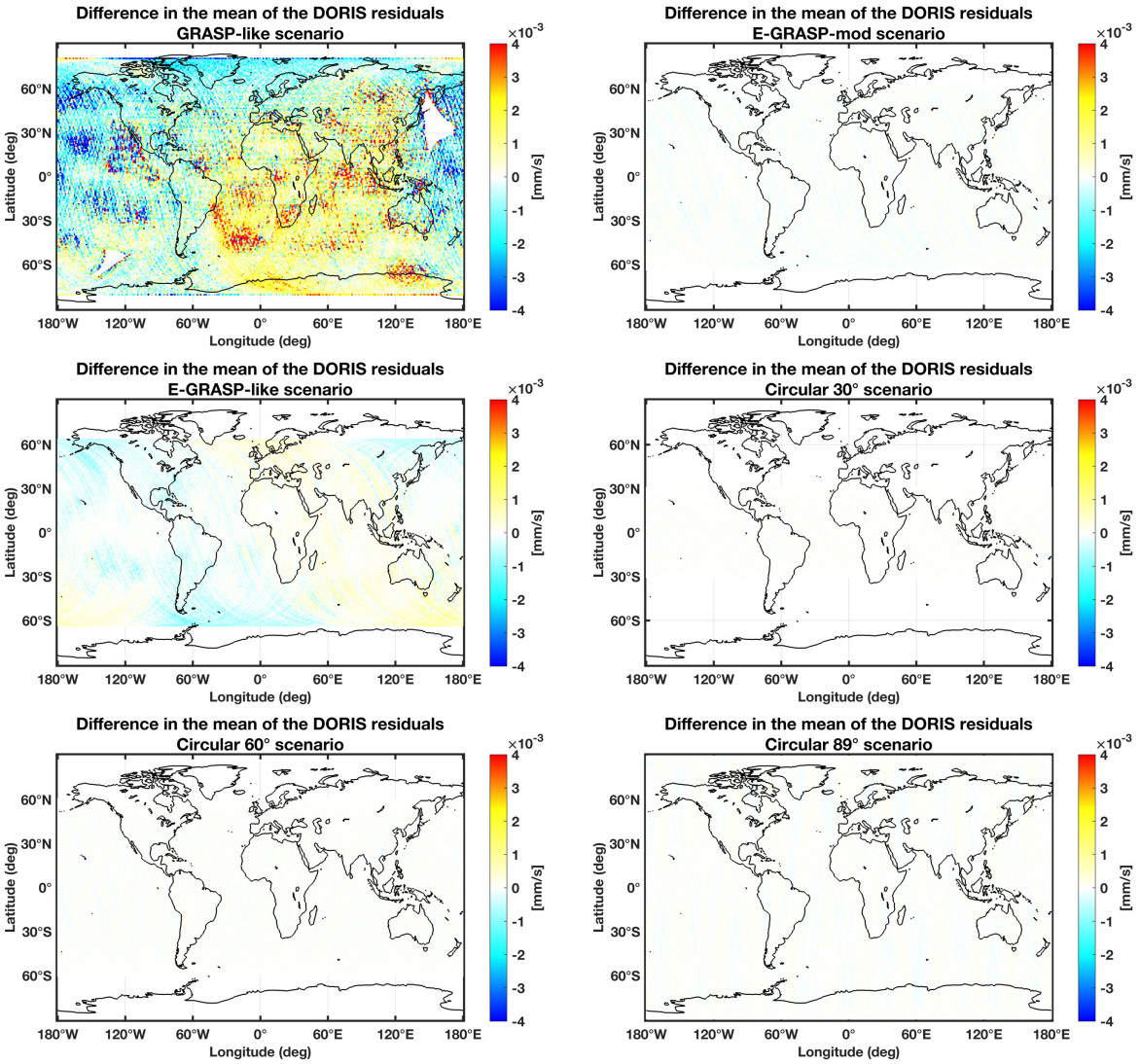

Figure 6.19: Global distribution of the difference in the mean of the observation residuals for the atmospheric drag mismodelling case compared to systematic error-free.

rotations are observed in the X- and Y-directions, but are below 0.15 mm, respectively 0.01 mm/year. One potential explanation for this is the poorly determined along-track component, which is close to the Z-axis for near polar orbits. For the GRASP-like scenario, minor effects can also be observed on the scale, which is also consistent with the higher orbital differences in the radial direction due to the introduced mismodelling. The other scenarios do not show any significant effect.

Formal errors Comparing the LIP in the formal errors reveals that the main effect is observed in low-orbiting scenarios, particularly in the pole coordinates. The LIP for station positions and velocities is in the very low single-digit percentage range, at approximately 2% or less for all scenarios (compare Tab. F.12 in App. F.1). In both pole coordinates, a loss of about 40% is observed for the GRASP-like scenario, 25% for the E-GRASP-like scenario and less than 5% for the E-GRASP-mod scenario. With regard to LOD, the LIP is smaller and only worth mentioning for the GRASP-like scenario, where it amounts to approximately 8%, and the E-GRASP-like scenario with about 2%. In the case of the higher orbiting circular scenarios, no significant effect on the formal errors can be observed.

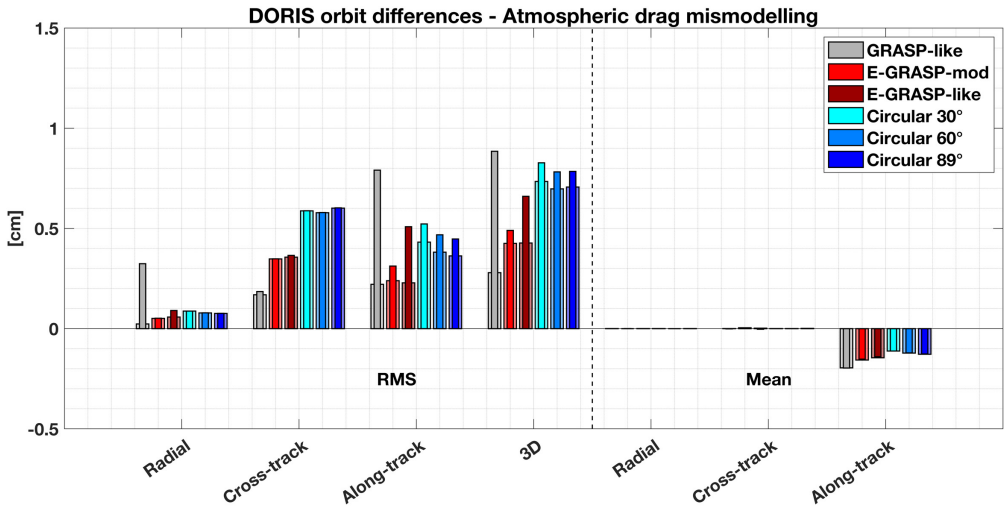

Figure 6.20: Mean RMS and mean values of the orbit comparison of the simulated and recovered orbit for the atmospheric drag mismodelled case. The thinner bars show the results of the drag mismodelling case, the slightly more transparent thicker bars in the background show the values achieved in the systematic error-free case.

ERP analysis The analysis of the a posteriori ERPs corroborates these findings (see Tab. F.13 in App. F.1). A notable rise in the standard deviation of the pole coordinates and LOD is evident in the GRASP-like and E-GRASP-like scenarios. In the GRASP-like scenario, this increase amounts to 36-38% in the pole coordinates and 29% in LOD. In the E-GRASP-like scenario, it is 23% and 5%, respectively.

A notable offset in the ERPs can only be observed in the Y-pole for the GRASP-like scenario, exhibiting an increase of approximately -0.3 mm. All the other offsets are either insignificant or not significantly different from the systematic error-free case, with values below 0.1 mm. Furthermore, no significant trends in the ERPs can be observed for any of the scenarios.

These findings are confirmed by the spectral analysis of the ERPs in comparison to the corresponding error-free scenario. The influence is limited to the GRASP-like and E-GRASP-like scenarios and to the pole coordinates. In the GRASP-like scenario, an annual period of 0.3 mm can be seen in both pole coordinates. Further signals also emerge with periods of 186, 155, and 106 days, with amplitudes ranging from 0.1 to 0.2 mm (see Fig. G.8). In the E-GRASP-like scenario, the most amplified signal is also an annual period, reaching 0.3 mm. Further amplified signals in the pole coordinates show periods of 122 and 92 days, with the largest amplitude at 0.2 mm (see Fig. G.9). The spectral analysis of the ERPs of the E-GRASP-mod and the circular scenarios shows no influence.

Conclusion - atmospheric drag mismodelling The lower the altitude of the satellite, the greater the interaction between the satellite and the atmosphere, which in turn affects the accuracy of the orbit, as well as the TRF and ERPs.

The orbital differences increase primarily in the radial and along-track components, particularly in the context of the GRASP-like scenario with a three-dimensional increase by a factor of three, slightly less for the E-GRASP-like scenario with a factor of 1.6.

Similarly holds for the TRF, where a systematic influence on the station network could only be detected for the GRASP-like scenario. This influence is predominantly reflected in a Z-translation by about 1.7 mm. The increase in formal errors pertaining to the station

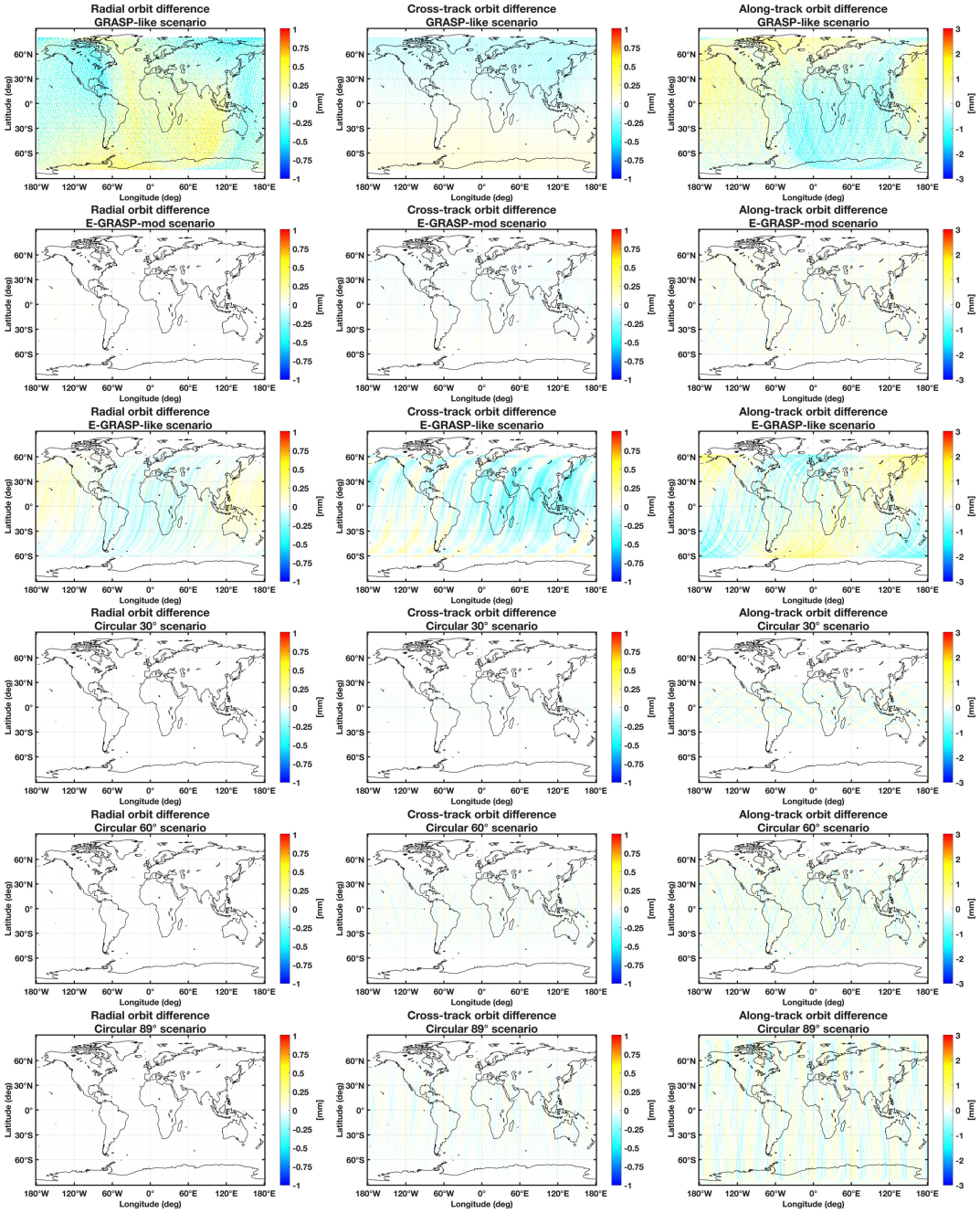

Figure 6.21: Mean orbit differences of the true simulated and recovered orbit over the full simulation time span of 7 years for the atmospheric drag mismodelling case. From left to right in radial, cross-track, and along-track direction. From the top to the bootom, GRASP-like, E-GRASP-mod, E-GRASP-like, Circular 30°, Circular 60°, Circular 89°

coordinates and velocities is deemed to be insignificant when considered across all scenarios examined.

With regard to the ERPs, excluseviley the GRASP-like and E-GRASP-like scenarios, a significant influence is evident. The LIP of the formal errors for the pole coordinates is approximately 40% for the GRASP-like scenario and 25% for the E-GRASP-like scenario. LOD with an LIP of 8% is only noteworthy in the GRASP-like scenario.

The estimated ERPs demonstrate an increase in noise of up to 38% in the GRASP-like scenario and up to 23% in the E-GRASP-like scenario. Furthermore, a systematic offset in the Y-pol can be observed in the GRASP-like scenario. These findings are reflected in the spectral analysis of the ERPs, where these two scenarios exhibit increased amplitudes.

In conclusion, the E-GRASP-mod and the higher orbiting circular scenarios show the least effect due to atmospheric drag mismodelling. The E-GRASP-mod scenario represents a compromise, as the higher perigee can mitigate the deteriorating influence of the atmosphere (compare Tab. 6.11).

Table 6.11: Vulnerability of the satellite scenarios for DORIS for systematic atmospheric drag mismodelling.

	G-like	E-G-mod	E-G-like	Circ. 30°	Circ. 60°	Circ. 89°
Orbit	③	①	②	①	①	①
Helmert	③	①	①	①	①	①
Station pos. form. err.	①	①	①	①	①	①
Station veloc. form. err.	①	①	①	①	①	①
Pole coord. form. err.	③	①	②	①	①	①
LOD form. err.	②	①	①	①	①	①
ERPs	③	①	②	①	①	①
Summary	2.3	1.0	1.4	1.0	1.0	1.0

6.1.2.4 Influence of solar radiation pressure mismodelling

To demonstrate the effect of SRP mismodelling, the macro-model of the satellite used for the simulations was modified for the recovery (see Sec. 4.4.2). In order not to induce any influence in the modelling of the atmospheric drag, the reflection properties of the solar panels of the satellite were modified for this purpose and not the sizes of individual surfaces. The calculation of the SRP disturbance force with the usage of a macro-model, as implemented in EPOS-OC, is based on surface reflectivity properties of certain areas in the visible and IR spectrum and their orientation (see also Sec. 2.4.3.4). This information can be derived from manufacturer's information or from technical notes of specific materials, describing the reflectivity characteristics of materials used at the outer layer of the satellite. The resulting disturbance force is calculated on the basis of the geometric reflection coefficient (ρ), the diffuse reflection coefficient (δ) and the absorption of incident radiation (α), in the visible and IR spectrum. In the case of the satellite here, the solar panels of the macro-model are positioned at the top of the satellite and the two slanted side panels (compare Fig. 4.5). In the direction of flight, this corresponds to the radial and normal directions. These surface properties were modified by increasing the geometric reflectivity and reducing the absorption properties, as detailed in Tab. 6.12. Here, all affected surfaces of the model were taken together as one large surface, since their surface properties are identical.

Table 6.12: Modified macro-model surface properties for the SRP mismodelling case.

		visible and IR		
	Total area $[m^2]$	ρ	δ	α
Simulation	7.6106	0.05	0.30	0.65
Recovery	7.6106	0.07	0.30	0.63

Fig. 6.22 illustrates the differences in the total disturbance acceleration resulting from the SRP mismodelling, exemplified over the course of one week. It should be noted that this effect depends on the β angle, and thus exhibits varying levels over time. The illustration demonstrates the same time epoch, but with different β angles. An epoch with identical β angles was not selected, as the range of the angle and its variation over time are quite different for the scenarios. The GRASP-like, and all circular scenarios are significantly less affected, with maximum acceleration differences of less than 0.3 mm/s^2. The E-GRASP-mod scenario demonstrates radial differences of up to 4-5 mm/s^2 after seven days, while the E-GRASP-like scenario exhibits up to 15-20 mm/s^2. To attribute the introduced mismodelling, the parameterisation according to Tab. 6.13 is used for all scenarios.

Table 6.13: Dynamic parameterisation and estimated parameters for the SRP mismodelling case.

SRP mismodelling parameterisation	
All scenarios	
Arc length	7 days
Initial state parameters	Estimated
SRP parameters	Two linear scaling factors per arc, beginning to end
Albedo parameters	Two linear scaling factors per arc, beginning to end
Atmospheric drag parameters	One global scaling factor per arc, piecewise linear scaling factor every 3h
Empirical accelerations	Piecewise linear continuous in transversal direction every 24h, cosine/sine after 24,48,72,96,120,144 h in transversal and normal direction

Orbital fit The introduced mismodelling of the SRP does not result in any notable differences in the orbital fits (minimum, maximum, RMS, mean, standard deviation) compared to the systematic error-free case for any of the satellite scenarios. Furthermore, the global distribution of the residuals (see Fig. 6.23) demonstrates no evidence of discernible geographical patterns.

Orbit recovery The orbit comparison reveals a notable increase in RMS values, particularly in scenarios involving high orbit altitudes (compare Fig. 6.24). A systematic bias is observable exclusively in the radial direction at the submillimetre level for the circular scenarios with 60° and 89° inclination. The geographical distribution of the orbit differences for all components (see Fig. 6.25) is largely reflecting the increased RMS of the orbit differences.

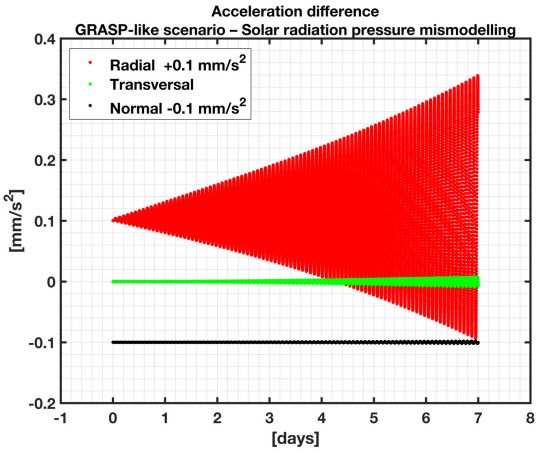

(a) GRASP-like β=18.75°

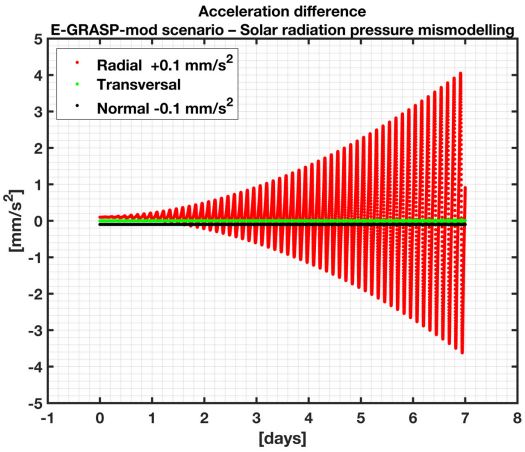

(b) E-GRASP-mod β=35.9°

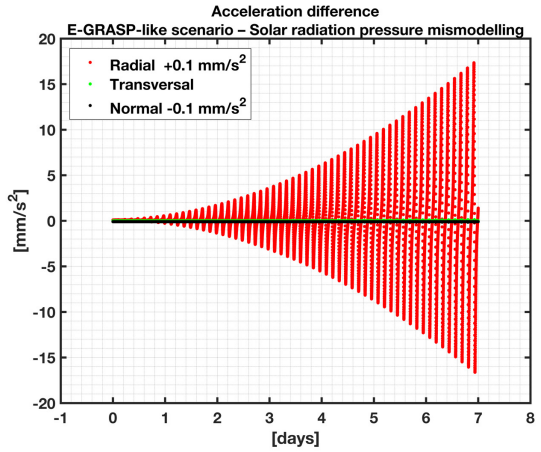

(c) E-GRASP-like β=36.1°

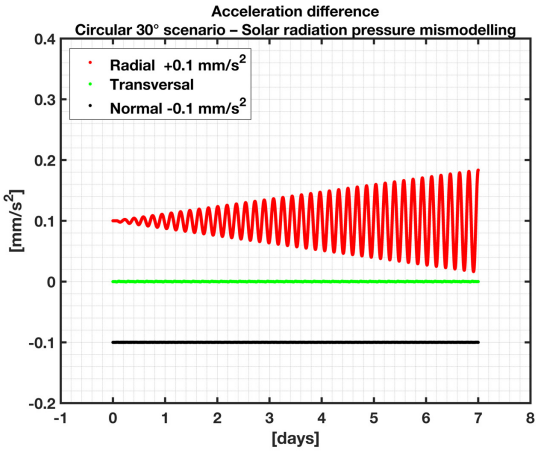

(d) Circular 30° β=5.8°

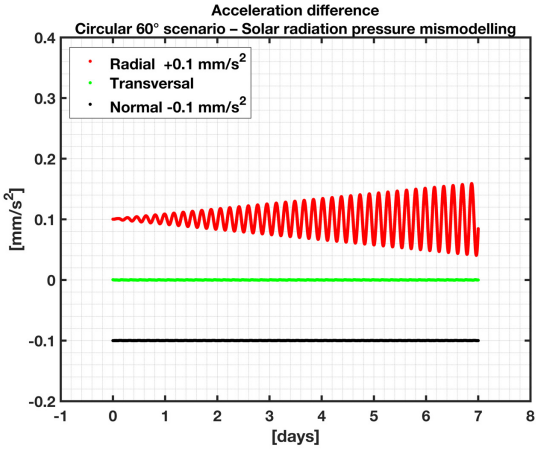

(e) Circular 60° β=33.9°

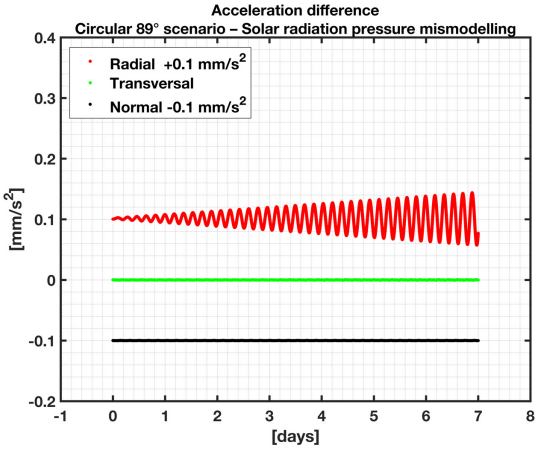

(f) Circular 89° β=59.6°

Figure 6.22: Difference in the sum of the accelerations acting on the satellite over 7 days in the case of SRP mismodelling. The parameter β denotes the angle between the orbital plane and the Sun. Note the different limits of the Y axes.

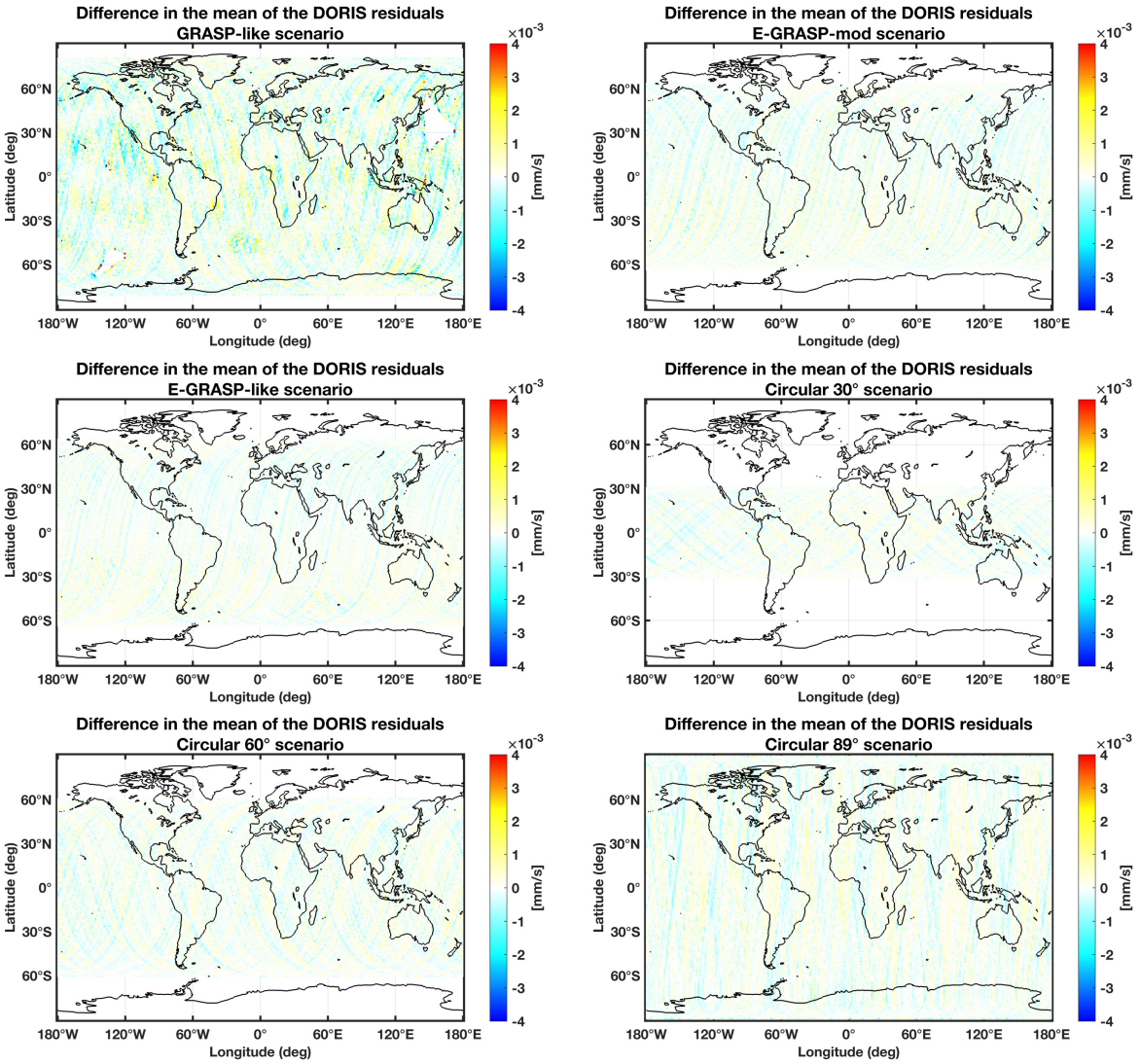

Figure 6.23: Global distribution of the difference in the mean of the observation residuals for the SRP mismodelling case compared to systematic error-free.

Slightly systematic patterns can only be observed in the E-GRASP-mod and E-GRASP-like scenarios. In the radial direction, a systematic pattern can be seen from the equator to the poles. In the cross-track direction, the systematic stripes previously mentioned in the systematic error-free scenario (Sec. 6.1.2.1) are slightly amplified.

Reference frame

Helmert parameters The influence of the introduced SRP mismodelling on translation, rotation and scale is quite small for all scenarios. The GRASP-like scenario exhibits the most significant deviations, though these remain below 1/10 mm (see Tab. F.14 in App. F.1).

Formal errors The changes in the formal errors demonstrate that the station coordinates and velocities exhibit a relatively minor LIP (see Fig. G.10 and Tab. F.15 in App. F.1). In this context, the GRASP-like scenario is marginally more affected. With regard to geographic coordinates, this is predominantly observed in the height components of positions and

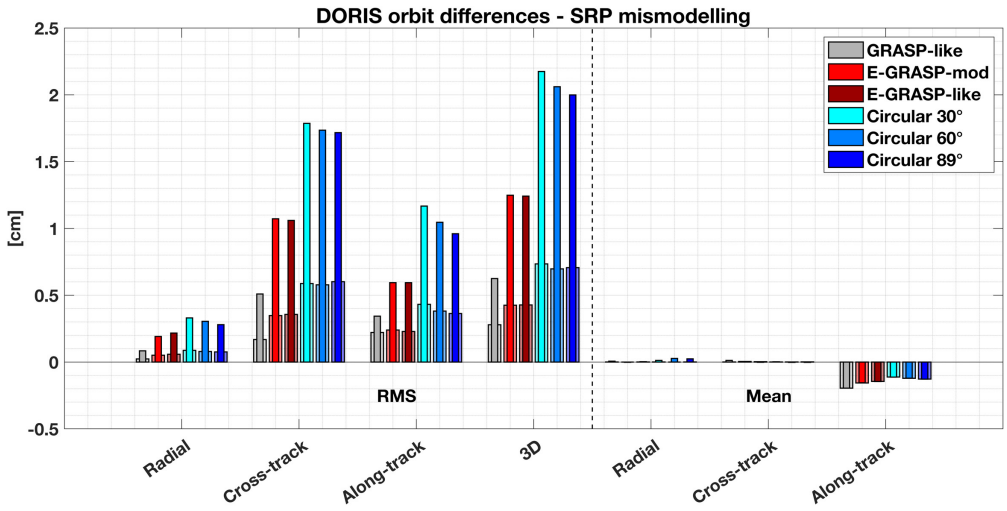

Figure 6.24: Mean RMS and mean values of the orbit comparison of the simulated and recovered orbit for the SRP mismodelled case. The thinner bars show the results of the SRP mismodelling cases, the slightly more transparent thicker bars in the background show the values achieved in the systematic error-free case.

velocities, as well as in the North-South component of velocities, where the LIP ranges up to 4%. In the Cartesian coordinates, however, there is no discernible evidence to suggest that any particular component is more affected with LIP of about 2% and below.

In regard to the ERPs, the pole coordinates are particularly susceptible to significant influence. In the GRASP-like scenario, a reduction of approximately 40% can be observed for both pole coordinates, followed by the E-GRASP-like scenario, for which the decrease ranges between 25 and 30%. The E-GRASP-mod scenario performs better, exhibiting a decrease below 20%. The most favourable outcomes are observed in the circular scenarios, with the scenario of 30 degree inclination exhibiting slightly higher decreases of 21 % in the X-pole and 15 % in the Y-pole. In the remaining two circular scenarios, the LIP in both pole coordinates is approximately 10%. With regard to LOD, it is only the GRASP-like scenario that is significantly affected, with an LIP of approximately 8%. All other scenarios are either close to or below 2%.

ERP analysis The estimated ERPs show a significant increase in the standard deviation of the determined pole coordinates in the GRASP-like and E-GRASP-like scenarios, reaching 6% for GRASP-like at the Y-pole and 5% for the E-GRASP-like scenario at the X-pole (see Tab. F.16). In comparison with the systematic error-free case, no significant offsets or trends can be detected for any of the scenarios. The spectral analysis of the ERPs shows that the impact of the introduced SRP mismodelling is insignificant across all scenarios.

Conclusion - SRP mismodelling The orbit comparison demonstrates a considerable degradation of the orbit due to the SRP mismodelling for all scenarios. However, the magnitude of this increase is significantly larger for the higher orbiting circular scenarios than for the eccentric E-GRASP-like and E-GRASP-mod scenarios, and even less for the GRASP-like scenario. A major systematic effect on the orbital differences and their geographical distribution was not observed for all scenarios.

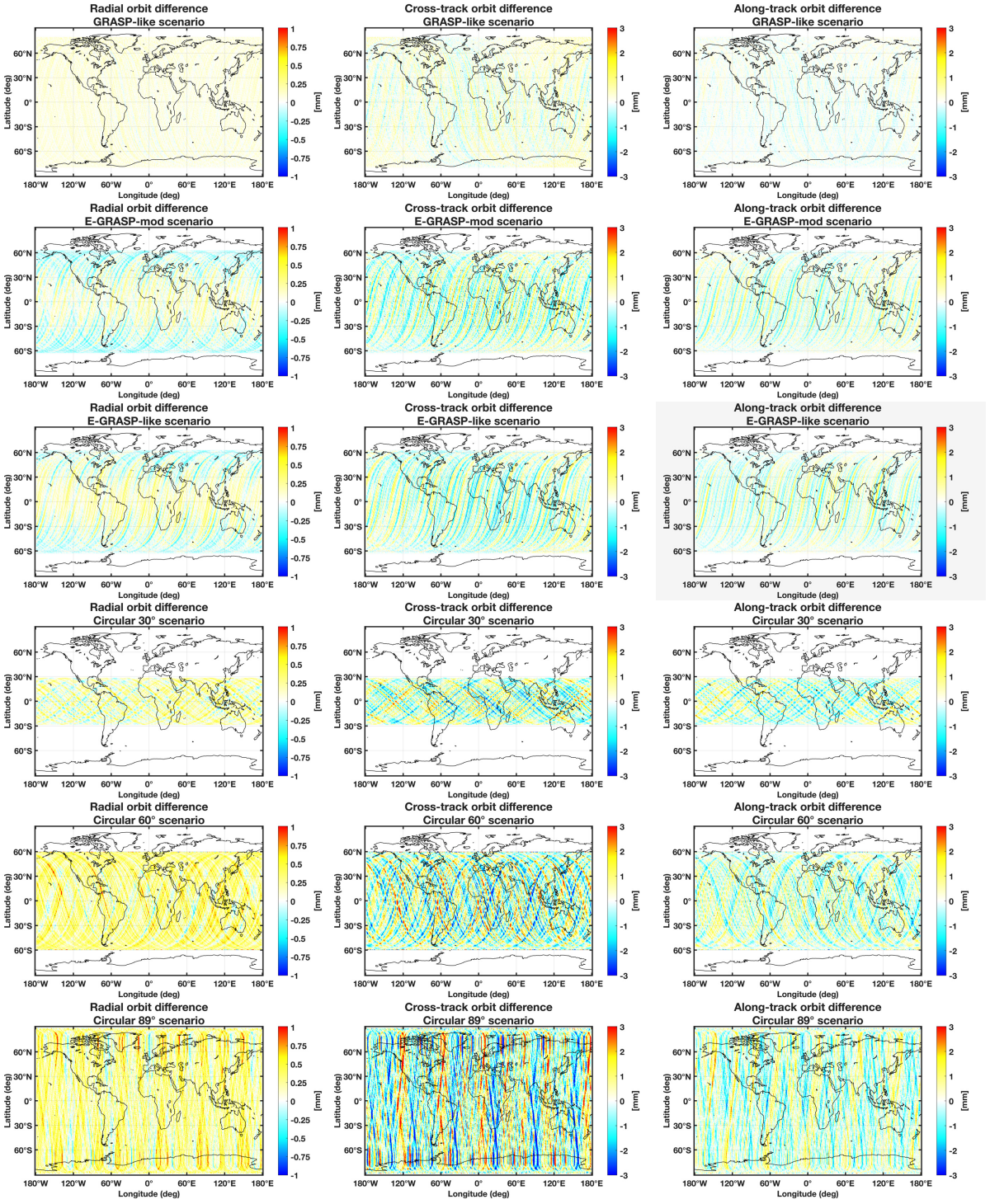

Figure 6.25: Mean orbit differences of the true simulated and recovered orbit over the full simulation time span of 7 years for the SRP mismodelling scenario. From left to right in radial, cross-track, and along-track direction. From the top to the bottom, GRASP-like, E-GRASP-mod, E-GRASP-like, Circular 30°, Circular 60°, Circular 89°.

For none of the scenarios significant systematic effects on the TRF could be detected. The LIP in formal errors turn out to be negligible for station coordinates and velocities, and is almost exclusively limited to the pole coordinates, and to a lesser extent, also to LOD. The highest level of degradation is observed in the GRASP-like scenario, with a maximum of approximately 40%. In comparison, the E-GRASP-mod, E-GRASP-like, and circular scenario with an inclination of 30 degrees exhibit a degradation of approximately 20 to 30%. The lowest level of degradation is observed in the higher orbiting circular scenarios with an inclination of 60 and 90 degrees, with degradation of close to and below 10%.

Systematics in the determined pole coordinates and LOD do not show up, the influences are limited to increased noise, which, is at the single-digit percentage level.

The results of the SRP mismodelling indicate that no scenario is inherently superior or inferior. While orbit accuracy is more susceptible to degradation in higher orbiting scenarios, this is not reflected in the derived TRF and ERPs. In the overall comparison in Tab. 6.14 only the GRASP-like scenario shows a minor increased deficit.

Table 6.14: Vulnerability of the satellite scenarios for DORIS for systematic SRP mismodelling.

	G-like	E-G-mod	E-G-like	Circ. 30°	Circ. 60°	Circ. 89°
Orbit	①	②	②	③	③	③
Helmert	①	①	①	①	①	①
Station pos. form. err.	①	①	①	①	①	①
Station veloc. form. err.	①	①	①	①	①	①
Pole coord. form. err.	③	②	②	②	①	①
LOD form. err.	②	①	①	①	①	①
ERPs est.	②	①	②	①	①	①
Summary	1.6	1.3	1.4	1.4	1.3	1.3

6.1.2.5 Influence of ground beacon frequency bias mismodelling

The transmitted frequency of the DORIS signal, as emitted by the beacons, may deviate from the nominal frequency (see also Sec. 3.1.1.1). This deviation should be taken into account during the orbit processing, as it can result in increased post-fit RMS values and systematic effects in the determined orbit. In the DORIS simulation free from systematic errors, it is assumed that in an ideal scenario, no frequency biases exist. Such a scenario would be theoretically feasible if all DORIS beacons were connected to highly accurate clocks. Although, this would be a highly costly endeavour and is also challenging to achieve, given that some beacons are situated in extremely remote locations. Nevertheless, it is part of the IDS strategic plan to extend the number of stations linked to highly accurate clocks (François & Claude, 2023). In the POD process, the frequency biases of stations are typically estimated. For the mismodelling case, the estimated frequency biases derived from the real data evaluation (see Sec. 5.1) are employed, with an average value determined for each station over time. The frequency bias values range between -150 and +188 Hz. Thereafter, the respective frequency biases for each station are applied to the simulated observations. In the recovery run, the modified observation data are used, and one frequency bias per station per pass is estimated in addition to the other parameters, as outlined in Tab. 6.15.

Table 6.15: Used dynamic parameterisation and estimated parameters for the frequency bias mismodelling case.

Parameterisation for frequency bias mismodelling case	
All scenarios	
Arc length	7 days
Initial state parameters	estimated
Atmospheric drag parameters	one global scaling parameter per arc
SRP parameters	one global scaling parameter per arc
Biases	one frequency bias per station per pass

Orbital fit The introduced frequency biases of the beacons and their estimation do not result in any significant differences in the orbital fits (minimum, maximum, RMS, mean, standard deviation) in any of the scenarios when compared to the case without systematic error. The global distribution of the residuals (see Fig. 6.26) demonstrates that, with the exception of the GRASP-like scenario, there is a minor difference in the residuals across all scenarios. Additionally, there is no discernible geographical distribution, with the residuals exhibiting only noise. In the case of the GRASP-like scenario, more pronounced differences in the residuals are observable in the equatorial region, exhibiting a slight North-South pattern with a variation over the longitude. Furthermoe, stronger differences are evident at the observation gaps in the Southwest and Northeast, situated at the edges of the gap.

Orbit recovery The orbit comparison demonstrates that the greatest impact on orbit accuracy is observed for satellites orbiting at higher altitudes. This is particularly evident in the cross-track and along-track directions, which demonstrate a more pronounced increase in the RMS of the orbit comparison. In the circular scenario with an inclination of 30 degrees in the along-track direction, the effect is slightly stronger. The eccentric E-GRASP-like and E-GRASP-mod scenarios show a lower increase in the RMS, which is particularly noteable in the along-track direction. The lower orbiting GRASP-like scenario demonstrates the most fabourable outcomes. This scenario exhibits a relatively minor increase in the RMS values, predominantly in the along-track direction. A bias was not found for any of the scenarios (see Fig. 6.27).

The geographical orbit comparisons presented in Fig. 6.28 illustrate a minor North-South variation in the radial component, particularly evident in the eccentric orbit scenarios E-GRASP-mod and E-GRASP-like. No significant variations are discernible for the GRASP-like and circular scenarios, with geographical variations confined to a range below 1/10 of a millimetre. In the cross-track direction, the largest influence is observed, with systematic North-South structures evident in the higher-orbiting circular scenarios and the E-GRASP-mod scenario. In the case of the circular scenarios, this distribution is most pronounced and increases with increasing inclination, reaching a maximum of approximately 5 mm. In comparison, the E-GRASP-like scenario exhibits less pronounced variations, which are expressed by North-South stripes of approximately one millimetre. The variations observed in the GRASP-like scenario reflect a similar geographic distribution as the residuals, but are approximately one order of magnitude smaller and therefore not statistically significant. In the along-track direction, the structures demonstrate a correlated pattern with the radial component, whereby the circular scenarios predominantly reflect the increased RMS of the orbit comparison. The eccentric E-GRASP-like and E-GRASP-mod scenarios exhibit a

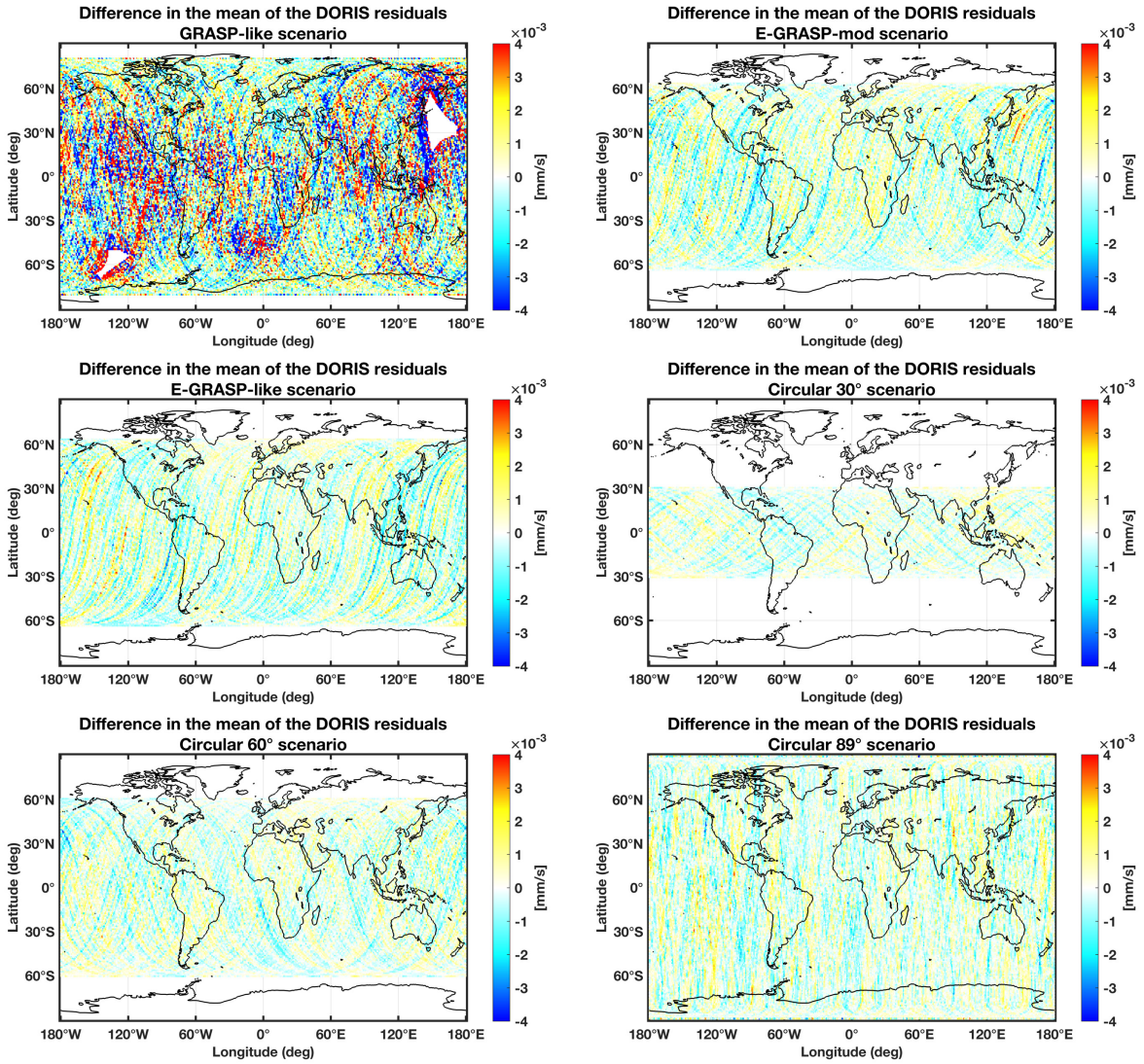

Figure 6.26: Global distribution of the difference in the mean of the observation residuals for the frequency bias case compared to systematic error-free.

North-South stripe structure with an amplitude of approximately 1 millimetre. In this case, an additional estimation of once-per-revolution parameters could be helpful. In contrast, the GRASP-like scenario shows no noticeable geographic distribution. A lower flight altitude seems advantageous to reduce the influence on the geographic orbit differences, while estimating ground beacon frequency offsets.

Reference frame

Helmert parameters Mismodelling and estimation of the frequency bias demonstrates only minor impact on the determined TRF across all scenarios. The Helmert parameters are below 0.15 mm for translation, rotation and scale. The effect on velocities is not significant (see Tab. F.17).

Formal errors The formal errors of the station coordinates demonstrate an LIP, particularly for the low-orbiting GRASP-like scenario (see Fig. 6.29 and Tab. F.18 in App. F.1).

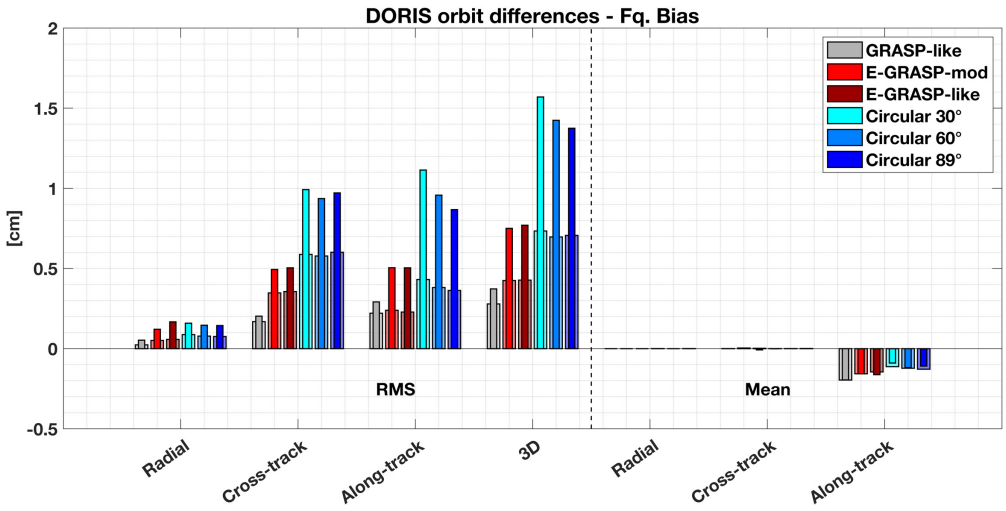

Figure 6.27: Mean RMS and mean values of the orbit comparison of the simulated and recovered orbit for the frequency bias mismodelled case. The thinner bars show the results of the frequency bias mismodelling scenarios, the slightly more transparent thicker bars in the background show the values achieved in the systematic error-free case.

The degradations observed in this case are approximately 20% in the X and Y directions and 5% in the Z direction. In geographic coordinates, the observed LIP is primarily in the West-East component. In contrast, the picture is different for all other scenarios. These show only very minor deterioration in the Z coordinates, and in some cases even improvements of up to around 25% in the X and Y coordinates, especially for the circular scenario with 30 and 60 degree inclination. In geographic coordinates, the deterioration is found in the West-East component. With regard to the velocities, the low-orbiting GRASP-like scenario is once again the most significantly affected, with an LIP of approximately 8% in the X and Y directions, and 23% in the Z direction. The remaining scenarios exhibit comparable levels of LIP in the X component and negligible changes in the Y component. In the Z direction, the two eccentric E-GRASP-like and E-GRASP-mod scenarios, as well as the circular scenario with 89 degree inclination, demonstrate an LIP between 5 and 10%. The circular scenario with 60 degree inclination exhibits lower LIP, while the scenario with 30 degree inclination demonstrates even an improvement of 9%. The geographic coordinates indicate that the aforementioned losses are almost exclusively confined to the West-East component, for the GRASP-like scenario also to the Nort-South and height component.

It was found that the improvements improvements in the formal errors of the station coordinates were found to have been caused by the noise generator. The generator creates a sequence of white noise for the entire 7-day observation period, which is then applied to the observations. The zero-mean condition of the generator (see App. B) tests the entire time series for the mean value, which should be close to zero. However, when the noise sequence is split into sections for individual observation passes, some sections are found to have mean values that differ from zero. When the frequency bias is now estimated per pass, this deviation from zero is accounted for in the estimated bias. Consequently, a positive effect is noted, as the formal error is reduced.

In the ERPs, the pole coordinates are clearly more affected. The GRASP-like scenario demonstrates LIP of approximately 55% for both the X- and Y-pole, closely followed by the eccentric E-GRASP-mod and E-GRASP-like scenarios with 45-50%. In the circular scenarios, the X-pole is in general more affected than the Y-pole, and the low inclination

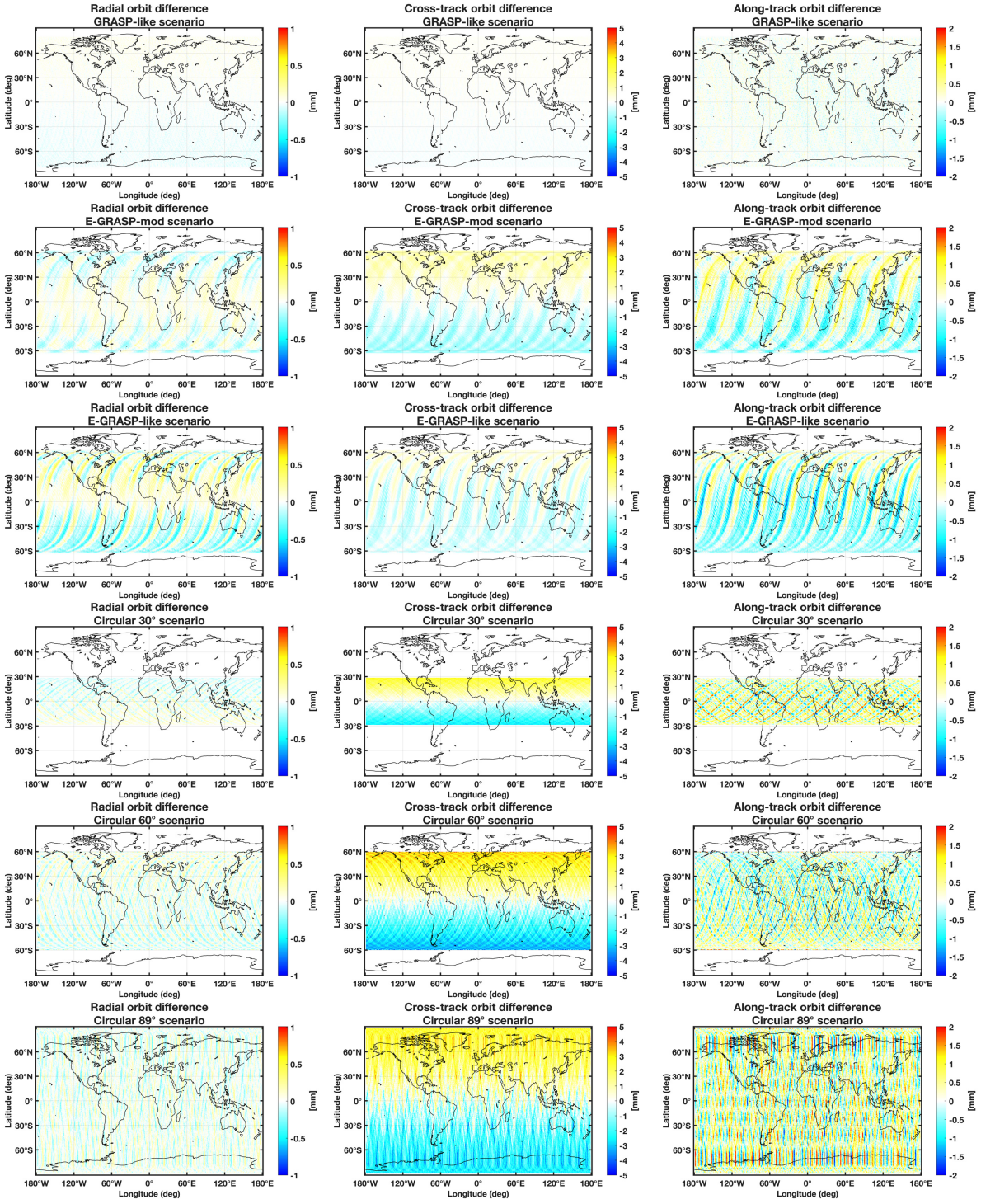

Figure 6.28: Mean orbit differences of the true simulated and recovered orbit over the full simulation time span of 7 years for the frequency bias mismodelling case. From left to right in radial, cross-track, and along-track direction. From the top to the bootom, GRASP-like, E-GRASP-mod, E-GRASP-like, Circular 30°, Circular 60°, Circular 89°

scenario of 30 degrees shows even higher losses at the X-pole than the GRASP-like scenario with about 60%. The remaining two circular scenarios (circular 60° and 89°) perform best, exhibiting comparable results with LIP between 30 and 40% in both pole coordinates. With regard to LOD, it is solely the GRASP-like scenario that exhibits an LIP of approximately 10%. All other scenarios are less affected, with an LIP in the low single-digit percentage range.

ERP analysis The estimated ERPs indicate a notable increase in the standard deviation of the pole coordinates, specifically in the GRASP-like scenario, where the value rises by approximately 16-20%. In contrast, the E-GRASP-mod and E-GRASP-like scenarios exhibit a relatively lower increase in the standard deviation of 6-7%. In LOD, a notable increase in noise is observed for the GRASP-like and the circular scenario with an 89° inclination, with values of 4% and 6%, respectively. No significant offset or trend in the pole coordinates with respect to the a priori can be identified, considering the limits of 1/10 mm for pole coordinates and 1/10 micrometre for LOD (see table F.19).

Spectral analysis of the ERPs reveals minimal influence on the pole coordinates and no significant effect on LOD. In all cases, variations in the pole coordinates are below 0.1 mm. The largest variations occur in the GRASP-like scenario, in the X-pole with a period of 110–120 days and in the Y-pole with quarterly periodicity, as well as in the E-GRASP-like scenario in the Y-pole with annual oscillation. The other scenarios remain largely unaffected.

Conclusion - Ground beacon frequency bias mismodelling The results of the frequency bias mismodelling indicate that primarily higher orbiting satellites are affected in terms of orbit accuracy. These satellites demonstrate considerable increases in orbit differences in both the cross-track and along-track directions. Systematic geographical orbit differences primarily occur in the cross-track direction, manifesting as a North-South division. In this case, continuously higher orbiting scenarios, such as the circular scenarios, are most affected, with this effect being intensified with increasing inclination. Conversely, systematic differences in the radial and along-track directions are significantly weaker and only noticeable in the eccentric scenarios.

In terms of the TRF, no evidence of a systematic effect could be identified. With respect to the LIP in the formal errors, only the GRASP-like scenario demonstrates a discernible impact on station positions and velocities. For the higher orbiting and also the investigated eccentric scenarios, this is less pronounced. In these scenarios, no clear deterioration can be observed, in fact, some components even exhibit improvements. The formal errors of the pole coordinates are the most affected, but also here a higher orbiting circular scenario with a medium to high inclination (here 60 and 89 degrees) is preferable. The analysis of the a posteriori ERPs demonstrates the greatest increase in noise in the pole coordinates, with a significantly greater impact observed in the GRASP-like scenario. However, discernible systematic effects in the ERPs could not be identified. The spectral analysis of the ERPs indicates the least influence for the E-GRASP-mod and the circular scenarios.

The results, which are summarised in Tab. 6.16, demonstrate, that the E-GRASP-mod, E-GRASP-like, and the circular higher orbiting scenarios are particularly advantageous. Although there is a notable reduction in orbit accuracy in the cross-track direction, the frequency bias mismodelling leads to the least degradation and influence on the TRF and the ERPs. Based on the spectral analysis, the scenario with 60 degree inclination would be marginally preferable in the case of the circular scenarios.

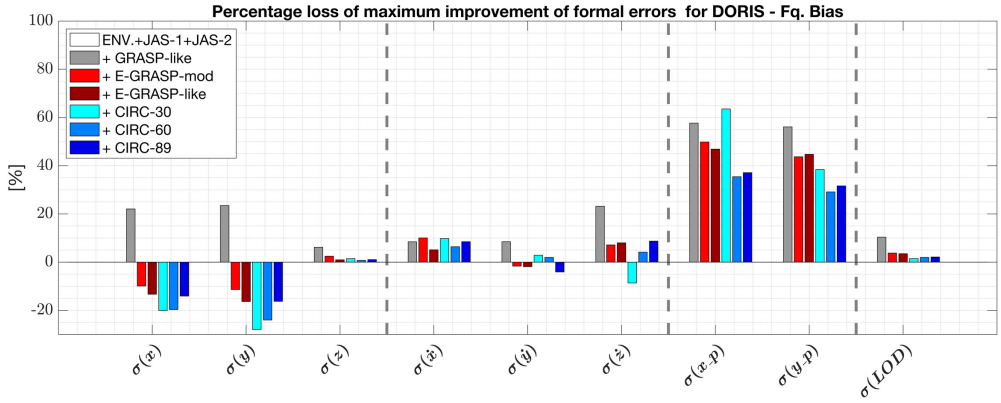

(a) Coordinates in X,Y, and Z

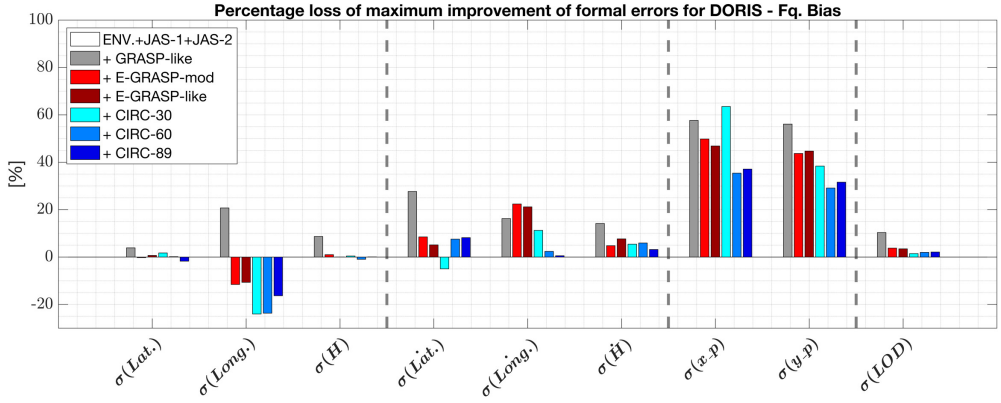

(b) Same as in Fig. a) but for geographic coordinates in Latitude, Longitude, Height.

Figure 6.29: Percentage loss of maximum improvement potential due to frequency bias mismodelling compared to the systematically error-free case. +10% means that the systematic error-free scenario achieved a 10% higher improvement. Figure a) shows the values for X,Y and Z, Figure b) the values for Latitude, Longitude, Height.

Table 6.16: Vulnerability of the satellite scenarios for DORIS for systematic frequency bias mismodelling.

	G-like	E-G-mod	E-G-like	Circ. 30°	Circ. 60°	Circ. 89°
Orbit	①	②	②	③	③	③
Helmert	①	①	①	①	①	①
Station pos. form. err.	②	①	①	①	①	①
Station veloc. form. err.	②	①	①	①	①	①
Pole coord. form. err.	③	②	②	③	②	②
LOD form. err.	②	①	①	①	①	①
ERPs est.	③	①	②	①	①	②
Summary	2.0	1.3	1.4	1.6	1.4	1.6

6.1.2.6 Influence of Earth gravity field mismodelling

To investigate the influence of Earth gravity field mismodelling, the static part of the EGM used for the simulation, the EIGEN-6C, is replaced by that of the GGM05S model. In both cases the gravity field is set up to degree and order 60.

Fig. 6.30 illustrates the absolute difference in the accelerations of the perturbation forces for each scenario.

In all cases, the largest discrepancies are observed in the radial direction, with the GRASP-like and E-GRASP-like scenarios exhibiting the most pronounced influence. Moreover, the GRASP-like scenario also shows smaller differences in the transversal and normal directions, in addition to the continuously increasing difference in the radial acceleration. The E-GRASP-like scenario demonstrates a more exponential increase in the radial acceleration difference, which accumulates rapidly over the seven-day period. In comparison, the E-GRASP-mod scenario is considerably less affected due to the higher perigee. The higher orbiting circular scenarios are the least affected, exhibiting only a slight difference in radial direction for each scenario after seven days, which is less than 10 $\mu m/s^2$. In order to account for the induced orbital disturbance, the parameterisation presented in Tab. 6.17 is employed for all scenarios. In accordance with the law of conservation of energy, empirical coefficients are used in the transversal direction, given their correlation with the radial component.

Table 6.17: Used dynamic parameterisation and estimated parameters for the EGM mismodelling case.

EGM mismodelling parameterisation	
All scenarios	
Arc length	7 days
Initial state parameters	Estimated
Atmospheric drag parameters	One global scaling parameter per arc
SRP parameters	One global scaling parameter per arc
Empirical accelerations	Piecewise linear continuous in transversal direction every 12h, cosine/sine every 12 h in transversal and normal direction

Orbital fit The introduction of EGM mismodelling does not result in a discernible discrepancy in the orbital fits (minimum, maximum, RMS, mean, standard deviation) in any of the scenarios when compared to the case without systematic error. The global distribution of residuals (see Fig. 6.31) shows by far the most significant influence in the GRASP-like scenario. Changes in the mean residuals of up to 3 micrometres per second can be seen. A correlation with the global observation distribution (see Sec. 6.1.2.1) could not be identified. The influence on the residuals of the E-GRASP-like and E-GRASP-mod scenarios is significantly reduced, with the exception of the E-GRASP-like scenario, where it is somewhat more pronounced. A minor West-East distribution is discernible for this scenario, with the residuals exhibiting a variation of less than 1 micrometre per second. The influence on the higher orbiting circular scenarios is almost undetectable.

Orbit recovery The orbit comparison shows a strong increase of the RMS of the orbit differences across all directions and scenarios (see Fig. 6.32). In the radial direction, all

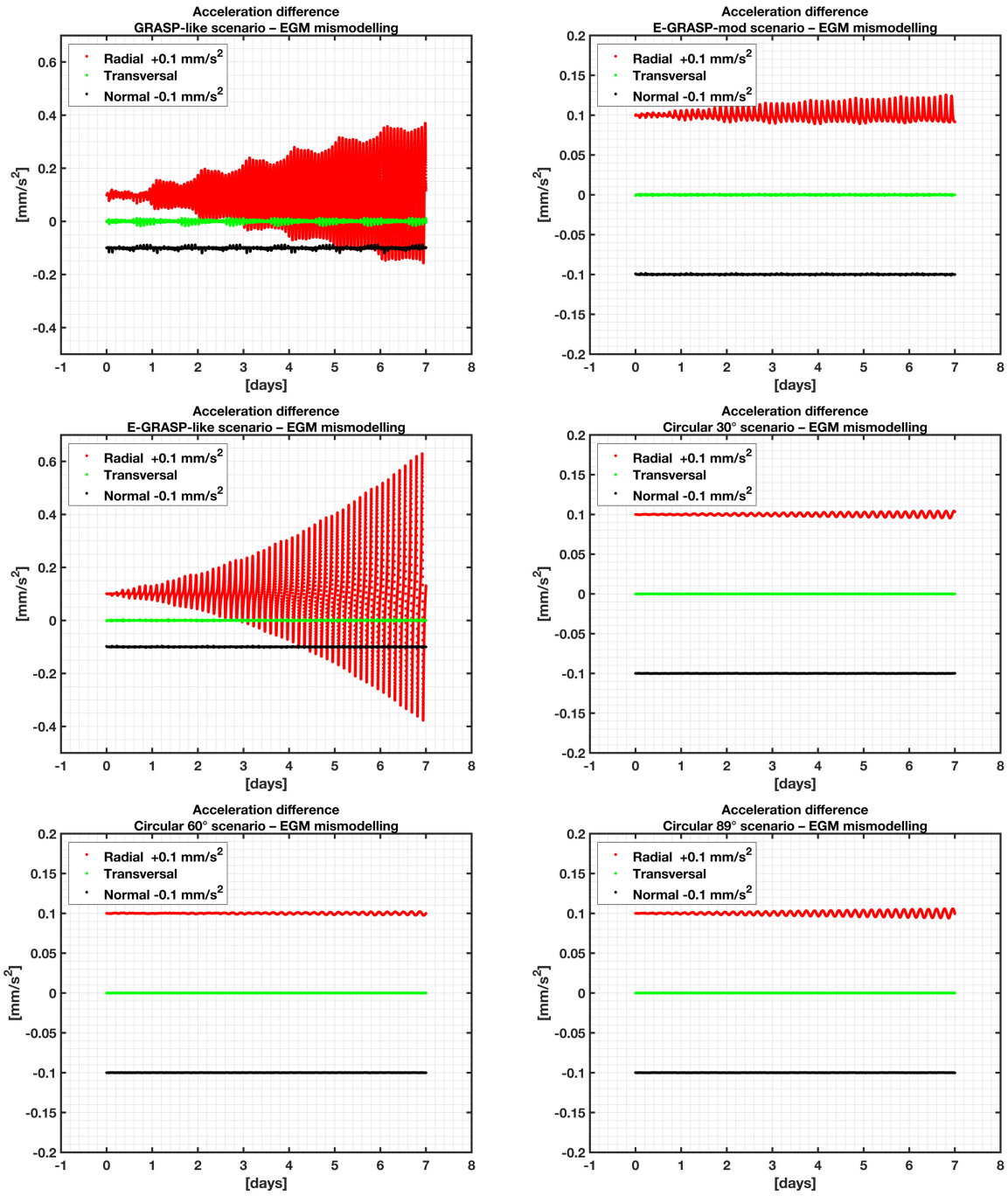

Figure 6.30: Difference in the sum of the accelerations acting on the satellite over a period of 7 days, when the EGM is mismodelled.

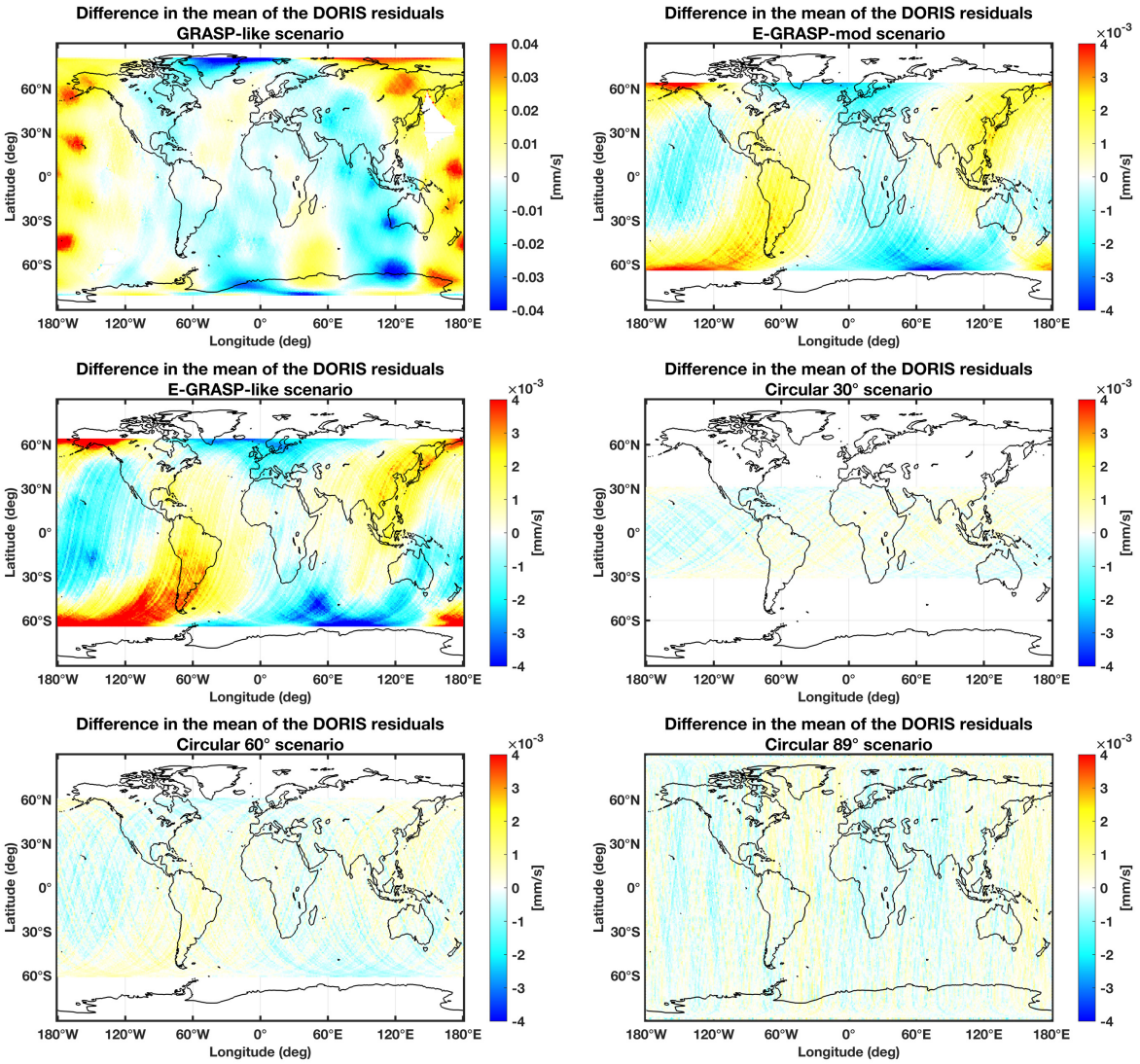

Figure 6.31: Global distribution of the difference in the mean of the observation residuals in the EGM mismodelling case compared to systematic error-free. The colour bar of the GRASP-like scenario is scaled 10 times higher.

scenarios demonstrate a comparable increase in the RMS values, reaching a similar level of approximately 0.4 cm. In comparison to the other components, the radial component is still by far the one that is best determined. In the cross-track and along-track direction, a similar deterioration is noted for all scenarios, with the RMS increasing by a factor of approximately four. In comparison to the values of the systematic error-free case, the three-dimensional increase is greatest in the GRASP-like scenario and least in the higher orbiting circular scenarios. Minor offsets are evident in the GRASP-like, E-GRASP-mod and E-GRASP-like scenarios, reaching up to 1 mm in the cross-track direction, and exclusively in the transversal direction for the GRASP-like scenario. Conversely, the circular scenarios demonstrate no significant biases.

The geographical distribution of the orbit differences (see Fig. 6.33) shows a significantly stronger influence for the GRASP-like scenario, and to a lesser extent for the E-GRASP-like and E-GRASP-mod scenarios. The higher orbiting circular scenarios exhibit significantly less pronounced differences. In the radial direction, the EGM mismodelling results in a West-East pattern, with a magnitude of approximately 4-5 mm for the GRASP-like scenario

and approximately 2 mm for the E-GRASP-like and E-GRASP-mod scenarios. The pattern is reversed for the GRASP-like scenario, which can be explained by the prograde and retrograde inclinations of the scenarios. Schreiner et al. (2023) identified similar structures in DORIS real data-based POD for Sentinel satellites when compared to reduced dynamic GPS orbits. Moreover, the estimation of low-degree harmonic coefficients proved to be beneficial in this context as demonstrated in Schreiner et al. (2024b). In contrast, the circular scenarios exhibit a comparable structure in the radial direction, albeit at a level that is significantly lower. A comparable West-East pattern of differences can be observed in the cross-track direction, although this is limited to the GRASP-like scenario. The pattern is anticorrelated with that of the radial component and is of a similar amplitude. The remaining scenarios demonstrate considerably smaller differences and no discernible geographical patterns. A clear correlation can be observed between the differences in the mean of the observation residuals and the differences in the orbit in the along-track direction. In this case, the GRASP-like scenario is the most significantly impacted, with differences reaching 10 mm and more. The E-GRASP-like scenario is slightly less affected, with larger differences in a West-East structure that follow the inclination of ascending arcs and are anti-correlated with the radial difference, reaching a maximum amplitude of approximately 10 mm. The E-GRASP-mod scenario presents a comparable pattern, albeit with diminished amplitudes reaching 4 mm. In contrast to the impact on the residuals, the two eccentric scenarios exhibit a considerably more pronounced influence on the orbit than could be anticipated based on their influence on the residuals. The West-East structure is also discernible in the circular scenarios, albeit to a markedly lesser degree.

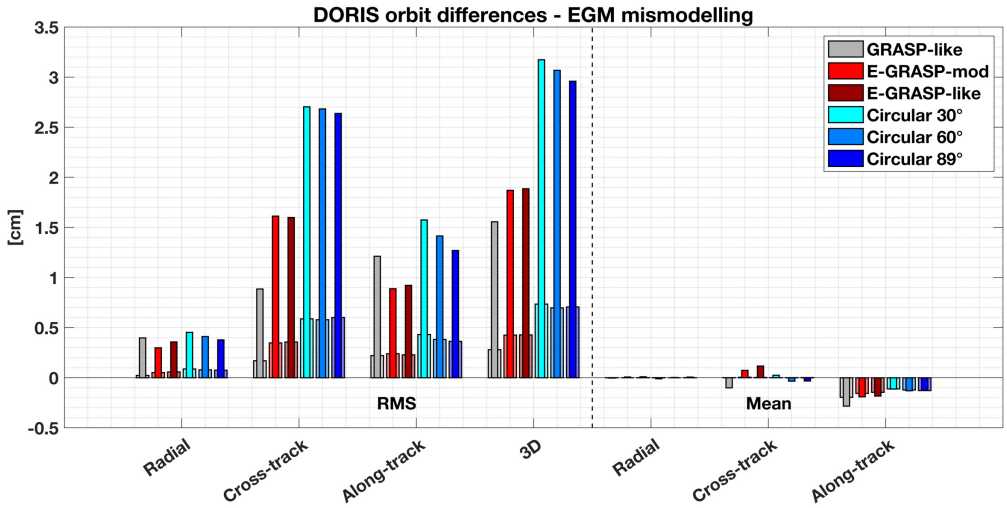

Figure 6.32: Mean RMS and mean values of the orbit comparison of the simulated and recovered orbit for the EGM mismodelling case. The thinner bars show the results of the EGM mismodelling case, the slightly more transparent thicker bars in the background show the values achieved in the systematic error-free case.

Reference frame

Helmert parameters The mismodelling of the EGM exerts the greatest influence on the derived TRF of all mismodelling cases, particularly in the case of the low-orbiting GRASP-like scenario. The Helmert parameters (see Fig. 6.34) demonstrate notable translations

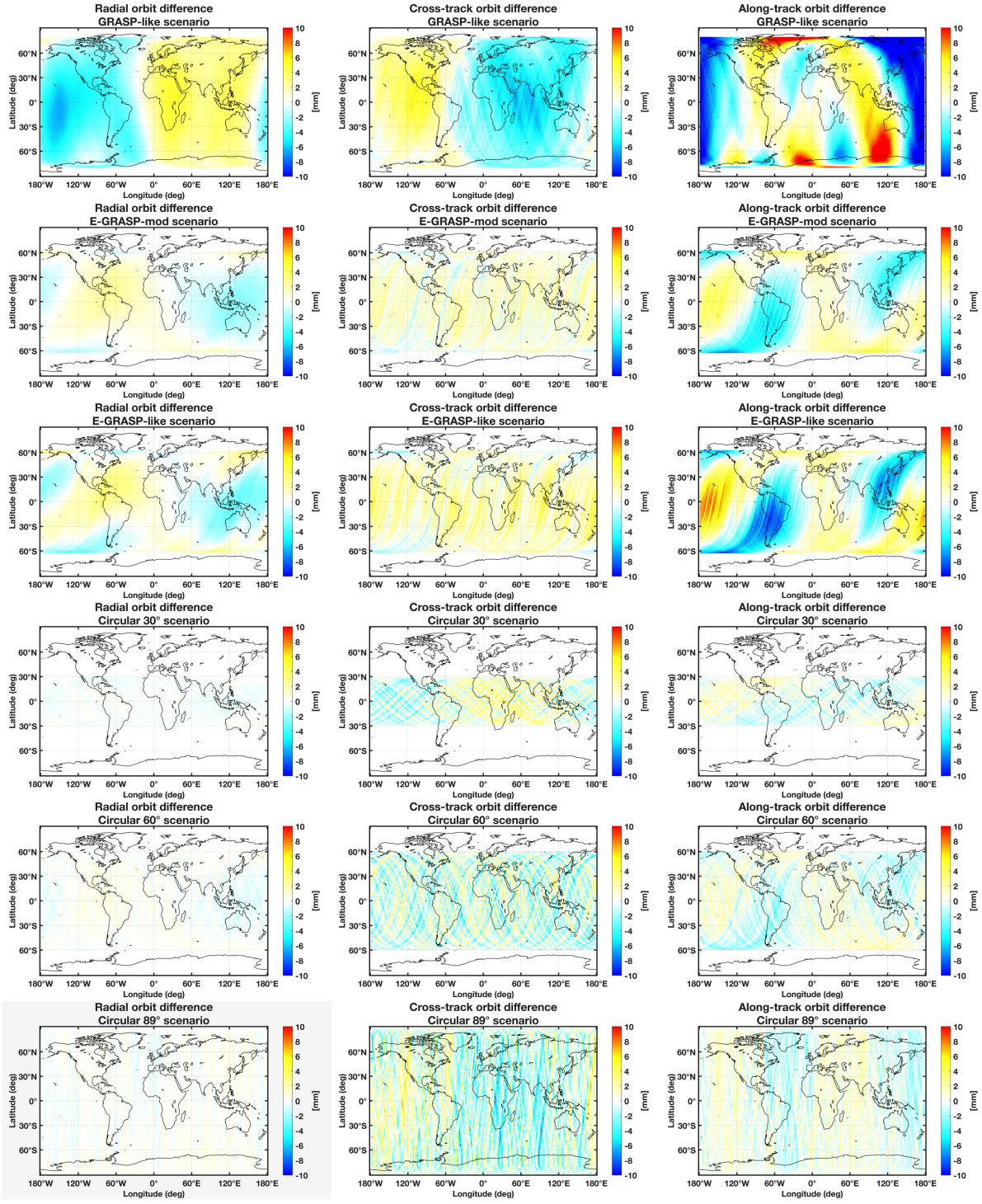

Figure 6.33: Mean orbit differences of the systematic error-free scenario and the recovered orbit for the EGM mismodelling scenario over the full simulation time span of 7 years. From left to right in radial, cross-track, and along-track direction. From the top to the bootom, GRASP-like, E-GRASP-mod, E-GRASP-like, Circular 30°, Circular 60°, Circular 89°.

and rotations, reaching up to 2.1 mm and 0.2 mm/a, particularly in the Y and Z axes. In comparison, the impact on the E-GRASP-mod and E-GRASP-like scenarios is considerably smaller. Both scenarios demonstrate translations and rotations in the Y and Z axes of up to 0.3 mm and 0.03 mm/year, respectively. Nevertheless, both are well below the targets set by GGOS. Furthermore, the scale demonstrates no considerable change in any of the scenarios (compare Tab. F.20).

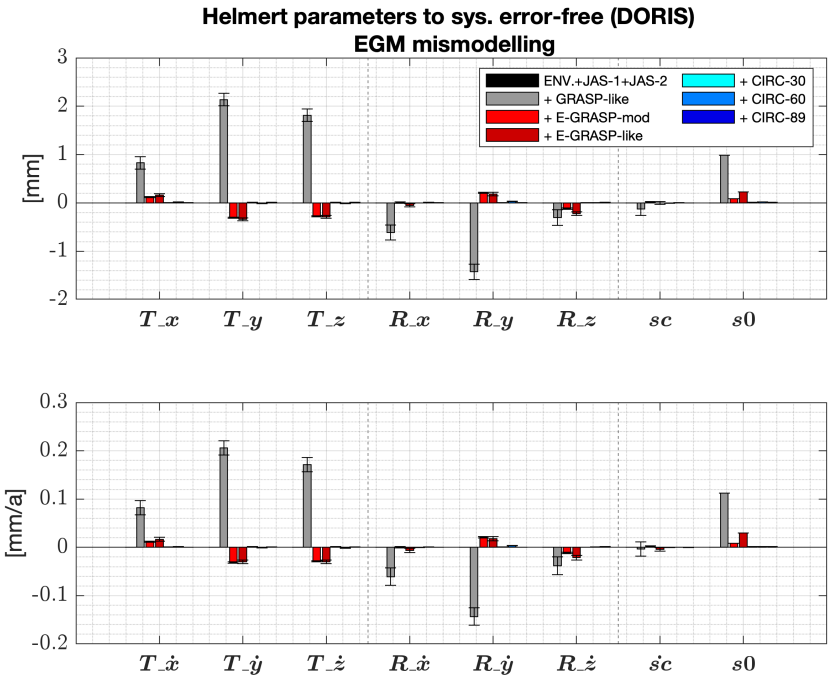

Figure 6.34: The upper figure shows the Helmert parameters of all stations for the EGM mismodelling case compared to systematic error-free. The lower figure shows the values for the velocities.

Formal errors The most significant LIP is evident in the station coordinates and velocities for the GRASP-like scenario, with a continuous LIP of approximately 30% in the X, Y, and Z components (see Fig. 6.35 and Tab. F.21 in App. F.1). In geographic coordinates, it is evident that these degradations are most pronounced in the North-South direction at around 55%, and less in the West-East and height components at around 35%. Regarding velocities, the components are affected similarly in Cartesian coordinates, in geographic coordinates the North-South component is less affected and shows a degradation equal to that of the other components. The remaining scenarios have an insignificant impact on the formal errors associated with positions and velocities, with observed changes occurring within the very low single-digit percentage range. In the ERPs, the GRASP-like and E-GRASP-like scenarios exhibit the most pronounced LIP, reaching approximately 50-55% for the pole coordinates. The E-GRASP-mod and the circular scenario with an inclination of 30 degrees are less affected, with an LIP in the range of 30-40%. The remaining two circular scenarios, with inclinations of 60 and 89 degrees, exhibit the least impact, with LIP of approximately 20%. With regard to LOD, the GRASP-like scenario is the only one

demonstrating a significant LIP of 29%. All other scenarios demonstrate only minimal deterioration in LOD, with LIP below 4%.

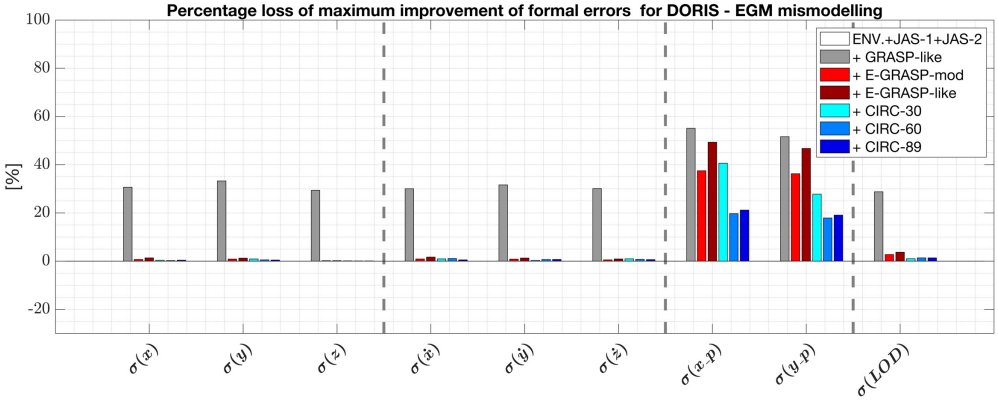

(a) Percentage loss of maximum improvement potential due to EGM mismodelling. Coordinates in X,Y, and Z

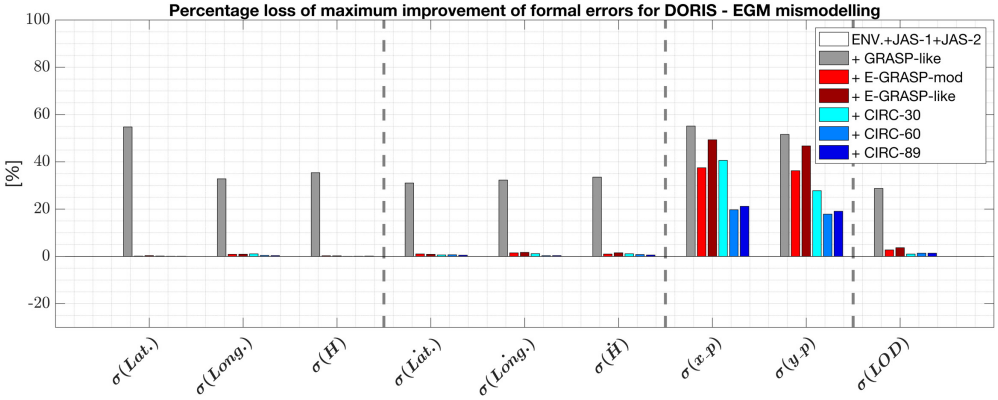

(b) Same as in Fig. a) but for coordinates in Latitude, Longitude, Height.

Figure 6.35: Differences of the percentage improvements compared to the systematically error-free case. +10% means that 10% of the maximum potential of improvement are lost in comparison to the systematic error-free scenario. Figure a) shows the values for X,Y and Z, Figure b) the values for Latitude, Longitude, Height.

ERP analysis In the context of the determined ERPs, a notable impact on the low-orbiting GRASP-like scenario can be observed, whereby a considerable rise in the standard deviation of the determined ERPs is evident, reaching up to 70% in the pole coordinates and 122% in LOD. To a lesser extent, this can also be observed in the E-GRASP-mod and E-GRASP-like scenarios, with increases in the range of 6 to 14% in the ERPs. In the circular scenarios, no significant increase in the standard deviation of the ERPs is evident. However, in the circular scenario with an inclination of 30 degrees, an increase in LOD of approximately 15% is observed.

The GRASP-like scenario exhibits the greatest observed biases in the ERPs, with values of approximately -0.6 mm in the X-pole, -2.2 mm in the Y-pole and 0.35 μm in LOD. In all other scenarios, the observed offsets are significantly smaller. If they are significant, they are on the order of up to 0.1 mm for the pole coordinates and 0.05 μm for LOD, respectively.

A significant trend can only be observed for the GRASP-like scenario in LOD. However, the drift is exceedingly small and negligible when considered in the context of the GGOS goals.

Spectral analysis of the a posteriori ERPs reveals that, for all scenarios, variations in LOD are insignificant, with variations in the micrometre range. Significant influences can be found in the pole coordinates for the GRASP-like, E-GRASP-mod and E-GRASP-like scenarios. The GRASP-like scenario exhibits the strongest influence, with signals occurring in the X- and Y-pole. The largest signal has a wavelength of approximately 155 days and an amplitude of up to 0.4 mm. The E-GRASP-mod scenario is less affected, with signals occurring in both pole coordinates, with a period of 98 days and an amplitude of up to 0.25 mm. The E-GRASP-like scenario is the least affected, exhibiting a signal in the X-pole with a quarterly period and an amplitude of approximately 0.16 mm. Overall, the circular scenarios show no significant variation.

Earth gravity field co-estimation The next step involes co-estimating the Earth gravity field to its maximum degree of development, which in this case is degree and order 60. In order to invert the normal equations, only degrees 0 and 1 are fixed to a priori to avoid the necessity for a NNT and NNS condition (where no mismodelling has taken place in these degrees). Furthermore, higher degrees are also fixed to a priori if the normal equation becomes singular. The maximum degree of development is given in Fig. 6.38. The maximum solvable degree is identified through a binary search. Additional information on binary search can be found, for example, in Cormen et al. (2022).

Reference frame

Helmert parameters By co-estimating the gravity field, it is almost completely possible to compensate for all systematic effects in the Helmert parameters. The translations and rotations decrease to values below 1/10 mm for the positions and 1/100 mm/year for the velocities in all scenarios (see Tab. F.20 in App. F.1).

Formal errors The formal errors clearly demonstrate a benefit from the co-estimation in the GRASP-like scenario. In this case, the LIP in the station positions can be reduced to values in the low single digits (see Fig. 6.36 and Tab. F.22 in App. F.1). However, this improvement is not reflected in the velocities. In fact, with the exception of the GRASP-like scenario, there is a deterioration that leads to an increase in the formal errors of the station velocities. One potential explanation for this could be too many estimated gravity field coefficients. In the ERPs, only the GRASP-like scenario demonstrates a significant improvement in LOD, with LIP dropping from 29% to approximately 9%. The pole coordinates remain unaffected.

ERP analysis The co-estimation of the gravity field allows to significantly reduce the increased standard deviations of the determined ERPs, as well as the larger systematic offsets and trends observed in the GRASP-like scenario. In all scenarios, periods identified in the spectral analysis of the ERP can be removed resulting in minimal changes in the periodogram when compared to the systematic error-free case. Regardless of whether co-estimated or not, the circular scenarios demonstrate no changes to the periodogram of the ERPs, while EGM is mismodelled.

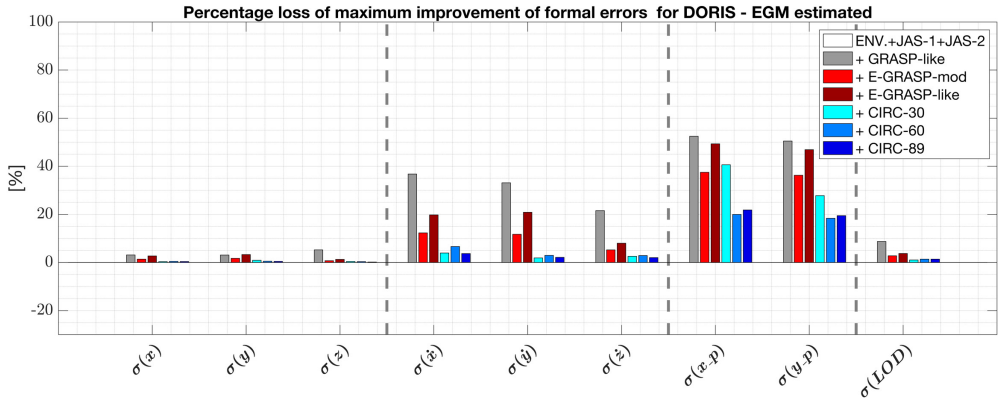

(a) Percentage loss of maximum improvement potential due to EGM mismodelling, whereby the EGM is co-estimated. Coordinates in X,Y, and Z

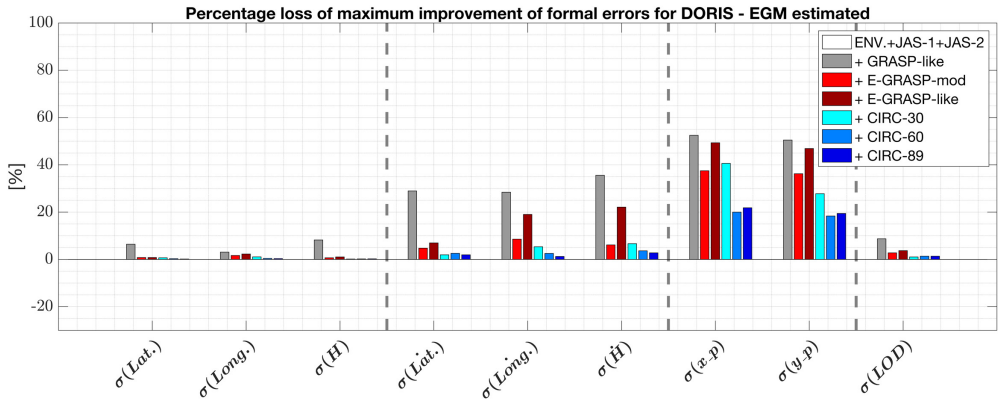

(b) Same as in Fig. a) but for coordinates in Latitude, Longitude, Height.

Figure 6.36: Differences of the percentage improvements compared to the systematically error-free case. +10% means that 10% of the maximum potential of improvement are lost in comparison to the systematic error-free scenario. Figure a) shows the values for X,Y and Z, Figure b) the values for Latitude, Longitude, Height.

Potential for gravity field determination To evaluate the potential of gravity field estimation, the station coordinates, station velocities and ERPs are not estimated in this step. Instead, the full gravity field is estimated using a single satellite from the scenarios at once. Furthermore, the resulting normal equation is not combined with the reference solution. In the context of the simulation and recovery, the maximum degree of development of the EGM is 60. The aforemenetioned mismodelling affects the static component of the gravity field, spanning degrees 2 to 60. The time-variable component of the gravity field, which in this case is represented by linear trends, remains unchanged. Subsequently, the weekly normal equations for each scenario are accumulated solely for that scenario over the entire simulation period. Eventually a single set of static gravity field coefficients is derived for each scenario. These solved for coefficients should ideally match the a priori values of the original static part of the gravity field of the simulation. For the inversion of the normal equations, degrees 0 and 1 are fixed as in the previous case, in which the TRF and the ERPs were also estimated. Furthermore, the SH coefficients in these two degrees are also free of any mismodelling. Subsequently, if necessary, a binary search is performed to identify the maximum degree up to which the normal equation is invertible and not becoming singular. This is not necessary for the GRASP-like and circular scenario with 89 degree inclination,

where all coefficients up to the maximum degree can be solved. For the E-GRASP-mod and the circular scenario with 60 degree inclination, the maximum degree of inversion is 47. For the E-GRASP-like, it is 39, and for the circular scenario with 30 degree inclination, it is 14.

Sensitivity analysis A sensitivity analysis (see Fig. 6.37) was conducted to demonstrate the analytically calculated perturbation of the orbit resulting from a given degree and order of the Earth gravity field spherical expansion. An increase in the perturbation of the orbit indicates a corresponding increase in the sensitivity of the orbit scenario to the specific SH coefficients in question. The GRASP-like scenario is found to exhibit the greatest overall sensitivity. In this scenario, resonance effects are present around orders 13, 26, 39 and 52, as well as high correlations in odd zonal coefficients. The E-GRASP-mod and E-GRASP-like scenarios demonstrate reduced sensitivity, mainly confined to the lower harmonics. Both scenarios demonstrate resonance effects at multiples of order 8, with this being markedly more pronounced in the E-GRASP-like scenario. Neither of the two scenarios exhibits a notable correlation in the zonal coefficients exceeding degree 6. In the circular scenarios, sensitivity is confined to the low SH coefficients below degree 10. The circular 30 and 89 degree scenarios show substantial correlations at odd zonal coefficients and resonances at order 6 and its multiples.

Estimated Earth gravity field analysis The differences of the estimated and simulated values of the SH coefficients are illustrated in Fig. 6.38. The triangular plots demonstrate the discrepancy of each estimated SH coefficient to its a priori value. This allows the evaluation of the extent to which a scenario can be employed to determine specific coefficients in a reasonable manner. The SH degree amplitudes and the cumulative errors given in equivalent water height are illustrated in Fig. 6.39 and 6.40. These figures demonstrate the error of the estimated SH coefficients on the geoid, per degree and as a cumulative error in the spatial scale.

Comparing the scenarios with each other reveals that the GRASP-like scenario exhibits the lowest errors in higher zonal, tesseral, and sectorial coefficients, which can be attributed to its flight altitude. The E-GRASP-mod scenario shows lower differences in the estimated SH coefficients especially in the sectorial coefficients and a rapid increase in the zonal coefficients, even at low coefficients below degree 10. In comparison, the E-GRASP-like scenario demonstrates a higher sensitivity due to its lower perigee and thus also lower differences in higher sectorial coefficients. It is noteworthy that the formal errors in the tesseral coefficients decrease at higher orders. This can be attributed to resonance effects, which are also evident in the sensitivity analysis. The circular scenarios exhibit a rapid increase in errors, which is a little less in the sectorial coefficients. The circular near polar scenario shows a somewhat different pattern, with more uniform differences across orders, increasing steadily with higher degrees.

The degree amplitude plots illustrate the actual error of the static part of the gravity field, which was used for the simulation (i.e. the actual truth), in black, for the estimated coefficients in red and the difference of the two in blue. The intersection of the difference to the simulation shows a SNR of 1, indicating that the SH coefficients with degrees lower than the degree at this point are reasonably determined. As a measure of quality a level of 100 mm equivalent water height is anticipated. This marks an upper limit for modern gravity field missions such as GRACE/GRACE-FO. This point is reached by the GRASP-like scenario at a maximum degree of 10 (compare also in Fig. 6.39 and Fig. 6.40). For the

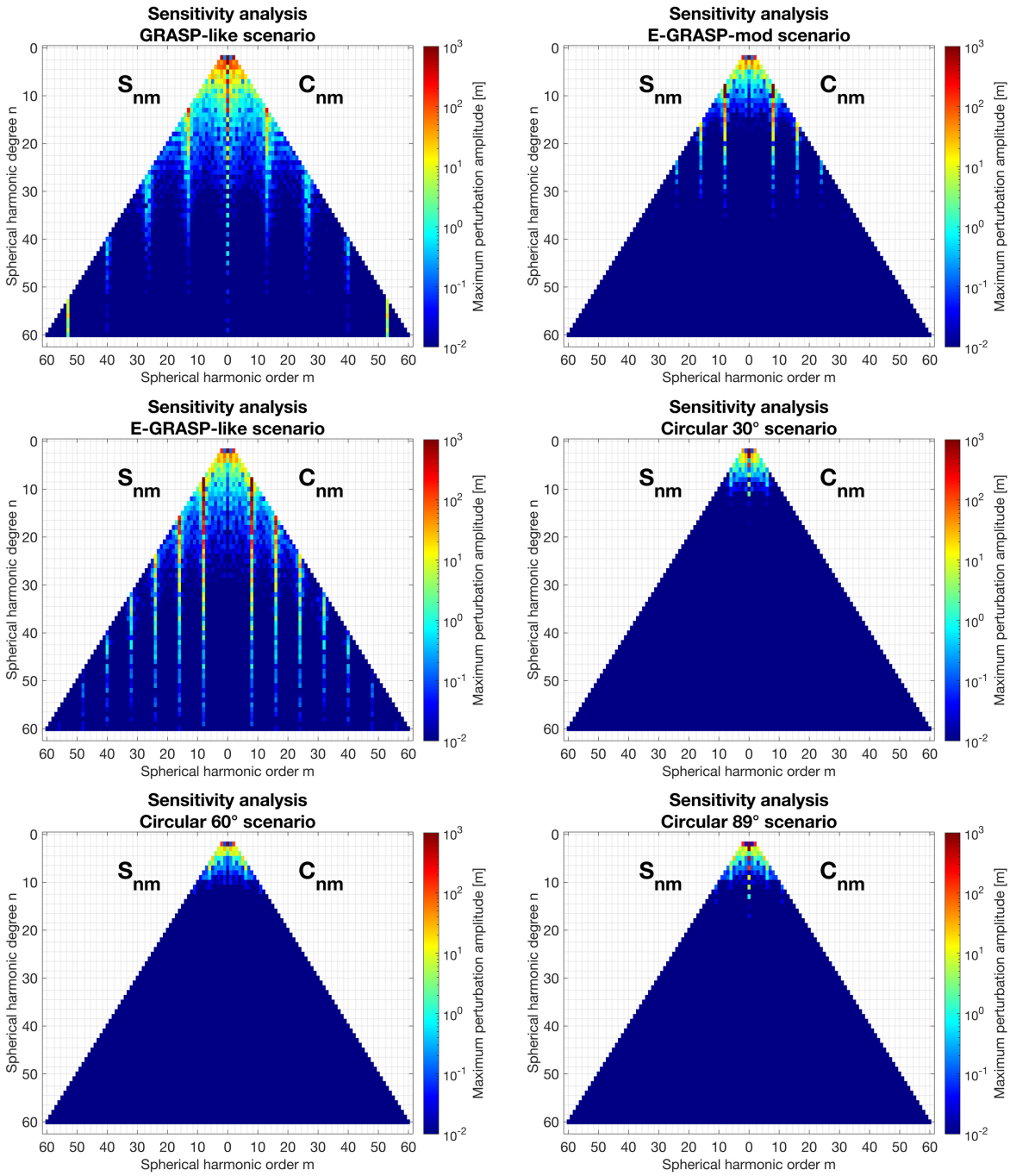

Figure 6.37: Analytical Earth gravity field sensitivity analysis for the scenarios.

other scenarios, the degree is 2-3 for E-GRASP-mod, 5 for E-GRASP-like, 2 for Circular 60 degree, 3-4 for Circular 89 degree and for the circular scenario with 30 degree inclination, the error at degree 2 is already greater than 100 mm. Furthermore, the circular scenario with 30 degrees inclination also exhibits a resonance at odd degrees, recognizable by peaks in the degree amplitudes. The resonance of the E-GRASP-like scenario, which was seen in the sensitivity analysis and triangular plots, is also visible in the degree amplitudes, manifesting as a decrease in the differences above degree 30 approximately.

The potential for determining the gravity field is therefore limited to low harmonic coefficients below degree 10 for all scenarios, with the GRASP-like scenario being the most sensitive. The E-GRASP-like scenario is the second most sensitive, exhibiting resonance effects over degree 30. The E-GRASP-mod scenario is somewhat less sensitive and only shows very limited resonance effects. The higher orbiting circular scenarios are clearly less sensitive, here only the near polar scenario would be suitable for the very low SH coefficients, specifically degrees 2 and 3.

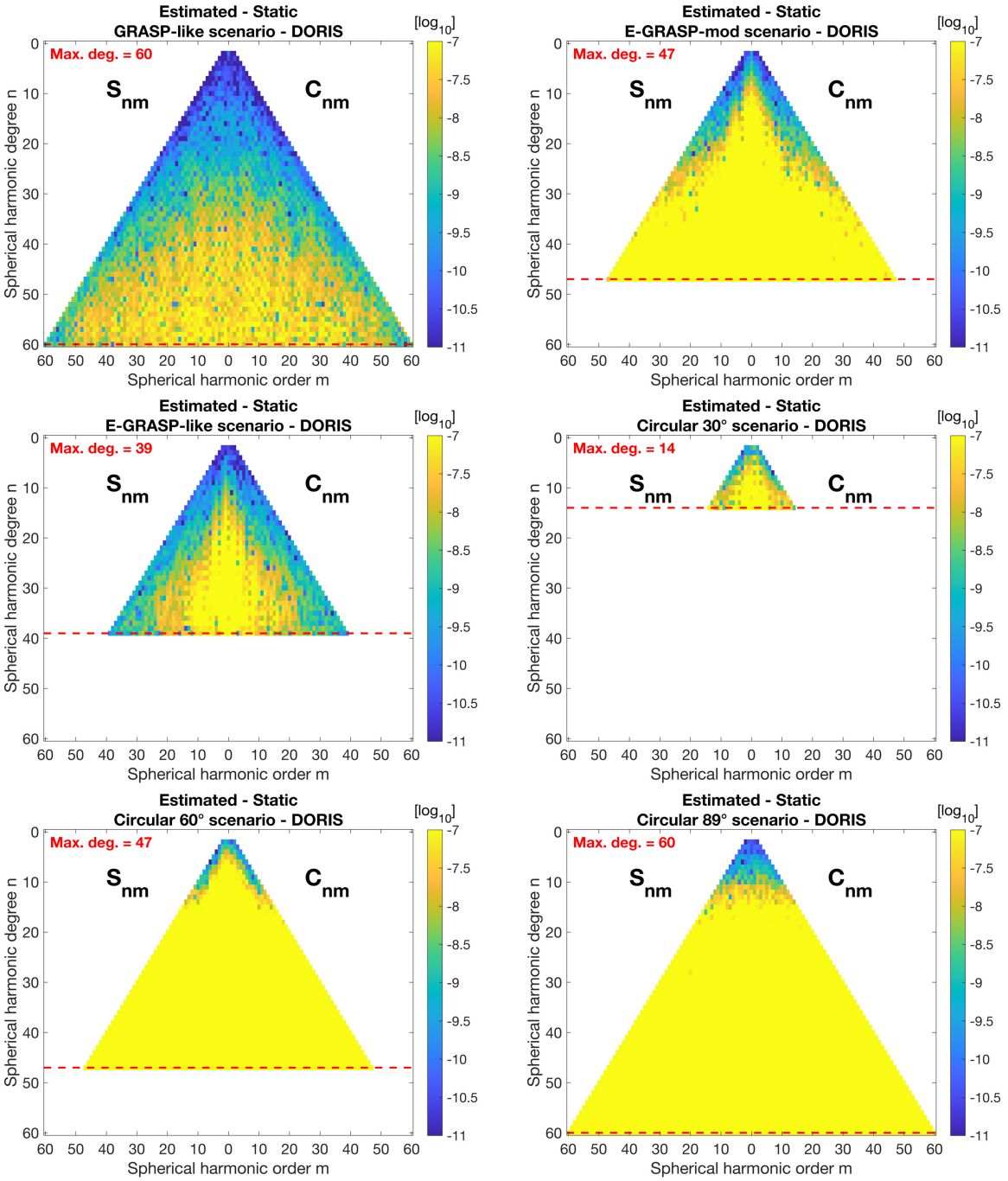

Figure 6.38: Triangular plots showing the difference between estimated and simulated SH coefficient.

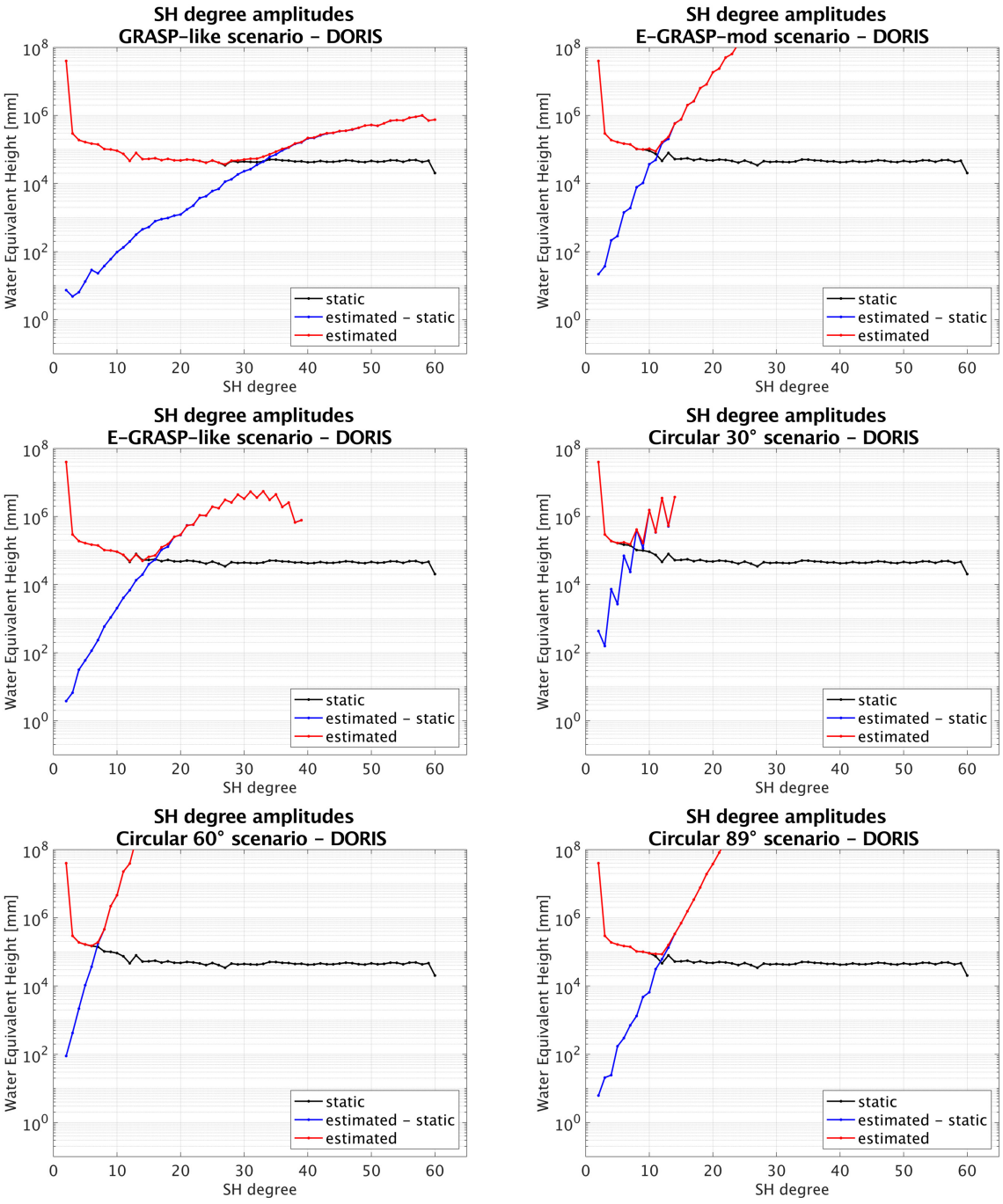

Figure 6.39: SH degree amplitudes in equivalent water height.

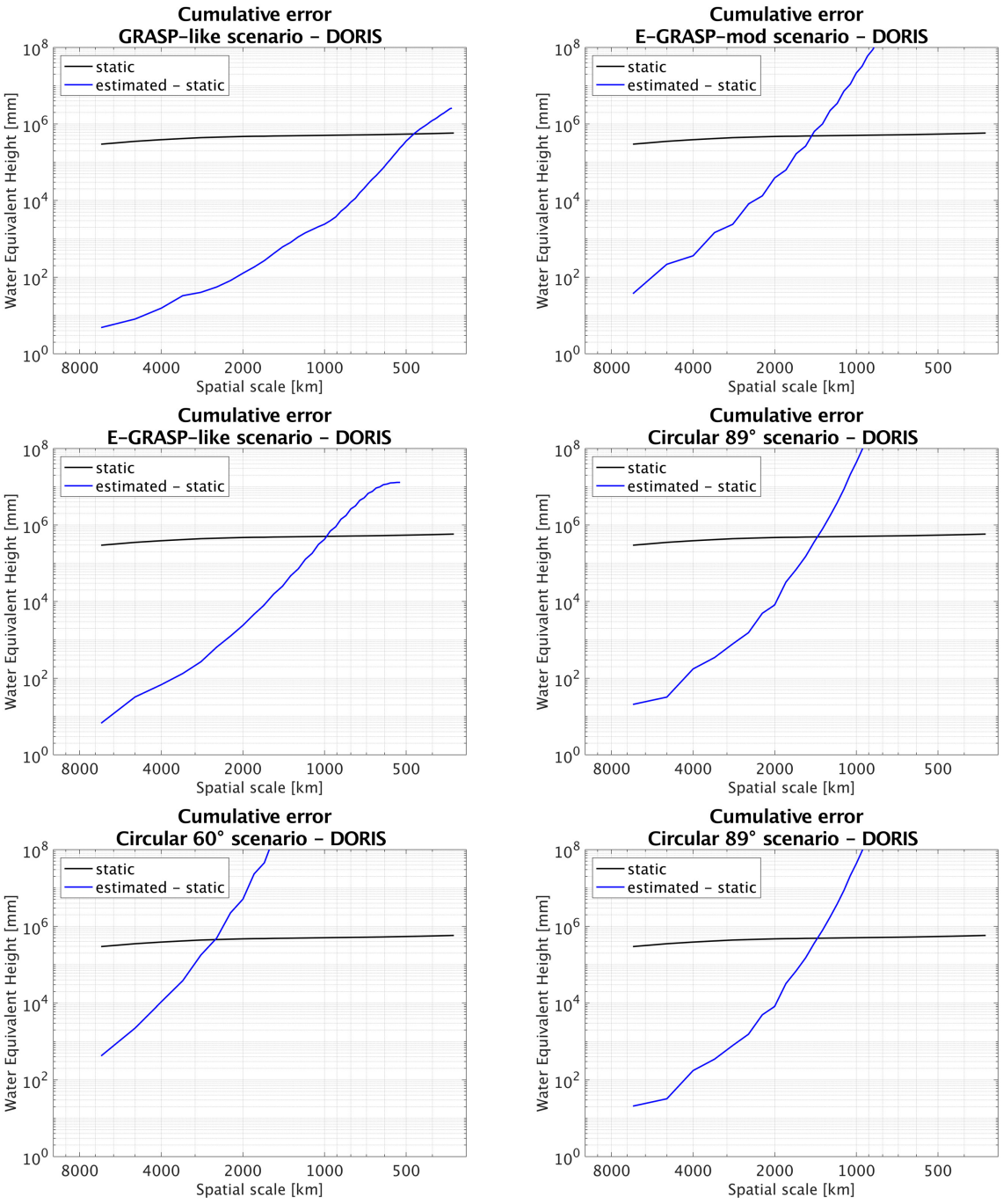

Figure 6.40: Cumulative error in equivalent water height

Conclusion - EGM mismodelling and potential for gravity field determination The assessment of the EGM mismodelling is presented in Tab. 6.18.

It can be observed that there is a notable decline in the orbit accuracy. This is clearly demonstrated in the orbit comparison, which reveals a comparable deterioration in all scenarios in relation to the orbit accuracy that can be attained in the systematic error-free case. In particular, the lower orbiting scenarios, which include the GRASP-like, E-GRASP-mod, and E-GRASP-like, demonstrate a consistent pattern of systematic differences in the orbit, which are predominantly reflected in geographical patterns. In contrast, the higher orbiting circular scenarios exhibit a significantly lower level of systematic influences on the orbit.

Almost exclusively the GRASP-like scenario shows significant LIP in formal errors of station positions and velocities. This is also indicated by the systematic impact on the TRF, which manifests as substantial translations and rotations. In comparison, the other scenarios are significantly less affected, only the E-GRASP-like and E-GRASP-mod scenarios show very minor systematic effects on the TRF.

In the ERPs, the most significant LIP is observed in the GRASP-like scenario, where the loss reaches up to 55% in the pole coordinates and 29% in LOD. The remaining scenarios are affected less and almost exclusively in the pole coordinates. Among the circular scenarios, those with 60 and 89 degree inclination demonstrate the least LIP, which is at the level of about 20% in the pole coordinates.

The estimated ERPs show a significant increase in noise, as well as systematic offsets in the pole coordinates and LOD, especially for the GRASP-like scenario. In comparison, the remaining scenarios are considerably less affected. The spectral analysis of the ERPs demonstrates a clear influence on the pole coordinates, primarily for the GRASP-like scenario, and to a lesser extent for the E-GRASP-mod and E-GRASP-like scenarios. The higher orbiting circular scenarios exhibit no significant influence.

The co-estimation of the gravity field has the potential to remove the systematic effects in the reference frame. However, the LIP of the most affected GRASP-like scenario can only be reduced, primarily for the station positions and LOD. In contrast, for the other scenarios, especially the eccentric ones, the co-estimation leads to an increase of the LIP, especially for the station velocities. The significantly larger noise in the ERPs for the GRASP-like scenario can be effectively reduced by the co-estimation, and systematic offsets can be eliminated. Furthermore, the apparent induced signals shown by the spectral analysis of the ERPs can be eliminated for all scenarios.

Table 6.18: Vulnerability of the satellite scenarios for DORIS for systematic EGM mismodelling and while co-estimating the EGM.

	G-like	E-G-mod	E-G-like	Circ. 30°	Circ. 60°	Circ. 89°
Orbit	③	②	②	①	①	①
EGM not estimated						
Helmert	③	②	②	①	①	①
Station pos. form. err.	③	①	①	①	①	①
Station veloc. form. err.	③	①	①	①	①	①
Pole coord. form. err.	③	②	③	②	①	①
LOD form. err.	③	①	①	①	①	①
ERPs est.	③	①	②	①	①	①
EGM co-estimated						
Helmert	②	②	②	①	①	①
Station pos. form. err.	①	①	①	①	①	①
Station veloc. form. err.	③	②	②	①	①	①
Pole coord. form. err.	③	②	③	②	①	①
LOD form. err.	②	①	①	①	①	①
ERPs est.	②	①	①	①	①	①
Summary	2.6	1.5	1.7	1.2	1.0	1.0

The potential of the Earth gravity field determination is limited for all scenarios to low harmonic coefficients up to a maximum degree 10 for the GRASP-like scenario and for the other scenarios even less (compare Tab. 6.19). However, if the influence of gravity field mismodelling is to be minimised, the higher orbiting circular scenarios, particularly those at 60 and 89 degrees inclination, are the ones most suitable. For the scenario with an inclination of 89 degrees, the errors in the gravity field determination up to degree 3 are also below 100 mm, showing that these coefficients can be estimated well and that the scenarios would be suitable candidates for combination with other missions. Given that co-estimation of the gravity field for TRF determination is not yet a common practice in the IAG services for ITRF determination, it might be a better option to choose a scenario where the systematic influence and the LIP due to Earth gravity field mismodelling are observed to be low.

Table 6.19: Earth gravity sensitivity of the satellite scenarios and the respective potential for gravity field estimation solely with DORIS.

	G-like	E-G-mod	E-G-like	Circ. 30°	Circ. 60°	Circ. 89°
Sensitivity	①	②	①	③	③	③
EGM determination	①	②	②	③	③	②

6.1.3 Single-technique conclusion for DORIS

An additional satellite for TRF and ERPs determination with DORIS can provide a geometric added value based improvement in formal errors, particularly in the case of station coordinate positions. The greatest improvement is observed in the North South and height components, which would also improve the precision of the scale. This is a crucial consideration, given that the scale of the ITRF is currently exclusively realised by SLR and VLBI. With regard to the height component, the eccentric E-GRASP-mod and E-GRASP-like scenarios were found to offer a slight advantage.

Improvements in the ERPs are primarily evident in LOD, while those for the pole coordinates are almost entirely due to additional observations. Only the GRASP-like scenario exhibits a geometric added value improvement across all ERPs, although the maximum improvement is not the largest, as other scenarios can reach a higher number of observations.

Moreover, especially the E-GRASP-mod and the circular scenarios with 60° and 89° have been shown to provide improved stability in station formal errors, particularly for stations in regions where observation coverage is limited.

The mismodelling cases demonstrate that the low-orbiting GRASP-like scenario is particularly susceptible, with an overall vulnerability factor of 2.0 (see Tab. 6.20). The E-GRASP-like scenario is the second most vulnerable due to its sensitivity to atmospheric drag and Earth gravity field modelling, with an overall factor of 1.5. This is less pronounced in the E-GRASP-mod scenario, with a factor of 1.3.

The higher orbiting circular scenarios demonstrate a notable decline in orbit accuracy due to the introduced mismodelling. However, this is not reflected in the losses of potential for TRF and ERPs determination. Consequently, these scenarios exhibit the lowest vulnerability, with values of 1.2 and 1.3, respectively.

In consideration of the potential for gravity field determination, the lower orbiting GRASP-like and E-GRASP-like scenarios are the most sensitive. The E-GRASP-mod exhibits reduced sensitivity, but still remains more affected than the higher orbiting circular scenarios, which demonstrate a markedly limited sensitivity confined to lower degrees. In light of the mission objective of enhancing the TRF and ERPs and establishing a connection with the Earth's gravity field, the E-GRASP-mod and the circular scenario with an 89degree inclination appear to be the best choices. They facilitate a reasonable estimation of low-degree SH coefficients while maintaining a low to moderate impact of EGM mismodelling.

Table 6.20: Maximum potential of the satellite scenarios for TRF and ERP determination in the case of DORIS, together with their vulnerability to mismodelling.

	G-like	E-G-mod	E-G-like	Circ. 30°	Circ. 60°	Circ. 89°
Maximum potential	1.4	1.5	1.7	2.2	1.7	1.7
CoM	1.5	1.4	1.4	1.1	1.1	1.1
Drag	2.3	1.0	1.4	1.0	1.0	1.0
SRP	1.6	1.3	1.4	1.4	1.3	1.3
Fq. bias	2.0	1.3	1.4	1.6	1.4	1.6
EGM mism.	2.6	1.5	1.7	1.2	1.0	1.0
Overall vulnerability	2.0	1.3	1.5	1.3	1.2	1.2

6.2 SLR

For reference frame determination with SLR, the satellites LAGEOS-1 and LAGEOS-2, Etalon-1 and -2, and LARES-2 are used for the operational processing at the GFZ ILRS AC. For the simulation of the SLR reference solution here, the two LAGEOS satellites are taken into account.

The real data evaluation is based on data from the two LAGEOS satellites, which are processed operationally by the GFZ ILRS AC. For the subsequent simulations, these data are reprocessed using consistent models described in Tab. 4.3 in Sec. 4.4.1. Further information on the evaluation of the real data can be found in Sec. 5.2. The two satellites are then simulated using the same procedure as described for DORIS in Sec. 6.1. For each of the two satellites, weekly normal equations are generated, which are accumulated over the entire simulation period and combined to form the reference solution for SLR. This solution is free of systematic errors, and the combined parameters are station coordinates, velocities and ERPs.

To evaluate the space-tie satellite scenarios observed solely with SLR, the generated SLR single-satellite normal equation of the respective space-tie satellite scenario is combined with the SLR reference solution. This allows the improvement of the scenario with respect to the reference solution to be assessed. In the following, the maximum potential of each space-tie satellite scenario is first analysed in a systematic error-free case in Sec. 6.2.2.1. This is followed by an analysis of the influence of CoM deviations (Sec. 6.2.2.2), atmospheric drag (Sec. 6.2.2.3), SRP (Sec. 6.2.2.4) and EGM mismodelling, and an analysis of the potential of Earth gravity field estimation (Sec. 6.2.2.5).

6.2.1 Reference solution

The procedure of the SLR simulation is similar to that of DORIS, described in Sec. 6.1. White noise only, according to the simulation procedure described in Sec. 4.3, is applied to the SLR observations. Otherwise this case is free of systematic errors. In the POD run, only the initial state elements of the orbit are estimated, reflecting the effect of only noise on the observations on the orbit, the TRF and the ERPs.

6.2.1.1 Orbital fit

The orbital fit of the scenarios and its comparison with the real data evaluation are presented in Sec. 5.2. The global distribution of the residuals is shown in Fig. 6.41 as the mean of the standard deviation of the residuals. The global distribution of the observation residuals shows a similar distribution for LAGEOS-1 and -2. Regions over North Africa and Europe as well as over Australia show a uniform distribution of the residuals around 0.8 cm. Regions such as over South Africa show lower values. The highest residuals are observed over China and Eastern Russia.

6.2.1.2 Orbit recovery

The orbit determined with the simulated observations is compared with the true orbit of the simulation. The mean values of the statistical evaluation of the orbit comparison over the entire time period are shown in Tab. 6.21. The radial component shows up best with RMS values of 0.3 mm. In cross-track and along-track direction the RMS values are at a similar level with values of 1.0 to 1.3 mm. There is no bias close to the level of 0.1 mm in any of the components.

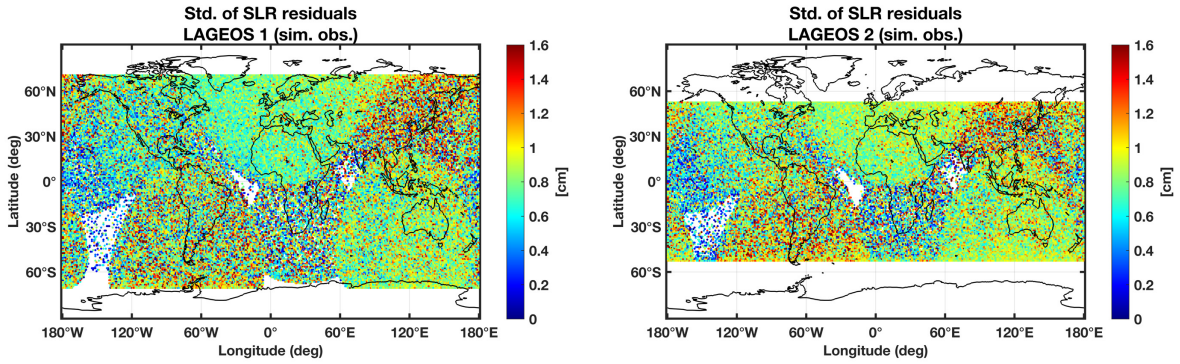

Figure 6.41: Global distribution of the mean standard deviation of the simulated SLR observations for the two LAGEOS satellites of the reference solution.

The geographical distribution of the mean orbital differences are shown in Fig. 6.42. There is no systematic geographical pattern in the orbital differences, they are homogeneously distributed and show no correlation with the distribution of the observation residuals.

Table 6.21: Mean orbit differences of the simulated and recovered orbit.

	RMS [cm]	Mean [cm]	Max [cm]
LAGEOS-1			
Radial	+0.0301	-0.0000	+0.0507
Cross-track	+0.1021	+0.0003	+0.1616
Along-track	+0.1299	-0.0040	+0.2746
LAGEOS-2			
Radial	+0.0314	-0.0000	+0.0506
Cross-track	+0.1286	+0.0002	+0.1974
Along-track	+0.1335	-0.0037	+0.2764

6.2.1.3 Reference frame

EPOS-OC is used in the normal equation mode in the same way as it was done for DORIS to solve station coordinates, velocities and ERPs for SLR (compare also Sec. 6.1). Eleven stations were selected to introduce the geodetic datum using a NNR condition (see Fig. 6.43). The strength of the condition is, as also used for DORIS, set to 1 mm for station position and 0.1 mm/a for station velocities, according to Altamimi (2003). The datum stations were selected on the basis of their performance in terms of number of observations and passes, longest possible observation periods and best orbit fit (compare Fig. 5.11 in Sec. 5.2). Starting from an initial set of datum stations, the selection was iteratively adjusted to minimise the Helmert parameter values for the derived TRF solution compared to the a priori. The final selected datum stations are listed in Tab. 6.22. In addition, three stations, also listed in Tab. 6.22, were treated in a special way. These stations observed for a maximum of 17 weeks or even less over the seven year time span of the simulation and mostly observed only one pass per week with very few observations. This is not sufficient to determine station velocities accurately, so these stations are reduced on normal equation level before the TRF evaluation.

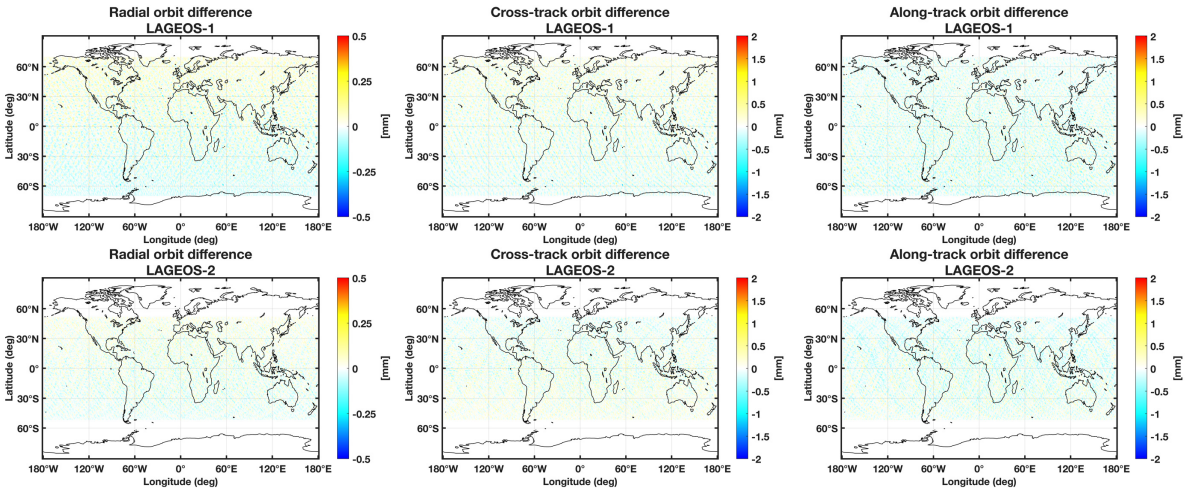

Figure 6.42: Mean orbit differences of the true simulated and recovered orbit over the full simulation time span. Top figures for LAGEOS-1 and bottom for LAGEOS-2. From left to right in radial, cross-track, and along-track direction. A factor of four is applied to the colour bar in the radial direction.

Table 6.22: SLR datum stations and stations which have been reduced

Station no.	Name	Country
Datum stations		
70802419	McDonald Observatory	Texas (USA)
70900513	Yarragadee	Australia
71191401	Haleakala	Hawaii (USA)
71240802	Tahiti	French Polynesia
72371901	Changchun	China
74068801	San Juan	Argentina
75010602	Hartebeesthoek	South Africa
78259001	Mount Stromlo	Australia
78383602	Simosato	Japan
78393402	Graz	Austria
78403501	Herstmonceux	United Kingdom
Reduced stations		
73592601	Daedeok	Republic of Korea
74072701	Brasilia	Brazil
78208201	Kunming	China

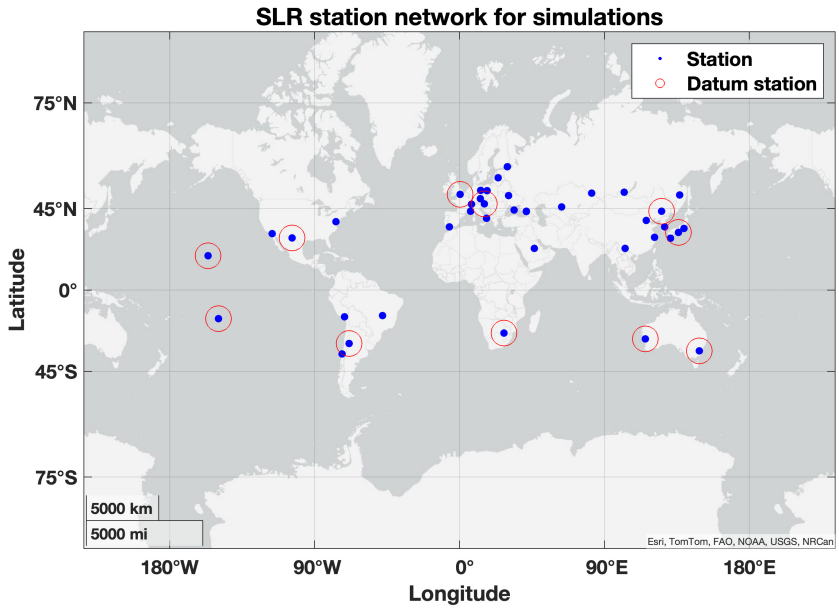

Figure 6.43: The SLR station network of the simulation. All stations used are shown in blue, datum stations are additionally encircled in red.

Helmert parameters The estimated station network is compared with the a priori network with respect to systematic differences in the parameters defining the reference frame (origin, orientation, and scale). Tab. 6.23 shows the Helmert parameters for the subnetwork of datum stations only, as well as for all stations. Translations, rotations and scale differences are in the sub-millimetre range. By varying the set of datum stations, slight changes in the Helmert parameters can be seen. However, all the rotations are below the strength of the NNR condition applied.

Table 6.23: Helmert parameters and their standard deviation to a priori for station positions and velocities of the SLR reference solution.

	T_x [mm] $T_{\dot{x}}$ [mm/a]	T_y [mm] $T_{\dot{y}}$ [mm/a]	T_z [mm] $T_{\dot{z}}$ [mm/a]	R_x [mm] $R_{\dot{x}}$ [mm/a]	R_y [mm] $R_{\dot{y}}$ [mm/a]	R_z [mm] $R_{\dot{z}}$ [mm/a]	sc [mm] $\dot{sc}$ [mm/a]	s_0 $\dot{s_0}$
Combined reference								
datum stations	0.03 ± 0.06	0.12 ± 0.06	0.06 ± 0.06	-0.36 ± 0.07	-0.57 ± 0.07	-0.81 ± 0.07	-0.06 ± 0.06	0.18
	-0.01 ± 0.02	-0.02 ± 0.02	-0.04 ± 0.02	-0.03 ± 0.03	-0.01 ± 0.02	0.01 ± 0.02	-0.01 ± 0.02	0.07
all stations	-0.14 ± 0.29	0.13 ± 0.30	0.24 ± 0.29	-0.52 ± 0.36	-0.44 ± 0.35	-0.94 ± 0.34	-0.23 ± 0.28	1.49
	0.03 ± 0.13	0.02 ± 0.13	-0.10 ± 0.13	0.20 ± 0.16	-0.02 ± 0.16	0.02 ± 0.15	0.05 ± 0.13	0.67

Formal errors Improvements are assessed based on formal errors, which are analysed in the same way as for DORIS (Sec. 6.2). Further information on this can also be found in App. D. The median formal errors of the estimated station coordinates, velocities, and ERPs, are listed in Tab. F.25. For the station positions, these are about 1 mm in X, Y and Z, for the velocities about 1.2 mm/decade. Geographical coordinates show that the formal errors of the height component are the best at 0.97 mm, and slightly worse in the Nort-South direction at 1.02 mm, and the West-East direction at 1.10 mm. The same applies to the velocities, with respective values of 1.17, 1.24, and 1.26 mm/decade. In terms of the ERPs, both pole coordinates are slightly better at 1.9 mm than LOD with 2.6 mm.

6.2.1.4 ERP analysis

The statistics of the differences to a priori of the determined ERPs are given in F.26. The scatter with respect to the a priori is at a comparable level as the formal errors and is at the level of 1.5 mm for the X-pole, 1.6 mm for the Y-pole and 2.9 mm for LOD. Significant biases can be seen in the X-pole with 0.6 mm and Y-pole with 0.4 mm. In addition, the Y-pole also shows a significant drift of about 0.056 mm/a. The significant biases and trends can be attributed to the geometry of the SLR ground station network, as well as the strength of the NNR condition used, as it is directly correlated with the rotations.

The spectral analysis of the ERPs (see Fig. 6.44) shows signals with amplitudes below 0.1 mm in all ERPs. In LOD, two prominent signals with amplitudes close to 0.1 mm and periods of 123 and 258 days, respectively, are visible. At the X-pole, three signals with amplitudes close to 0.1 mm can be seen, with periods of 62 and 69 days, as well as an almost semiannual signal with a period of 174 days. At the Y-pole, only the nearly semiannual period can be found, as well as an almost annual period.

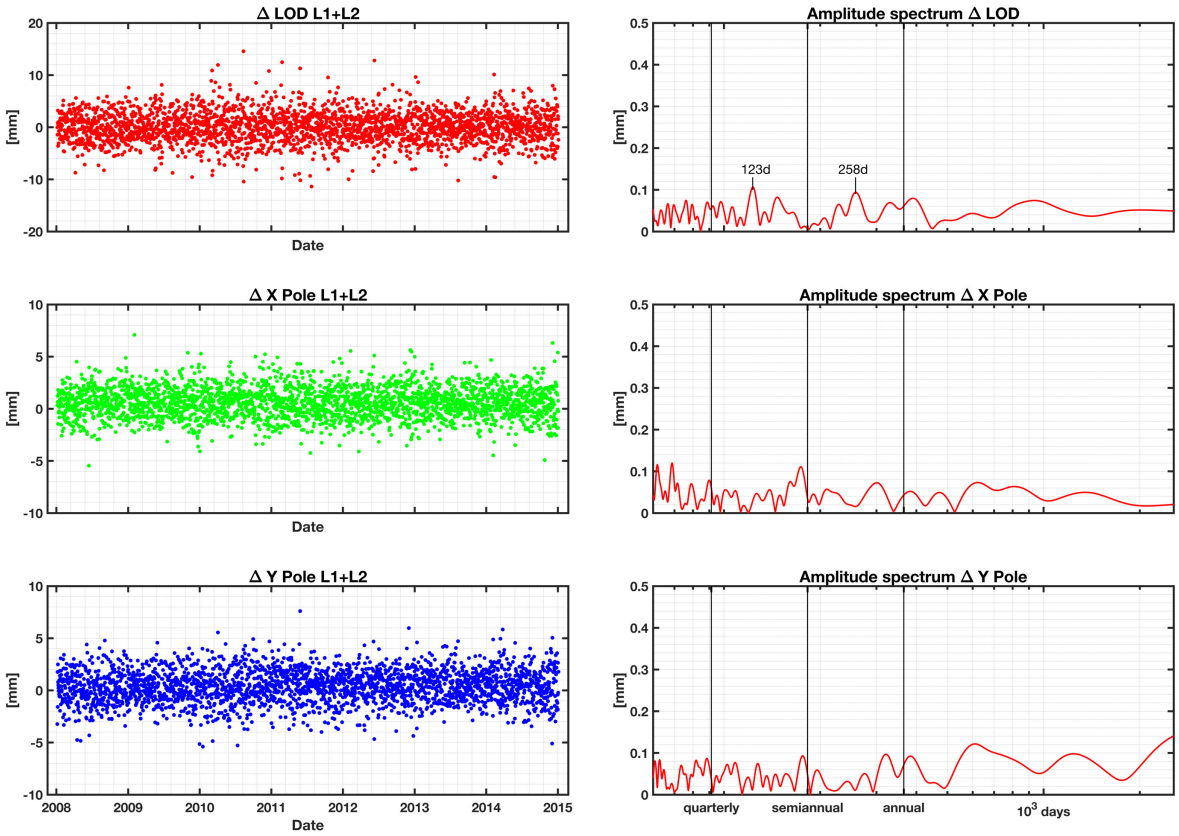

Figure 6.44: Time series of the differences of the estimated LOD, X-pole, and Y-pole to a priori and their spectral analysis for the combined solution of LAGEOS-1 and LAGEOS-2.

6.2.2 SLR space-tie satellite results

The individual SLR single-technique solutions for the space-tie scenarios are generated in the same way as the reference solution.

The influence of the space-tie satellite scenarios is investigated by adding the normal equation of one space-tie satellite scenario at a time to the simulated SLR reference solu-

tion. The changes to the reference solution are then analysed. As for DORIS, the case free of systematic errors represents the maximum achievable potential of each scenario. Subsequent analyses of systematic mismodelling are used to analyse how much of the full potential is lost and in which parameters losses occur. This also includes the analysis of changes and systematics in the TRFs and ERPs. For further details, see also App. E.

6.2.2.1 Case free of systematic errors

In the systematic error-free case for SLR, the observations are simulated for each orbit scenario as described in Chap. 4 and only white noise is added to the observations. These observations therefore have no systematic error effects such as range biases. Accordingly, only the initial state elements for the orbit are estimated in the recovery, as shown in Tab. 6.24.

Table 6.24: Estimated parameters and dynamic parameterisation used in the systematic error-free case for SLR.

Parameterisation for the systematic error-free case	
All scenarios	
Arc length	7 days
Initial state parameters	estimated

Orbital fit The global orbital fit values for each simulation scenario are shown in Tab. 6.25 and the variation with time is shown in Fig. G.11. The global RMS of the simulated SLR observations is at a level of 0.87 cm for all scenarios. The number of observations varies only slightly between scenarios, ranging from 510'000 to 576'000 over the entire simulation period. The number of passes is approximately 50'000, for the two circular scenarios with 30 and 60 degrees inclination it is slightly lower with about 40'000. This is due to the geometry of the orbit and the longer orbital period. The observation and pass yield factors of the simulation are the same for all scenarios, only the bin size is used to adjust the total number of observations and keep them at a similar level. The bin size for the circular 30° scenario is chosen to be 120 seconds, 10 seconds less than the other circular scenarios, to keep the total number of observations at a similar level. Over time, the scenarios show no significant difference in orbital fit or number of observations.

Global observation coverage The global distribution of simulated SLR observations is shown in Fig. 6.45 for each of the space-tie satellite scenarios. In particular, the GRASP-like scenario shows a spot-like distribution of observations around the SLR stations, due to the much lower altitude of the scenario. Most of the observations are over central Europe and Australia. For each of the other scenarios an almost complete global observation coverage can be achieved within the inclination band. In the eccentric E-GRASP-mod and E-GRASP-like scenarios, as well as in the circular scenario with 60 degree inclination, there are more observations over Europe and North Africa, and to a lesser extent over Australia. In the 30 degree circular scenario, observations are clustered over North Africa and South East Asia due to the low inclination. In contrast, the near-polar circular scenario shows the most homogeneous distribution of observations, with most observations over Europe and further North.

Table 6.25: SLR post fit statistics, total number of observations and passes for the simulated space-tie satellite scenarios. Full simulation time span from beginning of 2008 to end of 2014.

	SLR [cm]					Number	
	Min.	Max.	RMS	Mean	Std.	Observations	Passes
GRASP-like	-10.61	9.76	0.86	0.00	0.86	509’737	47’157
E-GRASP-mod	-9.55	11.97	0.87	0.00	0.87	565’262	54’494
E-GRASP-like	-12.26	9.43	0.87	0.00	0.87	576’424	51’072
Circular 30°	-11.48	12.71	0.87	0.00	0.87	521’254	37’000
Circular 60°	-12.35	10.52	0.87	0.00	0.87	535’180	41’635
Circular 89°	-11.10	9.87	0.86	0.00	0.86	534’854	50’422

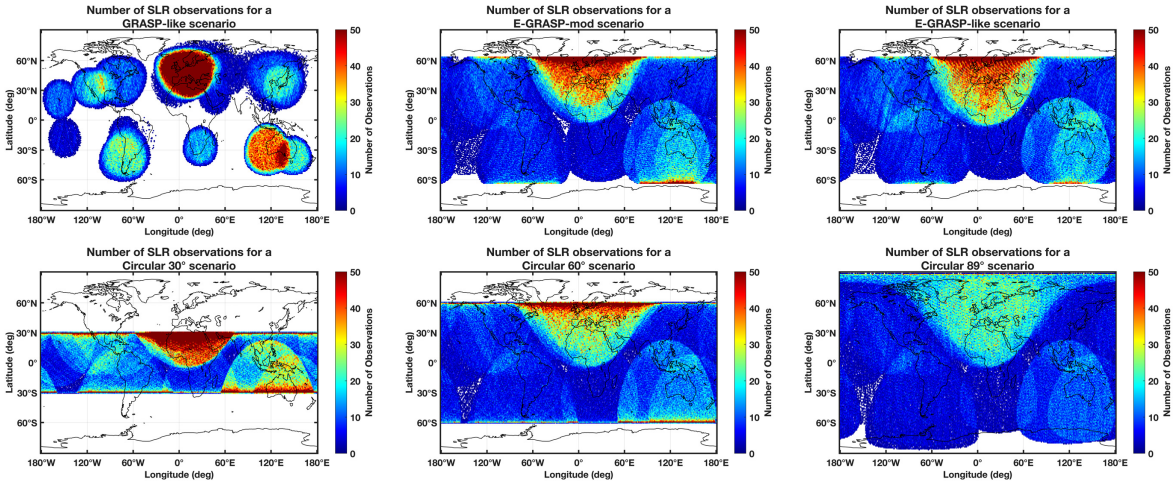

Figure 6.45: Global observation coverage of simulated SLR observations for the space-tie satellite scenarios.

The global distribution of the mean standard deviation of the simulated observations for each scenario is shown in Fig. 6.46. For the low-orbiting GRASP-like scenario, slightly increased values can be seen over South America and China, and to the North over Eastern Russia. The lowest values are observed over the station of Tahiti, and regions over Europe and Australia show the lowest mean scatter. A similar picture emerges for the other scenarios. However, due to the higher flight altitude, these effects are somewhat weaker and more regionally distributed, as the regional visibility of the satellite for the stations increases and the observation noise performance of the different stations mixes.

Orbit recovery The achievable orbit accuracy for each scenario is shown in Fig. G.12. The recovered orbit is compared with the orbit of the simulation. The deviations in terms of mean RMS values are remarkably small for all scenarios in the radial direction, less than 1 mm. In cross-track and along-track direction the RMS is higher with values up to 1.5 mm. The low-orbiting GRASP-like scenario shows the best results. The two eccentric E-GRASP-mod and E-GRASP-like scenarios show slightly higher mean RMS values, the different eccentricity does not lead to differences in RMS and mean. The higher orbiting

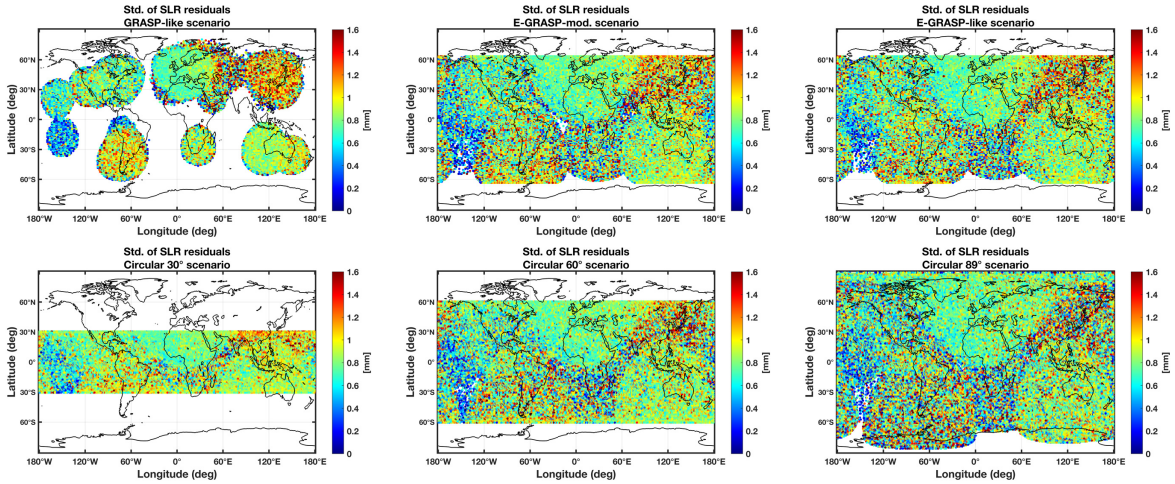

Figure 6.46: Global distribution of the mean standard deviation of the simulated SLR observations.

circular scenarios show the highest differences, which are all at a similar level. The 60 degree scenario is slightly worse in the cross-track direction, but slightly better in the along-track direction. None of the scenarios show a systematic offset.

The geographical distribution of the mean orbit differences for each scenario in radial, cross-track, and along-track directions is shown in Fig. 6.47. Systematic effects can be seen for the E-GRASP-mod, E-GRASP-like, and the 60 and 89 degree circular scenarios.

The two eccentric scenarios E-GRASP-mod and E-GRASP-like show patterns in the radial direction, which were also observed in a similar way for DORIS. Here, striped patterns occur along the inclination with an amplitude of 0.05 mm, which are slightly more pronounced for the E-GRASP-like scenario and therefore appear to increase with increasing orbital eccentricity. In the cross-track and along-track direction, the patterns along the inclination show 8 maxima. These are slightly weaker for the E-GRASP-mod scenario and show an amplitude of approximately 0.12 mm in the cross-track and 0.15 mm in the along-track. A similar pattern was found for DORIS, but mainly in the cross-track direction.

In the circular scenarios, a North-South pattern can be observed in the radial and cross-track directions. However, this is very small in the radial direction, with a maximum amplitude well below 0.1 mm. In the cross-track direction, the pattern is more pronounced, with an amplitude of up to about 0.3 mm in the scenario with 60 and 89 degree inclination, about twice as strong as in the scenario with 30 degree inclination. In the along-track direction, there is no clear geographical pattern for any of the three circulation scenarios, only the increased noise of the orbit difference.

A correlation between the geographical differences and distribution of the residuals can not be found for any of the scenarios.

Based on the orbit differences of the orbits determined with SLR in the systematically error-free case, each of the investigated scenarios is initially suitable, lower orbiting scenarios show a slightly better accuracy in terms of RMS values in the orbit comparison. The eccentric orbit scenarios show small systematic regional orbital differences in the radial and along-track direction. For the higher orbiting circular scenarios, small North-South patterns can be observed, however only in cross-track direction and with amplitudes on submillimetre level. Otherwise there are no other irregularities in the orbits found.

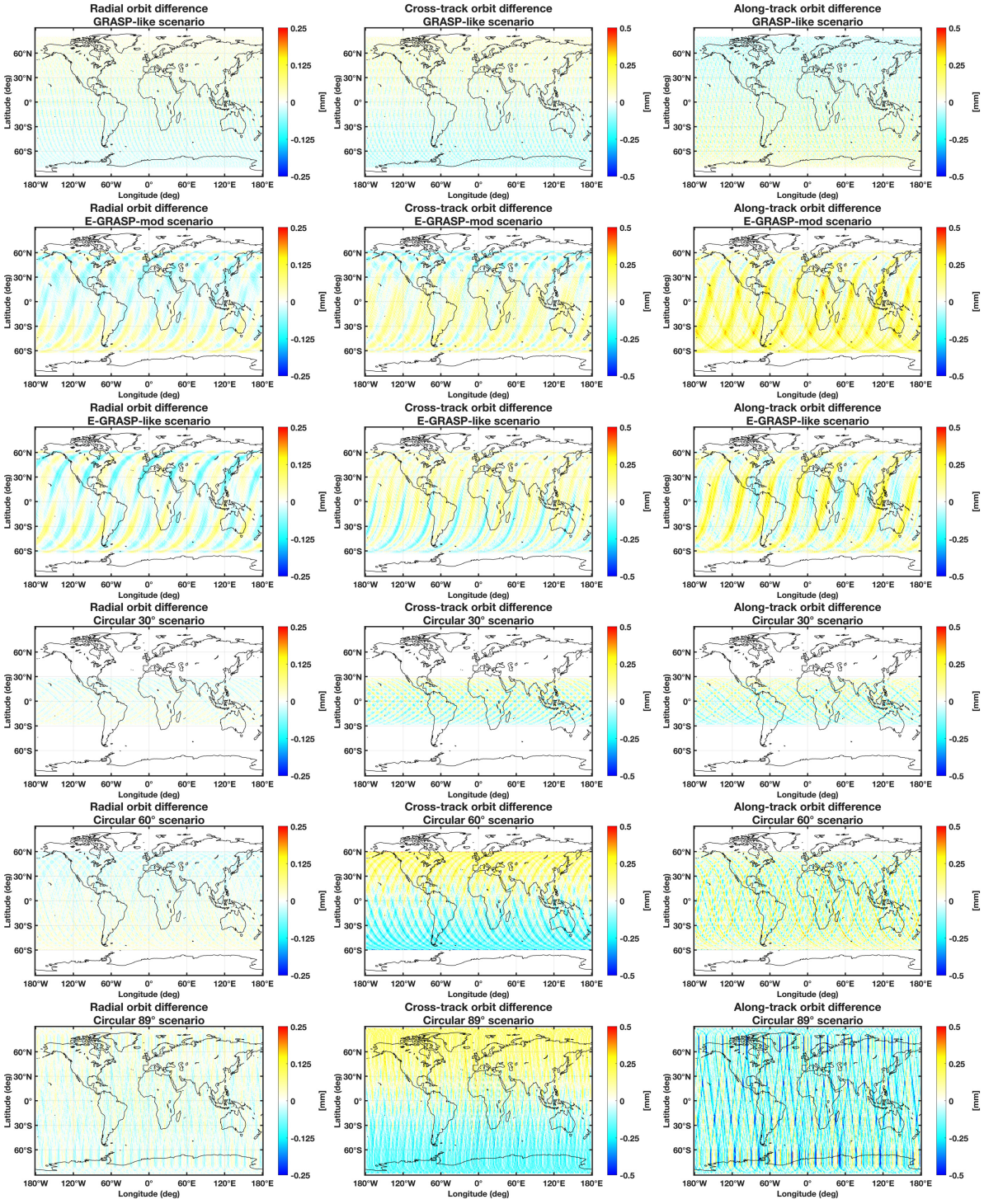

Figure 6.47: Mean orbit differences of the true simulated and recovered orbit over the full simulation time span of 7 years for SLR in the systematic error-free case. From the top to the bottom, GRASP-like, E-GRASP-mod, E-GRASP-like, Circular 30°, Circular 60°, Circular 89° scenario. From left to right in radial, cross-track, and along-track direction.

Reference frame evaluation

Helmert parameters The Helmert parameters are shown for the entire SLR network in Fig. 6.48 and listed in Tab. F.24 in App. F.2. Compared to the Helmert parameters of the reference solution and a priori, there is no significant change in translation and scale for positions and velocities in any of the scenarios. The rotations for positions and velocities are larger, but considering the standard deviation of the estimate, they are not significantly different from the reference solution. Furthermore, all rotations are below the level of the strength of the NNR condition of 1 mm and 0.1 mm/year respectively.

The smallest empirical variance coefficient of the transformation can be obtained by including the GRASP-like scenario with a maximum reduction of 23% in positions and 49% in velocities. For positions, all the circular scenarios also show a similar reduction of about 20%, while for velocities all other scenarios are in the range of 15 to 30%.

The inclusion of each of the space-tie scenarios in the SLR reference solution does not lead to a significant change in the parameters defining the reference frame.

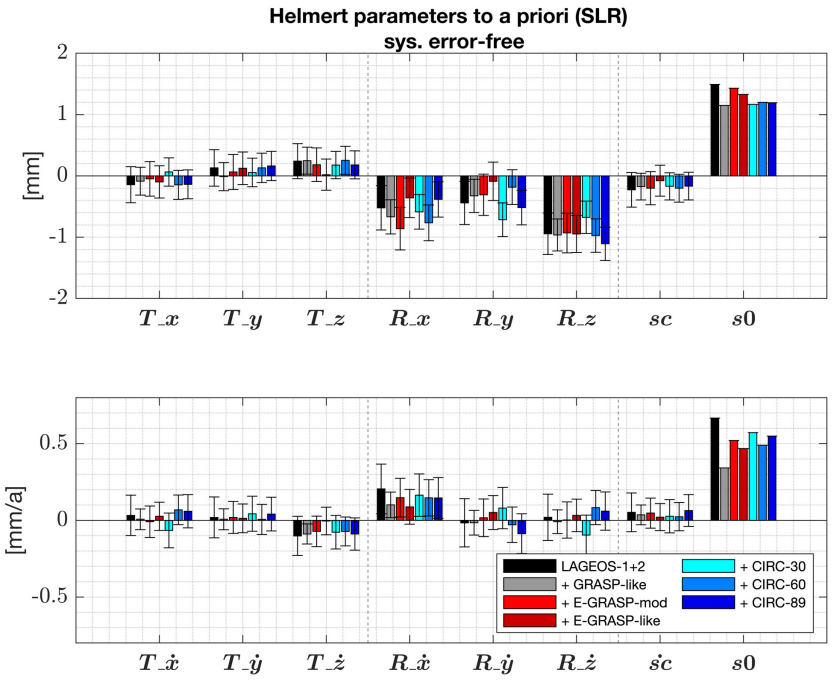

Figure 6.48: The upper figure shows the Helmert parameters of all station positions for the systematic error-free case compared to a priori. The error bars represent the standard deviation (1 σ).

Formal errors The formal error results for each scenario are shown for coordinates in X, Y, and Z in Fig. 6.49 and for latitude, longitude, and height in Fig. 6.50 (absolute values for all scenarios can be found in App. F.2). The values for the ERPs are identical in both figures and are converted to millimetre equivalents on the Earth's surface. The expected improvement for all scenarios is between 19 and 21 % (compare Tab. F.25 in App. F.2).

Formal errors of station coordinates The formal errors for each of the scenarios are at a comparable level to the reference solution of about 1 millimetre for positions and about

1 millimetre per decade for velocities. In Cartesian coordinates, the smallest formal errors are in the height component with about 0.87 mm, in the latitude (North-South) direction with about 0.92 mm, and in the longitude (West-East) direction with 1.02 mm. The velocities show a similar picture, with respective values of 1.01, 1.10, and 1.13 mm/decade respectively.

The scaled improvement shows that each of the scenarios leads to an improvement of the formal errors. The improvement is moderate for the station positions with 3 to 10% in X, Y, and Z directions, the largest improvement being in the Z component. In geographic coordinates, the improvement is greatest in the latitude and height component. Improvements in the latitude component are at about 11% for the GRASP-like, E-GRASP-mod and the E-GRASP-like scenario and 8 to 10% for the circular scenarios. In the longitude component the improvements are between 5 and 8% for all scenarios and in the height component between 8 and 12%. Also in the 30 degree circular scenario, the satellite is visible and trackable for all stations.

The OSI shows that none of the scenarios can achieve a geometric added value in terms of station positions. The GRASP-like scenario achieves the best overall OSI, while the 30 degree circular scenario appears to be the most beneficial for the height component.

Formal errors of station velocities The picture is similar for the velocities. Improvements in X, Y, and Z are between 7 and 14%, with the largest improvement in the Y component. In geographic coordinates, the picture is similar to that for positions, with a mean improvement in the latitude and longitude component of about 11%, and about 14% in the height component.

Again, none of the scenarios can provide a geometric added value in the OSI. However, in geographic coordinates, the 30 degree circular scenario once again achieves the best overall OSI in the height component.

Peak improvement analysis for station coordinates and velocities The difference between the percentage change in mean and median is shown in Fig. 6.51. Thereby jumps in improvement can be identified, showing whether individual stations experience superior improvement due to the geometry of the observations.

The differences are about 15% or less for all scenarios and components. In the Z direction and for the height component, the circular scenario with 89 degree inclination shows slightly larger differences, the 30 degree scenario the lowest, with values close to zero.

The results of the difference analysis indicate that no major peak improvement can be detected.

Formal errors of ERPs The formal errors of the ERPs are at a similar level for all scenarios, at 1.6 mm for the pole coordinates, and about 2 mm for LOD. The scaled improvement is between 11 and 16% for the pole coordinates, and 19 and 24% for LOD. The OSI shows that in the pole coordinates none of the scenarios shows a geometric added value, the GRASP-like comes closest to the expected improvement. Only for LOD, a very small geometric added value can be seen, with the largest effect found for the circular scenario at an inclination of 30 degrees. However, the improvements across all scenarios are very close to the expected improvement, indiating that the geometric added value is nearly insignificant.

In contrast to DORIS, no peak improvement in the ERPs can be noted. The reason for the peak improvement seen in DORIS is, that the satellites available in the reference

solution vary over time. In contrast, geodetic satellites do not manoeuvre and do not operate electronics that could be unavailable, so the satellites in the reference solution are continuously available throughout the simulation period. This leads to constant formal error values in the ERP, without jumping variations.

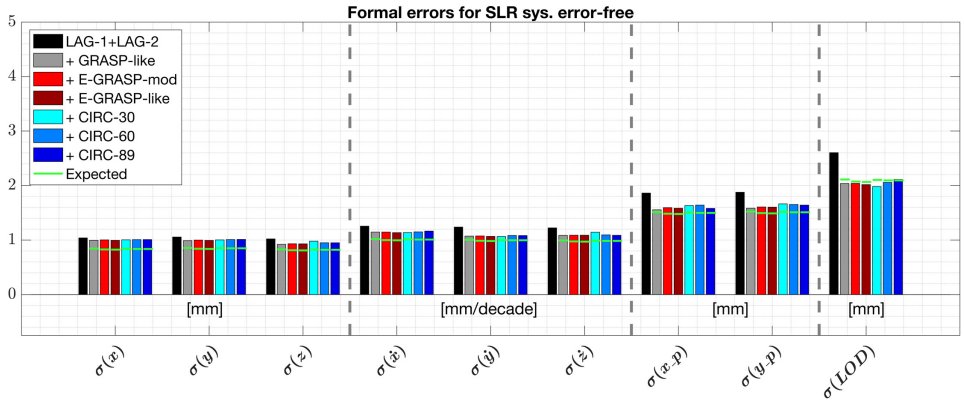

(a) Absolute values of the median of the formal errors. The green bars indicate the expected improvement.

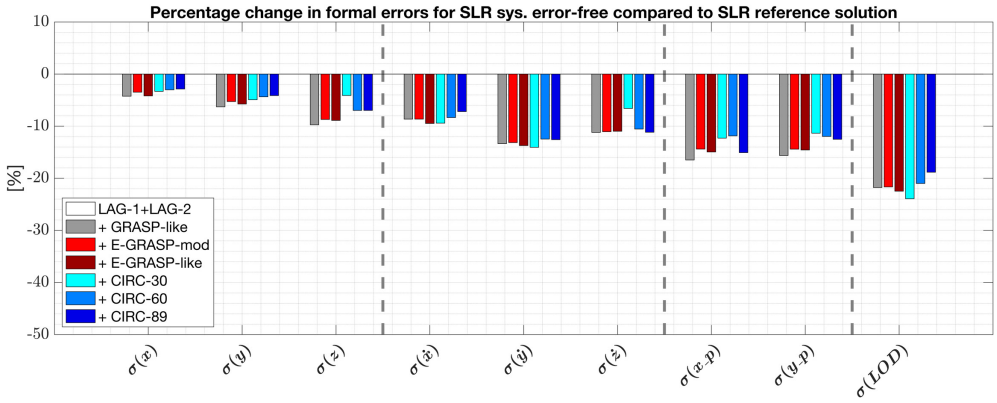

(b) Scaled improvement

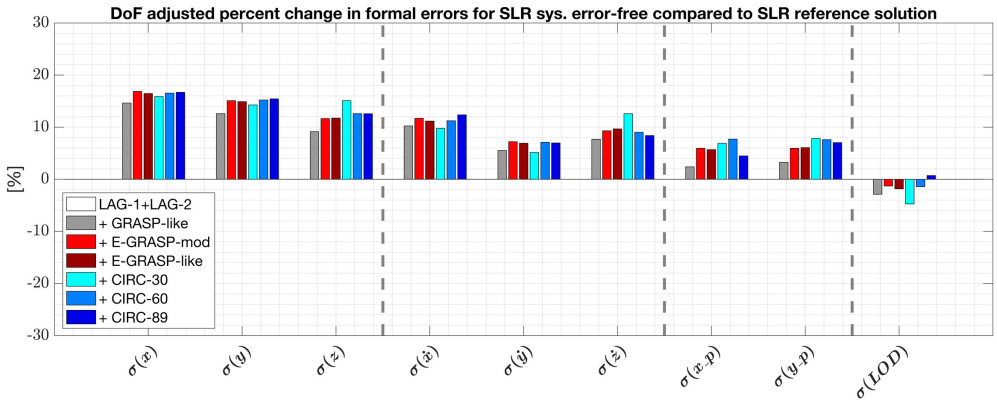

(c) Observation scaled improvement

Figure 6.49: Fig. a) shows the absolute values of the median of the formal errors in X, Y, and Z for the reference scenario and each of the space-tie satellite scenarios. Fig. b) shows the scaled improvement, Fig. c) shows the observation scaled improvement.

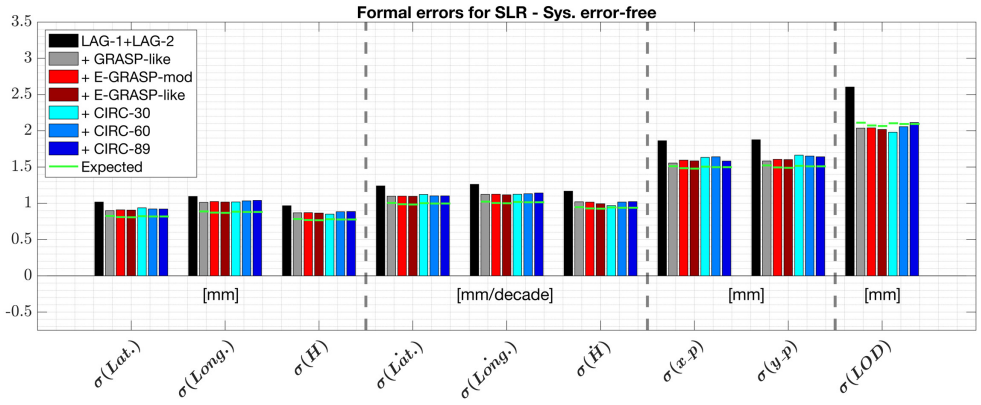

(a) Absolute values of the median of the formal errors. The green bars indicate the expected improvement.

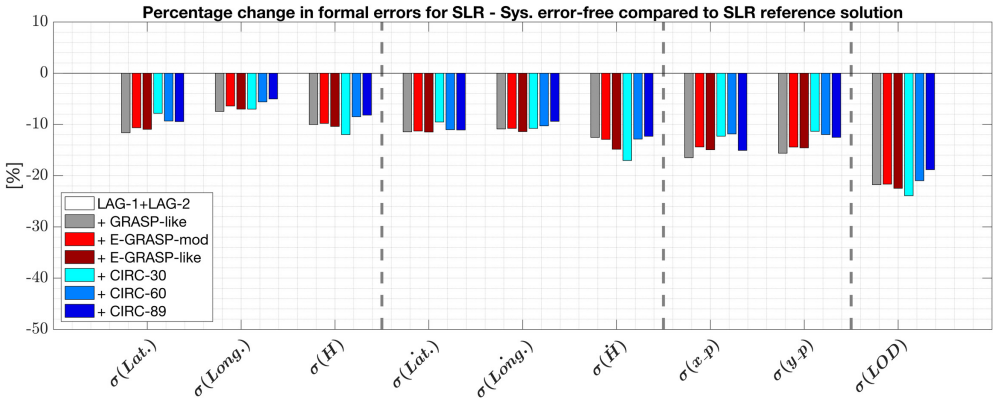

(b) Scaled improvement

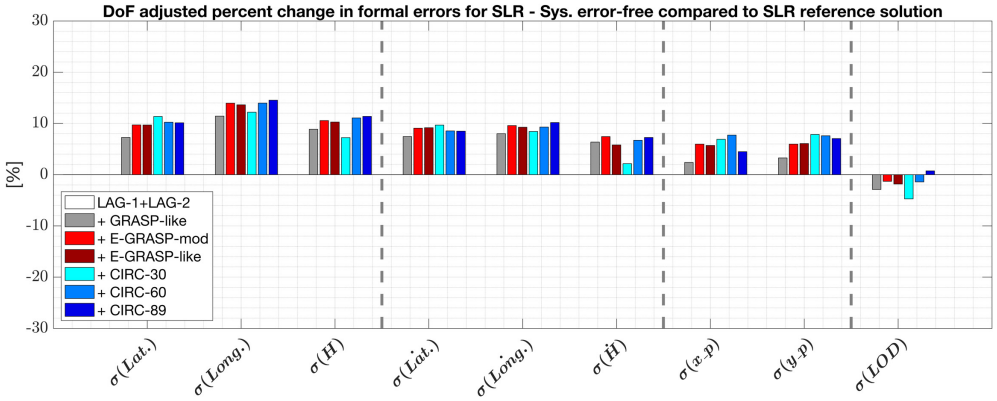

(c) Observation scaled improvement

Figure 6.50: Fig. a) shows the absolute values of the median of the formal errors in latitude, longitude, and height for the reference scenario and each of the space-tie satellite scenarios. Fig. b) shows the scaled improvement, Fig. c) shows the observation scaled improvement.

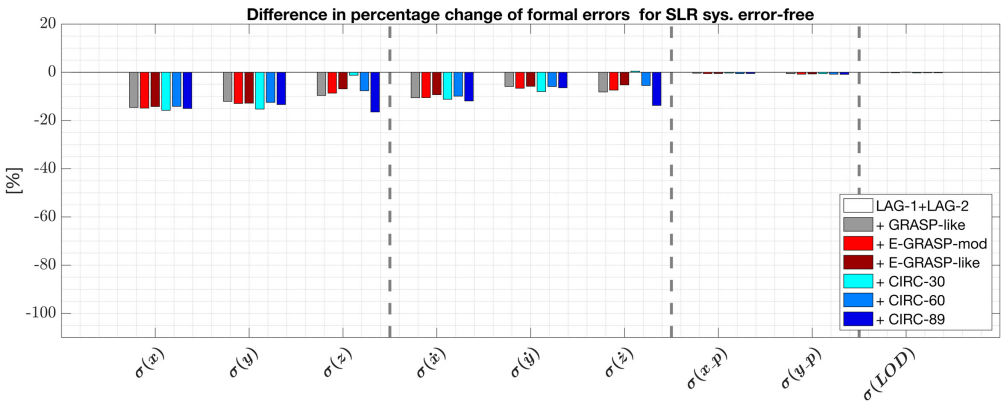

(a) Difference in improvement in Cartesian coordinates

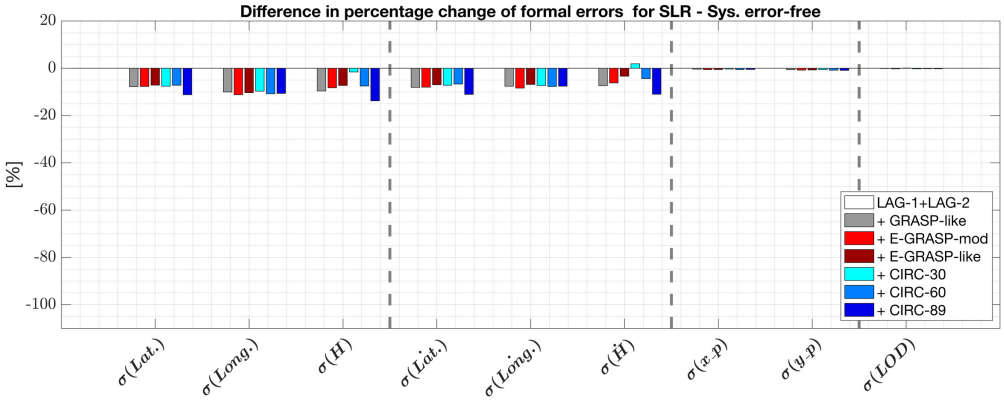

(b) Difference in improvement in geographic coordinates

Figure 6.51: Fig. a) and b) show the difference in scaled improvements based on the mean and median of the formal errors. Large negative values indicate a peak improvement for outlier values.

A posteriori ERP analysis Tab. F.26 shows the values of the statistical evaluation of the corrections of the ERPs. It can be seen that the standard deviation of the pole coordinates of 1.5-1.6 mm in the X- and Y-poles of the reference solution can be reduced by approximately 25% to a level of 1.1-1.2 mm with each of the scenarios. The 89 degree circular scenario shows a very minor advantage.

Based on the significant offset in the pole coordinates of the reference solution of 0.6 and 0.4 mm in X and Y respectively, none of the scenarios can significantly remove the offset. However, they are all below the millimetre that the GGOS is aiming for. This offset can be reduced by increasing the strength of the NNR condition.

The linear regression of the pole coordinates reveales significant drifts, mainly in the Y-pole, but at a level below 6/100 mm/year, which is a factor of 10 smaller than the average standard deviation of the pole corrections.

LOD shows a similar picture, the noise of the reference solution of 2.9 mm can be reduced by about 25% to 2.1-2.3 mm with each scenario, where the circular scenario with 89 degrees inclination shows a slightly worse improvement. None of the scenarios shows a significant offset or trend in LOD.

ERP spectral analysis The spectral analyses of the determined ERPs are shown in Fig. G.13–G.18 in App. G.2. The strongest signals found in the ERPs of the reference solution have maximum amplitudes close to 0.1 mm. Each space-tie scenario leads to a reduction in these signals to a level below 0.1 mm. No amplification or introduction of new signals were found for any of the scenarios. In LOD slightly more effective scenarios are the GRASP-like, E-GRASP-like and 60 degree circular scenario.

Conclusion - systematic error-free The results of the systematic error-free simulation show that the global observation coverage for SLR for lower orbiting satellites shows increasingly spot-like coverage around the ground stations, which means that parts of the orbit are unobserved. With increasing altitude, a global homogeneous observation coverage can be achieved.

The orbit comparison shows the best results for the low-orbiting GRASP-like scenario. Higher orbiting scenarios show slightly higher orbit differences in the mean RMS. Geographical differences were found for the eccentric E-GRASP-mod and E-GRASP-like, which show a similar stripe-like pattern as for DORIS, the circular scenarios show a minor North-Shouth pattern in cross-track direction, which increases with increasing inclination. However these geographical patterns are in the low submillimetre range.

The derived TRFs show no systematic influence in the Helmert parameters by including one of the space-tie satellite scenarios.

The possibility to improve the formal errors in the estimated station coordinates and velocities is mainly due to the additional observations. A geometric added value could not be found for any of the scenarios. The mean improvements for station coordinates and velocities are at the level of 10% for most of the components.

The potential for improving the formal errors in the ERPs is at a similar level for all scenarios and is around 14% for the pole coordinates and 20% for LOD. A geometric added value in the ERPs could only be found for LOD, and here for all scenarios except the 89 degree circular scenario. However, this is in the low single digit percentage range.

The scatter of the estimated pole coordinates and LOD can be reduced by about 25% with each of the scenarios. A systematic influence on the ERPs compared to the reference solution could not be found for any of the scenarios.

Each of the scenarios shows the potential to reduce signals in the determined ERPs of the SLR reference solution, differences in the scenarios are rather specific and small. For LOD, the GRASP-like, E-GRASP-like and 60 degree circular scenario are particularly suitable. At the pole coordinates, none of the scenarios is significantly better or worse than the others.

The ratings of the individual scenarios for improving the TRF and the ERPs are given in Tab. 6.26. The results demonstrate a high degree of balance, with each scenario proving to be suitable for achieving improvements of a comparable magnitude. In terms of station coordinates, the 30 degree circular scenario was found to be particularly effective in improving formal errors in the latitude component. In the context of the ERPs, the 60 degree circular scenario proved to be a good compromise for reducing the signals of the reference solution in both pole coordinates and LOD.

Table 6.26: Maximum potential of the satellite scenarios for SLR to improve the TRF and ERPs in the case free of systematic errors. The lower the stated value, the better the rating. The summary represents the unweighted mean value.

	G-like	E-G-mod	E-G-like	Circ. 30°	Circ. 60°	Circ. 89°
Obs. cov.	②	①	①	①	①	①
Orbit	①	②	②	②	②	②
Helmert	①	①	①	①	①	①
Station pos. f.e.	②	②	②	②	②	②
Station veloc. f.e.	②	②	②	②	②	②
Stat. stab. f.e.	②	②	②	②	②	②
Pole coord. f.e.	①	②	②	②	②	②
Pole coord. est.	①	①	①	①	①	①
LOD f.e.	①	①	①	①	①	①
LOD est.	①	①	①	①	①	①
ERP stab. f.e.	②	②	②	②	②	②
Summary	1.5	1.5	1.5	1.5	1.5	1.5

6.2.2.2 Influence of center-of-mass displacements

To investigate the influence of systematic eccentricity errors of the vector from the satellite's CoM to the SLR reference point, the same method used for DORIS in Sec. 6.1.2.2 is applied. The CoM coordinates are shifted by 3 mm in the first case and by 6 mm in the second in the X, Y, and Z directions of the satellite fixed reference system, corresponding respectively to 5 mm and 10 mm in three dimensions. As mentioned above, due to the chosen attitude control of the simulated satellite, the X, Y, and Z directions of the satellite correspond directly to the radial, cross-track and along-track components. The dynamic modelling is not modified in this case.

Orbital fit The displacement introduced can be seen in the parameters of the orbital fit. For a displacement of 3 and 6 mm, the RMS increases in all scenarios from about 0.86 to 0.90 and about 0.99 cm, respectively. The same applies to the mean, which increases by about 1.7-1.9 and 3.4-3.8 mm for the GRASP-like, E-GRASP-mod and 30 degree circular

scenarios, respectively. For the E-GRASP-like scenario the increase is slightly smaller at 1.3 and 2.6 mm. This is thought to be due to the eccentricity of the orbit, where the shift in the satellite's Z component is not only corresponding to the radial component. The 60 and 89 degree circular scenarios show a larger increase of 2.4 and 4.8 mm, which is close to the introduced one dimensional displacement. Furthermore, a shift of 10 mm (3D) is found to cause an increase in the standard deviation of up to 7%, which is slightly less for the 60 and 89 degree circular scenarios.

Orbital recovery The results of the orbit comparisons, Fig. 6.52, show that, similar to DORIS, it is mainly the eccentric orbit scenarios that show an increase in the RMS of the radial orbit differences. Compared to DORIS this increase is stronger and increases along with the introduced displacement. The increase is largest for the two eccentric orbits, E-GRASP-mod and E-GRASP-like, which show an increase by a factor of 5 and 7 respectively for the 5 mm displacement. The second largest increase can be seen for the circular scenarios at 60 and 89 degrees inclination with a factor of 2.7 and 3.1 repsectively, the smallest for the GRASP-like and circular scenario at 30 degree inclination with a factor of 1.9 and 1.4 respectively.

In the cross-track direction, all scenarios show an increase in RMS, but it is significantly stronger for the 30 degree circular scenario. For this scenario the increase is by a factor of 6 for 5 mm displacement, for all other scenarios it is approximately a factor of two to three. A comparison of the three circular orbit scenarios shows that the effect of orbital differences decreases with increasing inclination.

In the along-track direction, the effect is substantial, similar to that of DORIS, and is most pronounced for the E-GRASP-like scenario with a factor of 4.7 for 5 mm displacement. The GRASP-like and E-GRASP-mod are the second most affected with a factor of about 4. All circular scenarios are least affected with factors below 3. Here the inclination seems to have the opposite effect in comparison to the cross-track component, the smaller the inclination, the smaller the increase in the along-track orbit differences.

For all scenarios, doubling the introduced displacement also shows an increase in the RMS factors by a factor of two.

A systematic mean orbit difference can only be seen in the along-track component, which for all scenarios reflects 100% of the introduced one dimensional displacement of 3 and 6 mm respectively.

Fig. 6.54 shows the geographical orbit differences. A North-South distribution can be seen in the radial direction for all scenarios. This is clearly stronger for the two eccentric scenarios, and for the E-GRASP-like scenarios seems to have a maximum of about 3 mm at a latitude of 20° North. For the circular scenarios this pattern increases with increasing inclination. The lowest influence is seen for the GRASP-like and circular scenario at 30 degree inclination.

In the cross-track orbit direction there is also a North-South distribution for each scenario, which is strongest for the 30 degree circular scenario, where the differences reach an amplitude of about 14 mm. Near polar orbits such as the GRASP-like or the 89 degree inclined circular scenario perform best, with a maximum amplitude of about 2.3 and 3.9 mm respectively. The eccentric E-GRASP-mod and E-GRASP-like show amplitudes of 5.9 and 4.9 mm respectively. In contrast, the 60 degree circular scenario, which has a similar inclination, shows a stronger amplitude of about 6.1 mm. Thus, in the cross-track component, a permanent higher altitude of the orbit seems to weaken the ability to determine the cross-track component with SLR.

In the along-track direction, only the two eccentric scenarios show a North-South distribution in addition to the offset. Here the maximum amplitude is about 4.7 and 7.5 mm for the E-GRASP-mod and E-GRASP-like scenarios, respectively.

The geographical differences in the mean residuals in Fig. 6.53 partly reflect the North-South distribution and appear to be anticorrelated with the radial orbital differences. This is most obvious for the circular scenarios. For the other scenarios, the distribution of the mean differences show an overlap of the North-South distribution of the orbital differences with the elevation of the observation. In areas where the observations are observed at low elevations and in peripheral areas where observations from neighbouring stations overlap, the mean differences increase.

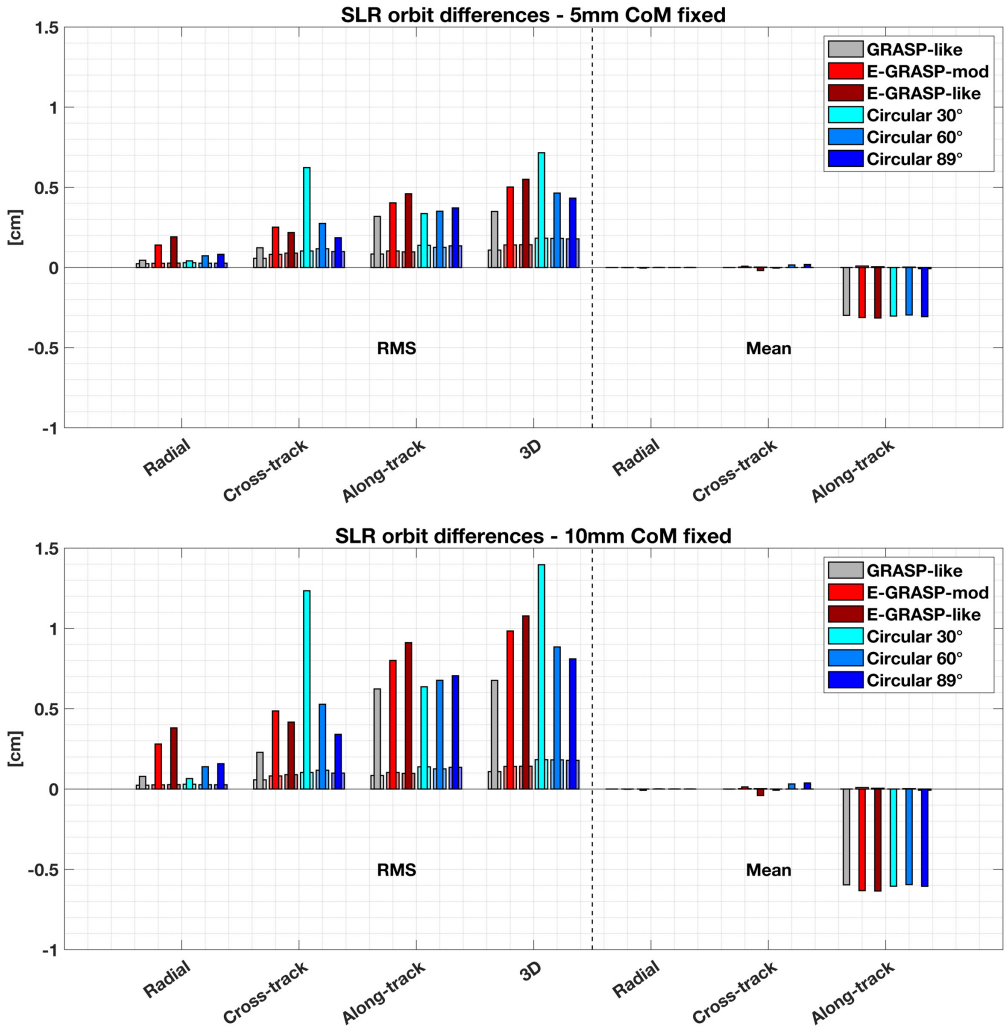

Figure 6.52: Mean RMS and mean values of the orbit comparison of the simulated and recovered orbit with 5 mm and 10 mm systematic displacement, respectively. The thinner bars show the results of the test scenarios with the systematic displacement, the thicker bars in the background show the values achieved in the systematic error-free case.

SLR reference point estimation The estimated reference points show an accuracy of better than 1/10 mm in the radial and normal directions for each of the scenarios (see Tab. 6.27). The differences between the scenarios are very small. The largest remaining deviation

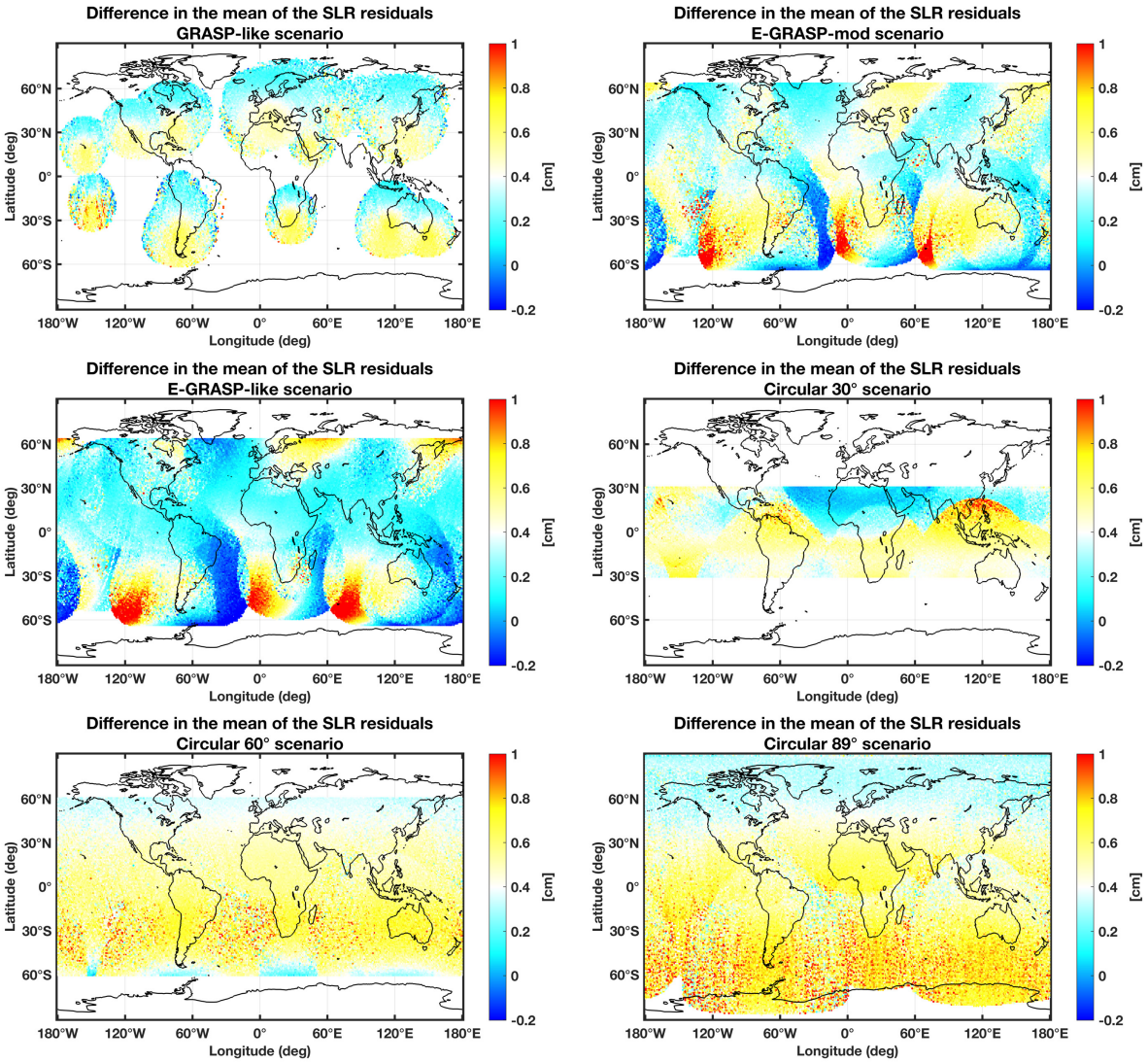

Figure 6.53: Global distribution of the difference in the mean of the observation residuals for the case of systematic CoM displacement compared to systematic error-free for SLR. The colorbar is shifted by 0.4 cm, corresponding to approximately the mean of all the scenarios seen in the orbital fit for this case.

in the radial direction is observed for the GRASP-like scenario, while in the normal direction it is the 60 degree circular scenario. However, these are still less than 1/10 mm.

In the transversal direction, only the two eccentric scenarios, E-GRASP-mod and E-GRASP-like, show a residual deviation on the sub-millimetre level, for the GRASP-like scenario an offset of about 1.7 mm remains. For the circular scenarios, it is not possible to estimate the reference point in the transversal direction in a meaningful way. Remaining offsets are 4 centimetres for the circular scenarios at 60 and 89 degree inclination and up to 64 centimetres for the scenario at 30 degree inclination.

Increasing the one-dimensional displacement from 3 to 6 mm per component has no significant effect on the estimated values for all scenarios.

For SLR, it can be concluded that the estimation of the reference point in the radial and normal direction is possible for all scenarios with an accuracy of 1/10 mm and better. In the transversal direction, the inaccuracy of the estimated value is larger and estimation is only reasonably possible for the GRASP-like scenario with millimetre accuracy and the

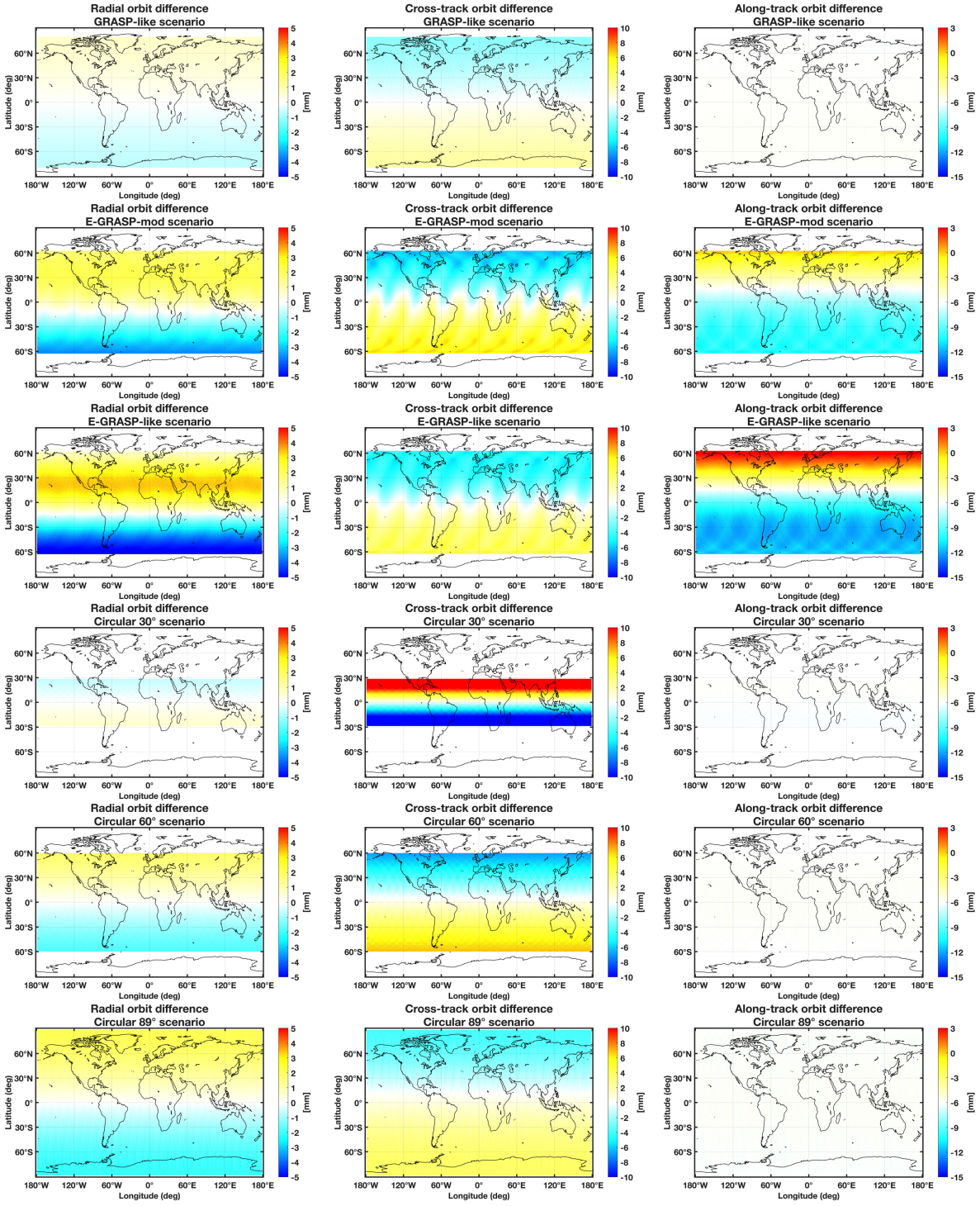

Figure 6.54: Mean orbit differences of the systematic error-free scenario and the recovered orbit for the 3D 10 mm CoM mismodelling scenario. From left to right in radial, cross-track, and along-track direction. From the top to the bootom, GRASP-like, E-GRASP-mod, E-GRASP-like, Circular 30°, Circular 60 °, Circular 89°.

E-GRASP-mod and E-GRASP-like scenarios with sub-millimetre accuracy. However, biases in SLR, such as range or time biases, would be correlated with the estimation of the CoM or SLR reference point, thus preventing estimation of the affected components.

Table 6.27: Difference of estimated CoM coordinates to the simulation. Estimates and their standard deviation in millimetres. Introduced CoM coordinate displacements of 3 and 6 mm all three axes.

	3 mm per axis introduced			**6 mm per axis introduced**		
	Radial	**Transversal**	**Normal**	**Radial**	**Transversal**	**Normal**
GRASP-like	0.09 ± 0.02	1.69 ± 2.08	-0.00 ± 0.03	0.09 ± 0.02	1.69 ± 2.08	-0.00 ± 0.03
E-GRASP-mod	0.06 ± 0.02	-0.22 ± 0.45	-0.02 ± 0.05	0.06 ± 0.02	-0.22 ± 0.45	-0.02 ± 0.05
E-GRASP-like	0.07 ± 0.02	0.30 ± 0.28	-0.03 ± 0.06	0.07 ± 0.02	0.30 ± 0.28	-0.03 ± 0.06
Circular 30°	0.05 ± 0.02	-644.76 ± 290.10	0.02 ± 0.08	0.05 ± 0.02	-643.27 ± 289.80	0.02 ± 0.08
Circular 60°	0.07 ± 0.02	-41.68 ± 118.40	0.07 ± 0.06	0.07 ± 0.02	-41.68 ± 118.40	0.07 ± 0.06
Circular 89°	0.06 ± 0.02	-38.47 ± 98.02	0.01 ± 0.05	0.06 ± 0.02	-38.51 ± 98.05	0.01 ± 0.05

Reference frame

Helmert parameters The systematic CoM displacement for SLR, shows a systematic influence on the TRF for all scenarios. These are primarily evident as translations in Z, rotations around X and Y, and in the scale. The effect is mainly on station positions, but to a lesser extent also on velocities (see Fig. 6.55 and Tab. F.27 and F.28 in App. F.2). The influence on the Helmert parameters shows a linear correlation with the introduced displacement, i. e. they double when the introduced displacement is doubled. The following values are given for the case of 5 mm displacement.

The largest influence can be seen for the GRASP-like scenario, where the rotations range up to about 7 mm for station positions and 0.4 mm/a for velocities. Other scenarios are less affected, but only the 30 degree circular scenario shows an influence on the rotation of less than 1 mm and 0.1 mm/a respectively. The influence on the translations is much smaller, translations for positions above 1 mm can only be seen for the two eccentric scenarios E-GRASP-mod and E-GRASP-like, and of exactly 1 mm for the 60 and 89 degree circular scenarios. The effect on the scale is up to 1.3 mm, with the GRASP-like and the 60 and 89 degree circular scenarios being affected the most. A more eccentric orbit or a lower inclination, here 30 degrees, reduces the effect.

The co-estimation of the CoM coordinates eliminates almost the entire systematic effect on the TRF in all scenarios. Only for the GRASP-like and E-GRASP-like scenarios a significant Y-rotation of maximum 0.14 mm remains.

Formal errors An LIP can be observed for all scenarios. This is strongest for station coordinates, and similarly strong for station velocities and ERPs (see Fig. 6.56 and 6.57).

With a shift of 5 mm, the LIP of the station positions is in the range of 14 to 36% in X, 10 to 25% in Y and 6 to 14% in Z. In geographical coordinates, it can be seen that the losses are strongest in the longitude direction, where they reach 8 to 20%. The 89 degree circular scenario is affected the most here. In the latitude and height components, the losses are smaller and are in the range of 4 to 12%.

For station velocities the LIP is smaller, ranging from 3 to 10% and at comparable levels in all components. Again the 89 degree circular scenario is the most affected.

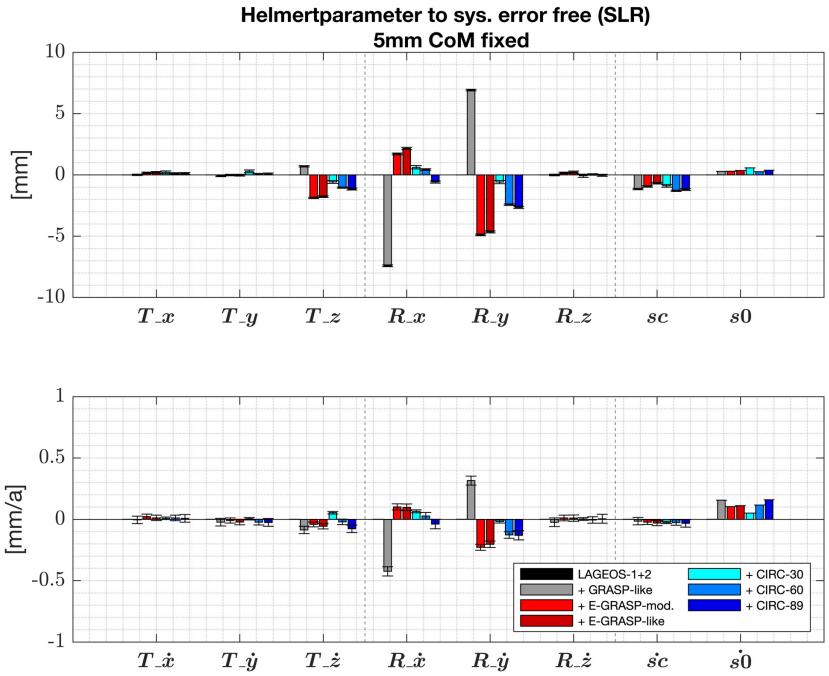

(a) 5 mm 3D CoM displacement

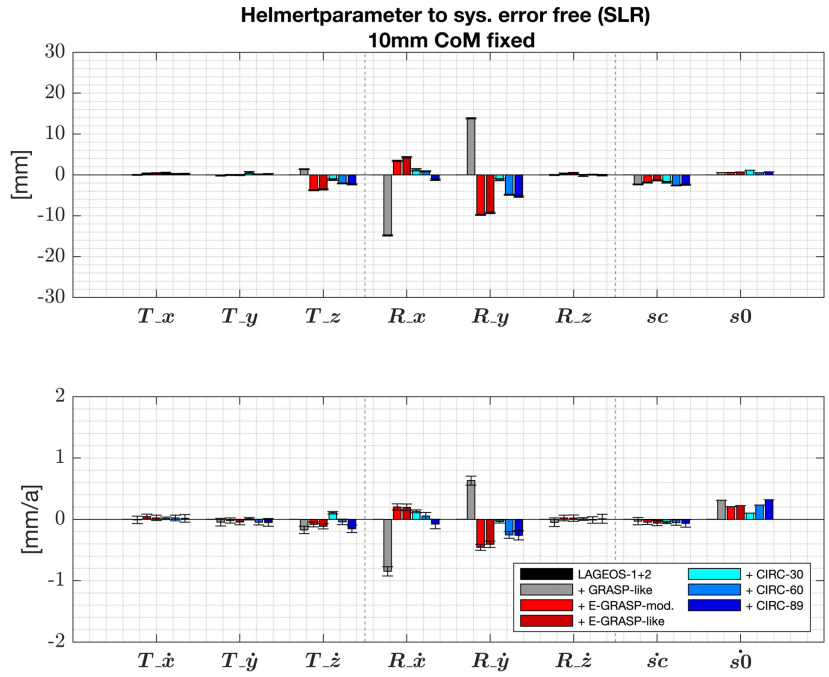

(b) 10 mm 3D CoM displacement

Figure 6.55: Helmert parameters for all stations for 5 mm (Figure a) and 10 mm (Figure b) CoM displacement compared to a priori. The upper figures show the values of the station positions, the lower ones those of the velocities.

The ERPs show the least influence, with the LIP ranging between 2 and 7% and 7 and 30% for 5 and 10 mm displacement respectively.

The E-GRASP-like is the least affected with 14% LIP in the pole coordinates and 8% in LOD for 10 mm displacement. The GRASP-like, E-GRASP-mod and 30 degree circular scenarios are not far off with LIP of 17 to 21% in the pole coordinates and 7 to 14% in LOD. The 60 and 89 degree circular scenarios are most affected with LIP in the range of 24 to 30% and 14 to 18% for the pole coordinates and LOD.

The increase in LIP as the displacement increases from 5 mm to 10 mm is not linear, but in fact overproportionate. For some parameters and scenarios it even exceeds the 100% level.

In general, the E-GRASP-like and 30 degree circular scenario are the least affected. The GRASP-like and E-GRASP-mod scenarios show similarly losses which are in all parameters higher, but the largest overall LIP can be seen for the 60 and especially the 89 degree circular scenario.

Estimating the reference points can reduce any LIP to values in the low single-digit percentage range.

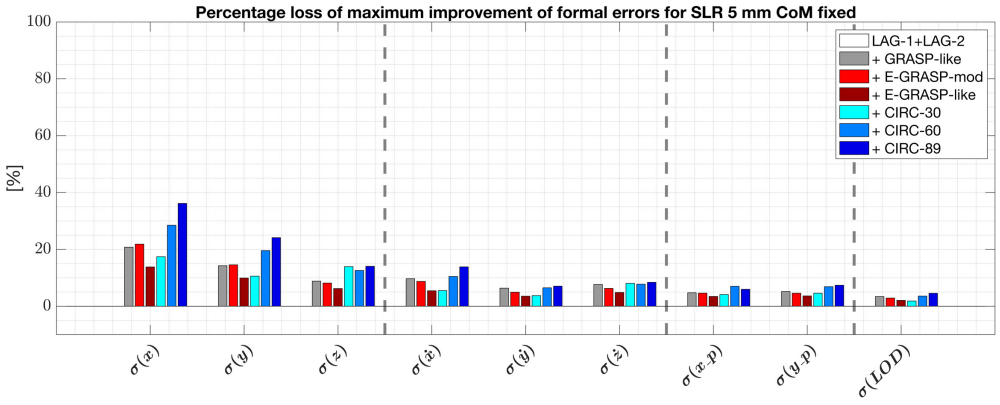

(a) Coordinates in X,Y, and Z.

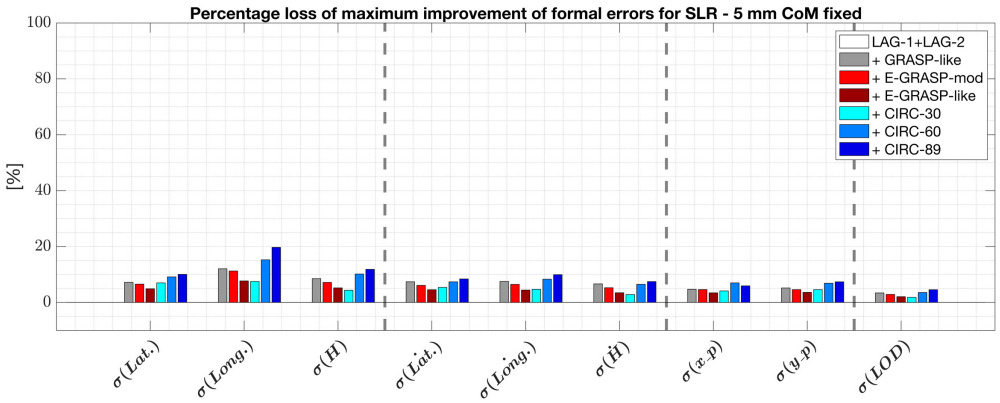

(b) Same as in Fig. a) but for geographic coordinates in Latitude, Longitude, Height.

Figure 6.56: Percentage loss of maximum improvement potential due to 5 mm CoM displacement compared to the systematically error-free case.

ERP analysis The introduced CoM displacement leads to a significant increase in noise in both X and Y-pole for all scenarios (compare Tab. F.33). At 10 mm displacement, this increase is most pronounced for the GRASP-like scenario, where it reaches 58% in X-pole

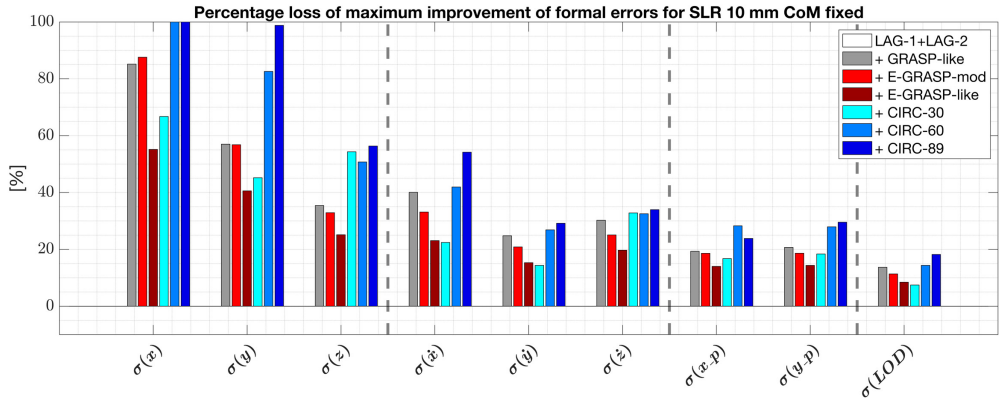

(a) Coordinates in X,Y, and Z.

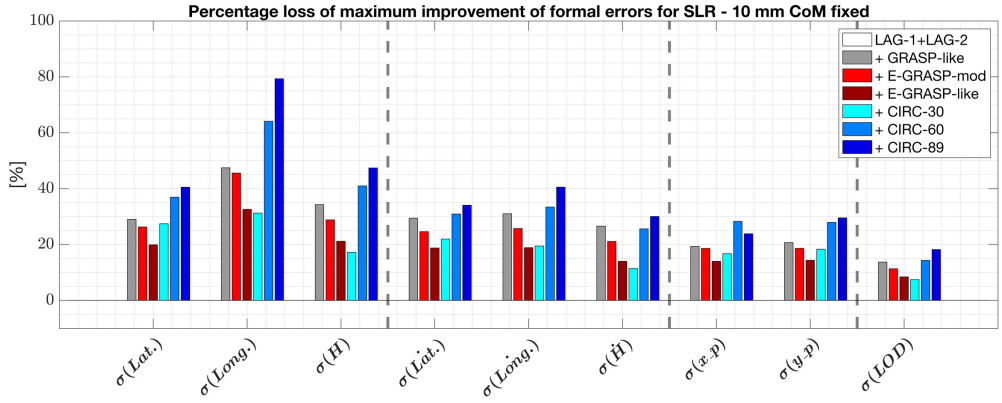

(b) Same as in Fig. a) but for geographic coordinates in Latitude, Longitude, Height.

Figure 6.57: Percentage loss of maximum improvement potential due to 10 mm CoM displacement compared to the systematically error-free case.

and 66% in Y-pole. The E-GRASP-mod and E-GRASP-like scenarios are less affected and show a similar increase in noise of 30-33% in the X-pole and 10-11% in the Y-pole. The circular scenarios are the least affected with increases between 11 and 23%, with the near-polar scenario showing the highest increases.

There is also an offset in the pole coordinates. In the GRASP-like scenario the bias amounts to 11.5 and 16.6 mm in the X and Y-pole. The E-GRASP-mod and E-GRASP-like scenarios show a primary bias in the X-Pol, which is approximately equal to the amount of the introduced 3D displacement. In the circular scenarios, smaller biases are observed, also mainly in the X-Pol. Here they reach about 50% of the introduced 3D displacement, in the Y-pole they are below 1.5 mm. The circular scenario at 30 degree inclination is less sensitive, since it shows a maximum deviation of 2 mm in the X-pole.

A significant trend in the pole coordinates is seen mainly for the GRASP-like scenario, with a drift of 0.6 and 0.7 mm/a in X and Y respectively. Again, the E-GRASP-mod and E-GRASP-like scenarios are comparatively less affected, with a maximum drift of 0.4 mm/a. For the circular scenarios, the scenarios at 60 and 89 degree inclination show a drift of about 0.2-3 mm/a, while the scenario at 30 degrees shows a drift of less than 0.1 mm/a.

In LOD, all scenarios show a significant increase in noise. This is largest for the GRASP-like and the two circular scenarios with 60 and 89 degrees inclination, ranging from 23 to 30%. The increase for the E-GRASP-mod, E-GRASP-like and the 30 degree circular scenario is in

the range of 10-15%. A significant bias can only be detected for the GRASP-like scenario, where it reaches 0.26 mm/a. No trend in LOD can be detected for any of the scenarios.

In each scenario, estimating the reference points can reduce the increased noise and remove the bias and drift to the values of the systematically error-free cases.

Spectral analysis of the ERPs shows that, for LOD solely the 60 degree circular scenario shows influences to amplitudes larger than 0.1 mm. Here, a signal arises at 263 days, with respective amplitudes of 0.1 and 0.16 mm for 5 and 10 mm CoM displacement, respectively. In the pole coordinates, variations in the spectra are largely dominated by the occuring biases and drifts. Coestimating the CoM coordinates can eliminate all variations seen in the amplitude spectra of the ERPs. (Amplitude spectra of the 10 mm displacement case can be found in App. G.2 in Fig. G.19–G.24.)

As with DORIS, it is noteworthy that the very poorly estimated CoM values of the circular scenarios in the transversal direction are not reflected in the TRF and the ERPs. They are most likely absorbed by the initial state elements.

Conclusion - systematic center-of-mass displacement The coordinates of the CoM have been shifted by 3 and 6 mm in all three axes, corresponding to approximately 5 and 10 mm in three dimensions.

A systematic shift only leads to a systematic shift in the along-track direction of the orbit, where it is reflected at 100%. The degradation of orbit accuracy for the two eccentric scenarios, E-GRASP-mod and E-GRASP-like, is greatest in the radial component. In the cross-track direction it is the 30 degree circular scenario. These three scenarios also appear to be the most affected in terms of geographical patterns in the orbit comparison. Overall, an increase in the mean RMS values of the orbit comparison in three dimensions is at the level of a factor of 2.4 to 3.9 in the case of a 3 mm displacement. The best results are obtained for the two circular scenarios with 60 and 89 degrees inclination, the GRASP-like scenario shows the least geographical patterns in the orbit comparisons.

The effect on the TRF is significant for all scenarios and is smallest for the 30 degree circular scenario. The LIP in the formal errors is strongest for the positions. The velocities are less affected and the ERPs the least. The E-GRASP-like and the 30 degree circular scenario show a slight advantage here.

The influence on the estimated ERPs shows a significant increase in noise for all scenarios, most pronounced up to 66% for a 3D shift of 10 mm for the GRASP-like scenario and up to 23% for the circular scenarios. Significant biases and drifts can be observed for all scenarios, and are particularly evident in the pole coordinates. Again, the circular scenarios are the least affected, but here too a systematic reference point shift is reflected with about 50% of the introduced 3D shift.

Reference point estimation is possible for all scenarios in the radial and normal directions. In the transversal direction this is not possible for the circular scenarios. The co-estimation of the reference points can account for almost all systematic effects on the TRF and the ERPs, as well as increased noise in the ERPs and LIP in the formal errors.

The introduction of systematic CoM displacements shows a significant influence for all scenarios, which should be avoided. The higher orbiting circular scenarios generally show a smaller influence, but since up to 50% of the introduced 3D shift can be found in the pole coordinates, the eccentricities of the satellite should be determined as accurately as possible before launch.

The evaluation of the SLR CoM mismodelling is given in Tab. 6.28.

Table 6.28: Vulnerability of the satellite scenarios for SLR for systematic CoM mismodelling. Ranking of formal errors for the CoM fixed and estimated cases are summarised.

	G-like	E-G-mod	E-G-like	Circ. 30°	Circ. 60°	Circ. 89°
Orbit	②	③	③	②	②	②
CoM est.	①	①	①	②	②	②
Helmert CoM fixed	③	③	③	①	②	②
Helmert CoM est.	①	①	①	①	①	①
Station pos. form. err.	②	②	②	②	③	③
Station veloc. form. err.	②	②	①	①	②	③
Pole coord. form. err.	②	②	②	②	③	③
LOD form. err.	②	②	①	①	③	③
ERPs est. CoM fixed	③	②	②	①	①	②
ERPs est. CoM est.	①	①	①	①	①	①
Summary	1.9	1.9	1.7	1.4	2.0	2.2

6.2.2.3 Influence of atmospheric drag mismodelling

The mismodelling of the atmospheric drag follows the same procedure as for DORIS. For details of the perturbations introduced, see Sec. 6.1.2.3. To compensate for the mismodelling introduced, the parameterisation in Tab. 6.29 is used for all satellites in the SLR processing. Compared to DORIS, further empirical accelerations have been introduced. In particular, the 1/rev terms are necessary to achieve a good orbital fit due to the lower density of observations.

Table 6.29: Used dynamic parameterisation and estimated parameters for the atmospheric drag mismodelling case.

Parameterisation for atmospheric drag mismodelling case	
All scenarios	
Arc length	7 days
Initial state parameters	estimated
Atmospheric drag parameters	one global scaling factor per arc and scaling factors every 12h set up as piecewise linear polygon
Empirical accelerations	Piecewise linear continuous in transversal direction every 24h, cosine and sine 1/rev after 24, 48, 72, 96, 120, 144 h in transversal direction

Orbital fit The atmospheric drag mismodelling does not lead to any difference in the orbital fits (minimum, maximum, RMS, mean, standard deviation) compared to the systematic error-free scenario. The global distribution of the differences in the residuals shows higher noise in the spot-like observation regions for the GRASP-like scenario (see Fig. 6.58). For the E-GRASP-like and 89 degree circular scenarios, the increased noise is only visible in regions with fewer observations. Regions with more observations, such as Europe and Australia,

show significantly less noise in the differences. For the other scenarios, the influence is much weaker.

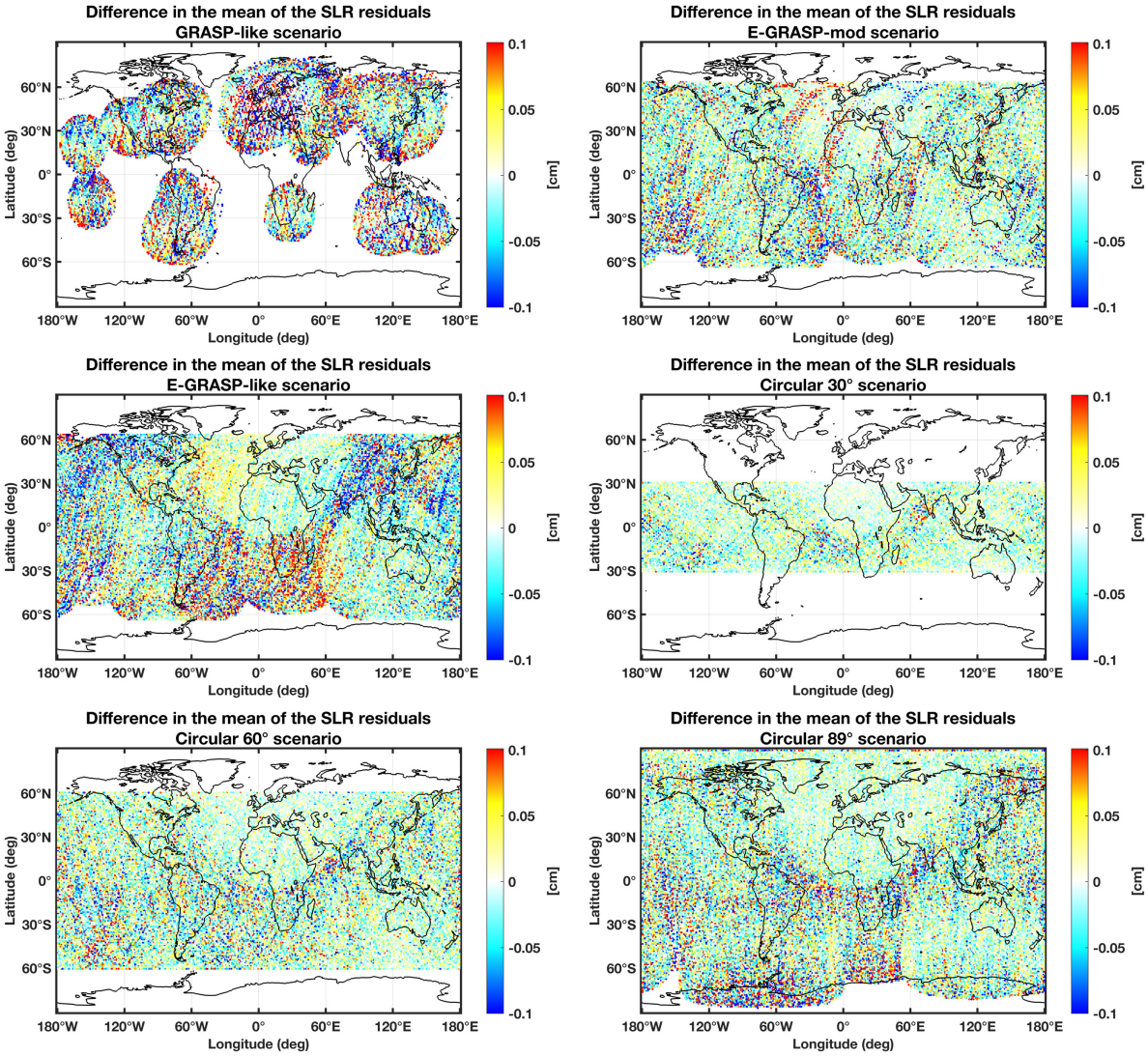

Figure 6.58: Global distribution of the difference in the mean of the observation residuals for the atmospheric drag mismodelling case compared to systematic error-free.

Orbit recovery Fig. 6.59 shows the mean orbit differences. The degradation in orbit accuracy is mainly in the radial and along-track direction. The GRASP-like and E-GRASP-like scenarios are most affected, with an increase of about a factor of five in both components. The other scenarios are less affected and show an increase of about a factor of three in both components. In the cross-track direction, all scenarios are similarly affected, with the difference increasing by approximately 30%. The radial and cross-track directions remain the better determined ones. A systematic bias in the orbits greater than 0.1 mm cannot be detected for any of the scenarios.

Geographical orbit differences can be found mainly for the GRASP-like and E-GRASP-like scenarios, as was also the case for DORIS. Again, a West-East pattern can be seen in the radial direction, with an amplitude of 0.15 and 0.2 mm (see Fig. 6.60). There is a correlation with the along-track direction, but the amplitude is significantly larger here at

0.67 and 0.95 mm. The other scenarios show almost no pattern in the radial direction, the circular scenarios show a very small North-South stripe pattern. In the along-track direction, these scenarios largely reflect the increased noise. In the cross-track direction, only the E-GRASP-like scenario shows a clear pattern with a North-South distribution of 0.2 mm amplitude.

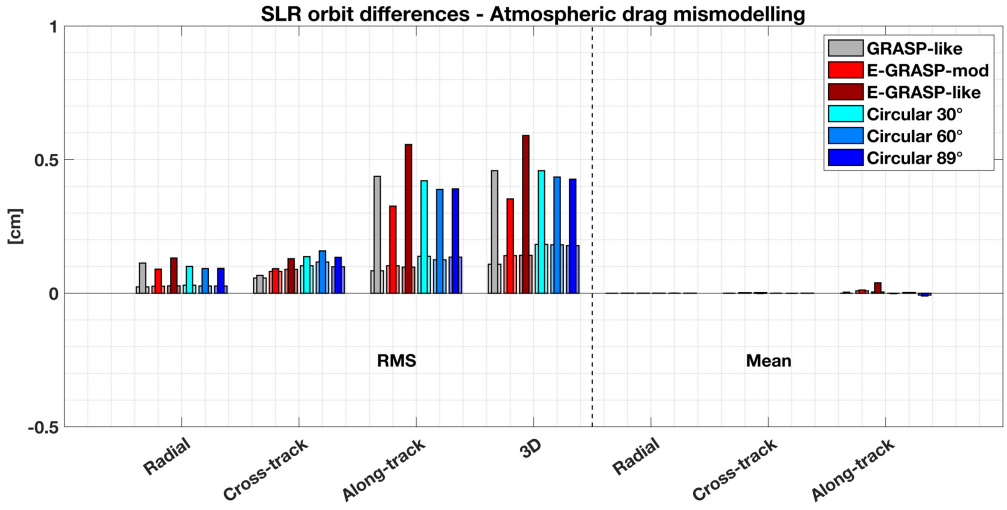

Figure 6.59: Mean RMS and mean values of the orbit comparison of the simulated and recovered orbit for the atmospheric drag mismodelled case. The thinner bars show the results of the drag mismodelling case, the slightly more transparent thicker bars in the background show the values achieved in the systematic error-free case.

Reference frame

Helmert parameters The influence on the TRF is mostly pronounced for the GRASP-like and E-GRASP-like scenarios in the Helmert parameters (see Tab. F.34). In these scenarios significant X-rotations of 1.0 and 2.8 mm can be seen, as well as a Y-rotation of 0.5 mm in both scenarios. The E-GRASP-mod and 30 degree circular scenarios are less affected, where significant rotations are found only in X, reaching 0.26 and 0.13 mm. A significant effect on station velocities is only found for the E-GRASP-like scenario, where an X-rotation of 0.16 mm/a occurs. The circular scenarios at 60 and 89 degrees inclination show no significant effect in the Helmert parameters. For all scenarios, there is no significant influence on the translations or the scale.

Formal errors The LIP in the station positions is 6 to 26% in Cartesian coordinates and 5 to 19% in geographic coordinates for all scenarios, with little difference between the components (see Tab. F.35 in App. F.2). The GRASP-like and E-GRASP-like scenarios demonstrate the greatest losses. The 30 degree circular scenario shows the second greatest loss, which is more pronounced in the Y, and longitude components. The 89 degree circular scenario achieves the best results.

In terms of velocities, losses range from 4 to 17% in Cartesian coordinates and from 5 to 15% in geographic coordinates. In Cartesian coordinates, the differences between the scenarios are less pronounced, with the GRASP-like and E-GRASP-like scenarios being most affected in the Z component. In geographic coordinates, the largest losses are found

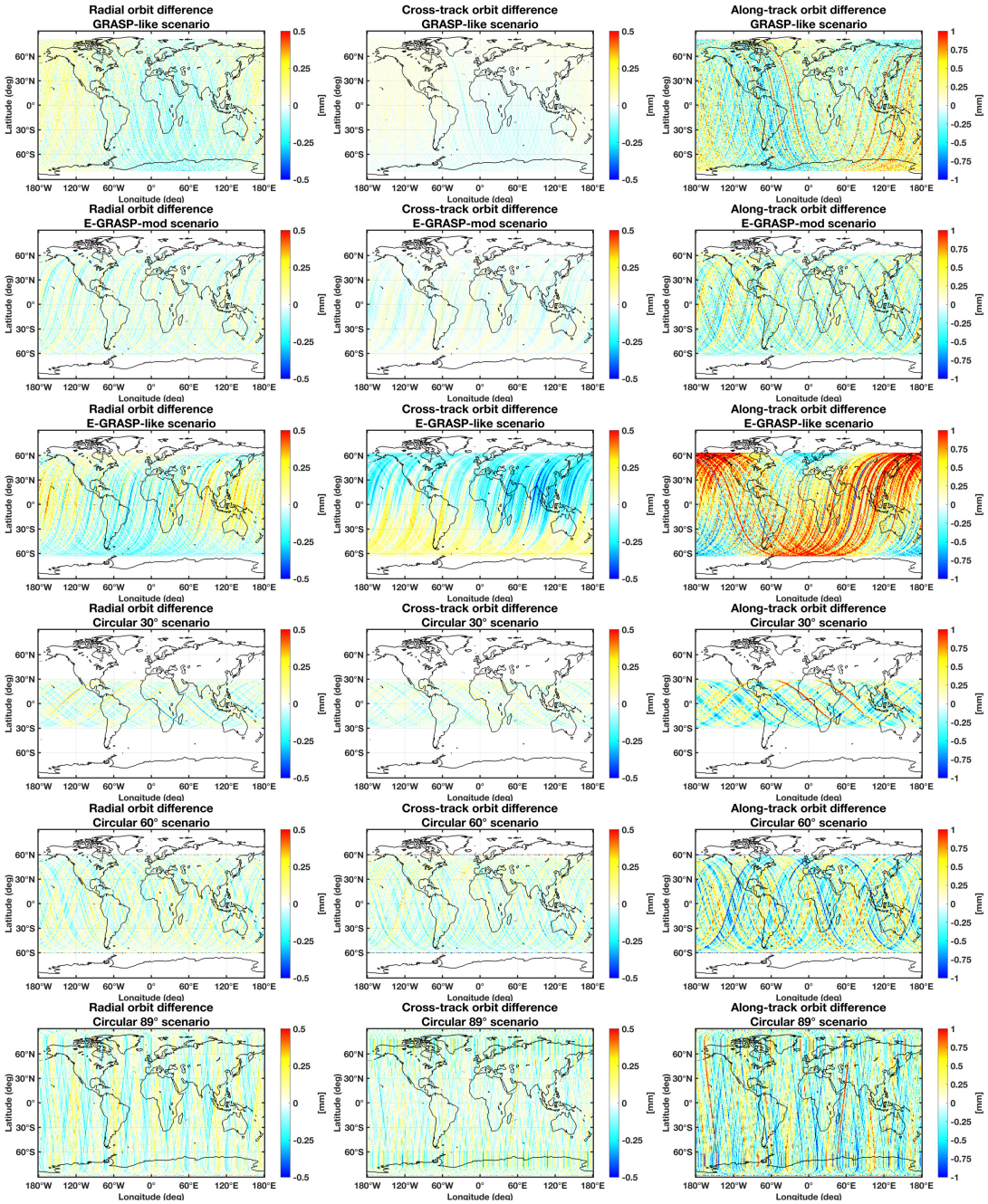

Figure 6.60: Mean orbit differences of the true simulated and recovered orbit over the full simulation time span of 7 years for the atmospheric drag mismodelling case. From left to right in radial, cross-track, and along-track direction. From the top to the bootom, GRASP-like, E-GRASP-mod, E-GRASP-like, Circular 30°, Circular 60°, Circular 89°

in the latitude and height components of the GRASP-like and E-GRASP-like scenarios, reaching up to 15%. Differences in the longitude component are rather small, with LIP in the range of 5 to 10% for all scenarios.

In the pole coordinates, again the GRASP-like and E-GRASP-like scenarios show the largest losses with 31 to 46%, while the other scenarios show less LIP, with 19 to 27%. In LOD, the 30 degree circular scenario is by far the most affected with 65% LIP, the E-GRASP-mod, E-GRASP-like and 60 degree circular scenarios show similar losses ranging from 31 to 39%. The GRASP-like and 89 degree circular scenarios are much less affected with 13 and 9%, respectively, where a near polar orbit seems to be advantageous regardless of the altitude of the orbit.

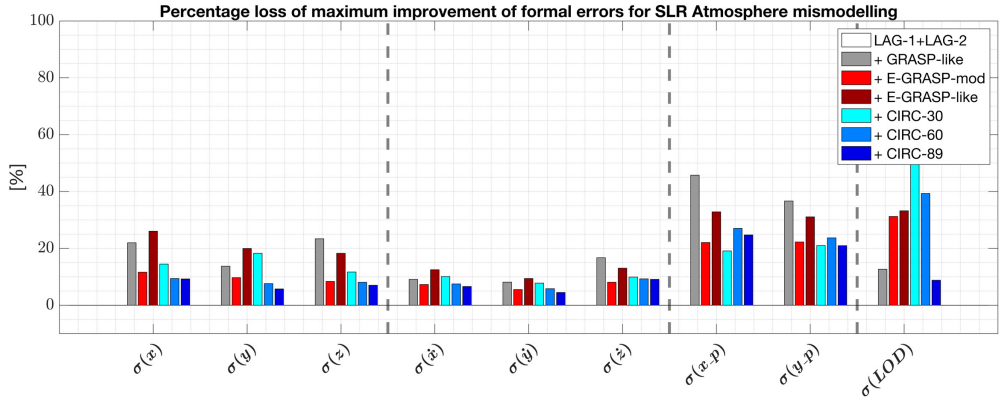

(a) Coordinates in X,Y, and Z.

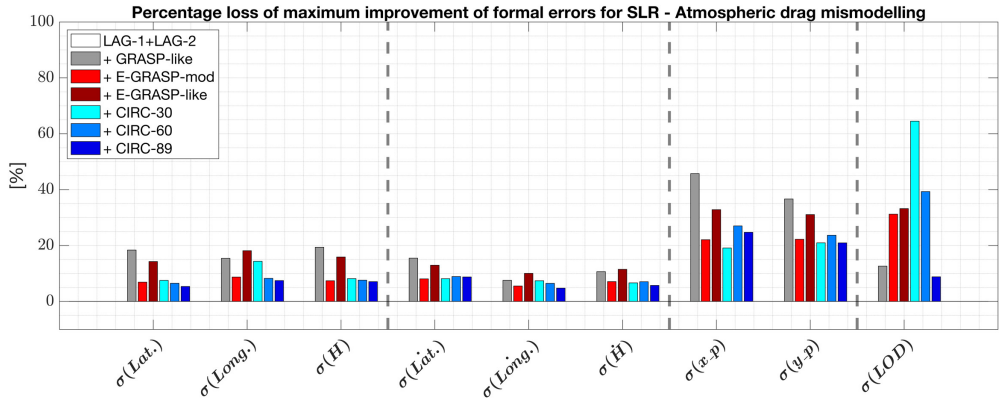

(b) Same as in Fig. a) but for geographic coordinates in Latitude, Longitude, Height.

Figure 6.61: Percentage loss of maximum improvement potential due to atmospheric drag mismodelling compared to the systematically error-free case.

ERP analysis The a posteriori ERP analysis (see Tab. F.36 in App. F.2) shows a significant increase of the noise in the pole coordinates for all scenarios. For the GRASP-like and E-GRASP-like scenarios this increase is between 14 and 17%, and for the other scenarios between 5 and 10%. There is also a bias in both pole coordinates for the GRASP-like and E-GRASP-like scenarios, which is 0.4 and 0.6 mm in the X-pole and 1 mm and 3.1 mm in the Y-pole. Of all the other scenarios, only the E-GRASP-mod scenario shows a bias of 0.5 mm only in the Y-pole, while the other biases are below 0.1 mm. A variation of the drift behaviour in the pole coordinates is only significant in a few cases and the variations are well

below 0.1 mm/a. A drift beyond this can only be determined for the E-GRASP-mod scenario, which is 0.18 mm/a.

In LOD, the influence is limited to an increase in noise. This is only significant for the E-GRASP-mod, E-GRASP-like and the 30 and 60 degree circular scenarios and is 9, 13, 23 and 10% respectively. No significant offset or drift can be detected.

Spectral analysis of the ERPs shows only minor influences. The largest influence is for the pole coordinates, where variation can be detected for the GRASP-like and E-GRASP-like scenarios only. The GRASP-like scenario shows induced signals with amplitudes close to 0.1 mm at 159 and 287 days, as well as close to annual (see Fig. G.25). In the E-GRASP-like scenario, the spectrum is largely dominated by occurring bias and drift (see Fig. G.26). In LOD, variations are below 0.1 mm for all scenarios.

Conclusion - atmospheric drag mismodelling The strongest influence due to atmospheric drag mismodelling is seen for the GRASP-like and E-GRASP-like scenarios.

The influence on orbit accuracy is mainly seen in the GRASP-like and E-GRASP-like scenarios, where the three-dimensional RMS of the orbit differences increases by a factor of about 4. In addition, the E-GRASP-like scenario has the largest geographical orbit differences in all three directions.

Similar results can be seen for the influence on the TRF. Significant rotations in the millimetre range are found for the GRASP-like and E-GRASP-like scenarios.

The formal errors of the station positions increase significantly for all scenarios, again most strongly for the GRASP-like and E-GRASP-like scenarios with LIP values up to 26%. LIP for velocities are significantly lower.

The pole coordinates show significant LIP for all scenarios, with the most pronounced values in the GRASP-like and E-GRASP-like scenarios, ranging from 31 to 46%. For LOD the 30 degree circular scenario is particularly affected.

The spectral analysis of the ERPs shows only minor influence at the pole coordinates for the GRASP-like and E-GRASP-like scenarios.

In summary, the GRASP-like and E-GRASP-like scenarios are most affected by the drag mismodelling. The other scenarios are much less affected, with the best results obtained by the E-GRASP-mod and the 60 and 89 degree circular scenarios (compare Tab. 6.30).

Table 6.30: Vulnerability of the satellite scenarios for SLR for systematic atmospheric drag mismodelling.

	G-like	E-G-mod	E-G-like	Circ. 30°	Circ. 60°	Circ. 89°
Orbit	②	①	③	①	①	①
Helmert	②	①	②	①	①	①
Station pos. form. err.	③	②	③	②	②	②
Station veloc. form. err.	②	①	②	①	①	①
Pole coord. form. err.	③	②	③	②	②	②
LOD form. err.	①	②	②	③	②	①
ERPs	②	①	②	①	①	①
Summary	2.1	1.4	2.4	1.6	1.4	1.3

6.2.2.4 Influence of solar radiation pressure mismodelling

The mismodelling of SRP follows the same procedure as for DORIS. For details of the perturbation introduced, see Sec. 6.1.2.4.

In order to absorb the introduced perturbations, the parameterisation of Tab. 6.31 is used for all satellites. Compared to the parameterisation used for DORIS, global scaling factors are estimated for SRP and albedo, and just one global scaling factor. This is necessary because estimating too many dynamic parameters in the case of SLR makes the solution more unstable due to the lower density of observations.

Table 6.31: Dynamic parameterisation and estimated parameters for the SRP mismodelling case.

SRP mismodelling parameterisation	
All scenarios	
Arc length	7 days
Initial state parameters	Estimated
SRP parameters	One global scaling factor per arc
Albedo parameters	One global scaling factor per arc
Atmospheric drag parameters	One global scaling factor per arc
Empirical accelerations	Piecewise linear continuous in transversal direction every 24h, cosine and sine 1/rev after 24, 48, 72, 96, 120, 144 h in transversal and normal direction

Orbital fit The introduced mismodelling of the SRP leads to almost no differences in the orbital fits (minimum, maximum, RMS, mean, standard deviation) compared to the systematic error-free case for any of the satellite scenarios. The differences are in the sub-millimetre range. The geographical distribution of the residuals shows no change for regions with higher observation coverage (see Fig. 6.62). In the GRASP-like scenario, increased noise of the residuals is observed at the edge of observation regions where stations observe at low elevation. For the other scenarios, increased noise is only observed in regions with lower observation density.

Orbit recovery The orbit comparison shows that for all scenarios the mean RMS of the orbit differences in radial, cross-track and along-track directions increases by a factor of about four (compare Fig. 6.63). No significant offsets in the orbit differences are evident in any of the scenarios, with the mean orbital differences reaching a maximum level of 1/100 mm.

The geographical distribution of the orbit differences in Fig. 6.64, shows for the E-GRASP-mod and 89 degree circular scenario a pattern in the radial component, where maxima around the equator and minima at the poles are visible, which have an amplitude of 0.14 and 0.22 mm respectively. Comparable patterns in the other scenarios are much weaker.

In the cross-track direction, the GRASP-like scenario shows a slight West-East pattern with an amplitude of about 0.3 mm. The E-GRASP-mod and E-GRASP-like scenarios largely reflect the increased noise in the orbit differences and an amplification of the aforementioned stripe pattern along ascending arcs (see also Sec. 6.1.2.1). Here the amplitudes of the

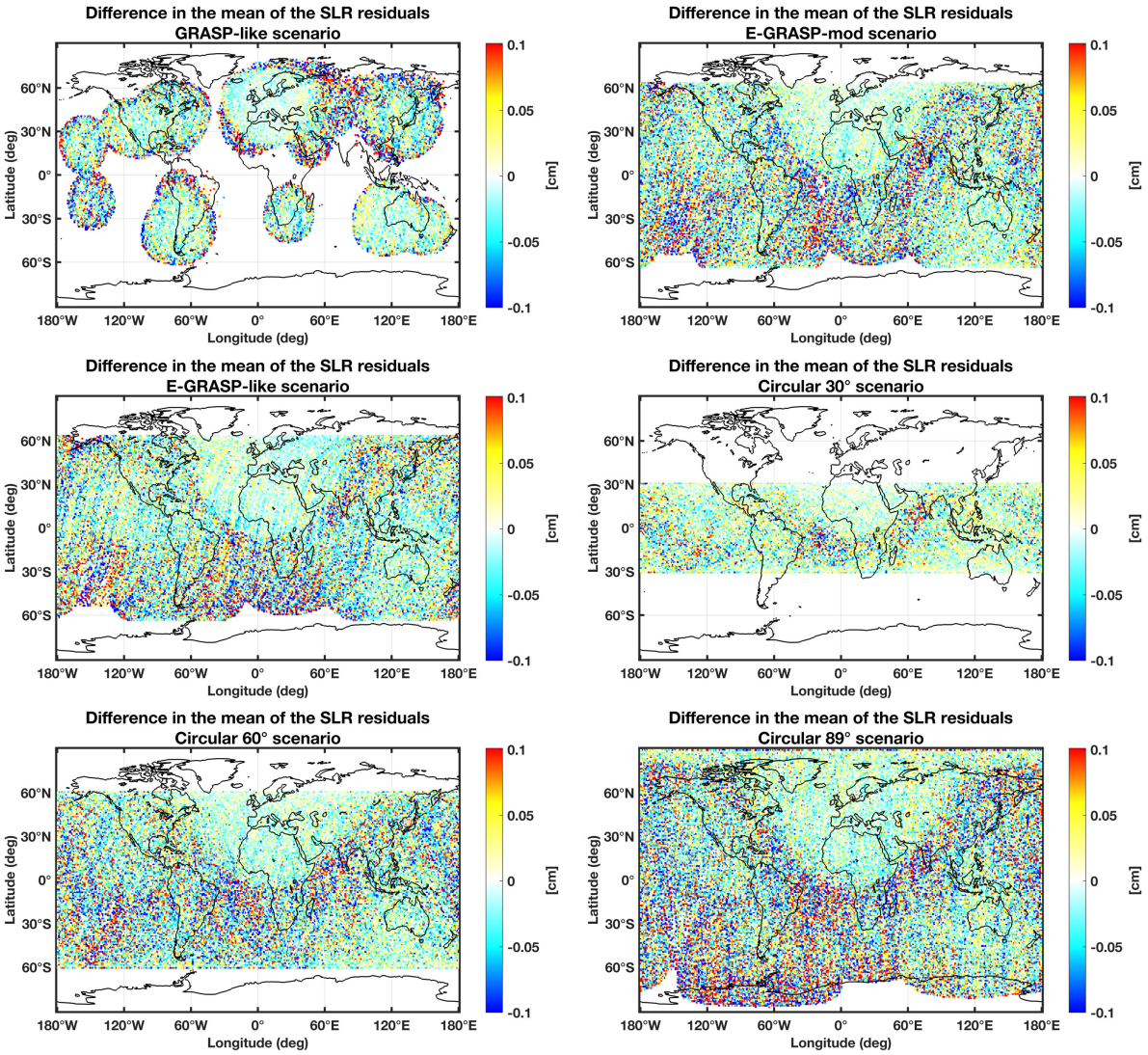

Figure 6.62: Global distribution of the difference in the mean of the observation residuals for the SRP mismodelling case compared to systematic error-free.

eight maxima are amplified to 0.45 mm in both scenarios. The two circular scenarios at 30 and 60 degrees inclination only reflect the increased noise of the orbit differences, with no discernible geographical pattern. The situation is similar for the 89 degree circular scenario, but here an additional pattern appears, with maxima at 90 degrees longitude intervals, alternating at the North and South poles. The amplitude of these extrema is about 0.6 mm.

In the along-track direction, only the E-GRASP-like scenario shows a North-South pattern with an amplitude of about 0.5 mm. The other scenarios only reflect the increased noise of the orbit differences. There is no clear correlation between the mean geographical orbit differences and the geographical distribution of the observation residuals.

Reference frame

Helmert parameters There is almost no systematic influence on the TRF. There are occasional rotations, but they are small or at the 3 sigma limit of the parameter in question. The maximum rotations are around 0.1 mm in the positions, while there are no significant

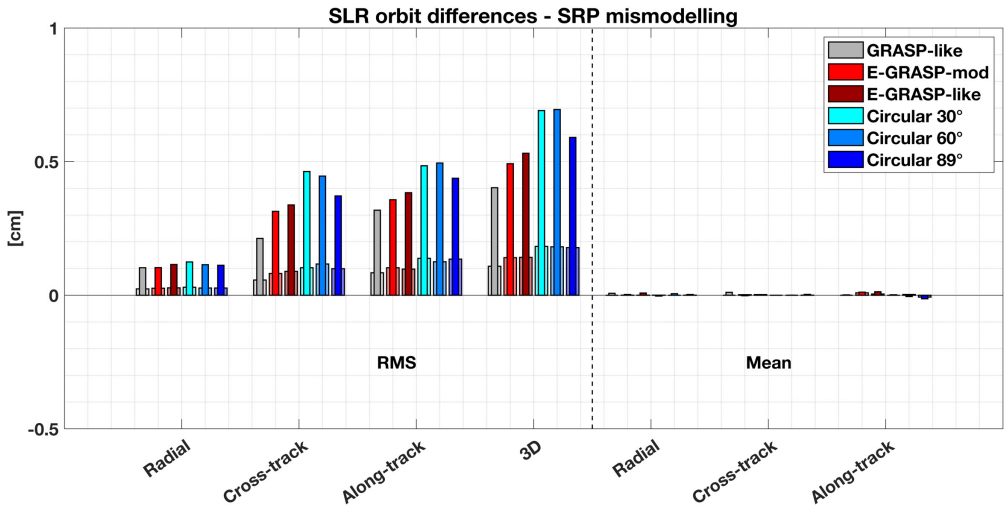

Figure 6.63: Mean RMS and mean values of the orbit comparison of the simulated and recovered orbit for the SRP mismodelled case. The thinner bars show the results of the SRP mismodelling cases, the slightly more transparent thicker bars in the background show the values achieved in the systematic error-free case.

rotations in the velocities. There is no significant influence on the translations, and the scale (see Tab. F.37 in App. F.2).

Formal errors The analysis of the LIP (see Fig. 6.65 and Tab. F.38 in App. F.2) in the formal errors shows that in the station coordinates, the losses in Cartesian coordinates in the X coordinate are at a similar level for all scenarios between 11 and 18%. In the Y component, the 30 degree circular scenario is the most affected with LIP of 24%, the other scenarios are in the range of 6 to 13%. In the Z component, the scenarios show a comparable loss, ranging from 9 to 15%.

In geographical coordinates, the LIP is in the range of 7 to 15% for all components and scenarios, except for the 30 degree circular scenario in the longitude component, where an LIP of 20% is reached. The E-GRASP-mod and the 60 and 89 degree circular scenarios achieve slightly better results for all components.

Similar losses are observed in all velocity directions in Cartesian coordinates for all scenarios, ranging from 6 to 14%. In geographic coordinates, losses are also uniform across all scenarios, ranging from 7 to 13% across all components, with the longitude component experiencing the least impact.

For the ERPs, all scenarios show similar losses, ranging from 25 to 34% for the pole coordinates and from 70 to 82% for LOD.

ERP analysis The estimated ERPs show a significant increase in noise in the X-pole of 8 to 15% and in the Y-pole of 7 to 11% (see Tab. F.39). All scenarios show significant biases in both pole coordinates compared to a priori, but the change compared to the respective systematic error-free cases is no more than 0.1 mm for all scenarios. Significant trends can be detected mainly in the Y-pole, but here the variations are below 0.01 mm/a.

In the case of LOD, the increase in noise is largest for the 30 degree circular scenario at 29%. The other scenarios show increases in the range of 18 to 23%. No significant offset or drift can be found for any of the scenarios.

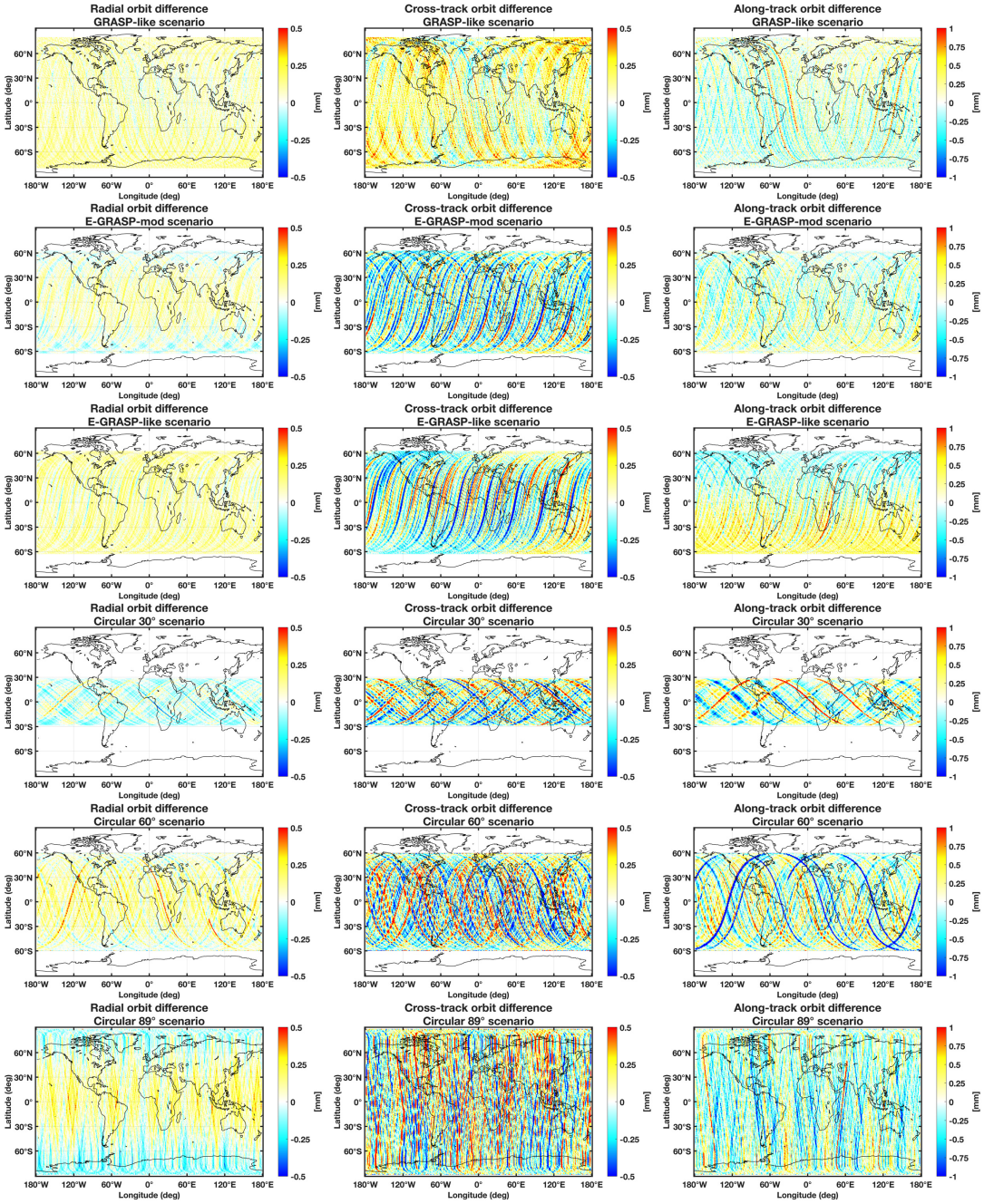

Figure 6.64: Mean orbit differences of the true simulated and recovered orbit over the full simulation time span of 7 years for the SRP mismodelling scenario. From left to right in radial, cross-track, and along-track direction. From the top to the bottom, GRASP-like, E-GRASP-mod, E-GRASP-like, Circular 30°, Circular 60°, Circular 89°.

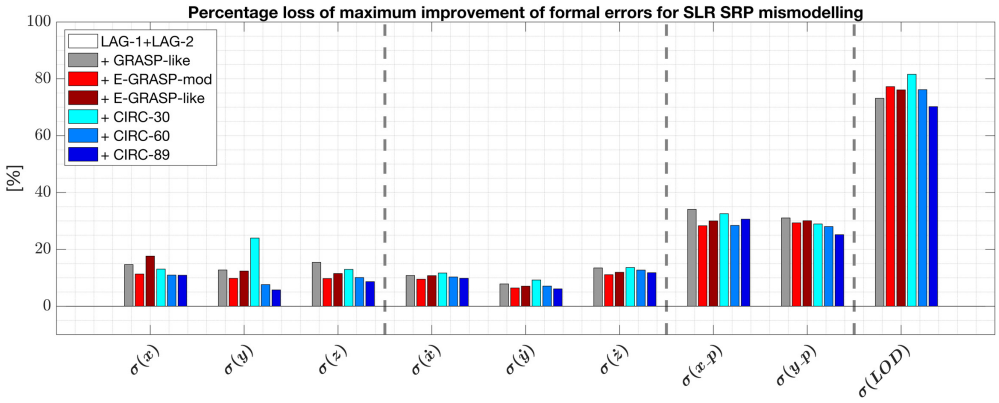

(a) Percentage loss of maximum improvement potential due to SRP mismodelling. Coordinates in X,Y, and Z

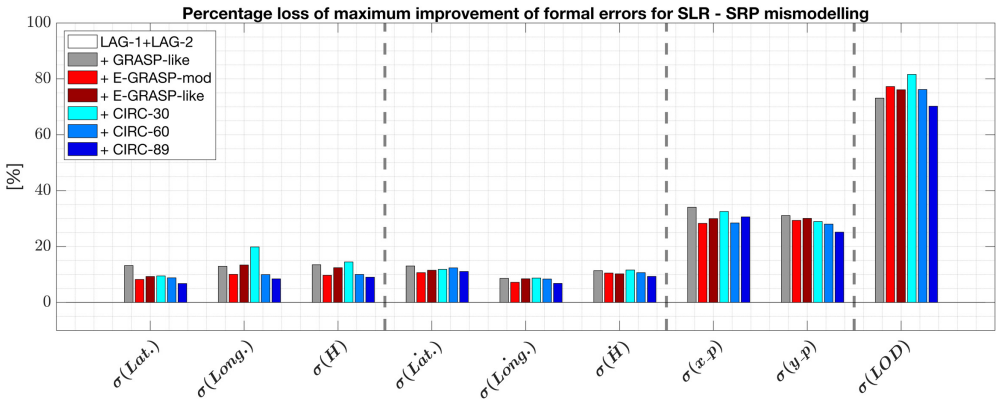

(b) Same as in Fig. a) but for coordinates in Latitude, Longitude, Height.

Figure 6.65: Differences of the percentage improvements compared to the systematically error-free case. +10% means that from the full potential of improvement of the systematic error-free case 10% are lost. Figure a) shows the values for X,Y and Z, Figure b) the values for Latitude, Longitude, Height.

For all scenarios, variations in the spectral analysis of the pole coordinates are well below 0.1 mm. In LOD, the variations are stronger, but still small. The largest variations, approaching 0.1 mm, are seen in the GRASP-like and 60degree circular scenarios. These signals have wavelengths close to annual for the GRASP-like scenario (nodal period) and of about 123 and 259 days for the 60degree circular scenario (half and full beta cycle).

Conclusion - SRP mismodelling The introduced SRP mismodelling leads to a comparable degradation of the orbit accuracy in all scenarios, with the RMS values increasing by a factor of about 4. Geographical patterns in the orbit differences could be found in the submillimetre range for several scenarios, and none of the scenarios is clearly advantageous.

No significant systematic effect on the TRF could be detected for any of the scenarios. The mean LIP in the station positions is below 20% for almost all scenarios and components and below 15% for the velocities. The losses in the pole coordinates are much larger and are about 30%, in LOD up to about 80%. The differences between the scenarios are very small.

Systematic effects on the ERPs are almost exclusively seen as an increase in noise, reaching up to 15% in the pole coordinates and 29% in LOD. Signal variations in the spectral

analysis of the ERPs show isolated signal mainly for the GRASP-like and 60 degree circular scenarios, with maximum amplitude close to 0.1 mm.

Based on the results of the SRP mismodelling, none of the scenarios is clearly advantageous. There are significant impacts for all scenarios, but these are mostly moderate. This is reflected in the average results of the vulnerability assessment, from which no clear recommendation can be made for reducing the impact of the SRP mismodelling on the TRF and ERPs (see Tab. 6.32).

Table 6.32: Vulnerability of the satellite scenarios for SLR for systematic SRP mismodelling.

	G-like	E-G-mod	E-G-like	Circ. 30°	Circ. 60°	Circ. 89°
Orbit	②	②	②	②	②	②
Helmert	①	①	①	①	①	①
Station pos. form. err.	②	②	②	②	②	②
Station veloc. form. err.	②	②	②	②	②	②
Pole coord. form. err.	②	②	②	②	②	②
LOD form. err.	③	③	③	③	③	③
ERPs	①	①	②	①	①	①
Summary	1.9	1.9	2.0	1.9	1.9	1.9

6.2.2.5 Influence of Earth gravity field mismodelling

The investigation of the influence of EGM mismodelling follows the same approach as for DORIS. Details of the introduced mismodelling and the quantification of the resulting perturbation acceleration are given in Sec. 6.1.2.6.

The parameterisation used to absorb the introduced perturbations is listed in Tab. 6.33. It is identical to the parameterisation used for the SRP mismodelling case (see Sec. 6.2.2.4). Compared to the parameterisation used for DORIS, the empirical coefficients used have a lower density in time, but a global albedo scaling factor is estimated here.

Table 6.33: Used dynamic parameterisation and estimated parameters for the EGM mismodelling case.

SRP mismodelling parameterisation	
All scenarios	
Arc length	7 days
Initial state parameters	Estimated
SRP parameters	One global scaling factor per arc
Albedo parameters	One global scaling factor per arc
Atmospheric drag parameters	One global scaling factor per arc
Empirical accelerations	Piecewise linear continuous in transversal direction every 24h, cosine and sine 1/rev after 24, 48, 72, 96, 120, 144 h in transversal and normal direction

Orbital fit The mismodelling shows the strongest influence on the orbital fit of the GRASP-like scenario. Here the RMS increases by about 28% and there is a systematic offset of -0.7 mm in the mean. The effect on the other scenarios is much smaller, with only the E-GRASP-mod and E-GRASP-like scenarios showing an increase in RMS of about 2%, otherwise there is no effect on the orbital fit.

The effect on the geographical distribution of the residuals (Fig. 6.66) is by far the largest in this case of mismodelling. The strongest influences can be seen in the GRASP-like scenario, where the variations in the mean values reach up to 1.5 cm. The E-GRASP-mod and E-GRASP-like scenarios are the second most affected, with variations showing a slight West-East pattern and a maximum amplitude of about 5 mm. The circular scenarios are much less affected. A similar pattern is most pronounced for the scenario at 60 degree inclination, which follows a similar West-East pattern.

A correlation with the geographical distribution of the number of observations can be found mainly for all scenarios except the GRASP-like scenario. In the GRASP-like scenario, the magnitude of the perturbation due to the orbital altitude and the patchy coverage of the observations probably mask the visibility of the correlation.

Orbit recovery The orbit comparison shows a similar result to the influence on the residuals. The influence on the GRASP-like scenario is by far the largest (see Fig. 6.67). Here, the mean RMS of the three-dimensional orbit comparison increases by a factor of 19. The radial and along-track directions are most affected. The E-GRASP-mod and E-GRASP-like scenarios are less affected. Here, the increase is by a factor of 7, with the cross-track direction again being less affected. The circular scenarios show the least influence, with an increase in RMS in all components by about a factor of 4. A systematic bias can primarily be determined for the GRASP-like, E-GRASP-mod and E-GRASP-like scenarios, which are at -0.3, 0.4 and 0.9 mm in the cross-track direction and at -1.8, -1.1 and -1.1 mm in the along-track direction. For the circular scenarios, a systematic bias exceeding 0.1 mm is only observed in the along-track direction and for the scenario at 60 and 89 degree inclination, with values of -0.5 mm and -0.2 mm, respectively.

The geographical distribution of the orbit differences (Fig. 6.68) show the largest influences for the GRASP-like scenario. There is a systematic West-East pattern in the radial and cross-track components, with amplitudes of 6 and 8 mm. In the along-track direction, the West-East pattern is less pronounced and shows four maxima at intervals of about 90 degrees longitude. The maximum amplitude is about 10 mm. The E-GRASP-mod and E-GRASP-like scenarios are less affected, with a West-East pattern also appearing in the radial direction, but in the opposite direction to the GRASP-like scenario. This was also observed for DORIS, where it was attributed to the prograde and retrograde inclination of the orbit. The amplitude of this variation is in the range of 1.6 and 2.0 mm. In the cross-track direction, these two scenarios show a less pronounced pattern, which correlates with the radial component. In the along-track direction, the strongest systematic patterns occur as a West-East pattern and an additional North-South distribution. The amplitude of this pattern is between 5 and 7 mm.

All circular scenarios are significantly less affected. The radial component shows a similar pattern to the E-GRASP-mod and E-GRASP-like scenarios, but here the amplitudes are 0.3, 0.6 and 0.3 mm for the 30, 60 and 89 degree scenarios. In the cross-track direction, a similar pattern to the circular 30 and 60 degree scenario is observed for the E-GRASP-mod and E-GRASP-like scenarios. However, the near-polar scenario shows a similar pattern to the GRASP-like scenario. The amplitude is 1.2, 1.0 and 1.3 mm. In the along-track direction, the

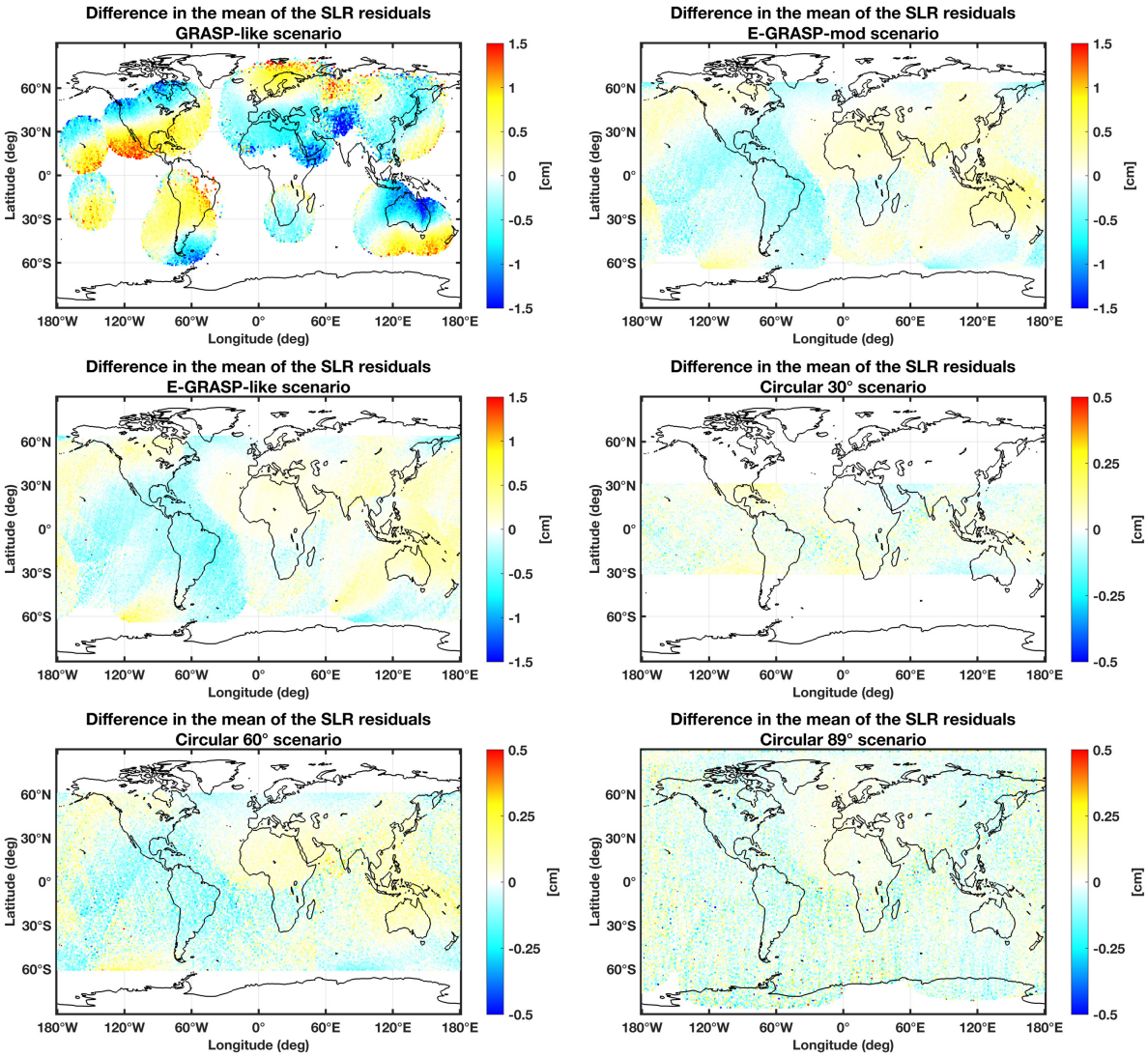

Figure 6.66: Global distribution of the difference in the mean of the observation residuals in the EGM mismodelling case compared to systematic error-free. The colour bar of the GRASP-like, E-GRASP-mod, and E-GRASP-like scenario are scaled 3 times higher.

30 degree circular scenario shows a Southwest to Northeast strip pattern that becomes more similar to the patterns of the E-GRASP-mod and E-GRASP-like scenarios as the inclination of the scenario increases to 60 degrees. The amplitude is 1.7 and 2.5 mm. The near-polar circular scenario shows the least systematics in this component, the distribution shows a slight West-East pattern with 4 extrema and an amplitude of 1.2 mm.

A correlation of the geographical distribution of the mean residuals can be found mainly in the radial component in the orbit comparisons.

Reference frame

Helmert parameters The mismodelling shows a clear influence on the derived TRF and is mainly seen in the rotations in X and Y (see Fig. 6.69). These are most pronounced for the GRASP-like, E-GRASP-like and E-GRASP-mod scenarios with up to 10 cm in the positions and up to 5 mm/a in the velocities. Of these, the GRASP-like scenario is the

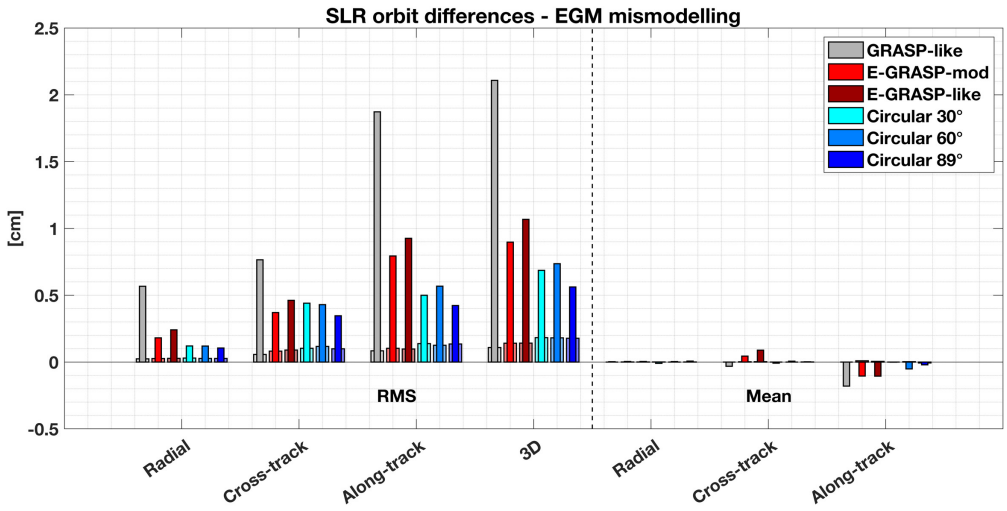

Figure 6.67: Mean RMS and mean values of the orbit comparison of the simulated and recovered orbit for the EGM mismodelling case. The thinner bars show the results of the EGM mismodelling case, the slightly more transparent thicker bars in the background show the values achieved in the systematic error-free case.

most affected, the difference between the other two scenarios is marginal. For the circular scenarios, the influence is much smaller, with the rotations in the 30 and 60 degree scenarios reaching a level of up to 5 mm in the positions and up to 0.3 mm/a in the velocities. The 89 degree circular scenario is the only one where all the effects are less than 1 mm in position and 0.1 mm/a in velocities.

For all scenarios the influence on translations is much smaller and only occasionally significant for the positions. The largest translation occurs for the GRASP-like scenario in the Y direction with 1.7 mm. The influence on the scale is well below 1 mm and 0.1 mm/a for all scenarios and is less than 3 sigma of the respective parameter of the Helmert transformation. The largest difference is again observed for the GRASP-like scenario, which is 0.5 mm in position and 0.09 mm/a in velocity (see Tab. F.40).

Formal errors The analysis of the formal errors shows that, due to the mismodelling, by far the largest LIPs occur in the GRASP-like scenario (see Fig. 6.70 and Tab. F.41 in App. F.2). These exceed the 100% level in the X and Y components of the positions, which means that the formal error of this parameter of the solution exceeds the formal error of the reference solution. In the Z direction, the LIP is 85%. The other scenarios are less affected, with the E-GRASP-mod and E-GRASP-like scenarios showing the second largest losses with LIP values between 18 and 43% in the Cartesian positions. The lowest losses are found for the circular scenarios, and in particular for the 60 and 89 degree scenario, where the LIP values are between 9 and 17%. In geographic coordinates, it can be seen that the component being affected the most is longitude. The GRASP-like scenario is also by far the most affected here, reaching an LIP of 70 to 104%. The lowest losses are seen for the circular scenarios, where LIP appears to increase in the latitude and longitude component the lower the inclination of the scenario.

The situation is similar for the velocities. Once again, the GRASP-like scenario shows the greatest losses, at up to 88%. The other scenarios show much lower losses, with a maximum of 22% for all components and scenarios. Also here, the least affected scenarios are the circular ones.

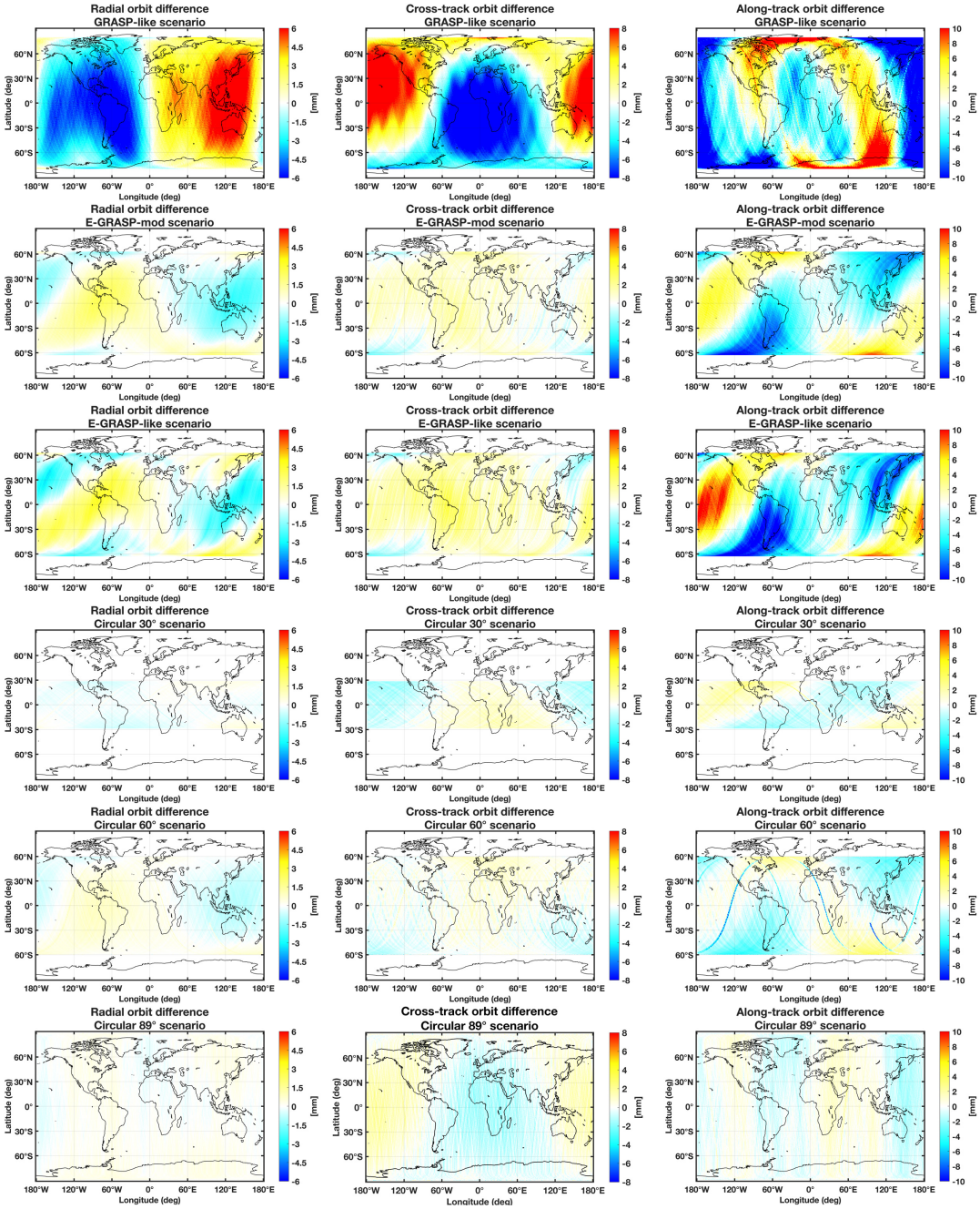

Figure 6.68: Mean orbit differences of the systematic error-free scenario and the recovered orbit for the EGM mismodelling scenario over the full simulation time span of 7 years. From left to right in radial, cross-track, and along-track direction. From the top to the bootom, GRASP-like, E-GRASP-mod, E-GRASP-like, Circular 30°, Circular 60°, Circular 89°.

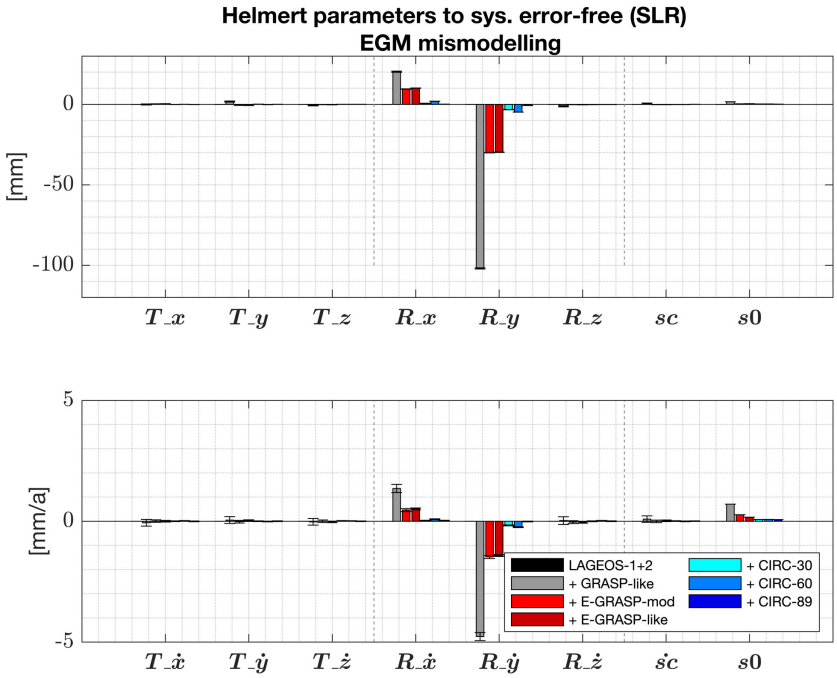

Figure 6.69: The upper figure shows the Helmert parameters of all stations for the EGM mismodelling case compared to systematic error-free. The lower figure shows the values for the velocities.

In the ERPs, it is also the GRASP-like scenario that shows the highest LIP of up to 80% in the pole coordinates and above 100% in LOD. The other scenarios show smaller losses, ranging from 24 to 36% in the pole coordinates and from 70 to 82% for LOD. Again, the circular scenarios are less affected, and the near-polar scenario at 89 degrees inclination is slightly the best.

ERP analysis The influence on the ERPs is strongest for the GRASP-like scenario. Here an increase in noise is mainly observed in the X-pole, which increases significantly to about 10 mm, and to a much lesser extent in the Y-pole, with an increase of about 2.9 mm. In the E-GRASP-mod and E-GRASP-like scenarios, the X-pole is also mainly affected, with an increase in noise to about 3 mm, and the Y-pole by 37 and 39%. The circular scenarios are the least affected, with noise increases of 6 to 15%.

There is also a significant bias and trend in both pole coordinates for all scenarios. This is strongly correlated with the determined rotation parameters of the Helmert transformation and reflects the Y-rotation in the X-pole and the X-rotation in the Y-pole. The reason for this rotation is the loose constraint network, which causes the station network to rotate in the opposite direction of the pole. A stronger NNR condition can counteract this. The only scenario where the significant offsets and drifts are close to or below 1 mm and 0.1 mm/a respectively is the circular scenario with an inclination of 89 degrees.

The spectral analysis of the ERPs shows that the GRASP-like, E-GRASP-mod and E-GRASP-like scenarios, in particular, are affected, primarily in the pole coordinates.

Variations in individual signals are superimposed by the extreme offsets and drifts, leading to a rapid increase in amplitude as the wavelength increases.

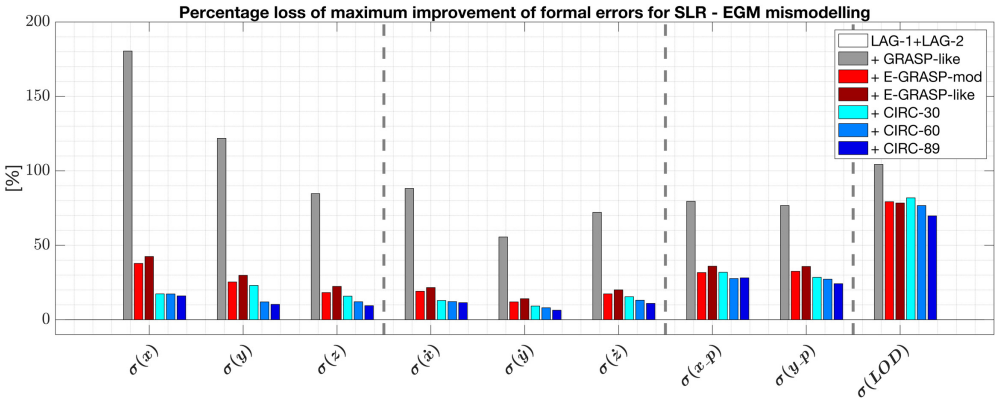

(a) Percentage loss of maximum improvement potential due to EGM mismodelling. Coordinates in X,Y, and Z

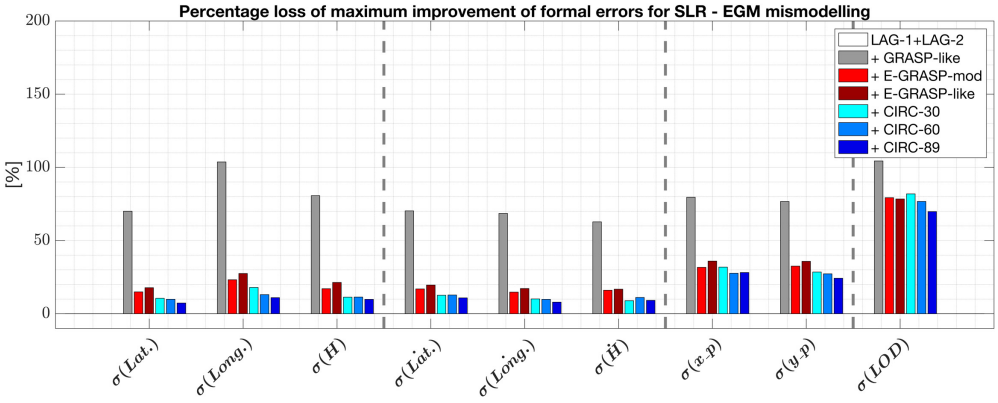

(b) Same as in Fig. a) but for coordinates in Latitude, Longitude, Height.

Figure 6.70: Differences of the percentage improvements compared to the systematically error-free case. +10% means that 10% of the maximum potential of improvement are lost in comparison to the systematic error-free scenario. Figure a) shows the values for X,Y and Z, Figure b) the values for Latitude, Longitude, Height.

This increase in the amplitudes accumulates the longer the wavelength, and reaches at a yearly period a maximum amplitude of 1.5 mm for the GRASP-like scenario and about 0.5 mm for the E-GRASP-mod and E-GRASP-like scenarios. The circular scenarios are less affected, with maximum amplitudes close to or below 0.1 mm. The circular scenario with 89 degrees inclination shows no variation in the spectrum of the pole coordinates at all.

The influence on LOD is largest for the GRASP-like scenario, with signals larger than 0.1 mm at periods of 123, 152, 225 and 254 days. For the other scenarios, variations are well below 0.1 mm.

Earth gravity field co-estimation In the next step, the Earth gravity field is co-estimated using the same procedure as for DORIS (see Sec. 6.1.2.6).

Reference frame

Helmert parameters By estimating the SHs of the Earth's gravity field, the systematic effect on the TRF can be reduced to less than 0.5 mm in positions and 0.11 mm/a in velocities

in all scenarios. In the circular scenario with 30 and 89 degrees inclination no remaining significant translation, rotation or effect on the scale remains (see Tab. F.40 in App. F.2).

Formal errors The LIP in the formal errors can be reduced mainly for the GRASP-like scenario. It reaches a level only slightly higher than that of the E-GRASP-mod and E-GRASP-like scenarios. For the other scenarios there is almost exclusively a slight increase in formal errors of up to 5%, in some cases up to 10%. Compare Fig. 6.71 and Tab. F.42 in App. F.2.

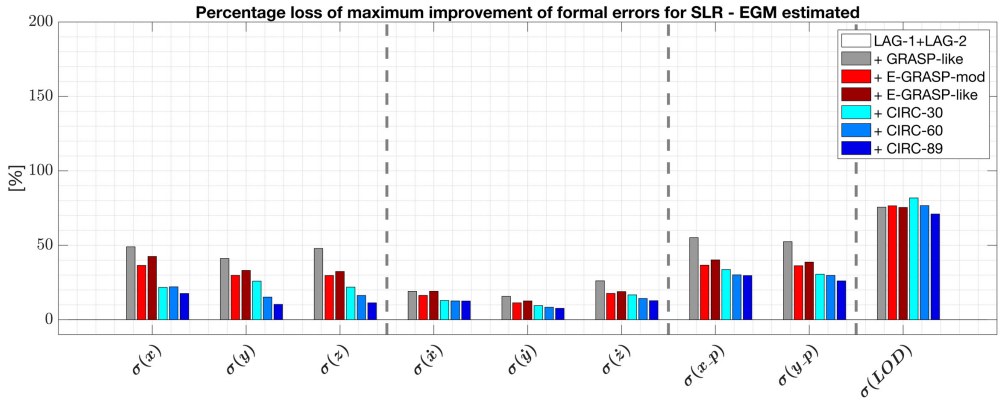

(a) Percentage loss of maximum improvement potential due to EGM mismodelling, whereby the EGM is co-estimated. Coordinates in X,Y, and Z

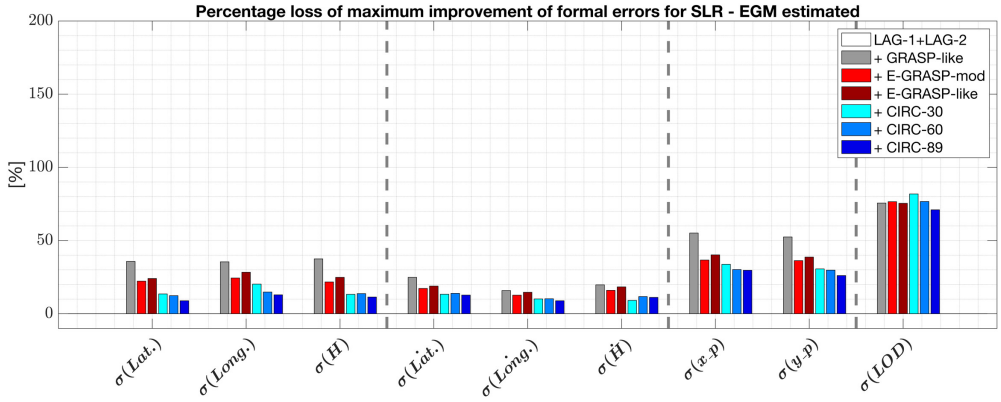

(b) Same as in Fig. a) but for coordinates in Latitude, Longitude, Height.

Figure 6.71: Differences of the percentage improvements compared to the systematically error-free case. +10% means that 10% of the maximum potential of improvement are lost in comparison to the systematic error-free scenario. Figure a) shows the values for X,Y and Z, Figure b) the values for Latitude, Longitude, Height.

ERP analysis The increase in noise can be reduced mainly for the GRASP-like, E-GRASP-mod and E-GRASP-like scenarios. Remaining noise increase are in the range of 7 to 13% for the estimated pole coordinates for all scenarios except the GRASP-like, where they are 20 and 15% for the X and Y-pole.

In LOD the remaining noise increase is between 17 and 29%. The improvements are greatest for the GRASP-like and E-GRASP-like scenarios.

Remaining offsets and trends can only be detected in the pole coordinates, where the biases correspond to the remaining rotations in the Helmert parameters mentioned. These

are at most about 0.5 mm compared to the respective systematic error-free solution. No significant offset or trend can be detected for LOD in any of the scenarios.

The spectral analysis shows significant improvements for all scenarios, with the amplitude of all signals being reduced to below 0.1 mm. However, only for the GRASP-lile scenario, a signal with a semiannual period remains at the X-pole. The 89 degree circular scenario shows the least overall influence in the spectral analysis of the ERPs, regardless of whether the EGM is co-estimated.

Potential for gravity field determination To assess the potential of SLR to estimate the SHs of the Earth's gravity field with the different scenarios, the same procedure is followed as for DORIS. For the sensitivity analysis of the scenarios see Sec. 6.1.2.6. The maximum degree to which the SH of the gravity field can be estimated is 37 for the GRASP-like and E-GRASP-mod scenario, 26 for the E-GRASP-like and 20, 45, and 60 for the circular scenario with inclinations of 30, 60, and 89 degrees respectively.

Estimated Earth gravity field analysis Compared to DORIS, the maximum degree of the SH expansion that is solved for is lower for SLR in all scenarios except the 30 degree circular scenario. The triangular plots in Fig. 6.72 show a similar behaviour for SLR in the differences of the SHs as for DORIS, but they increase significantly faster with increasing degree. This is most evident in the GRASP-like scenario, where the deviations in the zonal and tesseral coefficients become very large already below degree 10. At higher degrees and lower orders the resonance effects lead to smaller errors. However, here only the beginning of the resonance effect can be captured up to the maximum degree of the solution. In the E-GRASP-mod scenario, SLR shows slightly smaller differences in the zonal and tesseral coefficients up to about degree 15, after which the deviations also increase rapidly. The E-GRASP-like scenario shows fairly homogeneous differences over the orders of a degree and larger differences the higher the degree. A larger increase in the zonal and tesseral coefficients, as seen for DORIS, is not reflected here, as the deviations are already too large at lower degrees. Again, slightly smaller differences are seen at higher levels and orders due to resonance effects, which are limited by the maximum degree of development. For the circular scenarios, all scenarios show a very identical result to DORIS, but here the deviations are mainly larger in the scenario with 30 degree inclination.

The degree amplitudes in Fig. 6.73 and the cumulative error in Fig. 6.74 show, that the GRASP-like scenario with SLR achieves significantly poorer results than with DORIS. Here the degree amplitudes increase much faster and reach a SNR of 1 at degree 14 instead of 33. The level of 100 mm equivalent water height, used as a quality measure, is already reached at degree 4 for SLR, in contrast to DORIS where it is reached at degree 10.

Very similar results to DORIS can be obtained with the E-GRASP-like and the two circular scenarios at 30 and 60 degrees inclination. Here, for both techniques, the 100 mm limit is reached at degree 5 for the E-GRASP-like scenario. For the circular scenarios at 30 and 60 degrees inclination, the degree amplitudes for degree 2 are already above the 100 mm limit for SLR. For DORIS they were only close to the 100 mm level for degree 2 and only for the 60 degree scenario. The E-GRASP-mod and the 89 degree circular scenario are the only two scenarios where the degree amplitudes show a slightly better solution with SLR than with DORIS. For the E-GRASP-mod scenario the 100 mm limit is reached at degree 5 instead of 3 and the SNR of 1 at degree 13 instead of 11. For the 89 degree circular scenario the advantages are limited to degrees 2 and 3 and the 100 mm limit is reached above degree 4.

In summary, the potential to determine the gravity field using SLR with one of the space-tie satellite scenarios is limited to the very low SHs even more than with DORIS. The 30 and 60 degree circular scenarios are less suitable, showing very large differences in the triangular plots and degree amplitudes already at degree 2.

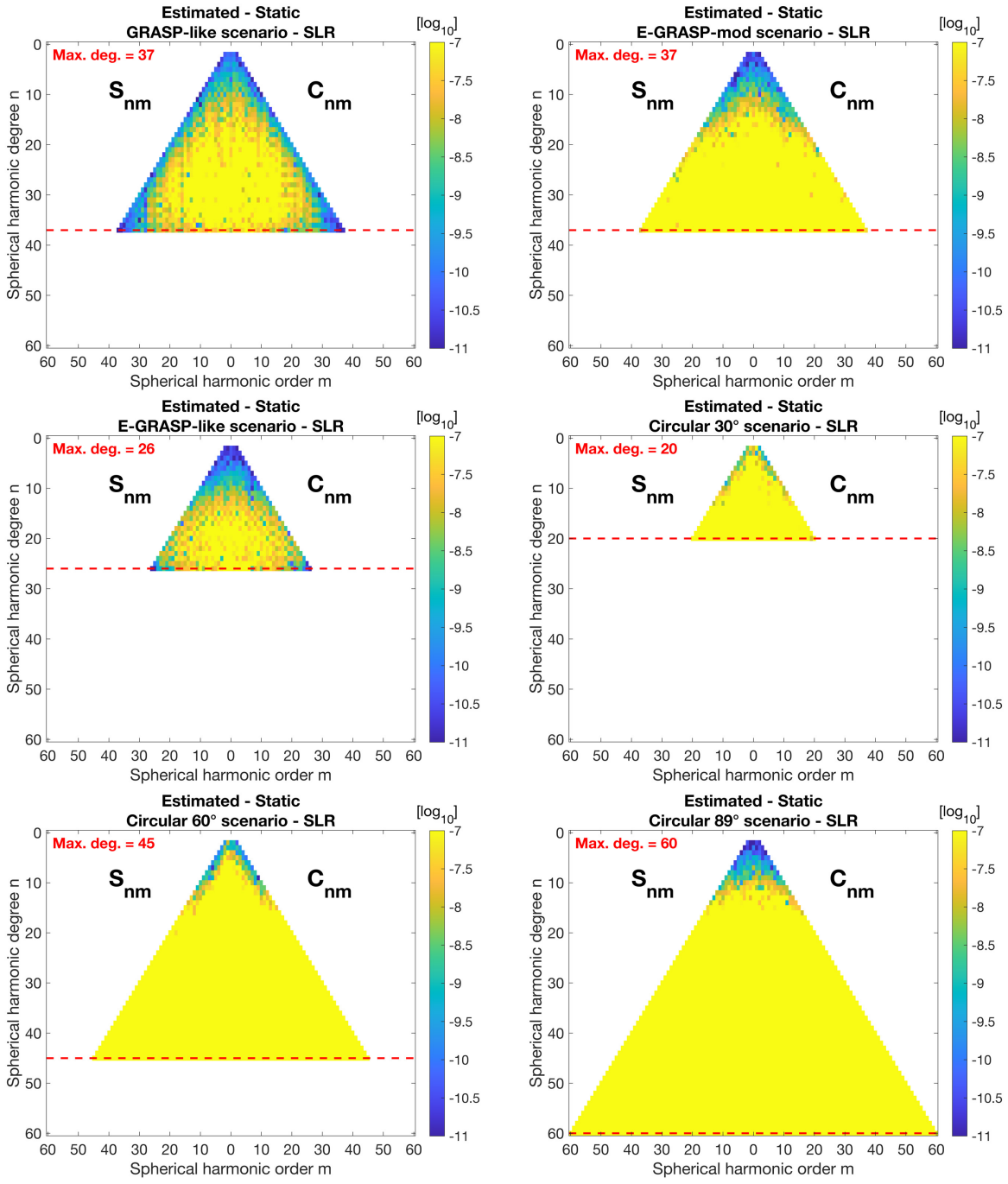

Figure 6.72: Triangular plots showing the difference between estimated and simulated SH coefficient.

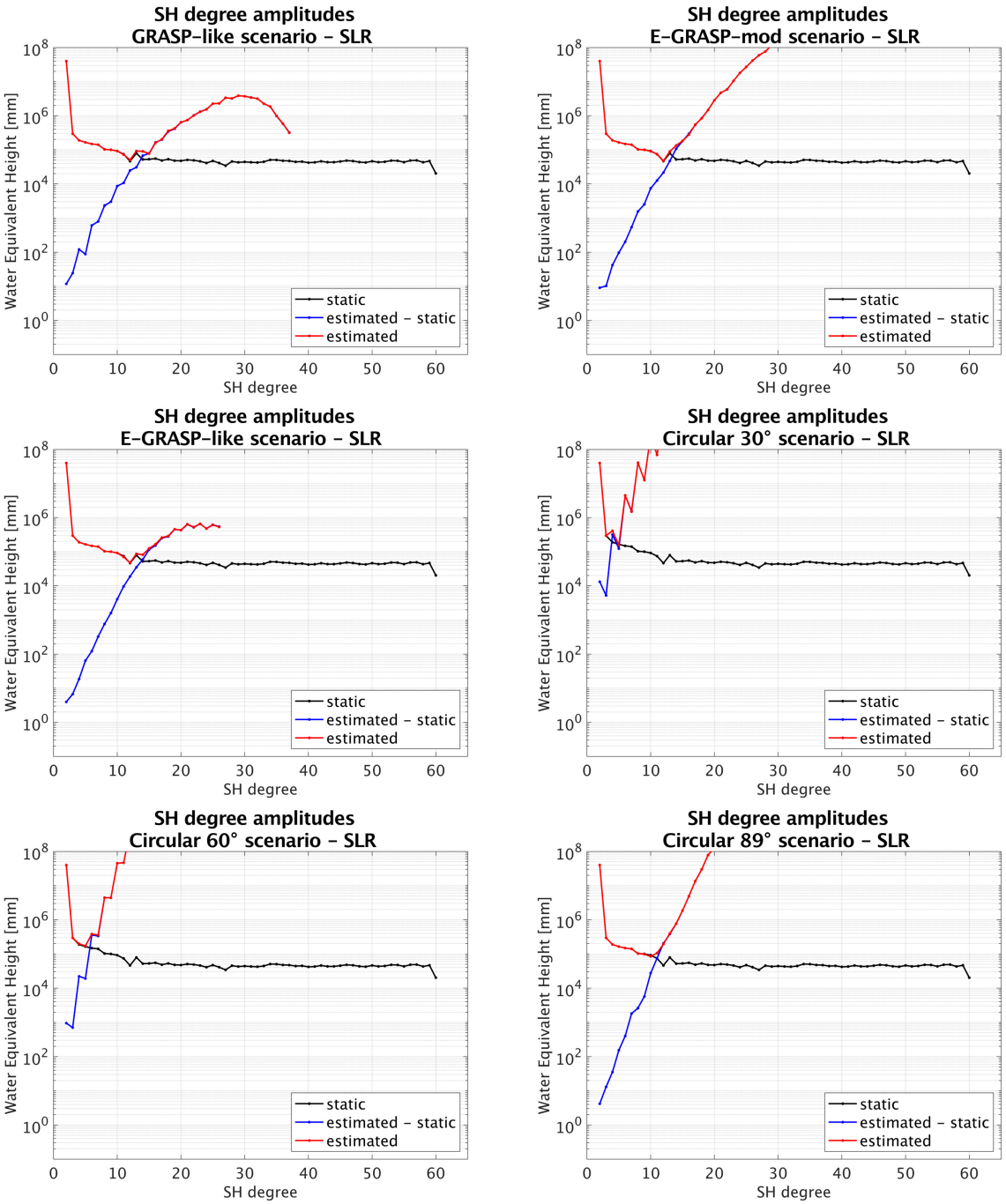

Figure 6.73: SH degree amplitudes in equivalent water height.

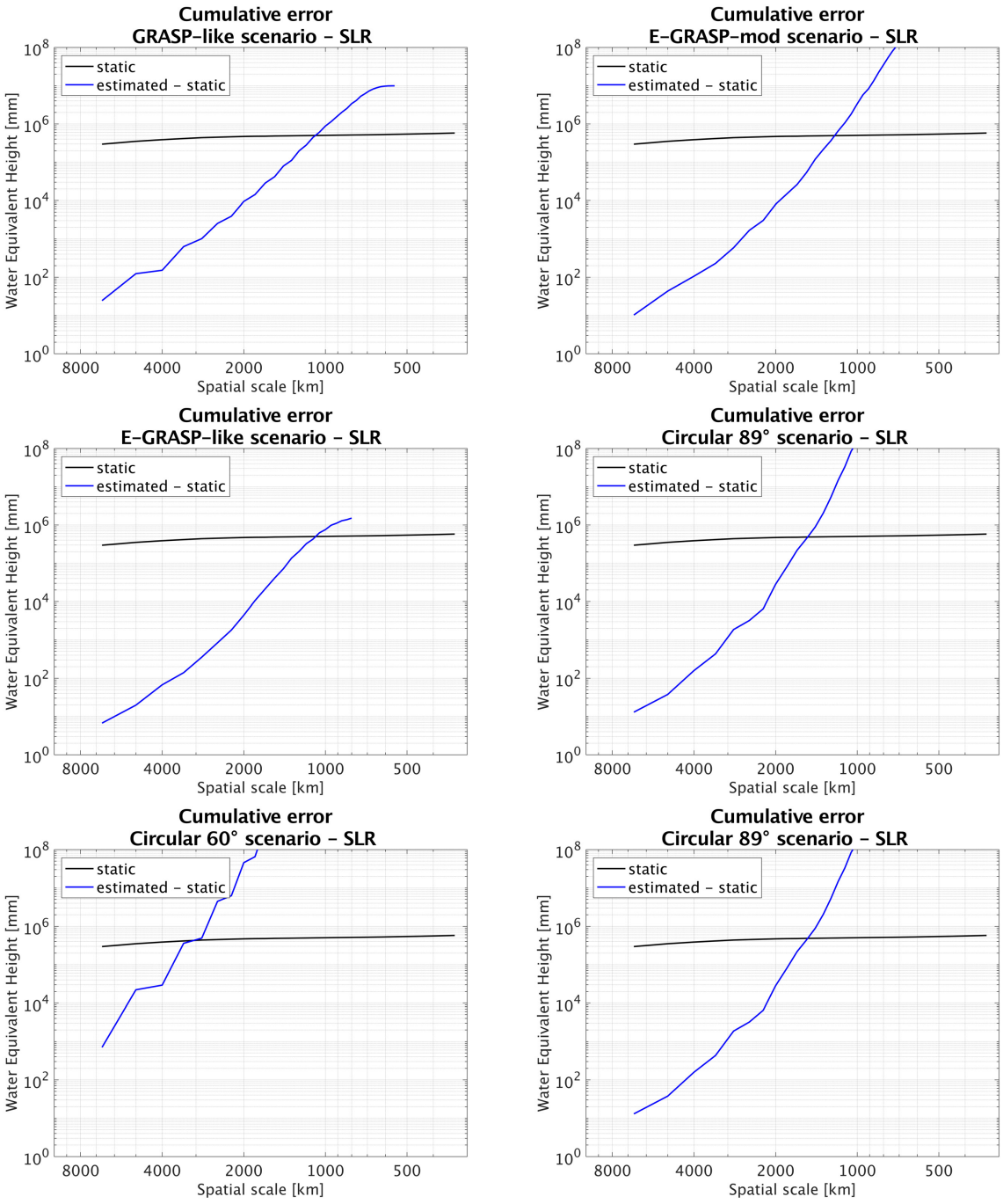

Figure 6.74: Cumulative error in equivalent water height

Conclusion - EGM mismodelling and potential for gravity field determination The evaluation of the EGM mismodelling for SLR is given in Tab. 6.34.

The EGM mismodelling shows a significant influence on the orbit, especially for the GRASP-like, E-GRASP-mod and E-GRASP-like scenarios, where significant degradations in orbit accuracy can be seen, as well as systematic patterns in the orbit differences. The higher orbiting circular scenarios are significantly less affected and only show geographical patterns in the orbit comparison with amplitudes in the low millimetre range.

A systematic influence on the TRF can be seen for all scenarios. This is largest for the GRASP-like, E-GRASP-mod and E-GRASP-like scenarios, where the rotations reache several centimetres in position and mm/a for the velocities. The 89 degree circular scenario is the only one where the effect on the TRF in terms of the Helmert parameter is less than 1 mm in position and 0.1 mm/a in velocities. LIP in the formal errors for positions and velocities occur mainly for the GRASP-like scenario, where the LIP reaches up to 100% and beyond (total loss of improvement with respect to the reference solution). If the reference solution is not highly sensitive to EGM mismodelling, a combination with a GRASP-like scenario would be counterproductive at this point. The other scenarios are less affected, where the E-GRASP-mod and E-GRASP-like scenarios are generally more affected than the circular scenarios.

In the pole coordinates, the LIP values for the GRASP-like scenario are above 50%, while for the others they are at a similar level at 25%. For LOD, all scenarios show significant losses, with the GRASP-like scenario leading the way with 80-90%, but the others are also greatly affected.

The impact on the ERPs is most evident in the GRASP-like, E-GRASP-mod and E-GRASP-like scenarios. Here there occure offsets and drifts in the pole coordinates, which can reach several centimetres and mm/a, as well as significant increases in noise. The circular scenarios are less affected, but also show significant effects. The 89 degree scenario is the least affected.

The spectral analyses of the scenarios show clear influences, mainly in the pole coordinates, which are strongest for the GRASP-like, E-GRASP-mod and E-GRASP-like scenarios. Again, the circular scenario with an inclination of 89 degrees shows the least interference.

By estimating the gravity field, the systematic effect on the TRF can be reduced to less than 0.47 and 0.11 mm/a in the Helmert parameters of the positions and velocities. In particular, the GRASP-like scenario shows a significant reduction of the LIP values in the formal errors of the station positions and velocities and ERPs. The other scenarios show no improvement in the formal errors. Systematic effects on the ERPs can be significantly reduced by co-estimating the Earth's gravity field, with remaining biases of less than 0.5 mm and 0.1 mm/a, respectively. Furthermore, for the GRASP-like, E-GRASP-mod and E-GRASP-like scenarios, the increase in noise of the ERPs can be reduced to the level of the circular scenarios (up to 21% increase in noise compared to the systematic error-free case). The same applies to the spectral analysis of the ERPs, where the co-estimation can significantly reduce amplified signals. Only the GRASP-like scenario exhibits a residual signal at the X-pole with a semiannual period. The circular scenarios show the least remaining variation compared to the systematic error-free case.

Table 6.34: Vulnerability of the satellite scenarios for SLR for systematic EGM mismodelling and while co-estimating the EGM.

	G-like	E-G-mod	E-G-like	Circ. 30°	Circ. 60°	Circ. 89°
Orbit	③	③	③	①	①	①
EGM not estimated						
Helmert	③	③	③	②	②	①
Station pos. form. err.	③	③	③	③	②	②
Station veloc. form. err.	②	①	①	①	①	①
Pole coord. form. err.	③	②	②	②	②	②
LOD form. err.	③	③	③	③	③	③
ERPs est.	③	③	③	②	②	①
EGM co-estimated						
Helmert	②	②	②	①	②	①
Station pos. form. err.	①	①	①	①	①	①
Station veloc. form. err.	③	②	②	①	①	①
Pole coord. form. err.	③	③	③	③	②	②
LOD form. err.	①	①	①	①	①	①
ERPs est.	②	②	②	①	②	①
Summary	2.5	2.3	2.3	1.8	1.8	1.4

The potential for estimating the Earth's gravity field for the scenarios with SLR is limited to the very low SHs up to a maximum degree 5 and for the GRASP-like, E-GRASP-mod, E-GRASP-like and 89 degree circular scenarios. For the other scenarios, the deviations of the estimated SHs compared to the reference of the simulation are significantly larger and exceed the used limit of 100 mm equivalent water height in degree amplitudes starting from degree 2.

The 89 degree circular scenario shows the best overall results for minimising the influence of the introduced EGM mismodelling. Despite the lower sensitivity to the Earth's gravity field, this scenario also shows a good suitability for estimating low SHs (see Tab. 6.35).

Table 6.35: Potential for Earth gravity field estimation solely with SLR with the satellite scenarios.

	G-like	E-G-mod	E-G-like	Circ. 30°	Circ. 60°	Circ. 89°
EGM determination	②	②	②	③	③	②

6.2.3 Single-technique conclusion for SLR

The inclusion of one of the simulated space-tie satellite scenarios for the TRF and ERPs determination using only SLR shows that the potential for improvement is largely due to additional observations. Geometric added value cannot be found or is very small. Improvements that would indicate enhanced geometry for stations in the reference solution that have non-optimal observation characteristics cannot be found either. The advantages and disadvantages of the different scenarios are well balanced in the absence of systematic errors. Accordingly, each of the scenarios shows a rating of 1.5 for the maximum achievable potential (see Tab. 6.36).

The investigated mismodelling cases show that in particular the GRASP-like, E-GRASP-mod and E-GRASP-like scenarios have a higher risk of not achieving the maximum potential due to systematic error influences, with overall vulnerability values of 2.1, 1.9 and 2.1, respectively. The circular scenarios show a lower overall risk with values of 1.7 to 1.8.

For the circular scenarios, the systematic CoM shift and the SRP mismodelling are the two strongest effects that can be positively influenced by measurements before the satellite is launched. In this context, the satellite eccentricities should be determined as accurately as possible prior to launch, as the results show that even in these scenarios about 50% of the introduced 3D displacement can be found in the pole coordinates.

For the determination of the Earth's gravity field, only the GRASP-like, E-GRASP-mod, E-GRASP-like and the 89 degree circular scenario are suitable. The deviations found for the other scenarios are already above the limit used from degree 2 onwards. For the remaining scenarios, the determination is limited to low-degree SH coefficients up to a maximum of degree 5.

Table 6.36: Maximum potential of the satellite scenarios for TRF and ERP determination in the case of SLR, together with their vulnerability to mismodelling.

	G-like	E-G-mod	E-G-like	Circ. 30°	Circ. 60°	Circ. 89°
Maximum potential	1.5	1.5	1.5	1.5	1.5	1.5
CoM	1.9	1.9	1.7	1.4	2.0	2.2
Drag	2.1	1.4	2.4	1.6	1.4	1.3
SRP	1.9	1.9	2.0	1.9	1.9	1.9
EGM mism.	2.5	2.3	2.3	1.8	1.8	1.4
Overall vulnerability	2.1	1.9	2.1	1.7	1.8	1.7

6.3 GPS

For its contribution to ITRF2020, the IGS used observations from the GPS satellite navigation system starting from 1994, the GLONASS system from 2002, and the Galileo system from 2013 (Altamimi et al., 2023).

As GPS can be considered representative of GNSS and to limit the number of scenarios, the simulated reference solution used here consists of GPS only. EPOS-OC offers the possibility of processing LEOs in an integrated approach together with the GPS constellation, which is the only way to consistently solve for coordinates and achieve a gravity field solution. Further information on the GPS real data evaluation used for the subsequent simulation can be found in Chap. 4 and Sec. 5.3. The result is a simulated GPS constellation over the entire simulation period that is free of systematic errors.

Subsequently, this simulated GPS constellation is used to simulate GPS SST observations free of systematic errors for the space-tie satellites. After that, the potential of the space-tie satellite scenarios for GPS is investigated using the integrated approach. In this approach, one space-tie satellite at a time is integrated into the network adjustment of the GPS constellation. Detailed information on this approach can be found in Sec. 5.3. The solutions generated in this way are compared with the GPS reference solution and changes are analysed.

As the GPS processing and combination methods differ from those used for DORIS and SLR, different mismodelling scenarios are investigated. First, the maximum potential in a systematic error-free simulation is investigated (Sec. 6.3.2.1). Subsequently, Sec. 6.3.2.2 considers SRP mismodelling of the GPS transmitter satellites, as described in Sec. 4.6.3. Finally, in Sec. 6.3.2.3, mismodelling of the EGM, as done for DORIS and SLR, is investigated and the potential to estimate the Earth's gravity field is analysed.

6.3.1 Reference solution

The procedure for simulating GPS observations of transmitter satellites to ground stations is described in Sec. 4.3. White noise is added to the observations and ambiguities are simulated. Otherwise, the observations are free of systematic errors. The parameterisation for the GPS processing was outlined in Tab. 4.4. More specifically, the parameters estimated in the network adjustment for GPS are given in Tab. 6.37. For the orbits, in addition to the initial state parameters, five reduced ECOM parameters and empirical accelerations in the transversal direction are estimated, following the setup of Steigenberger et al. (2020), from which the box-wing model used for the simulation was also adapted. Satellite clock biases are estimated for every epoch. Similar to the processing procedure for real data, a NNR, NNS, and NNT condition with a strength of 0.1 mm is used in the POD to constrain the network as closely as possible to the a priori network while retaining the freedom of a network adjustment. These conditions are not used in the subsequent step of the normal equation gerenation. For each arc, the clock of one ground station is fixed as the reference clock. Ambiguities are estimated and subsequently fixed using Double Differences (DD) (see also Sec. 4.5.2).

6.3.1.1 Orbital fit

The a posteriori RMS of the orbital fit of the simulated GPS constellation and its comparison with real data are described in Sec. 5.3. Fig. 6.75 shows the global distribution of the number of code observations, the median of the residuals and the standard deviation of the residuals for all satellites over a period of one year.

Table 6.37: Estimated parameters and dynamic parameterisation for the reference solutions used in the systematic error-free case for the GPS constellation and the ground stations.

Parameterisation for systematic error-free case only GPS constellation	
General	
Arc length	24 hours
GPS satellites	
Initial state parameters	Estimated
SRP parameters	5 reduced ECOM
Empirical accelerations	Constant and 1/rev cosine and sine
	in transversal direction once per arc
Clocks	Estimated per epoch
Ground stations	
Station positions	Estimated
	For the POD constrained with NNR, NNS, and NNT 0.1 mm to a priori
Troposphere	Piecewise linear scaling 10 per arc around each station
Ambiguities	Estimated and fixed using DD
Clocks	Estimated per epoch
	One reference clock fixed per arc

The observations demonstrate almost complete global coverage. More observations are possible in the northern hemisphere, particularly over Europe and North America. Gaps only appear in areas over which the GPS satellites did not pass in the evaluated time interval due to their repeat cycle.

The geographical distribution of the standard deviation of the code and phase residuals reflects the clusters of receivers for which increased observation noise was simulated. This is particularly evident in the southern hemisphere and over Eastern China. The median residuals show an identical geographical distribution for code and phase observations and only deviate from zero in regions with a lower number of observations near the equator in North-South direction.

6.3.1.2 Orbit recovery

The accuracy of the orbits of the GPS constellation is assessed using the mean of the RMS and mean differences of the orbit comparison. Further values used for statistical quantification include the global RMS values of the Signal-in-Space Range Error (SISRE) of the orbit (denoted as SISRE_{orb}), the SISRE also taking into account the clocks of the GPS satellites (denoted as $\text{SISRE}_{p/m}$), and the RMS of the satellite and ground station clocks. The SISRE is calculated according to Equation 45 from Montenbruck et al. (2018), and the RMS is calculated over all epochs and satellites for geographical averaging of the SISRE. The constellation-specific weight factors used in the calculation of the SISRE are typical GPS values of 0.98 and 1/49, as detailed in, for example, Liu et al. (2022). To account for the anticorrelating effect of the radial component and the satellite clock on the pseudorange observations, the clock error is added to the radial component in the calculation of the SISRE, giving SISRE_p. This provides an indication of the total error experienced by a ground station, which is important for ground station positioning and determining a TRF. To evaluate the cumulative error of the constellation additionally, the clock error is subtracted from the

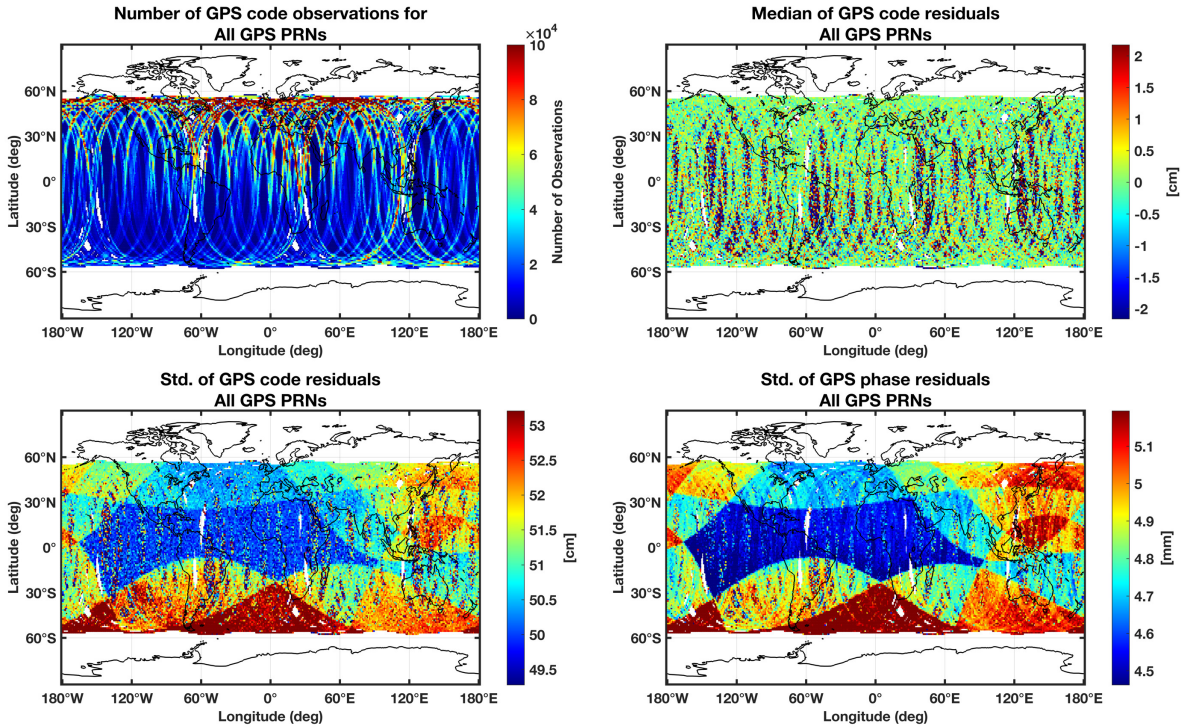

Figure 6.75: Global distribution of the number of simulated GPS code observations for all GPS PRNs of the reference solution (top left), the median of the code observations (top right), and the standard deviation of the simulated code (bottom left) and phase observations (bottom right).

radial component to give SISRE$_m$. The values for the reference solution in the systematic error-free case are given in Tab. 6.38.

The mean RMS is approximately 1 millimetre in all components and is highest in the radial component. No mean deviation in the orbits can be detected. The RMS of the estimated clocks is at a similar level to the noise in the phase observations, at 5 mm for the satellite clocks and 6 mm for the ground stations. SISRE$_p$ and SISRE$_m$ are close to 5 mm, indicating no significant systematic anticorrelation of the radial orbit component with the estimated satellite clocks. No temporal variation of the SISRE can be detected.

Table 6.38: Statistics of the recovered orbit and clocks in the systematic error-free case for the GPS constellation. Values computed over the whole time span in radial (R), transversal (T), and normal (N) direction. SV stands for GPS satellite vehicle, Sta. for ground station. SISRE in the version SISRE$_{orb}$ represents the orbital accuracy without taking into account the clock estimate, while SISRE$_p$ takes into account the clock estimate and the correlation with the radial component, and SISRE$_m$ takes into account the clock estimate but not the correlation with the radial component. All values are given in centimetres.

	RMS						Clock RMS		Mean		
	R	T	N	SISRE$_{orb}$	SISRE$_p$	SISRE$_m$	SV	Sta.	R	T	N
Systematic error-free case											
GPS const.	0.12	0.07	0.08	0.12	0.49	0.54	0.50	0.61	-0.00	0.00	0.00

Fig. 6.76 shows the mean orbital differences for all GPS satellites in the radial, cross-track and along-track directions. In the radial component, a minor East-West pattern with an amplitude of 0.4 mm can be observed, showing maxima at locations differing by approximately 90 degrees along the equator. Additionally, a correlation with the median of the residuals and with the number of GPS observations (see Fig. 6.75 top left) is evident. No clear geographical patterns are apparent in the cross-track and along-track directions.

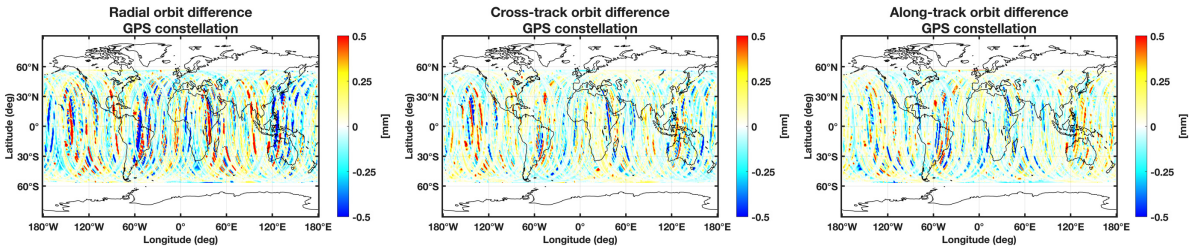

Figure 6.76: Median orbit differences of the true simulated and recovered orbit over a time span of one year for the GPS constellation in the case of no systematic errors. The differences are shown from left to right in the radial, cross-track, and along-track directions.

The accuracy of GPS satellites' orbits and clocks depends to a large extent on modelling the SRP. Therefore, the accuracy of satellite clock estimates can be analysed in terms of the angle between the orbital plane and the Sun (the beta angle) and the angle between the Sun, the centre of the Earth, and the satellite (the Sun elongation angle). This is illustrated for PRN 4 in Fig. 6.77. In the absence of systematic errors, the estimated clock offsets are uniformly distributed across the beta angle and Sun elongation angle.

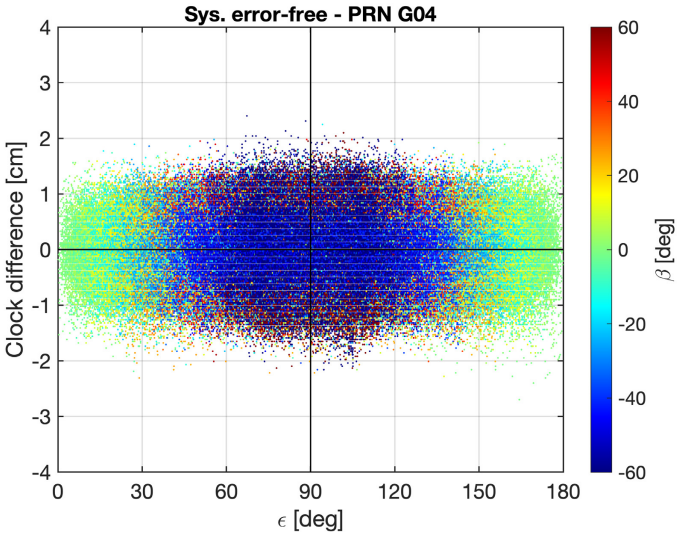

Figure 6.77: Clock difference for PRN 4 in cm as a function of the Sun elongation angle ϵ. Different β angles according to colour bar.

6.3.1.3 Reference frame

The GPS reference frame is generated in a similar way to that for DORIS and SLR. EPOS-OC is used in normal equation mode to set up daily normal equations, in which the parameters of the POD run, station velocities and ERPs are estimated, in addition to

the usual parameters. For details of the normal equation mode with regard to GPS ambiguities, please refer to Sec. 4.5.2 and App. A. Subsequently, these normal equations are accumulated and the initial values of the parameters, which have already been estimated in the POD run, are mapped onto the a priori values of the simulation. A NNR condition is then applied to the station positions and velocities for a subnetwork of datum stations (see Tab. 6.39), with respective strengths of 1 mm and 0.1 mm/a. As observations for the ground stations are densely distributed over time with a similar noise level, the datum stations are selected to ensure a homogeneous global distribution (see Fig. 6.78).

Table 6.39: GPS datum stations

Country	Station code
Antartica	CAS1, DAV1, OHI2, SYOG
Argentina	LPGS
Australia	ALIC, CEDU, DARW, HOB2, MAC1, YAR1
Brazil	BRAZ
Canada	DRAO, STJO, WHIT
Chile	ISPA
China	KUNM
Colombia	BOGT
Cuba	SCUB
French Southern Territories	KERG
French Polynesia	THTI
Gabon	NKLG
Greenland	QAQ1
Guam	GUAM
Israel	RAMO
Kyrgyzstan	POL2
Russian Federation	ARTU, IRKT, NRIL, TIXI
Spain	YEBE
South Africa	RBAY
New Zealand	AUCK
USA	KOKB, MDO1, MKEA, NLIB
Virgin Islands	CRO1

Helmert parameters The Helmert parameters for the comparison of the estimated TRF to the a priori reference (see. Tab 6.40) for the subnetwork of datum stations, as well as for all stations, show an X-rotation in the positions of 0.13 and 0.14 mm, respectively. These rotations are smaller than the rotations seen in the SLR reference solution and are below the strength of the applied NNR condition. Significant translations show up to a maximum of 0.02 mm, a difference in the scale cannot be seen.

Due to the much larger and more homogeneously distributed GPS ground station network, and the very small formal error in the rotation parameters, the observed rotation appears more suspicious than with the other techniques. The reason for this lies in the strength of the NNR condition. To this end, a test scenario was created that is completely free of

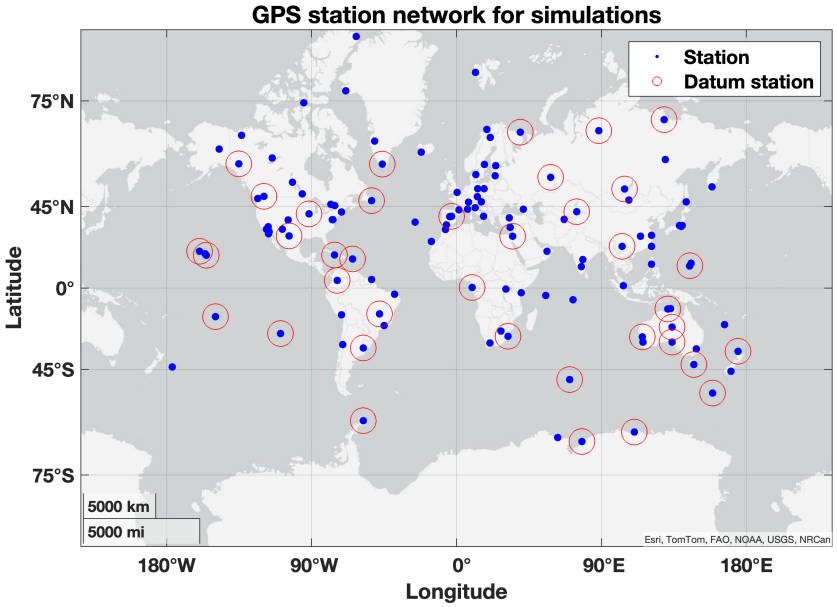

Figure 6.78: The GPS station network of the simulation. All stations used are shown in blue, datum stations are additionally encircled in red.

errors, and the estimated ERPs were tested for significant changes compared to the a priori values, using linear regression hypothesis tests. The strength of the NNR condition was then gradually increased until no significant offset or trend was found, based on a 5% significance level. For the Helmert transformation to the a priori station network, a three sigma threshold was used as a criterion for the Helmert parameters. The necessary strength of the NNR condition to achieve statistical insignificance with respect to the a priori found here is 1/10'000 mm for positions and for the velocities smaller by a factor of 10. However, to be consistent with the other techniques, the recommendation of Altamimi (2003) is also followed here, using a strength of 1 mm or 0.1 mm/a.

Table 6.40: Helmert parameters and their standard deviations for the station positions and velocities of the GPS reference solution compared to the a priori reference frame.

	T_x [mm] $T_{\dot{x}}$ [mm/a]	T_y [mm] $T_{\dot{y}}$ [mm/a]	T_z [mm] $T_{\dot{z}}$ [mm/a]	R_x [mm] $R_{\dot{x}}$ [mm/a]	R_y [mm] $R_{\dot{y}}$ [mm/a]	R_z [mm] $R_{\dot{z}}$ [mm/a]	sc [mm] $\dot{sc}$ [mm/a]	s_0 $\dot{s_0}$
Combined reference								
datum stations	-0.00 ± 0.00	-0.01 ± 0.00	-0.02 ± 0.00	0.14 ± 0.00	0.00 ± 0.00	0.01 ± 0.00	0.00 ± 0.00	0.02
	0.00 ± 0.00	-0.00 ± 0.00	0.00 ± 0.00	0.01 ± 0.00	0.00 ± 0.00	0.00 ± 0.00	-0.00 ± 0.00	0.01
all stations	-0.00 ± 0.00	-0.01 ± 0.00	-0.02 ± 0.00	0.13 ± 0.00	0.00 ± 0.00	0.01 ± 0.00	0.00 ± 0.00	0.01
	0.00 ± 0.00	-0.00 ± 0.00	0.00 ± 0.00	0.01 ± 0.00	0.00 ± 0.00	0.00 ± 0.00	-0.00 ± 0.00	0.01

Formal errors The improvements in the formal errors of the station coordinates, velocities and ERPs are evaluated in the same way as for DORIS and SLR. The median formal errors of the reference solution for GPS are listed in Tab. F.45 in App. F.3. The formal errors of the station coordinates are in the range of 0.23 to 0.27 mm in Cartesian coordinates and 0.21 to 0.28 mm in geographic coordinates. The velocity errors range from 0.25 to 0.27 mm/a in Cartesian coordinates and from 0.23 to 0.29 mm/a in geographic coordinates. For the ERPs, the formal errors of both pole coordinates are approximately 0.33 mm and 0.46 mm in LOD .

6.3.1.4 ERP analysis

The statistical evaluation of the ERPs is listed in Tab. F.46. The estimated ERPs noise compared to the a priori values is 0.06 mm for both pole coordinates. A significant offset can be seen in both pole coordinates, but only in the Y-pole it is above the 0.1 mm level at -0.145 mm. This reflects the previously mentioned X-rotation of the Helmert parameters, which was found to be due to the strength of the NNR condition used. A significant trend can only be determined in the Y-pole, but this is within the range of micrometres/a. The noise in LOD, at 0.48 mm, is approximately ten times larger than that in the pole coordinates, however, no significant offset or trend can be determined here.

Spectral analysis of the ERPs shows no significant signals. Amplitudes are below the micrometre level.

6.3.2 GPS space-tie satellite results

The potential of the space-tie satellite scenarios in the case of GPS is investigated in a different way from that in the case of DORIS and SLR. To evaluate the potential of a satellite with a SST GPS receiver for TRF estimation, the integrated approach is necessary. Starting from the systematic error-free case in Sec. 6.3.2.1, one of the satellites is added to the constellation and the integrated calculation is performed. This allows the influence on the GPS constellation and network to be examined and the maximum potential improvement to be determined.

For SRP mismodelling of the GPS satellites (Sec. 6.3.2.2), the influence is first analysed for the case of the GPS constellation alone. Then, the systematic error-free space-tie satellites are integrated into this case, and the extent to which the scenarios can reduce the effects of the introduced SRP mismodelling is examined.

The same procedure is carried out for the EGM mismodelling (Sec. 6.3.2.3), whereby the space-tie satellites are also affected by the mismodelling. Finally, the potential to estimate the SHs of the Earth's gravity field using the individual scenarios in the integrated approach is analysed.

6.3.2.1 Case free of systematic errors

The GPS SST observations are simulated in a systemic error-free case, as described in Sec. 4.3. These observations contain only white noise, ambiguities, and cycle slips, which are fixed in the integrated POD run together with those of the GPS constellation using DDs. The dynamic parameterisation of the LEO orbit differs from that used in DORIS and SLR, employing a more reduced-dynamic parameterisation (see Tab. 6.41). The parameterisation of the constellation and the ground stations is identical to that of the reference solution in Tab. 6.37.

Orbital fit The orbital fit values are listed for all scenarios in Tab. 6.42 and are shown for the space-tie satellites over the full time span in Fig. 6.79. The global RMS of the space-tie satellites is approximately 38 cm in code and 2.7 mm in phase, with no visible temporal variation. The GRASP-like scenario has the highest number of possible observations and is most stable over time. The E-GRASP-mod and E-GRASP-like scenarios show 13% and 16% fewer observations, respectively, while the circular scenarios show about 26% fewer. As the GPS receivers used in the simulation are configured identically for all scenarios, this difference is solely of a geometric nature, due to the higher altitude and reduced GPS satellite visibility. To counteract this, a different orientation or an additional GPS antenna

Table 6.41: Estimated parameters and dynamic parameterisation used for the space-tie satellites in the systematic error-free case for GPS.

Parameterisation for space-tie satellite in the systematic error-free case for GPS	
All scenarios	
General	
Arc length	24 hours
LEO satellites	
Initial state parameters	Estimated
Atmosphere parameters	Piecewise linear every 6h
Empirical accelerations	1/rev cosine and sine in transversal and normal direction every 75 min with linear amplitude modelling
Clocks	Estimated per epoch
Ambiguities	Estimated and fixed using DD

with a different orientation could be considered, as proposed for the Genesis mission (Montenbruck et al., 2023).

The orbital fit values of the GPS constellation are approximately 51 cm in code and 4.8 mm in phase, showing no temporal variation. Adding space-tie satellites, results in a minor increase in the RMS in phase for all scenarios. This is strongest for the GRASP-like scenario and weakest for the circular scenarios, however, all variations are below 0.1%.

Table 6.42: GPS orbit fit statistics and total number of observations for the simulated space-tie satellite scenarios and the GPS satellites. The number of observations refers to the ionosphere-free linear combination of code and phase observations, which is the same for both. Full simulation time span from beginning of 2008 to the end of 2014. For the GPS constellation, the change when adding the space-tie satellite is given in percentages.

	Code [cm]			Phase [mm]			Number of
	RMS	Mean	Std.	RMS	Mean	Std.	observations
LEO satellites							
GRASP-like	37.95	0.00	37.95	2.73	0.00	2.73	57’364’193
E-GRASP-mod	37.94	0.00	37.94	2.70	0.00	2.70	49’731’838
E-GRASP-like	37.95	0.00	37.95	2.60	0.00	2.69	48’147’810
Circular 30°	37.97	0.00	37.97	2.65	0.00	2.65	42’300’660
Circular 60°	38.01	0.00	38.01	2.65	0.00	2.65	41’411’860
Circular 89°	38.00	0.00	38.00	2.65	0.00	2.65	42’297’554
GPS satellites							
Reference	51.09	0.00	51.09	4.82	0.00	4.82	6’096’564’540
+ GRASP-like	+0.00%	0.00	+0.00%	+0.06%	0.00	+0.06%	idem
+ E-GRASP-mod	+0.00%	0.00	+0.00%	+0.05%	0.00	+0.06%	idem
+ E-GRASP-like	+0.00%	0.00	+0.00%	+0.05%	0.00	+0.06%	idem
+ Circular 30°	+0.00%	0.00	+0.00%	+0.04%	0.00	+0.04%	idem
+ Circular 60°	+0.00%	0.00	+0.00%	+0.04%	0.00	+0.04%	idem
+ Circular 89°	+0.00%	0.00	+0.00%	+0.04%	0.00	+0.04%	idem

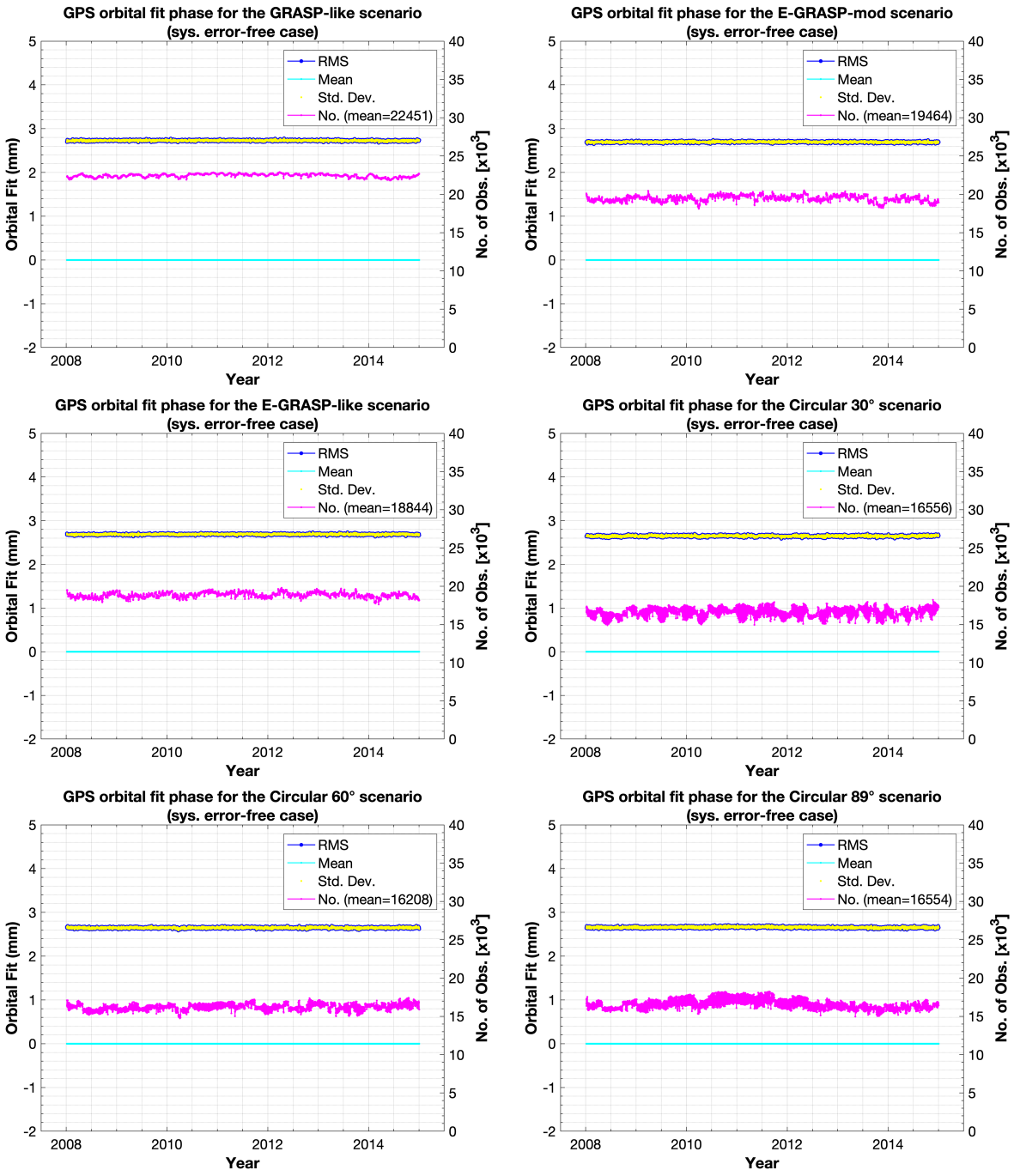

Figure 6.79: Orbital fits for the GPS phase observations of the simulation scenarios in the systematic error-free case.

Global observation coverage The GPS receiver on the space-tie satellite is mounted at the top of the satellite and aligned with the zenith. Due to the different orbit scenarios, the visibility of GPS satellites varies. In the simulation, all SST GPS observations are simulated first, and then these are edited to replicate the 8-channel receiver of Sentinel-3A. Fig. 6.80 shows the number of PRNs visible and observed in parallel after editing the receiver channels, with the former shown in blue and the latter in orange. For the GRASP-like scenario in particular, it can be seen that significantly more satellites could be observed in parallel if the receiver had more channels. This effect is smaller for the eccentric E-GRASP-mod and E-GRASP-like scenarios, where peaks of up to 15 PRNs occur every 12 hours, which is related to the altitude of the eccentric scenarios. In the circular scenarios, the number of PRNs visible in parallel is almost always a maximum of eight, and often falls below the critical value of four PRNs, which should be avoided for continuous tracking.

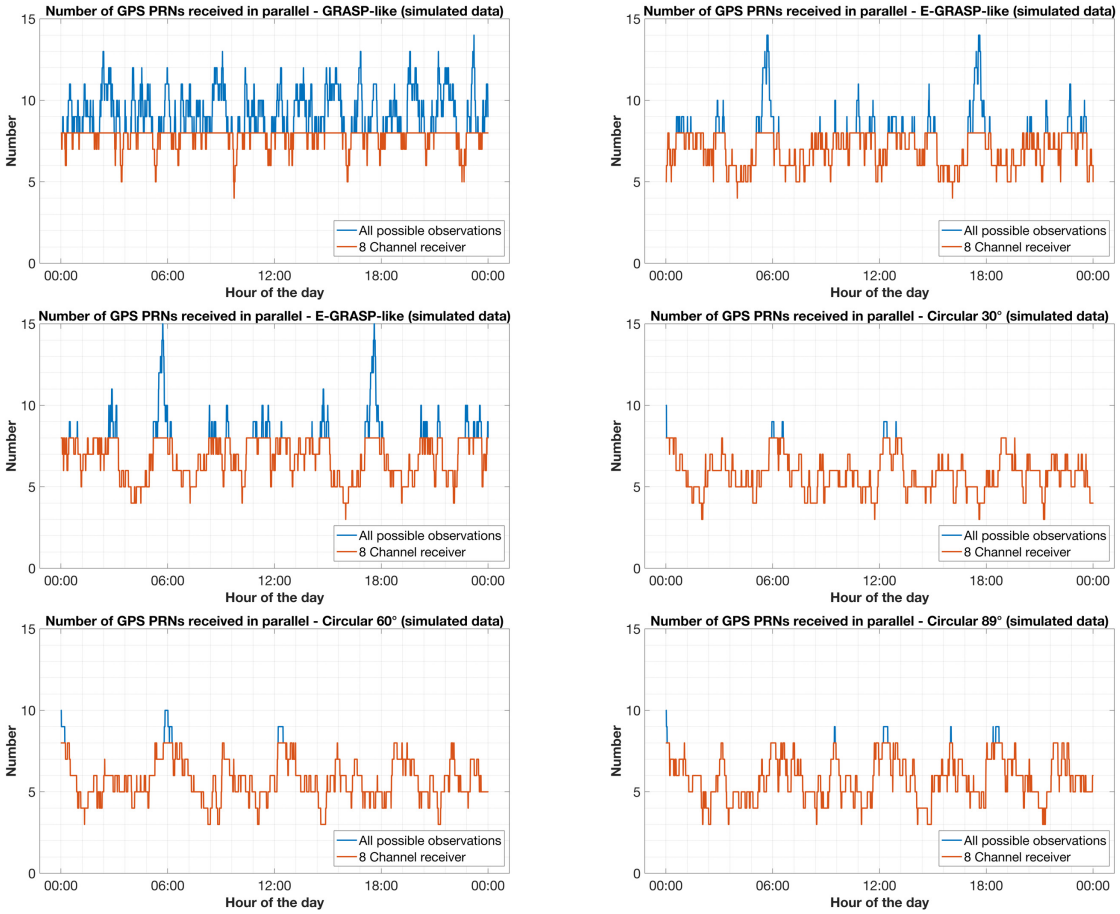

Figure 6.80: Number of PRNs visible per epoch in blue and tracked per epoch in orange. The number of channels of the receiver for the tracking is limited to eight.

The evaluation of the GPS observations over the elevation is shown in Fig. 6.81. Due to the orientation of the GPS antenna on the space-tie satellite, 90 degrees of elevation points towards the zenith. The histogram for the GRASP-like scenario reflects a typical distribution of observations seen with conventional LEO satellites with GPS receivers. Most observations are possible at lower elevations, increasing rapidly below 50 degrees.

By contrast, all other scenarios show fewer observations, except for the E-GRASP-mod and E-GRASP-like scenarios, which show an increased possibility for observation starting

from an elevation of about 60 degrees. The same applies, albeit to a much lesser extent, to the 60 degree circular scenario.

One possible reason for this is the inclination of the scenarios, which is close to that of the GPS satellites (55 degrees). Thus, from the perspective of the LEO antenna at a constant azimuth, the line of sight of the GPS satellites starts at 0 degrees in the flight direction, passes through the entire elevation range, and finally sinks below the horizon at an azimuth of 180 degrees. Consequently, these scenarios exhibit a higher number of observations at high elevation angles.

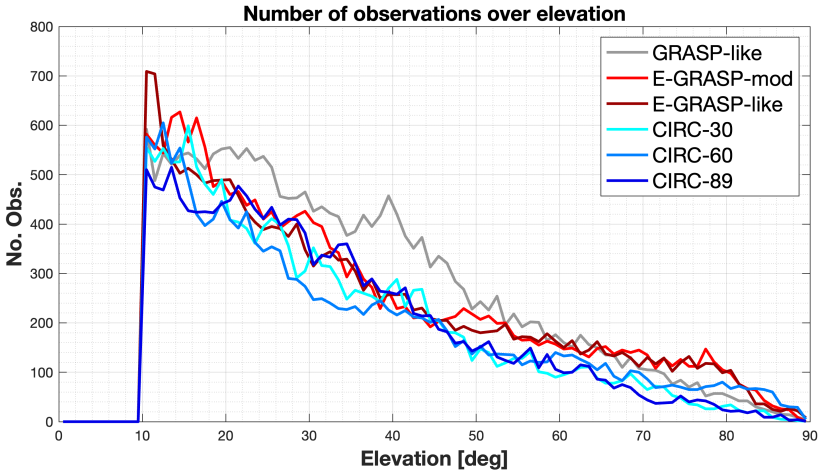

Figure 6.81: Number of observations over the elevation angle for the zenith-pointing GPS antenna of the space-tie satellite scenarios.

Sky plots of the GPS observations for one day are shown in Fig. 6.82. The most homogeneous distribution of observations can be seen here for the GRASP-like scenario.

For the E-GRASP-mod, E-GRASP-like, and 60 degree circular scenarios, the aforementioned concentration of observations along the 0 and 180-degree azimuths is evident. The 30 and 89 degree circular scenarios do not exhibit this pattern, reflecting the significantly lower number of possible observations.

As shown in Fig. 6.83, the global distribution of observations indicates that, for all scenarios, the majority of observations are possible at the northern and southern boundaries defined by the inclination. The geographic distribution of observations is most homogeneous for the GRASP-like scenario, for which no regional patterns can be identified. The E-GRASP-mod and E-GRASP-like scenarios both show similar distribution patterns, similar to those observed in DORIS. Here, eight maxima occur around the equator, following the inclination to the North and South. The circular scenarios show a lower number of observations around the equator. With increasing inclination, four maximal regions around the equator arise which correlate with the ground tracks of the GPS satellites.

No regional structure can be found in the standard deviation, mean or median of the residuals for any of the scenarios.

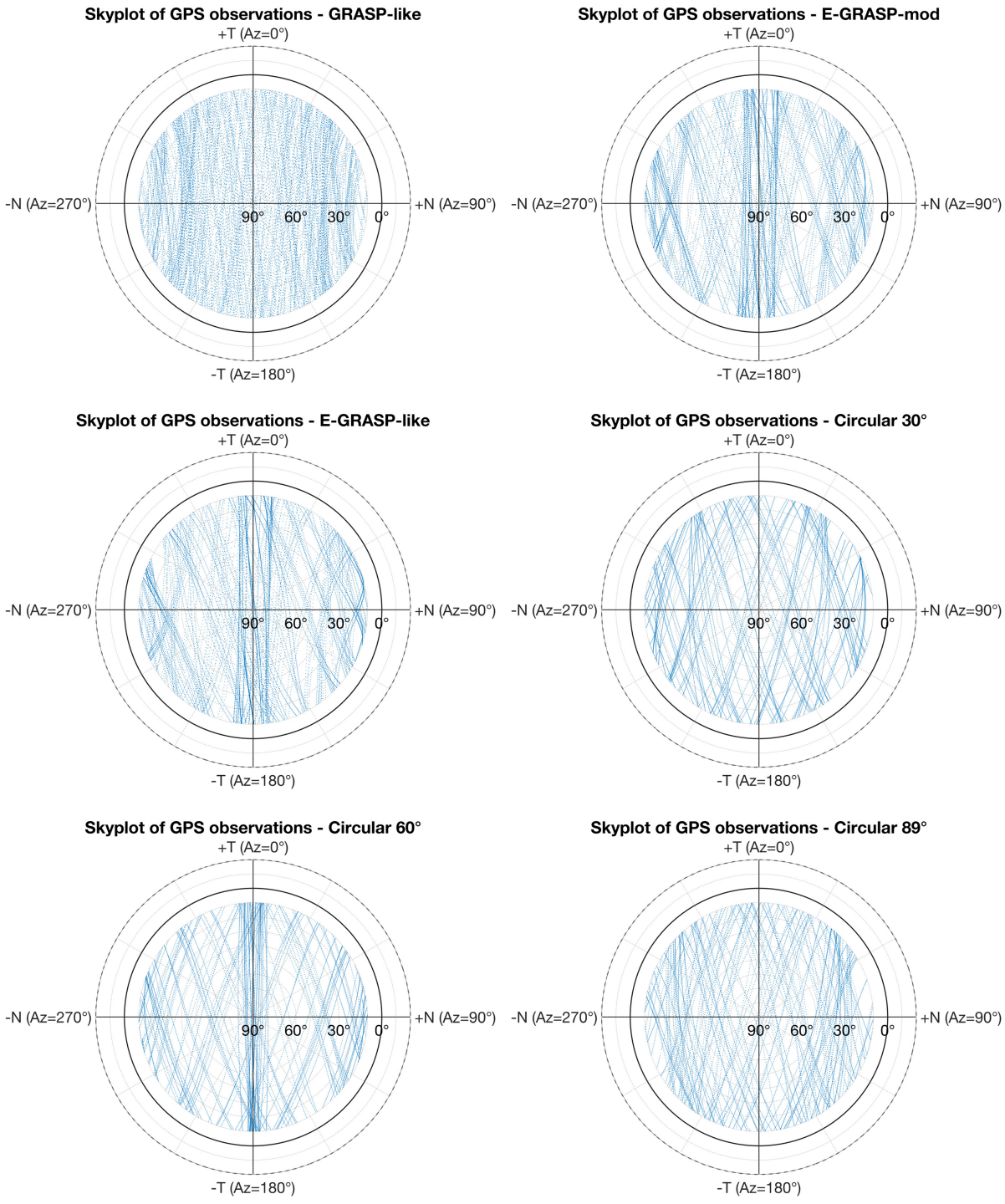

Figure 6.82: Skyplot of the tracked GPS observations for the space-tie satellite scenarios. T = transversal, N= normal

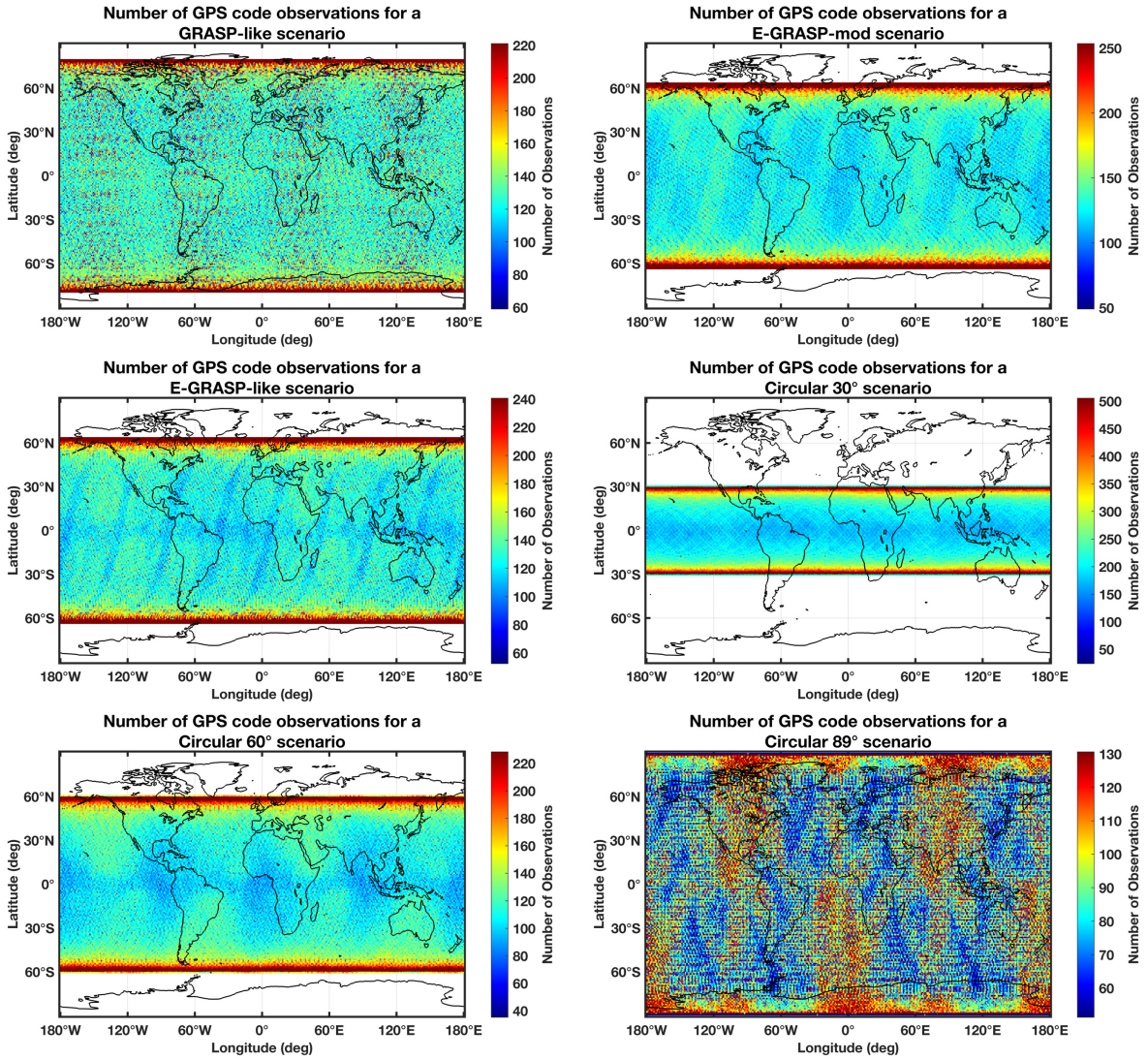

Figure 6.83: Global observation coverage of simulated GPS observations, analysed over a one-year period.

Orbit recovery

LEO satellite The recovered orbit of the space-tie satellites, determined alongside the constellation, is compared with the simulated orbit. The orbit differences in the form of the mean RMS are below 0.1 mm for all scenarios and components, with the radial component being the most accurately determined (see Fig. 6.84). The GRASP-like scenario shows the best results, while the circular scenarios show the worst. In the two eccentric scenarios, the E-GRASP-like scenario performs slightly worse than the E-GRASP-mod scenario, particularly with regard to the radial component. It can be concluded that, for LEO POD with GPS in the case free of systematic errors, a low orbit and a non-highly eccentric orbit seems advantageous. Nevertheless, 3D orbit accuracy is clearly superior to that of DORIS and SLR in all scenarios. No systematic bias can be identified in any of the scenarios.

Fig. 6.85 shows the geographical distribution of median orbit differences for all scenarios. The radial component exhibits the least variation across all scenarios. In the cross-track and along-track directions, increased noise in the differences is evident in all scenarios except

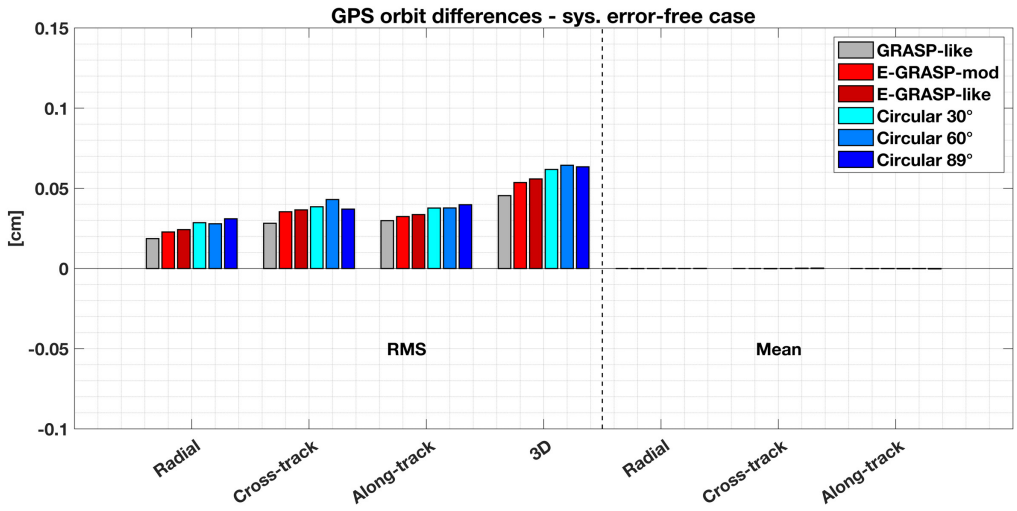

Figure 6.84: Mean RMS value of the orbit comparison in the radial, cross-track, along track and 3D directions, as well as the mean orbit deviation. The true orbit of the simulation is compared to the orbit recovered in the systematic error-free case.

the GRASP-like one. A systematic pattern is evident only for the 89 degree circular scenario and for the cross-track and along-track components. Here, an amplitude of approximately 0.2 mm can be seen, which correlates with the geographical distribution of the observations. This is due to the significantly lower number of observations in the affected regions in this scenario.

Orbit comparisons of the recovered and simulated orbits, show that the GRASP-like scenario achieves the greatest orbital accuracy. The other scenarios achieve slightly worse results in terms of RMS of the orbit comparison and higher noise in the geographical orbit comparison. However, systematic geographical patterns in the orbit can only be found in the 89 degree circular scenario and are correlated with the lower number of observations in affected regions.

GPS satellites In the integrated processing, space-tie satellites also affect the orbit and clock estimation of the GPS constellation. The statistical evaluation of the orbit and clock comparison of the GPS constellation is shown in Tab. 6.43. Adding a space-tie satellite improves the orbit and clock accuracy of the GPS constellation in each scenario. Notably, the improvement in estimated clocks is rather small for all scenarios, at less than 1% for the GPS satellite clocks and less than 0.1% for ground station clocks. The greatest improvement in the orbits is seen in the radial component, with circular scenarios being about twice as effective as the GRASP-like scenario, resulting in a reduction of up to 11% in RMS. However, the SISRE_p value improves by less than 1% in all scenarios, reflecting the low potential for improved positioning with a GPS receiver due to the improved orbits and clocks of the GPS constellation. The constellation integrity (SISRE_m) shows improvements of between 1 and 3%, with the greatest improvement again being achieved with the circular scenarios.

The geographic changes in the GPS constellation's orbit differences compared to the simulated orbit, when the space-tie satellite scenarios are added, are shown in Fig. G.27 in App. G.3. The figures show the absolute difference: negative values indicate a reduction (improvement), while positive values indicate an increase in the median orbit difference. None of the space-tie scenarios results in obvious regional changes to the GPS constellation's orbital differences. Changes are mostly limited to the radial component and regions where

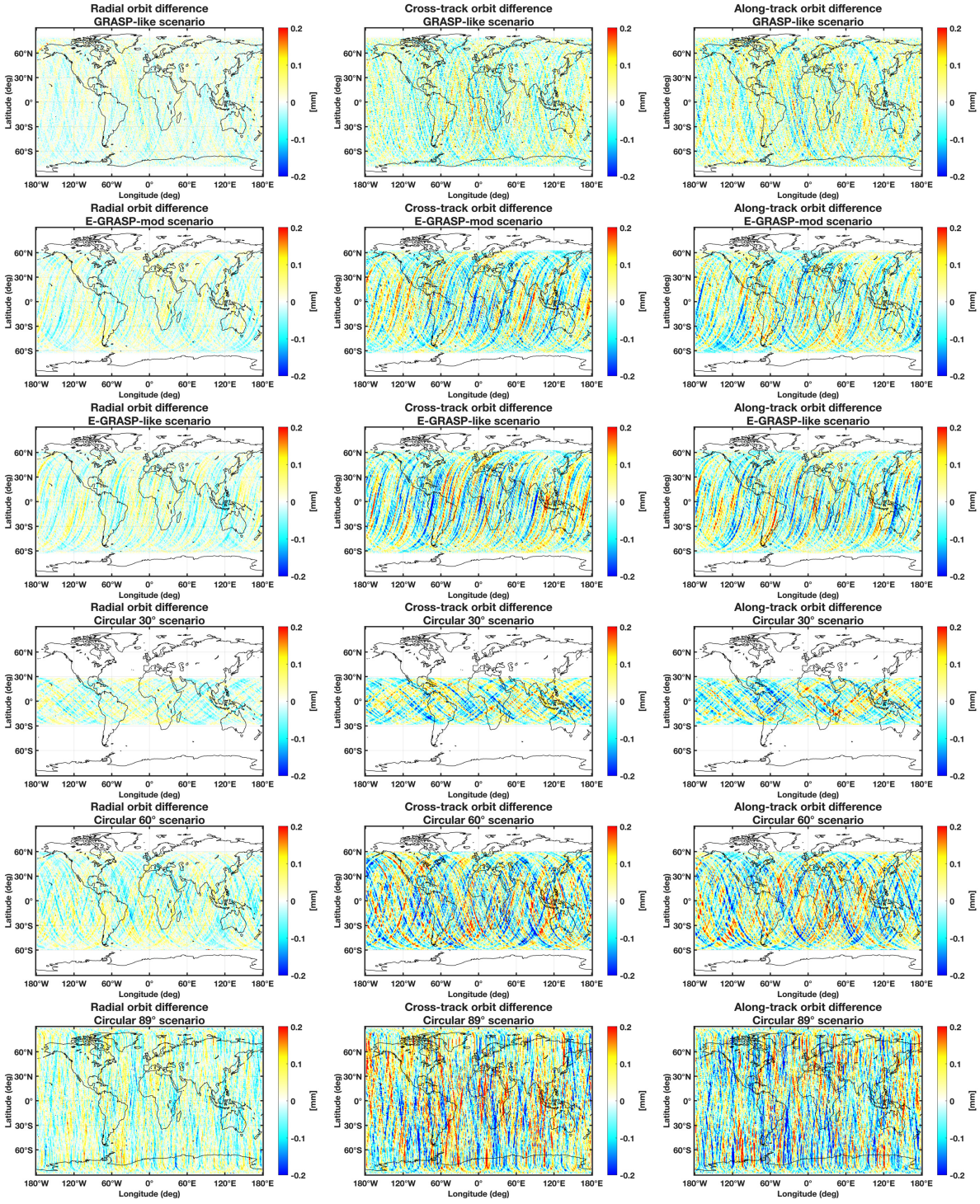

Figure 6.85: Median orbit differences of the LEO satellites between the true simulated and recovered orbit over a one-year time span for GPS in the systematic error-free case. From the top to the bottom: GRASP-like; E-GRASP-mod; E-GRASP-like; Circular 30°; Circular 60°; Circular 89° scenario. From left to right in radial, cross-track, and along-track direction.

Table 6.43: Statistics of the recovered orbit and clocks of the GPS constellation in the systematic error-free case, with one of the space-tie satellite scenarios added respectively. Values are computed over the entire time span in radial (R), transversal (T), and normal (N) direction. SV stands for GPS satellite vehicle, Sta. for ground station. Values are given in percentages and centimetres.

	RMS						Clock RMS		Mean		
	R	T	N	SISRE_{orb}	SISRE_{p}	SISRE_{m}	SV	Sta.	R	T	N
Systematic error-free case											
GPS constellation	0.12	0.07	0.08	0.12	0.49	0.54	0.50	0.61	-0.00	0.00	0.00
+ GRASP-like	-4.76%	-4.88%	-5.03%	-4.82%	-0.36%	-1.24%	-0.61%	-0.06%	-0.00	+0.00	+0.00
+ E-GRASP-mod	-7.62%	-5.77%	-5.95%	-7.79%	-0.29%	-1.75%	-0.71%	-0.05%	-0.00	+0.00	-0.00
+ E-GRASP-like	-7.63%	-5.51%	-5.81%	-7.86%	-0.28%	-1.77%	-0.71%	-0.05%	-0.00	+0.00	+0.00
+ Circular 30°	-9.97%	-5.29%	-6.57%	-10.34%	-0.25%	-2.21%	-0.82%	-0.04%	-0.00	+0.00	+0.00
+ Circular 60°	-10.05%	-5.63%	-6.20%	-10.37%	-0.23%	-2.20%	-0.80%	-0.03%	-0.00	+0.00	-0.00
+ Circular 89°	-11.80%	-6.46%	-7.50%	-12.12%	-0.26%	-2.55%	-0.93%	-0.04%	-0.00	+0.00	+0.00

increased deviations in the median of the residuals were observed. However, these changes are in the low submillimetre range.

As mentioned above, the inclusion of the space-tie scenarios leads to a reduction in the Satellite Vehicle (SV) clock RMS of less than 1% for all scenarios, with the highest reduction achieved by the circular scenarios. However, the SISRE_{p} does not reflect these findings, as the largest improvements are seen in the GRASP-like scenario and the smallest in the circular scenarios. This suggests that the anticorrelation of the radial position with the SV clock cannot be improved to the same extent as the improvements seen in the orbit and SV clock. This can be seen in the analysis of clock differences relative to the simulated clock along the Sun elongation and beta angles (see Fig. 6.86). For the circular scenarios, and to a lesser extent for the E-GRASP-mod and E-GRASP-like scenarios, an increased clock difference is evident for elongation angles between 70 and 110 degrees, at both low and high beta angles. This difference can be as large as 2 mm. Furthermore, positive and negative differences are evident for eclipse phases at low and high elevation angles. The GRASP-like scenario exhibits the most homogeneous influence across Sun elongation and beta angles.

Reference frame evaluation

Helmert parameters The Helmert parameters for each scenario are shown in Fig. 6.87 and Tab. F.44. Significant X-rotations remain in each scenario, as in the reference solution. Differences from the reference solution are below 0.03 mm for positions and are primarily in Z-translation, as well as in X- and Y-rotations. For velocities, differences from the reference solution are below 5 micrometres/a and are primarily in Z-translation. This is because the Z-translation generally shows high correlations with GPS SRP modelling (Glaser et al., 2020). Adding a LEO satellite can improve this by decorrelation. The inclusion of the space-tie satellite scenarios does not significantly alter the TRF of any of the scenarios, given the strength of the applied NNR condition.

Formal errors Formal errors of the station coordinates and velocities are evaluated in the X, Y and Z directions (see Fig. 6.88) and in latitude, longitude and height (see Fig. 6.89). The absolute values for all scenarios can be found in App. F.3. The ERPs are converted to millimetre equivalents on the Earth's surface. The expected improvement is greatest

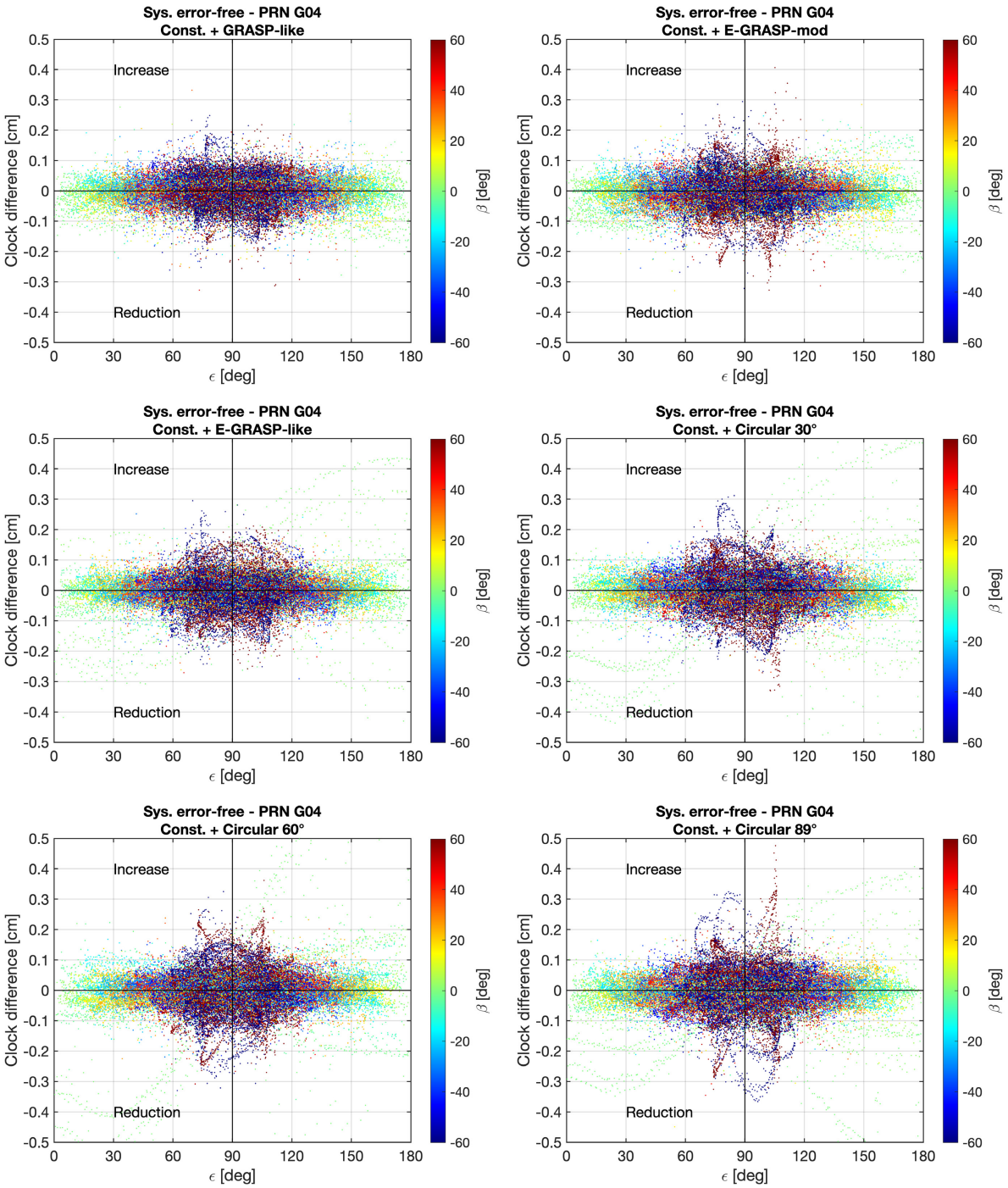

Figure 6.86: Clock difference of absolute clock offset in comparison to GPS constellation alone in the systematic error-free case. Positive values indicate an increase in clock differences, negative values a reduction.

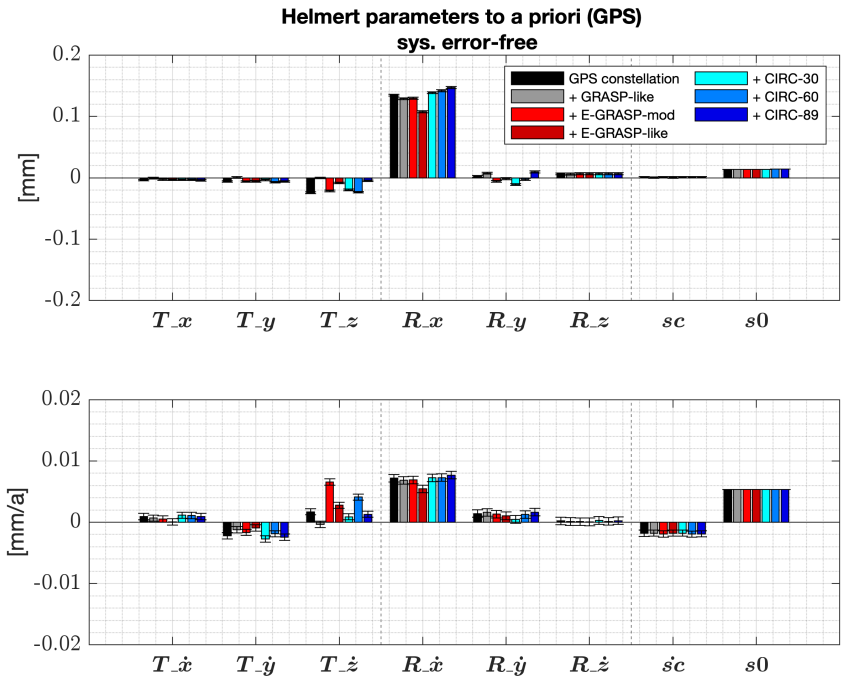

Figure 6.87: The upper figure shows the Helmert parameters for all station positions in the systematic error-free case compared to a priori. The line around the bar shows the standard deviation according to one σ.

for the GRASP-like scenario at 0.47%, the E-GRASP-mod and E-GRASP-like scenarios being similar at 0.40 and 0.39%, respectively, and lowest for all circular scenarios at 0.34% (see Tab. F.45). This is due to the smaller number of possible observations in the higher orbiting circular scenarios. Compared to the other techniques, the expected potential for improvement is significantly lower. This is because the influence of one additional receiver on a satellite is statistically very low, compared to the large number of ground stations (up to 121).

Formal errors of station coordinates The formal errors of the station coordinates are at a similar level for all the examined scenarios, compared with the reference solution (see Tab. F.45).

The scaled improvement shows that the greatest percentage improvement can be achieved in the Z component at around 2-3% (see Fig. 6.88). In geographic coordinates, the strongest improvements of up to 3% are seen in the latitude and height components (see Fig. 6.89). The GRASP-like scenario achieves the highest improvements, while the 30 degree circular scenario achieves the lowest.

The OSI is only slightly lower than the percentage improvements, as the expected improvements are below 1% for all scenarios. A geometric added value can be found for all scenarios, even if it is in the single-digit percentage range. This is most prominent in the Z coordinate and, respectively, in the latitude and height components. The GRASP-like scenario achieves the best results, whereas the 30degree circular scenario achieves the least. However, the differences between the scenarios are very small.

Formal errors of station velocities A similar picture emerges for the station velocities. The strongest scaled improvements are in the Z component, at up to 6%, with improvements in the X and Y components below 1%. In the geographic coordinates of the velocities, the largest improvements of up to 4% can be seen in the latitude and height components. As with the coordinates, the GRASP-like scenario shows the greatest improvement, while the 30degree circular scenario shows the least.

A geometric added value can be seen for each scenario, the conclusions are identical to those based on scaled improvements.

Peak improvement analysis for station coordinates and velocities Peak improvement analysis of the mean and median indicates no significant improvement. The differences are smaller than 1%. Therefore, there is no ground station for which the inclusion of one of the space-tie satellite scenarios results in a sudden change in formal errors in station positions or velocities.

Formal errors of ERPs The scaled improvement of the pole coordinates is below 1% for all scenarios. A geometric added value can also be seen, but it is almost insignificant. In LOD, improvements in formal errors of up to 3% can be seen, with each scenario resulting in a geometric added value. Comparing the scenarios shows that those LEOs continuously flying at higher altitudes, as well as in near-polar orbits, are more advantageous. In the ERPs, no sudden improvement can be detected either.

A posteriori ERP analysis The statistical evaluation of the estimated ERPs is listed in Tab. F.46. Although a reduction in noise in the pole coordinates of up to 4% can be achieved, the changes are not statistically significant for any of the scenarios.

The change in the determined offsets in the pole coordinates compared to the reference solution is less than 0.1 mm for all scenarios. A significant bias of up to 0.01 mm in the X-pole and 0.12–0.16 mm in the Y-pole remains for all scenarios, except for the E-GRASP-like scenario and the 60degree circular scenario in the X-pole. However, the changes here are extremely small.

The linear regression shows a significant trend in the Y-pole for all scenarios, but this is below 1/100 mm/a.

A similar picture emerges in LOD, where a reduction in noise of up to 4% can be achieved, although this is not statistically significant for any of the scenarios. None of the scenarios show significant offsets or drifts.

ERP spectral analysis No signals can be detected in the spectral analysis of the reference solution. The inclusion of the space-tie scenarios has no detectable effect on the spectral analysis of the pole coordinates or LOD for either scenario, variations are well below the micrometre level.

Conclusion - systematic error-free The results of the error-free GPS simulation show that the global observation coverage is homogeneous for each scenario, with slight hotspot regions in the higher-altitude near-polar orbit scenarios. Additionally, the number of possible observations decreases by up to 28% with increasing flight altitude, compared to the GRASP-like scenario, in which the number of observations increases for elevation angles

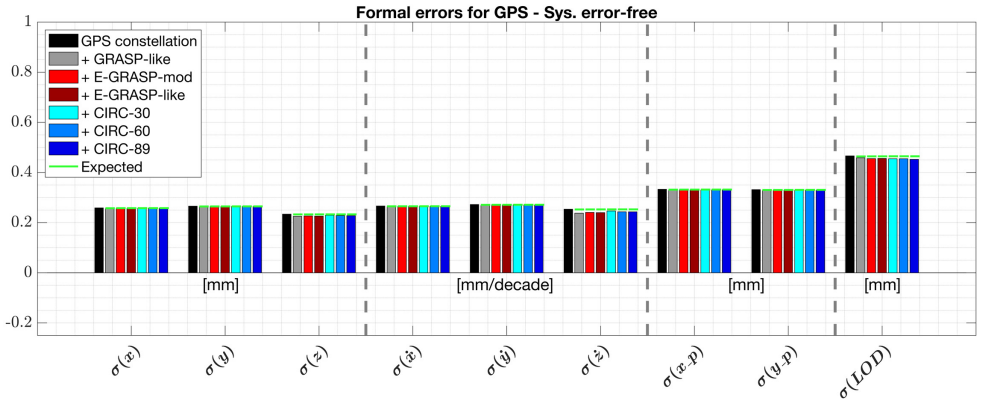

(a) Absolute values of the median of the formal errors. The green bars indicate the expected improvement.

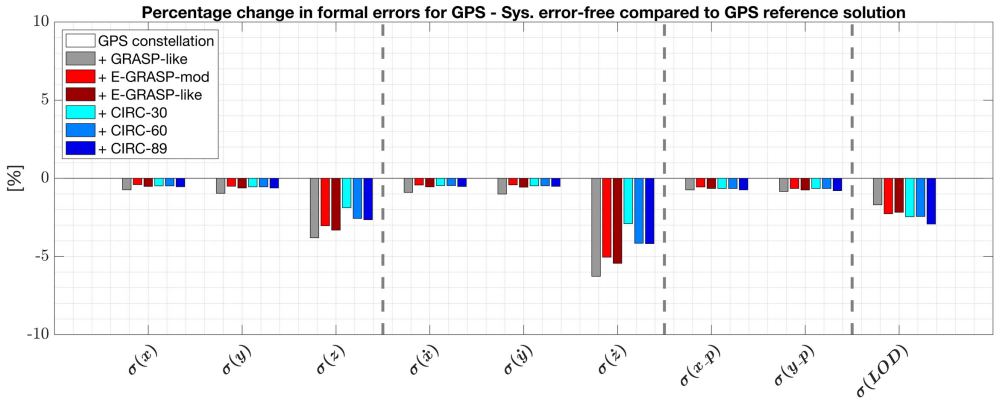

(b) Scaled improvement

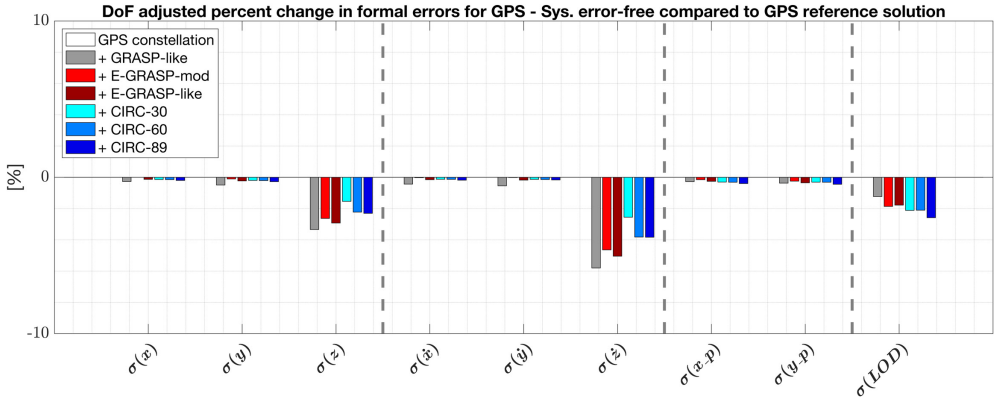

(c) Observation scaled improvement

Figure 6.88: Fig. a) shows the absolute values of the median formal error in X, Y and Z directions for the reference scenario and each space-tie satellite scenario. Fig. b) shows the scaled improvement, Fig. c) shows the observation scaled improvement.

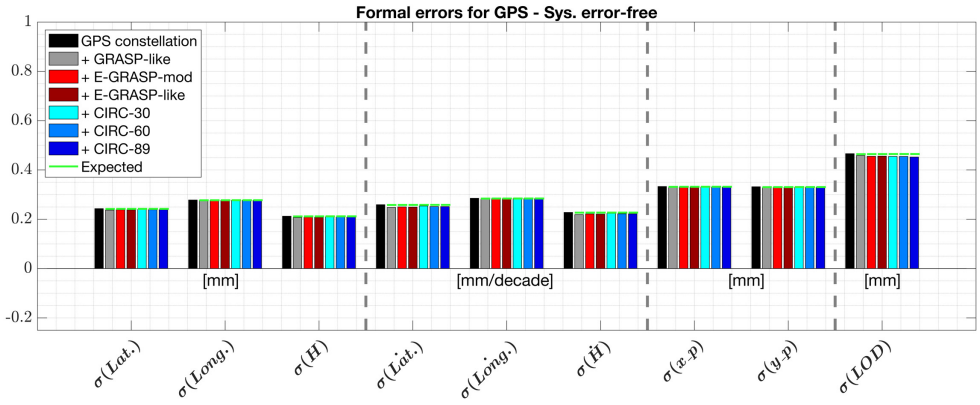

(a) Absolute values of the median of the formal errors. The green bars indicate the expected improvement.

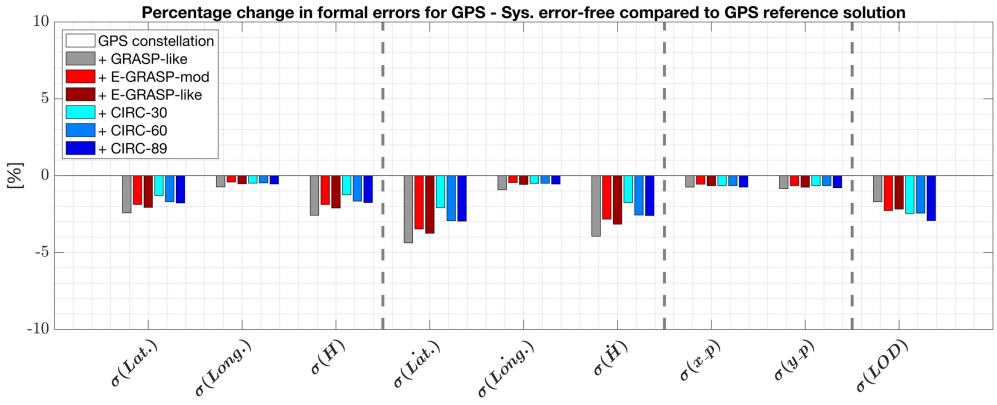

(b) Scaled improvement

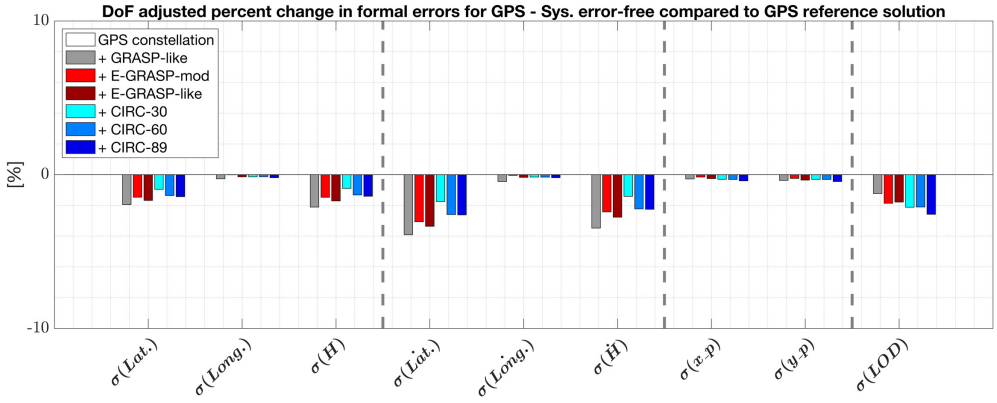

(c) Observation scaled improvement

Figure 6.89: Fig. a) shows the absolute values of the median formal error in latitude, longitude, and height for the reference scenario and each space-tie satellite scenario. Fig. b) shows the scaled improvement, Fig. c) shows the observation scaled improvement.

below 50 degrees.

The GRASP-like scenario achieves the highest orbit accuracy, but the other scenarios are not far behind. The average RMS of 3D orbit comparison against the simulation is below 0.1 mm for all scenarios. Geographical distributions in orbit analysis can only be found below this level, and are correlated with the observation distributions.

The geographical influence on the orbits of the specific GPS constellation is primarily limited to the radial component and regions where fewer observations are possible by the ground network. As the flight altitude of the space-tie satellite scenario increases, the orbits of the GPS constellations can be improved in the radial component by up to 12% in the mean RMS for the 89 degree circular scenario, as also evident in SISRE_{orb}. However, the potential to improve SISRE_{p}, and thus to achieve enhanced positioning capabilities for ground stations, is less than 1% for all scenarios.

The inclusion of any of the space-tie satellite scenarios has not revealed significant changes in the Helmert parameters.

For each scenario, a geometric added value can be determined in the formal errors of the estimated station positions and velocities. This is most evident in the Z component, amounting to up to 3% for positions and 6% for velocities. In geographical coordinates, the greatest added value is evident in the latitude and height components, amounting to up to 3% for positions and up to 4% for velocities. The GRASP-like scenario proves to be the most advantageous here, while the 30 degree circular scenario is the least advantageous.

The potential for improving the formal errors of the pole coordinates is less than 1% for all scenarios, and up to 3% for LOD. The estimated ERPs are not significantly altered. Spectral analysis of the estimated ERPs also shows no significant influence.

Tab. 6.44 shows the evaluation of the individual scenarios for improving the TRF and ERPs with GPS. The potential of each scenario is at a similar level, ranging from 2.1 to 2.5. The potential for improvement is limited to station positions and velocities, with the GRASP-like scenario proving to be favourable and the 30 degree circular scenario proving to be the least effective.

Table 6.44: Maximum potential of the satellite scenarios for GPS to improve the TRF and ERPs in the case free of systematic errors. The lower the stated value, the better the rating. The summary represents the unweighted mean value.

	G-like	E-G-mod	E-G-like	Circ. 30°	Circ. 60°	Circ. 89°
Obs. cov.	①	①	①	②	②	②
Orbit	①	①	①	①	①	①
Helmert	①	①	①	①	①	①
Station pos. f.e.	①	②	②	③	②	②
Station veloc. f.e.	①	②	②	③	②	②
Stat. stab. f.e.	③	③	③	③	③	③
Pole coord. f.e.	③	③	③	③	③	③
Pole coord. est.	③	③	③	③	③	③
LOD f.e.	③	③	③	③	③	③
LOD est.	③	③	③	③	③	③
ERP stab. f.e.	③	③	③	③	③	③
Summary	2.1	2.3	2.3	2.5	2.4	2.4

6.3.2.2 Influence of solar radiation pressure mismodelling

For SRP mismodelling for GPS, the macro-model of all GPS satellites was modified, as described in Sec. 4.6.3. Fig. 6.90 shows the influence of this mismodelling on PRN 1 over one day at a beta angle of 32.6 degrees. The most significant effect is a radial acceleration, reaching an amplitude of approximately 0.1 mm/s^2 after one day. The influence in the transversal and normal directions is significantly smaller.

In this case, the space-tie satellite remains unaffected and is still considered free of systematic errors. The parameterisation of the GPS constellation and the space-tie satellite remains unchanged.

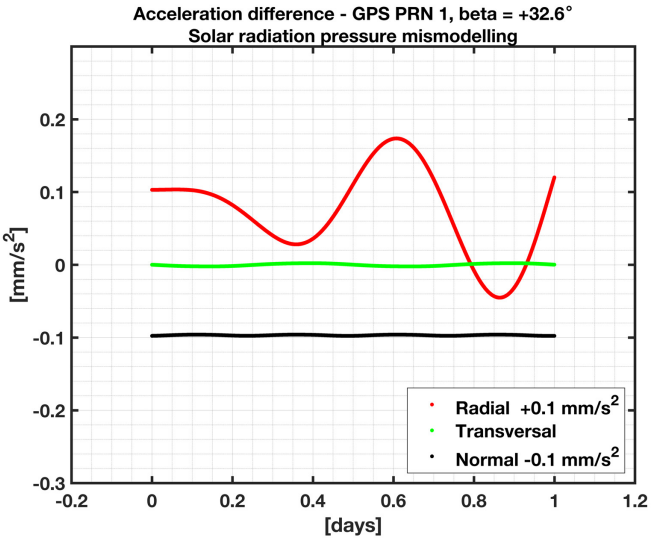

Figure 6.90: Difference in the sum of the accelerations acting on a GPS satellite over a period of 1 day, in the case of SRP mismodelling.

Orbital fit

LEO satellite The influence of the introduced SRP mismodelling to the GPS constellation on the orbital fit of the space-tie satellite is limited to the phase residuals, which increase by up to 0.3%. This effect is most pronounced in the circular scenario (0.3%), less so in the E-GRASP-mod and E-GRASP-like scenarios (both 0.2%), and least in the GRASP-like scenario (0.1%). The code residuals show no discernible influence. No geographical pattern can be identified in the code and phase residuals.

GPS satellites The orbital fit of the GPS constellation shows that the residuals are not significantly affected by the mismodelling. Variations are well below 0.1%, and no temporal variation can be detected. Integrating the space-tie satellites has the same effect as in the systematic error-free scenario.

Orbit recovery

LEO satellite The mismodelling of the constellation leads to an increase in the mean RMS of the orbit comparison by up to 34% in 3D for the space-tie satellites (see Fig. 6.91). The GRASP-like scenario is the least affected, with an increase of 7%. The E-GRASP-mod and E-GRASP-like scenarios show an increase of 23-25%, and the circular scenarios as large as 34%. Comparing the scenarios shows that the radial component is most affected, by increasing flight altitude. The lower the altitude, the more prominent the differences in the cross-track component become. The most noticeable systematic mean orbit difference occurs exclusively in the radial and cross-track components of the circular scenarios, and is less than 0.1 mm.

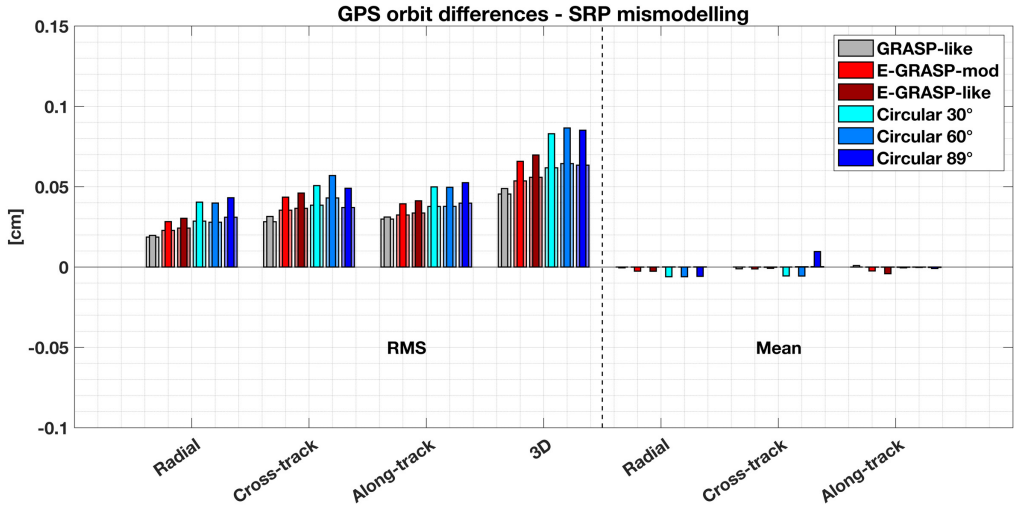

Figure 6.91: Mean RMS values of the LEO orbit comparison in radial, cross-track, along track and 3D directions, as well as the mean orbit deviation. The thinner bars show the results of the SRP mismodelling cases, the slightly more transparent thicker bars in the background show the values achieved in the systematic error-free case.

Geographical analysis of the orbital differences shown in Fig. G.28 reveals that, in the stronger affected scenarios, the orbital differences increase in the radial component, particularly in regions around the equator and, for the 89 degree circular scenario, also at

the North Pole. The amplitude is strongest for the 89 degree circular scenario at 0.13 mm, for the other scenarios, it is below 0.1 mm .

In the cross-track component, an increase in orbit differences is primarily observed in the direction of the polar regions, with amplitudes in the range of 0.1-0.2 mm. The circular scenario exhibits the most pronounced differences, as well as a correlation with the observation coverage.

In the along-track direction, no clear regional distribution can be observed, only the E-GRASP-like scenario exhibits a regional pattern, with an amplitude of approximately 0.2 mm near 30 degrees north latitude.

GPS satellites In the GPS constellation, the introduced mismodelling leads to an increase in the mean RMS of the orbit comparison by a factor of 5 in the radial component, and by a factor of approximately 2 in the cross-track and along-track directions (see Tab. 6.45). Additionally, a mean orbit difference of 0.5 cm is observed in the radial component. This is reflected in SISRE_{orb}, which increases by a factor of 5 to a level similar to that of the radial component. However, there is almost no increase in SISRE_{p}, despite an increase in SISRE_{m} by a factor of 2 and an increase in the SV clock RMS by about 50%. This reflects the anticorrelation of the now larger SV clock differences with the radial orbit position. The increase in the clock RMS of the ground stations is less than 1%.

The inclusion of one of the space-tie satellite scenarios leads to a significantly lower improvement compared to the systematic error-free case. Improvements in the mean RMS are at most 1.4% in the radial component and 3.7% in the cross-track and along-track directions. None of the scenarios can improve the observed radial orbit bias. The SISRE_{orb}, the general constellation integrity (SISRE_{m}) and the SV clock RMS can be improved most with the circular scenarios. However, the largest improvements in SISRE_{p} are seen in the GRASP-like scenario and the smallest in the circular scenarios. This indicates that improvements in constellation integrity for the circular scenarios do not lead to an improvement of the anticorrelation between the SV clock estimates and the radial orbit position. Changes in the ground station clock estimates are negligible.

Table 6.45: Statistics of the recovered orbit and clocks of the GPS constellation in the SRP mismodelling case, with one of the space-tie satellite scenarios added respectively. Values are computed over the entire time span in radial (R), transversal (T), and normal (N) direction. SV stands for GPS satellite vehicle, Sta. for ground station. Values are given in centimetres unless otherwise stated.

	RMS						Clock RMS		Mean		
	R	T	N	SISRE_{orb}	SISRE_{p}	SISRE_{m}	SV	Sta.	R	T	N
Systematic error-free case											
GPS cons. SRP mism.	0.58	0.15	0.14	0.57	0.49	1.24	0.75	0.61	0.50	0.00	0.01
+ GRASP-like	-0.33%	-2.61%	-3.73%	-0.34%	-0.37%	-0.63%	-0.75%	-0.05%	0.50	0.00	0.01
+ E-GRASP-mod	-0.76%	-2.21%	-2.89%	-0.77%	-0.26%	-0.73%	-0.60%	-0.03%	0.50	0.00	0.01
+ E-GRASP-like	-0.78%	-1.50%	-2.11%	-0.79%	-0.27%	-0.72%	-0.58%	-0.04%	0.50	0.00	0.01
+ Circular 30°	-1.27%	-1.40%	-3.23%	-1.28%	-0.23%	-1.23%	-0.99%	-0.03%	0.50	0.00	0.01
+ Circular 60°	-1.23%	-1.65%	-2.94%	-1.25%	-0.23%	-1.10%	-0.83%	-0.04%	0.50	0.00	0.01
+ Circular 89°	-1.41%	-1.85%	-2.88%	-1.43%	-0.24%	-1.26%	-0.95%	-0.03%	0.50	0.00	0.01

The geographical distribution of the orbital differences shown in Fig. 6.92 reveals a 5 mm bias in the radial component, as well as smaller differences around the equator and larger differences towards the poles. In the cross-track component, a slight pattern towards

the poles can be seen, with an amplitude of approximately 1.2 mm. Additionally, two larger differences that follow the North South direction can be observed at longitudes of 60° West and 120° East. These differences are correlated with the observation coverage and occur in regions with fewer observations. No pattern can be found in the along-track component.

The inclusion of space-tie satellite scenarios has only a very minor influence on the orbits of the GPS constellation in the SRP mismodelling case (see Fig. G.29). In the radial component, a slight North-South structure with amplitudes between 0.2 and 0.4 mm is evident for all scenarios, with improvements in the northern hemisphere and deteriorations in the southern hemisphere. In the cross-track component, improvements are evident in the two regions detected at 60° West and 120° East longitude, particularly for the E-GRASP-like scenario. This is less or not the case for the other scenarios. No influence is seen in the along-track component.

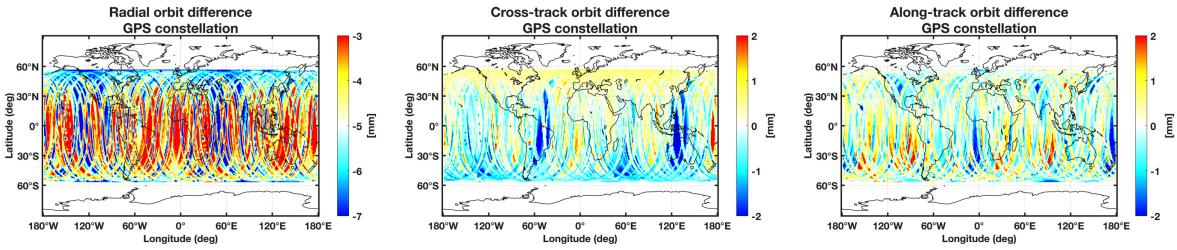

Figure 6.92: Median orbit differences of the GPS constellation in the SRP mismodelling case in comparison to the systematic error-free case over a time span of one year. From left to right in radial, cross-track, and along-track direction.

Analysis of the estimated SV clocks along the Sun elongation and beta angles shows that, at low and high elongation angles, the clock differences increase (see Fig. 6.93). This is slightly more pronounced during eclipse phases. The reason for this is that, in these positions, the satellite lies on the same axis as the Sun and Earth. Therefore, SRP force and the attraction of the Earth are on the same axis. This leads to high correlation with the radial position estimate and thus the estimated satellite clock.

As observed in the systematic error-free case, the inclusion of the space-tie scenarios reduces the SV clock RMS, which is highest for the circular scenarios. However, the improvement in SISRE$_p$ is lowest for these scenarios. This phenomenon has been found to be caused by smaller anticorrelations of the radial position with the SV clock estimates. In the case of SRP mismodelling, the observed patterns in the clock corrections along the Sun elongation angle are amplified further and reach up to 5 mm (see Fig. G.30). Increased clock differences can also be observed for beta angles of the eclipse phases. These reflect not only reductions, but also increases in the SV clock differences. This effect is least pronounced for the GRASP-like scenario, which mostly reflects noise homogeneously across the Sun elongation and beta angle.

Reference frame

Helmert parameters Significant systematic effects on the TRF can be observed (see Fig. 6.94). In the case of the GPS constellation alone, the strongest translations arise in the Z direction, reaching 0.13 mm in position and 0.04 mm/a in velocity. These are known to be caused by strong correlations of the ECOM parameters of the SRP modelling and the station position Z component. Additionally, significant rotations in X and Y are observed,

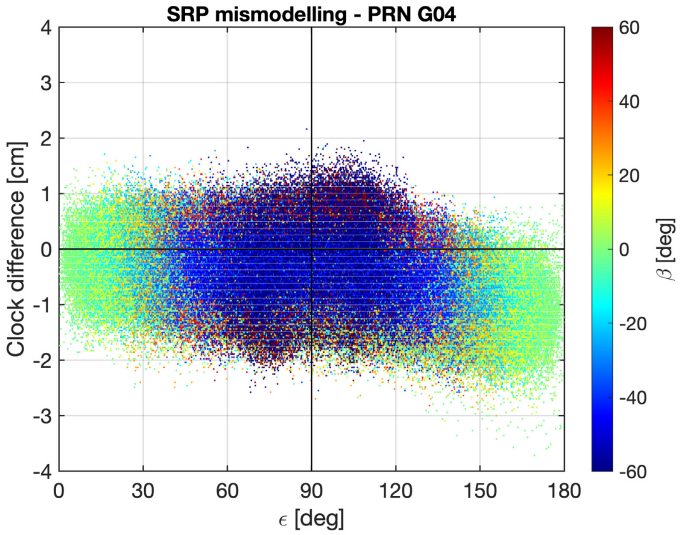

Figure 6.93: Clock difference for PRN 4 in cm over the Sun elongation angle ϵ in the SRP mismodelling case. Different β angles according to colorbar.

reaching up to 0.67 mm in position and 0.04 mm/a in velocity. An effect on the scale is only observed in position, at -0.40 mm.

The integration of a space-tie satellite scenario improves the translations observed in all scenarios, with the greatest improvement seen in the GRASP-like scenario for the X and Z components. Furthermore, none of the space-tie satellite scenarios leads to an obvious improvement in the established systematics in the rotations nor in the scale. Changes in rotation of the positions are below 0.05 mm, which is negligible in view of the remaining systematic error. The influence on the scale is at the level of 0.01 mm or less (see Tab. F.47 in App. F.3).

Formal errors Due to the mismodelling, the formal errors of the GPS constellation without space-tie satellites increase by about 20% in station positions, velocities and ERPs (see Tab. F.48 in App. F.3).

The OSI in station positions due to the integration of the space-tie scenarios is limited to maximum 3% and can be achieved primarily in the Z component (see Fig. 6.95). In geographic coordinates it is about 2% and primarily in the latitude and height components. Differences between the scenarios are very small.

For station velocities, the greatest OSI can also be seen in the Z component, at between 3 and 6%, and in geographic coordinates in the latitude and height components, at a maximum of 4%. The difference between the scenarios is somewhat stronger for the velocities, with the GRASP-like scenario being slightly more advantageous and the 30 degree circular scenario being the least advantageous. However, these differences are small in the context of the overall level of OSI.

For the pole coordinates, the OSI for all scenarios is below 1%. In LOD, the GRASP-like scenario shows the smallest values, at around 1%, while the 89 degree circular scenario shows the largest values, at around 3%.

ERP analysis The introduced mismodelling significantly affects the ERPs of the GPS constellation without an integrated space-tie satellite. The noise in the pole coordinates increases by 120% in the X-pole and 29% in the Y-pole. Systematic biases also occur,

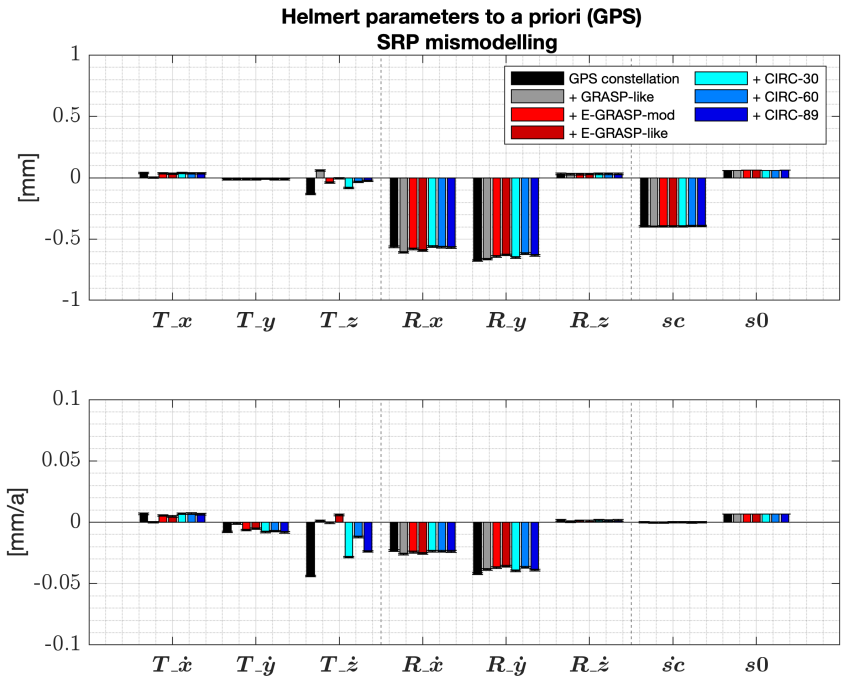

Figure 6.94: The upper figure shows the Helmert parameters for all stations in the SRP mismodelling case compared to a priori. The lower figure shows the values for the velocities.

correlating with the rotations seen in the Helmert parameters, and reaching up to 0.76 mm. Furthermore, a significant drift is observed in both pole coordinates, reaching up to 0.04 mm/a in the X-pole. In LOD, the noise increases by a factor of about 5, and a significant offset of approximately 7 mm occurs. Additionally, a significant drift of 0.06 mm/a can be noted.

Spectral analysis of the ERPs (see. Fig. 6.96) shows an annual signal in the X-pole with an amplitude of 0.1 mm and a semiannual signal of up to 4 mm in LOD. This semiannual signal is also present in the corrections to the node of the GPS satellite's orbital elements. These signals can be traced back to one half cycle of the beta angle period of the satellite's orbital plane.

By the integration of the space-tie scenarios, the noise in the pole coordinates can only be significantly reduced in the X-pole by 4-7%. In the Y-pole, only the GRASP-like scenario shows a significant change in the standard deviation, which increases by around 4%. Changes in the offset and drift of the pole coordinates are less than 0.1 mm and 0.01 mm/a, respectively. In LOD, no significant change in noise can be detected in any of the scenarios. Variation in the offset in LOD are at a maximum of 0.1 mm, with a trend below 0.01 mm/a.

An effect on the spectral analysis of the ERPs cannot be found for any of the scenarios.

Conclusion - SRP mismodelling Introducing SRP mismodelling to the GPS constellation results in a deterioration in the 3D orbit accuracy of the space-tie satellites by up to 34%, with the GRASP-like scenario experiencing significantly less impact at around 7%. The accuracy of the orbits and clocks of the GPS constellation decreases significantly due to the mismodelling. The positive effect of all space-tie satellites on the orbit and clock accuracy of

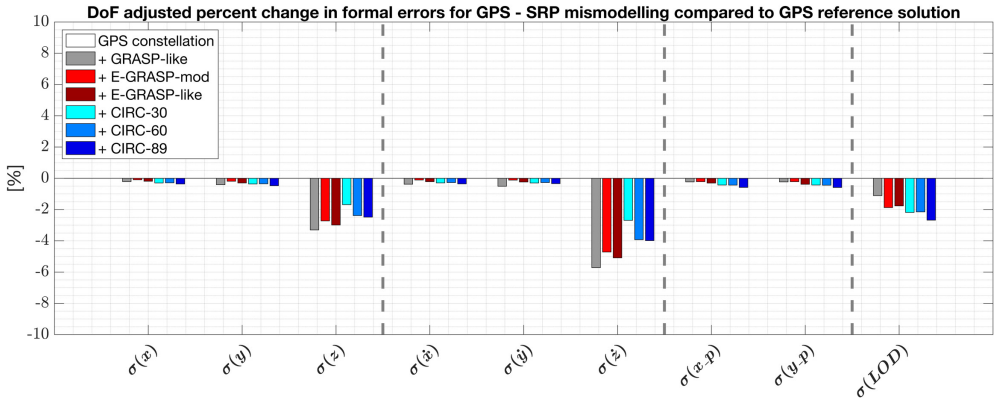

(a) Observation scaled improvement

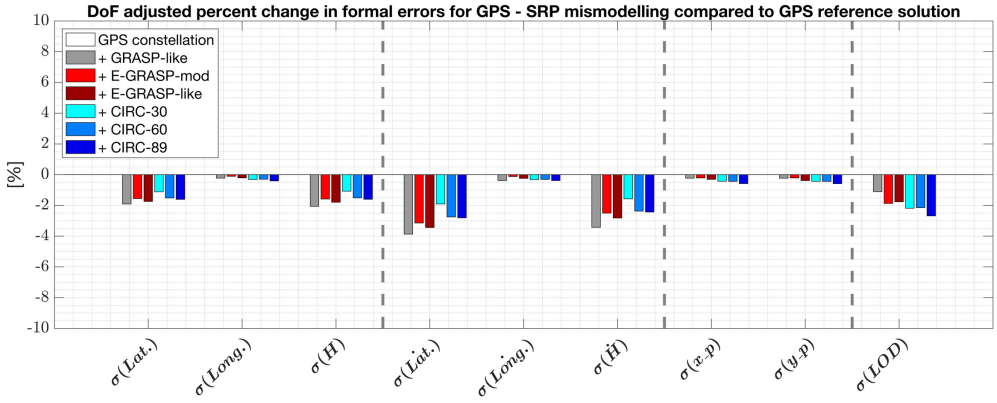

(b) Observation scaled improvement

Figure 6.95: Fig. a) shows the OSI of the median formal error in X, Y and Z for the space-tie satellite scenarios, compared to the GPS constellation with SRP mismodelling, Fig. b) shows the values for geographical coordinates.

the GPS satellites is limited to less than 1% in SISRE_p.

The mismodelling of the GPS constellation leads to systematic translations, rotations, and scale effects. The systematic effect on the scale is 0.5 mm. Integrating a space-tie satellite has a positive effect on translations, but systematic rotations and scale differences cannot be significantly mitigated.

The formal errors in station coordinates and velocities increase by about 20%. Each space-tie satellite scenario exhibits an OSI primarily in the Z coordinate or the latitude and altitude components, with values in the low single-digit percentage range for positions and velocities for all scenarios.

The formal errors of the ERPs also show an increase of around 20%, while the space-tie satellite scenarios show an OSI of less than 3%.

The estimated ERPs show significant increases in noise of up to 120% in the pole coordinates and a factor of five in LOD. Additionally, there are systematic offsets of up to 0.76 mm and drifts of 0.04 mm/a in the pole coordinates, as well as a significant drift of 0.06 mm/a in LOD. Spectral analysis reveals clear signals at the X-pole and in LOD. The strongest

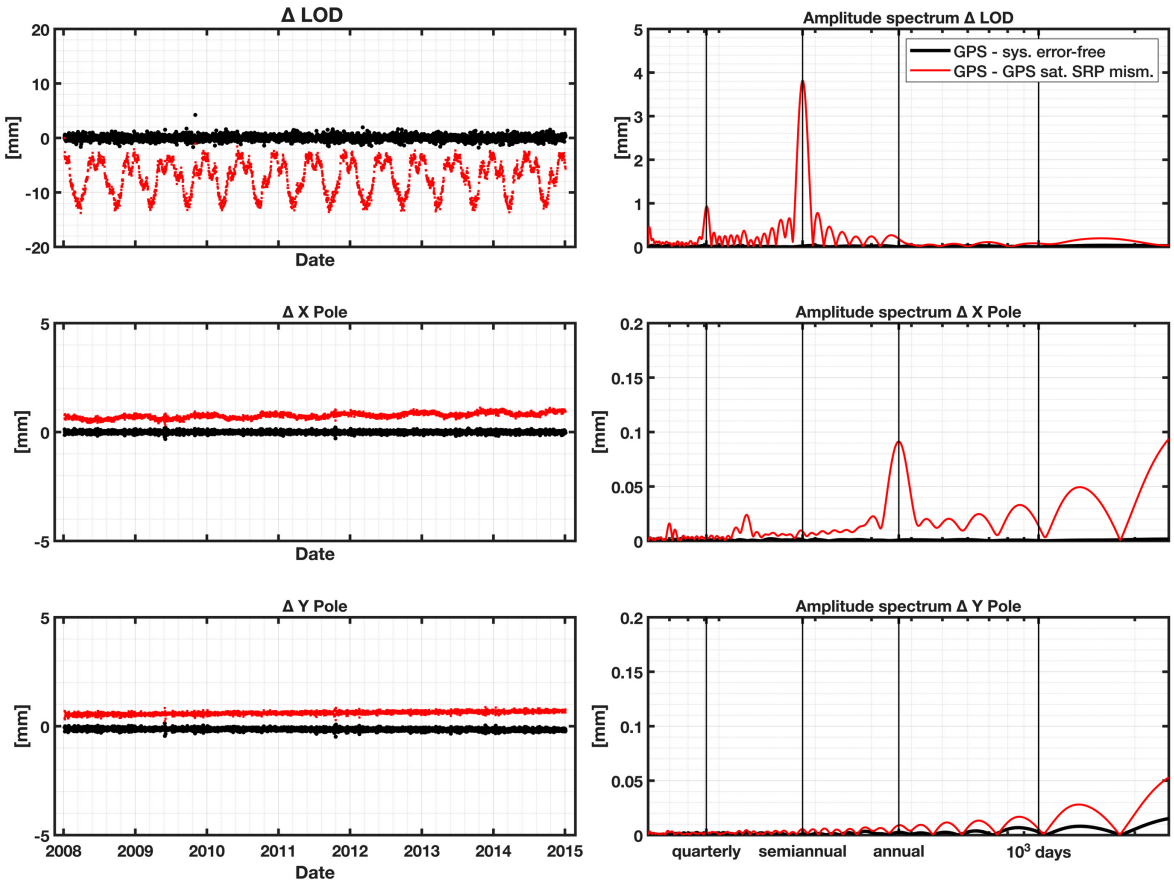

Figure 6.96: Time series of estimated differences of LOD, X-Pole, and Y-Pole and their spectral analysis for the GPS constellation in the systematic error-free case in black and in the SRP mismodelled case in red.

signal is in LOD, with an amplitude of 4 mm and a semi-annual period corresponding to a half beta angle cycle.

Integrating the space-tie satellites has only a very small influence on the determined ERPs. Differences in noise are in the low single-digit percentage range. A significant influence on offsets and drifts can only be observed for the pole coordinates at below 0.1 mm and 0.01 mm/a, respectively. No influence on the spectral analysis of the ERPs can be observed.

Based on the results of the SRP mismodelling of the GPS constellation, none of the scenarios is clearly advantageous (see Tab. 6.46). The positive influences are in the low single-digit percentage range in all areas and for all scenarios. None of the scenarios can lead to a significant improvement in the systematic signals in the ERPs .

Table 6.46: Vulnerability of the satellite scenarios in the systematic SRP mismodelling case for GPS.

	G-like	E-G-mod	E-G-like	Circ. 30°	Circ. 60°	Circ. 89°
Orbit	①	②	②	③	③	③
Helmert	①	①	①	②	②	②
Station pos. form. err.	②	②	②	②	②	②
Station veloc. form. err.	②	②	②	②	②	②
Pole coord. form. err.	③	③	③	③	③	③
LOD form. err.	②	②	②	②	②	②
ERPs	③	②	②	②	②	②
Summary	2.0	2.0	2.0	2.3	2.3	2.3

6.3.2.3 Influence of Earth gravity field mismodelling

The EGM mismodelling follows the same approach as for DORIS and SLR. Different from the case of SRP mismodelling above, the satellites of the GPS constellation and the space-tie satellites are exposed to the mismodelling. The absolute difference in the perturbation acceleration introduced by the mismodelling is for a GPS satellite as an example shown for the satellite PRN 1 over a seven-day period in Fig.6.97. The influence in all directions is significantly lower than for the space-tie satellites, as presented in Sec. 6.1.2.6. Only in the radial direction the disturbance accumulates, reaching a maximum amplitude of approximately 0.2 μm/s^2 after seven days.

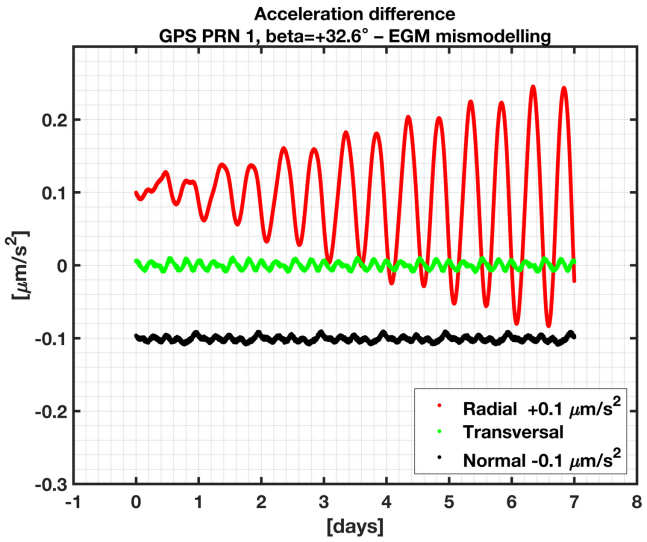

Figure 6.97: Difference in the sum of the accelerations acting on a GPS satellite over a period of 7 days, in the case of EGM mismodelling.

Orbital fit

LEO satellite The introduced EGM mismodelling primarily affects the orbital fit of scenarios that involve low-altitude passages. This is most evident for the GRASP-like scenario, resulting in an increase of 0.7% in phase residuals. All other scenarios are significantly less affected. This influence is also evident in the geographical distribution of the median phase residuals. For the GRASP-like scenario, the strongest influence is evident in an East-West pattern. The other scenarios exhibit weaker influences, though regional patterns can still be identified here (see Fig. 6.98). No correlation can be found with the geographical distribution of observations.

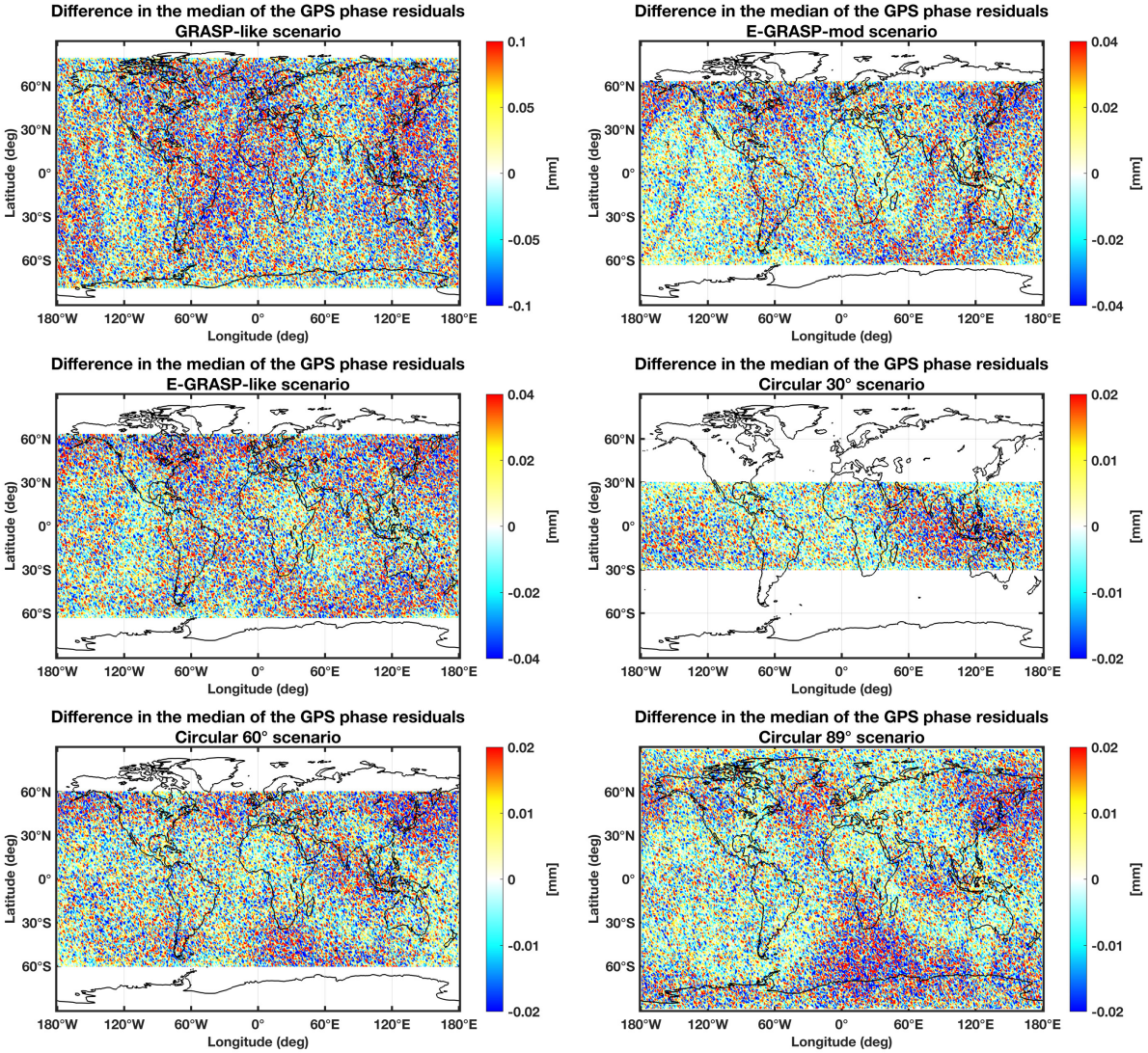

Figure 6.98: Global distribution of the difference in the median of the phase observation residuals in the EGM mismodelling case compared to systematic error-free. The colour bar of the GRASP-like scenario is scaled 5 times higher, for the E-GRASP-mod and E-GRASP-like scenario 2 times higher.

GPS satellites The orbital fit of the GPS constellation shows no change due to the mismodelling introduced. As also observed in the systematic error-free case, integrating the

space-tie satellites results in a slight increase in phase residuals. No geographical influence on the residuals could be identified.

Orbit recovery

LEO satellite The mismodelling primarily leads to a decrease in the accuracy of the determined orbit for the GRASP-like scenario (see. Fig. 6.99). This manifests itself as an increase in the mean RMS of the orbit comparison by a factor of approximately 3.5 in the radial and cross-track components, and by a factor of 2 in the along-track direction. The other scenarios primarily demonstrate a degradation in the radial component, which is 43-49% for the E-GRASP-mod and E-GRASP-like scenarios, and between 10 and 13% for the circular scenarios in terms of mean RMS. A systematic offset greater than 0.1 mm is only evident in the cross-track direction for the GRASP-like scenario, at 0.3 mm.

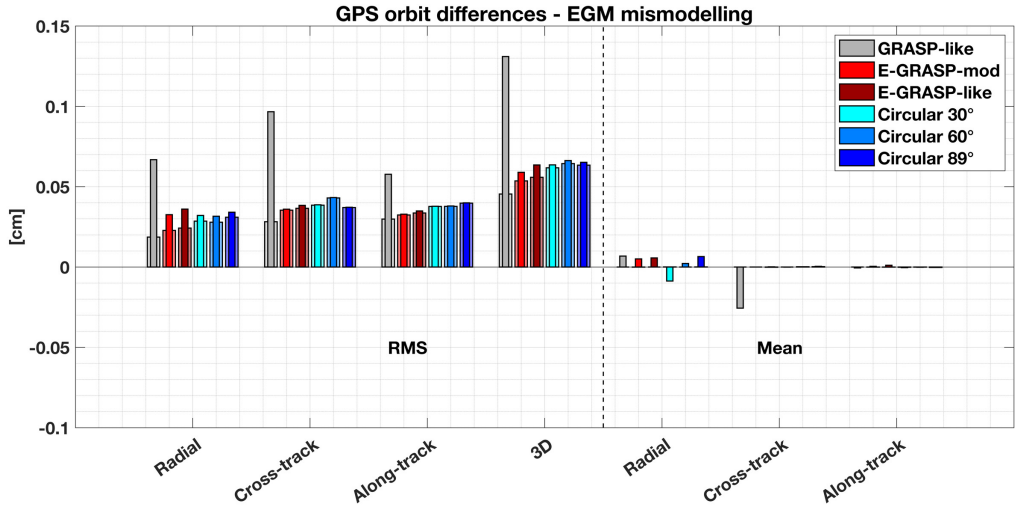

Figure 6.99: Mean RMS value of the orbit comparison in radial, cross-track, along track and 3D directions, as well as the mean orbit deviation. The thinner bars show the results of the EGM mismodelling cases, the slightly more transparent thicker bars in the background show the values achieved in the systematic error-free case.

The geographical orbit differences shown in Fig. 6.100 reveal clear regional patterns in all components, especially in the GRASP-like scenario, where maximum amplitudes of between 0.6 and 1 mm are observed in all components. Similar regional patterns are evident in the E-GRASP-mod and E-GRASP-like scenarios, which are strongest in the radial component. Here, the maximum amplitude is approximately 0.3 mm, which is about five times stronger than in the cross-track and along-track components. The same is the case for the circular scenarios, although the maximum amplitude in the radial component is weaker at 0.2 mm. For all scenarios, the radial orbital differences correlate with the geographical distribution of the median phase residuals.

GPS satellites The mismodelling only leads to a very minor deterioration in the mean RMS of the orbit comparison for the GPS constellation, with an impact of less than 1%. The SV and ground station clock estimates, as well as the SISRE_p show no influence at all (see Tab. 6.47).

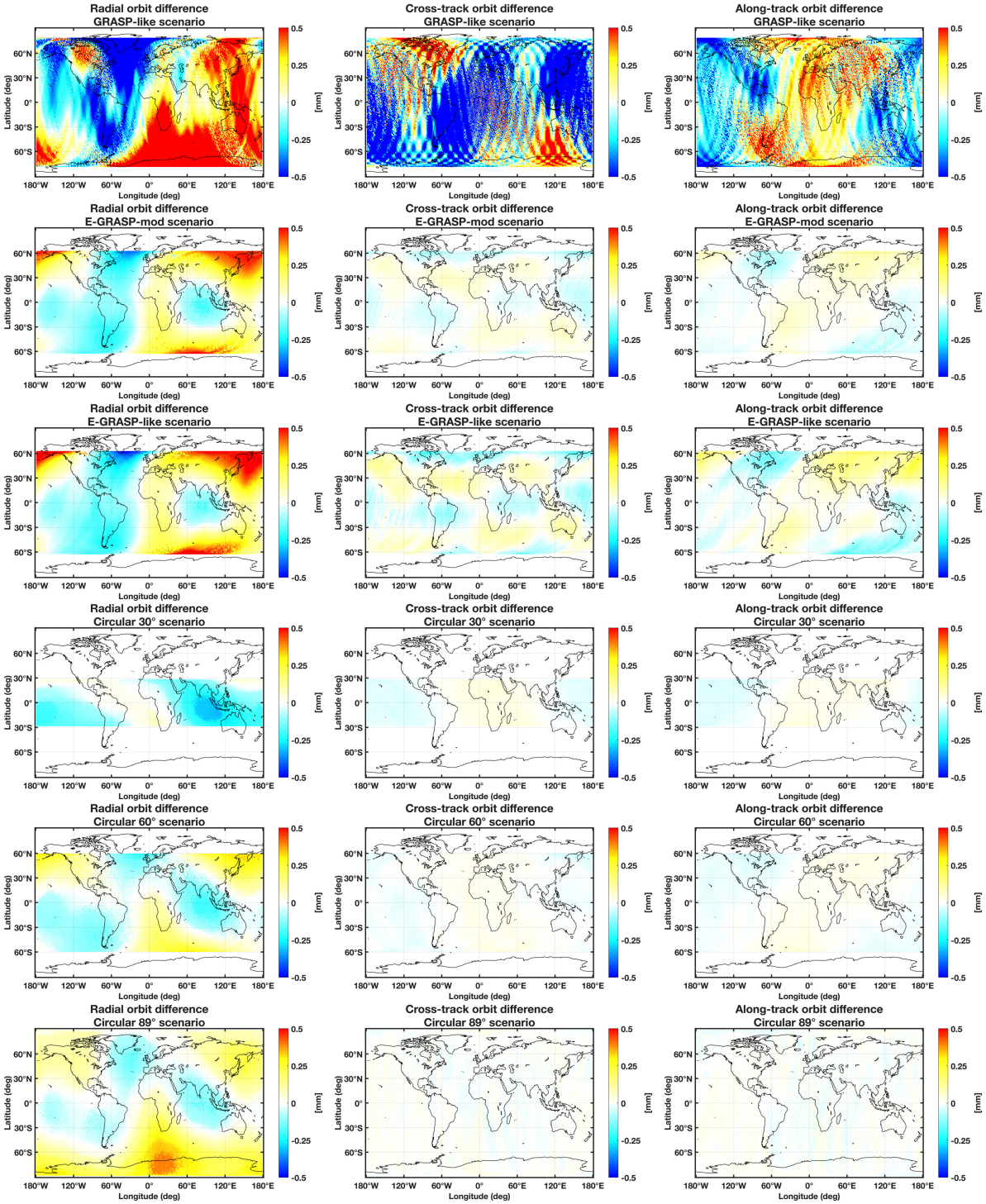

Figure 6.100: Median orbit difference of the LEO satellites compared to the systematic error-free case over a one-year period for GPS in the EGM mismodelling case. From top to bottom: GRASP-like; E-GRASP-mod; E-GRASP-like; Circular 30°; Circular 60°; Circular 89°. From left to right in the radial, cross-track and along-track directions.

The inclusion of the space-tie satellite scenarios shows similar effects as in the systematic error-free case for all scenarios except the GRASP-like scenario. In this case, there is a slight improvement in the orbit, while the SV clock RMS increases by 0.88%, resulting in a 1.29% deterioration in the SISRE_p. Additionally, a 0.68% increase in the ground station clock RMS can be observed. This underlines that integrating a satellite with a GPS receiver that is subject to greater disturbances due to modelling errors, in this case due to the Earth's gravity field, can result in a deterioration of the GPS constellation when using the integrated approach.

Table 6.47: Statistics of the recovered orbit and clocks of the GPS constellation in the EGM mismodelling case, with one of the space-tie satellite scenarios added, respectively. Values computed over the whole time span in radial (R), transversal (T), and normal (N) direction. SV stands for GPS satellite vehicle, Sta. for ground station. Values are given in percentages and centimetres.

	RMS						Clock RMS		Mean		
	R	T	N	SISRE_{orb}	SISRE_p	SISRE_m	SV	Sta.	R	T	N
EGM mismodelling case											
GPS constellation	0.12	0.08	0.08	0.12	0.49	0.54	0.50	0.61	-0.00	0.00	0.00
+ GRASP-like	-2.39%	-2.81%	-2.05%	-2.43%	+1.29%	+0.22%	+0.88%	+0.68%	-0.00	-0.00	-0.00
+ E-GRASP-mod	-7.46%	-5.68%	-5.85%	-7.64%	-0.29%	-1.74%	-0.71%	-0.05%	-0.00	+0.00	+0.00
+ E-GRASP-like	-7.39%	-5.37%	-5.69%	-7.62%	-0.28%	-1.74%	-0.70%	-0.04%	-0.00	+0.00	+0.00
+ Circular 30°	-9.83%	-5.18%	-6.43%	-10.20%	-0.25%	-2.21%	-0.82%	-0.04%	-0.00	+0.00	+0.00
+ Circular 60°	-9.89%	-5.57%	-6.13%	-10.21%	-0.23%	-2.20%	-0.80%	-0.03%	-0.00	+0.00	+0.00
+ Circular 89°	-11.64%	-6.34%	-7.38%	-11.95%	-0.26%	-2.55%	-0.93%	-0.04%	-0.00	+0.00	-0.00

The geographical distribution of orbital differences for the GPS satellites, as shown in Fig. 6.101, differs from the systematic error-free case at a submillimetre level. The regional patterns are similar to those of the 60 degree circular scenario due to the similar inclination. The largest amplitude of 0.2 mm is found in the radial component, the cross-track and along-track components are significantly larger for the GPS constellation than for the 60 degree circular scenario, and are only slightly smaller than the radial component.

The inclusion of space-tie satellite scenarios shows that, for the GRASP-like scenario, the geographical orbit differences are transferred to the orbits of the GPS constellation (see Fig. G.31). The orbit differences increase in all components, reaching a maximum amplitude of 0.25 mm in the radial component. In the other scenarios, there is almost no geographical influence. However, in the circular scenarios, a minor improvement in the radial orbit component can be observed in regions around the equator.

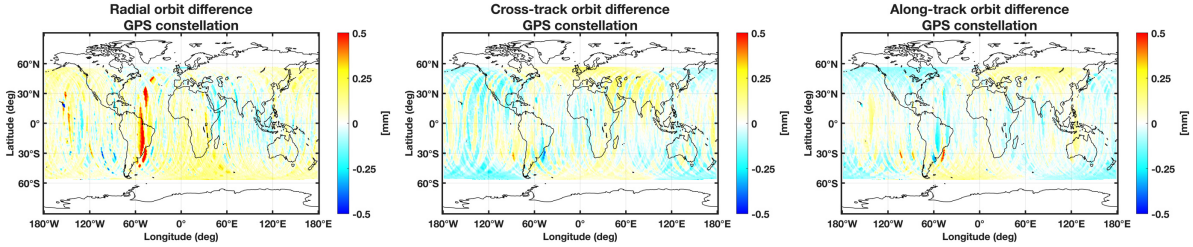

Figure 6.101: Median orbit differences of the GPS constellation in the EGM mismodelling case in comparison to the systematic error-free case over a time span of one year. From left to right in radial, cross-track, and along-track direction.

The influence on the estimated clock differences of the GPS constellation shows no dependence on solar elongations or beta angles greater than 1 mm (see Fig. 6.102).

Integrating the space-tie scenarios has a similar effect on the estimated clock differences of the GPS satellites to that seen in the SRP mismodelling case, albeit slightly weaker. This is true for all scenarios except the GRASP-like scenario, in which a uniform increase in clock differences of approximately 1–2 mm is observed, regardless of Sun elongation and beta angle (see Fig. G.32).

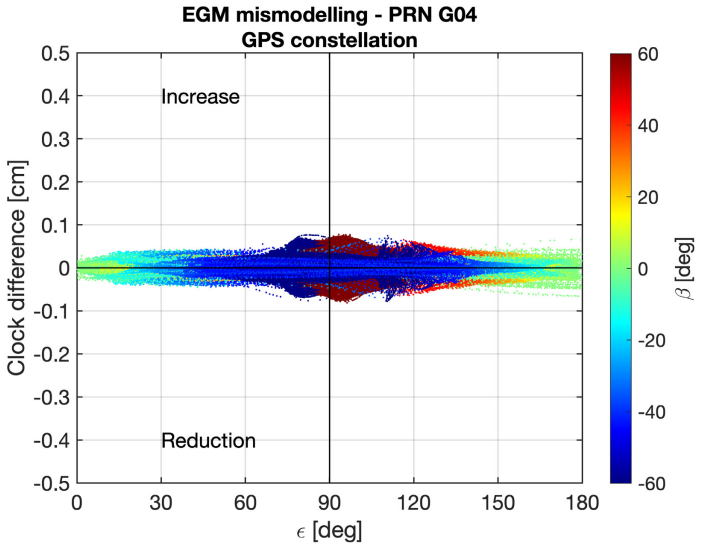

Figure 6.102: Difference in clock estimate for PRN 4 in cm over the Sun elongation angle ϵ in the EGM mismodelling case in comparison to the systematic error-free case. Different β angles according to colorbar.

Reference frame

Helmert parameters A significant influence on the TRF can be observed for the GPS constellation (see Fig. 6.103). This primarily affects the positions, manifesting as rotations of up to 1.2 mm around the X and Y axes, as well as translations of up to 0.07 mm in all directions. In terms of velocities, only a significant Y-rotation of 0.06 mm/a is apparent. There is no apparent impact on the scale (see Tab. F.40). At this point, it is difficult to determine whether the rotations are caused by the relatively weak NNR constraints or whether there are strong systematic effects. This once again emphasises that the strength of the datum constraint is not a trivial issue.

None of the space-tie scenarios can improve these systematics to such an extent that the Helmert parameters become insignificant. Depending on the flight altitude of the scenario, the inclusion leads to an increase in rotation of approximately 0.1 mm for the circular scenarios and up to 0.7 mm for the GRASP-like scenario. For nearly all scenarios, the influence on translations is in the range of hundredths of a millimetre, except for the GRASP-like scenario, where an increase of up to 1 mm can be observed, particularly in the Y and Z components. The influence on velocities is significantly lower for all scenarios, being in the range of hundredths of a millimetre per year.

Formal errors The EGM mismodelling does not show any significant change in the formal errors of the station coordinates, velocities and ERPs. For each of the space-tie

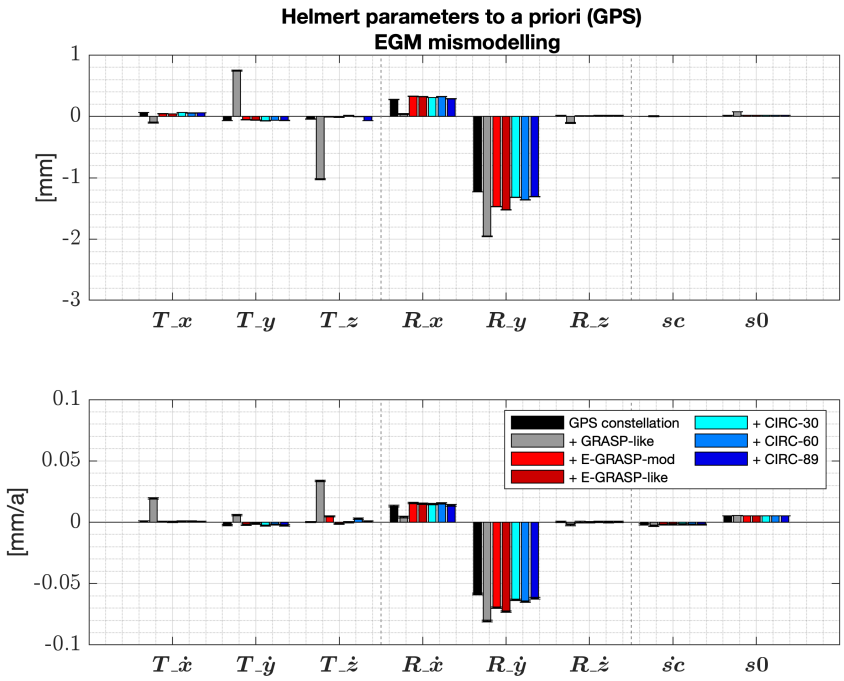

Figure 6.103: The upper figure shows the Helmert parameters of all stations for the EGM mismodelling case compared to systematic error-free. The lower figure shows the values for the velocities.

satellite scenarios, an OSI in formal errors can be noted, which is on the level of the systematic error-free case.

ERP analysis The introduced mismodelling increases the noise in the X-pole and Y-pole coordinates of the reference solution by 135% and 7%, respectively. Additionally, a significant bias of up to 1.3 mm and a trend of up to 0.06 mm/a can be observed in both pole coordinates, reflecting the rotations evident in the Helmert parameters. In LOD, however, the increase in noise is not significant and only a bias of 0.4 mm is evident.

The integration of the space-tie satellites increases the influence of the mismodelling, the more sensitive the scenario is to the Earth gravity field. This effect is most pronounced in the GRASP-like scenario, where an increase in noise of up to 29% can be observed in the pole coordinates, as well as an offset increase of up to 0.7 mm. The circular scenarios demonstrate the least deterioration, with noise increases below 10% and biases of no more than 0.15 mm. In LOD, a slight reduction in noise can be observed for all scenarios, though this is not significant.

Spectral analysis of the ERPs shows no variation compared to the systematic error-free case, for either the GPS constellation with or without space-tie satellites. The variations are in the micrometre range.

Earth gravity field co-estimation The Earth's gravity field is subsequently co-estimated in the same way as for DORIS and SLR, except that, the GPS constellation is also part of the integrated processing for gravity field estimation. Information on how the maximum degree of solution is obtained can be found in Sec. 6.1.2.6.

Reference frame

Helmert parameters By co-estimating the Earth gravity field, the translations and rotations of the GPS constellation can be reduced to less than 0.1 mm and 0.01mm/a relative to the a priori. Only a Z-component translation of 0.08 mm remains, and the X-component rotation shows a deviation of 0.07 mm compared to the rotation of the systematically error-free case (see Fig. 6.104). Integrating the space-tie scenarios further improves the Z translation in the positions. But in the velocities the GRASP-like scenario leads to an increase in translations in X and Z up to 0.02 mm/a. In terms of rotations, the GRASP-like and E-GRASP-like scenarios show slight increases in rotational differences relative to the systematically error-free case, but these are less than 0.1 mm. The E-GRASP-mod and 89 degree circular scenarios demonstrate the smallest rotation deviations relative to the systematically error-free case. No influence on velocities and scale can be found (see Tab. F.50 in App. F.3).

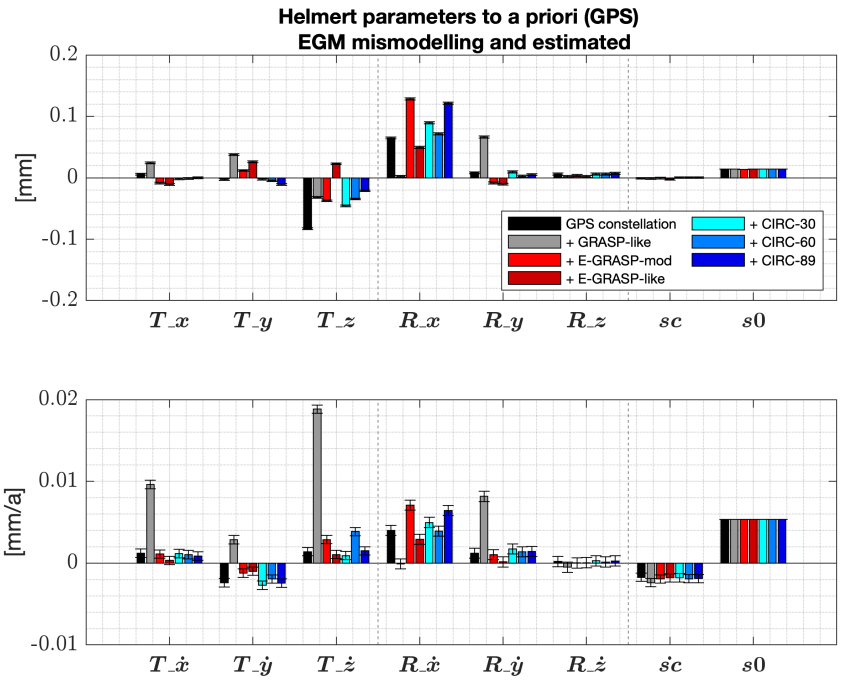

Figure 6.104: The upper figure shows the Helmert parameters of all stations for the EGM mismodelling case compared to systematic error-free with SHs co-estimated. The lower figure shows the values for the velocities.

Formal errors The additional estimation of the gravity field results in an increase in formal errors for the GPS constellation, compared to the case of EGM mismodelling without co-estimation of the gravity field. This suggests correlations between the estimated parameters, or that too many SHs are being estimated. This increase is up to 1% for all station coordinates and velocities, except for the Z component of positions, where the increase is 4%. In the pole coordinates, the increase is as high as 3-4%, and in LOD it is as high as 20% (see Tab. F.52 in App. F.3).

Integrating each of the space-tie scenarios, achieves improvements such that the formal errors are reduced to the level of the systematic error-free case. Any remaining differences are no larger than 1%.

ERP analysis Significant improvements can be achieved by estimating the SH of the Earth's gravity field in the case of only the GPS constellation. The estimated ERPs do not show any significant difference in noise compared to the systematic error-free solution. Offset differences compared to the systematic error-free case are below 0.1 mm for trends below 0.01 mm/a. An offset increase of -0.2 mm is only noted in LOD.

Integrating the space-tie satellite leads to a slight improvement in noise in all ERPs, by up to 4%. The influence on offsets in the pole coordinates is below 0.1 mm for all scenarios. For the GRASP-like scenario only, an increase in X and Y-pole offsets compared to the systematically error-free case can be observed. In LOD, an offset of between 0.1 and 0.3 mm remains for the E-GRASP-mod, E-GRASP-like, and 60 degree circular scenarios. Overall, the 89 degree circular scenario most closely resembles the ERP solution of the systematically error-free case.

Spectral analysis of the ERPs shows nearly perfect coincidence with the systematic error-free case. Integration of the space-tie satellites shows no further influence.

Potential for gravity field determination Assessing the potential to estimate the SHs of the Earth's gravitational field using GPS differs from the DORIS and SLR methods. Due to integrated processing, the GPS constellation is used in the estimation. The sensitivity analysis of one GPS satellite is shown in Fig. 6.105 top left, for the space-tie scenarios it can be found in Sec. 6.1.2.6. The sensitivity of a GPS satellite is limited to very low SHs, primarily to C_{20}. Using the reference solution (i.e. all GPS satellites), the gravity field can be solved up to degree 20. The differences between the estimated SHs and the simulation are shown as a triangle plot in Fig. 6.105 top right. As can be seen, the estimated degree 2 and 3 coefficients show very good agreement with the simulation due to the large number of GPS satellites in the constellation, even though, one satellite alone was not found to be that sensitive. The degree amplitudes demonstrate that the 100 mm equivalent water height level used prior for DORIS and SLR is exceeded above degree 3, corresponding to a cumulative error of approximately 4'000 km.

In the case of the space-tie scenarios the Earth's gravity field is thus solved together with the GPS constellation. The maximum degree to which the gravity field can be solved is 60 for the GRASP-like scenario, 48 for the E-GRASP-mod, 42 for the E-GRASP-like, and 32, 35 and 60 for the circular scenarios with 30, 60 and 89 degrees inclination, respectively. Therefore, for most scenarios, it is possible to solve the SH expansion to a higher degree with GPS than with DORIS and SLR, except for the 60 degree circular scenario. In this scenario, the maximum degree is 35 for GPS, 47 for DORIS and 45 for SLR. One possible reason for this could be the inclination of the scenario, which is close to that of the GPS constellation. In this case, special observation distributions were found in Sec. 6.3.2.1.

Estimated Earth gravity field analysis The triangular plots of the SH differences in Fig. 6.106 show a picture very similar to that of DORIS for all scenarios. In the GRASP-like scenario, the differences are smallest and increase steadily with slightly lower deviations in sectoral coefficients. For all other scenarios, the progression of deviations is almost identical to DORIS, albeit generally lower. At very low SHs, the GPS constellation appears to make a

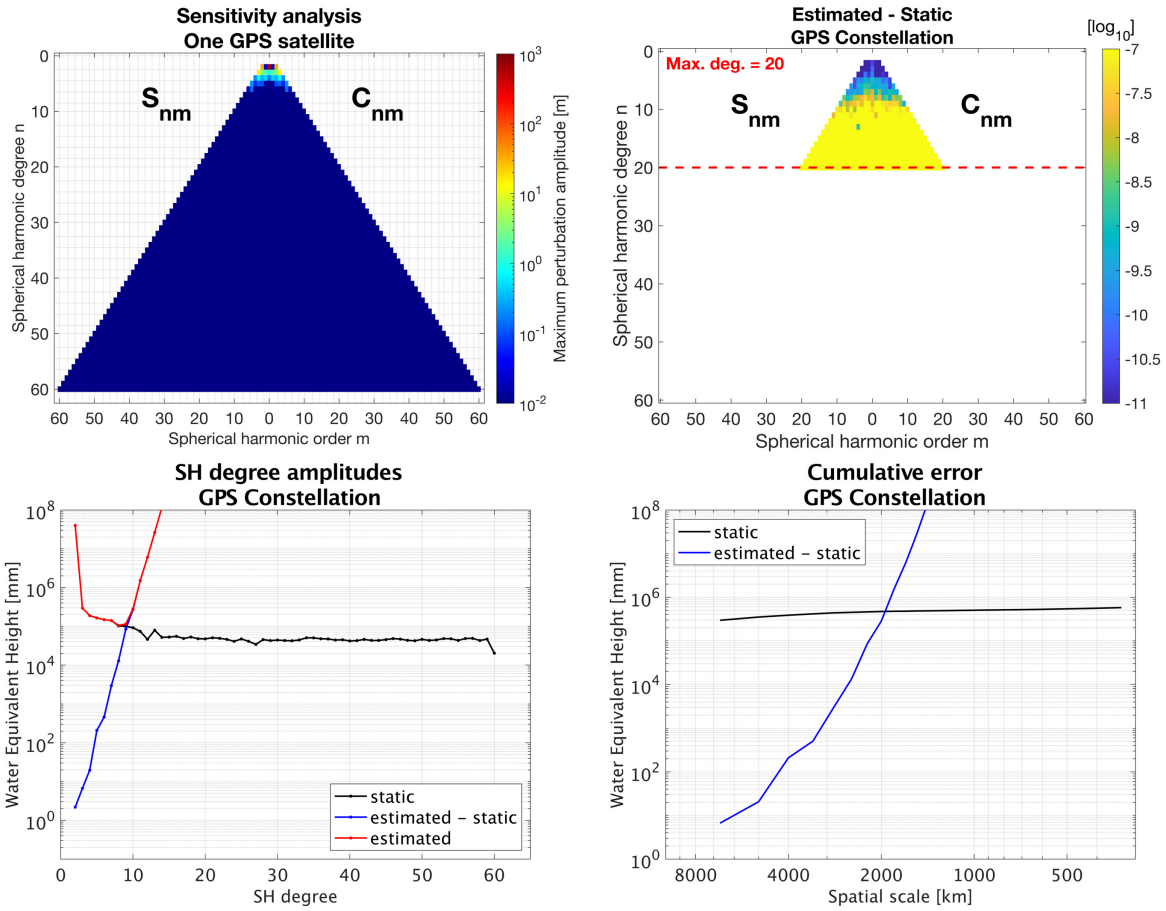

Figure 6.105: Sensitivity analysis of one GPS satellite (top left), triangular plot showing the difference between estimated and simulated SH coefficient (top right). SH degree amplitudes and cumulative error in equivalent water height in the bottom left and right.

positive contribution. Thus, the differences in zonal and tesseral SH at degrees below 10 are significantly lower compared to DORIS and SLR.

The degree amplitudes (Fig. 6.107) and cumulative error (Fig. 6.108) demonstrate that the GRASP-like scenario achieves the lowest overall deviation of all techniques and scenarios. A SNR of 1 is only achieved above degree 47 here, and a deviation equivalent to a water height of 100 mm is only achieved from degree 20 onwards. By comparison, this level is achieved above degree 6 for the E-GRASP-mod scenario, above degree 5 for the E-GRASP-like scenario, and above degrees 4, 5, and 7 for the circular scenarios with 30, 60 and 89 degree inclination, respectively. Compared to the degree amplitudes of the GPS constellation (see Fig. 6.105), the E-GRASP-mod and E-GRASP-like scenarios offer no further improvement at degree 2, as the degree amplitudes are almost identical to those of the GPS constellation. Improvements can be observed in all circular scenarios up to degree 3, and in the 89 degree scenario up to degree 4, with errors close to and below 1 mm of equivalent water height. Compared to DORIS and SLR, the circular scenarios in particular show significantly lower deviations below approximately degree 5, and no spike pattern due to resonance occurs in the 30 degree scenario.

It can thus be concluded that the potential for deriving Earth gravity field SHs using GPS is strongest, albeit with a focus on low degrees, in all scenarios except the GRASP-like scenario, for which higher degrees can also be reasonablly be estimated. Clearly, in

low coefficients up to degree 3, the GPS constellation can make a valuable contribution. Compared with DORIS and SLR, and due to the contribution of the GPS constellation, all scenarios demonstrate minimal errors in low SHs up to approximately degree 4. The E-GRASP-mod and E-GRASP-like scenarios exhibit slightly diminished performance in degree 2, and the 30 and 60 degree circular scenarios demonstrate slightly lower efficiency up to degree 4.

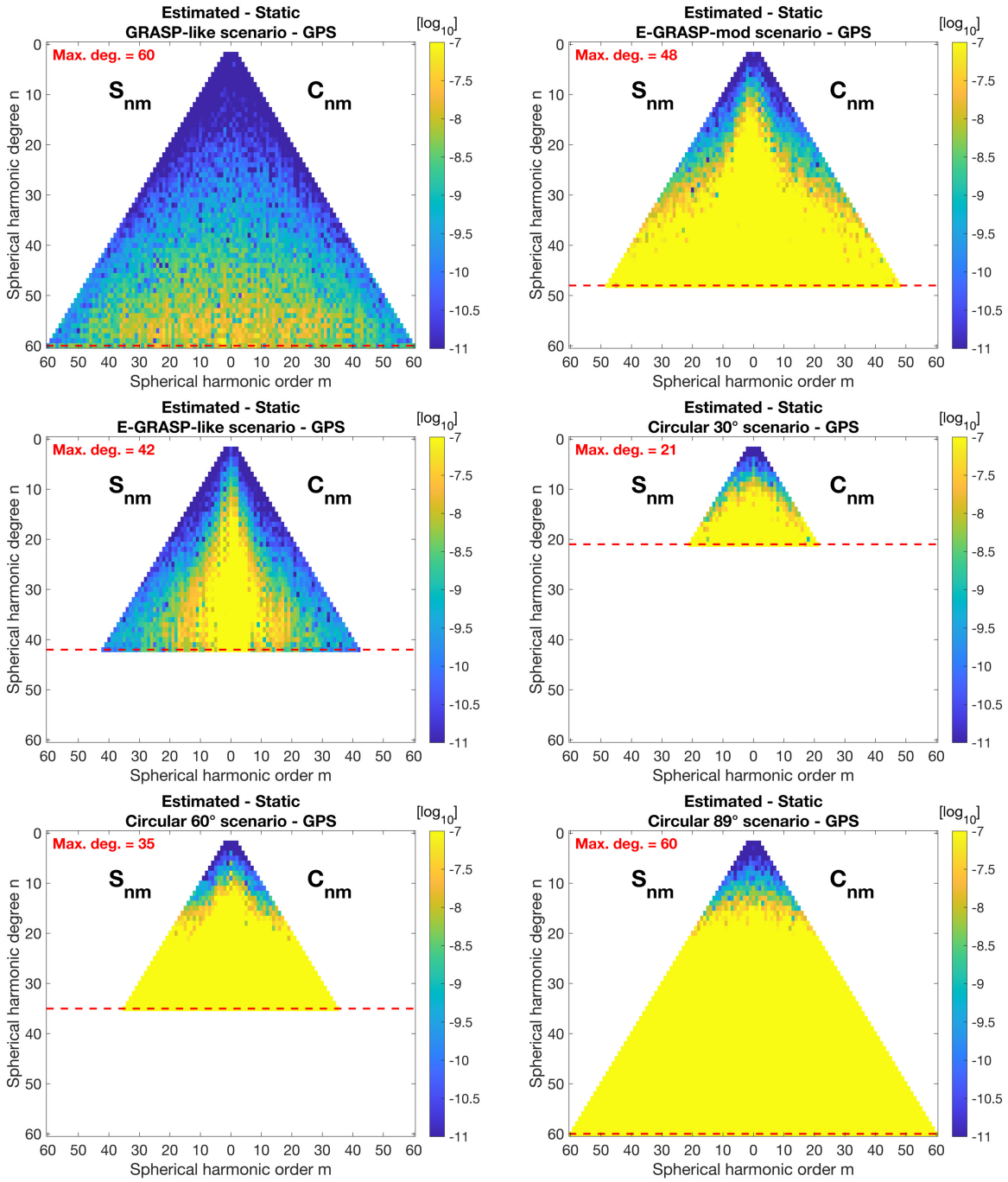

Figure 6.106: Triangular plots showing the difference between estimated and simulated SH coefficient.

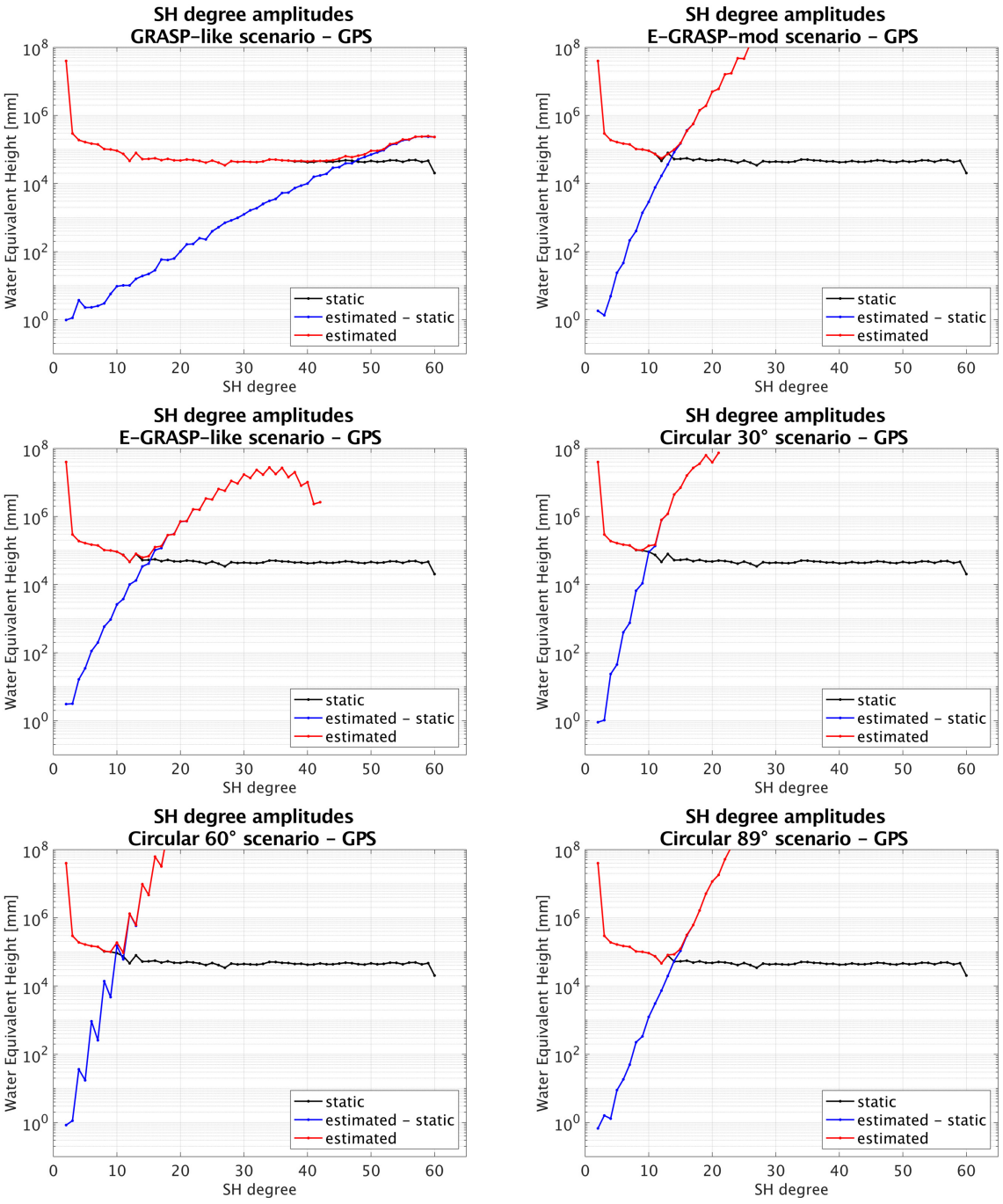

Figure 6.107: SH degree amplitudes in equivalent water height.

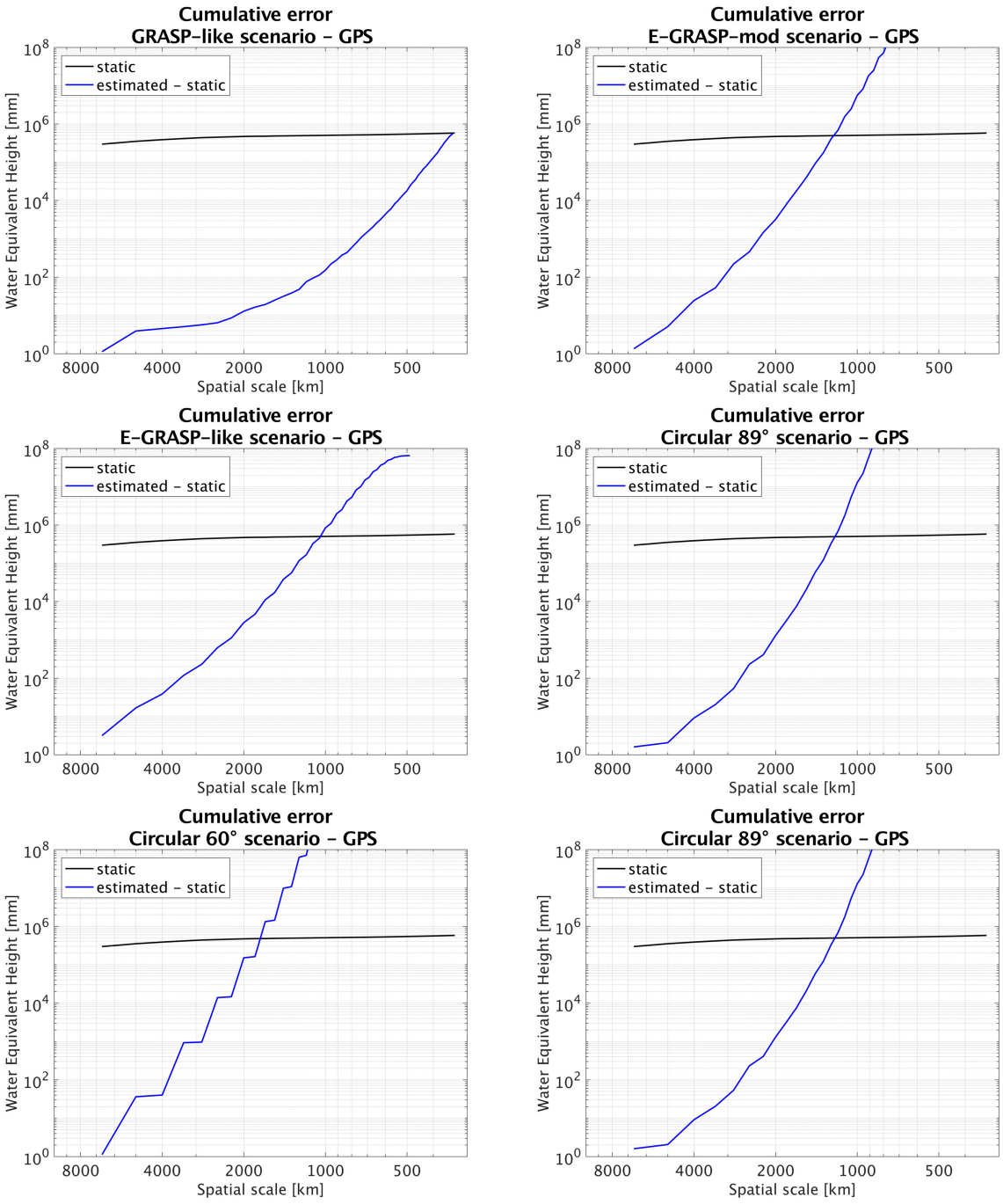

Figure 6.108: Cumulative error in equivalent water height

Conclusion - EGM mismodelling and potential for gravity field determination The EGM mismodelling has a significant impact on the orbit accuracy of the space-tie satellites, particularly in the GRASP-like scenario. The influence of the mismodelling on the orbit and clock accuracy of the GPS constellation is however negligible. Integration of the space-tie satellites improves the $SISRE_p$ for all scenarios by less than 1%, except for the GRASP-like scenario, for which it increases by slightly more than 1%. Furthermore, it was found that the geographical patterns induced by mismodelling in the space-tie satellite orbits were transferred to the orbits of the GPS constellation. The strongest amplitude in case of the GRASP-like scenario was 0.25 mm.

The impact on the TRF is primarily reflected in rotations. None of the space-tie scenarios can help to improve the Helmert parameters, as the EGM mismodelling is transferred. This is most evident in the GRASP-like scenario, where translations of up to 1 mm occur.

Formal errors in the station coordinates, velocities and ERPs of the GPS constellation do not change significantly as a result of EGM mismodelling. The improvements achieved through the space-tie scenarios are comparable to those in the systematically error-free case.

For the GPS constellation, the mismodelling leads to an increase in noise of the pole coordinates of up to 135%, as well as offsets and trends of up to 1.3 mm and 0.06 mm/a, respectively. In LOD, an offset of 0.4 mm is primarily introduced. For every space-tie satellite scenario, a deterioration in the pole coordinates can be observed, which is more pronounced the more lower-altitude passages the scenario has. This leads to stronger mismodelling influences. Consequently, noise in the X-pole increases by up to 29% and an increased bias of up to 0.7 mm is introduced. The circular scenarios demonstrate the least interference, as their altitude minimises the influence of the mismodelling. Spectral analysis of the ERPs shows no significant amplitudes for either the GPS constellation alone or when the space-tie scenario is integrated.

Co-estimating the gravity field, improves the systematics in the TRF to less than 0.1 mm or 0.01 mm/a. However, the GRASP-like scenario in particular results in an increase in velocity translations.

The formal errors increase due to mismodelling by up to 4% for station coordinates, velocities and pole coordinates, and by up to 20% in LOD. Integrating the space-tie satellites can reduce formal errors to the level of the systematic error-free case. The same applies to the estimated ERPs, which can be traced back almost entirely to the values of the systematically error-free case. In the case of the GPS constellation, only a 0.2 mm LOD bias remains. As with the TRF, integrating the space-tie scenarios results in isolated minor improvements, but increases in offsets can also be observed. The 89 degree circular scenario achieves the best results. No influence on the spectral analysis of the ERPs was observed in any of the cases.

The potential for estimating the gravitational field with GPS is limited to low SHs up to approximately degree 4 for the GPS constellation. Compared to DORIS and SLR, with the space-tie scenarios integration the lowest deviations in the degree amplitudes up to degree 3 can be seen for all scenarios, for the GRASP-like and 89 degree circular scenario also up to degree 4. The GRASP-like scenario demonstrates the greatest potential for determining

the Earth's gravity field. An error of 100 mm in equivalent water height is reached only above degree 20 (see Tab. 6.48).

Table 6.48: Potential for Earth gravity field estimation solely with GPS with the satellite scenarios.

	G-like	E-G-mod	E-G-like	Circ. 30°	Circ. 60°	Circ. 89°
EGM determination	①	②	②	②	②	②

The 89 degree circular scenario achieves the best overall results in minimising the influence of introduced EGM mismodelling. Despite being less sensitive to the Earth's gravity field, this scenario is also suitable for estimating low SHs (see Tab. 6.49).

Table 6.49: Vulnerability of the satellite scenarios for GPS for systematic EGM mismodelling and while co-estimating the EGM.

	G-like	E-G-mod	E-G-like	Circ. 30°	Circ. 60°	Circ. 89°
Orbit	②	②	②	①	①	①
EGM not estimated						
Helmert	③	②	②	②	②	②
Station pos. form. err.	①	②	②	③	②	②
Station veloc. form. err.	①	②	②	③	②	②
Pole coord. form. err.	③	③	③	③	③	③
LOD form. err.	③	③	③	③	③	③
ERPs est.	③	③	③	②	②	②
EGM co-estimated						
Helmert	③	②	②	②	②	②
Station pos. form. err.	①	①	①	②	①	①
Station veloc. form. err.	①	①	①	②	①	①
Pole coord. form. err.	①	①	①	②	①	①
LOD form. err.	①	①	①	②	②	①
ERPs est.	②	②	②	①	②	①
Summary	1.9	1.9	1.9	2.1	1.8	1.7

6.3.3 Single-technique conclusion for GPS

The integration of the space-tie satellite scenarios into the GPS constellation improves the determination of orbits and clocks. However, the improvement in $SISRE_p$ is less than 1% for all scenarios. Improvements in TRF and ERPs are primarily evident in a reduction in formal errors of up to 6% in the Z component. A reduction in noise of up to 4% can be observed in the estimated ERPs. As the observation characteristics of the circular scenarios are less favourable, these scenarios receive a slightly worse rating of between 2.4 and 2.5. Nevertheless, the overall potential of all scenarios in the systematic error-free simulation is moderate.

The mismodelling scenarios examined showed that, in the case of SRP mismodelling, orbital accuracy decreases most significantly in the circular scenarios, and slight translations remain in the Z component of station velocities in the TRF. However, none of the scenarios could significantly reduce the larger systematic errors in the ERPs. Analysis of EGM mismodelling revealed that scenarios affected by strong mismodelling transfer errors to the GPS constellation. This was observed for the orbits and clocks of the GPS constellation, as well as for the TRF and the determined ERPs.

The overall vulnerability is balanced at a value of 2.0 for the scenarios. The circular scenarios with 60 and 30 degrees of inclination show slightly worse results, at 2.1 and 2.2, respectively.

In the case of GPS, gravity field determination shows significantly lower degree amplitude errors for all scenarios compared to DORIS and SLR. This is partly due to the GPS constellation's contribution. The 100 mm equivalent water height limit is reached at the earliest above degree 5 in all scenarios, with the GRASP-like and 89degree circular scenarios proving most advantageous at low harmonics up to degree 4.

Table 6.50: Maximum potential of the satellite scenarios for TRF and ERP determination in the case of GPS, together with their vulnerability to mismodelling.

	G-like	E-G-mod	E-G-like	Circ. 30°	Circ. 60°	Circ. 89°
Maximum potential	2.1	2.3	2.3	2.5	2.4	2.4
SRP	2.0	2.0	2.0	2.3	2.3	2.3
EGM mism.	1.9	1.9	1.9	2.1	1.8	1.7
Overall vulnerability	2.0	2.0	2.0	2.2	2.1	2.0

7 Co-location in space combination and analysis

This chapter investigates the potential of co-location in space using the space-tie satellite scenarios. For this purpose, the individual systematic error-free single-technique solutions of DORIS (Sec. 6.1), SLR (Sec. 6.2) and GPS (Sec. 6.3) are combined. To determine the potential of the ST in the combination, a combination is first carried out without the ST, using only GTs. At this stage, the GTs are the pole coordinates and LOD. For this purpose, all satellite-specific parameters are reduced at the normal equation level prior to the combination. Secondly, the combination with the ST is carried out by combining the weekly initial state orbital elements of the respective space-tie satellite scenario at normal equation level. For GPS, these are available daily, but can only be combined weekly. On the other days of the week, the GPS arcs are free. In both cases, the TRF solution is obtained by applying the datum as a NNR condition to GPS only, using the same procedure as for the GPS single-technique solution described in Sec. 6.3.1.3. Next, the accuracy with which the datum can be transferred from GPS to DORIS and SLR using only GTs and in combination with the ST is investigated. Furthermore, the formal errors and the estimated ERPs are examined for changes between the combination with and without the ST and the single-technique solutions.

To this end, the results of the single-technique analysis for the space-tie satellite scenarios are summarised first with respect to the orbit in Sec. 7.1, the TRF in Sec. 7.2, the ERPs in Sec. 7.3 and gravity field estimation in Sec. 7.4. Subsequently, in Sec. 7.5, the combination is carried out, and the potential for the TRF (Sec. 7.5.1), ERPs (Sec. 7.5.2) and EGM estimation (Sec. 7.5.3) is examined. Sec. 7.6 summarises the results of the combination.

7.1 Inter-technique orbit comparison

In the systematic error-free case, the achievable orbit accuracy is highest with GPS in all components and scenarios. When comparing DORIS and SLR, it can be seen that DORIS performs particularly well in the radial component and in low-orbiting scenarios, such as the GRASP-like scenario. For the cross-track and along-track components, both techniques demonstrate substantially higher RMS values in the orbit comparison than GPS, while this effect is less pronounced for SLR. The largest decrease in orbit accuracy occurs in the circular scenarios for all techniques. The achievable orbit accuracy for the two eccentric scenarios (E-GRASP-mod and E-GRASP-like) lies between the other scenarios. Generally, the relationship between the orbit accuracy of the individual space-tie satellite scenarios is similar for all techniques. The best accuracy is achieved in the low-orbiting GRASP-like scenario, followed by the E-GRASP-mod and E-GRASP-like scenarios. All circular scenarios achieve the lowest accuracy.

Systematic geographical differences in the orbits are primarily evident for DORIS and SLR. This is most evident in the two eccentric scenarios, E-GRASP-mod and E-GRASP-like, in the form of stripe patterns that follow the inclination in all components. In the circular scenarios, regional patterns exhibit a North-South distribution, which increases primarily for SLR in the cross-track direction, the larger the inclination of the scenario. The GRASP-like scenario shows the least geographical influence. For GPS, geographical orbit differences

are significantly lower for all scenarios and only show isolated correlations with observation coverage, primarily for higher-orbiting circular scenarios, especially the near-polar one.

The orbit of the space-tie satellite resulting from the multi-technique combination with GT and ST cannot be analysed after the combination and solution of the normal equation. This would be possible if the parameters of the normal equation solution were reintroduced into consistent orbit integration. However, due to the integrated processing of GPS and the associated reduction in parameters required for this, this would only be possible if the parameters were substituted back after solving the normal equation. Currently, this is not possible with EPOS-CS.

7.2 Inter-technique TRF comparison

Helmert parameters Comparing the individual single-technique TRF solutions with a priori values shows insignificant variation for DORIS, at below 0.2 mm or 0.03 mm/a. For SLR, only significant rotations were found, with maximum values of 1.1 mm and 0.20 mm/a, respectively. While it was demonstrated that rotations are influenced by the choice of datum stations, the remaining rotations do not significantly exceed the strength of the NNR condition applied when using this network. In the case of GPS, a significant X-rotation was primarily observed, reaching up to 0.15 mm in the coordinates and below 0.01 mm/a in the velocities. Additionally, the strongest translations were observed in the Z direction, reaching a maximum of 0.02 mm, which remains significantly below 0.01 mm/a. The strength of the NNR condition was identified as the reason for the significance of the deviation (see also Sec. 6.3.1.3). In the systematic error-free case of the simulation, taking into account the standard deviation of the estimated Helmert parameters, no significant deviations greater than the GGOS goals of 1 mm or 0.1 mm/a could be found in the TRF generated for any of the techniques. The influence of integrating the space-tie satellite scenario was found to be either insignificant or below 0.1 mm or 0.01 mm/a.

Formal errors The formal errors in the coordinates were particularly small for DORIS, with values below 0.1 mm in all components. SLR and GPS both achieved comparable error levels in all components, which are approximately 1 mm for SLR and 0.2 mm for GPS.

Similar values were found for DORIS and GPS in the station velocities, at approximately 0.2 mm/decade. Further improvements to below 0.2 mm/decade could only be achieved through the integration of a space-tie satellite scenario in the case of DORIS. For GPS, the improvements were significantly less pronounced. In the case of SLR, the errors are at a level of about 1 mm/decade. No component of the velocities could be identified as significantly better-determined for each technique.

In the ERPs, the formal errors of the pole coordinates for DORIS and SLR are less than 2 mm, while GPS shows significantly better results at less than 0.4 mm. However, in LOD, extremely small formal errors were achieved with DORIS, in the low micrometre range. With GPS, these are below 0.5 mm and with SLR, with an integrated space-tie satellite, they are at approximately 2 mm.

7.3 Inter-technique ERP comparison

The a posteriori ERPs of the individual single-technique solutions reflect the results of the formal error and Helmert parameter analysis. For DORIS and SLR, the noise in the pole coordinates is at a level of 1–2 mm, whereas for GPS it is around 0.06 mm. Systematic offsets and trends in the pole coordinates are evident for each technique and align with the

rotations determined by the Helmert transformation. However, all offsets are smaller than 0.7 mm and all trends are below 0.06 mm/a. In LOD, the noise level is lowest with DORIS at below 1 micrometre, with SLR at below 3 mm and with GPS at below 0.5 mm. Statistically significant offsets and trends were only observed with DORIS, but these were well below the micrometre level. Therefore, all offset and trend patterns observed in the ERPs are below the GGOS goals.

Spectral analysis of the individual single-technique solutions revealed no signals with amplitudes exceeding 0.1 mm in any of the respective reference solutions. Furthermore, no signals were found to be introduced by integrating the space-tie satellite scenarios.

7.4 Inter-technique comparison of estimated Earth gravity field

In Sec. 6.1, 6.2 and 6.3, the Earth's gravity field was estimated separately for each of the observation techniques for the different space-tie satellite scenarios. In the case of GPS, the GPS constellation is also involved, in addition to the space-tie satellite, due to the integrated processing.

The GRASP-like scenario was found to be by far the most sensitive to the Earth's gravity field due to its lower flight altitude. The lowest errors in the estimated SHs were achieved using GPS. An increase in degree amplitudes with increasing degrees was observed, similar to that seen with DORIS, but generally larger. With SLR, errors below 100 mm Equivalent Water Height (EWH) could only be achieved for low degrees, with a maximum of degree 6. For higher degrees, the deviations increase rapidly.

The sensitivity was found to be significantly lower for the E-GRASP-mod and E-GRASP-like scenarios. The E-GRASP-like orbit is more sensitive than the E-GRASP-mod orbit due to its lower perigee. Strong resonances were found for multiples of order 8 in the E-GRASP-like scenario, which are significantly larger than those in the E-GRASP-mod scenario. In these scenarios, the lowest deviations in the estimated SHs were achieved using GPS. As in the GRASP-like scenario, DORIS showed a similar increase in the differences, albeit slightly larger. However, a strong increase in zonal and tesseral SHs differences was observed for DORIS and GPS beyond about degree 10. By contrast, differences in sectorial SHs for SLR were generally found to be significantly larger for both scenarios. As before, errors in the degree amplitudes are below 100 mm EWH in coefficients below about degree 6. These errors are at a similar level for DORIS and SLR, and are only lower with GPS. Here, the GPS constellation was found to provide a positive contribution.

The three circular scenarios revealed the lowest sensitivity, limited to SHs up to about degree 3. For the scenarios with 30 and 89 degrees inclination, resonances were found at odd zonal coefficients. The degree amplitudes of these scenarios were found to be very similar for DORIS and SLR. For the scenarios with 30 and 60 degrees inclination, the errors are already above 100 mm EWH for degree 2. For the 89 degree scenario, the errors in degree 2 are below this level, at about 10 mm EWH for both DORIS and SLR. For all these scenarios, errors in the degree amplitudes achieved with GPS were also found to be lower, at around 1 mm EWH at degree 2, and the GPS constellation was again found to be the main contributor.

7.5 Combination with co-location in space

7.5.1 Reference frame evaluation

7.5.1.1 Helmert parameters

The station networks of the individual techniques for the two combinations, GTs only and GTs with ST, are compared using the Helmert transformation to a priori. This makes it possible to validate whether the geodetic datum applied to GPS can be transferred to the other techniques and with what level of accuracy, and to assess the potential of the ST in this regard. The Helmert parameters for the combinations with GTs in comparison to GTs and ST are shown for each technique in Fig. 7.1. Absolute values can be found in Tab. F.54, F.55, and F.56.

When combined with only the GTs, it can be seen that the datum can be transferred from GPS to DORIS with an accuracy of better than 1 mm or 0.1 mm/a. The ERPs, which are well-determined by the multi-technique contribution, appear to be sufficient for transferring the datum information. Deviations from a priori in the Helmert parameters are a maximum of 0.17 mm for translations and below 0.12 mm for rotations and scale. The velocities show no significant deviation. In the GPS network, to which the datum was applied, significant X- and Y-rotations of up to 0.12 mm in the coordinates can be found. Otherwise, there are no significant differences in agreement with the a priori network. For SLR, it is found that the datum cannot be transferred sufficiently. Significant Z-rotations in the positions and velocities are found in all space-tie satellite scenarios, except the E-GRASP-like scenario, which are in the centimetre to decimetre range and up to 9 mm/a, respectively. The E-GRASP-like scenario exhibits the lowest Z-rotation of 3.2 mm for positions and 4.5 mm/a for velocities. For the positions at least, the datum can be transferred with this scenario to an accuracy of a few millimetres. This is consistent with the findings of Glaser et al. (2017), who concluded that LTs and GTs did not allow Z-rotation to be transferred from VLBI to SLR.

Adding the ST to the combination has a very minor influence on the DORIS network. Most of the information for datum transfer clearly originates from the ERPs. Furthermore, both the E-GRASP-mod and the E-GRASP-like scenario demonstrate an increase in Z-translation of up to 0.46 mm, with velocities remaining below 0.1 mm/a. This appears to be more pronounced in the E-GRASP-like scenario. In the other scenarios, the additional ST shows no significant difference compared to the combination with GTs alone.

For GPS, the combination with the ST compared to GTs alone shows that the ST induces significant Z-rotations. This is true for every scenario and amounts to up to 2.4 mm or 0.23 mm/a. Only for the circular scenarios are all Helmert parameters in agreement with the GGOS goals and the respective strength of the applied NNR condition (i.e. 1 mm and 0.1 mm/a, respectively).

For SLR, the ST leads to a significant improvement in Z-rotation and enables the datum to be transferred. The maximum remaining rotations are 2.1 mm and 0.2 mm/a, respectively. The best results are achieved in all circular scenarios, where values below 1 mm and 0.1 mm/a are achieved for all Helmert parameters. Unlike previous investigations by Thaller et al. (2011) and Bruni et al. (2017), which used GNSS satellites for the ST co-location, the space-tie satellite scenarios investigated here allow the full datum to be transferred from GPS to SLR.

Combining with the ST thus significantly improves datum transfer, particularly for SLR, where GTs could not transfer the datum sufficiently. For GPS, ST-induced Z-rotations are observed, which also appear in the SLR network and show a strong correlation. One possible reason for this is the global distribution of the SLR network, with many observations around

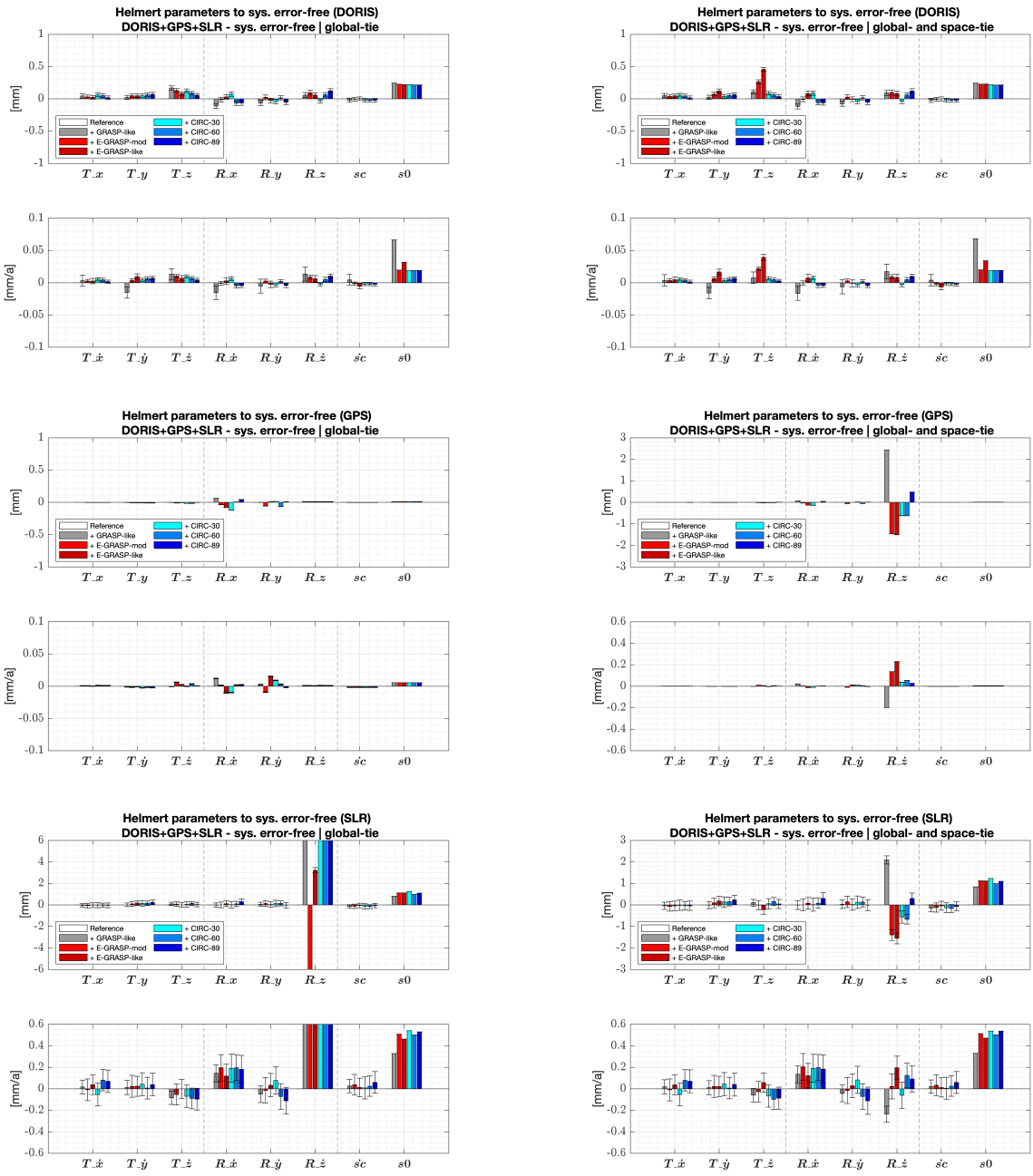

Figure 7.1: Helmert parameters to a priori for the DORIS, GPS and SLR network in the case of a combination using only global ties on the left and also space-ties on the right. The upper figures show the values for positions, the lower for velocities.

the equator, as demonstrated in the SLR single-technique analyses (see Sec. 6.2.2.1). The SLR network therefore adheres to the Z-rotation transferred by the ST, and distorts it by up to a few millimetres. Since GPS is sensitive to this rotation, it can also be found in the GPS network, whereas DORIS does not appear to be sensitive to it.

To confirm this, the strength of the NNR condition for the GPS datum stations was gradually increased. Saturation occurs at a factor of 1'000 (strength of the NNR condition of 1/1'000 mm and 1/10'000 mm/a). The Helmert parameters of the GPS network thereby become insignificant. In the SLR network, only significant Z-rotations remain for the GRASP-like scenario, at 0.85 mm and 0.2 mm/a, respectively, for position and velocity. This is also the only scenario with very few SLR observations around the equator.

The transfer of the datum between the techniques is also evident in the LTs. Tab. 7.1 shows the RMS values of the LTs for distances up to 30 km (Altamimi, 2008) between the techniques in comparison to the simulation. This is shown for the combination with GTs only and for the combination with GTs and ST.

As can be seen, the RMS of the LTs between DORIS and GPS (D-G), when combined with only the GTs, achieves a level of less than 1 mm for all scenarios. This value increases to a maximum of 1.33 mm when the ST is introduced. This is due to the Z-rotation, which is also present in the Helmert parameters and relates to the influence of SLR and the strength of the NNR condition applied. The effect is least pronounced in the circular scenarios, where the LT RMS in the combination with the ST is below half a millimetre.

The LTs between DORIS and SLR (D-S), as well as SLR and GPS (S-G), are only at the millimetre level in the GT combination for the E-GRASP-like scenario. For all other scenarios, the LT RMS in the GT combination is at the centimetre to decimetre level. As the E-GRASP-mod and E-GRASP-like scenarios only differ in their eccentricity, it seems that a highly eccentric orbit has a positive effect. In these inter-technique comparisons, introducing the ST in the combination substantially improves the LT RMS. Between DORIS and SLR, a LT RMS of about 0.3–1.2 millimetres is achieved. Between SLR and GPS it is about 1–2 millimetres. Variations in the overall RMS between the scenarios for combinations involving GTs and ST are in the submillimetre range. Considering the systematic discrepancies between the techniques in reality and the difficulty of measuring inaccessible reference points (e.g. at ground stations), this is a promising result, as it would allow the LTs to be validated at the millimetre level using a space-tie satellite.

Table 7.1: RMS of LTs using GTs alone or GTs and ST. All values are given in millimetres. D stands for DORIS, G for GPS and S for SLR. The threshold for the LTs is 30 kilometres. The overall RMS values are calculated as unweighted RMS.

	with GTs				**with GTs and ST**			
	D-S	**S-G**	**G-D**	**RMS**	**D-S**	**S-G**	**G-D**	**RMS**
GRASP-like	34.83	33.20	0.22	27.78	1.23	1.15	1.33	1.24
E-GRASP-mod	22.92	22.34	0.18	18.48	0.78	1.22	0.84	0.97
E-GRASP-like	1.88	1.95	0.14	1.57	0.86	1.20	0.84	0.98
Circular 30°	289.66	278.18	0.20	231.87	0.39	1.63	0.32	0.98
Circular 60°	467.70	450.92	0.16	375.09	0.48	1.02	0.43	0.70
Circular 89°	349.43	336.19	0.19	279.95	0.32	1.36	0.25	0.82

7.5.1.2 Formal errors

The influence of the multi-technique combination is examined in two steps. First, the influence of the combination is analysed in comparison to the respective single-technique solution. In this analysis, only the formal errors of the station network for each technique are considered in the combined solution. The OSI is also used at this point, as the combination significantly alters the DoF, particularly for DORIS and SLR. Secondly, the multi-technique combination using both GTs and ST is compared with the combination using GTs alone, and changes are discussed. If significant changes are identified in this combination, the combined solution is compared again with the respective single-technique solution.

Combination with global ties Combining the techniques using GTs results in a reduction of formal errors in station positions and velocities of approximately 70% in all components for DORIS (see Fig. G.33). An improvement of approximately 95% can be noted in both pole coordinates for all scenarios, and between 70 and 75% in LOD. The differences between the scenarios are in the low single-digit percentage range and are only noticeable in LOD. The expected improvement for DORIS is around 92%. A geometric added value of between 5 and 10% can only be seen in the pole coordinates. In the station coordinates, velocities and LOD, the improvement is about 10–20% below expectations. The GRASP-like scenario is slightly less advantageous in this respect.

For GPS, the improvement is approximately 35–40% in the X and Y components for station positions and velocities in Cartesian coordinates. For the Z component, the improvement is approximately 70% and 60%, respectively. In geographical coordinates, improvements are mainly evident in the latitude and height components. In the ERPs, the combination leads to a reduction of about 80% in the pole coordinates and over 95% in LOD. The expected improvement due to the change in the DoF is approximately 1% for all scenarios. Therefore, a geometric added value can be determined for all parameters in all scenarios.

For SLR, only the Z component of the Cartesian coordinate system shows an improvement of around 80% in station positions and velocities. As mentioned above, it is not possible to transfer the geodetic datum adequately from GPS to SLR using GTs alone. Consequently, a significant increase in formal errors of up to 700% is observed in the X and Y components. This is also evident in all components in geographical coordinates. In the ERPs, however, a reduction of over 95% is evident for all scenarios. The expected improvement due to the change in the DoF is around 99% for all scenarios. A geometric added value can only be noted in LOD, in the pole coordinates, the improvement is close to expectations.

Combination with global ties and spacetie Combining the techniques with both the GTs and ST leads to a further reduction in formal errors. For DORIS, this reduction is exclusively seen in the Z component of station velocities, compared to combining with GTs alone. However, this reduction is in the low single-digit percentage range, with the strongest reduction occurring in the GRASP-like scenario.

For GPS, the ST combination significantly reduces formal errors in the X and Y components of the station positions and velocities by approximately 50% and 30%, respectively (see Fig. 7.2). In geographical coordinates, this improvement is most evident in the longitude component. Reductions in the Z component are less than 3% for all scenarios and less than 1% for the ERPs. Compared to the GPS single-technique solution, combining with the ST thus achieves a similar level of improvement in all station position components at around 70% and 60% for velocities. In geographical coordinates, the latitude component shows

slightly stronger improvements of around 70% in positions and 65% in velocities than the longitude and height components, where the improvements are around 65% and 50% for positions and velocities, respectively. The same applies to the OSI due to the low change in the DoF (see Fig. G.34).

With SLR, combining with the ST has a similar effect to that observed for GPS (see Fig. 7.3). As can be seen from the Helmert parameters, the geodetic datum can be transferred adequately from GPS to SLR if the ST is used for the combination. Compared to combining with GTs alone, this substantially improves the formal errors in the X and Y components of positions and velocities. Changes in the Z component are at most 2%, and in the ERPs less than 1%. Therefore, compared to the single-technique solution of SLR, combining with the ST achieves an improvement in formal errors of about 80% in positions and 75–80% in velocities. Differences between the satellite scenarios and between the components are in the low single-digit percentage range. No geometric added value can be achieved in the positions and velocities with any of the scenarios. The improvements are 15–25% below expectations (see Fig. G.35). The formal errors of the ERPs do not change when combined with the ST.

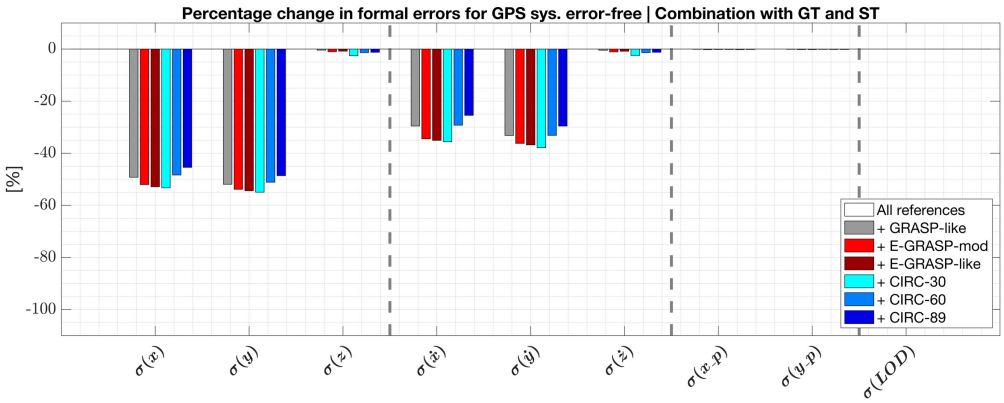

(a) Difference in formal errors when using GTs and ST compared to GTs alone. Coordinates in X,Y, and Z

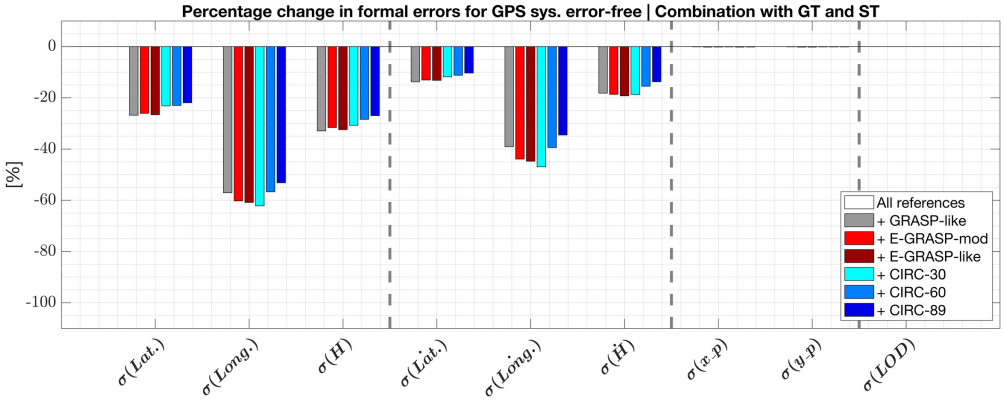

(b) Same as in Fig. a) but for coordinates in Latitude, Longitude, Height.

Figure 7.2: Percent differences in formal errors for GPS when using GTs and ST for the combination compared to using GTs alone. Negative values indicate a reduction in formal errors due to the ST. Figure a) shows the values for X,Y and Z, Figure b) the values for Latitude, Longitude, Height.

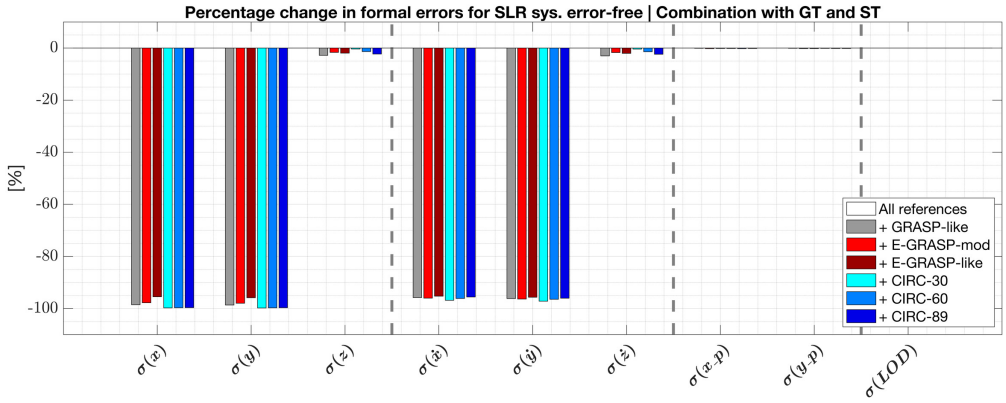

(a) Difference in formal errors when using GTs and ST compared to GTs alone. Coordinates in X,Y, and Z

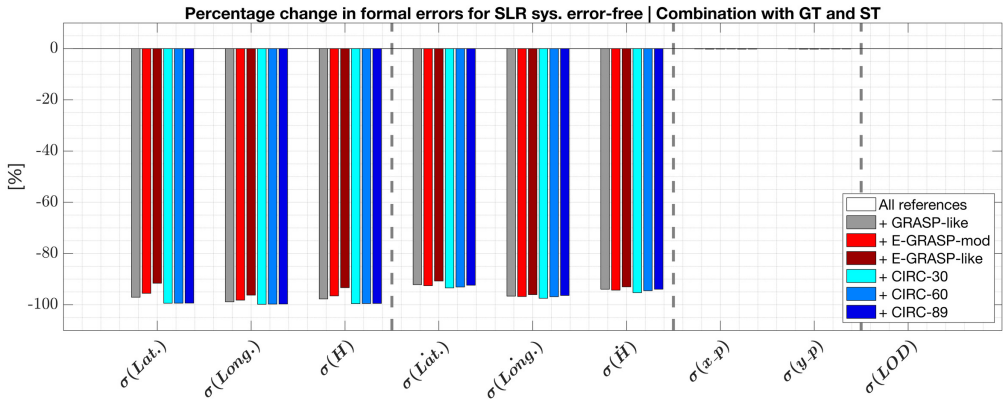

(b) Same as in Fig. a) but for coordinates in Latitude, Longitude, Height.

Figure 7.3: Percent differences in formal errors for SLR when using GTs and ST for the combination compared to using GTs alone. Negative values indicate a reduction in formal errors due to the ST. Figure a) shows the values for X,Y and Z, Figure b) the values for Latitude, Longitude, Height.

7.5.2 ERP analysis

The multi-technique combination with GTs can combine the strengths of the individual techniques with regard to determining the ERPs. In the single-technique solutions, the lowest noise in the pole coordinates was achieved using GPS, and DORIS for LOD. Compared to the DORIS single-technique solution, the combined solution reduces the noise in the pole coordinates by over 95% to below 0.1 mm (see Tab. F.63). The influence on the noise level of LOD is less pronounced, with a reduction in noise of 3–16% being achieved for all scenarios except the 60 degree circular scenario, which shows an increase of 12%. Compared to the GPS single-technique solutions, the combination leads to a slight increase in noise in the pole coordinates of between 18 and 37%. However, noise in LOD can be reduced by around 95% to below 1 μm for all scenarios. The strongest improvement can be seen for SLR. Compared to the single-technique solution, noise in the pole coordinates is reduced by around 95%, and in LOD by over 99% (a reduction from the millimetre level to below the micrometre). Statistically significant remaining biases and trends can be observed in the combined solution for all scenarios, but these are below 0.12 mm and 0.01 mm/a, respectively. Spectral analysis revealed no signals with an amplitude greater than 0.01 mm for any scenario (see also Figs. G.36 to G.41 in App. G.4).

The additional combination with the ST shows only a very minor influence on the determined ERPs. Significant changes in noise compared to the solution with GTs alone can only be sporadically detected in the pole coordinates, with differences in the range of a few micrometres. The same applies to offsets and trends, where differences are in the range of a few micrometres and micrometres/a, respectively. The largest difference is seen in the Y-pole for the E-GRASP-like scenario, at 51 micrometres. No influence on the spectral analysis of the ERPs can be detected for any of the scenarios.

7.5.3 Earth gravity field determination in combination

The estimated Earth gravity field of the multi-technique solution combined with GTs shows a strong dominance of GPS. (The triangular plots, degree amplitudes and cumulative error can be found in App. G.4 in Fig. G.42, G.44, and G.46). The maximum degree of development to which the gravity field can be resolved is almost identical to that of the GPS single-technique solution in most scenarios and is therefore the highest of all techniques. For the 60 degree circular scenario only, it is equivalent to the single-technique solution of GPS (degree 35), which is, however, lower than the maximum degree of the DORIS solution at degree 47 and the SLR solution at degree 45. The 100 mm EWH level is reached above degrees 16, 6, 7, 5, 6, 7 for the GRASP-like, E-GRASP-mod, E-GRASP-like and the 30, 60 and 89 degree circular scenario, respectively. For all scenarios, this corresponds almost exactly to the values achieved in the GPS single-technique solution. For the GRASP-like scenario only, this level is reached at a lower degree in the multi-technique solution (degree 16) than with GPS alone (degree 20). The same applies to the degree to which a SNR of 1 is achieved. For all scenarios except the GRASP-like scenario, this is almost identical to the GPS single-technique solution. In this scenario, it is achieved at degree 43 in the multi-technique solution compared to degree 47 in the GPS single-technique solution. Other than that, combining with GTs shows an improvement in the degree amplitudes in each scenario, primarily in degrees 2 and 3. For degree 2, values below 1 mm EWH can be achieved in all scenarios. They are largest for the E-GRASP-mod and E-GRASP-like scenarios. This is also reflected in the degree amplitudes, which generally show an improvement, especially in low-degree SHs. However, in the GRASP-like scenario, the combination leads to a deterioration in degree amplitudes above degree 10.

The additional combination with the ST results only in very minor changes in the degree amplitudes in any of the scenarios. (Compare also in App. G.4 the triangular plots in Fig. G.43, degree amplitudes in Fig. G.45 and cumulative error in Fig. G.47). The percentage change in the absolute difference per coefficient is shown in Fig. 7.4. Here, a negative value indicates that the difference between the estimated coefficient in the solution with both GTs and ST comes closer to the simulation, thus representing an improvement. Conversely, a positive value indicates that the deviation from the simulation increases, suggesting a deterioration. In the GRASP-like scenario, the primary influence of the ST is evident in low-degree SHs and higher sectorial coefficients. However, no uniform improvement can be observed, as the differences exhibit significant variability. In the E-GRASP-mod, E-GRASP-like and circular scenarios with 30 and 60 degrees inclination, combining with the ST leads to both improvements and deteriorations, primarily for zonal and tesseral coefficients of low order. Changes are mostly evident for resonance coefficients and uniform for degrees of a certain order. The 89 degree circular scenario shows almost no change. Nevertheless, the median changes are below 1% in all scenarios. Therefore, it is not possible to determine an obvious improvement or deterioration through the additional combination of techniques with the ST.

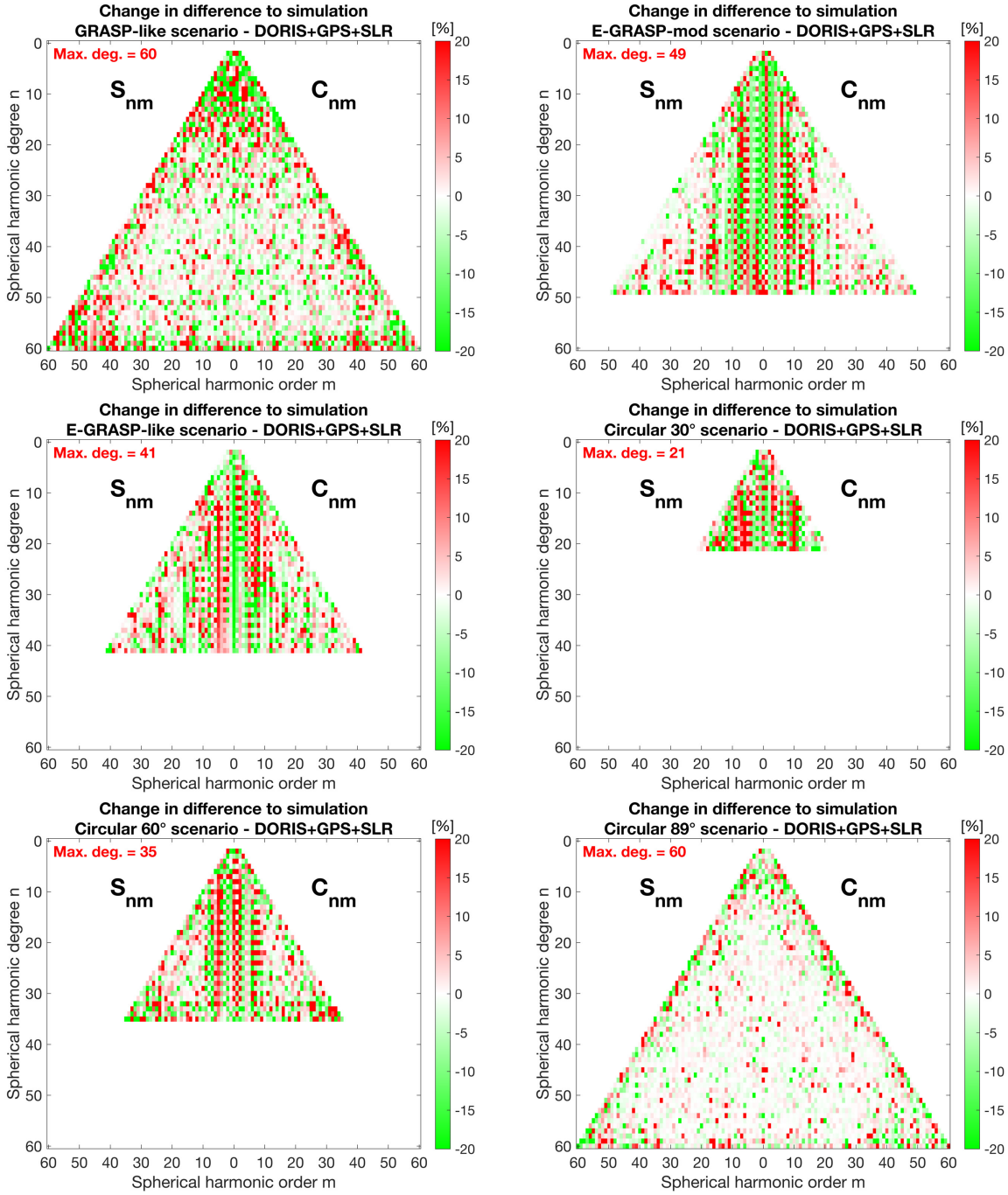

Figure 7.4: Triangular plots showing the differences between the estimated SH coefficients for the combination using GTs alone and the combination using GTs and the ST with respect to the simulation. Negative values indicate improvement, while positive values indicate degradation.

7.6 Conclusion - Co-location in space

The potential of co-location of the techniques DORIS, GPS and SLR in space was investigated. To this end, a combination using only GTs was first carried out and compared with the respective individual single-technique solutions. Then, the ST was used in addition to the GTs for the combination. For this purpose, the geodetic datum was applied solely to GPS in the same way as for the single-technique solution and it was investigated whether it is possible to transfer the datum to the other techniques and whether this would improve the TRF, ERPs and, subsequently, the estimated gravity field.

The results show that it is possible to transfer the geodetic datum from GPS to DORIS using GTs alone. For SLR, this is not possible in all scenarios. It is only possible for station positions in the E-GRASP-like scenario. In all scenarios, the SLR network undergoes significant Z-rotation. Using the ST in addition to the GTs for the combination enables the datum to be transferred to SLR as well. However, the station network determined in this way exhibited residual Z-rotations for SLR in the low millimetre and submillimetre range. These were found to be induced into the GPS network by combining it with the ST. By increasing the strength of the applied NNR condition, these rotations are reduced to an insignificant level. For the SLR network, only the GRASP-like scenario exhibits a Z-rotation of approximately 0.85 mm and 0.2 mm/a. For GPS, insignificance was achieved in all rotations for all scenarios. Given the goals set forth by GGOS, the required level of accuracy can be achieved.

This was further validated in the LTs, computed as RMS for inter-technique distances in comparison to the simulation. By combining the techniques using the ST, an improvement in the LT RMS from up to several decimetres down to the millimetre level could be achieved for all scenarios and between all techniques. This offers the novel possibility to validate LTs measured by local surveys between the techniques with millimetre accuracy through ST co-location.

In terms of formal errors in station coordinates and velocities, it was found that for DORIS the maximum potential for improvement is already achieved through the combination with GTs. Since the DoF varies greatly compared to the DORIS single-technique solution due to the large number of GPS observations, no geometric added value could be found for DORIS for any of the scenarios. Improvements are approximately 20% below expectation. For GPS, the ST combination significantly improves the formal errors of station coordinates and velocities in the X and Y components, the improvement in the Z component can also be provided by GTs. Compared to the GPS single-technique solutions, the percentage improvements are thus around 70% for positions and 60% for velocities. A geometric added value can be found for each scenario, which is approximately the same for all scenarios. The same applies to SLR, where the potential for improvement in formal errors in the X and Y components can only be achieved through the combination with the ST. The OSI is approximately 15% below expectation for positions and approximately 20% below expectation for velocities. However, as the expected improvement is around 99%, the combination still provides a substantial improvement compared to the single-technique solution.

In terms of formal errors in ERPs, the combination with GTs provides almost the complete improvement. Compared to the single-technique solutions, a geometric added value in the pole coordinates of approximately 10% for DORIS and 80% for GPS is achieved. For SLR, it is slightly below expectation. For LOD, the improvement for DORIS is about 12–20% below expectations, for GPS about 80% above, and for SLR at the expected level.

The same applies to the a posteriori ERPs, where the combination with GTs provides the main influence. The noise in the ERPs can be reduced to approximately the level

of the best contributing technique for all scenarios. For the pole coordinates, the best contributing technique is GPS, representing an improvement of around 95% compared to the single-technique solutions of DORIS and SLR. For LOD, the best contributing technique is DORIS, which corresponds to an improvement of over 95% compared to GPS and SLR single-technique solutions. Any remaining statistically significant offsets and trends are found to be below 0.12 mm and 0.01 mm/a, respectively. Spectral analysis shows no signals with amplitudes above 0.1 mm remaining for any of the scenarios. There is no significant influence from the additional combination with ST.

Evaluating the space-tie satellite scenarios shows that, when combined with GTs, only the E-GRASP-like scenario proves to offer the possibility of transferring the datum of station positions. However, the accuracy of the resulting station velocities cannot reach the GGOS goals. Variations in the summarised rating between all other scenarios are small. Combining with the ST substantially improves the transfer of the datum and the determination of inter-technique LT distances. Furthermore, it also leads to greater improvements in the formal errors of station positions and velocities for GPS and SLR (compare Tab. 7.2).

Table 7.2: Maximum potential of the satellite scenarios for multi-technique co-location with GTs and the additional potential through the combination with the ST.

	G-like	E-G-mod	E-G-like	Circ. 30°	Circ. 60°	Circ. 89°
Combination with GTs						
Helmert	②	②	①	②	②	②
LTs	②	②	①	③	③	③
Station pos. form. err.	②	②	②	②	②	②
Station veloc. form. err.	②	②	②	②	②	②
Pole coord. form. err.	①	①	①	①	①	①
LOD form. err.	①	①	①	①	①	①
ERPs	①	①	①	①	①	①
Summary GTs	1.6	1.6	1.3	1.7	1.7	1.7
Combination with GTs and ST						
Helmert	②	②	②	①	①	①
LTs	①	①	①	①	①	①
Station pos. form. err.	①	①	①	①	①	①
Station veloc. form. err.	①	①	①	①	①	①
Pole coord. form. err.	⊙	⊙	⊙	⊙	⊙	⊙
LOD form. err.	⊙	⊙	⊙	⊙	⊙	⊙
ERPs	⊙	⊙	⊙	⊙	⊙	⊙
Summary GTs+ST	1.3	1.3	1.3	1.0	1.0	1.0

The combination of techniques for the determination of the Earth gravity field shows that the combined solution is largely dominated by GPS, as well as by the combination using GTs. Thus, the rating for the potential to determine the Earth gravity field in Tab. 7.3 is equivalent to that of the GPS single-technique solution. Compared to the individual single-technique solutions, improvements are primarily limited to SHs of degrees 2 and 3. No distinct improvements were identified through the additional combination with the ST.Changes in the differences between the estimated SHs and the simulation are not uniform

and become apparent only at higher zonal and tesseral degrees, despite the fact that the errors in these coefficients are still very large. Furthermore, the degree amplitudes in the ST combination are in general smaller, but differences are close to insignificant.

Table 7.3: Potential for EGM estimation in the multi-technique combination with GTs and GTs with ST.

	G-like	E-G-mod	E-G-like	Circ. 30°	Circ. 60°	Circ. 89°
EGM determination GTs	①	②	②	②	②	②
EGM determination GTs+ST	①	②	②	②	②	②

The greatest potential of the ST combination is found to lie in the transfer of the geodetic datum between techniques and in determining LT distances between co-location sites with millimetre accuracy. Additionally, substantial improvements can be achieved in the formal errors of station coordinates and velocities. Improvements in the formal errors of ERPs, the determined ERPs, and in the determination of the Earth gravity field are almost exclusively attributable to the combination with GTs.

8 Conclusion and outlook

This dissertation investigates the influence and potential of six different space-tie satellite scenarios on improving TRF and Earth gravity field determination.

To this end, a simulation environment was implemented, as described in Chap. 4. Used in conjunction with the EPOS-OC software, this environment can realistically simulate observations of the space geodetic techniques DORIS, GPS and SLR. The real data evaluation performed to obtain information on real observation characteristics is described in Chap. 5, where the characteristics of real observation data and their use as the basis for the simulation are described. Based on these evaluations, reference solutions for an existing space and ground segment were simulated for each technique.

Using the characteristics of the real data, highly realistic observations were simulated for the space geodetic techniques DORIS in Sec. 6.1, SLR in Sec. 6.2 and GPS in Sec. 6.3 for six different space-tie satellite scenarios for a mission time span of seven years. Subsequently, the potential of the various techniques for orbit determination in the scenarios, as well as for TRF and gravity field determination, was analysed. In each case, this was done in a systematic error-free manner in order to assess the maximum potential that each scenario could provide individually. Next, the influence of selected mismodelling effects was investigated to assess the robustness of the scenarios with regard to achieving this level of improvement. Based on the systematic error-free single-technique solutions, the combination of the techniques was carried out in Chap. 7. This was done with GTs, and then with both GTs and the ST provided by the space-tie satellite, in order to isolate the potential of the ST combination.

This concluding chapter summarises the results of the single-technique analysis and multi-technique combinations, highlighting the benefits of combining the techniques with a ST. Sec. 8.1 discusses this with regard to the potential for TRF determination, while Sec. 8.2 discusses this with regard to Earth gravity field determination. These results are placed in the context of the scientific questions set out in Chap. 1, which are answered here. Based on the results, Sec. 8.3 provides an outlook on what can be expected from co-location in space and makes recommendations for future space-tie missions. It also outlines the limitations of the analysis performed and recommends future analyses to bring us closer to achieving the GGOS goals.

8.1 Potential for reference frame determination

The potential of a single-technique solution using space-tie satellite scenarios to improve the respective technique-specific TRF and estimated ERPs was assessed in each case using summarising benchmark factors for the potential and vulnerability, which are summarised in Tab. 8.1. The research questions Q1, Q2 and Q3 set forth in the introduction can therefore be answered as follows:

Q1 To what extent can a possible space-tie satellite contribute to TRF solutions — technique-specific and in combination?

Technique-specific contribution – Of the space-tie satellites examined, the greatest individual technique-specific potential for improvement was found for DORIS and SLR, although this is largely due to the additional observations. For DORIS, the greatest improvements were seen in station coordinates, particularly in the North-South and height components, while improvements for the ERPs were primarily in LOD. SLR showed fewer specific improvements. All scenarios were found to provide very similar improvements, which were also mostly due to the additional observations. The potential for GPS was found to be lowest. The proportion of additional observations provided by the space-tie satellite, and the contribution that one satellite can make to a large number of GPS ground stations and an entire GPS satellite constellation, proved to be very limited. Improvements were in the low single-digit percentage range for all scenarios. The greatest improvements were found in formal errors in the Z component. The circular scenarios performed slightly worse due to the observation geometry caused by the high altitude.

Comparing the scenarios shows that for DORIS the highest potential for improvement is provided by the low-orbiting GRASP-like scenario. The E-GRASP-mod, E-GRASP-like, and circular scenarios with inclinations of 60 and 89 degrees demonstrate slightly lower potential, with factors ranging from 1.5 to 1.7. The 30-degree circular scenario shows the lowest potential for improvement for DORIS, with a factor of 2.2.

For SLR, the potential is similar for all scenarios, with all scenarios being rated by a factor of 1.5.

GPS generally shows the lowest potential for improvement in the single-technique analysis across all techniques. The highest potential is achieved by the low-orbiting GRASP-like scenario, with a factor of 2.1, and the lowest by the 30degree circular scenario, with a factor of 2.5. The E-GRASP-mod and E-GRASP-like scenarios demonstrate slightly higher potential than the circular scenarios at inclinations of 60 and 89 degrees, but the differences are minimal.

Contribution in combination – When combined with GTs, it was shown that the geodetic datum could be transferred from GPS to DORIS with millimetre accuracy in all scenarios. Only the E-GRASP-like scenario demonstrated the possibility of transferring the datum information for station positions to SLR, but not for velocities. With GTs, the full improvement can already be achieved in the ERPs for all techniques, as well as for DORIS in all components of station coordinates and velocities. For GPS and SLR, the full improvement can only be achieved for the Z component.

The additional combination using the ST primarily made it possible to transfer the geodetic datum from GPS to DORIS and SLR with millimetre accuracy in all scenarios. In comparison to the combination with GTs only, further substantial improvements were also achieved in the formal errors of station coordinates and velocities for GPS and SLR, as well as a clear geometric added value in the case of GPS. Furthermore, combining the techniques with the ST made it possible to determine inter-technique LT distances with millimetre accuracy in every satellite scenario. Given systematic differences between the techniques in reality and the difficulty of measuring inaccessible reference points (e.g. at ground stations), this is a

promising result, as it would enable the validation of LTs with millimetre accuracy using a space-tie satellite.

The circular scenarios achieved the best overall rating in the ST combination, primarily due to the very good determination of inter-technique LTs. However, the other scenarios are not far behind.

Q2 To what extent does mismodelling of the space-tie satellite affect the single-technique TRF determination?

The largest variability in vulnerability ratings due to mismodelling was found for DORIS and SLR. When the scenarios are averaged across all techniques, the highest potential for improvement is seen for the GRASP-like scenario with a factor of 1.6, but it is also the scenario most affected by mismodelling, resulting in the highest vulnerability rating of 2.0. The E-GRASP-like scenario is the second most affected. Due to its highly eccentric orbit with low perigee, this scenario is particularly susceptible to the effects of atmospheric drag, SRP, and the Earth's gravity field. The E-GRASP-mod scenarios and all circular scenarios demonstrate the lowest vulnerability overall. The 89degree circular scenario is the best by a narrow margin.

Q3 Which orbit scenarios are most beneficial for contributing to the GGOS goals?

The summarised evaluations of the space-tie satellite scenarios examined for the individual techniques, in combination with GTs and in combination with both GTs and ST, are listed in Tab. 8.1. The overall rating, calculated as the sum of the ratings for the individual techniques, the combinations, and the summarised vulnerability rating shows the circular scenario with an inclination of 89 degrees and a final rating of 6.2 as the best overall choice. Second place goes to the E-GRASP-like and 60degree circular scenarios, and third place to the GRASP-like, E-GRASP-mod and 30degree circular scenarios.

Table 8.1: Multi-technique potential of the space-tie satellite scenarios for TRF and ERP determination. The summarised single-technique potential and vulnerability (abbreviated as v) is calculated as the unweighted mean of the individual values. The overall rating is calculated as the sum of the potential of the single-technique and the combinations, as well as the summarised vulnerability rating.

	G-like	E-G-mod	E-G-like	Circ. 30°	Circ. 60°	Circ. 89°
DORIS	1.4 v: 2.0	1.5 v: 1.3	1.7 v: 1.5	2.2 v: 1.3	1.7 v: 1.2	1.7 v: 1.2
SLR	1.5 v: 2.1	1.5 v: 1.9	1.5 v: 2.1	1.5 v: 1.7	1.5 v: 1.8	1.5 v: 1.7
GPS	2.1 v: 2.0	2.3 v: 2.0	2.3 v: 2.0	2.5 v: 2.2	2.4 v: 2.1	2.4 v: 2.0
Single-technique	1.6 v: 2.0	1.8 v: 1.7	1.8 v: 1.9	2.1 v: 1.7	1.9 v: 1.7	1.9 v: 1.6
Combination GTs	1.6	1.6	1.3	1.7	1.7	1.7
Combination GTs+ST	1.3	1.3	1.3	1.0	1.0	1.0
Overall rating	**6.5**	**6.4**	6.3	**6.5**	6.3	6.2

8.2 Potential for gravity field determination

The potential for gravity field determination was investigated, since the gravity field forms one of the three pillars of geodesy and is closely linked to the realisation of geodetic reference frames. The research question in this regard was:

Q4 To what extent can a possible space-tie mission contribute to gravity field recovery, and what is the effect of the spacetie?

An analytical sensitivity analysis was used to investigate the sensitivity of the space-tie satellite scenarios. The GRASP-like scenario showed by far the greatest sensitivity. The E-GRASP-like scenario is less sensitive, especially in zonal and tesseral coefficients due to the high numerical eccentricity of the orbit. The E-GRASP-mod scenario exhibited a sensitivity range similar to that of the E-GRASP-like scenario, albeit generally lower due to its higher perigee. The circular scenarios are the least sensitive, particularly at 30 degrees inclination.

Based on the results, determining the Earth's gravity field using only the individual space-tie satellite scenarios with the individual space geodetic techniques is limited to low-degree SHs. For most scenarios, this is up to a maximum of degree 7, based on an error in the degree amplitudes of up to 100 mm EWH. The estimation with the individual techniques shows the best results for the GRASP-like scenario with all techniques, and the worst for the circular scenarios at 30 and 60 degrees of inclination. In these two circular scenarios in particular, the GPS constellation showed a positive contribution through the integrated processing at the degree 2 and 3 SHs.

When combined with GTs, it was found that the resulting gravity field is almost completely dominated by the GPS solution. Improvements through the combination are limited to degrees 2 and 3.

The additional combination with the ST showed no consistent advantage. In some cases, the degree amplitudes are slightly lower, but the improvement achieved by the ST is marginal, especially with regard to degrees 2 and 3.

The results of the gravity field estimation show that a meaningful estimation of SHs is limited to low-degree SHs. From this perspective, it would be better to choose a scenario with lower sensitivity to the Earth's gravity field for a space-tie satellite mission to reduce the influence of gravity field mismodelling and reduce the overall vulnerability. The connection between the three pillars of geodesy via low SHs would persist.

Table 8.2: Summary of the sensitivity and potential for EGM determination for the space-tie satellite scenarios in the single-technique solutions and in combination.

	G-like	E-G-mod	E-G-like	Circ. 30°	Circ. 60°	Circ. 89°
Sensitivity	①	②	①	③	③	③
DORIS	①	②	②	③	③	②
SLR	②	②	②	③	③	②
GPS	①	②	②	②	②	②
Combination GTs	①	②	②	②	②	②
Combination GTs+ST	①	②	②	②	②	②

8.3 Outlook

The results show that what can expect from co-location in space using a space-tie satellite is primarily the ability to transfer the geodetic datum between space geodetic techniques with millimetre accuracy. This makes it possible to determine inter-technique LTs with millimetre accuracy, thus allowing values measured by local surveys to be validated with high accuracy. This will allow discrepancies between the techniques that lead to systematic differences to be identified. Consequently, the consistency between the techniques can be improved, which helps to make the determined TRF more accurate. Furthermore, it was shown that the combination with the ST provides significant geometric added value and reduces formal errors of station coordinates, velocities and ERPs.

The findings can serve as a basis for the selection of optimal orbit scenarios for future space-tie satellite missions. The Genesis satellite mission, approved by ESA in 2022 as part of the FutureNAV programme, will be a pioneering mission combining the four techniques on a single satellite for the first time. The currently planned orbit is a circular orbit, with an altitude of 6'000 km and an inclination of 95 degrees. This orbit is the closest match to the circular scenario investigated with an inclination of 89 degrees and an altitude of 7'000 km, which was identified as the optimal choice in the overall rating.

Based on the results, the following recommendations can be made for a future space-tie satellite mission: With the focus on TRF determination, the potential influence of mismodelling should be minimised as much as possible, as this poses a risk of preventing the full potential for improvement from being achieved or of inducing unwanted signals in the ERPs. Systematic geographic orbit differences could also be identified for eccentric orbits. Although no correlating effect on the TRF could be found in the mismodelling cases investigated for these scenarios, this risk should be avoided in reality, where multiple sources of mismodelling may occur and potentially lead to amplified effects. Additionally, for scenarios that are more susceptible to gravity field mismodelling, it was found that orbit errors of the space-tie satellite are transferred to the GPS constellation orbits in the integrated GPS processing, which should be avoided.

In addition, it was found that there is a very large margin for incorrectly determined reference points on the satellite in the individual single-technique solutions, particularly for higher-orbiting satellites such as the investigated circular scenarios. This issue should be investigated further in future work with respect to its effect in the ST combination.

Further investigations into the combined effects of multiple mismodelling influences in parallelhould also be conducted. In this analysis, the influences were examined individually for each disturbance force to determine their direct impact on the TRF and the ERPs. Combining several mismodelling effects could provide valuable insights into whether systematic errors, such as deviations in station coordinates or PCOs, can be estimated simultaneously. Therefore, it should be analysed whether the ST can decouple possible correlations. Another factor which should be investigated in future studies is that the initial state elements of the GPS space-tie satellite solutions could only be combined with the other techniques on a weekly basis. Using suitable long-arc solutions, the influence of the highly precise GPS arcs could be increased.

On a final note, extensive simulations provide valuable insights into the origins of many issues encountered in real data analysis, helping us to understand possibilities and limitations involved. For this purpose, some satellites, such as the Sentinel satellites, are already equipped with multiple space geodetic techniques, although not with VLBI, offering an opportunity to complement the findings of this thesis using real data. This could be used to

verify whether the possibilities identified for co-location in space can be reproduced, even before the launch of Genesis.

Many of these issues will be addressed within the GENESIS-D project, which is funded by the German Space Agency at the German Aerospace Center (DLR) and is being carried out by GFZ in collaboration with the Federal Agency for Cartography and Geodesy (BKG) and the Deutsches Geodätisches Forschungsinstitut at Technical University of Munich (DGFI-TUM). To this end, further analyses of real data and combinations will be carried out, as well as simulations, particularly for Genesis orbit scenarios. The combined effects of systematic mismodelling will be investigated, as will the potential of combining all four space geodetic techniques (including VLBI) with the ST and strategies for optimal orbit combination at the normal equation level between ACs. This will provide an optimal basis for future space-tie missions and ultimately help to achieve the accuracy goals for future TRFs, as set forth by GGOS.

Bibliography

Aitken AC (1936) IV.—On Least Squares and Linear Combination of Observations. In: Proceedings of the Royal Society of Edinburgh 55, 42–48. ISSN: 0370-1646. DOI: 10.1017/s0370164600014346.

Altamimi Z (2003) Discussion on How to Express a Regional GPS Solution in the ITRF. In: EUREF Publication n °12, Report on the Symposium ofthe IAG Subcommission for Europe (EUREF) held in Ponta Delgada,5–8 June 2002, 162–167. URL: http://www.euref.eu/symposia/book2002/162-167.pdf.

Altamimi Z (2008) Importance of local ties for the ITRF. In: In Proceedings of the joint Symposia: 13th FIG Symposium on Deformation Measurement and Analysis and 4th IAG Symposium on Geodesy for Geotechnical and Structural Engineering, Portugal, Lisbon. report on the joint symposium “Measuring the Changes”of the FIG 13th symposium on deformation measurementand analysis and the IAG 4th symposium on geodesy forgeotechnical and structural engineering. URL: https://www.fig.net/resources/proceedings/2008/lisbon_2008_comm6/papers/pas02/pas02_01_altamimi_mc108.pdf (accessed 28 July 2025).

Altamimi Z, Rebischung P, Métivier L, Collilieux X (2016) ITRF2014: A new release of the International Terrestrial Reference Frame modeling nonlinear station motions. In: Journal of Geophysical Research: Solid Earth 121(8), 6109–6131. DOI: 10.1002/2016jb013098.

Altamimi Z, Rebischung P, Collilieux X, Métivier L, Chanard K (2023) ITRF2020: an augmented reference frame refining the modeling of nonlinear station motions. In: Journal of Geodesy 97(47). DOI: 10.1007/s00190-023-01738-w.

Appleby G, Rodríguez J, Altamimi Z (2016) Assessment of the accuracy of global geodetic satellite laser ranging observations and estimated impact on ITRF scale: estimation of systematic errors in LAGEOS observations 1993–2014. In: Journal of Geodesy 90(12), 1371–1388. ISSN: 1432-1394. DOI: 10.1007/s00190-016-0929-2.

Arnold D, Meindl M, Beutler G, Dach R, Schaer S, Lutz S, Prange L, Sośnica K, Mervart L, Jäggi A (2015) CODE’s new solar radiation pressure model for GNSS orbit determination. In: Journal of Geodesy 89(8), 775–791. ISSN: 1432-1394. DOI: 10.1007/s00190-015-0814-4.

Arnold D, Montenbruck O, Hackel S, Sośnica K (2018) Satellite laser ranging to low Earth orbiters: orbit and network validation. In: Journal of Geodesy 93(11), 2315–2334. ISSN: 1432-1394. DOI: 10.1007/s00190-018-1140-4.

Balbach O, Eissfeller B, Hein G, Enderle W, Schmidhuber M, Lemke N (1998) Tracking GPS above GPS Satellite Altitude: First Results of the GPS Experiment on the HEO Mission Equator-S. In: IEEE.

Bar-Sever YE (1996) A new model for GPS yaw attitude. In: Journal of Geodesy 70(11), 714–723. ISSN: 1432-1394. DOI: 10.1007/bf00867149.

Bar-Sever YE, Haines BJ, Bertiger W, Desai S, Wu SC (2009) GEODETIC REFERENCE ANTENNA IN SPACE (GRASP) – A MISSION TO ENHANCE SPACE-BASED GEODESY. In: COSPAR colloquium: scientific and fundamental aspects of the Galileo program, Padua. URL: https://api.semanticscholar.org/CorpusID:149451469 (accessed 17 Jan. 2025).

Barlier F, Berger C, Falin J, Kockarts G, Thuillier G (1978) A thermospheric model based on satellite drag data. In: Annales de Geophysique 34, 9–24.

Belli A, Zelensky NP, Lemoine FG, Chinn DS (2020) Impact of Jason-2/T2L2 Ultra-Stable-Oscillator Frequency Model on DORIS stations coordinates and Earth Orientation Parameters. In: Advances in Space Research 67(3), 930–944. DOI: 10.1016/j.asr.2020.11.034.

Beutler G (2005) Methods of Celestial Mechanics. Heidelberg: Springer.

Biancale R, Bode A (2006) Mean Annual and Seasonal Atmospheric Tide Models Based on 3-hourly and 6-hourly ECMWF Surface Pressure Data. en. Tech. rep. STR06/01. Deutsches GeoForschungsZentrum GFZ. DOI: 10.2312/GFZ.B103-06011.

Biancale R, Pollet A, Coulot D, Mandea M (2017) E-GRASP/Eratosthenes: a mission proposal for millimetric TRF realization. In: 19th EGU General Assembly, EGU2017, proceedings from the conference held 23-28 April, 2017 in Vienna, Austria., p.8752.

BIPM, ed. (1960) 10h CIPM proceedings. Bureau International des Poids et Mesures. DOI: 10.59161/cgpm1960res9e.

BIPM, ed. (1967) 13th CIPM proceedings. Bureau International des Poids et Mesures. DOI: 10.59161/cgpm1967res1e.

BIPM, ed. (2018) 26th CIPM proceedings. Conférence générale des poids et mesures. Bureau International des Poids et Mesures. DOI: 10.59161/cgpm2018res1e.

Bizouard C, Lambert S, Gattano C, Becker O, Richard JY (2018) The IERS EOP 14C04 solution for Earth orientation parameters consistent with ITRF 2014. In: Journal of Geodesy 93(5), 621–633. DOI: 10.1007/s00190-018-1186-3.

Blewitt G, Lavallée D (2002) Effect of annual signals on geodetic velocity. In: Journal of Geophysical Research: Solid Earth 107(B7). ISSN: 0148-0227. DOI: 10.1029/2001jb000570.

Boehm J, Niell A, Tregoning P, Schuh H (2006) Global Mapping Function (GMF): A new empirical mapping function based on numerical weather model data. In: Geophysical Research Letters 33(7). ISSN: 1944-8007. DOI: 10.1029/2005gl025546.

Boldbaatar E, Grant D, Choy S, Zaminpardaz S, Holden L (2023) Evaluating Optical Clock Performance for GNSS Positioning. In: Sensors 23(13), 5998. ISSN: 1424-8220. DOI: 10.3390/s23135998.

Borderies N (1977) Time regularization of an Adams-Moulton-Cowell algorithm. In: Celestial Mechanics 16(3), 291–308. ISSN: 1572-9478. DOI: 10.1007/bf01232656.

Boucher C, Altamimi Z (1993) Development of a Conventional Terrestrial Reference Frame. In: Contributions of Space Geodesy to Geodynamics: Earth Dynamics. American Geophysical Union, 89–97. DOI: 10.1029/gd024p0089.

Box GEP, Cox DR (1964) An Analysis of Transformations. In: Journal of the Royal Statistical Society: Series B (Methodological) 26(2), 211–243. ISSN: 2517-6161. DOI: 10.1111/j.2517-6161.1964.tb00553.x.

Brouwer D, Clemence GM (1961) Methods of Celestial Mechanics. Amsterdam: Elsevier. ISBN: 9781483200750. DOI: https://doi.org/10.1016/C2013-0-08160-1.

Brown MB, Forsythe AB (1974) Robust Tests for the Equality of Variances. In: Journal of the American Statistical Association 69(346), 364–367. ISSN: 1537-274X. DOI: 10.1080/01621459.1974.10482955.

Bruni S, Rebischung P, Zerbini S, Altamimi Z, Errico M, Santi E (2017) Assessment of the possible contribution of space ties on-board GNSS satellites to the terrestrial reference frame. In: Journal of Geodesy 92(4), 383–399. ISSN: 1432-1394. DOI: 10.1007/s00190-017-1069-z.

Bury G, Sośnica K, Zajdel R, Strugarek D, Hugentobler U (2021) Geodetic Datum Realization Using SLR-GNSS Co-Location Onboard Galileo and GLONASS. In: Journal of Geophysical Research: Solid Earth 126(10). ISSN: 2169-9356. DOI: 10.1029/2021jb022211.

Capdeville H, Štěpánek P, Hecker L, Lemoine J.-M (2016) Update of the corrective model for Jason-1 DORIS data in relation to the South Atlantic Anomaly and a corrective model for SPOT-5. In: Advances in Space Research 58(12), 2628–2650. ISSN: 0273-1177. DOI: 10.1016/j.asr.2016.02.009.

Capuano V, Botteron C, Farine PA (2013) GNSS PERFORMANCES FOR MEO, GEO AND HEO. In.

Cerri L, Couhert A, Ferrage P (2021) DORIS satellites models implemented in POE processing Ed.: 1/Rev.: 17. Tech. rep. CNES. URL: ftp://ftp.ids-doris.org/pub/ids/satellites/DORISSatelliteModels.pdf (accessed 28 Apr. 2022).

Cheng M, Tapley BD (2004) Variations in the Earth's oblateness during the past 28 years. In: Journal of Geophysical Research: Solid Earth 109(B9). ISSN: 0148-0227. DOI: 10.1029/2004jb003028.

Cheng M, Tapley BD, Ries JC (2013) Deceleration in the Earth's oblateness. In: Journal of Geophysical Research: Solid Earth 118(2), 740–747. ISSN: 2169-9356. DOI: 10.1002/jgrb.50058.

Ciufolini I, Pavlis EC (2004) A confirmation of the general relativistic prediction of the Lense–Thirring effect. In: Nature 431(7011), 958–960. ISSN: 1476-4687. DOI: 10.1038/nature03007.

CNES (2008) DORIS data export formats. URL: https://ids-doris.org/documents/BC/data/doris22.fmt (accessed 27 July 2022).

CNES (2024a) ADFB-2. Ed. by CNES. URL: https://ids-doris.org/ids/gallery/category/24-doris-equipment.html (accessed 28 Mar. 2024).

CNES (2024b) DORIS SYSTEM DEFINITION (VERSION 1.2). Tech. rep. CNES.

CNES-CLS (2024) International DORIS Service. URL: https://ids-doris.org/doris-system/tracking-network/maps.html.

Conover WJ (1980) Practical nonparametric statistics. Wiley series in probability and mathematical statistics. New York: Wiley. 493 pp. ISBN: 0471028673.

Cormen TH, Leiserson CE, Rivest RL, Stein C (2022) Introduction to algorithms. Ed. by Leiserson CE, Rivest RL, Stein C. Fourth edition. Cambridge, Massachusetts: The MIT Press. 11291 pp. ISBN: 9780262367509.

Coulot D, Berio P, Bonnefond P, Exertier P, Féraudy D, Laurain O, Deleflie F (2009) Satellite Laser Ranging Biases and Terrestrial Reference Frame Scale Factor. In: Observing our Changing Earth. Heidelberg: Springer, 39–46. ISBN: 9783540854265. DOI: 10.1007/978-3-540-85426-5_5.

Dahle C, Murböck M (2020) Post-processed GRACE/GRACE-FO Geopotential GSM Coefficients COST-G RL01 (Level-2B Product). en. DOI: 10.5880/COST-G.GRAVIS_01_L2B.

de Sitter W (1916) On Einstein's Theory of Gravitation and its Astronomical Consequences. First Paper. In: Monthly Notices of the Royal Astronomical Society 76(9), 699–728. DOI: 10.1093/mnras/76.9.699.

de Sitter W (1917) On Einstein's Theory of Gravitation and its Astronomical Consequences. Third Paper. In: Monthly Notices of the Royal Astronomical Society 78(1), 3–28. DOI: 10.1093/mnras/78.1.3.

Delva P, Altamimi Z, Blazquez A, Blossfeld M, Böhm J, Bonnefond P, Boy JP, Bruinsma S, Bury G, Chatzinikos M, Couhert A, Courde C, Dach R, Dehant V, Dell'Agnello S, Elgered G, Enderle W, Exertier P, Glaser S, Haas R, Huang W, Hugentobler U, Jäggi A, Karatekin O, Lemoine FG, Le Poncin-Lafitte C, Lunz S, Männel B, Mercier F, Métivier L, Meyssignac B, Müller J, Nothnagel A, Perosanz F, Rietbroek R, Rothacher M, Schuh H, Sert H, Sosnica K, Testani P, Ventura-Traveset J, Wautelet G, Zajdel R (2023) GENESIS:

co-location of geodetic techniques in space. In: Earth, Planets and Space 75(1). ISSN: 1880-5981. DOI: 10.1186/s40623-022-01752-w.

Desai SD (2002) Observing the pole tide with satellite altimetry. In: Journal of Geophysical Research 107(C11), 7-1 –7-13. ISSN: 0148-0227. DOI: 10.1029/2001jc001224.

Dow JM, Neilan RE, Gendt G (2005) The International GPS Service: Celebrating the 10th anniversary and looking to the next decade. In: Advances in Space Research 36(3), 320–326. ISSN: 0273-1177. DOI: 10.1016/j.asr.2005.05.125.

Eicker A, Jensen L, Wöhnke V, Dobslaw H, Kvas A, Mayer-Gürr T, Dill R (2020) Daily GRACE satellite data evaluate short-term hydro-meteorological fluxes from global atmospheric reanalyses. In: Scientific Reports 10(1). ISSN: 2045-2322. DOI: 10.1038/s41598-020-61166-0.

Einstein A (1905) Zur Elektrodynamik bewegter Körper. In: Annalen der Physik 322(10), 891–921. ISSN: 1521-3889. DOI: 10.1002/andp.19053221004.

Einstein A (1916) Die Grundlage der allgemeinen Relativitätstheorie. In: Annalen der Physik 354(7), 769–822. ISSN: 1521-3889. DOI: 10.1002/andp.19163540702.

EUSPA (2023) Galileo Satellite Metadata. https://www.gsc-europa.eu/support-to-developers/galileo-satellite-metadata. Accessed: 2023-10-31. URL: https://www.gsc-europa.eu/support-to-developers/galileo-satellite-metadata.

Exertier P, Belli A, Lemoine J (2017) Time biases in laser ranging observations: A concerning issue of Space Geodesy. In: Advances in Space Research 60(5), 948–968. ISSN: 0273-1177. DOI: 10.1016/j.asr.2017.05.016.

Ferrari AJ (1977) Lunar gravity: A harmonic analysis. In: Journal of Geophysical Research 82(20), 3065–3084. DOI: 10.1029/jb082i020p03065.

Fliegel HF, Gallini TE, Swift ER (1992) Global Positioning System Radiation Force Model for geodetic applications. In: Journal of Geophysical Research: Solid Earth 97(B1), 559–568. ISSN: 0148-0227. DOI: 10.1029/91jb02564.

Folkner WM, Williams JG, Boggs DH (2009) The Planetary and Lunar Ephemeris DE 421. In: PN Progress Report 42-178.

Folkner WM, Williams JG, Boggs DH, Park RS, Kuchynka P (2014) The Planetary and Lunar Ephemerides DE430 and DE431. In: The Interplanetary Network Progress Report 42-196.

François D, Claude B (2023) IDS AWG DORIS SYSTEM NEWS. URL: https://ids-doris.org/images/documents/report/AWG202311/IDSAWG202311-Didelot-DorisSystemStatus.pdf (accessed 13 Nov. 2024).

Gauß CF (1809) Theoria motus corporum coelestium in sectionibus conicis solem ambientium. la. sumtibus Frid. Perthes et I. H. Besser. DOI: 10.3931/E-RARA-522.

Gauß CF (1823) Theoria combinationis observationum erroribus minimis obnoxiae. la. apud Henricum Dieterich. DOI: 10.3931/E-RARA-2857.

Gauß CF (1828) Bestimmung des Breitenunterschiedes zwischen den Sternwarten von Göttingen und Altona durch Beobachtungen am Ramsdenschen Zenithsector. Göttingen: Vandenhoeck und Ruprecht. URL: https://goobi.tib.eu/viewer/image/897680731/8/#topDocAnchor (accessed 5 Feb. 2025).

Gauß CF (1887) Abhandlungen zur Methode der kleinsten Quadrate / von Carl Friedrich Gauss. In deutscher Sprache hrsg. von A. Börsch und P. Simon. Ed. by Anton Börsch PS. Berlin: Stankiewicz. URL: https://archive.org/details/abhandlungenmet00gausrich (accessed 5 Feb. 2025).

GFZ (2026) Die Satelliten-Laser-Radarstation Potsdam. Ed. by GFZ. GFZ. URL: https://www.gfz.de/sektion/globales-geomonitoring-und-schwerefeld/infrastruktur/die-satelliten-laser-radarstation-potsdam (accessed 7 July 2026).

Gilbert F, Dziewonski A (1975) An application of normal mode theory to the retrieval of structural parameters and source mechanisms from seismic spectra. In: Philosophical Transactions of the Royal Society of London. Series A, Mathematical and Physical Sciences 278(1280), 187–269. DOI: https://doi.org/10.1098/rsta.1975.0025.

Ginisty F, Wrobel F, Ecoffet R, Mandea M, Michez A, Balcon N, Ruffenach M, Mekki J (2024) South Atlantic Anomaly Evolution Seen by the Proton Flux. In: Journal of Geophysical Research: Space Physics 129(6). ISSN: 2169-9402. DOI: 10.1029/2023ja032186.

Giorgi G, Schmidt T, Trainotti C, Mata-Calvo R, Fuchs C, Hoque M, Berdermann J, Furthner J, Günther C, Schuldt T, Sanjuan J, Gohlke M, Oswald M, Braxmaier C, Balidakis K, Dick G, Flechtner F, Ge M, Glaser S, König R, Michalak G, Murböck M, Semmling M, Schuh H (2019) Advanced technologies for satellite navigation and geodesy. In: Advances in Space Research 64(6), 1256–1273. ISSN: 0273-1177. DOI: 10.1016/j.asr.2019.06.010.

Glaser S, Ampatzidis D, König R, Nilsson T, Heinkelmann R, Flechtner F, Schuh H (2016) Simulation of VLBI Observations to Determine a Global TRF for GGOS. In: International Symposium on Earth and Environmental Sciences for Future Generations. Springer International Publishing, 3–9. ISBN: 9783319691701. DOI: 10.1007/1345_2016_256.

Glaser S, König R, Ampatzidis D, Nilsson T, Heinkelmann R, Flechtner F, Schuh H (2017) A Global Terrestrial Reference Frame from simulated VLBI and SLR data in view of GGOS. In: Journal of Geodesy 91(7), 723–733. ISSN: 1432-1394. DOI: 10.1007/s00190-017-1021-2.

Glaser S, König R, Neumayer KH, Nilsson T, Heinkelmann R, Flechtner F, Schuh H (2018) On the impact of local ties on the datum realization of global terrestrial reference frames. In: Journal of Geodesy 93(5), 655–667. ISSN: 1432-1394. DOI: 10.1007/s00190-018-1189-0.

Glaser S, König R, Neumayer KH, Balidakis K, Schuh H (2019) Future SLR station networks in the framework of simulated multi-technique terrestrial reference frames. In: Journal of Geodesy 93(11), 2275–2291. ISSN: 1432-1394. DOI: 10.1007/s00190-019-01256-8.

Glaser S, Michalak G, Männel B, König R, Neumayer KH, Schuh H (2020) Reference system origin and scale realization within the future GNSS constellation “Kepler”. In: Journal of Geodesy 94(12). ISSN: 1432-1394. DOI: 10.1007/s00190-020-01441-0.

Gross R, Beutler G, Plag H.-P (2009) Integrated scientific and societal user requirements and functional specifications for the GGOS. In: Global Geodetic Observing System. Heidelberg: Springer, 209–224. ISBN: 9783642026874. DOI: 10.1007/978-3-642-02687-4_7.

Haines B, Bertiger W, Desai S, Ellmer M, Heflin M, Kuang D, Lanyi G, Naudet C, Peidou A, Ries P, Sibois A, Wu X (2024) A Global Combination of Geodetic Techniques at the Observation Level: New Perspectives on the Terrestrial Reference Frame. In: Journal of Geophysical Research: Solid Earth 129(12). ISSN: 2169-9356. DOI: 10.1029/2024jb029527.

Haines BJ, Bar-Sever YE, Bertiger WI, Desai SD, Harvey N, Sibois AE, Weiss JP (2015) Realizing a terrestrial reference frame using the Global Positioning System. In: Journal of Geophysical Research: Solid Earth 120(8), 5911–5939. ISSN: 2169-9356. DOI: 10.1002/2015jb012225.

Hauschild A, Montenbruck O (2008) Real-time Clock Estimation for Precise Orbit Determination of LEO-Satellites. In: Proceedings of the 21st International Technical Meeting of

the Satellite Division of The Institute of Navigation (ION GNSS 2008), Savannah, GA, September 2008, 581–589.

Hedin AE (1991) Extension of the MSIS Thermosphere Model into the middle and lower atmosphere. In: Journal of Geophysical Research: Space Physics 96(A2), 1159–1172. DOI: 10.1029/90ja02125.

Herrera Pinzón ID (2023) Methods for an Enhanced Co-Location of Space Geodetic Techniques. en. PhD thesis. DOI: 10.3929/ETHZ-B-000606121.

Hesselbarth A, Wanninger L (2008) Short-term Stability of GNSS Satellite Clocks andits Effects on Precise Point Positioning. In: Proceedings of the 21st International Technical Meeting of the Satellite Division of The Institute of Navigation (ION GNSS 2008), Savannah, GA, September 2008, 1855–1863.

Hoyt DV (1979) The Smithsonian Astrophysical Observatory Solar Constant Program. In: Reviews of Geophysics 17(3), 427–458. ISSN: 1944-9208. DOI: 10.1029/rg017i003p00427.

Huang W (2022) Enhancing GNSS by integrating low Earth orbiters. en. DOI: 10.14279/DEPOSITONCE-15101.

Huang W, Männel B, Brack A, Schuh H (2020) Two methods to determine scale-independent GPS PCOs and GNSS-based terrestrial scale: comparison and cross-check. In: GPS Solutions 25(1). ISSN: 1521-1886. DOI: 10.1007/s10291-020-01035-5.

International GNSS Service (IGS) (1992a) Daily 30-Second GNSS Observation Data. DOI: 10.5067/GNSS/GNSS_DAILY_O_001.

International GNSS Service (IGS) (1992b) GNSS Final Combined Orbit Solution Product. DOI: 10.5067/GNSS/GNSS_IGSORB_001.

International GNSS Service (IGS) (2022) IGS international GNSS service. URL: https://igs.org/network/ (accessed 4 July 2022).

Jayles C, Chauveau JP, Yaya P (2021) DOPPLER CROSSINGS ON-BOARD DORIS RECEIVERCARRIER SATELLITES. In: Newsletter of the International DORIS Service.

Johnson FS (1954) THE SOLAR CONSTANT. In: Journal of Meteorology 11(6), 431–439. ISSN: 0095-9634. DOI: 10.1175/1520-0469(1954)011<0431:tsc>2.0.co;2.

Johnston G, Riddell A, Hausler G (2017) The International GNSS Service. In: Springer Handbook of Global Navigation Satellite Systems. Basel, Switzerland: Springer International Publishing, 967–982. ISBN: 9783319429281. DOI: 10.1007/978-3-319-42928-1_33.

Kaula W (1966) Theory of satellite geodesy. New York: Dover Publications Inc. ISBN: 0-486-41465-5.

König R, Schreiner P, Dahle C (2019) Monthly estimates of C(2,0) generated by GFZ from SLR satellites based on GFZ GRACE/GRACE-FO RL06 background models. en. DOI: 10.5880/GFZ.GRAVIS_06_C20_SLR.

König R, Michalak G, Neumayer KH, Flechtner F, Reigber C, Rothacher M, Schwintzer P (2022a) GFZ GRACE-A Rapid Science Orbits (version 1). DOI: 10.5880/GFZ_ORBIT/RSO/L09_G_V01.

König R, Michalak G, Neumayer KH, Flechtner F, Reigber C, Rothacher M, Schwintzer P (2022b) GFZ GRACE-B Rapid Science Orbits (version 1.0). DOI: 10.5880/GFZ_ORBIT/RSO/L10_G_V01.

Kouba J (2008) A simplified yaw-attitude model for eclipsing GPS satellites. In: GPS Solutions 13(1), 1–12. ISSN: 1521-1886. DOI: 10.1007/s10291-008-0092-1.

Kucharski D, Otsubo T, Kirchner G, Bianco G (2012) Spin rate and spin axis orientation of LARES spectrally determined from Satellite Laser Ranging data. In: Advances in Space Research 50(11), 1473–1477. ISSN: 0273-1177. DOI: 10.1016/j.asr.2012.07.018.

Kucharski D, Kirchner G, Otsubo T, Koidl F (2015) A method to calculate zero-signature satellite laser ranging normal points for millimeter geodesy - a case study with Ajisai. In: Earth, Planets and Space 67(1), 34. ISSN: 1880-5981. DOI: 10.1186/s40623-015-0204-4.

Kulikov DK (1963) Integration of equations of celestial mechanics by Cowell's method with variable intervals. In: Dynamics of Satellites / Dynamique des Satellites. Heidelberg: Springer, 123–135. ISBN: 9783642481307. DOI: 10.1007/978-3-642-48130-7_11.

Kur T, Liwosz T, Kalarus M (2020) The application of inter-satellite links connectivity schemes in various satellite navigation systems for orbit and clock corrections determination: simulation study. In: Acta Geodaetica et Geophysica 56(1), 1–28. ISSN: 2213-5820. DOI: 10.1007/s40328-020-00322-4.

Landerer FW, Flechtner FM, Save H, Webb FH, Bandikova T, Bertiger WI, Bettadpur SV, Byun SH, Dahle C, Dobslaw H, Fahnestock E, Harvey N, Kang Z, Kruizinga GLH, Loomis BD, McCullough C, Murböck M, Nagel P, Paik M, Pie N, Poole S, Strekalov D, Tamisiea ME, Wang F, Watkins MM, Wen HY, Wiese DN, Yuan DN (2020) Extending the Global Mass Change Data Record: GRACE Follow-On Instrument and Science Data Performance. In: Geophysical Research Letters 47(12). ISSN: 1944-8007. DOI: 10.1029/2020gl088306.

Lemoine JM, Capdeville H (2006) A corrective model for Jason-1 DORIS Doppler data in relation to the South Atlantic Anomaly. In: Journal of Geodesy 80(8–11), 507–523. ISSN: 1432-1394. DOI: 10.1007/s00190-006-0068-2.

Lense J, Thirring H (1918) Über den Einfluss der Eigenrotation der Zentralkörper auf die Bewegung der Planeten und Monde nach der Einsteinschen Gravitationstheorie. In: Physikalische Zeitschrift 19, 156–163.

Lilliefors HW (1967) On the Kolmogorov-Smirnov Test for Normality with Mean and Variance Unknown. In: Journal of the American Statistical Association 62(318), 399–402. ISSN: 1537-274X. DOI: 10.1080/01621459.1967.10482916.

Liu W, Jiao B, Hao J, Lv Z, Xie J, Liu J (2022) Signal-in-space range error and positioning accuracy of BDS-3. In: Scientific Reports 12(1). ISSN: 2045-2322. DOI: 10.1038/s41598-022-12012-y.

Lockheed Martin Corporation (2024) GPS III/IIIF. URL: https://www.lockheedmartin.com/en-us/products/gps.html (accessed 5 June 2024).

Luceri V, Pirri M, Rodríguez J, Appleby G, Pavlis EC, Müller H (2019) Systematic errors in SLR data and their impact on the ILRS products. In: Journal of Geodesy 93(11), 2357–2366. ISSN: 1432-1394. DOI: 10.1007/s00190-019-01319-w.

Lyard FH, Allain DJ, Cancet M, Carrère L, Picot N (2021) FES2014 global ocean tide atlas: design and performance. In: Ocean Science 17(3), 615–649. DOI: 10.5194/os-17-615-2021.

Mammadaliyev N (2024) Co-location of space geodetic techniques in space. PhD thesis. Technische Universität Berlin.

Männel B (2016) Co-location of Geodetic Observation Techniques in Space. en. PhD thesis. DOI: 10.3929/ETHZ-A-010811791.

Mathews PM, Herring TA, Buffett BA (2002) Modeling of nutation and precession: New nutation series for nonrigid Earth and insights into the Earth's interior. In: Journal of Geophysical Research: Solid Earth 107(B4). ISSN: 0148-0227. DOI: 10.1029/2001jb000390.

McCarthy DD, Petit G, eds. (2004) IERS Conventions (2003). IERS technical note 32. Frankfurt am Main: Verl. des Bundesamtes für Kartographie und Geodäsie. 127 pp. ISBN: 3898888843.

McGarry JF, Hoffman ED, Degnan JJ, Cheek JW, Clarke CB, Diegel IF, Donovan HL, Horvath JE, Marzouk M, Nelson AR, Patterson DS, Ricklefs RL, Shappirio MD, Wetzel SL, Zagwodzki TW (2018) NASA's satellite laser ranging systems for the twenty-first century. In: Journal of Geodesy 93(11), 2249–2262. ISSN: 1432-1394. DOI: 10.1007/s00190-018-1191-6.

Mendes V, Pavlis E (2004) High-accuracy zenith delay prediction at optical wavelengths. In: Geophysical Research Letters 31(L14602). DOI: 10.1029/2004gl020308.

Meyer U, Lasser M, Dahle C, Förste C, Behzadpour S, Koch I, Jäggi A (2023) Combined monthly GRACE-FO gravity fields for a Global Gravity-based Groundwater Product. In: Geophysical Journal International 236(1), 456–469. ISSN: 1365-246X. DOI: 10.1093/gji/ggad437.

Montenbruck O, Hackel S, Jäggi A (2017) Precise orbit determination of the Sentinel-3A altimetry satellite using ambiguity-fixed GPS carrier phase observations. In: Journal of Geodesy 92(7), 711–726. DOI: 10.1007/s00190-017-1090-2.

Montenbruck O, Steigenberger P, Hauschild A (2018) Multi-GNSS signal-in-space range error assessment – Methodology and results. In: Advances in Space Research 61(12), 3020–3038. ISSN: 0273-1177. DOI: 10.1016/j.asr.2018.03.041.

Montenbruck O, Steigenberger P, Thoelert S, Arnold D, Bury G (2023) GNSS visibility and performance implications for the GENESIS mission. In: Journal of Geodesy 97(10). ISSN: 1432-1394. DOI: 10.1007/s00190-023-01784-4.

Montgomery DC, Runger GC (2003) Applied statistics and probability for engineers. 3. ed. Includes bibliographical references and index. - Includes free interactive e-text on CD-ROM with student solutions manual and data sets; installation of Excel viewer or Adobe Acrobat. - Previous ed.: 1999. New York: Wiley. 706 pp. ISBN: 0471204544.

Moreaux G, Lemoine FG, Zelensky NP, Moyard J, Couhert A (2023a) DPOD2020: A DORIS extension of the ITRF2020 for precise orbit determination. In: Advances in Space Research 72(11), 4625–4650. ISSN: 0273-1177. DOI: 10.1016/j.asr.2023.10.006.

Moreaux G, Lemoine FG, Capdeville H, Otten M, Štěpánek P, Saunier J, Ferrage P (2023b) The international DORIS service contribution to ITRF2020. In: Advances in Space Research 72(1), 65–91. ISSN: 0273-1177. DOI: https://doi.org/10.1016/j.asr.2022.07.012.

Moritz H, Mueller II (1988) Earth rotation. Theory and observation. New York, NY: Ungar. 617 pp. ISBN: 0804446717.

Mueller II (1989) Conventional Terrestrial Reference Frames. In: Astrophysics and Space Science Library. Heidelberg: Springer, 163–169. ISBN: 9789400909335. DOI: 10.1007/978-94-009-0933-5_8.

Müller EA (1977) Transactions of the International Astronomical Union. Proceedings of the Sixteenth General Assembly Grenoble 1976. Ed. by Jappel A. International Astronomical Union Transactions Ser. v.16B. Description based on publisher supplied metadata and other sources. Heidelberg: Springer. 1567 pp. ISBN: 9789401012577.

NASA (2024) Current Missions. URL: https://ilrs.gsfc.nasa.gov/missions/satellite_missions/current_missions/ (accessed 31 Jan. 2023).

NCO (2022) GPS.gov. URL: https://www.gps.gov/systems/gps/ (accessed 4 July 2022).

NERC (2024) Geodetic Satellites. URL: http://sgf.rgo.ac.uk/supportsci/geodetic.html.

Neumayer KH, Schreiner P, König R, Dahle C, Glaser S, Mammadaliyev N, Flechtner F (2024) EPOS-OC, a Universal Software Tool for Satellite Geodesy at GFZ. In: International Association of Geodesy Symposia. Heidelberg: Springer. DOI: 10.1007/1345_2024_260.

Noll CE (2010) The crustal dynamics data information system: A resource to support scientific analysis using space geodesy. In: Advances in Space Research 45(12), 1421–1440. ISSN: 0273-1177. DOI: 10.1016/j.asr.2010.01.018.

Otsubo T, Appleby GM (2003) System-dependent center-of-mass correction for spherical geodetic satellites. In: Journal of Geophysical Research: Solid Earth 108(B4). ISSN: 0148-0227. DOI: 10.1029/2002jb002209.

Pavlis E, Luceri V, Sciarretta C, Kelm R (2008) The ILRS contribution to ITRF2008. Tech. rep. ILRS. URL: https://ilrs.gsfc.nasa.gov/docs/ILRS_contribution_to_ITRF2008.pdf (accessed 21 June 2024).

Pavlis E, Luceri V (2022) The ILRS contribution to ITRF2020. In: URL: https://itrf.ign.fr/docs/solutions/itrf2020/The_ILRS_contribution_to_ITRF2020_description_2022.09.23.pdf (accessed 9 Aug. 2024).

Pearlman M, Degnan J, Bosworth J (2002) The International Laser Ranging Service. In: Advances in Space Research 30(2), 135–143. ISSN: 0273-1177. DOI: 10.1016/s0273-1177(02)00277-6.

Petit G, Luzum B (2010) IERS Conventions (2010). Frankfurt am Main: Bundesamts für Kartographie und Geodäsie. URL: https://www.iers.org/IERS/EN/Publications/TechnicalNotes/tn36.html (accessed 20 May 2022).

Picone JM, Hedin AE, Drob DP, Aikin AC (2002) NRLMSISE-00 empirical model of the atmosphere: Statistical comparisons and scientific issues. In: Journal of Geophysical Research: Space Physics 107(A12), SIA 15–1–SIA 15–16. DOI: https://doi.org/10.1029/2002JA009430.

Rebischung P, Griffiths J, Ray J, Schmid R, Collilieux X, Garayt B (2011) IGS08: the IGS realization of ITRF2008. In: GPS Solutions 16(4), 483–494. ISSN: 1521-1886. DOI: 10.1007/s10291-011-0248-2.

Rebischung P, Altamimi Z, Ray J, Garayt B (2016) The IGS contribution to ITRF2014. In: Journal of Geodesy 90(7), 611–630. ISSN: 1432-1394. DOI: 10.1007/s00190-016-0897-6.

Rebischung P, Altamimi Z, Métivier L, Collilieux X, Gobron K, Chanard K (2024) Analysis of the IGS contribution to ITRF2020. In: Journal of Geodesy 98(6). ISSN: 1432-1394. DOI: 10.1007/s00190-024-01870-1.

Reigber C (1989) Reference Frames for Artificial Satellites of the Earth. In: Astrophysics and Space Science Library. Heidelberg: Springer, 91–114. ISBN: 9789400909335. DOI: 10.1007/978-94-009-0933-5_5.

Reigber C, Lühr H, Grunwaldt L, Förste C, König R, Massmann H, Falck C (2006) CHAMP Mission 5 Years in Orbit. In: Observation of the Earth System from Space. Heidelberg: Springer, 3–15. ISBN: 3540295208. DOI: 10.1007/3-540-29522-4_1.

Ries J (2017) Conventional Model Update for Rotational Deformation. Presented at AGU Fall Meeting 2017, New Orleans, Louisiana, USA. DOI: 10.26153/TSW/2659.

Rodríguez J, Appleby G, Otsubo T (2019) Upgraded modelling for the determination of centre of mass corrections of geodetic SLR satellites: impact on key parameters of the terrestrial reference frame. In: Journal of Geodesy 93(12), 2553–2568. ISSN: 1432-1394. DOI: 10.1007/s00190-019-01315-0.

Rodriguez-Solano C, Hugentobler U, Steigenberger P (2012) Adjustable box-wing model for solar radiation pressure impacting GPS satellites. In: Advances in Space Research 49(7), 1113–1128. ISSN: 0273-1177. DOI: 10.1016/j.asr.2012.01.016.

Rothacher M (2003) Towards a rigorous combination of space geodetic techniques. IERS Workshop on Combination Research and Global Geophysical Fluids. In: IERS Workshop

on Combination Research and Global Geophysical Fluids. Ed. by Richter B, Schwegmann W, Dick WR. IERS technical note 30. Frankfurt am Main: Verl. des Bundesamts für Kartographie und Geodäsie. ISBN: 3-89888-877-0.

Samain É, Weick J, Vrancken P, Para F, Albanese D, Paris J, Torre J.-M, Zhao C, Guillemot P, Petitbon I (2008) TIME TRANSFER BY LASER LINK – THE T2L2 EXPERIMENT ON JASON-2 AND FURTHER EXPERIMENTS. In: International Journal of Modern Physics D 17(07), 1043–1054. ISSN: 1793-6594. DOI: 10.1142/s0218271808012681.

Schmid R (2009) Zur Kombination von VLBI und GNSS. Deutsche Geodätische Kommission bei der Bayerischen Akademie der Wissenschaft. München: Verl. der Bayer. Akad. der Wiss. ISBN: 978-3-7696-5048-8.

Schmid R, Steigenberger P, Gendt G, Ge M, Rothacher M (2007) Generation of a consistent absolute phase-center correction model for GPS receiver and satellite antennas. In: Journal of Geodesy 81(12), 781–798. ISSN: 1432-1394. DOI: 10.1007/s00190-007-0148-y.

Schreiner P, König R, Abrykosov O, Neumayer KH, Flechtner F (2022a) GFZ GRACE-FO-1 Rapid Science Orbits (version 2). DOI: 10.5880/GFZ_ORBIT/RSO/L64_G_V02.

Schreiner P, König R, Abrykosov O, Neumayer KH, Flechtner F (2022b) GFZ GRACE-FO-2 Rapid Science Orbits (version 2). DOI: 10.5880/GFZ_ORBIT/RSO/L65_G_V02.

Schreiner P, Neumayer H, König R (2022c) GFZ Rapid Science Orbits. DOI: 10.5880/GFZ_ORBIT/RSO.

Schreiner P, König R, Abrykosov O, Neumayer KH, Flechtner F (2022d) GFZ TanDEM-X Rapid Science Orbits (version 2). DOI: 10.5880/GFZ_ORBIT/RSO/L20_G_V02.

Schreiner P, König R, Abrykosov O, Neumayer KH, Flechtner F (2022e) GFZ TerraSAR-X Rapid Science Orbits (version 2). DOI: 10.5880/GFZ_ORBIT/RSO/L13_G_V02.

Schreiner P, König R, Neumayer KH, Reinhold A (2023) On precise orbit determination based on DORIS, GPS and SLR using Sentinel-3A/B and -6A and subsequent reference frame determination based on DORIS-only. In: Advances in Space Research 72(1), 47–64. DOI: https://doi.org/10.1016/j.asr.2023.04.002.

Schreiner P, Glaser S, König R, Neumayer KH, Raut S, Schuh H (2024a) On the Potential of Accelerometers for GNSS on Satellite Positioning and Ensuing Reference Frame Determination. In: International Association of Geodesy Symposia. Heidelberg: Springer. DOI: 10.1007/1345_2024_270.

Schreiner P, Reinhold A, Schöne T, Esselborn S, König R (2024b) Three Decades of Altimetry Orbits: Consistent DORIS-Based Orbit Series and Validation. In: CNES. DOI: 10.24400/312072/l03-2024.3917.

Schuh H, König R, Ampatzidis D, Glaser S, Flechtner F, Heinkelmann R, Nilsson TJ (2015) GGOS-SIM: Simulation of the Reference Frame for the Global Geodetic Observing System. In: REFAG 2014. Heidelberg: Springer, 95–100. ISBN: 9783319456294. DOI: 10.1007/1345_2015_217.

Schwarzschild K (1916) Über das Gravitationsfeld eines Massenpunktes nach der Einsteinschen Theorie. In: Deutsche Akademie der Wissenschaften zu Berlin.

Seeber G (2003) Satellite Geodesy. Walter de Gruyter. ISBN: 9783110175493. DOI: 10.1515/9783110200089.

Seidelmann PK, ed. (1992) Explanatory supplement to the astronomical almanac. A revision to the Explanatory Supplement to the Astronomical Ephemeris and the American Ephemeris and Nautical Almanac. Mill Valley, California: University Science Books. 752 pp. ISBN: 0935702687.

Seitz F, Schuh H (2010) Earth Rotation. In: Sciences of Geodesy - I. Heidelberg: Springer, 185–227. ISBN: 9783642117411. DOI: 10.1007/978-3-642-11741-1_6.

Seitz F, Müller J (2016) Erdrotation. In: Handbuch der Geodäsie. Heidelberg: Springer, 1–29. ISBN: 9783662469002. DOI: 10.1007/978-3-662-46900-2_12-2.

Seitz M, Angermann D, Gerstl M, Bloßfeld M, Sánchez L, Seitz F (2015) Geometrical Reference Systems. In: Handbook of Geomathematics. Heidelberg: Springer, 2995–3034. ISBN: 9783642545511. DOI: 10.1007/978-3-642-54551-1_79.

Shako R, Förste C, Abrikosov O, Bruinsma S, Marty J.-C, Lemoine J.-M, Flechtner F, Neumayer H, Dahle C (2013) EIGEN-6C: A High-Resolution Global Gravity Combination Model Including GOCE Data. In: Observation of the System Earth from Space - CHAMP, GRACE, GOCE and future missions. Heidelberg: Springer, 155–161. ISBN: 9783642321351. DOI: 10.1007/978-3-642-32135-1_20.

Springer TA, Beutler G, Rothacher M (1999) A New Solar Radiation Pressure Model for GPS Satellites. In: GPS Solutions 2(3), 50–62. ISSN: 1521-1886. DOI: 10.1007/pl00012757.

Steigenberger P, Fritsche M, Dach R, Schmid R, Montenbruck O, Uhlemann M, Prange L (2016) Estimation of satellite antenna phase center offsets for Galileo. In: Journal of Geodesy 90(8), 773–785. ISSN: 1432-1394. DOI: 10.1007/s00190-016-0909-6.

Steigenberger P, Thoelert S, Montenbruck O (2020) GPS III Vespucci: Results of half a year in orbit. In: Advances in Space Research 66(12), 2773–2785. DOI: 10.1016/j.asr.2020.03.026.

Steigenberger P, Thoelert S, Dach R, Montenbruck O (2024) Validation of GPS III transmit antenna calibrations. In: Advances in Space Research 73(5), 2488–2498. ISSN: 0273-1177. DOI: 10.1016/j.asr.2023.11.048.

Student (1908) The Probable Error of a Mean. In: Biometrika 6(1), 1. ISSN: 0006-3444. DOI: 10.2307/2331554.

Tapley B, Flechtner F, Bettadpur S, Watkins M (2013) The status and future prospect for GRACE after the first decade. In: EGU General Assembly 2012. Vol. 14. Chap. EGU2012-12776.

Thaller D (2008) Inter-technique combination based on homogeneous normal equation systems including station coordinates, Earth orientation and troposphere parameters. GFZ, Helmholtz-Zentrum, Potsdam. DOI: 10.23689/FIDGEO-501.

Thaller D, Dach R, Seitz M, Beutler G, Mareyen M, Richter B (2011) Combination of GNSS and SLR observations using satellite co-locations. In: Journal of Geodesy 85(5), 257–272. ISSN: 1432-1394. DOI: 10.1007/s00190-010-0433-z.

Thomas C, Wolf P, Tavella P (1994) TIME SCALES. In: URL: https://www.bipm.org/documents/20126/53814635/Monographie+94-1+(1994).pdf/c4069c93-155d-5565-7e3b-5bf5d4ff76c7 (accessed 8 July 2024).

Tourain C, Moreaux G, Auriol A, Saunier J (2016) DORIS Starec ground antenna characterization and impact on positioning. In: Advances in Space Research (58).

Trainotti C, Dassié M, Giorgi G, Khodabandeh A, Günther C (2023) Autonomous Synchronization of Satellite Constellations via Optical Inter-Satellite Links. In: 2023 Joint Conference of the European Frequency and Time Forum and IEEE International Frequency Control Symposium (EFTF/IFCS). IEEE, 1–6. DOI: 10.1109/eftf/ifcs57587.2023.10272176.

Villiger A, Dach R, Schaer S, Prange L, Zimmermann F, Kuhlmann H, Wübbena G, Schmitz M, Beutler G, Jäggi A (2020) GNSS scale determination using calibrated receiver and Galileo satellite antenna patterns. In: Journal of Geodesy 94(9). ISSN: 1432-1394. DOI: 10.1007/s00190-020-01417-0.

Wahr JM (1981) The forced nutations of an elliptical, rotating, elastic and oceanless earth. In: Geophysical Journal of the Royal Astronomical Society 64(3), 705–727. DOI: 10.1111/j.1365-246x.1981.tb02691.x.

Wang K, Rothacher M (2013) Stochastic modeling of high-stability ground clocks in GPS analysis. In: Journal of Geodesy 87(5), 427–437. ISSN: 1432-1394. DOI: 10.1007/s00190-013-0616-5.

Weinbach U (2013) Feasibility and impact of receiver clock modeling in precise GPS data analysis. PhD thesis. Fakultät für Bauingenieurwesen und Geodäsieder Gottfried Wilhelm Leibniz Universität Hannover.

Wilcoxon F (1945) Individual Comparisons by Ranking Methods. In: Biometrics Bulletin 1(6), 80. ISSN: 0099-4987. DOI: 10.2307/3001968.

Willis P, Fagard H, Ferrage P, Lemoine FG, Noll CE, Noomen R, Otten M, Ries JC, Rothacher M, Soudarin L, Tavernier G, Valette JJ (2010) The International DORIS Service (IDS): Toward maturity. In: Advances in Space Research 45(12), 1408–1420. ISSN: 0273-1177. DOI: 10.1016/j.asr.2009.11.018.

Willis P, Zelensky NP, Ries J, Soudarin L, Cerri L, Moreaux G, Lemoine FG, Otten M, Argus DF, Heflin MB (2015a) DPOD2008: A DORIS-Oriented Terrestrial Reference Frame for Precise Orbit Determination. In: IAG 150 Years. Heidelberg: Springer, 175–181. ISBN: 9783319308951. DOI: 10.1007/1345_2015_125.

Willis P, Lemoine FG, Moreaux G, Soudarin L, Ferrage P, Ries J, Otten M, Saunier J, Noll C, Biancale R, Luzum B (2015b) The International DORIS Service (IDS): Recent Developments in Preparation for ITRF2013. In: IAG 150 Years. Springer International Publishing, 631–640. ISBN: 9783319308951. DOI: 10.1007/1345_2015_164.

Winternitz LMB, Bamford WA, Heckler GW (2009) A GPS Receiver for High-Altitude Satellite Navigation. In: IEEE Journal of Selected Topics in Signal Processing 3(4), 541–556. DOI: 10.1109/jstsp.2009.2023352.

Yang S, Zhang Q, Zhang X, Liu D (2021) Impact of GPS/BDS Satellite Attitude Quaternions on Precise Point Positioning with Ambiguity Resolution. In: Remote Sensing 13(15), 3035. ISSN: 2072-4292. DOI: 10.3390/rs13153035.

Zhu S, Reigber C, König R (2004) Integrated adjustment of CHAMP, GRACE, and GPS data. In: Journal of Geodesy 78(1–2). ISSN: 1432-1394. DOI: https://doi.org/10.1007/s00190-004-0379-0.

A GPS ambiguity handling at normal equation level with EPOS

The current version of EPOS-OC does not permit the storage of the final number of ambiguities found through the iterations of the POD, nor their status, i.e. whether they are fixed values or float values. Consequently, all ambiguities existing in the final convergence state are written to the observation file with their current value. However, if a further calculation from this point on is started, as it is the case for the normal equation mode, the information if the ambiguity is fixed or not cannot be ascertained. This is due to the manner in which ambiguities are handled in EPOS-OC. During the iterations, new ambiguities are continuously searched for and added to the parameter list. Consequently, if the subsequent processing utilises the generated observation file, the resulting ambiguity parameter list does not necessarily correspond to the one used for the generation of the ambiguity-fixed observation file.

It is therefore possible to transfer all identified ambiguities, along with their final values, to the subsequent step. However, the status of the ambiguities is lost in this process. Therefore, three cases are possible: In the first case, the ambiguities are read from the observation file and estimated as float values. In the second case, the ambiguities are also read from the observation file and estimated as float values, but it is assumed that a fixing rate of 100% has been achieved. Thus, there is no need to distinguish between fixed and non-fixed ambiguities, as they are effectively fixed. Accordingly, all ambiguity parameters in the normal equation are fixed to their a priori values. The ambiguity estimation of EPOS-OC is deactivated in the next step in the third case, and all ambiguity values are read from the observation file. A comparison of the three methods was conducted, showing that the differences between scenario 1 and the other two scenarios are insignificant and that no difference can be found between scenarios 2 and 3. Therefore, method 3 was chosen for the GPS simulations.

B Zero mean condition for random noise sequences

Zero mean conditions are used for the generation of random noise sequences which are applied to the simulated DORIS and SLR observations. This is done because the mean of a generated random noise sequence is itself Gaussian. This implies that the actual empirical mean of the sequence varies by $\sigma_{\mathbf{mean}} = \sigma_{\mathbf{noise}}/\sqrt{\mathbf{N_{obs}}}$ where $\sigma_{\mathbf{noise}}$ is the noise to be added and $\mathbf{N_{obs}}$ is the sample size. Consequently, the mean of the sequence can be as large as $3 \cdot \sigma_{\mathbf{mean}}$, in accordance with three sigma of a normal distribution, which is close to the value of the actual noise.

For example, in the case of SLR with a global mean standard deviation of the SLR observations of approximately 0.9 cm, a station with very few observations in an arc, e.g. 10, may have a mean of up to 0.85 cm.

Therefore, to ensure that the simulation scenario accurately reflects a situation free of any systematics, the zero mean condition for SLR has been set to 0.5 mm, for example. It should be noted that the application of this condition results in the individual random numbers no longer being strictly Gaussian and uncorrelated. This effect becomes more pronounced the closer the mean constraint is with respect to $\sigma_{\mathbf{noise}}/\sqrt{\mathbf{N_{obs}}}$. In this case it has been decided that this is acceptable, as spreading e.g. 10 observations over a seven day arc and investigating systematic sources of error could lead to more unwanted effects.

C Influence of EPOS-OC time granularity on DORIS simulations

In the DORIS simulation, an along-track bias of approximately 2 millimetres was identified. Further investigations revealed that this was caused by a quantisation problem with the time epochs for the simulated DORIS observations in EPOS-OC. When a DORIS observation is simulated, EPOS-OC calculates the epoch of the observation and stores it internally in a binary file. The output of the simulated observations is written in an EPOS-OC input format for DORIS observations, which is based on the DORIS Data Exchange Format. In this format, the fractions of seconds of the epochs are given in microseconds in Fortran I6 format. This means that epochs can only be written and read with an accuracy of one microsecond. However, further investigation revealed that a quantisation error occurs at this stage, as epoch information smaller than one microsecond is rounded to the nearest integer. Fig. C.1a illustrates this effect, showing the difference between the epochs written to the output file and the epochs stored in the internal binary. This causes the epochs written to the output file to deviate slightly from the epoch of the simulated observation. This is also evident in the residuals of the observations after the first iteration of the POD with simulated data (see Fig. C.1b), where a perfect correlation is apparent.

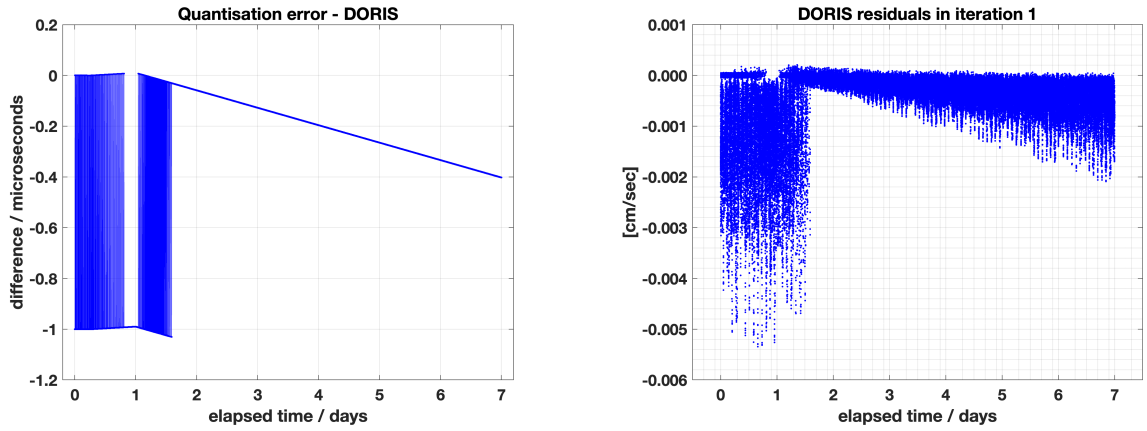

(a) (b)

Figure C.1: Figure (a) on the left shows the quantisation error as the difference between the epoch held internally during the simulation and the epoch written to the output. Figure (b) on the right demonstrates the effect on simulated DORIS residuals.

The issue could be resolved in an experimental version of EPOS-OC by increasing the granularity of output epochs to the Fortran I12 format. Thus, fractions of epochs down to one picosecond can be written and read. However, this solution cannot be transferred directly to the official version of EPOS-OC, since modifying the fixed-format Doppler input would be necessary. This would mean that real data, including that used for this thesis, could no longer be processed. Such a modification would necessitate adjusting the pre-processing chain for all real data currently in use, as well as for any new real data observations provided in Doppler RINEX format. However, as it has not yet been confirmed that the same effect occurs with real data, this modification has been disregarded for the time being.

D Statistical evaluation of changes in formal errors

A suitable statistical method is required to investigate whether the different analyses lead to improvements or deteriorations in terms of formal errors. As an example, the formal errors of the station velocities in Y of a scenario 1, are defined as variable $X1$, and the respective formal errors for scenario 2, defined as variable $X2$. Since the number of stations in the two scenarios is identical, this is an analysis of paired variables. If the distribution of $X1$ and $X2$ follows a normal distribution, the mean of the distribution of $X1$ and $X2$ can be used, which is also equivalent to the median, and a t-test (Student, 1908) can be used to test the hypothesis of a significant change in the mean of the two variables. However, the formal errors of the station coordinates do not follow a normal distribution. Reasons are, for example, differences in the observation noise, their position on the Earth or the length of the observation period. A suitable distribution function for the variables of the scenarios (compare left figures in Fig. D.1) is the log normal distribution.

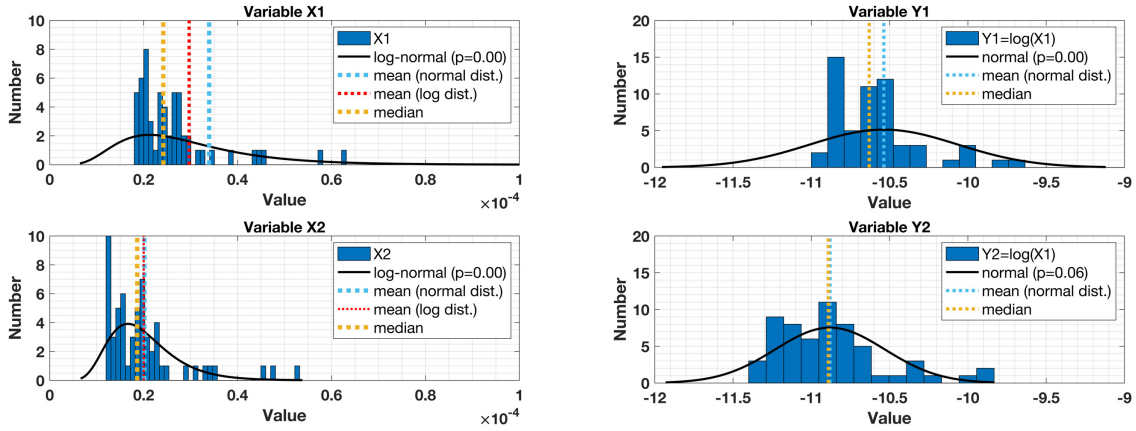

Figure D.1: The figure on the left shows the histogram for the variables $X1$ and $X2$. The mean is shown in cyan, assuming a normal distribution, and in red, assuming a log normal distribution. The median is shown in yellow. The figure on the right shows the histogram of the respective logarithmic transformation ($Y1$ and $Y2$), with the mean assuming a normal distribution in cyan and the median in yellow.

A robust means of assessing changes in a set of values, where some values might be outliers and the distribution might be non-normal in addition, is the median of the variable. However, this poses some difficulties, as a hypothesis test for the significance of a change in the median is typically a non-parametric test, such as the Wilcoxon signed rank test (Wilcoxon, 1945), which face less test strength compared to parametric test like the t-test. An alternative method is to make use of the underlying distribution of the measurement series, which in this case is a log-normal distribution. Whether the values of $X1$ and $X2$ follow a specific distribution can be tested by using the respective transformation of the distribution to be tested. The variable $X1$ and $X2$ are transformed, in this case by means

of the logarithm ($Y1 = log(X1)$). If appropriate, the logarithmic transformation $Y1$ and $Y2$ should approximately follow a normal distribution, which can be assessed using a Lilliefors test (Lilliefors, 1967), for example (compare right figures in Fig. D.1). The median or mean value is again suitable for the assessment of changes in the totality of variables $X1$ and $X2$. However, the two are not identical for a log-normal distribution as the mean is calculated as $mean = e^{(\mu+\frac{\sigma^2}{2})}$ and the median as $median = e^{\mu}$ with μ and σ being the parameters of the log-normal distribution. In order to allow a general statement for the variables $X1$ and $X2$, the median is more suitable, as it is less susceptible to outliers. However, this again raises the same problem for hypothesis testing of the change in the median as in the case of the normal distribution. Therefore, the transformation of the variables can be used again. Assuming that the transformation of X corresponds to an ideal normal distribution, its median is equal to its mean, as follows:

$$median(X) = e^{median(\log_X)} \tag{D.1}$$

(D.2)

and, under the assumption that $log(X)$ follows a normal distribution:

$$median(X) = e^{mean(\log_X)} \tag{D.3}$$

This results in the elegant possibility that the variables $X1$ and $X2$ of two scenarios, can be tested for significance with regard to their change in the median by applying a parametric test with high test strength, such as a paired-sample t-test, to the logarithmic transformation $Y1$ and $Y2$ (Box & Cox, 1964; Conover, 1980; Montgomery & Runger, 2003). However, since large outliers in X come closer to the totality of the values in Y through the logarithm transformation, they can still have a considerable influence on the difference between the mean and median, which leads to a non-normal distribution in Y. To cover this case as well, the parametric approach is applied only if the hypothesis test for the normal distribution of Y does not reject the null hypothesis at the 5% significance level. Otherwise, instead of the paired sample t-test, the non-parametric Wilcoxon signed rank test is used because it makes less stringent assumptions about the normal distribution of the variables. To distinguish between these two cases, the p-values in the tables of formal errors are given a positive sign if they come from a parametric test and a negative sign if they come from a non-parametric test.

E Evaluation of formal errors

For the evaluation of the formal errors, the following formulas are introduced. The expected improvement can be calculated by the change in the DoF. Since the number of estimated parameters changes only slightly in contrast to the number of observations, this value roughly describes the expected value of the improvement due to the additional observations.

$$\text{expected improvement} = \left(\sqrt{\frac{DOF_{old}}{DOF_{new}}} - 1 \right) \cdot 100 \tag{E.1}$$

Comparing two values of the median formal errors and scaling them in percentage, we get the scaled improvement factor. We define an improvement as a negative percentage that results in a reduction in the formal error.

$$\text{scaled improvement} = \left(\frac{\tilde{\sigma}_{NEQ_{new}}}{\tilde{\sigma}_{NEQ_{old}}} - 1 \right) \cdot 100 \tag{E.2}$$

By combining these two quantities, we can remove from the scaled improvement the expected improvement due to the change in DoF, which is mostly caused by the additional observations. We thus subtract the expected value from the calculated improvement and get a value which we define as the observation scaled improvement. This value indicates the difference by which the reduction in formal errors is greater than the expected improvement. If this value is negative, the reduction in formal errors is greater than expected, thereby indicating a geometric added value. These scenarios are particularly suitable for a space geodetic technique because they lead to higher improvements due to the geometry of the observations in space. Positive values, on the other hand, indicate an improvement below expectation.

$$\text{observation scaled improvement} = \left(\frac{\tilde{\sigma}_{NEQ_{new}}}{\tilde{\sigma}_{NEQ_{old}}} - 1 \right) \cdot 100 - \left(\sqrt{\frac{DOF_{old}}{DOF_{new}}} - 1 \right) \cdot 100 \tag{E.3}$$

F Compilation of assessment statistics

The following tables present the statistics of the TRF assessment, i.e. the Helmert parameters and the formal errors, and ERP analyses for all scenarios and cases.

The Helmert parameters are presented alongside their standard deviation and the inner variance coefficient of the transformation. For the case free of systematic errors, the are calculated in relation to a priori, in the case of mismodelling in relation to the respective systematically error-free solution of the respective scenario.

The formal errors associated with the station coordinates, velocities, and ERPs are each assigned a p-value. As outlined in App. D, this value signifies whether the distribution of the parameter in question exhibits a notable deviation from the distribution of the comparison solution. In the systematic error-free case, the comparison solution for the calculation of the p-values is represented by the reference solution. Conversely, in instances of mismodelling, it is the systematic error-free solution of the respective scenario.

The statistical evaluation of the ERPs includes the calculation of the standard deviation of the difference between the adjusted ERPs and the a priori values. A p-value is provided for this, which should be interpreted in the same way as that for formal errors, i.e. against the reference solution in the systematic error-free case and against the systematic error-free case in the case of mismodelling. Additionally, estimated mean and trend value are given, along with the respective standard deviation of the parameter, derived from the estimation of the linear regression. The p-values for the mean and trend estimates are also provided, but are related to a priori, as the aim is to have no bias and no trend.

F.1 DORIS

F.1.1 Systematic error-free

Table F.1: Helmert parameters to a priori for the systematic error-free scenarios for DORIS. The reference is a combination of ENVISAT, Jason-1 and Jason-2.

	T_x [mm]	T_y [mm]	T_z [mm]	R_x [mm]	R_y [mm]	R_z [mm]	sc [mm]	s_0
	$\dot{T}_x$ [mm/a]	$\dot{T}_y$ [mm/a]	$\dot{T}_z$ [mm/a]	$\dot{R}_x$ [mm/a]	$\dot{R}_y$ [mm/a]	$\dot{R}_z$ [mm/a]	$\dot{sc}$ [mm/a]	$\dot{s}_0$
Reference	0.05 ± 0.03	0.05 ± 0.03	0.27 ± 0.03	0.16 ± 0.04	0.02 ± 0.04	-0.15 ± 0.04	-0.03 ± 0.03	0.25
	0.01 ± 0.01	0.00 ± 0.01	0.02 ± 0.01	0.00 ± 0.01	0.00 ± 0.01	0.00 ± 0.01	-0.02 ± 0.01	0.07
+ GRASP-like	0.04 ± 0.03	0.05 ± 0.03	0.16 ± 0.03	-0.12 ± 0.03	0.02 ± 0.03	0.02 ± 0.03	-0.02 ± 0.03	0.21
	0.00 ± 0.01	-0.02 ± 0.01	0.01 ± 0.01	-0.02 ± 0.01	0.00 ± 0.01	0.01 ± 0.01	0.01 ± 0.01	0.07
+ E-GRASP-mod	0.02 ± 0.03	0.04 ± 0.03	0.12 ± 0.03	-0.03 ± 0.03	0.07 ± 0.03	0.06 ± 0.03	0.00 ± 0.03	0.20
	0.00 ± 0.00	0.00 ± 0.00	0.01 ± 0.00	-0.00 ± 0.00	0.01 ± 0.00	0.01 ± 0.00	-0.00 ± 0.00	0.02
+ E-GRASP-like	0.02 ± 0.02	0.03 ± 0.02	0.08 ± 0.02	0.06 ± 0.03	0.01 ± 0.03	0.03 ± 0.03	0.02 ± 0.02	0.19
	0.00 ± 0.00	0.01 ± 0.00	0.01 ± 0.00	0.01 ± 0.00	0.00 ± 0.00	0.00 ± 0.00	-0.00 ± 0.00	0.02
+ Circular 30°	0.05 ± 0.03	0.05 ± 0.03	0.12 ± 0.03	0.06 ± 0.03	-0.01 ± 0.03	-0.02 ± 0.03	-0.02 ± 0.03	0.20
	0.01 ± 0.00	0.00 ± 0.00	0.01 ± 0.00	0.01 ± 0.00	-0.00 ± 0.00	-0.00 ± 0.00	-0.00 ± 0.00	0.02
+ Circular 60°	0.04 ± 0.03	0.06 ± 0.03	0.09 ± 0.03	-0.06 ± 0.03	0.08 ± 0.03	0.06 ± 0.03	-0.02 ± 0.03	0.19
	0.00 ± 0.00	0.01 ± 0.00	0.01 ± 0.00	-0.01 ± 0.00	0.01 ± 0.00	0.01 ± 0.00	-0.00 ± 0.00	0.02
+ Circular 89°	0.01 ± 0.02	0.06 ± 0.02	0.06 ± 0.02	-0.06 ± 0.03	0.00 ± 0.03	0.12 ± 0.03	-0.01 ± 0.02	0.19
	0.00 ± 0.00	0.01 ± 0.00	0.01 ± 0.00	-0.00 ± 0.00	0.00 ± 0.00	0.01 ± 0.00	-0.00 ± 0.00	0.02

Table F.2: Formal errors for the systematic error-free scenarios for DORIS. The reference is a combination of ENVISAT, Jason-1 and Jason-2.

	σ_x & p-value		σ_y & p-value		σ_z & p-value		$\sigma_{\dot{x}}$ & p-value		$\sigma_{\dot{y}}$ & p-value		$\sigma_{\dot{z}}$ & p-value		σ_{x_p} & p-value		σ_{y_p} & p-value		σ_{LOD} & p-value		exp. imp.
	[mm]						[mm/dec]						[cm]				[μm]		[%]
Reference	0.000002	—	0.023860	—	0.078150	—	0.230	—	0.243	—	0.213	—	0.161	—	0.161	—	0.384	—	—
GRASP-like	0.000001	-0.000	0.018060	-0.000	0.060180	0.000	0.183	0.000	0.196	-0.000	0.157	-0.000	0.121	0.000	0.122	0.000	0.277	0.000	-18.78
E-GRASP-mod	0.000001	-0.000	0.018070	0.001	0.039360	-0.000	0.185	0.000	0.182	-0.000	0.156	-0.000	0.145	-0.000	0.142	-0.000	0.232	-0.000	-38.10
E-GRASP-like	0.000001	0.000	0.019020	0.000	0.037510	-0.000	0.183	0.000	0.180	-0.000	0.157	-0.000	0.142	-0.000	0.141	-0.000	0.236	-0.000	-38.11
Circular 30°	0.000001	0.023	0.020570	0.010	0.033070	-0.000	0.177	-0.000	0.180	-0.000	0.182	-0.000	0.158	-0.000	0.156	-0.000	0.247	-0.000	-43.38
Circular 60°	0.000001	0.002	0.018070	0.001	0.035760	-0.000	0.192	-0.000	0.182	-0.000	0.158	-0.000	0.150	-0.000	0.148	-0.000	0.219	-0.000	-44.45
Circular 89°	0.000001	0.001	0.017220	0.001	0.037430	-0.000	0.192	0.000	0.186	0.000	0.149	-0.000	0.147	-0.000	0.143	-0.000	0.209	-0.000	-44.90

	$\sigma_{Lat.}$ & p-value		$\sigma_{Lon.}$ & p-value		σ_{Height}		$\sigma_{\dot{Lat.}}$ & p-value		$\sigma_{\dot{Lon.}}$ & p-value		$\sigma_{\dot{Height}}$ & p-value	
	[mm]						[mm/dec]					
Reference	0.072512	—	0.011520	—	0.043606	—	0.205	—	0.251	—	0.227	—
GRASP-like	0.050958	-0.000	0.008735	0.000	0.034904	-0.000	0.157	-0.000	0.204	-0.000	0.182	-0.000
E-GRASP-mod	0.038507	-0.000	0.008606	0.001	0.024145	-0.000	0.153	-0.000	0.187	-0.000	0.177	-0.000
E-GRASP-like	0.036320	-0.000	0.008598	0.000	0.023361	-0.000	0.154	-0.000	0.183	-0.000	0.176	-0.000
Circular 30°	0.030482	-0.000	0.009707	0.010	0.021288	-0.000	0.174	-0.000	0.182	-0.000	0.181	-0.000
Circular 60°	0.034542	-0.000	0.008602	0.001	0.022665	-0.000	0.155	-0.000	0.192	-0.000	0.179	-0.000
Circular 89°	0.036323	-0.000	0.008195	0.001	0.022506	-0.000	0.151	-0.000	0.196	-0.000	0.180	-0.000

Table F.3: Statistics for ERPs by adding space-tie satellit scenarios in the DORIS systematic error-free case.

	$\Delta X - Pole$					$\Delta Y - Pole$					ΔLOD				
	std. [mm]	p-value	mean ± std. [mm]	p-value	trend ± std. [mm/a]	p-value	std. [mm]	p-value	mean ± std. [mm]	p-value	trend ± std. [mm/a]	p-value	std. [μm]	p-value	mean ± std. [μm]	p-value	trend ± std. [μm/a]	p-value
ENV.+JAS-1+JAS-2	1.747	NaN	0.049 ± 0.035	0.159	0.003 ± 0.017	0.880	1.854	NaN	0.231 ± 0.037	0.000	0.019 ± 0.018	0.307	0.852	NaN	0.025 ± 0.018	0.156	-0.005 ± 0.009	0.605
- sys. eror-free																		
+ GRASP-like	1.339	0.000	0.089 ± 0.026	0.001	0.004 ± 0.013	0.761	1.327	0.000	-0.093 ± 0.026	0.000	-0.013 ± 0.013	0.321	0.465	0.000	0.020 ± 0.009	0.033	0.009 ± 0.005	0.051
- sys. eror-free																		
+ E-GRASP-mod	1.508	0.000	0.111 ± 0.030	0.000	0.013 ± 0.015	0.382	1.490	0.000	0.018 ± 0.029	0.547	-0.000 ± 0.015	0.987	0.333	0.000	0.026 ± 0.007	0.000	0.002 ± 0.003	0.512
- sys. eror-free																		
+ E-GRASP-like	1.480	0.000	0.020 ± 0.029	0.492	-0.015 ± 0.014	0.288	1.488	0.000	0.126 ± 0.029	0.000	0.014 ± 0.015	0.351	0.329	0.000	-0.017 ± 0.007	0.011	-0.003 ± 0.003	0.358
- sys. eror-free																		
+ Circular 30°	1.611	0.000	0.009 ± 0.032	0.780	-0.009 ± 0.016	0.557	1.644	0.000	0.113 ± 0.033	0.000	0.010 ± 0.016	0.550	0.295	0.000	-0.002 ± 0.006	0.677	0.001 ± 0.003	0.658
- sys. eror-free																		
+ Circular 60°	1.553	0.000	0.138 ± 0.031	0.000	0.002 ± 0.015	0.900	1.559	0.000	-0.011 ± 0.031	0.733	0.001 ± 0.015	0.966	0.268	0.000	-0.040 ± 0.005	0.000	-0.001 ± 0.003	0.633
- sys. eror-free																		
+ Circular 89°	1.512	0.000	0.046 ± 0.030	0.122	0.007 ± 0.015	0.654	1.518	0.000	-0.046 ± 0.030	0.126	-0.002 ± 0.015	0.903	0.269	0.000	-0.044 ± 0.005	0.000	-0.005 ± 0.003	0.063
- sys. eror-free																		

F.1.2 Influence of systematic center-of-mass displacement

Table F.4: Helmert parameters to the reference solution for introducing a CoM displacement to the space-tie satellite of 5mm, either fixed or solved for, in the case of DORIS. The reference is a combination of ENVISAT, Jason-1 and Jason-2.

	T_x [mm] $\dot{T}_x$ [mm/a]	T_y [mm] $\dot{T}_y$ [mm/a]	T_z [mm] $\dot{T}_z$ [mm/a]	R_x [mm] $\dot{R}_x$ [mm/a]	R_y [mm] $\dot{R}_y$ [mm/a]	R_z [mm] $\dot{R}_z$ [mm/a]	sc [mm] $\dot{sc}$ [mm/a]	s_0 s_0
Reference	0.00 ± 0.00	0.00 ± 0.00	0.00 ± 0.00	0.00 ± 0.00	0.00 ± 0.00	0.00 ± 0.00	0.00 ± 0.00	0.00
	0.00 ± 0.00	0.00 ± 0.00	0.00 ± 0.00	0.00 ± 0.00	0.00 ± 0.00	0.00 ± 0.00	0.00 ± 0.00	0.00
+ GRASP-like	0.00 ± 0.01	0.03 ± 0.01	0.30 ± 0.01	-0.57 ± 0.01	-0.01 ± 0.01	0.15 ± 0.01	-0.48 ± 0.01	0.09
	0.00 ± 0.00	0.00 ± 0.00	0.03 ± 0.00	-0.06 ± 0.00	0.00 ± 0.00	0.02 ± 0.00	-0.05 ± 0.00	0.01
+ E-GRASP-mod	-0.00 ± 0.01	-0.01 ± 0.01	-0.06 ± 0.01	-0.14 ± 0.01	-0.01 ± 0.01	0.02 ± 0.01	-0.12 ± 0.01	0.04
	-0.00 ± 0.00	-0.00 ± 0.00	-0.01 ± 0.00	-0.01 ± 0.00	-0.00 ± 0.00	0.00 ± 0.00	-0.01 ± 0.00	0.00
+ E-GRASP-like	-0.00 ± 0.01	-0.02 ± 0.01	-0.09 ± 0.01	-0.23 ± 0.01	-0.02 ± 0.01	0.03 ± 0.01	-0.19 ± 0.01	0.07
	-0.00 ± 0.00	-0.00 ± 0.00	-0.01 ± 0.00	-0.02 ± 0.00	-0.00 ± 0.00	0.00 ± 0.00	-0.02 ± 0.00	0.01
+ Circular 30°	-0.00 ± 0.00	-0.00 ± 0.00	-0.02 ± 0.00	-0.01 ± 0.00	-0.00 ± 0.00	0.00 ± 0.00	-0.02 ± 0.00	0.02
	-0.00 ± 0.00	-0.00 ± 0.00	-0.00 ± 0.00	-0.00 ± 0.00	-0.00 ± 0.00	0.00 ± 0.00	-0.00 ± 0.00	0.00
+ Circular 60°	-0.00 ± 0.00	-0.01 ± 0.00	-0.01 ± 0.00	-0.03 ± 0.00	-0.00 ± 0.00	0.00 ± 0.00	-0.03 ± 0.00	0.01
	-0.00 ± 0.00	-0.00 ± 0.00	-0.00 ± 0.00	-0.00 ± 0.00	0.00 ± 0.00	0.00 ± 0.00	-0.00 ± 0.00	0.00
+ Circular 89°	-0.00 ± 0.00	-0.00 ± 0.00	-0.01 ± 0.00	-0.04 ± 0.00	0.00 ± 0.00	0.00 ± 0.00	-0.03 ± 0.00	0.01
	-0.00 ± 0.00	-0.00 ± 0.00	-0.00 ± 0.00	-0.00 ± 0.00	0.00 ± 0.00	0.00 ± 0.00	-0.00 ± 0.00	0.00
+ GRASP-like CoM est.	0.00 ± 0.00	-0.00 ± 0.00	-0.00 ± 0.00	0.04 ± 0.00	0.00 ± 0.00	-0.01 ± 0.00	0.03 ± 0.00	0.00
	0.00 ± 0.00	0.00 ± 0.00	-0.00 ± 0.00	0.00 ± 0.00	-0.00 ± 0.00	-0.00 ± 0.00	0.00 ± 0.00	0.00
+ E-GRASP-mod CoM est.	-0.00 ± 0.00	-0.00 ± 0.00	-0.01 ± 0.00	-0.00 ± 0.00	-0.00 ± 0.00	0.00 ± 0.00	-0.00 ± 0.00	0.00
	-0.00 ± 0.00	-0.00 ± 0.00	-0.00 ± 0.00	-0.00 ± 0.00	-0.00 ± 0.00	0.00 ± 0.00	-0.00 ± 0.00	0.00
+ E-GRASP-like CoM est.	-0.00 ± 0.00	-0.00 ± 0.00	-0.00 ± 0.00	-0.00 ± 0.00	-0.00 ± 0.00	0.00 ± 0.00	-0.00 ± 0.00	0.00
	-0.00 ± 0.00	-0.00 ± 0.00	-0.00 ± 0.00	-0.00 ± 0.00	-0.00 ± 0.00	0.00 ± 0.00	-0.00 ± 0.00	0.00
+ Circular 30° CoM est.	0.00 ± 0.00	0.00 ± 0.00	0.01 ± 0.00	0.00 ± 0.00	0.00 ± 0.00	-0.00 ± 0.00	0.00 ± 0.00	0.01
	0.00 ± 0.00	0.00 ± 0.00	0.00 ± 0.00	0.00 ± 0.00	0.00 ± 0.00	-0.00 ± 0.00	0.00 ± 0.00	0.00
+ Circular 60° CoM est.	0.00 ± 0.00	0.00 ± 0.00	0.00 ± 0.00	0.01 ± 0.00	0.00 ± 0.00	-0.00 ± 0.00	0.00 ± 0.00	0.00
	0.00 ± 0.00	0.00 ± 0.00	0.00 ± 0.00	0.00 ± 0.00	0.00 ± 0.00	-0.00 ± 0.00	0.00 ± 0.00	0.00
+ Circular 89° CoM est.	0.00 ± 0.00	0.00 ± 0.00	0.00 ± 0.00	0.00 ± 0.00	-0.00 ± 0.00	-0.00 ± 0.00	0.00 ± 0.00	0.00
	0.00 ± 0.00	0.00 ± 0.00	0.00 ± 0.00	0.00 ± 0.00	-0.00 ± 0.00	-0.00 ± 0.00	0.00 ± 0.00	0.00

Table F.5: Helmert parameters to the reference solution for introducing a CoM displacement to the space-tie satellite of 10mm, either fixed or solved for, in the case of DORIS. The reference is a combination of ENVISAT, Jason-1 and Jason-2.

	T_x [mm] $T_{\dot{x}}$ [mm/a]	T_y [mm] $T_{\dot{y}}$ [mm/a]	T_z [mm] $T_{\dot{z}}$ [mm/a]	R_x [mm] $R_{\dot{x}}$ [mm/a]	R_y [mm] $R_{\dot{y}}$ [mm/a]	R_z [mm] $R_{\dot{z}}$ [mm/a]	sc [mm] $\dot{sc}$ [mm/a]	s_0 s_0
Reference	0.00 ± 0.00	0.00 ± 0.00	0.00 ± 0.00	0.00 ± 0.00	0.00 ± 0.00	0.00 ± 0.00	0.00 ± 0.00	0.00
	0.00 ± 0.00	0.00 ± 0.00	0.00 ± 0.00	0.00 ± 0.00	0.00 ± 0.00	0.00 ± 0.00	0.00 ± 0.00	0.00
+ GRASP-like	0.00 ± 0.02	0.05 ± 0.02	0.60 ± 0.02	-1.13 ± 0.03	-0.03 ± 0.03	0.30 ± 0.03	-0.96 ± 0.02	0.18
	0.00 ± 0.00	0.00 ± 0.00	0.06 ± 0.00	-0.11 ± 0.00	0.00 ± 0.00	0.03 ± 0.00	-0.09 ± 0.00	0.02
+ E-GRASP-mod	-0.01 ± 0.01	-0.03 ± 0.01	-0.12 ± 0.01	-0.27 ± 0.01	-0.02 ± 0.01	0.04 ± 0.01	-0.24 ± 0.01	0.08
	-0.00 ± 0.00	-0.00 ± 0.00	-0.01 ± 0.00	-0.03 ± 0.00	-0.00 ± 0.00	0.00 ± 0.00	-0.02 ± 0.00	0.01
+ E-GRASP-like	-0.00 ± 0.02	-0.03 ± 0.02	-0.17 ± 0.02	-0.46 ± 0.02	-0.04 ± 0.02	0.06 ± 0.02	-0.38 ± 0.02	0.14
	-0.00 ± 0.00	-0.00 ± 0.00	-0.02 ± 0.00	-0.05 ± 0.00	-0.00 ± 0.00	0.01 ± 0.00	-0.04 ± 0.00	0.02
+ Circular 30°	-0.00 ± 0.00	-0.01 ± 0.00	-0.03 ± 0.00	-0.02 ± 0.01	-0.00 ± 0.01	0.01 ± 0.01	-0.04 ± 0.00	0.03
	-0.00 ± 0.00	-0.00 ± 0.00	-0.00 ± 0.00	-0.00 ± 0.00	-0.00 ± 0.00	0.00 ± 0.00	-0.00 ± 0.00	0.00
+ Circular 60°	-0.00 ± 0.00	-0.01 ± 0.00	-0.03 ± 0.00	-0.05 ± 0.00	-0.00 ± 0.00	0.01 ± 0.00	-0.05 ± 0.00	0.02
	-0.00 ± 0.00	-0.00 ± 0.00	-0.00 ± 0.00	-0.01 ± 0.00	0.00 ± 0.00	0.00 ± 0.00	-0.01 ± 0.00	0.00
+ Circular 89°	-0.00 ± 0.00	-0.01 ± 0.00	-0.02 ± 0.00	-0.08 ± 0.00	0.00 ± 0.00	0.01 ± 0.00	-0.06 ± 0.00	0.02
	-0.00 ± 0.00	-0.00 ± 0.00	-0.00 ± 0.00	-0.01 ± 0.00	0.00 ± 0.00	0.00 ± 0.00	-0.01 ± 0.00	0.00
+ GRASP-like CoM est.	0.00 ± 0.00	-0.00 ± 0.00	-0.00 ± 0.00	0.04 ± 0.00	0.00 ± 0.00	-0.01 ± 0.00	0.03 ± 0.00	0.00
	0.00 ± 0.00	0.00 ± 0.00	-0.00 ± 0.00	0.00 ± 0.00	-0.00 ± 0.00	-0.00 ± 0.00	0.00 ± 0.00	0.00
+ E-GRASP-mod CoM est.	-0.00 ± 0.00	-0.00 ± 0.00	-0.01 ± 0.00	-0.00 ± 0.00	-0.00 ± 0.00	0.00 ± 0.00	-0.00 ± 0.00	0.00
	-0.00 ± 0.00	-0.00 ± 0.00	-0.00 ± 0.00	-0.00 ± 0.00	-0.00 ± 0.00	0.00 ± 0.00	-0.00 ± 0.00	0.00
+ E-GRASP-like CoM est.	-0.00 ± 0.00	-0.00 ± 0.00	-0.00 ± 0.00	-0.00 ± 0.00	-0.00 ± 0.00	0.00 ± 0.00	-0.00 ± 0.00	0.00
	-0.00 ± 0.00	-0.00 ± 0.00	-0.00 ± 0.00	-0.00 ± 0.00	-0.00 ± 0.00	0.00 ± 0.00	-0.00 ± 0.00	0.00
+ Circular 30° CoM est.	0.00 ± 0.00	0.00 ± 0.00	0.01 ± 0.00	0.00 ± 0.00	0.00 ± 0.00	-0.00 ± 0.00	0.00 ± 0.00	0.01
	0.00 ± 0.00	0.00 ± 0.00	0.00 ± 0.00	0.00 ± 0.00	0.00 ± 0.00	-0.00 ± 0.00	0.00 ± 0.00	0.00
+ Circular 60° CoM est.	0.00 ± 0.00	0.00 ± 0.00	0.00 ± 0.00	0.01 ± 0.00	0.00 ± 0.00	-0.00 ± 0.00	0.00 ± 0.00	0.00
	0.00 ± 0.00	0.00 ± 0.00	0.00 ± 0.00	0.00 ± 0.00	0.00 ± 0.00	-0.00 ± 0.00	0.00 ± 0.00	0.00
+ Circular 89° CoM est.	0.00 ± 0.00	0.00 ± 0.00	0.00 ± 0.00	0.00 ± 0.00	-0.00 ± 0.00	-0.00 ± 0.00	0.00 ± 0.00	0.00
	0.00 ± 0.00	0.00 ± 0.00	0.00 ± 0.00	0.00 ± 0.00	-0.00 ± 0.00	-0.00 ± 0.00	0.00 ± 0.00	0.00

Table F.6: Formal errors for the 5 mm CoM case for DORIS, coordinates are fixed.

	σ_x & p-value		σ_y & p-value		σ_z & p-value		$\sigma_{\dot{x}}$ & p-value		$\sigma_{\dot{y}}$ & p-value		$\sigma_{\dot{z}}$ & p-value		σ_{x_p} & p-value		σ_{y_p} & p-value		σ_{LOD} & p-value		exp. imp.
	[mm]						[mm/dec]						[cm]				[μm]		[%]
GRASP-like	0.000001	-0.000	0.018060	-0.000	0.060180	0.000	0.183	0.000	0.196	-0.000	0.157	-0.000	0.121	0.000	0.122	0.000	0.277	0.000	-18.78
E-GRASP-mod	0.000001	-0.000	0.018070	0.001	0.039360	-0.000	0.185	0.000	0.182	-0.000	0.156	-0.000	0.145	-0.000	0.142	-0.000	0.232	-0.000	-38.10
E-GRASP-like	0.000001	0.000	0.019020	0.000	0.037510	-0.000	0.183	0.000	0.180	-0.000	0.157	-0.000	0.142	-0.000	0.141	-0.000	0.236	-0.000	-38.11
Circular 30°	0.000001	0.023	0.020570	0.010	0.033070	-0.000	0.177	-0.000	0.180	-0.000	0.182	-0.000	0.158	-0.000	0.156	-0.000	0.247	-0.000	-43.38
Circular 60°	0.000001	0.002	0.018070	0.001	0.035760	-0.000	0.192	-0.000	0.182	-0.000	0.158	-0.000	0.150	-0.000	0.148	-0.000	0.219	-0.000	-44.45
Circular 89°	0.000001	0.001	0.017220	0.001	0.037430	-0.000	0.192	0.000	0.186	0.000	0.149	-0.000	0.147	-0.000	0.143	-0.000	0.209	-0.000	-44.90

	$\sigma_{Lat.}$ & p-value		$\sigma_{Lon.}$ & p-value		σ_{Height}		$\sigma_{\dot{Lat.}}$ & p-value		$\sigma_{\dot{Lon.}}$ & p-value		$\sigma_{\dot{Height}}$ & p-value	
	[mm]						[mm/dec]					
GRASP-like	0.050958	-0.000	0.008735	0.000	0.034904	-0.000	0.157	-0.000	0.204	-0.000	0.182	-0.000
E-GRASP-mod	0.038507	-0.000	0.008606	0.001	0.024145	-0.000	0.153	-0.000	0.187	-0.000	0.177	-0.000
E-GRASP-like	0.036320	-0.000	0.008598	0.000	0.023361	-0.000	0.154	-0.000	0.183	-0.000	0.176	-0.000
Circular 30°	0.030482	-0.000	0.009707	0.010	0.021288	-0.000	0.174	-0.000	0.182	-0.000	0.181	-0.000
Circular 60°	0.034542	-0.000	0.008602	0.001	0.022665	-0.000	0.155	-0.000	0.192	-0.000	0.179	-0.000
Circular 89°	0.036323	-0.000	0.008195	0.001	0.022506	-0.000	0.151	-0.000	0.196	-0.000	0.180	-0.000

Table F.7: Formal errors for the 10 mm CoM case for DORIS, coordinates are fixed.

	σ_x & p-value		σ_y & p-value		σ_z & p-value		$\sigma_{\dot{x}}$ & p-value		$\sigma_{\dot{y}}$ & p-value		$\sigma_{\dot{z}}$ & p-value		σ_{x_p} & p-value		σ_{y_p} & p-value		σ_{LOD} & p-value		exp. imp.
	[mm]						[mm/dec]						[cm]				[μm]		[%]
GRASP-like	0.000001	-0.000	0.018060	-0.000	0.060180	0.000	0.183	0.000	0.196	-0.000	0.157	-0.000	0.121	0.000	0.122	0.000	0.277	0.000	-18.78
E-GRASP-mod	0.000001	-0.000	0.018070	0.001	0.039360	-0.000	0.185	0.000	0.182	-0.000	0.156	-0.000	0.145	-0.000	0.142	-0.000	0.232	-0.000	-38.10
E-GRASP-like	0.000001	0.000	0.019020	0.000	0.037510	-0.000	0.183	0.000	0.180	-0.000	0.157	-0.000	0.142	-0.000	0.141	-0.000	0.236	-0.000	-38.11
Circular 30°	0.000001	0.023	0.020570	0.010	0.033070	-0.000	0.177	-0.000	0.180	-0.000	0.182	-0.000	0.158	-0.000	0.156	-0.000	0.247	-0.000	-43.38
Circular 60°	0.000001	0.002	0.018070	0.001	0.035760	-0.000	0.192	-0.000	0.182	-0.000	0.158	-0.000	0.150	-0.000	0.148	-0.000	0.219	-0.000	-44.45
Circular 89°	0.000001	0.001	0.017220	0.001	0.037430	-0.000	0.192	0.000	0.186	0.000	0.149	-0.000	0.147	-0.000	0.143	-0.000	0.209	-0.000	-44.90

	$\sigma_{Lat.}$ & p-value		$\sigma_{Lon.}$ & p-value		σ_{Height}		$\sigma_{\dot{Lat.}}$ & p-value		$\sigma_{\dot{Lon.}}$ & p-value		$\sigma_{\dot{Height}}$ & p-value	
	[mm]						[mm/dec]					
GRASP-like	0.050958	-0.000	0.008735	0.000	0.034904	-0.000	0.157	-0.000	0.204	-0.000	0.182	-0.000
E-GRASP-mod	0.038507	-0.000	0.008606	0.001	0.024145	-0.000	0.153	-0.000	0.187	-0.000	0.177	-0.000
E-GRASP-like	0.036320	-0.000	0.008598	0.000	0.023361	-0.000	0.154	-0.000	0.183	-0.000	0.176	-0.000
Circular 30°	0.030482	-0.000	0.009707	0.010	0.021288	-0.000	0.174	-0.000	0.182	-0.000	0.181	-0.000
Circular 60°	0.034542	-0.000	0.008602	0.001	0.022665	-0.000	0.155	-0.000	0.192	-0.000	0.179	-0.000
Circular 89°	0.036323	-0.000	0.008195	0.001	0.022506	-0.000	0.151	-0.000	0.196	-0.000	0.180	-0.000

Table F.8: Formal errors for the 5 mm CoM case for DORIS, coordinates are estimated.

	σ_x & p-value		σ_y & p-value		σ_z & p-value		$\sigma_{\dot{x}}$ & p-value		$\sigma_{\dot{y}}$ & p-value		$\sigma_{\dot{z}}$ & p-value		σ_{x_p} & p-value		σ_{y_p} & p-value		σ_{LOD} & p-value		exp. imp.
	[mm]						[mm/dec]						[cm]				[μm]		[%]
GRASP-like	0.000001	-0.000	0.018060	-0.000	0.060200	0.000	0.183	0.000	0.196	-0.000	0.159	-0.000	0.121	0.000	0.122	0.000	0.277	0.000	-18.78
E-GRASP-mod	0.000001	-0.000	0.018070	0.001	0.039370	-0.000	0.185	0.000	0.183	-0.000	0.156	-0.000	0.145	-0.000	0.142	-0.000	0.232	-0.000	-38.10
E-GRASP-like	0.000001	0.000	0.019020	0.000	0.037530	-0.000	0.183	0.000	0.180	-0.000	0.157	-0.000	0.142	-0.000	0.141	-0.000	0.236	-0.000	-38.11
Circular 30°	0.000001	0.023	0.020570	0.010	0.033080	-0.000	0.177	-0.000	0.180	-0.000	0.182	-0.000	0.158	-0.000	0.156	-0.000	0.247	-0.000	-43.38
Circular 60°	0.000001	0.002	0.018070	0.001	0.035770	-0.000	0.192	-0.000	0.182	-0.000	0.158	-0.000	0.150	-0.000	0.148	-0.000	0.219	-0.000	-44.45
Circular 89°	0.000001	0.001	0.017220	0.001	0.037440	-0.000	0.192	0.000	0.186	0.000	0.149	-0.000	0.147	-0.000	0.143	-0.000	0.209	-0.000	-44.90

	$\sigma_{Lat.}$ & p-value		$\sigma_{Lon.}$ & p-value		σ_{Height}	$\sigma_{\dot{Lat.}}$ & p-value		$\sigma_{\dot{Lon.}}$ & p-value		$\sigma_{\dot{Height}}$ & p-value	
	[mm]					[mm/dec]					
GRASP-like	0.050968	-0.000	0.008735	0.000	0.034904	-0.000	0.158	-0.000	0.204	-0.000	0.183	-0.000
E-GRASP-mod	0.038516	-0.000	0.008606	0.001	0.024145	-0.000	0.154	-0.000	0.187	-0.000	0.178	-0.000
E-GRASP-like	0.036323	-0.000	0.008598	0.000	0.023366	-0.000	0.154	-0.000	0.183	-0.000	0.176	-0.000
Circular 30°	0.030482	-0.000	0.009707	0.010	0.021288	-0.000	0.174	-0.000	0.183	-0.000	0.182	-0.000
Circular 60°	0.034542	-0.000	0.008602	0.001	0.022665	-0.000	0.155	-0.000	0.192	-0.000	0.179	-0.000
Circular 89°	0.036323	-0.000	0.008195	0.001	0.022506	-0.000	0.152	-0.000	0.196	-0.000	0.180	-0.000

Table F.9: Formal errors for the 10 mm CoM case for DORIS, coordinates are estimated.

	σ_x & p-value		σ_y & p-value		σ_z & p-value		$\sigma_{\dot{x}}$ & p-value		$\sigma_{\dot{y}}$ & p-value		$\sigma_{\dot{z}}$ & p-value		σ_{x_p} & p-value		σ_{y_p} & p-value		σ_{LOD} & p-value		exp. imp.
	[mm]						[mm/dec]						[cm]				[μm]		[%]
GRASP-like	0.000001	-0.000	0.018060	-0.000	0.060200	0.000	0.183	0.000	0.196	-0.000	0.159	-0.000	0.121	0.000	0.122	0.000	0.277	0.000	-18.78
E-GRASP-mod	0.000001	-0.000	0.018070	0.001	0.039370	-0.000	0.185	0.000	0.183	-0.000	0.156	-0.000	0.145	-0.000	0.142	-0.000	0.232	-0.000	-38.10
E-GRASP-like	0.000001	0.000	0.019020	0.000	0.037530	-0.000	0.183	0.000	0.180	-0.000	0.157	-0.000	0.142	-0.000	0.141	-0.000	0.236	-0.000	-38.11
Circular 30°	0.000001	0.023	0.020570	0.010	0.033080	-0.000	0.177	-0.000	0.180	-0.000	0.182	-0.000	0.158	-0.000	0.156	-0.000	0.247	-0.000	-43.38
Circular 60°	0.000001	0.002	0.018070	0.001	0.035770	-0.000	0.192	-0.000	0.182	-0.000	0.158	-0.000	0.150	-0.000	0.148	-0.000	0.219	-0.000	-44.45
Circular 89°	0.000001	0.001	0.017220	0.001	0.037440	-0.000	0.192	0.000	0.186	0.000	0.149	-0.000	0.147	-0.000	0.143	-0.000	0.209	-0.000	-44.90

	$\sigma_{Lat.}$ & p-value		$\sigma_{Lon.}$ & p-value		σ_{Height}		$\sigma_{\dot{Lat.}}$ & p-value		$\sigma_{\dot{Lon.}}$ & p-value		$\sigma_{\dot{Height}}$ & p-value	
	[mm]						[mm/dec]					
GRASP-like	0.050968	-0.000	0.008735	0.000	0.034904	-0.000	0.158	-0.000	0.204	-0.000	0.183	-0.000
E-GRASP-mod	0.038516	-0.000	0.008606	0.001	0.024145	-0.000	0.154	-0.000	0.187	-0.000	0.178	-0.000
E-GRASP-like	0.036323	-0.000	0.008598	0.000	0.023366	-0.000	0.154	-0.000	0.183	-0.000	0.176	-0.000
Circular 30°	0.030482	-0.000	0.009707	0.010	0.021288	-0.000	0.174	-0.000	0.183	-0.000	0.182	-0.000
Circular 60°	0.034542	-0.000	0.008602	0.001	0.022665	-0.000	0.155	-0.000	0.192	-0.000	0.179	-0.000
Circular 89°	0.036323	-0.000	0.008195	0.001	0.022506	-0.000	0.152	-0.000	0.196	-0.000	0.180	-0.000

Table F.10: Statistics of the estimated ERPs with DORIS in the case of 5 mm and 10mm CoM displacement introduced to the space-tie satellite and when estimating for the CoM coordinates.

	$\Delta X - Pole$						$\Delta Y - Pole$						ΔLOD					
	std. [mm]	p-value	mean ± std. [mm]	p-value	trend ± std. [mm/a]	p-value	std. [mm]	p-value	mean ± std. [mm]	p-value	trend ± std. [mm/a]	p-value	std. [μm]	p-value	mean ± std. [μm]	p-value	trend ± std. [μm/a]	p-value
Reference + GRASP-like																		
- 5 mm CoM deviation	1.338	0.000	0.075 ± 0.026	0.005	0.006 ± 0.013	0.668	1.335	0.000	-0.748 ± 0.026	0.000	-0.070 ± 0.013	0.000	0.461	0.000	0.002 ± 0.009	0.796	0.008 ± 0.005	0.079
- 5 mm CoM deviation est.	1.339	0.000	0.090 ± 0.026	0.001	0.004 ± 0.013	0.769	1.327	0.000	-0.047 ± 0.026	0.073	-0.009 ± 0.013	0.494	0.465	0.000	0.021 ± 0.009	0.028	0.009 ± 0.005	0.051
- 10 mm CoM deviation	1.338	0.000	0.061 ± 0.026	0.021	0.007 ± 0.013	0.580	1.353	0.000	-1.403 ± 0.026	0.000	-0.127 ± 0.013	0.000	0.505	0.000	-0.019 ± 0.010	0.060	0.008 ± 0.005	0.126
- 10 mm CoM deviation est.	1.339	0.000	0.090 ± 0.026	0.001	0.004 ± 0.013	0.770	1.327	0.000	-0.047 ± 0.026	0.073	-0.009 ± 0.013	0.494	0.465	0.000	0.021 ± 0.009	0.028	0.009 ± 0.005	0.051
Reference + E-GRASP-mod																		
- 5 mm CoM deviation	1.508	0.000	0.116 ± 0.030	0.000	0.014 ± 0.015	0.341	1.491	0.000	-0.155 ± 0.029	0.000	-0.016 ± 0.015	0.273	0.333	0.000	0.023 ± 0.007	0.000	0.002 ± 0.003	0.532
- 5 mm CoM deviation est.	1.508	0.000	0.112 ± 0.030	0.000	0.013 ± 0.015	0.380	1.490	0.000	0.016 ± 0.029	0.587	-0.000 ± 0.015	0.978	0.333	0.000	0.026 ± 0.007	0.000	0.002 ± 0.003	0.510
- 10 mm CoM deviation	1.508	0.000	0.120 ± 0.030	0.000	0.015 ± 0.015	0.304	1.492	0.000	-0.327 ± 0.029	0.000	-0.032 ± 0.015	0.030	0.332	0.000	0.021 ± 0.007	0.002	0.002 ± 0.003	0.553
- 10 mm CoM deviation est.	1.508	0.000	0.112 ± 0.030	0.000	0.013 ± 0.015	0.380	1.490	0.000	0.016 ± 0.029	0.587	-0.000 ± 0.015	0.978	0.336	0.000	0.026 ± 0.007	0.000	0.002 ± 0.003	0.643
Reference + E-GRASP-like																		
- 5 mm CoM deviation	1.479	0.000	0.019 ± 0.029	0.520	-0.014 ± 0.014	0.326	1.489	0.000	-0.170 ± 0.029	0.000	-0.013 ± 0.015	0.377	0.398	0.000	-0.021 ± 0.008	0.008	-0.004 ± 0.004	0.341
- 5 mm CoM deviation est.	1.480	0.000	0.020 ± 0.029	0.492	-0.015 ± 0.014	0.289	1.488	0.000	0.124 ± 0.029	0.000	0.013 ± 0.015	0.356	0.329	0.000	-0.017 ± 0.007	0.011	-0.003 ± 0.003	0.359
- 10 mm CoM deviation	1.479	0.000	0.018 ± 0.029	0.549	-0.013 ± 0.014	0.368	1.492	0.000	-0.465 ± 0.029	0.000	-0.039 ± 0.015	0.007	0.381	0.000	-0.026 ± 0.008	0.001	-0.002 ± 0.004	0.557
- 10 mm CoM deviation est.	1.480	0.000	0.020 ± 0.029	0.492	-0.015 ± 0.014	0.289	1.488	0.000	0.124 ± 0.029	0.000	0.013 ± 0.015	0.356	0.329	0.000	-0.017 ± 0.007	0.011	-0.003 ± 0.003	0.359
Reference + Circular 30°																		
- 5 mm CoM deviation	1.611	0.000	0.010 ± 0.032	0.743	-0.009 ± 0.016	0.572	1.644	0.000	0.096 ± 0.033	0.003	0.008 ± 0.016	0.623	0.295	0.000	-0.004 ± 0.006	0.520	0.001 ± 0.003	0.689
- 5 mm CoM deviation est.	1.611	0.000	0.009 ± 0.032	0.787	-0.009 ± 0.016	0.554	1.644	0.000	0.119 ± 0.033	0.000	0.010 ± 0.016	0.526	0.295	0.000	-0.002 ± 0.006	0.743	0.001 ± 0.003	0.643
- 10 mm CoM deviation	1.610	0.000	0.012 ± 0.032	0.707	-0.009 ± 0.016	0.587	1.644	0.000	0.080 ± 0.033	0.015	0.006 ± 0.016	0.701	0.295	0.000	-0.005 ± 0.006	0.384	0.001 ± 0.003	0.720
- 10 mm CoM deviation est.	1.611	0.000	0.009 ± 0.032	0.787	-0.009 ± 0.016	0.554	1.644	0.000	0.119 ± 0.033	0.000	0.010 ± 0.016	0.526	0.295	0.000	-0.002 ± 0.006	0.743	0.001 ± 0.003	0.643
Reference + Circular 60°																		
- 5 mm CoM deviation	1.553	0.000	0.141 ± 0.031	0.000	0.002 ± 0.015	0.875	1.559	0.000	-0.044 ± 0.031	0.155	-0.003 ± 0.015	0.870	0.269	0.000	-0.041 ± 0.005	0.000	-0.001 ± 0.003	0.610
- 5 mm CoM deviation est.	1.553	0.000	0.137 ± 0.031	0.000	0.002 ± 0.015	0.906	1.559	0.000	-0.004 ± 0.031	0.903	0.001 ± 0.015	0.931	0.268	0.000	-0.040 ± 0.005	0.000	-0.001 ± 0.003	0.639
- 10 mm CoM deviation	1.553	0.000	0.144 ± 0.031	0.000	0.003 ± 0.015	0.849	1.559	0.000	-0.077 ± 0.031	0.012	-0.006 ± 0.015	0.711	0.269	0.000	-0.042 ± 0.005	0.000	-0.001 ± 0.003	0.587
- 10 mm CoM deviation est.	1.553	0.000	0.137 ± 0.031	0.000	0.002 ± 0.015	0.906	1.559	0.000	-0.004 ± 0.031	0.903	0.001 ± 0.015	0.931	0.268	0.000	-0.040 ± 0.005	0.000	-0.001 ± 0.003	0.639
Reference + Circular 89°																		
- 5 mm CoM deviation	1.512	0.000	0.051 ± 0.030	0.091	0.007 ± 0.015	0.624	1.518	0.000	-0.096 ± 0.030	0.001	-0.006 ± 0.015	0.674	0.270	0.000	-0.045 ± 0.005	0.000	-0.005 ± 0.003	0.060
- 5 mm CoM deviation est.	1.512	0.000	0.046 ± 0.030	0.126	0.007 ± 0.015	0.657	1.518	0.000	-0.041 ± 0.030	0.168	-0.001 ± 0.015	0.924	0.269	0.000	-0.044 ± 0.005	0.000	-0.005 ± 0.003	0.063
- 10 mm CoM deviation	1.512	0.000	0.055 ± 0.030	0.066	0.008 ± 0.015	0.595	1.518	0.000	-0.146 ± 0.030	0.000	-0.011 ± 0.015	0.471	0.270	0.000	-0.046 ± 0.005	0.000	-0.005 ± 0.003	0.057
- 10 mm CoM deviation est.	1.512	0.000	0.046 ± 0.030	0.126	0.007 ± 0.015	0.657	1.518	0.000	-0.041 ± 0.030	0.168	-0.001 ± 0.015	0.924	0.269	0.000	-0.044 ± 0.005	0.000	-0.005 ± 0.003	0.063

F.1.3 Atmospheric drag mismodelling

Table F.11: Helmert parameters to the reference solution for the atmospheric drag mismodelling case for DORIS. The reference is a combination of ENVISAT, Jason-1 and Jason-2.

	T_x [mm] $T_{\dot{x}}$ [mm/a]	T_y [mm] $T_{\dot{y}}$ [mm/a]	T_z [mm] $T_{\dot{z}}$ [mm/a]	R_x [mm] $R_{\dot{x}}$ [mm/a]	R_y [mm] $R_{\dot{y}}$ [mm/a]	R_z [mm] $R_{\dot{z}}$ [mm/a]	sc [mm] $\dot{sc}$ [mm/a]	s_0 s_0
Reference	0.00 ± 0.00 0.00 ± 0.00	0.00 ± 0.00 0.00 ± 0.00	0.00 ± 0.00 0.00 ± 0.00	0.00 ± 0.00 0.00 ± 0.00	0.00 ± 0.00 0.00 ± 0.00	0.00 ± 0.00 0.00 ± 0.00	0.00 ± 0.00 0.00 ± 0.00	0.00 0.00
+ GRASP-like	0.08 ± 0.02 0.01 ± 0.00	-0.16 ± 0.02 -0.01 ± 0.00	-1.67 ± 0.02 -0.17 ± 0.00	-0.15 ± 0.03 -0.01 ± 0.00	-0.09 ± 0.03 -0.01 ± 0.00	-0.05 ± 0.03 -0.01 ± 0.00	0.02 ± 0.02 0.01 ± 0.00	0.17 0.03
+ E-GRASP-mod	-0.00 ± 0.00 -0.00 ± 0.00	-0.00 ± 0.00 -0.00 ± 0.00	-0.00 ± 0.00 -0.00 ± 0.00	0.00 ± 0.00 0.00 ± 0.00	0.00 ± 0.00 0.00 ± 0.00	0.00 ± 0.00 0.00 ± 0.00	0.00 ± 0.00 0.00 ± 0.00	0.00 0.00
+ E-GRASP-like	-0.06 ± 0.01 -0.01 ± 0.00	-0.01 ± 0.01 0.00 ± 0.00	-0.01 ± 0.01 0.00 ± 0.00	0.01 ± 0.01 0.00 ± 0.00	-0.08 ± 0.01 -0.01 ± 0.00	0.01 ± 0.01 0.00 ± 0.00	-0.01 ± 0.01 -0.00 ± 0.00	0.05 0.01
+ Circular 30°	-0.00 ± 0.00 -0.00 ± 0.00	0.00 ± 0.00 -0.00 ± 0.00	0.00 ± 0.00 0.00 ± 0.00	0.00 ± 0.00 0.00 ± 0.00	-0.00 ± 0.00 -0.00 ± 0.00	0.00 ± 0.00 0.00 ± 0.00	-0.00 ± 0.00 -0.00 ± 0.00	0.00 0.00
+ Circular 60°	-0.00 ± 0.00 -0.00 ± 0.00	0.00 ± 0.00 0.00 ± 0.00	0.00 ± 0.00 0.00 ± 0.00	0.00 ± 0.00 0.00 ± 0.00	-0.00 ± 0.00 -0.00 ± 0.00	0.00 ± 0.00 0.00 ± 0.00	0.00 ± 0.00 0.00 ± 0.00	0.00 0.00
+ Circular 89°	-0.00 ± 0.00 -0.00 ± 0.00	0.00 ± 0.00 0.00 ± 0.00	-0.00 ± 0.00 -0.00 ± 0.00	0.00 ± 0.00 0.00 ± 0.00	0.00 ± 0.00 0.00 ± 0.00	0.00 ± 0.00 0.00 ± 0.00	-0.00 ± 0.00 -0.00 ± 0.00	0.00 0.00

Table F.12: Formal errors for the atmospheric drag case DORIS.

	σ_x & p-value		σ_y & p-value		σ_z & p-value		$\sigma_{\dot{x}}$ & p-value		$\sigma_{\dot{y}}$ & p-value		$\sigma_{\dot{z}}$ & p-value		σ_{x_p} & p-value		σ_{y_p} & p-value		σ_{LOD} & p-value		exp. imp.
	[mm]						[mm/dec]						[cm]				[μm]		[%]
GRASP-like	0.000001	-0.000	0.018120	-0.000	0.060420	0.000	0.183	0.000	0.196	-0.000	0.158	-0.000	0.140	0.000	0.137	0.000	0.285	0.000	-18.78
E-GRASP-mod	0.000001	-0.000	0.018070	0.001	0.039360	-0.000	0.185	0.000	0.182	-0.000	0.156	-0.000	0.145	-0.000	0.143	-0.000	0.232	-0.000	-38.10
E-GRASP-like	0.000001	0.000	0.019050	0.000	0.037550	-0.000	0.183	0.000	0.180	-0.000	0.157	-0.000	0.147	-0.000	0.145	-0.000	0.239	-0.000	-38.11
Circular 30°	0.000001	0.023	0.020570	0.010	0.033070	-0.000	0.177	-0.000	0.180	-0.000	0.182	-0.000	0.158	-0.000	0.156	-0.000	0.247	-0.000	-43.38
Circular 60°	0.000001	0.002	0.018070	0.001	0.035760	-0.000	0.192	-0.000	0.182	-0.000	0.158	-0.000	0.150	-0.000	0.148	-0.000	0.219	-0.000	-44.45
Circular 89°	0.000001	0.001	0.017220	0.001	0.037430	-0.000	0.192	0.000	0.186	0.000	0.149	-0.000	0.147	-0.000	0.143	-0.000	0.209	-0.000	-44.90

	$\sigma_{Lat.}$ & p-value		$\sigma_{Lon.}$ & p-value		σ_{Height}	$\sigma_{\dot{Lat.}}$ & p-value		$\sigma_{\dot{Lon.}}$ & p-value		$\sigma_{\dot{Height}}$ & p-value	
	[mm]					[mm/dec]					
GRASP-like	0.051445	-0.000	0.008770	0.000	0.035246	-0.000	0.158	-0.000	0.205	-0.000	0.183	-0.000
E-GRASP-mod	0.038507	-0.000	0.008606	0.001	0.024151	-0.000	0.153	-0.000	0.187	-0.000	0.177	-0.000
E-GRASP-like	0.036384	-0.000	0.008612	0.000	0.023383	-0.000	0.154	-0.000	0.184	-0.000	0.176	-0.000
Circular 30°	0.030482	-0.000	0.009707	0.010	0.021288	-0.000	0.174	-0.000	0.182	-0.000	0.181	-0.000
Circular 60°	0.034542	-0.000	0.008602	0.001	0.022665	-0.000	0.155	-0.000	0.192	-0.000	0.179	-0.000
Circular 89°	0.036323	-0.000	0.008195	0.001	0.022506	-0.000	0.151	-0.000	0.196	-0.000	0.180	-0.000

Table F.13: Statistics of estimated ERPs for the DORIS drag mismodelling case.

	$\Delta X - Pole$						$\Delta Y - Pole$						ΔLOD					
	std. [mm]	p-value	mean ± std. [mm]	p-value	trend ± std. [mm/a]	p-value	std. [mm]	p-value	mean ± std. [mm]	p-value	trend ± std. [mm/a]	p-value	std. [μm]	p-value	mean ± std. [μm]	p-value	trend ± std. [μm/a]	p-value
Comb. reference																		
+ GRASP-like																		
- drag mism.	1.862	0.000	0.028 ± 0.037	0.444	0.011 ± 0.018	0.549	1.822	0.000	-0.419 ± 0.036	0.000	-0.016 ± 0.018	0.366	0.602	0.000	-0.034 ± 0.012	0.005	0.004 ± 0.006	0.508
+ E-GRASP-mod																		
- drag mism.	1.511	0.916	0.113 ± 0.030	0.000	0.013 ± 0.015	0.374	1.493	0.880	0.016 ± 0.030	0.592	-0.001 ± 0.015	0.952	0.336	0.753	0.027 ± 0.007	0.000	0.002 ± 0.003	0.497
+ E-GRASP-like																		
- drag mism.	1.840	0.000	-0.028 ± 0.036	0.449	0.005 ± 0.018	0.780	1.879	0.000	-0.017 ± 0.037	0.640	-0.015 ± 0.018	0.403	0.347	0.004	-0.030 ± 0.007	0.000	-0.003 ± 0.003	0.395
+ Circular 30°																		
- drag mism.	1.611	0.985	0.008 ± 0.032	0.791	-0.009 ± 0.016	0.563	1.644	0.981	0.114 ± 0.033	0.000	0.009 ± 0.016	0.555	0.294	0.979	-0.002 ± 0.006	0.687	0.001 ± 0.003	0.645
+ Circular 60°																		
- drag mism.	1.554	0.971	0.138 ± 0.031	0.000	0.002 ± 0.015	0.892	1.559	0.985	-0.009 ± 0.031	0.767	0.001 ± 0.015	0.964	0.271	0.943	-0.039 ± 0.005	0.000	-0.002 ± 0.003	0.501
+ Circular 89°																		
- drag mism.	1.512	0.998	0.046 ± 0.030	0.122	0.007 ± 0.015	0.646	1.519	0.974	-0.046 ± 0.030	0.125	-0.002 ± 0.015	0.888	0.269	0.991	-0.044 ± 0.005	0.000	-0.005 ± 0.003	0.066

F.1.4 Solar radiation pressure mismodelling

Table F.14: Helmert parameters to the reference solution for the solar radiation pressure mismodelling case for DORIS. The reference is a combination of ENVISAT, Jason-1 and Jason-2.

	T_x [mm]	T_y [mm]	T_z [mm]	R_x [mm]	R_y [mm]	R_z [mm]	sc [mm]	s_0
	$T_{\dot{x}}$ [mm/a]	$T_{\dot{y}}$ [mm/a]	$T_{\dot{z}}$ [mm/a]	$R_{\dot{x}}$ [mm/a]	$R_{\dot{y}}$ [mm/a]	$R_{\dot{z}}$ [mm/a]	$\dot{sc}$ [mm/a]	s_0
Reference	0.00 ± 0.00	0.00 ± 0.00	0.00 ± 0.00	0.00 ± 0.00	0.00 ± 0.00	0.00 ± 0.00	0.00 ± 0.00	0.00
	0.00 ± 0.00	0.00 ± 0.00	0.00 ± 0.00	0.00 ± 0.00	0.00 ± 0.00	0.00 ± 0.00	0.00 ± 0.00	0.00
+ GRASP-like	-0.00 ± 0.00	0.00 ± 0.00	0.06 ± 0.00	0.05 ± 0.00	-0.02 ± 0.00	-0.05 ± 0.00	0.01 ± 0.00	0.01
	-0.00 ± 0.00	0.00 ± 0.00	0.01 ± 0.00	0.00 ± 0.00	-0.00 ± 0.00	-0.00 ± 0.00	0.00 ± 0.00	0.00
+ E-GRASP-mod	0.00 ± 0.00	0.01 ± 0.00	0.00 ± 0.00	-0.02 ± 0.00	0.01 ± 0.00	-0.00 ± 0.00	-0.00 ± 0.00	0.01
	0.00 ± 0.00	0.00 ± 0.00	0.00 ± 0.00	-0.00 ± 0.00	0.00 ± 0.00	-0.00 ± 0.00	-0.00 ± 0.00	0.00
+ E-GRASP-like	0.00 ± 0.00	0.00 ± 0.00	0.00 ± 0.00	-0.02 ± 0.00	0.01 ± 0.00	0.01 ± 0.00	0.00 ± 0.00	0.01
	0.00 ± 0.00	0.00 ± 0.00	0.00 ± 0.00	-0.00 ± 0.00	0.00 ± 0.00	0.00 ± 0.00	-0.00 ± 0.00	0.00
+ Circular 30°	0.00 ± 0.00	0.01 ± 0.00	0.01 ± 0.00	0.00 ± 0.00	0.00 ± 0.00	0.00 ± 0.00	0.00 ± 0.00	0.01
	0.00 ± 0.00	0.00 ± 0.00	0.00 ± 0.00	0.00 ± 0.00	0.00 ± 0.00	0.00 ± 0.00	0.00 ± 0.00	0.00
+ Circular 60°	0.00 ± 0.00	0.00 ± 0.00	0.00 ± 0.00	0.01 ± 0.00	-0.00 ± 0.00	0.00 ± 0.00	0.00 ± 0.00	0.01
	0.00 ± 0.00	0.00 ± 0.00	0.00 ± 0.00	0.00 ± 0.00	-0.00 ± 0.00	0.00 ± 0.00	0.00 ± 0.00	0.00
+ Circular 89°	-0.00 ± 0.00	0.00 ± 0.00	0.00 ± 0.00	0.00 ± 0.00	-0.00 ± 0.00	-0.00 ± 0.00	0.00 ± 0.00	0.01
	-0.00 ± 0.00	0.00 ± 0.00	0.00 ± 0.00	0.00 ± 0.00	-0.00 ± 0.00	-0.00 ± 0.00	0.00 ± 0.00	0.00

Table F.15: Formal errors for the DORIS SRP mismodelling case.

	σ_x & p-value		σ_y & p-value		σ_z & p-value		$\sigma_{\dot{x}}$ & p-value		$\sigma_{\dot{y}}$ & p-value		$\sigma_{\dot{z}}$ & p-value		σ_{x_p} & p-value		σ_{y_p} & p-value		σ_{LOD} & p-value		exp. imp.
	[mm]						[mm/dec]						[cm]				[μm]		[%]
GRASP-like	0.000001	-0.000	0.018120	-0.000	0.060420	0.000	0.183	0.000	0.196	-0.000	0.158	-0.000	0.138	0.000	0.137	0.000	0.285	0.000	-18.76
E-GRASP-mod	0.000001	-0.000	0.018090	0.001	0.039380	-0.000	0.185	0.000	0.182	-0.000	0.156	-0.000	0.147	-0.000	0.145	-0.000	0.234	-0.000	-38.10
E-GRASP-like	0.000001	0.000	0.019050	0.000	0.037550	-0.000	0.183	0.000	0.180	-0.000	0.157	-0.000	0.147	-0.000	0.146	-0.000	0.240	-0.000	-38.11
Circular 30°	0.000001	0.024	0.020590	0.010	0.033080	-0.000	0.177	-0.000	0.180	-0.000	0.182	-0.000	0.159	-0.000	0.157	-0.000	0.248	-0.000	-43.38
Circular 60°	0.000001	0.002	0.018090	0.001	0.035780	-0.000	0.192	-0.000	0.182	-0.000	0.158	-0.000	0.151	-0.000	0.149	-0.000	0.220	-0.000	-44.45
Circular 89°	0.000001	0.001	0.017230	0.001	0.037450	-0.000	0.192	0.000	0.186	0.000	0.149	-0.000	0.149	-0.000	0.145	-0.000	0.210	-0.000	-44.89

	$\sigma_{Lat.}$ & p-value		$\sigma_{Lon.}$ & p-value		σ_{Height}		$\sigma_{\dot{Lat.}}$ & p-value		$\sigma_{\dot{Lon.}}$ & p-value		$\sigma_{\dot{Height}}$ & p-value	
	[mm]						[mm/dec]					
GRASP-like	0.051455	-0.000	0.008770	0.000	0.035210	-0.000	0.159	-0.000	0.205	-0.000	0.183	-0.000
E-GRASP-mod	0.038526	-0.000	0.008614	0.001	0.024166	-0.000	0.154	-0.000	0.187	-0.000	0.178	-0.000
E-GRASP-like	0.036384	-0.000	0.008613	0.000	0.023390	-0.000	0.154	-0.000	0.184	-0.000	0.176	-0.000
Circular 30°	0.030492	-0.000	0.009717	0.010	0.021291	-0.000	0.174	-0.000	0.183	-0.000	0.182	-0.000
Circular 60°	0.034551	-0.000	0.008608	0.001	0.022666	-0.000	0.155	-0.000	0.192	-0.000	0.179	-0.000
Circular 89°	0.036340	-0.000	0.008198	0.001	0.022517	-0.000	0.152	-0.000	0.196	-0.000	0.180	-0.000

Table F.16: Statistics of estimated ERPs for the DORIS SRP mismodelling case.

	$\Delta X - Pole$						$\Delta Y - Pole$						ΔLOD					
	std. [mm]	p-value	mean ± std. [mm]	p-value	trend ± std. [mm/a]	p-value	std. [mm]	p-value	mean ± std. [mm]	p-value	trend ± std. [mm/a]	p-value	std. [μm]	p-value	mean ± std. [μm]	p-value	trend ± std. [μm/a]	p-value
Comb. reference																		
+ GRASP-like																		
- SRP mism.	1.381	0.237	0.050 ± 0.027	0.068	-0.001 ± 0.014	0.956	1.411	0.009	-0.024 ± 0.028	0.390	-0.006 ± 0.014	0.683	0.462	0.863	0.011 ± 0.009	0.219	0.007 ± 0.005	0.149
+ E-GRASP-mod																		
- SRP mism.	1.553	0.143	0.109 ± 0.031	0.000	0.007 ± 0.015	0.628	1.529	0.208	-0.016 ± 0.030	0.589	-0.003 ± 0.015	0.819	0.345	0.537	0.029 ± 0.007	0.000	0.002 ± 0.003	0.486
+ E-GRASP-like																		
- SRP mism.	1.547	0.044	0.037 ± 0.031	0.226	-0.012 ± 0.015	0.415	1.547	0.113	0.097 ± 0.031	0.002	0.017 ± 0.015	0.266	0.326	0.626	-0.019 ± 0.007	0.003	-0.003 ± 0.003	0.315
+ Circular 30°																		
- SRP mism.	1.626	0.770	0.006 ± 0.032	0.855	-0.009 ± 0.016	0.556	1.649	0.986	0.117 ± 0.033	0.000	0.010 ± 0.016	0.541	0.294	0.874	0.002 ± 0.006	0.733	0.002 ± 0.003	0.584
+ Circular 60°																		
- SRP mism.	1.575	0.492	0.139 ± 0.031	0.000	0.004 ± 0.015	0.786	1.573	0.687	-0.001 ± 0.031	0.971	0.002 ± 0.015	0.907	0.268	0.901	-0.039 ± 0.005	0.000	-0.001 ± 0.003	0.657
+ Circular 89°																		
- SRP mism.	1.526	0.752	0.038 ± 0.030	0.203	0.003 ± 0.015	0.833	1.538	0.752	-0.038 ± 0.030	0.209	0.001 ± 0.015	0.964	0.271	0.946	-0.045 ± 0.005	0.000	-0.005 ± 0.003	0.054

F.1.5 Ground beacon frequency bias mismodelling

Table F.17: Helmert parameters to the reference solution for the ground beacon frequency mismodelling case for DORIS. The reference is a combination of ENVISAT, Jason-1 and Jason-2.

	T_x [mm]	T_y [mm]	T_z [mm]	R_x [mm]	R_y [mm]	R_z [mm]	sc [mm]	s_0
	$\dot{T}_x$ [mm/a]	$\dot{T}_y$ [mm/a]	$\dot{T}_z$ [mm/a]	$\dot{R}_x$ [mm/a]	$\dot{R}_y$ [mm/a]	$\dot{R}_z$ [mm/a]	$\dot{sc}$ [mm/a]	$\dot{s}_0$
Reference	0.00 ± 0.00	0.00 ± 0.00	0.00 ± 0.00	0.00 ± 0.00	0.00 ± 0.00	0.00 ± 0.00	0.00 ± 0.00	0.00
	0.00 ± 0.00	0.00 ± 0.00	0.00 ± 0.00	0.00 ± 0.00	0.00 ± 0.00	0.00 ± 0.00	0.00 ± 0.00	0.00
+ GRASP-like	0.01 ± 0.01	-0.00 ± 0.01	0.03 ± 0.01	-0.06 ± 0.01	-0.01 ± 0.01	-0.01 ± 0.01	-0.10 ± 0.01	0.07
	0.00 ± 0.00	0.00 ± 0.00	0.00 ± 0.00	-0.00 ± 0.00	-0.00 ± 0.00	-0.00 ± 0.00	-0.01 ± 0.00	0.01
+ E-GRASP-mod	0.00 ± 0.01	0.01 ± 0.01	-0.02 ± 0.01	-0.13 ± 0.01	0.01 ± 0.01	0.06 ± 0.01	-0.12 ± 0.01	0.07
	0.00 ± 0.00	0.00 ± 0.00	-0.00 ± 0.00	-0.01 ± 0.00	0.00 ± 0.00	0.01 ± 0.00	-0.01 ± 0.00	0.01
+ E-GRASP-like	-0.00 ± 0.01	-0.00 ± 0.01	-0.02 ± 0.01	-0.13 ± 0.01	0.00 ± 0.01	0.02 ± 0.01	-0.08 ± 0.01	0.05
	-0.00 ± 0.00	0.00 ± 0.00	-0.00 ± 0.00	-0.01 ± 0.00	0.00 ± 0.00	0.00 ± 0.00	-0.01 ± 0.00	0.01
+ Circular 30°	-0.01 ± 0.01	-0.01 ± 0.01	-0.02 ± 0.01	-0.04 ± 0.01	-0.01 ± 0.01	0.05 ± 0.01	-0.08 ± 0.01	0.06
	-0.00 ± 0.00	-0.00 ± 0.00	-0.00 ± 0.00	-0.00 ± 0.00	-0.00 ± 0.00	0.01 ± 0.00	-0.01 ± 0.00	0.01
+ Circular 60°	-0.00 ± 0.01	-0.00 ± 0.01	-0.02 ± 0.01	-0.11 ± 0.01	-0.00 ± 0.01	0.01 ± 0.01	-0.10 ± 0.01	0.05
	-0.00 ± 0.00	-0.00 ± 0.00	-0.00 ± 0.00	-0.01 ± 0.00	0.00 ± 0.00	0.00 ± 0.00	-0.01 ± 0.00	0.01
+ Circular 89°	0.00 ± 0.01	-0.00 ± 0.01	-0.02 ± 0.01	-0.14 ± 0.01	0.02 ± 0.01	0.04 ± 0.01	-0.11 ± 0.01	0.06
	0.00 ± 0.00	0.00 ± 0.00	-0.00 ± 0.00	-0.01 ± 0.00	0.00 ± 0.00	0.00 ± 0.00	-0.01 ± 0.00	0.01

Table F.18: Formal errors for the DORIS ground beacon frequency bias case.

	σ_x & p-value		σ_y & p-value		σ_z & p-value		$\sigma_{\dot{x}}$ & p-value		$\sigma_{\dot{y}}$ & p-value		$\sigma_{\dot{z}}$ & p-value		σ_{x_p} & p-value		σ_{y_p} & p-value		σ_{LOD} & p-value		exp. imp.
	[mm]						[mm/dec]						[cm]				[μm]		[%]
GRASP-like	0.000001	-0.000	0.019420	-0.000	0.061290	0.000	0.187	0.000	0.200	-0.000	0.170	-0.000	0.144	0.000	0.144	0.000	0.288	0.000	-18.53
E-GRASP-mod	0.000001	-0.000	0.017410	0.001	0.040320	-0.000	0.190	0.000	0.181	-0.000	0.160	-0.000	0.153	-0.000	0.150	-0.000	0.238	-0.000	-38.01
E-GRASP-like	0.000001	0.000	0.018230	0.000	0.037900	-0.000	0.185	0.000	0.178	-0.000	0.161	-0.000	0.151	-0.000	0.149	-0.000	0.241	-0.000	-38.02
Circular 30°	0.000001	0.012	0.019650	0.005	0.033730	-0.000	0.182	-0.000	0.182	-0.000	0.179	-0.000	0.160	-0.583	0.158	-0.000	0.249	-0.000	-43.33
Circular 60°	0.000001	0.000	0.016680	0.000	0.036070	-0.000	0.195	0.000	0.183	-0.000	0.160	-0.000	0.154	-0.000	0.151	-0.000	0.223	-0.000	-44.40
Circular 89°	0.000001	0.000	0.016140	0.000	0.037850	-0.000	0.195	0.000	0.184	-0.000	0.154	-0.000	0.152	-0.000	0.149	-0.000	0.213	-0.000	-44.84

	$\sigma_{Lat.}$ & p-value		$\sigma_{Lon.}$ & p-value		σ_{Height}		$\sigma_{\dot{Lat.}}$ & p-value		$\sigma_{\dot{Lon.}}$ & p-value		$\sigma_{\dot{Height}}$ & p-value	
	[mm]						[mm/dec]					
GRASP-like	0.051797	-0.000	0.009313	0.000	0.035661	-0.000	0.170	-0.000	0.212	-0.000	0.188	-0.000
E-GRASP-mod	0.038429	-0.000	0.008270	0.001	0.024346	-0.000	0.158	-0.000	0.202	-0.000	0.180	-0.000
E-GRASP-like	0.036573	-0.000	0.008287	0.000	0.023372	-0.000	0.156	-0.000	0.198	-0.000	0.180	-0.000
Circular 30°	0.031218	-0.000	0.009272	0.005	0.021390	-0.000	0.172	-0.000	0.190	-0.000	0.184	-0.000
Circular 60°	0.034610	-0.000	0.007911	0.000	0.022467	-0.000	0.159	-0.000	0.193	-0.000	0.182	-0.000
Circular 89°	0.035695	-0.000	0.007653	0.000	0.022521	-0.000	0.156	-0.000	0.196	0.000	0.182	-0.000

Table F.19: Statistics of estimated ERPs for the DORIS frequency bias mismodelling case.

	$\Delta X - Pole$						$\Delta Y - Pole$						ΔLOD					
	std. [mm]	p-value	mean ± std. [mm]	p-value	trend ± std. [mm/a]	p-value	std. [mm]	p-value	mean ± std. [mm]	p-value	trend ± std. [mm/a]	p-value	std. [μm]	p-value	mean ± std. [μm]	p-value	trend ± std. [μm/a]	p-value
Comb. reference																		
+ GRASP-like																		
- Fq. bias mismodelling	1.559	0.000	0.073 ± 0.031	0.018	0.003 ± 0.015	0.858	1.600	0.000	-0.157 ± 0.032	0.000	-0.018 ± 0.016	0.259	0.482	0.008	-0.045 ± 0.010	0.000	0.000 ± 0.005	0.993
+ E-GRASP-mod																		
- Fq. bias mismodelling	1.598	0.013	0.132 ± 0.032	0.000	0.007 ± 0.016	0.639	1.597	0.003	-0.134 ± 0.032	0.000	-0.013 ± 0.016	0.394	0.333	0.286	-0.002 ± 0.007	0.710	-0.000 ± 0.003	0.935
+ E-GRASP-like																		
- Fq. bias mismodelling	1.604	0.000	0.043 ± 0.032	0.178	-0.006 ± 0.016	0.686	1.595	0.002	-0.031 ± 0.032	0.324	0.001 ± 0.016	0.954	0.332	0.457	-0.020 ± 0.007	0.003	-0.003 ± 0.003	0.430
+ Circular 30°																		
- Fq. bias mismodelling	1.644	0.465	0.001 ± 0.033	0.967	-0.006 ± 0.016	0.698	1.680	0.553	0.065 ± 0.033	0.051	0.005 ± 0.016	0.753	0.298	0.748	-0.009 ± 0.006	0.151	0.001 ± 0.003	0.682
+ Circular 60°																		
- Fq. bias mismodelling	1.608	0.122	0.132 ± 0.032	0.000	0.003 ± 0.016	0.873	1.620	0.115	-0.144 ± 0.032	0.000	-0.009 ± 0.016	0.554	0.261	0.175	-0.031 ± 0.005	0.000	-0.001 ± 0.003	0.770
+ Circular 89°																		
- Fq. bias mismodelling	1.584	0.062	0.063 ± 0.031	0.046	0.006 ± 0.016	0.706	1.588	0.091	-0.189 ± 0.031	0.000	-0.012 ± 0.016	0.433	0.284	0.009	-0.067 ± 0.006	0.000	-0.007 ± 0.003	0.011

F.1.6 Earth gravity field mismodelling

Table F.20: Helmert parameters to the reference solution for the EGM mismodelling case, either fixed or solved for, in the case of DORIS. The reference is a combination of ENVISAT, Jason-1 and Jason-2.

	T_x [mm] $T_{\dot{x}}$ [mm/a]	T_y [mm] $T_{\dot{y}}$ [mm/a]	T_z [mm] $T_{\dot{z}}$ [mm/a]	R_x [mm] $R_{\dot{x}}$ [mm/a]	R_y [mm] $R_{\dot{y}}$ [mm/a]	R_z [mm] $R_{\dot{z}}$ [mm/a]	sc [mm] $\dot{sc}$ [mm/a]	s_0 s_0
Reference	0.00 ± 0.00	0.00 ± 0.00	0.00 ± 0.00	0.00 ± 0.00	0.00 ± 0.00	0.00 ± 0.00	0.00 ± 0.00	0.00
	0.00 ± 0.00	0.00 ± 0.00	0.00 ± 0.00	0.00 ± 0.00	0.00 ± 0.00	0.00 ± 0.00	0.00 ± 0.00	0.00
+ GRASP-like								
- EGM mism.	0.83 ± 0.13	2.14 ± 0.13	1.81 ± 0.13	-0.61 ± 0.16	-1.42 ± 0.16	-0.31 ± 0.16	-0.13 ± 0.13	0.99
	0.08 ± 0.01	0.21 ± 0.01	0.17 ± 0.01	-0.06 ± 0.02	-0.14 ± 0.02	-0.04 ± 0.02	-0.00 ± 0.01	0.11
- EGM mism. and co-est.	0.00 ± 0.01	0.01 ± 0.01	0.05 ± 0.01	0.07 ± 0.01	-0.02 ± 0.01	-0.07 ± 0.01	0.02 ± 0.01	0.08
	0.00 ± 0.00	-0.00 ± 0.00	0.01 ± 0.00	0.01 ± 0.00	-0.00 ± 0.00	-0.01 ± 0.00	0.00 ± 0.00	0.01
+ E-GRASP-mod								
- EGM mism.	0.12 ± 0.01	-0.31 ± 0.01	-0.27 ± 0.01	0.01 ± 0.01	0.21 ± 0.01	-0.12 ± 0.01	0.01 ± 0.01	0.09
	0.01 ± 0.00	-0.03 ± 0.00	-0.03 ± 0.00	0.00 ± 0.00	0.02 ± 0.00	-0.01 ± 0.00	0.00 ± 0.00	0.01
- EGM mism. and co-est.	0.01 ± 0.00	0.01 ± 0.00	0.00 ± 0.00	-0.02 ± 0.01	0.02 ± 0.01	0.00 ± 0.01	-0.02 ± 0.00	0.03
	0.00 ± 0.00	0.00 ± 0.00	0.00 ± 0.00	-0.00 ± 0.00	0.00 ± 0.00	0.00 ± 0.00	-0.00 ± 0.00	0.00
+ E-GRASP-like								
- EGM mism.	0.16 ± 0.03	-0.34 ± 0.03	-0.29 ± 0.03	-0.05 ± 0.04	0.19 ± 0.04	-0.22 ± 0.04	-0.00 ± 0.03	0.23
	0.02 ± 0.00	-0.03 ± 0.00	-0.03 ± 0.00	-0.01 ± 0.00	0.02 ± 0.00	-0.02 ± 0.00	-0.00 ± 0.00	0.03
- EGM mism. and co-est.	0.00 ± 0.01	0.02 ± 0.01	0.02 ± 0.01	-0.01 ± 0.01	0.01 ± 0.01	0.03 ± 0.01	-0.01 ± 0.01	0.07
	0.00 ± 0.00	0.01 ± 0.00	0.00 ± 0.00	-0.00 ± 0.00	0.00 ± 0.00	0.00 ± 0.00	-0.00 ± 0.00	0.02
+ Circular 30°								
- EGM mism.	0.00 ± 0.00	0.01 ± 0.00	0.01 ± 0.00	0.00 ± 0.00	0.01 ± 0.00	0.00 ± 0.00	-0.00 ± 0.00	0.02
	0.00 ± 0.00	0.00 ± 0.00	0.00 ± 0.00	-0.00 ± 0.00	0.00 ± 0.00	0.00 ± 0.00	-0.00 ± 0.00	0.00
- EGM mism. and co-est.	-0.01 ± 0.00	-0.00 ± 0.00	-0.00 ± 0.00	0.00 ± 0.00	-0.01 ± 0.00	-0.00 ± 0.00	0.01 ± 0.00	0.02
	-0.00 ± 0.00	-0.00 ± 0.00	-0.00 ± 0.00	0.00 ± 0.00	-0.00 ± 0.00	-0.00 ± 0.00	0.00 ± 0.00	0.00
+ Circular 60°								
- EGM mism.	0.02 ± 0.00	-0.01 ± 0.00	-0.01 ± 0.00	0.01 ± 0.00	0.03 ± 0.00	0.00 ± 0.00	0.00 ± 0.00	0.02
	0.00 ± 0.00	-0.00 ± 0.00	-0.00 ± 0.00	0.00 ± 0.00	0.00 ± 0.00	0.00 ± 0.00	0.00 ± 0.00	0.00
- EGM mism. and co-est.	0.00 ± 0.00	-0.00 ± 0.00	-0.00 ± 0.00	-0.01 ± 0.00	0.00 ± 0.00	-0.00 ± 0.00	0.00 ± 0.00	0.01
	0.00 ± 0.00	0.00 ± 0.00	-0.00 ± 0.00	-0.00 ± 0.00	0.00 ± 0.00	-0.00 ± 0.00	0.00 ± 0.00	0.00
+ Circular 89°								
- EGM mism.	0.00 ± 0.00	0.01 ± 0.00	0.01 ± 0.00	0.00 ± 0.00	0.00 ± 0.00	0.01 ± 0.00	-0.00 ± 0.00	0.01
	0.00 ± 0.00	0.00 ± 0.00	0.00 ± 0.00	0.00 ± 0.00	0.00 ± 0.00	0.00 ± 0.00	-0.00 ± 0.00	0.00
- EGM mism. and co-est.	0.00 ± 0.00	-0.00 ± 0.00	-0.00 ± 0.00	-0.01 ± 0.00	0.01 ± 0.00	-0.00 ± 0.00	0.00 ± 0.00	0.01
	0.00 ± 0.00	-0.00 ± 0.00	-0.00 ± 0.00	-0.00 ± 0.00	0.00 ± 0.00	-0.00 ± 0.00	0.00 ± 0.00	0.00

Table F.21: Formal errors for the DORIS EGM mismodelling case.

	σ_x & p-value		σ_y & p-value		σ_z & p-value		$\sigma_{\dot{x}}$ & p-value		$\sigma_{\dot{y}}$ & p-value		$\sigma_{\dot{z}}$ & p-value		σ_{x_p} & p-value		σ_{y_p} & p-value		σ_{LOD} & p-value		exp. imp.
	[mm]		[mm]		[mm]		[mm/dec]		[mm/dec]		[mm/dec]		[cm]		[cm]		[μm]		[%]
GRASP-like	0.000001	-0.000	0.019990	-0.000	0.065460	0.000	0.197	0.000	0.211	-0.000	0.174	-0.000	0.143	-0.000	0.142	-0.000	0.308	-0.000	-14.79
E-GRASP-mod	0.000001	-0.000	0.018120	0.002	0.039430	-0.000	0.185	0.000	0.183	-0.000	0.156	-0.000	0.151	-0.000	0.149	-0.000	0.236	-0.000	-38.10
E-GRASP-like	0.000001	0.000	0.019080	0.000	0.037590	-0.000	0.184	0.000	0.180	-0.000	0.157	-0.000	0.152	-0.000	0.150	-0.000	0.242	-0.000	-38.11
Circular 30°	0.000001	0.024	0.020600	0.010	0.033130	-0.000	0.177	-0.000	0.180	-0.000	0.182	-0.000	0.159	-0.000	0.157	-0.000	0.249	-0.000	-43.38
Circular 60°	0.000001	0.002	0.018100	0.001	0.035800	-0.000	0.193	-0.000	0.182	-0.000	0.158	-0.000	0.153	-0.000	0.150	-0.000	0.222	-0.000	-44.45
Circular 89°	0.000001	0.001	0.017250	0.001	0.037470	-0.000	0.192	0.000	0.187	0.000	0.149	-0.000	0.150	-0.000	0.147	-0.000	0.211	-0.000	-44.90

	$\sigma_{Lat.}$ & p-value		$\sigma_{Lon.}$ & p-value		σ_{Height}	$\sigma_{\dot{Lat.}}$ & p-value		$\sigma_{\dot{Lon.}}$ & p-value		$\sigma_{\dot{Height}}$ & p-value	
	[mm]		[mm]			[mm/dec]		[mm/dec]		[mm/dec]	
GRASP-like	0.062760	-0.000	0.009649	0.000	0.037986	-0.000	0.172	-0.000	0.219	-0.000	0.197	-0.000
E-GRASP-mod	0.038563	-0.000	0.008633	0.002	0.024201	-0.000	0.154	-0.000	0.188	-0.000	0.178	-0.000
E-GRASP-like	0.036445	-0.000	0.008626	0.000	0.023413	-0.000	0.154	-0.000	0.184	-0.000	0.177	-0.000
Circular 30°	0.030560	-0.000	0.009727	0.010	0.021300	-0.000	0.174	-0.000	0.183	-0.000	0.182	-0.000
Circular 60°	0.034570	-0.000	0.008615	0.001	0.022682	-0.000	0.155	-0.000	0.192	-0.000	0.180	-0.000
Circular 89°	0.036357	-0.000	0.008206	0.001	0.022540	-0.000	0.152	-0.000	0.196	-0.000	0.181	-0.000

Table F.22: Formal errors for the DORIS EGM mismodelling case, SHs estimated.

	σ_x & p-value		σ_y & p-value		σ_z & p-value		$\sigma_{\dot{x}}$ & p-value		$\sigma_{\dot{y}}$ & p-value		$\sigma_{\dot{z}}$ & p-value		σ_{x_p} & p-value		σ_{y_p} & p-value		σ_{LOD} & p-value		exp. imp.
	[mm]						[mm/dec]						[cm]				[μm]		[%]
GRASP-like	0.000001	-0.000	0.018240	-0.000	0.061120	0.000	0.200	0.000	0.211	-0.000	0.169	-0.000	0.142	0.000	0.141	0.000	0.286	0.000	-18.77
E-GRASP-mod	0.000001	-0.000	0.018170	0.002	0.039640	-0.000	0.191	0.000	0.189	-0.000	0.159	-0.000	0.151	-0.000	0.149	-0.000	0.236	-0.000	-38.10
E-GRASP-like	0.000001	0.000	0.019180	0.000	0.038030	-0.000	0.192	0.000	0.193	-0.000	0.161	-0.000	0.152	-0.000	0.150	-0.000	0.242	-0.000	-38.11
Circular 30°	0.000001	0.024	0.020600	0.010	0.033270	-0.000	0.179	-0.000	0.181	-0.000	0.183	-0.000	0.159	-0.000	0.157	-0.000	0.249	-0.000	-43.38
Circular 60°	0.000001	0.002	0.018100	0.001	0.035910	-0.000	0.195	-0.000	0.183	-0.000	0.159	-0.000	0.153	-0.000	0.150	-0.000	0.222	-0.000	-44.45
Circular 89°	0.000001	0.001	0.017250	0.001	0.037510	-0.000	0.193	0.000	0.187	0.000	0.150	-0.000	0.150	-0.000	0.147	-0.000	0.211	-0.000	-44.89

	$\sigma_{Lat.}$ & p-value		$\sigma_{Lon.}$ & p-value		σ_{Height}	$\sigma_{\dot{Lat.}}$ & p-value		$\sigma_{\dot{Lon.}}$ & p-value		$\sigma_{\dot{Height}}$ & p-value	
	[mm]					[mm/dec]					
GRASP-like	0.052341	-0.000	0.008821	0.000	0.035621	-0.000	0.171	-0.000	0.218	-0.000	0.198	-0.000
E-GRASP-mod	0.038787	-0.000	0.008655	0.002	0.024280	-0.000	0.156	-0.000	0.193	-0.000	0.180	-0.000
E-GRASP-like	0.036617	-0.000	0.008665	0.000	0.023572	-0.000	0.157	-0.000	0.196	-0.000	0.187	-0.000
Circular 30°	0.030781	-0.000	0.009727	0.010	0.021331	-0.000	0.175	-0.000	0.186	-0.000	0.184	-0.000
Circular 60°	0.034663	-0.000	0.008615	0.001	0.022709	-0.000	0.156	-0.000	0.193	-0.000	0.181	-0.000
Circular 89°	0.036391	-0.000	0.008206	0.001	0.022562	-0.000	0.152	-0.000	0.196	-0.000	0.182	-0.000

Table F.23: Statistics of estimated ERPs for the DORIS EGM mismodelling case.

	$\Delta X - Pole$						$\Delta Y - Pole$						ΔLOD					
	std. [mm]	p-value	mean ± std. [mm]	p-value	trend ± std. [mm/a]	p-value	std. [mm]	p-value	mean ± std. [mm]	p-value	trend ± std. [mm/a]	p-value	std. [μm]	p-value	mean ± std. [μm]	p-value	trend ± std. [μm/a]	p-value
Comb. reference																		
+ GRASP-like																		
- EGM mism.	2.281	0.000	-0.592 ± 0.045	0.000	0.009 ± 0.022	0.686	2.236	0.000	-2.237 ± 0.044	0.000	0.005 ± 0.022	0.825	1.033	0.000	0.350 ± 0.021	0.000	0.047 ± 0.011	0.000
- EGM mism. and co-est.	1.494	0.000	0.031 ± 0.030	0.302	0.001 ± 0.015	0.962	1.538	0.000	-0.011 ± 0.030	0.725	-0.004 ± 0.015	0.803	0.472	0.472	0.018 ± 0.010	0.063	0.007 ± 0.005	0.154
+ E-GRASP-mod																		
- EGM mism.	1.611	0.005	0.055 ± 0.032	0.082	-0.018 ± 0.016	0.255	1.609	0.003	0.101 ± 0.032	0.002	0.007 ± 0.016	0.647	0.366	0.000	0.041 ± 0.007	0.000	0.003 ± 0.004	0.472
- EGM mism. and co-est.	1.584	0.024	0.119 ± 0.031	0.000	0.003 ± 0.016	0.868	1.581	0.016	-0.019 ± 0.031	0.542	-0.004 ± 0.015	0.821	0.344	0.182	0.030 ± 0.007	0.000	0.003 ± 0.003	0.336
+ E-GRASP-like																		
- EGM mism.	1.615	0.000	0.012 ± 0.032	0.714	-0.029 ± 0.016	0.071	1.629	0.000	0.139 ± 0.032	0.000	0.025 ± 0.016	0.120	0.374	0.287	-0.003 ± 0.007	0.669	-0.006 ± 0.004	0.120
- EGM mism. and co-est.	1.603	0.000	0.040 ± 0.032	0.202	-0.005 ± 0.016	0.731	1.621	0.000	0.102 ± 0.032	0.002	0.015 ± 0.016	0.331	0.337	0.147	-0.036 ± 0.007	0.000	-0.005 ± 0.003	0.158
+ Circular 30°																		
- EGM mism.	1.631	0.631	0.001 ± 0.032	0.985	-0.009 ± 0.016	0.583	1.665	0.795	0.119 ± 0.033	0.000	0.011 ± 0.016	0.495	0.340	0.698	0.005 ± 0.007	0.434	-0.001 ± 0.003	0.856
- EGM mism. and co-est.	1.632	0.617	-0.002 ± 0.032	0.958	-0.008 ± 0.016	0.603	1.663	0.831	0.120 ± 0.033	0.000	0.012 ± 0.016	0.471	0.295	0.936	0.005 ± 0.006	0.363	0.002 ± 0.003	0.460
+ Circular 60°																		
- EGM mism.	1.585	0.336	0.121 ± 0.031	0.000	-0.004 ± 0.016	0.805	1.592	0.404	0.016 ± 0.032	0.615	0.005 ± 0.016	0.738	0.274	0.577	-0.045 ± 0.005	0.000	-0.003 ± 0.003	0.359
- EGM mism. and co-est.	1.585	0.320	0.131 ± 0.031	0.000	0.000 ± 0.016	0.985	1.594	0.377	-0.023 ± 0.032	0.460	0.002 ± 0.016	0.900	0.275	0.403	-0.045 ± 0.006	0.000	-0.002 ± 0.003	0.391
+ Circular 89°																		
- EGM mism.	1.554	0.320	0.031 ± 0.031	0.308	-0.002 ± 0.015	0.914	1.556	0.408	-0.027 ± 0.031	0.373	0.000 ± 0.015	0.990	0.268	0.787	-0.044 ± 0.005	0.000	-0.005 ± 0.003	0.052
- EGM mism. and co-est.	1.555	0.303	0.036 ± 0.031	0.240	-0.001 ± 0.015	0.924	1.556	0.410	-0.045 ± 0.031	0.144	-0.001 ± 0.015	0.927	0.268	0.726	-0.042 ± 0.005	0.000	-0.005 ± 0.003	0.060

F.2 SLR

F.2.1 Systematic error-free

Table F.24: Helmert parameters to a priori for the systematic error-free scenarios for SLR.
The reference is a combination of LAGEOS-1 and LAGEOS-2.

	T_x [mm] $T_{\dot{x}}$ [mm/a]	T_y [mm] $T_{\dot{y}}$ [mm/a]	T_z [mm] $T_{\dot{z}}$ [mm/a]	R_x [mm] $R_{\dot{x}}$ [mm/a]	R_y [mm] $R_{\dot{y}}$ [mm/a]	R_z [mm] $R_{\dot{z}}$ [mm/a]	sc [mm] $\dot{sc}$ [mm/a]	s_0 s_0
Reference	-0.14 ± 0.29	0.13 ± 0.30	0.24 ± 0.29	-0.52 ± 0.36	-0.44 ± 0.35	-0.94 ± 0.34	-0.23 ± 0.28	1.49
	0.03 ± 0.13	0.02 ± 0.13	-0.10 ± 0.13	0.20 ± 0.16	-0.02 ± 0.16	0.02 ± 0.15	0.05 ± 0.13	0.67
+ GRASP-like	-0.08 ± 0.23	-0.01 ± 0.23	0.25 ± 0.22	-0.67 ± 0.28	-0.33 ± 0.27	-0.96 ± 0.26	-0.17 ± 0.22	1.15
	0.01 ± 0.07	0.01 ± 0.07	-0.09 ± 0.07	0.10 ± 0.08	-0.02 ± 0.08	-0.01 ± 0.08	0.04 ± 0.06	0.34
+ E-GRASP-mod	-0.05 ± 0.28	0.06 ± 0.29	0.18 ± 0.27	-0.86 ± 0.35	-0.31 ± 0.34	-0.93 ± 0.32	-0.20 ± 0.27	1.43
	-0.01 ± 0.10	0.02 ± 0.10	-0.07 ± 0.10	0.15 ± 0.13	0.02 ± 0.12	0.00 ± 0.12	0.05 ± 0.10	0.52
+ E-GRASP-like	-0.10 ± 0.26	0.13 ± 0.27	0.02 ± 0.25	-0.36 ± 0.32	-0.09 ± 0.31	-0.95 ± 0.30	-0.08 ± 0.25	1.33
	0.03 ± 0.09	0.01 ± 0.09	-0.00 ± 0.09	0.09 ± 0.11	0.05 ± 0.11	0.03 ± 0.11	0.02 ± 0.09	0.47
+ Circular 30°	0.06 ± 0.23	0.06 ± 0.23	0.18 ± 0.22	-0.59 ± 0.28	-0.71 ± 0.27	-0.68 ± 0.26	-0.17 ± 0.22	1.17
	-0.07 ± 0.11	0.04 ± 0.11	-0.08 ± 0.11	0.16 ± 0.14	0.08 ± 0.13	-0.10 ± 0.13	0.03 ± 0.11	0.57
+ Circular 60°	-0.15 ± 0.24	0.13 ± 0.24	0.25 ± 0.23	-0.76 ± 0.29	-0.18 ± 0.28	-0.97 ± 0.27	-0.20 ± 0.23	1.20
	0.07 ± 0.10	0.01 ± 0.10	-0.07 ± 0.09	0.15 ± 0.12	-0.03 ± 0.12	0.08 ± 0.11	0.02 ± 0.09	0.49
+ Circular 89°	-0.14 ± 0.24	0.16 ± 0.24	0.18 ± 0.23	-0.38 ± 0.29	-0.52 ± 0.28	-1.11 ± 0.27	-0.17 ± 0.23	1.19
	0.06 ± 0.11	0.04 ± 0.11	-0.09 ± 0.11	0.15 ± 0.13	-0.09 ± 0.13	0.06 ± 0.12	0.06 ± 0.10	0.55

Table F.25: Formal errors for the systematic error-free scenarios for SLR. The reference is a combination of LAGEOS-1 and LAGEOS-2.

	σ_x & p-value		σ_y & p-value		σ_z & p-value		$\sigma_{\dot{x}}$ & p-value		$\sigma_{\dot{y}}$ & p-value		$\sigma_{\dot{z}}$ & p-value		σ_{x_p} & p-value		σ_{y_p} & p-value		σ_{LOD} & p-value		exp. imp.
	[mm]						[mm/dec]						[mm]				[mm]		[%]
Reference	1.039	—	1.055	—	1.022	—	1.255	—	1.239	—	1.224	—	1.863	—	1.877	—	2.604	—	—
GRASP-like	0.995	-0.000	0.989	-0.000	0.922	-0.000	1.147	-0.000	1.073	-0.000	1.087	-0.000	1.556	0.000	1.584	0.000	2.037	0.000	-18.88
E-GRASP-mod	1.003	-0.000	1.000	-0.000	0.933	-0.000	1.146	-0.000	1.076	-0.000	1.089	-0.000	1.595	-0.000	1.607	-0.000	2.040	-0.000	-20.36
E-GRASP-like	0.996	-0.000	0.995	-0.000	0.931	-0.000	1.136	-0.000	1.069	-0.000	1.090	-0.000	1.585	-0.000	1.604	-0.000	2.019	-0.000	-20.65
Circular 30°	1.005	-0.000	1.003	-0.000	0.980	-0.000	1.137	-0.000	1.065	-0.000	1.143	-0.000	1.634	-0.000	1.664	-0.000	1.981	-0.000	-19.19
Circular 60°	1.008	-0.000	1.009	-0.000	0.950	-0.000	1.150	-0.000	1.084	-0.000	1.095	-0.000	1.642	-0.000	1.652	-0.000	2.057	-0.000	-19.57
Circular 89°	1.010	-0.000	1.012	-0.000	0.950	-0.000	1.165	-0.000	1.083	-0.000	1.088	-0.000	1.582	-0.000	1.642	-0.000	2.113	-0.000	-19.56

	$\sigma_{Lat.}$ & p-value		$\sigma_{Lon.}$ & p-value		σ_{Height}		$\sigma_{\dot{Lat.}}$ & p-value		$\sigma_{\dot{Lon.}}$ & p-value		$\sigma_{\dot{Height}}$ & p-value	
	[mm]						[mm/dec]					
Reference	1.017	—	1.095	—	0.966	—	1.239	—	1.261	—	1.167	—
GRASP-like	0.899	-0.000	1.013	-0.000	0.869	-0.000	1.098	-0.000	1.124	-0.000	1.021	-0.000
E-GRASP-mod	0.909	-0.000	1.025	-0.000	0.871	-0.000	1.100	-0.000	1.125	-0.000	1.016	-0.000
E-GRASP-like	0.906	-0.000	1.018	-0.000	0.866	-0.000	1.097	-0.000	1.118	-0.000	0.994	-0.000
Circular 30°	0.938	-0.000	1.018	-0.000	0.850	-0.000	1.121	-0.000	1.125	-0.000	0.968	-0.000
Circular 60°	0.923	-0.000	1.034	-0.000	0.884	-0.000	1.103	-0.000	1.132	-0.000	1.017	-0.000
Circular 89°	0.921	-0.000	1.040	-0.000	0.887	-0.000	1.102	-0.000	1.143	-0.000	1.024	-0.000

Table F.26: Statistics for ERPs by adding space-tie satellit scenarios in the SLR systematic error-free case.

	$\Delta X - Pole$						$\Delta Y - Pole$						ΔLOD					
	std. [mm]	p-value	mean $\pm$ std. [mm]	p-value	trend $\pm$ std. [mm/a]	p-value	std. [mm]	p-value	mean $\pm$ std. [mm]	p-value	trend $\pm$ std. [mm/a]	p-value	std. [mm]	p-value	mean $\pm$ std. [mm]	p-value	trend $\pm$ std. [mm/a]	p-value
LAG.-1+LAG.-2																		
- sys. error-free	1.463	NaN	0.601 $\pm$ 0.029	0.000	-0.003 $\pm$ 0.014	0.817	1.578	NaN	0.372 $\pm$ 0.031	0.000	0.056 $\pm$ 0.015	0.000	2.912	NaN	0.033 $\pm$ 0.058	0.570	0.003 $\pm$ 0.029	0.929
+ GRASP like																		
- sys. error-free	1.122	0.000	0.413 $\pm$ 0.022	0.000	-0.023 $\pm$ 0.011	0.038	1.215	0.000	0.429 $\pm$ 0.024	0.000	0.038 $\pm$ 0.012	0.001	2.268	0.000	0.005 $\pm$ 0.045	0.905	-0.002 $\pm$ 0.022	0.939
+ E-GRASP-mod																		
- sys. error-free	1.136	0.000	0.461 $\pm$ 0.022	0.000	-0.018 $\pm$ 0.011	0.098	1.193	0.000	0.671 $\pm$ 0.024	0.000	0.052 $\pm$ 0.012	0.000	2.218	0.000	0.003 $\pm$ 0.044	0.950	-0.004 $\pm$ 0.022	0.864
+ E-GRASP-like																		
- sys. error-free	1.104	0.000	0.057 $\pm$ 0.022	0.009	-0.034 $\pm$ 0.011	0.001	1.221	0.000	0.404 $\pm$ 0.024	0.000	0.044 $\pm$ 0.012	0.000	2.237	0.000	0.005 $\pm$ 0.044	0.912	-0.002 $\pm$ 0.022	0.937
+ Circular 30°																		
- sys. error-free	1.151	0.000	0.659 $\pm$ 0.023	0.000	0.003 $\pm$ 0.011	0.770	1.241	0.000	0.480 $\pm$ 0.024	0.000	0.049 $\pm$ 0.012	0.000	2.138	0.000	0.011 $\pm$ 0.042	0.798	-0.008 $\pm$ 0.021	0.689
+ Circular 60°																		
- sys. error-free	1.162	0.000	0.379 $\pm$ 0.023	0.000	-0.017 $\pm$ 0.011	0.128	1.217	0.000	0.608 $\pm$ 0.024	0.000	0.044 $\pm$ 0.012	0.000	2.257	0.000	0.047 $\pm$ 0.045	0.289	-0.006 $\pm$ 0.022	0.778
+ Circular 89°																		
- sys. error-free	1.056	0.000	0.574 $\pm$ 0.021	0.000	-0.014 $\pm$ 0.010	0.180	1.199	0.000	0.408 $\pm$ 0.024	0.000	0.045 $\pm$ 0.012	0.000	2.322	0.000	0.023 $\pm$ 0.046	0.620	-0.002 $\pm$ 0.023	0.931

F.2.2 Influence of systematic center-of-mass displacement

Table F.27: Helmert parameters to the reference solution for introducing a CoM displacement to the space-tie satellite of 5mm, either fixed or solved for, in the case of SLR. The reference is a combination of LAGEOS-1 and LAGEOS-2.

	T_x [mm]	T_y [mm]	T_z [mm]	R_x [mm]	R_y [mm]	R_z [mm]	sc [mm]	s_0
	$T_{\dot{x}}$ [mm/a]	$T_{\dot{y}}$ [mm/a]	$T_{\dot{z}}$ [mm/a]	$R_{\dot{x}}$ [mm/a]	$R_{\dot{y}}$ [mm/a]	$R_{\dot{z}}$ [mm/a]	$\dot{sc}$ [mm/a]	$\dot{s}_0$
Reference	0.00 ± 0.00	0.00 ± 0.00	0.00 ± 0.00	0.00 ± 0.00	0.00 ± 0.00	0.00 ± 0.00	0.00 ± 0.00	0.00
	0.00 ± 0.00	0.00 ± 0.00	0.00 ± 0.00	0.00 ± 0.00	0.00 ± 0.00	0.00 ± 0.00	0.00 ± 0.00	0.00
+ GRASP-like	0.00 ± 0.06	-0.09 ± 0.06	0.70 ± 0.05	-7.41 ± 0.07	6.92 ± 0.07	-0.00 ± 0.06	-1.16 ± 0.05	0.29
	-0.00 ± 0.03	-0.02 ± 0.03	-0.09 ± 0.03	-0.42 ± 0.04	0.32 ± 0.04	-0.02 ± 0.04	-0.02 ± 0.03	0.16
+ E-GRASP-mod	0.17 ± 0.06	-0.01 ± 0.06	-1.87 ± 0.06	1.71 ± 0.07	-4.89 ± 0.07	0.16 ± 0.07	-0.94 ± 0.06	0.30
	0.02 ± 0.02	-0.01 ± 0.02	-0.04 ± 0.02	0.10 ± 0.03	-0.23 ± 0.02	0.01 ± 0.02	-0.02 ± 0.02	0.10
+ E-GRASP-like	0.21 ± 0.07	-0.02 ± 0.07	-1.78 ± 0.07	2.16 ± 0.09	-4.65 ± 0.08	0.23 ± 0.08	-0.67 ± 0.07	0.35
	0.01 ± 0.02	-0.02 ± 0.02	-0.06 ± 0.02	0.10 ± 0.03	-0.20 ± 0.03	0.01 ± 0.03	-0.03 ± 0.02	0.11
+ Circular 30°	0.21 ± 0.11	0.29 ± 0.11	-0.58 ± 0.11	0.63 ± 0.14	-0.59 ± 0.14	-0.07 ± 0.13	-0.89 ± 0.11	0.58
	0.01 ± 0.01	0.01 ± 0.01	0.05 ± 0.01	0.07 ± 0.01	-0.02 ± 0.01	0.00 ± 0.01	-0.03 ± 0.01	0.05
+ Circular 60°	0.12 ± 0.05	0.06 ± 0.05	-1.04 ± 0.05	0.44 ± 0.06	-2.43 ± 0.06	0.03 ± 0.06	-1.30 ± 0.05	0.27
	0.01 ± 0.02	-0.02 ± 0.02	-0.02 ± 0.02	0.03 ± 0.03	-0.13 ± 0.03	-0.01 ± 0.03	-0.03 ± 0.02	0.12
+ Circular 89°	0.12 ± 0.08	0.08 ± 0.08	-1.15 ± 0.07	-0.58 ± 0.09	-2.65 ± 0.09	-0.04 ± 0.09	-1.20 ± 0.07	0.38
	0.01 ± 0.03	-0.03 ± 0.03	-0.08 ± 0.03	-0.04 ± 0.04	-0.13 ± 0.04	0.00 ± 0.04	-0.03 ± 0.03	0.16
Reference	0.00 ± 0.00	0.00 ± 0.00	0.00 ± 0.00	0.00 ± 0.00	0.00 ± 0.00	0.00 ± 0.00	0.00 ± 0.00	0.00
	0.00 ± 0.00	0.00 ± 0.00	0.00 ± 0.00	0.00 ± 0.00	0.00 ± 0.00	0.00 ± 0.00	0.00 ± 0.00	0.00
+ GRASP-like CoM est.	0.00 ± 0.00	0.00 ± 0.00	-0.02 ± 0.00	-0.05 ± 0.00	0.14 ± 0.00	-0.00 ± 0.00	-0.03 ± 0.00	0.01
	-0.00 ± 0.00	-0.00 ± 0.00	-0.00 ± 0.00	-0.00 ± 0.00	0.01 ± 0.00	-0.00 ± 0.00	-0.00 ± 0.00	0.00
+ E-GRASP-mod CoM est.	0.00 ± 0.00	-0.00 ± 0.00	0.01 ± 0.00	0.02 ± 0.00	-0.05 ± 0.00	0.00 ± 0.00	-0.02 ± 0.00	0.00
	0.00 ± 0.00	-0.00 ± 0.00	-0.00 ± 0.00	0.00 ± 0.00	-0.00 ± 0.00	0.00 ± 0.00	-0.00 ± 0.00	0.00
+ E-GRASP-like CoM est.	0.00 ± 0.00	-0.00 ± 0.00	-0.02 ± 0.00	0.06 ± 0.00	-0.13 ± 0.00	0.00 ± 0.00	-0.02 ± 0.00	0.01
	0.00 ± 0.00	-0.00 ± 0.00	-0.00 ± 0.00	0.00 ± 0.00	-0.01 ± 0.00	0.00 ± 0.00	-0.00 ± 0.00	0.00
+ Circular 30 °CoM est.	0.00 ± 0.00	0.01 ± 0.00	0.00 ± 0.00	0.02 ± 0.00	-0.02 ± 0.00	-0.01 ± 0.00	-0.02 ± 0.00	0.01
	-0.00 ± 0.00	0.00 ± 0.00	0.00 ± 0.00	0.00 ± 0.00	-0.00 ± 0.00	-0.00 ± 0.00	-0.00 ± 0.00	0.00
+ Circular 60 °CoM est.	0.00 ± 0.00	0.00 ± 0.00	-0.03 ± 0.00	0.01 ± 0.00	-0.06 ± 0.00	-0.00 ± 0.00	-0.03 ± 0.00	0.01
	0.00 ± 0.00	-0.00 ± 0.00	-0.00 ± 0.00	0.00 ± 0.00	-0.00 ± 0.00	-0.00 ± 0.00	-0.00 ± 0.00	0.00
+ Circular 89 °CoM est.	0.00 ± 0.00	0.00 ± 0.00	-0.02 ± 0.00	-0.00 ± 0.00	-0.04 ± 0.00	-0.00 ± 0.00	-0.02 ± 0.00	0.01
	0.00 ± 0.00	-0.00 ± 0.00	-0.00 ± 0.00	-0.00 ± 0.00	-0.00 ± 0.00	0.00 ± 0.00	-0.00 ± 0.00	0.00

Table F.28: Helmert parameters to the reference solution for introducing a CoM displacement to the space-tie satellite of 10mm, either fixed or solved for, in the case of SLR. The reference is a combination of LAGEOS-1 and LAGEOS-2.

	T_x [mm] $T_{\dot{x}}$ [mm/a]	T_y [mm] $T_{\dot{y}}$ [mm/a]	T_z [mm] $T_{\dot{z}}$ [mm/a]	R_x [mm] $R_{\dot{x}}$ [mm/a]	R_y [mm] $R_{\dot{y}}$ [mm/a]	R_z [mm] $R_{\dot{z}}$ [mm/a]	sc [mm] $\dot{sc}$ [mm/a]	s_0 s_0
Reference	0.00 ± 0.00	0.00 ± 0.00	0.00 ± 0.00	0.00 ± 0.00	0.00 ± 0.00	0.00 ± 0.00	0.00 ± 0.00	0.00
	0.00 ± 0.00	0.00 ± 0.00	0.00 ± 0.00	0.00 ± 0.00	0.00 ± 0.00	0.00 ± 0.00	0.00 ± 0.00	0.00
+ GRASP-like	0.01 ± 0.11	-0.17 ± 0.11	1.41 ± 0.11	-14.82 ± 0.14	13.84 ± 0.13	-0.00 ± 0.13	-2.32 ± 0.11	0.57
	-0.01 ± 0.06	-0.05 ± 0.06	-0.17 ± 0.06	-0.85 ± 0.08	0.63 ± 0.07	-0.05 ± 0.07	-0.03 ± 0.06	0.31
+ E-GRASP-mod	0.34 ± 0.12	-0.01 ± 0.12	-3.74 ± 0.11	3.42 ± 0.15	-9.77 ± 0.14	0.32 ± 0.14	-1.89 ± 0.11	0.60
	0.04 ± 0.04	-0.02 ± 0.04	-0.08 ± 0.04	0.20 ± 0.05	-0.46 ± 0.05	0.02 ± 0.05	-0.05 ± 0.04	0.21
+ E-GRASP-like	0.42 ± 0.14	-0.05 ± 0.14	-3.56 ± 0.14	4.32 ± 0.17	-9.30 ± 0.17	0.45 ± 0.16	-1.34 ± 0.13	0.71
	0.02 ± 0.04	-0.04 ± 0.04	-0.11 ± 0.04	0.20 ± 0.05	-0.41 ± 0.05	0.02 ± 0.05	-0.06 ± 0.04	0.22
+ Circular 30°	0.43 ± 0.23	0.59 ± 0.23	-1.16 ± 0.22	1.25 ± 0.28	-1.17 ± 0.27	-0.14 ± 0.26	-1.78 ± 0.22	1.15
	0.02 ± 0.02	0.01 ± 0.02	0.11 ± 0.02	0.13 ± 0.02	-0.04 ± 0.02	0.01 ± 0.02	-0.05 ± 0.02	0.10
+ Circular 60°	0.24 ± 0.10	0.12 ± 0.11	-2.08 ± 0.10	0.88 ± 0.13	-4.85 ± 0.13	0.07 ± 0.12	-2.60 ± 0.10	0.53
	0.02 ± 0.05	-0.05 ± 0.05	-0.04 ± 0.04	0.05 ± 0.06	-0.26 ± 0.06	-0.01 ± 0.05	-0.05 ± 0.04	0.23
+ Circular 89°	0.24 ± 0.15	0.15 ± 0.15	-2.31 ± 0.15	-1.16 ± 0.19	-5.30 ± 0.18	-0.07 ± 0.17	-2.40 ± 0.15	0.77
	0.02 ± 0.06	-0.05 ± 0.06	-0.16 ± 0.06	-0.08 ± 0.08	-0.26 ± 0.08	0.01 ± 0.07	-0.07 ± 0.06	0.32
Reference	0.00 ± 0.00	0.00 ± 0.00	0.00 ± 0.00	0.00 ± 0.00	0.00 ± 0.00	0.00 ± 0.00	0.00 ± 0.00	0.00
	0.00 ± 0.00	0.00 ± 0.00	0.00 ± 0.00	0.00 ± 0.00	0.00 ± 0.00	0.00 ± 0.00	0.00 ± 0.00	0.00
+ GRASP-like CoM est.	0.00 ± 0.00	0.00 ± 0.00	-0.02 ± 0.00	-0.05 ± 0.00	0.14 ± 0.00	-0.00 ± 0.00	-0.03 ± 0.00	0.01
	-0.00 ± 0.00	-0.00 ± 0.00	-0.00 ± 0.00	-0.00 ± 0.00	0.01 ± 0.00	-0.00 ± 0.00	-0.00 ± 0.00	0.00
+ E-GRASP-mod CoM est.	0.00 ± 0.00	-0.00 ± 0.00	0.01 ± 0.00	0.02 ± 0.00	-0.05 ± 0.00	0.00 ± 0.00	-0.02 ± 0.00	0.00
	0.00 ± 0.00	-0.00 ± 0.00	-0.00 ± 0.00	0.00 ± 0.00	-0.00 ± 0.00	0.00 ± 0.00	-0.00 ± 0.00	0.00
+ E-GRASP-like CoM est.	0.00 ± 0.00	-0.00 ± 0.00	-0.02 ± 0.00	0.06 ± 0.00	-0.13 ± 0.00	0.00 ± 0.00	-0.02 ± 0.00	0.01
	0.00 ± 0.00	-0.00 ± 0.00	-0.00 ± 0.00	0.00 ± 0.00	-0.01 ± 0.00	0.00 ± 0.00	-0.00 ± 0.00	0.00
+ Circular 30°CoM est.	0.00 ± 0.00	0.01 ± 0.00	0.00 ± 0.00	0.02 ± 0.00	-0.02 ± 0.00	-0.01 ± 0.00	-0.02 ± 0.00	0.01
	-0.00 ± 0.00	0.00 ± 0.00	0.00 ± 0.00	0.00 ± 0.00	-0.00 ± 0.00	-0.00 ± 0.00	-0.00 ± 0.00	0.00
+ Circular 60°CoM est.	0.00 ± 0.00	0.00 ± 0.00	-0.03 ± 0.00	0.01 ± 0.00	-0.06 ± 0.00	-0.00 ± 0.00	-0.03 ± 0.00	0.01
	0.00 ± 0.00	-0.00 ± 0.00	-0.00 ± 0.00	0.00 ± 0.00	-0.00 ± 0.00	-0.00 ± 0.00	-0.00 ± 0.00	0.00
+ Circular 89°CoM est.	0.00 ± 0.00	0.00 ± 0.00	-0.02 ± 0.00	-0.00 ± 0.00	-0.04 ± 0.00	-0.00 ± 0.00	-0.02 ± 0.00	0.01
	0.00 ± 0.00	-0.00 ± 0.00	-0.00 ± 0.00	-0.00 ± 0.00	-0.00 ± 0.00	-0.00 ± 0.00	-0.00 ± 0.00	0.00

Table F.29: Formal errors for the 5 mm CoM case for SLR, coordinates are fixed.

	σ_x & p-value	σ_y & p-value	σ_z & p-value	$\sigma_{\dot{x}}$ & p-value	$\sigma_{\dot{y}}$ & p-value	$\sigma_{\dot{z}}$ & p-value	σ_{x_p} & p-value	σ_{y_p} & p-value	σ_{LOD} & p-value	exp. imp.
	[mm]			[mm/dec]			[cm]		[μm]	[%]
GRASP-like	1.004 -0.000	0.999 -0.000	0.931 -0.000	1.157 -0.000	1.084 -0.000	1.098 -0.000	1.570 0.000	1.599 0.000	2.056 0.000	-18.88
E-GRASP-mod	1.011 -0.000	1.008 -0.000	0.940 -0.000	1.156 -0.000	1.084 -0.000	1.097 -0.000	1.607 -0.000	1.619 -0.000	2.056 -0.000	-20.36
E-GRASP-like	1.002 -0.000	1.001 -0.000	0.936 -0.000	1.142 -0.000	1.075 -0.000	1.096 -0.000	1.594 -0.000	1.613 -0.000	2.031 -0.000	-20.65
Circular 30°	1.011 -0.000	1.009 -0.000	0.986 -0.000	1.143 -0.000	1.071 -0.000	1.150 -0.000	1.643 -0.000	1.674 -0.000	1.992 -0.000	-19.19
Circular 60°	1.017 -0.000	1.018 -0.000	0.959 -0.000	1.161 -0.000	1.094 -0.000	1.105 -0.000	1.658 -0.000	1.668 -0.000	2.077 -0.000	-19.57
Circular 89°	1.020 -0.000	1.022 -0.000	0.960 -0.000	1.177 -0.000	1.094 -0.000	1.099 -0.000	1.599 -0.000	1.660 -0.000	2.136 -0.000	-19.56

	$\sigma_{Lat.}$ & p-value	$\sigma_{Lon.}$ & p-value	σ_{Height}	$\sigma_{\dot{Lat.}}$ & p-value	$\sigma_{\dot{Lon.}}$ & p-value	$\sigma_{\dot{Height}}$ & p-value
	[mm]			[mm/dec]		
GRASP-like	0.908 -0.000	1.023 -0.000	0.877 -0.000	1.108 -0.000	1.134 -0.000	1.031 -0.000
E-GRASP-mod	0.916 -0.000	1.033 -0.000	0.878 -0.000	1.108 -0.000	1.134 -0.000	1.024 -0.000
E-GRASP-like	0.911 -0.000	1.024 -0.000	0.871 -0.000	1.104 -0.000	1.124 -0.000	1.000 -0.000
Circular 30°	0.943 -0.000	1.024 -0.000	0.855 -0.000	1.128 -0.000	1.132 -0.000	0.974 -0.000
Circular 60°	0.931 -0.000	1.043 -0.000	0.892 -0.000	1.113 -0.000	1.142 -0.000	1.027 -0.000
Circular 89°	0.931 -0.000	1.051 -0.000	0.896 -0.000	1.114 -0.000	1.155 -0.000	1.034 -0.000

Table F.30: Formal errors for the 10 mm CoM case for SLR, coordinates are fixed.

	σ_x & p-value		σ_y & p-value		σ_z & p-value		$\sigma_{\dot{x}}$ & p-value		$\sigma_{\dot{y}}$ & p-value		$\sigma_{\dot{z}}$ & p-value		σ_{x_p} & p-value		σ_{y_p} & p-value		σ_{LOD} & p-value		exp. imp.
	[mm]						[mm/dec]						[cm]				[μm]		[%]
GRASP-like	1.033	-0.000	1.027	-0.000	0.957	-0.000	1.190	-0.000	1.114	-0.000	1.129	-0.000	1.615	0.000	1.645	0.000	2.115	0.000	-18.88
E-GRASP-mod	1.035	-0.000	1.031	-0.000	0.962	-0.000	1.182	-0.000	1.110	-0.000	1.123	-0.000	1.645	-0.000	1.657	-0.000	2.104	-0.000	-20.36
E-GRASP-like	1.020	-0.000	1.019	-0.000	0.954	-0.000	1.163	-0.000	1.095	-0.000	1.116	-0.000	1.624	-0.000	1.643	-0.000	2.068	-0.000	-20.65
Circular 30°	1.028	-0.000	1.027	-0.000	1.002	-0.000	1.163	-0.000	1.090	-0.000	1.170	-0.000	1.672	-0.000	1.703	-0.000	2.027	-0.000	-19.19
Circular 60°	1.046	-0.000	1.047	-0.000	0.987	-0.000	1.194	-0.000	1.126	-0.000	1.137	-0.000	1.705	-0.000	1.715	-0.000	2.136	-0.000	-19.57
Circular 89°	1.052	-0.000	1.055	-0.001	0.991	-0.000	1.214	-0.000	1.128	-0.000	1.134	-0.000	1.649	-0.000	1.712	-0.000	2.203	-0.000	-19.56

	$\sigma_{Lat.}$ & p-value		$\sigma_{Lon.}$ & p-value		σ_{Height}		$\sigma_{\dot{Lat.}}$ & p-value		$\sigma_{\dot{Lon.}}$ & p-value		$\sigma_{\dot{Height}}$ & p-value	
	[mm]						[mm/dec]					
GRASP-like	0.934	-0.000	1.052	-0.000	0.902	-0.000	1.139	-0.000	1.167	-0.000	1.060	-0.000
E-GRASP-mod	0.938	-0.000	1.057	-0.000	0.899	-0.000	1.134	-0.000	1.160	-0.000	1.048	-0.000
E-GRASP-like	0.928	-0.000	1.043	-0.000	0.887	-0.000	1.124	-0.000	1.145	-0.000	1.018	-0.000
Circular 30°	0.960	-0.000	1.042	-0.000	0.870	-0.000	1.147	-0.000	1.152	-0.000	0.991	-0.000
Circular 60°	0.958	-0.000	1.073	-0.001	0.918	-0.000	1.145	-0.000	1.175	-0.000	1.056	-0.000
Circular 89°	0.960	-0.000	1.083	-0.003	0.924	-0.000	1.149	-0.000	1.191	-0.000	1.067	-0.000

Table F.31: Formal errors for the 5 mm CoM case for SLR, coordinates are estimated.

	σ_x & p-value		σ_y & p-value		σ_z & p-value		$\sigma_{\dot{x}}$ & p-value		$\sigma_{\dot{y}}$ & p-value		$\sigma_{\dot{z}}$ & p-value		σ_{x_p} & p-value		σ_{y_p} & p-value		σ_{LOD} & p-value		exp. imp.
	[mm]						[mm/dec]						[cm]				[μm]		[%]
GRASP-like	0.995	-0.000	0.989	-0.000	0.923	-0.000	1.147	-0.000	1.074	-0.000	1.088	-0.000	1.556	0.000	1.585	0.000	2.037	0.000	-18.88
E-GRASP-mod	1.003	-0.000	1.000	-0.000	0.934	-0.000	1.147	-0.000	1.076	-0.000	1.089	-0.000	1.596	-0.000	1.607	-0.000	2.040	-0.000	-20.36
E-GRASP-like	0.996	-0.000	0.995	-0.000	0.932	-0.000	1.136	-0.000	1.069	-0.000	1.090	-0.000	1.586	-0.000	1.604	-0.000	2.019	-0.000	-20.65
Circular 30°	1.005	-0.000	1.003	-0.000	0.980	-0.000	1.137	-0.000	1.065	-0.000	1.143	-0.000	1.634	-0.000	1.664	-0.000	1.981	-0.000	-19.19
Circular 60°	1.008	-0.000	1.009	-0.000	0.951	-0.000	1.150	-0.000	1.084	-0.000	1.095	-0.000	1.643	-0.000	1.652	-0.000	2.057	-0.000	-19.57
Circular 89°	1.010	-0.000	1.012	-0.000	0.951	-0.000	1.165	-0.000	1.083	-0.000	1.088	-0.000	1.583	-0.000	1.642	-0.000	2.113	-0.000	-19.56

	$\sigma_{Lat.}$ & p-value		$\sigma_{Lon.}$ & p-value		σ_{Height}		$\sigma_{\dot{Lat.}}$ & p-value		$\sigma_{\dot{Lon.}}$ & p-value		$\sigma_{\dot{Height}}$ & p-value	
	[mm]						[mm/dec]					
GRASP-like	0.900	-0.000	1.014	-0.000	0.870	-0.000	1.098	-0.000	1.124	-0.000	1.021	-0.000
E-GRASP-mod	0.910	-0.000	1.025	-0.000	0.872	-0.000	1.100	-0.000	1.125	-0.000	1.016	-0.000
E-GRASP-like	0.906	-0.000	1.018	-0.000	0.866	-0.000	1.097	-0.000	1.118	-0.000	0.994	-0.000
Circular 30°	0.938	-0.000	1.018	-0.000	0.851	-0.000	1.121	-0.000	1.125	-0.000	0.968	-0.000
Circular 60°	0.923	-0.000	1.034	-0.000	0.884	-0.000	1.103	-0.000	1.132	-0.000	1.017	-0.000
Circular 89°	0.922	-0.000	1.040	-0.000	0.887	-0.000	1.102	-0.000	1.143	-0.000	1.024	-0.000

Table F.32: Formal errors for the 10 mm CoM case for SLR, coordinates are estimated.

	σ_x & p-value		σ_y & p-value		σ_z & p-value		$\sigma_{\dot{x}}$ & p-value		$\sigma_{\dot{y}}$ & p-value		$\sigma_{\dot{z}}$ & p-value		σ_{x_p} & p-value		σ_{y_p} & p-value		σ_{LOD} & p-value		exp. imp.
	[mm]						[mm/dec]						[cm]				[μm]		[%]
GRASP-like	0.995	-0.000	0.989	-0.000	0.923	-0.000	1.147	-0.000	1.074	-0.000	1.088	-0.000	1.556	0.000	1.585	0.000	2.037	0.000	-18.88
E-GRASP-mod	1.003	-0.000	1.000	-0.000	0.934	-0.000	1.147	-0.000	1.076	-0.000	1.089	-0.000	1.596	-0.000	1.607	-0.000	2.040	-0.000	-20.36
E-GRASP-like	0.996	-0.000	0.995	-0.000	0.932	-0.000	1.136	-0.000	1.069	-0.000	1.090	-0.000	1.586	-0.000	1.604	-0.000	2.019	-0.000	-20.65
Circular 30°	1.005	-0.000	1.003	-0.000	0.980	-0.000	1.137	-0.000	1.065	-0.000	1.143	-0.000	1.634	-0.000	1.664	-0.000	1.981	-0.000	-19.19
Circular 60°	1.008	-0.000	1.009	-0.000	0.951	-0.000	1.150	-0.000	1.084	-0.000	1.095	-0.000	1.643	-0.000	1.652	-0.000	2.057	-0.000	-19.57
Circular 89°	1.010	-0.000	1.012	-0.000	0.951	-0.000	1.165	-0.000	1.083	-0.000	1.088	-0.000	1.583	-0.000	1.642	-0.000	2.113	-0.000	-19.56

	$\sigma_{Lat.}$ & p-value		$\sigma_{Lon.}$ & p-value		σ_{Height}		$\sigma_{\dot{Lat.}}$ & p-value		$\sigma_{\dot{Lon.}}$ & p-value		$\sigma_{\dot{Height}}$ & p-value	
	[mm]						[mm/dec]					
GRASP-like	0.900	-0.000	1.014	-0.000	0.870	-0.000	1.098	-0.000	1.124	-0.000	1.021	-0.000
E-GRASP-mod	0.910	-0.000	1.025	-0.000	0.872	-0.000	1.100	-0.000	1.125	-0.000	1.016	-0.000
E-GRASP-like	0.906	-0.000	1.018	-0.000	0.866	-0.000	1.097	-0.000	1.118	-0.000	0.994	-0.000
Circular 30°	0.938	-0.000	1.018	-0.000	0.851	-0.000	1.121	-0.000	1.125	-0.000	0.968	-0.000
Circular 60°	0.923	-0.000	1.034	-0.000	0.884	-0.000	1.103	-0.000	1.132	-0.000	1.017	-0.000
Circular 89°	0.922	-0.000	1.040	-0.000	0.887	-0.000	1.102	-0.000	1.143	-0.000	1.024	-0.000

Table F.33: Statistics of estimated ERPs introducing a CoM displacement to the space-tie satellite of 5mm, 10mm, and while estimating for the CoM coordinates

	$\Delta X - Pole$						$\Delta Y - Pole$						ΔLOD					
	std. [mm]	p-value	mean ± std. [mm]	p-value	trend ± std. [mm/a]	p-value	std. [mm]	p-value	mean ± std. [mm]	p-value	trend ± std. [mm/a]	p-value	std. [μm]	p-value	mean ± std. [μm]	p-value	trend ± std. [μm/a]	p-value
Reference + GRASP-like																		
- 5mm CoM deviation	1.327	0.000	-7.024 ± 0.023	0.000	-0.328 ± 0.011	0.000	1.560	0.000	8.574 ± 0.025	0.000	0.453 ± 0.012	0.000	2.466	0.000	-0.126 ± 0.049	0.010	0.011 ± 0.024	0.643
- 5mm CoM deviation est.	1.123	0.981	0.263 ± 0.022	0.000	-0.029 ± 0.011	0.008	1.216	0.985	0.481 ± 0.024	0.000	0.041 ± 0.012	0.001	2.269	0.988	0.005 ± 0.045	0.911	-0.001 ± 0.022	0.950
- 10mm CoM deviation	1.784	0.000	-14.460 ± 0.025	0.000	-0.634 ± 0.012	0.000	2.241	0.000	16.720 ± 0.028	0.000	0.868 ± 0.014	0.000	2.938	0.000	-0.256 ± 0.058	0.000	0.024 ± 0.029	0.402
- 10mm CoM deviation est.	1.123	0.983	0.264 ± 0.022	0.000	-0.029 ± 0.011	0.008	1.216	0.986	0.482 ± 0.024	0.000	0.041 ± 0.012	0.001	2.268	0.989	0.005 ± 0.045	0.910	-0.001 ± 0.022	0.950
Reference + E-GRASP-mod																		
- 5mm CoM deviation	1.231	0.000	5.528 ± 0.023	0.000	0.206 ± 0.011	0.000	1.220	0.371	-1.184 ± 0.024	0.000	-0.040 ± 0.012	0.001	2.305	0.079	-0.006 ± 0.046	0.897	-0.012 ± 0.023	0.583
- 5mm CoM deviation est.	1.136	0.986	0.517 ± 0.022	0.000	-0.016 ± 0.011	0.162	1.193	0.999	0.644 ± 0.024	0.000	0.051 ± 0.012	0.000	2.218	1.000	0.003 ± 0.044	0.951	-0.004 ± 0.022	0.862
- 10mm CoM deviation	1.507	0.000	10.595 ± 0.024	0.000	0.431 ± 0.012	0.000	1.317	0.000	-3.038 ± 0.026	0.000	-0.132 ± 0.013	0.000	2.549	0.000	-0.015 ± 0.050	0.772	-0.021 ± 0.025	0.399
- 10mm CoM deviation est.	1.136	0.987	0.517 ± 0.022	0.000	-0.016 ± 0.011	0.162	1.193	0.999	0.644 ± 0.024	0.000	0.051 ± 0.012	0.000	2.218	1.000	0.003 ± 0.044	0.952	-0.004 ± 0.022	0.863
Reference + E-GRASP-like																		
- 5mm CoM deviation	1.184	0.001	4.856 ± 0.022	0.000	0.183 ± 0.011	0.000	1.250	0.265	-1.881 ± 0.025	0.000	-0.065 ± 0.012	0.000	2.316	0.123	0.010 ± 0.046	0.831	-0.001 ± 0.023	0.952
- 5mm CoM deviation est.	1.104	0.979	0.195 ± 0.022	0.000	-0.028 ± 0.011	0.010	1.221	0.995	0.345 ± 0.024	0.000	0.042 ± 0.012	0.001	2.237	0.998	0.005 ± 0.044	0.911	-0.002 ± 0.022	0.937
- 10mm CoM deviation	1.438	0.000	9.655 ± 0.024	0.000	0.400 ± 0.012	0.000	1.350	0.000	-4.165 ± 0.026	0.000	-0.174 ± 0.013	0.000	2.518	0.000	0.015 ± 0.050	0.768	-0.001 ± 0.025	0.967
- 10mm CoM deviation est.	1.104	0.979	0.195 ± 0.022	0.000	-0.028 ± 0.011	0.010	1.221	0.995	0.345 ± 0.024	0.000	0.042 ± 0.012	0.001	2.237	0.999	0.005 ± 0.044	0.911	-0.002 ± 0.022	0.937
Reference + Circular 30°																		
- 5mm CoM deviation	1.187	0.194	1.365 ± 0.023	0.000	0.033 ± 0.012	0.004	1.291	0.052	-0.531 ± 0.026	0.000	-0.015 ± 0.013	0.242	2.198	0.134	0.039 ± 0.043	0.372	-0.012 ± 0.022	0.564
- 5mm CoM deviation est.	1.151	1.000	0.683 ± 0.023	0.000	0.004 ± 0.011	0.693	1.241	0.995	0.456 ± 0.024	0.000	0.047 ± 0.012	0.000	2.138	1.000	0.011 ± 0.042	0.788	-0.008 ± 0.021	0.690
- 10mm CoM deviation	1.277	0.000	2.070 ± 0.025	0.000	0.063 ± 0.012	0.000	1.430	0.000	-1.543 ± 0.028	0.000	-0.078 ± 0.014	0.000	2.349	0.000	0.067 ± 0.046	0.150	-0.016 ± 0.023	0.475
- 10mm CoM deviation est.	1.151	1.000	0.683 ± 0.023	0.000	0.004 ± 0.011	0.694	1.241	0.995	0.456 ± 0.024	0.000	0.047 ± 0.012	0.000	2.138	0.999	0.011 ± 0.042	0.788	-0.008 ± 0.021	0.690
Reference + Circular 60°																		
- 5mm CoM deviation	1.215	0.046	2.971 ± 0.024	0.000	0.095 ± 0.012	0.000	1.244	0.462	0.143 ± 0.025	0.000	0.021 ± 0.012	0.087	2.385	0.018	0.062 ± 0.047	0.192	-0.009 ± 0.023	0.698
- 5mm CoM deviation est.	1.162	0.999	0.439 ± 0.023	0.000	-0.015 ± 0.011	0.195	1.216	0.987	0.592 ± 0.024	0.000	0.043 ± 0.012	0.000	2.257	0.992	0.048 ± 0.045	0.285	-0.006 ± 0.022	0.775
- 10mm CoM deviation	1.372	0.000	5.564 ± 0.026	0.000	0.207 ± 0.013	0.000	1.345	0.000	-0.322 ± 0.027	0.000	-0.002 ± 0.013	0.854	2.767	0.000	0.076 ± 0.055	0.167	-0.012 ± 0.027	0.661
- 10mm CoM deviation est.	1.162	0.999	0.439 ± 0.023	0.000	-0.015 ± 0.011	0.195	1.216	0.986	0.592 ± 0.024	0.000	0.043 ± 0.012	0.000	2.257	0.992	0.048 ± 0.045	0.285	-0.006 ± 0.022	0.775
Reference + Circular 89°																		
- 5mm CoM deviation	1.112	0.015	3.215 ± 0.021	0.000	0.127 ± 0.011	0.000	1.253	0.041	1.252 ± 0.025	0.000	0.086 ± 0.012	0.000	2.468	0.002	0.010 ± 0.049	0.836	0.002 ± 0.024	0.920
- 5mm CoM deviation est.	1.056	0.985	0.613 ± 0.021	0.000	-0.012 ± 0.010	0.256	1.199	0.999	0.418 ± 0.024	0.000	0.046 ± 0.012	0.000	2.321	0.999	0.022 ± 0.046	0.624	-0.002 ± 0.023	0.933
- 10mm CoM deviation	1.300	0.000	5.856 ± 0.023	0.000	0.268 ± 0.012	0.000	1.398	0.000	2.096 ± 0.027	0.000	0.126 ± 0.013	0.000	2.898	0.000	-0.003 ± 0.057	0.964	0.007 ± 0.028	0.810
- 10mm CoM deviation est.	1.056	0.985	0.613 ± 0.021	0.000	-0.012 ± 0.010	0.256	1.199	0.999	0.418 ± 0.024	0.000	0.046 ± 0.012	0.000	2.321	0.999	0.022 ± 0.046	0.624	-0.002 ± 0.023	0.933

F.2.3 Atmospheric drag mismodelling

Table F.34: Helmert parameters to the reference solution for the atmospheric drag mismodelling case for SLR. The reference is a combination of LAGEOS-1 and LAGEOS-2.

	T_x [mm]	T_y [mm]	T_z [mm]	R_x [mm]	R_y [mm]	R_z [mm]	sc [mm]	s_0
	$\dot{T}_x$ [mm/a]	$\dot{T}_y$ [mm/a]	$\dot{T}_z$ [mm/a]	$\dot{R}_x$ [mm/a]	$\dot{R}_y$ [mm/a]	$\dot{R}_z$ [mm/a]	$\dot{sc}$ [mm/a]	$\dot{s}_0$
+ GRASP-like	-0.00 ± 0.06	0.02 ± 0.06	0.02 ± 0.06	1.00 ± 0.07	-0.49 ± 0.07	-0.05 ± 0.07	0.04 ± 0.06	0.30
	-0.01 ± 0.02	0.00 ± 0.02	-0.01 ± 0.02	0.04 ± 0.03	-0.01 ± 0.03	0.01 ± 0.03	-0.00 ± 0.02	0.12
+ E-GRASP-mod	-0.02 ± 0.03	-0.00 ± 0.03	0.04 ± 0.03	-0.26 ± 0.04	0.01 ± 0.04	0.06 ± 0.04	-0.01 ± 0.03	0.17
	0.01 ± 0.01	0.00 ± 0.01	-0.01 ± 0.01	0.00 ± 0.01	-0.01 ± 0.01	-0.01 ± 0.01	-0.00 ± 0.01	0.05
+ E-GRASP-like	-0.05 ± 0.05	-0.02 ± 0.05	0.00 ± 0.04	-2.80 ± 0.06	-0.52 ± 0.05	-0.07 ± 0.05	-0.02 ± 0.04	0.23
	-0.01 ± 0.02	-0.00 ± 0.02	-0.01 ± 0.02	-0.16 ± 0.02	-0.05 ± 0.02	-0.02 ± 0.02	0.01 ± 0.02	0.10
+ Circular 30°	-0.01 ± 0.03	-0.00 ± 0.03	0.00 ± 0.03	-0.13 ± 0.04	-0.03 ± 0.04	-0.03 ± 0.04	0.00 ± 0.03	0.17
	-0.00 ± 0.01	0.00 ± 0.01	-0.00 ± 0.01	0.00 ± 0.01	-0.02 ± 0.01	-0.01 ± 0.01	0.00 ± 0.01	0.05
+ Circular 60°	-0.02 ± 0.03	-0.00 ± 0.03	-0.01 ± 0.03	0.08 ± 0.04	0.03 ± 0.04	0.01 ± 0.03	-0.02 ± 0.03	0.15
	0.01 ± 0.01	-0.00 ± 0.01	0.01 ± 0.01	-0.01 ± 0.01	-0.01 ± 0.01	0.00 ± 0.01	-0.00 ± 0.01	0.05
+ Circular 89°	0.03 ± 0.04	0.01 ± 0.04	-0.01 ± 0.04	0.01 ± 0.05	-0.06 ± 0.05	0.01 ± 0.04	0.02 ± 0.04	0.20
	-0.01 ± 0.01	-0.00 ± 0.01	0.01 ± 0.01	-0.00 ± 0.01	0.02 ± 0.01	0.00 ± 0.01	0.00 ± 0.01	0.06

Table F.35: Formal errors for the SLR atmospheric drag mismodelling case.

	σ_x & p-value		σ_y & p-value		σ_z & p-value		$\sigma_{\dot{x}}$ & p-value		$\sigma_{\dot{y}}$ & p-value		$\sigma_{\dot{z}}$ & p-value		σ_{x_p} & p-value		σ_{y_p} & p-value		σ_{LOD} & p-value		exp. imp.
	[mm]						[mm/dec]						[cm]				[μm]		[%]
GRASP-like	1.005	-0.000	0.998	-0.000	0.946	-0.000	1.156	-0.000	1.087	-0.000	1.110	-0.000	1.696	0.000	1.691	0.000	2.109	0.000	-18.52
E-GRASP-mod	1.007	-0.000	1.005	-0.000	0.940	-0.000	1.154	-0.000	1.085	-0.000	1.100	-0.000	1.654	-0.000	1.667	-0.000	2.216	-0.000	-20.02
E-GRASP-like	1.007	-0.000	1.007	-0.000	0.947	-0.000	1.151	-0.000	1.085	-0.000	1.107	-0.000	1.676	-0.000	1.689	-0.000	2.213	-0.000	-20.31
Circular 30°	1.010	-0.000	1.013	-0.000	0.985	-0.000	1.149	-0.000	1.078	-0.000	1.151	-0.000	1.678	-0.000	1.709	-0.000	2.383	-0.000	-18.84
Circular 60°	1.011	-0.000	1.013	-0.000	0.956	-0.000	1.158	-0.000	1.093	-0.000	1.107	-0.000	1.702	-0.000	1.706	-0.000	2.272	-0.000	-19.22
Circular 89°	1.012	-0.000	1.014	-0.000	0.955	-0.000	1.171	-0.000	1.090	-0.000	1.100	-0.000	1.652	-0.000	1.691	-0.000	2.157	-0.000	-19.21

	$\sigma_{Lat.}$ & p-value		$\sigma_{Lon.}$ & p-value		σ_{Height}		$\sigma_{\dot{Lat.}}$ & p-value		$\sigma_{\dot{Lon.}}$ & p-value		$\sigma_{\dot{Height}}$ & p-value	
	[mm]						[mm/dec]					
GRASP-like	0.921	-0.000	1.026	-0.000	0.888	-0.000	1.120	-0.000	1.134	-0.000	1.037	-0.000
E-GRASP-mod	0.917	-0.000	1.031	-0.000	0.878	-0.000	1.111	-0.000	1.133	-0.000	1.027	-0.000
E-GRASP-like	0.922	-0.000	1.032	-0.000	0.882	-0.000	1.116	-0.000	1.132	-0.000	1.014	-0.000
Circular 30°	0.944	-0.000	1.029	-0.000	0.860	-0.000	1.131	-0.000	1.135	-0.000	0.982	-0.000
Circular 60°	0.929	-0.000	1.039	-0.000	0.890	-0.000	1.115	-0.000	1.140	-0.000	1.028	-0.000
Circular 89°	0.927	-0.000	1.044	-0.000	0.893	-0.000	1.114	-0.000	1.148	-0.000	1.032	-0.000

Table F.36: Statistics of estimated ERPs for the SLR atmospheric drag mismodelling case.

	$\Delta X - Pole$						$\Delta Y - Pole$						ΔLOD					
	std. [mm]	p-value	mean ± std. [mm]	p-value	trend ± std. [mm/a]	p-value	std. [mm]	p-value	mean ± std. [mm]	p-value	trend ± std. [mm/a]	p-value	std. [μm]	p-value	mean ± std. [μm]	p-value	trend ± std. [μm/a]	p-value
Comb. reference																		
+ GRASP-like																		
- Atmospheric drag mismodelling	1.306	0.000	0.830 ± 0.026	0.000	0.002 ± 0.013	0.847	1.390	0.000	-0.564 ± 0.028	0.000	-0.002 ± 0.014	0.858	2.328	0.245	0.013 ± 0.046	0.774	0.001 ± 0.023	0.961
+ E-GRASP-mod																		
- Atmospheric drag mismodelling	1.203	0.003	0.471 ± 0.024	0.000	-0.014 ± 0.012	0.232	1.270	0.003	0.915 ± 0.025	0.000	0.062 ± 0.012	0.000	2.409	0.000	0.003 ± 0.048	0.945	0.001 ± 0.024	0.976
+ E-GRASP-like																		
- Atmospheric drag mismodelling	1.259	0.000	0.622 ± 0.025	0.000	-0.000 ± 0.012	0.994	1.431	0.000	3.508 ± 0.027	0.000	0.225 ± 0.013	0.000	2.523	0.000	0.011 ± 0.050	0.823	0.005 ± 0.025	0.847
+ Circular 30°																		
- Atmospheric drag mismodelling	1.205	0.021	0.713 ± 0.024	0.000	0.001 ± 0.012	0.952	1.305	0.012	0.586 ± 0.026	0.000	0.057 ± 0.013	0.000	2.640	0.000	0.024 ± 0.052	0.646	-0.002 ± 0.026	0.923
+ Circular 60°																		
- Atmospheric drag mismodelling	1.236	0.013	0.371 ± 0.024	0.000	-0.016 ± 0.012	0.187	1.305	0.003	0.523 ± 0.026	0.000	0.052 ± 0.013	0.000	2.493	0.000	0.043 ± 0.049	0.382	0.001 ± 0.024	0.982
+ Circular 89°																		
- Atmospheric drag mismodelling	1.159	0.000	0.574 ± 0.023	0.000	-0.013 ± 0.011	0.258	1.283	0.001	0.418 ± 0.025	0.000	0.051 ± 0.013	0.000	2.380	0.416	0.020 ± 0.047	0.671	0.001 ± 0.023	0.977

F.2.4 Solar radiation pressure mismodelling

Table F.37: Helmert parameters to the reference solution for the SRP mismodelling case for SLR. The reference is a combination of LAGEOS-1 and LAGEOS-2.

	T_x [mm]	T_y [mm]	T_z [mm]	R_x [mm]	R_y [mm]	R_z [mm]	sc [mm]	s_0
	$T_{\dot{x}}$ [mm/a]	$T_{\dot{y}}$ [mm/a]	$T_{\dot{z}}$ [mm/a]	$R_{\dot{x}}$ [mm/a]	$R_{\dot{y}}$ [mm/a]	$R_{\dot{z}}$ [mm/a]	$\dot{sc}$ [mm/a]	$\dot{s_0}$
+ GRASP-like	0.01 ± 0.03	0.04 ± 0.03	0.08 ± 0.03	0.09 ± 0.04	0.08 ± 0.04	0.01 ± 0.04	0.03 ± 0.03	0.17
	-0.01 ± 0.01	-0.01 ± 0.01	0.01 ± 0.01	0.00 ± 0.02	0.01 ± 0.02	-0.00 ± 0.02	-0.00 ± 0.01	0.07
+ E-GRASP-mod	-0.03 ± 0.05	-0.01 ± 0.05	0.04 ± 0.05	0.04 ± 0.06	0.14 ± 0.06	0.08 ± 0.06	-0.01 ± 0.05	0.27
	0.01 ± 0.02	0.00 ± 0.02	-0.00 ± 0.02	0.01 ± 0.02	-0.01 ± 0.02	-0.02 ± 0.02	-0.01 ± 0.02	0.08
+ E-GRASP-like	-0.01 ± 0.05	-0.01 ± 0.05	0.07 ± 0.04	0.13 ± 0.06	0.02 ± 0.05	-0.04 ± 0.05	-0.01 ± 0.04	0.23
	-0.00 ± 0.02	0.01 ± 0.02	0.01 ± 0.01	-0.01 ± 0.02	-0.01 ± 0.02	-0.01 ± 0.02	0.01 ± 0.01	0.08
+ Circular 30°	-0.02 ± 0.05	0.00 ± 0.05	-0.02 ± 0.05	-0.08 ± 0.06	-0.07 ± 0.06	-0.00 ± 0.06	-0.00 ± 0.05	0.25
	0.01 ± 0.01	0.00 ± 0.01	0.01 ± 0.01	-0.01 ± 0.02	-0.01 ± 0.02	0.00 ± 0.02	-0.00 ± 0.01	0.07
+ Circular 60°	-0.03 ± 0.03	-0.02 ± 0.03	-0.02 ± 0.03	0.12 ± 0.04	0.09 ± 0.04	-0.02 ± 0.04	-0.01 ± 0.03	0.17
	0.01 ± 0.01	-0.01 ± 0.01	0.00 ± 0.01	0.01 ± 0.02	-0.00 ± 0.02	0.00 ± 0.02	-0.01 ± 0.01	0.07
+ Circular 89°	0.02 ± 0.04	0.02 ± 0.04	-0.03 ± 0.04	0.02 ± 0.05	-0.08 ± 0.05	0.01 ± 0.05	0.04 ± 0.04	0.21
	-0.00 ± 0.01	-0.00 ± 0.01	-0.00 ± 0.01	0.02 ± 0.02	0.01 ± 0.02	0.01 ± 0.02	0.00 ± 0.01	0.07

Table F.38: Formal errors for the SLR SRP mismodelling case.

	σ_x & p-value		σ_y & p-value		σ_z & p-value		$\sigma_{\dot{x}}$ & p-value		$\sigma_{\dot{y}}$ & p-value		$\sigma_{\dot{z}}$ & p-value		σ_{x_p} & p-value		σ_{y_p} & p-value		σ_{LOD} & p-value		exp. imp.
	[mm]						[mm/dec]						[cm]				[μm]		[%]
GRASP-like	1.002	-0.000	0.998	-0.000	0.938	-0.000	1.158	-0.000	1.086	-0.000	1.106	-0.000	1.660	0.000	1.675	0.000	2.451	0.000	-18.53
E-GRASP-mod	1.007	-0.000	1.005	-0.000	0.941	-0.000	1.157	-0.000	1.086	-0.000	1.104	-0.000	1.671	-0.000	1.686	-0.000	2.475	-0.000	-20.03
E-GRASP-like	1.004	-0.000	1.002	-0.000	0.941	-0.000	1.149	-0.000	1.081	-0.000	1.106	-0.000	1.668	-0.000	1.686	-0.000	2.464	-0.000	-20.32
Circular 30°	1.009	-0.000	1.016	-0.000	0.985	-0.000	1.151	-0.000	1.081	-0.000	1.154	-0.000	1.709	-0.000	1.726	-0.000	2.489	-0.000	-18.85
Circular 60°	1.011	-0.000	1.013	-0.000	0.958	-0.000	1.161	-0.000	1.095	-0.000	1.112	-0.000	1.705	-0.000	1.715	-0.000	2.474	-0.000	-19.23
Circular 89°	1.013	-0.000	1.014	-0.000	0.957	-0.000	1.174	-0.000	1.092	-0.000	1.104	-0.000	1.668	-0.000	1.701	-0.000	2.458	-0.000	-19.22

	$\sigma_{Lat.}$ & p-value		$\sigma_{Lon.}$ & p-value		σ_{Height}		$\sigma_{\dot{Lat.}}$ & p-value		$\sigma_{\dot{Lon.}}$ & p-value		$\sigma_{\dot{Height}}$ & p-value	
	[mm]						[mm/dec]					
GRASP-like	0.915	-0.000	1.024	-0.000	0.882	-0.000	1.116	-0.000	1.136	-0.000	1.038	-0.000
E-GRASP-mod	0.918	-0.000	1.032	-0.000	0.881	-0.000	1.114	-0.000	1.135	-0.000	1.032	-0.000
E-GRASP-like	0.916	-0.000	1.028	-0.000	0.878	-0.000	1.114	-0.000	1.130	-0.000	1.012	-0.000
Circular 30°	0.945	-0.000	1.033	-0.000	0.867	-0.000	1.135	-0.000	1.137	-0.000	0.991	-0.000
Circular 60°	0.931	-0.000	1.040	-0.000	0.892	-0.000	1.120	-0.000	1.142	-0.000	1.033	-0.000
Circular 89°	0.928	-0.000	1.044	-0.000	0.894	-0.000	1.117	-0.000	1.151	-0.000	1.037	-0.000

Table F.39: Statistics of estimated ERPs for the SLR SRP mismodelling case.

	$\Delta X - Pole$						$\Delta Y - Pole$						ΔLOD					
	std. [mm]	p-value	mean ± std. [mm]	p-value	trend ± std. [mm/a]	p-value	std. [mm]	p-value	mean ± std. [mm]	p-value	trend ± std. [mm/a]	p-value	std. [μm]	p-value	mean ± std. [μm]	p-value	trend ± std. [μm/a]	p-value
Comb. reference																		
+ GRASP-like																		
- SRP mismodelling	1.277	0.000	0.297 ± 0.025	0.000	-0.020 ± 0.012	0.102	1.354	0.000	0.325 ± 0.027	0.000	0.037 ± 0.013	0.006	2.768	0.000	0.043 ± 0.055	0.437	0.006 ± 0.027	0.819
+ E-GRASP-mod																		
- SRP mismodelling	1.248	0.000	0.341 ± 0.025	0.000	-0.019 ± 0.012	0.121	1.320	0.000	0.566 ± 0.026	0.000	0.043 ± 0.013	0.001	2.722	0.000	-0.021 ± 0.054	0.694	0.002 ± 0.027	0.936
+ E-GRASP-like																		
- SRP mismodelling	1.260	0.000	0.081 ± 0.025	0.001	-0.031 ± 0.012	0.012	1.350	0.000	0.270 ± 0.027	0.000	0.038 ± 0.013	0.004	2.762	0.000	-0.008 ± 0.055	0.890	0.012 ± 0.027	0.649
+ Circular 30°																		
- SRP mismodelling	1.278	0.000	0.788 ± 0.025	0.000	0.002 ± 0.013	0.885	1.331	0.000	0.544 ± 0.026	0.000	0.055 ± 0.013	0.000	2.769	0.000	-0.001 ± 0.055	0.981	-0.002 ± 0.027	0.945
+ Circular 60°																		
- SRP mismodelling	1.261	0.001	0.311 ± 0.025	0.000	-0.015 ± 0.012	0.221	1.342	0.000	0.492 ± 0.026	0.000	0.054 ± 0.013	0.000	2.758	0.000	-0.016 ± 0.055	0.769	0.004 ± 0.027	0.875
+ Circular 89°																		
- SRP mismodelling	1.220	0.000	0.560 ± 0.024	0.000	-0.012 ± 0.012	0.327	1.317	0.000	0.404 ± 0.026	0.000	0.051 ± 0.013	0.000	2.747	0.000	-0.039 ± 0.054	0.472	0.006 ± 0.027	0.815

F.2.5 Earth gravity field mismodelling

Table F.40: Helmert parameters to the reference solution for the EGM mismodelling case, either fixed or solved for, in the case of SLR. The reference is a combination of LAGEOS-1 and LAGEOS-2.

	T_x [mm] $T_{\dot{x}}$ [mm/a]	T_y [mm] $T_{\dot{y}}$ [mm/a]	T_z [mm] $T_{\dot{z}}$ [mm/a]	R_x [mm] $R_{\dot{x}}$ [mm/a]	R_y [mm] $R_{\dot{y}}$ [mm/a]	R_z [mm] $R_{\dot{z}}$ [mm/a]	sc [mm] $\dot{sc}$ [mm/a]	s_0 s_0
+ GRASP-like								
- EGM mism.	-0.03 ± 0.32	1.74 ± 0.32	-0.64 ± 0.31	20.31 ± 0.39	-101.92 ± 0.38	-1.16 ± 0.37	0.49 ± 0.31	1.62
	-0.06 ± 0.14	0.05 ± 0.14	-0.02 ± 0.14	1.35 ± 0.17	-4.77 ± 0.17	0.03 ± 0.16	0.09 ± 0.13	0.71
- EGM mism. and co-est.	0.00 ± 0.05	0.02 ± 0.05	0.02 ± 0.05	0.35 ± 0.06	-0.05 ± 0.06	0.06 ± 0.05	-0.05 ± 0.05	0.24
	-0.00 ± 0.03	-0.01 ± 0.03	0.00 ± 0.03	0.11 ± 0.04	0.02 ± 0.03	-0.00 ± 0.03	0.01 ± 0.03	0.15
+ E-GRASP-mod								
- EGM mism.	0.24 ± 0.07	-0.59 ± 0.07	-0.09 ± 0.07	9.54 ± 0.09	-30.06 ± 0.09	-0.06 ± 0.08	-0.14 ± 0.07	0.37
	0.01 ± 0.05	-0.02 ± 0.05	0.00 ± 0.05	0.46 ± 0.06	-1.48 ± 0.06	-0.04 ± 0.06	-0.01 ± 0.05	0.27
- EGM mism. and co-est.	-0.04 ± 0.04	0.01 ± 0.05	0.06 ± 0.04	0.19 ± 0.05	-0.02 ± 0.05	0.05 ± 0.05	-0.05 ± 0.04	0.23
	0.01 ± 0.02	-0.00 ± 0.02	-0.01 ± 0.01	0.02 ± 0.02	-0.02 ± 0.02	-0.02 ± 0.02	-0.01 ± 0.01	0.08
+ E-GRASP-like								
- EGM mism.	0.36 ± 0.09	-0.69 ± 0.09	-0.24 ± 0.08	10.12 ± 0.11	-29.75 ± 0.10	-0.20 ± 0.10	-0.15 ± 0.08	0.44
	-0.00 ± 0.03	0.02 ± 0.03	-0.03 ± 0.03	0.51 ± 0.04	-1.42 ± 0.04	-0.04 ± 0.04	0.02 ± 0.03	0.17
- EGM mism. and co-est.	0.01 ± 0.05	0.00 ± 0.05	0.04 ± 0.04	0.03 ± 0.06	-0.47 ± 0.05	-0.02 ± 0.05	-0.03 ± 0.04	0.23
	-0.00 ± 0.01	0.02 ± 0.01	0.01 ± 0.01	0.01 ± 0.02	-0.03 ± 0.01	-0.00 ± 0.01	0.01 ± 0.01	0.06
+ Circular 30°								
- EGM mism.	-0.04 ± 0.05	0.10 ± 0.05	0.01 ± 0.05	0.64 ± 0.06	-3.28 ± 0.06	-0.09 ± 0.06	-0.03 ± 0.05	0.26
	0.00 ± 0.02	0.00 ± 0.02	0.01 ± 0.01	0.02 ± 0.02	-0.17 ± 0.02	-0.00 ± 0.02	0.01 ± 0.01	0.08
- EGM mism. and co-est.	-0.02 ± 0.05	0.01 ± 0.05	-0.01 ± 0.05	0.01 ± 0.06	0.04 ± 0.06	-0.01 ± 0.05	-0.00 ± 0.05	0.24
	0.00 ± 0.02	-0.00 ± 0.02	0.01 ± 0.01	-0.01 ± 0.02	-0.01 ± 0.02	0.00 ± 0.02	0.00 ± 0.01	0.08
+ Circular 60°								
- EGM mism.	0.06 ± 0.05	-0.18 ± 0.05	0.02 ± 0.05	1.93 ± 0.06	-4.78 ± 0.06	-0.06 ± 0.05	-0.03 ± 0.04	0.24
	0.01 ± 0.01	-0.01 ± 0.01	0.01 ± 0.01	0.08 ± 0.02	-0.25 ± 0.02	0.01 ± 0.02	-0.01 ± 0.01	0.07
- EGM mism. and co-est.	0.00 ± 0.04	-0.01 ± 0.04	-0.01 ± 0.04	0.21 ± 0.05	-0.22 ± 0.05	-0.01 ± 0.05	-0.05 ± 0.04	0.21
	0.01 ± 0.02	-0.01 ± 0.02	0.01 ± 0.02	0.00 ± 0.02	-0.01 ± 0.02	0.00 ± 0.02	-0.01 ± 0.02	0.08
+ Circular 89°								
- EGM mism.	-0.02 ± 0.04	0.01 ± 0.04	0.02 ± 0.04	0.09 ± 0.05	-0.73 ± 0.05	-0.01 ± 0.04	0.02 ± 0.04	0.20
	-0.01 ± 0.01	0.00 ± 0.01	-0.00 ± 0.01	0.02 ± 0.02	-0.01 ± 0.02	0.00 ± 0.02	0.00 ± 0.01	0.07
- EGM mism. and co-est.	0.02 ± 0.05	0.01 ± 0.05	-0.06 ± 0.04	0.01 ± 0.06	-0.06 ± 0.05	0.02 ± 0.05	0.00 ± 0.04	0.23
	-0.01 ± 0.01	0.00 ± 0.01	0.00 ± 0.01	0.00 ± 0.01	0.02 ± 0.01	0.00 ± 0.01	0.00 ± 0.01	0.06

Table F.41: Formal errors for the SLR EGM mismodelling case.

	σ_x & p-value		σ_y & p-value		σ_z & p-value		$\sigma_{\dot{x}}$ & p-value		$\sigma_{\dot{y}}$ & p-value		$\sigma_{\dot{z}}$ & p-value		σ_{x_p} & p-value		σ_{y_p} & p-value		σ_{LOD} & p-value		exp. imp.
	[mm]						[mm/dec]						[cm]				[μm]		[%]
GRASP-like	1.075	-0.003	1.070	-0.012	1.006	-0.000	1.242	-0.000	1.165	-0.001	1.186	-0.000	1.800	0.000	1.809	0.000	2.628	-0.000	-18.40
E-GRASP-mod	1.017	-0.000	1.014	-0.000	0.949	-0.000	1.167	-0.000	1.095	-0.000	1.112	-0.000	1.680	-0.000	1.695	-0.000	2.487	-0.000	-19.90
E-GRASP-like	1.014	-0.000	1.013	-0.000	0.951	-0.000	1.162	-0.000	1.093	-0.000	1.117	-0.000	1.685	-0.000	1.701	-0.000	2.477	-0.000	-20.19
Circular 30°	1.011	-0.000	1.015	-0.000	0.986	-0.000	1.152	-0.000	1.081	-0.000	1.156	-0.000	1.707	-0.000	1.725	-0.000	2.491	-0.000	-18.72
Circular 60°	1.013	-0.000	1.015	-0.000	0.959	-0.000	1.163	-0.000	1.097	-0.000	1.112	-0.000	1.703	-0.000	1.714	-0.000	2.476	-0.000	-19.10
Circular 89°	1.014	-0.000	1.016	-0.000	0.957	-0.000	1.175	-0.000	1.093	-0.000	1.103	-0.000	1.661	-0.000	1.699	-0.000	2.455	-0.000	-19.09

	$\sigma_{Lat.}$ & p-value		$\sigma_{Lon.}$ & p-value		σ_{Height}		$\sigma_{\dot{Lat.}}$ & p-value		$\sigma_{\dot{Lon.}}$ & p-value		$\sigma_{\dot{Height}}$ & p-value	
	[mm]						[mm/dec]					
GRASP-like	0.982	-0.001	1.098	-0.035	0.947	-0.001	1.197	-0.000	1.218	-0.005	1.113	-0.000
E-GRASP-mod	0.925	-0.000	1.041	-0.000	0.888	-0.000	1.123	-0.000	1.145	-0.000	1.041	-0.000
E-GRASP-like	0.926	-0.000	1.039	-0.000	0.887	-0.000	1.125	-0.000	1.142	-0.000	1.023	-0.000
Circular 30°	0.946	-0.000	1.032	-0.000	0.863	-0.000	1.136	-0.000	1.139	-0.000	0.986	-0.000
Circular 60°	0.932	-0.000	1.042	-0.000	0.893	-0.000	1.120	-0.000	1.144	-0.000	1.034	-0.000
Circular 89°	0.928	-0.000	1.046	-0.000	0.895	-0.000	1.117	-0.000	1.152	-0.000	1.037	-0.000

Table F.42: Formal errors for the SLR EGM mismodelling case, SHs estimated.

	σ_x & p-value		σ_y & p-value		σ_z & p-value		$\sigma_{\dot{x}}$ & p-value		$\sigma_{\dot{y}}$ & p-value		$\sigma_{\dot{z}}$ & p-value		σ_{x_p} & p-value		σ_{y_p} & p-value		σ_{LOD} & p-value		exp. imp.
	[mm]						[mm/dec]						[cm]				[μm]		[%]
GRASP-like	1.017	-0.000	1.016	-0.000	0.970	-0.000	1.167	-0.000	1.099	-0.000	1.123	-0.000	1.725	0.000	1.738	0.000	2.465	0.000	-18.36
E-GRASP-mod	1.016	-0.000	1.016	-0.000	0.959	-0.000	1.164	-0.000	1.094	-0.000	1.113	-0.000	1.693	-0.000	1.705	-0.000	2.471	-0.000	-19.86
E-GRASP-like	1.014	-0.000	1.015	-0.000	0.960	-0.000	1.159	-0.000	1.090	-0.000	1.115	-0.000	1.697	-0.000	1.709	-0.000	2.460	-0.000	-20.17
Circular 30°	1.012	-0.000	1.017	-0.000	0.989	-0.000	1.152	-0.000	1.081	-0.000	1.157	-0.000	1.711	-0.000	1.729	-0.000	2.490	-0.000	-18.71
Circular 60°	1.015	-0.000	1.016	-0.000	0.962	-0.000	1.163	-0.000	1.097	-0.000	1.114	-0.000	1.709	-0.000	1.719	-0.000	2.476	-0.000	-19.04
Circular 89°	1.015	-0.000	1.016	-0.000	0.958	-0.000	1.176	-0.000	1.095	-0.000	1.105	-0.000	1.666	-0.000	1.703	-0.000	2.461	-0.000	-18.99

	$\sigma_{Lat.}$ & p-value		$\sigma_{Lon.}$ & p-value		σ_{Height}		$\sigma_{\dot{Lat.}}$ & p-value		$\sigma_{\dot{Lon.}}$ & p-value		$\sigma_{\dot{Height}}$ & p-value	
	[mm]						[mm/dec]					
GRASP-like	0.941	-0.000	1.042	-0.000	0.905	-0.000	1.133	-0.000	1.146	-0.000	1.050	-0.000
E-GRASP-mod	0.933	-0.000	1.042	-0.000	0.892	-0.000	1.124	-0.000	1.143	-0.000	1.041	-0.000
E-GRASP-like	0.933	-0.000	1.040	-0.000	0.891	-0.000	1.124	-0.000	1.139	-0.000	1.026	-0.000
Circular 30°	0.949	-0.000	1.034	-0.000	0.866	-0.000	1.137	-0.000	1.139	-0.000	0.986	-0.000
Circular 60°	0.934	-0.000	1.043	-0.000	0.895	-0.000	1.122	-0.000	1.145	-0.000	1.035	-0.000
Circular 89°	0.930	-0.000	1.047	-0.000	0.896	-0.000	1.120	-0.000	1.153	-0.000	1.040	-0.000

Table F.43: Statistics of estimated ERPs for the SLR EGM mismodelling case.

	$\Delta X - Pole$						$\Delta Y - Pole$						ΔLOD					
	std. [mm]	p-value	mean $\pm$ std. [mm]	p-value	trend $\pm$ std. [mm/a]	p-value	std. [mm]	p-value	mean $\pm$ std. [mm]	p-value	trend $\pm$ std. [mm/a]	p-value	std. [μm]	p-value	mean $\pm$ std. [μm]	p-value	trend $\pm$ std. [μm/a]	p-value
Comb. reference																		
+ GRASP-like																		
- EGM mism.	10.215	0.000	107.765 $\pm$ 0.042	0.000	4.946 $\pm$ 0.021	0.000	2.889	0.000	-21.095 $\pm$ 0.039	0.000	-1.035 $\pm$ 0.020	0.000	3.286	0.000	0.197 $\pm$ 0.065	0.002	0.021 $\pm$ 0.032	0.510
- EGM mism. and co-est.	1.347	0.000	0.467 $\pm$ 0.027	0.000	-0.012 $\pm$ 0.013	0.348	1.403	0.000	-0.028 $\pm$ 0.028	0.311	0.029 $\pm$ 0.014	0.037	2.750	0.000	0.029 $\pm$ 0.054	0.591	0.001 $\pm$ 0.027	0.959
+ E-GRASP-mod																		
- EGM mism.	3.226	0.000	33.584 $\pm$ 0.026	0.000	1.457 $\pm$ 0.013	0.000	1.637	0.000	-9.874 $\pm$ 0.027	0.000	-0.454 $\pm$ 0.013	0.000	2.855	0.000	-0.173 $\pm$ 0.056	0.002	-0.003 $\pm$ 0.028	0.928
- EGM mism. and co-est.	1.225	0.000	0.559 $\pm$ 0.024	0.000	-0.002 $\pm$ 0.012	0.838	1.299	0.000	0.407 $\pm$ 0.026	0.000	0.054 $\pm$ 0.013	0.000	2.686	0.000	0.031 $\pm$ 0.053	0.565	0.001 $\pm$ 0.026	0.962
+ E-GRASP-like																		
- EGM mism.	2.964	0.000	32.643 $\pm$ 0.027	0.000	1.305 $\pm$ 0.013	0.000	1.701	0.000	-10.621 $\pm$ 0.028	0.000	-0.452 $\pm$ 0.014	0.000	3.040	0.000	-0.233 $\pm$ 0.060	0.000	0.006 $\pm$ 0.030	0.845
- EGM mism. and co-est.	1.233	0.000	0.569 $\pm$ 0.024	0.000	-0.018 $\pm$ 0.012	0.140	1.332	0.000	0.340 $\pm$ 0.026	0.000	0.039 $\pm$ 0.013	0.003	2.734	0.000	0.032 $\pm$ 0.054	0.559	0.004 $\pm$ 0.027	0.871
+ Circular 30°																		
- EGM mism.	1.311	0.000	4.279 $\pm$ 0.025	0.000	0.161 $\pm$ 0.012	0.000	1.319	0.001	-0.268 $\pm$ 0.026	0.000	0.025 $\pm$ 0.013	0.056	2.762	0.000	-0.025 $\pm$ 0.055	0.653	-0.003 $\pm$ 0.027	0.907
- EGM mism. and co-est.	1.263	0.000	0.671 $\pm$ 0.025	0.000	-0.001 $\pm$ 0.012	0.952	1.322	0.001	0.440 $\pm$ 0.026	0.000	0.054 $\pm$ 0.013	0.000	2.757	0.000	0.033 $\pm$ 0.055	0.549	-0.003 $\pm$ 0.027	0.916
+ Circular 60°																		
- EGM mism.	1.342	0.000	5.878 $\pm$ 0.025	0.000	0.229 $\pm$ 0.012	0.000	1.332	0.000	-1.537 $\pm$ 0.026	0.000	-0.039 $\pm$ 0.013	0.003	2.755	0.000	-0.033 $\pm$ 0.055	0.550	0.004 $\pm$ 0.027	0.883
- EGM mism. and co-est.	1.251	0.004	0.644 $\pm$ 0.025	0.000	-0.006 $\pm$ 0.012	0.652	1.337	0.000	0.364 $\pm$ 0.026	0.000	0.053 $\pm$ 0.013	0.000	2.743	0.000	0.033 $\pm$ 0.054	0.545	0.004 $\pm$ 0.027	0.896
+ Circular 89°																		
- EGM mism.	1.193	0.000	1.314 $\pm$ 0.024	0.000	0.022 $\pm$ 0.012	0.058	1.293	0.000	0.292 $\pm$ 0.026	0.000	0.042 $\pm$ 0.013	0.001	2.722	0.000	0.022 $\pm$ 0.054	0.686	0.004 $\pm$ 0.027	0.872
- EGM mism. and co-est.	1.195	0.000	0.580 $\pm$ 0.024	0.000	-0.010 $\pm$ 0.012	0.371	1.300	0.000	0.412 $\pm$ 0.026	0.000	0.050 $\pm$ 0.013	0.000	2.725	0.000	0.030 $\pm$ 0.054	0.573	0.005 $\pm$ 0.027	0.860

F.3 GPS

F.3.1 Systematic error-free

Table F.44: Helmert parameters to a priori for the systematic error-free scenarios for GPS.
The reference is the GPS constellation.

	T_x [mm] $T_{\dot{x}}$ [mm/a]	T_y [mm] $T_{\dot{y}}$ [mm/a]	T_z [mm] $T_{\dot{z}}$ [mm/a]	R_x [mm] $R_{\dot{x}}$ [mm/a]	R_y [mm] $R_{\dot{y}}$ [mm/a]	R_z [mm] $R_{\dot{z}}$ [mm/a]	sc [mm] $\dot{sc}$ [mm/a]	s_0 s_0
Reference	-0.00 ± 0.00	-0.01 ± 0.00	-0.02 ± 0.00	0.13 ± 0.00	0.00 ± 0.00	0.01 ± 0.00	0.00 ± 0.00	0.01
	0.00 ± 0.00	-0.00 ± 0.00	0.00 ± 0.00	0.01 ± 0.00	0.00 ± 0.00	0.00 ± 0.00	-0.00 ± 0.00	0.01
+ GRASP-like	-0.00 ± 0.00	0.00 ± 0.00	-0.00 ± 0.00	0.13 ± 0.00	0.01 ± 0.00	0.01 ± 0.00	0.00 ± 0.00	0.01
	0.00 ± 0.00	-0.00 ± 0.00	-0.00 ± 0.00	0.01 ± 0.00	0.00 ± 0.00	0.00 ± 0.00	-0.00 ± 0.00	0.01
+ E-GRASP-mod	-0.00 ± 0.00	-0.01 ± 0.00	-0.02 ± 0.00	0.13 ± 0.00	-0.01 ± 0.00	0.01 ± 0.00	0.00 ± 0.00	0.01
	0.00 ± 0.00	-0.00 ± 0.00	0.01 ± 0.00	0.01 ± 0.00	0.00 ± 0.00	0.00 ± 0.00	-0.00 ± 0.00	0.01
+ E-GRASP-like	-0.00 ± 0.00	-0.01 ± 0.00	-0.01 ± 0.00	0.11 ± 0.00	-0.00 ± 0.00	0.01 ± 0.00	0.00 ± 0.00	0.01
	0.00 ± 0.00	-0.00 ± 0.00	0.00 ± 0.00	0.01 ± 0.00	0.00 ± 0.00	0.00 ± 0.00	-0.00 ± 0.00	0.01
+ Circular 30°	-0.00 ± 0.00	-0.00 ± 0.00	-0.02 ± 0.00	0.14 ± 0.00	-0.01 ± 0.00	0.01 ± 0.00	0.00 ± 0.00	0.01
	0.00 ± 0.00	-0.00 ± 0.00	0.00 ± 0.00	0.01 ± 0.00	0.00 ± 0.00	0.00 ± 0.00	-0.00 ± 0.00	0.01
+ Circular 60°	-0.00 ± 0.00	-0.01 ± 0.00	-0.02 ± 0.00	0.14 ± 0.00	-0.00 ± 0.00	0.01 ± 0.00	0.00 ± 0.00	0.01
	0.00 ± 0.00	-0.00 ± 0.00	0.00 ± 0.00	0.01 ± 0.00	0.00 ± 0.00	0.00 ± 0.00	-0.00 ± 0.00	0.01
+ Circular 89°	-0.00 ± 0.00	-0.01 ± 0.00	-0.00 ± 0.00	0.15 ± 0.00	0.01 ± 0.00	0.01 ± 0.00	0.00 ± 0.00	0.01
	0.00 ± 0.00	-0.00 ± 0.00	0.00 ± 0.00	0.01 ± 0.00	0.00 ± 0.00	0.00 ± 0.00	-0.00 ± 0.00	0.01

Table F.45: Formal errors for the systematic error-free scenarios for GPS. The reference is the GPS constellation.

	σ_x & p-value	σ_y & p-value	σ_z & p-value	$\sigma_{\dot{x}}$ & p-value	$\sigma_{\dot{y}}$ & p-value	$\sigma_{\dot{z}}$ & p-value	σ_{x_p} & p-value	σ_{y_p} & p-value	σ_{LOD} & p-value	exp. imp.
	[mm]			[mm/dec]			[mm]		[mm]	[%]
Reference	0.259 —	0.266 —	0.234 —	0.266 —	0.272 —	0.254 —	0.333 —	0.332 —	0.466 —	—
GRASP-like	0.257 -0.000	0.263 -0.000	0.225 -0.000	0.264 -0.000	0.269 -0.000	0.238 -0.000	0.331 0.000	0.329 0.000	0.458 0.000	-0.47
E-GRASP-mod	0.258 -0.000	0.264 -0.000	0.227 -0.000	0.265 -0.000	0.271 -0.000	0.241 -0.000	0.331 -0.000	0.330 -0.000	0.456 -0.000	-0.40
E-GRASP-like	0.257 -0.000	0.264 -0.000	0.226 -0.000	0.265 -0.000	0.271 -0.000	0.240 -0.000	0.331 -0.000	0.329 -0.000	0.456 -0.000	-0.39
Circular 30°	0.257 -0.000	0.264 -0.000	0.229 -0.000	0.265 -0.000	0.271 -0.000	0.246 -0.000	0.331 -0.000	0.330 -0.000	0.455 -0.000	-0.34
Circular 60°	0.257 -0.000	0.264 -0.000	0.228 -0.000	0.265 -0.000	0.271 -0.000	0.243 -0.000	0.331 -0.000	0.330 -0.000	0.455 -0.000	-0.34
Circular 89°	0.257 -0.000	0.264 -0.000	0.228 -0.000	0.265 -0.000	0.271 -0.000	0.243 -0.000	0.331 -0.000	0.329 -0.000	0.453 -0.000	-0.34

	$\sigma_{Lat.}$ & p-value	$\sigma_{Lon.}$ & p-value	σ_{Height}	$\sigma_{\dot{Lat.}}$ & p-value	$\sigma_{\dot{Lon.}}$ & p-value	$\sigma_{\dot{Height}}$ & p-value
	[mm]			[mm/dec]		
Reference	0.243 —	0.278 —	0.213 —	0.259 —	0.285 —	0.228 —
GRASP-like	0.237 -0.000	0.276 -0.000	0.207 -0.000	0.248 -0.000	0.283 -0.000	0.219 -0.000
E-GRASP-mod	0.238 -0.000	0.277 -0.000	0.209 -0.000	0.250 -0.000	0.284 -0.000	0.221 -0.000
E-GRASP-like	0.238 -0.000	0.277 -0.000	0.208 -0.000	0.250 -0.000	0.284 -0.000	0.221 -0.000
Circular 30°	0.240 -0.000	0.277 -0.000	0.210 -0.000	0.254 -0.000	0.284 -0.000	0.224 -0.000
Circular 60°	0.239 -0.000	0.277 -0.000	0.209 -0.000	0.252 -0.000	0.284 -0.000	0.222 -0.000
Circular 89°	0.239 -0.000	0.277 -0.000	0.209 -0.000	0.252 -0.000	0.284 -0.000	0.222 -0.000

Table F.46: Statistics for ERPs by adding space-tie satellit scenarios in the GPS systematic error-free case.

	$\Delta X - Pole$						$\Delta Y - Pole$						ΔLOD					
	std. [mm]	p-value	mean ± std. [mm]	p-value	trend ± std. [mm/a]	p-value	std. [mm]	p-value	mean ± std. [mm]	p-value	trend ± std. [mm/a]	p-value	std. [mm]	p-value	mean ± std. [mm]	p-value	trend ± std. [mm/a]	p-value
GPS constellation																		
- sys. error-free	0.056	—	-0.004 ± 0.001	0.000	-0.001 ± 0.001	0.350	0.058	—	-0.145 ± 0.001	0.000	-0.007 ± 0.001	0.000	0.476	—	0.011 ± 0.009	0.233	-0.003 ± 0.005	0.579
+ GRASP like																		
- sys. error-free	0.055	0.286	-0.009 ± 0.001	0.000	-0.001 ± 0.001	0.201	0.056	0.353	-0.139 ± 0.001	0.000	-0.007 ± 0.001	0.000	0.467	0.370	0.012 ± 0.009	0.196	-0.003 ± 0.005	0.497
+ E-GRASP-mod																		
- sys. error-free	0.055	0.305	0.004 ± 0.001	0.000	-0.000 ± 0.001	0.471	0.056	0.263	-0.140 ± 0.001	0.000	-0.007 ± 0.001	0.000	0.462	0.201	0.009 ± 0.009	0.322	-0.004 ± 0.005	0.415
+ E-GRASP-like																		
- sys. error-free	0.055	0.146	0.000 ± 0.001	0.709	-0.000 ± 0.001	0.801	0.055	0.060	-0.116 ± 0.001	0.000	-0.005 ± 0.001	0.000	0.463	0.239	0.010 ± 0.009	0.257	-0.002 ± 0.005	0.586
+ Circular 30°																		
- sys. error-free	0.054	0.103	0.011 ± 0.001	0.000	0.000 ± 0.001	0.387	0.056	0.240	-0.149 ± 0.001	0.000	-0.007 ± 0.001	0.000	0.462	0.186	0.013 ± 0.009	0.151	-0.002 ± 0.005	0.680
+ Circular 60°																		
- sys. error-free	0.055	0.184	0.001 ± 0.001	0.308	-0.000 ± 0.001	0.430	0.056	0.234	-0.153 ± 0.001	0.000	-0.007 ± 0.001	0.000	0.460	0.132	0.009 ± 0.009	0.305	-0.003 ± 0.005	0.554
+ Circular 89°																		
- sys. error-free	0.055	0.117	-0.012 ± 0.001	0.000	-0.001 ± 0.001	0.173	0.056	0.174	-0.159 ± 0.001	0.000	-0.008 ± 0.001	0.000	0.457	0.089	0.013 ± 0.009	0.148	-0.002 ± 0.004	0.644

F.3.2 Solar radiation pressure mismodelling

Table F.47: Helmert parameters to the reference solution for the solar radiation pressure mismodelling case for GPS. The reference is the GPS constellation.

	T_x [mm]	T_y [mm]	T_z [mm]	R_x [mm]	R_y [mm]	R_z [mm]	sc [mm]	s_0
	$\dot{T}_x$ [mm/a]	$\dot{T}_y$ [mm/a]	$\dot{T}_z$ [mm/a]	$\dot{R}_x$ [mm/a]	$\dot{R}_y$ [mm/a]	$\dot{R}_z$ [mm/a]	$\dot{sc}$ [mm/a]	$\dot{s}_0$
Reference (SRP mism.)	0.04 ± 0.01	-0.01 ± 0.01	-0.13 ± 0.01	-0.56 ± 0.01	-0.67 ± 0.01	0.03 ± 0.01	-0.40 ± 0.01	0.06
	0.01 ± 0.00	-0.01 ± 0.00	-0.04 ± 0.00	-0.02 ± 0.00	-0.04 ± 0.00	0.00 ± 0.00	0.00 ± 0.00	0.01
+ GRASP-like	0.00 ± 0.01	-0.01 ± 0.01	0.06 ± 0.01	-0.61 ± 0.01	-0.66 ± 0.01	0.03 ± 0.01	-0.40 ± 0.01	0.06
	0.00 ± 0.00	-0.00 ± 0.00	0.00 ± 0.00	-0.03 ± 0.00	-0.04 ± 0.00	0.00 ± 0.00	-0.00 ± 0.00	0.01
+ E-GRASP-mod	0.04 ± 0.01	-0.01 ± 0.01	-0.04 ± 0.01	-0.58 ± 0.01	-0.64 ± 0.01	0.03 ± 0.01	-0.39 ± 0.01	0.06
	0.01 ± 0.00	-0.01 ± 0.00	-0.00 ± 0.00	-0.02 ± 0.00	-0.04 ± 0.00	0.00 ± 0.00	-0.00 ± 0.00	0.01
+ E-GRASP-like	0.03 ± 0.01	-0.01 ± 0.01	-0.00 ± 0.01	-0.59 ± 0.01	-0.63 ± 0.01	0.03 ± 0.01	-0.39 ± 0.01	0.06
	0.00 ± 0.00	-0.01 ± 0.00	0.01 ± 0.00	-0.03 ± 0.00	-0.04 ± 0.00	0.00 ± 0.00	-0.00 ± 0.00	0.01
+ Circular 30°	0.04 ± 0.01	-0.01 ± 0.01	-0.08 ± 0.01	-0.56 ± 0.01	-0.65 ± 0.01	0.03 ± 0.01	-0.39 ± 0.01	0.06
	0.01 ± 0.00	-0.01 ± 0.00	-0.03 ± 0.00	-0.02 ± 0.00	-0.04 ± 0.00	0.00 ± 0.00	-0.00 ± 0.00	0.01
+ Circular 60°	0.04 ± 0.01	-0.01 ± 0.01	-0.03 ± 0.01	-0.56 ± 0.01	-0.62 ± 0.01	0.03 ± 0.01	-0.39 ± 0.01	0.06
	0.01 ± 0.00	-0.01 ± 0.00	-0.01 ± 0.00	-0.02 ± 0.00	-0.04 ± 0.00	0.00 ± 0.00	-0.00 ± 0.00	0.01
+ Circular 89°	0.04 ± 0.01	-0.01 ± 0.01	-0.02 ± 0.01	-0.57 ± 0.01	-0.63 ± 0.01	0.03 ± 0.01	-0.39 ± 0.01	0.06
	0.01 ± 0.00	-0.01 ± 0.00	-0.02 ± 0.00	-0.02 ± 0.00	-0.04 ± 0.00	0.00 ± 0.00	-0.00 ± 0.00	0.01

Table F.48: Formal errors for the GPS SRP mismodelling case.

	σ_x & p-value		σ_y & p-value		σ_z & p-value		$\sigma_{\dot{x}}$ & p-value		$\sigma_{\dot{y}}$ & p-value		$\sigma_{\dot{z}}$ & p-value		σ_{x_p} & p-value		σ_{y_p} & p-value		σ_{LOD} & p-value		exp. imp.
	[mm]						[mm/dec]						[mm]				[mm]		[%]
Reference	0.311	—	0.319	—	0.281	—	0.320	—	0.327	—	0.305	—	0.400	—	0.399	—	0.560	—	—
GRASP-like	0.309	-0.000	0.316	-0.000	0.270	-0.000	0.317	-0.000	0.324	-0.000	0.286	-0.000	0.397	0.000	0.396	0.000	0.551	0.000	-0.47
E-GRASP-mod	0.309	-0.000	0.317	-0.000	0.272	-0.000	0.318	-0.000	0.325	-0.000	0.289	-0.000	0.398	-0.000	0.396	-0.000	0.547	-0.000	-0.40
E-GRASP-like	0.309	-0.000	0.317	-0.000	0.272	-0.000	0.318	-0.000	0.325	-0.000	0.288	-0.000	0.397	-0.000	0.395	-0.000	0.548	-0.000	-0.39
Circular 30°	0.309	-0.000	0.317	-0.000	0.275	-0.000	0.318	-0.000	0.325	-0.000	0.296	-0.000	0.397	-0.000	0.395	-0.000	0.546	-0.000	-0.34
Circular 60°	0.309	-0.000	0.317	-0.000	0.273	-0.000	0.318	-0.000	0.325	-0.000	0.292	-0.000	0.397	-0.000	0.395	-0.000	0.546	-0.000	-0.34
Circular 89°	0.309	-0.000	0.317	-0.000	0.273	-0.000	0.318	-0.000	0.325	-0.000	0.292	-0.000	0.396	-0.000	0.395	-0.000	0.543	-0.000	-0.34

	$\sigma_{Lat.}$ & p-value		$\sigma_{Lon.}$ & p-value		σ_{Height}		$\sigma_{\dot{Lat.}}$ & p-value		$\sigma_{\dot{Lon.}}$ & p-value		$\sigma_{\dot{Height}}$ & p-value	
	[mm]						[mm/dec]					
Reference	0.292	—	0.334	—	0.255	—	0.312	—	0.343	—	0.274	—
GRASP-like	0.285	-0.000	0.332	-0.000	0.249	-0.000	0.298	-0.000	0.340	-0.000	0.263	-0.000
E-GRASP-mod	0.286	-0.000	0.333	-0.000	0.250	-0.000	0.301	-0.000	0.341	-0.000	0.266	-0.000
E-GRASP-like	0.286	-0.000	0.332	-0.000	0.250	-0.000	0.300	-0.000	0.341	-0.000	0.265	-0.000
Circular 30°	0.288	-0.000	0.332	-0.000	0.252	-0.000	0.305	-0.000	0.341	-0.000	0.269	-0.000
Circular 60°	0.287	-0.000	0.332	-0.000	0.251	-0.000	0.302	-0.000	0.341	-0.000	0.266	-0.000
Circular 89°	0.286	-0.000	0.332	-0.000	0.251	-0.000	0.302	-0.000	0.340	-0.000	0.266	-0.000

Table F.49: Statistics of estimated ERPs for the GPS SRP mismodelling case.

	$\Delta X - Pole$					$\Delta Y - Pole$					ΔLOD				
	std. [mm]	p-value	mean ± std. [mm]	p-value	trend ± std. [mm/a]	p-value	std. [mm]	p-value	mean ± std. [mm]	p-value	trend ± std. [mm/a]	p-value	std. [mm]	p-value	mean ± std. [mm]	p-value	trend ± std. [mm/a]	p-value
GPS constellation																		
- SRP	0.124	0.000	0.755 ± 0.002	0.000	0.043 ± 0.001	0.000	0.075	0.000	0.612 ± 0.001	0.000	0.024 ± 0.001	0.000	3.039	0.000	-7.186 ± 0.060	0.000	0.059 ± 0.030	0.048
+ GRASP like																		
- SRP	0.119	0.031	0.739 ± 0.002	0.000	0.040 ± 0.001	0.000	0.078	0.026	0.660 ± 0.001	0.000	0.027 ± 0.001	0.000	3.022	0.742	-7.167 ± 0.060	0.000	0.060 ± 0.030	0.043
+ E-GRASP-mod																		
- SRP	0.117	0.002	0.714 ± 0.002	0.000	0.038 ± 0.001	0.000	0.075	0.569	0.632 ± 0.001	0.000	0.025 ± 0.001	0.000	3.005	0.512	-7.128 ± 0.059	0.000	0.060 ± 0.029	0.043
+ E-GRASP-like																		
- SRP	0.115	0.000	0.700 ± 0.002	0.000	0.037 ± 0.001	0.000	0.077	0.105	0.646 ± 0.001	0.000	0.026 ± 0.001	0.000	2.997	0.472	-7.118 ± 0.059	0.000	0.060 ± 0.029	0.041
+ Circular 30°																		
- SRP	0.119	0.077	0.726 ± 0.002	0.000	0.041 ± 0.001	0.000	0.074	0.724	0.611 ± 0.001	0.000	0.024 ± 0.001	0.000	3.004	0.517	-7.139 ± 0.059	0.000	0.061 ± 0.029	0.038
+ Circular 60°																		
- SRP	0.116	0.001	0.692 ± 0.002	0.000	0.038 ± 0.001	0.000	0.074	0.754	0.616 ± 0.001	0.000	0.024 ± 0.001	0.000	2.988	0.355	-7.087 ± 0.059	0.000	0.063 ± 0.029	0.032
+ Circular 89°																		
- SRP	0.119	0.031	0.708 ± 0.002	0.000	0.040 ± 0.001	0.000	0.074	0.672	0.621 ± 0.001	0.000	0.024 ± 0.001	0.000	2.993	0.367	-7.016 ± 0.059	0.000	0.064 ± 0.029	0.029

F.3.3 Earth gravity field mismodelling

Table F.50: Helmert parameters to the reference solution for the EGM mismodelling case, either fixed or solved for, in the case of GPS. The reference is the GPS constellation.

	T_x [mm] $T_{\dot{x}}$ [mm/a]	T_y [mm] $T_{\dot{y}}$ [mm/a]	T_z [mm] $T_{\dot{z}}$ [mm/a]	R_x [mm] $R_{\dot{x}}$ [mm/a]	R_y [mm] $R_{\dot{y}}$ [mm/a]	R_z [mm] $R_{\dot{z}}$ [mm/a]	sc [mm] $\dot{sc}$ [mm/a]	s_0 s_0
Reference								
- EGM mism.	0.06 ± 0.00	-0.07 ± 0.00	-0.04 ± 0.00	0.27 ± 0.00	-1.23 ± 0.00	0.02 ± 0.00	-0.00 ± 0.00	0.02
	0.00 ± 0.00	-0.00 ± 0.00	0.00 ± 0.00	0.01 ± 0.00	-0.06 ± 0.00	0.00 ± 0.00	-0.00 ± 0.00	0.01
- EGM mism. and co-est.	0.01 ± 0.00	-0.00 ± 0.00	-0.08 ± 0.00	0.06 ± 0.00	0.01 ± 0.00	0.01 ± 0.00	-0.00 ± 0.00	0.01
	0.00 ± 0.00	-0.00 ± 0.00	0.00 ± 0.00	0.00 ± 0.00	0.00 ± 0.00	0.00 ± 0.00	-0.00 ± 0.00	0.01
+ GRASP-like								
- EGM mism.	-0.10 ± 0.01	0.74 ± 0.01	-1.02 ± 0.01	0.04 ± 0.01	-1.95 ± 0.01	-0.11 ± 0.01	0.00 ± 0.01	0.07
	0.02 ± 0.00	0.01 ± 0.00	0.03 ± 0.00	0.00 ± 0.00	-0.08 ± 0.00	-0.00 ± 0.00	-0.00 ± 0.00	0.01
- EGM mism. and co-est.	0.02 ± 0.00	0.04 ± 0.00	-0.03 ± 0.00	0.00 ± 0.00	0.07 ± 0.00	0.00 ± 0.00	-0.00 ± 0.00	0.01
	0.01 ± 0.00	0.00 ± 0.00	0.02 ± 0.00	-0.00 ± 0.00	0.01 ± 0.00	-0.00 ± 0.00	-0.00 ± 0.00	0.01
+ E-GRASP-mod								
- EGM mism.	0.04 ± 0.00	-0.06 ± 0.00	-0.01 ± 0.00	0.33 ± 0.00	-1.47 ± 0.00	0.01 ± 0.00	-0.00 ± 0.00	0.02
	0.00 ± 0.00	-0.00 ± 0.00	0.00 ± 0.00	0.02 ± 0.00	-0.07 ± 0.00	0.00 ± 0.00	-0.00 ± 0.00	0.01
- EGM mism. and co-est.	-0.01 ± 0.00	0.01 ± 0.00	-0.04 ± 0.00	0.13 ± 0.00	-0.01 ± 0.00	0.00 ± 0.00	-0.00 ± 0.00	0.01
	0.00 ± 0.00	-0.00 ± 0.00	0.00 ± 0.00	0.01 ± 0.00	0.00 ± 0.00	0.00 ± 0.00	-0.00 ± 0.00	0.01
+ E-GRASP-like								
- EGM mism.	0.04 ± 0.00	-0.06 ± 0.00	-0.01 ± 0.00	0.32 ± 0.00	-1.52 ± 0.00	0.01 ± 0.00	-0.00 ± 0.00	0.02
	0.00 ± 0.00	-0.00 ± 0.00	-0.00 ± 0.00	0.02 ± 0.00	-0.07 ± 0.00	0.00 ± 0.00	-0.00 ± 0.00	0.01
- EGM mism. and co-est.	-0.01 ± 0.00	0.03 ± 0.00	0.02 ± 0.00	0.05 ± 0.00	-0.01 ± 0.00	0.00 ± 0.00	-0.00 ± 0.00	0.01
	0.00 ± 0.00	-0.00 ± 0.00	0.00 ± 0.00	0.00 ± 0.00	0.00 ± 0.00	0.00 ± 0.00	-0.00 ± 0.00	0.01
+ Circular 30°								
- EGM mism.	0.06 ± 0.00	-0.07 ± 0.00	0.01 ± 0.00	0.31 ± 0.00	-1.32 ± 0.00	0.02 ± 0.00	-0.00 ± 0.00	0.02
	0.00 ± 0.00	-0.00 ± 0.00	-0.00 ± 0.00	0.01 ± 0.00	-0.06 ± 0.00	0.00 ± 0.00	-0.00 ± 0.00	0.01
- EGM mism. and co-est.	-0.00 ± 0.00	-0.00 ± 0.00	-0.05 ± 0.00	0.09 ± 0.00	0.01 ± 0.00	0.01 ± 0.00	0.00 ± 0.00	0.01
	0.00 ± 0.00	-0.00 ± 0.00	0.00 ± 0.00	0.00 ± 0.00	0.00 ± 0.00	0.00 ± 0.00	-0.00 ± 0.00	0.01
+ Circular 60°								
- EGM mism.	0.06 ± 0.00	-0.06 ± 0.00	-0.00 ± 0.00	0.32 ± 0.00	-1.36 ± 0.00	0.01 ± 0.00	-0.00 ± 0.00	0.02
	0.00 ± 0.00	-0.00 ± 0.00	0.00 ± 0.00	0.02 ± 0.00	-0.06 ± 0.00	0.00 ± 0.00	-0.00 ± 0.00	0.01
- EGM mism. and co-est.	-0.00 ± 0.00	-0.00 ± 0.00	-0.03 ± 0.00	0.07 ± 0.00	0.00 ± 0.00	0.01 ± 0.00	0.00 ± 0.00	0.01
	0.00 ± 0.00	-0.00 ± 0.00	0.00 ± 0.00	0.00 ± 0.00	0.00 ± 0.00	0.00 ± 0.00	-0.00 ± 0.00	0.01
+ Circular 89°								
- EGM mism.	0.06 ± 0.00	-0.07 ± 0.00	-0.07 ± 0.00	0.29 ± 0.00	-1.31 ± 0.00	0.02 ± 0.00	-0.00 ± 0.00	0.02
	0.00 ± 0.00	-0.00 ± 0.00	0.00 ± 0.00	0.01 ± 0.00	-0.06 ± 0.00	0.00 ± 0.00	-0.00 ± 0.00	0.01
- EGM mism. and co-est.	0.00 ± 0.00	-0.01 ± 0.00	-0.02 ± 0.00	0.12 ± 0.00	0.01 ± 0.00	0.01 ± 0.00	0.00 ± 0.00	0.01
	0.00 ± 0.00	-0.00 ± 0.00	0.00 ± 0.00	0.01 ± 0.00	0.00 ± 0.00	0.00 ± 0.00	-0.00 ± 0.00	0.01

Table F.51: Formal errors for the GPS EGM mismodelling case.

	σ_x & p-value		σ_y & p-value		σ_z & p-value		$\sigma_{\dot{x}}$ & p-value		$\sigma_{\dot{y}}$ & p-value		$\sigma_{\dot{z}}$ & p-value		σ_{x_p} & p-value		σ_{y_p} & p-value		σ_{LOD} & p-value		exp. imp.
	[mm]						[mm/dec]						[mm]				[mm]		[%]
Reference	0.259	—	0.266	—	0.234	—	0.266	—	0.272	—	0.254	—	0.333	—	0.332	—	0.466	—	—
GRASP-like	0.257	-0.000	0.264	-0.000	0.225	-0.000	0.264	-0.000	0.270	-0.000	0.238	-0.000	0.331	0.000	0.330	0.000	0.459	0.000	-0.47
E-GRASP-mod	0.258	-0.000	0.264	-0.000	0.227	-0.000	0.265	-0.000	0.271	-0.000	0.241	-0.000	0.331	-0.000	0.330	-0.000	0.456	-0.000	-0.40
E-GRASP-like	0.257	-0.000	0.264	-0.000	0.226	-0.000	0.265	-0.000	0.271	-0.000	0.240	-0.000	0.331	-0.000	0.329	-0.000	0.456	-0.000	-0.39
Circular 30°	0.257	-0.000	0.264	-0.000	0.229	-0.000	0.265	-0.000	0.271	-0.000	0.246	-0.000	0.331	-0.000	0.330	-0.000	0.455	-0.000	-0.34
Circular 60°	0.257	-0.000	0.264	-0.000	0.228	-0.000	0.265	-0.000	0.271	-0.000	0.243	-0.000	0.331	-0.000	0.330	-0.000	0.455	-0.000	-0.34
Circular 89°	0.257	-0.000	0.264	-0.000	0.228	-0.000	0.265	-0.000	0.271	-0.000	0.243	-0.000	0.331	-0.000	0.329	-0.000	0.453	-0.000	-0.34

	$\sigma_{Lat.}$ & p-value		$\sigma_{Lon.}$ & p-value		σ_{Height}		$\sigma_{\dot{Lat.}}$ & p-value		$\sigma_{\dot{Lon.}}$ & p-value		$\sigma_{\dot{Height}}$ & p-value	
	[mm]						[mm/dec]					
Reference	0.243	—	0.278	—	0.213	—	0.259	—	0.285	—	0.228	—
GRASP-like	0.237	-0.000	0.277	-0.000	0.207	-0.000	0.248	-0.000	0.283	-0.000	0.219	-0.000
E-GRASP-mod	0.238	-0.000	0.277	-0.000	0.209	-0.000	0.250	-0.000	0.284	-0.000	0.221	-0.000
E-GRASP-like	0.238	-0.000	0.277	-0.000	0.208	-0.000	0.250	-0.000	0.284	-0.000	0.221	-0.000
Circular 30°	0.240	-0.000	0.277	-0.000	0.210	-0.000	0.254	-0.000	0.284	-0.000	0.224	-0.000
Circular 60°	0.239	-0.000	0.277	-0.000	0.209	-0.000	0.252	-0.000	0.284	-0.000	0.222	-0.000
Circular 89°	0.239	-0.000	0.277	-0.000	0.209	-0.000	0.252	-0.000	0.284	-0.000	0.222	-0.000

Table F.52: Formal errors for the GPS EGM mismodelling case, SHs estimated.

	σ_x & p-value		σ_y & p-value		σ_z & p-value		$\sigma_{\dot{x}}$ & p-value		$\sigma_{\dot{y}}$ & p-value		$\sigma_{\dot{z}}$ & p-value		σ_{x_p} & p-value		σ_{y_p} & p-value		σ_{LOD} & p-value		exp. imp.
	[mm]						[mm/dec]						[mm]				[mm]		[%]
Reference	0.262	—	0.269	—	0.242	—	0.268	—	0.273	—	0.256	—	0.344	—	0.344	—	0.558	—	—
GRASP-like	0.257	-0.000	0.264	-0.000	0.226	-0.000	0.264	-0.000	0.270	-0.000	0.239	-0.000	0.332	0.000	0.330	0.000	0.459	0.000	-0.47
E-GRASP-mod	0.258	-0.000	0.265	-0.000	0.228	-0.000	0.265	-0.000	0.271	-0.000	0.242	-0.000	0.332	-0.000	0.331	-0.000	0.458	-0.000	-0.40
E-GRASP-like	0.258	-0.000	0.264	-0.000	0.227	-0.000	0.265	-0.000	0.271	-0.000	0.241	-0.000	0.331	-0.000	0.330	-0.000	0.459	-0.000	-0.39
Circular 30°	0.258	-0.000	0.266	-0.000	0.232	-0.000	0.265	-0.000	0.271	-0.000	0.247	-0.000	0.334	-0.000	0.332	-0.000	0.464	-0.000	-0.34
Circular 60°	0.258	-0.000	0.265	-0.000	0.229	-0.000	0.265	-0.000	0.271	-0.000	0.243	-0.000	0.332	-0.000	0.331	-0.000	0.467	-0.000	-0.34
Circular 89°	0.258	-0.000	0.265	-0.000	0.228	-0.000	0.265	-0.000	0.271	-0.000	0.243	-0.000	0.331	-0.000	0.330	-0.000	0.455	-0.000	-0.34

	$\sigma_{Lat.}$ & p-value		$\sigma_{Lon.}$ & p-value		σ_{Height}		$\sigma_{\dot{Lat.}}$ & p-value		$\sigma_{\dot{Lon.}}$ & p-value		$\sigma_{\dot{Height}}$ & p-value	
	[mm]						[mm/dec]					
Reference	0.250	—	0.282	—	0.217	—	0.261	—	0.288	—	0.229	—
GRASP-like	0.238	-0.000	0.277	-0.000	0.208	-0.000	0.249	-0.000	0.283	-0.000	0.219	-0.000
E-GRASP-mod	0.239	-0.000	0.277	-0.000	0.209	-0.000	0.251	-0.000	0.284	-0.000	0.222	-0.000
E-GRASP-like	0.239	-0.000	0.277	-0.000	0.209	-0.000	0.251	-0.000	0.284	-0.000	0.222	-0.000
Circular 30°	0.242	-0.000	0.278	-0.000	0.211	-0.000	0.254	-0.000	0.284	-0.000	0.224	-0.000
Circular 60°	0.240	-0.000	0.277	-0.000	0.210	-0.000	0.252	-0.000	0.284	-0.000	0.222	-0.000
Circular 89°	0.239	-0.000	0.277	-0.000	0.209	-0.000	0.252	-0.000	0.284	-0.000	0.222	-0.000

Table F.53: Statistics of estimated ERPs for the GPS EGM mismodelling case. The p-values of the standard deviation are for the reference solution (GPS constellation) in comparison to the systematically error-free reference solution. The p-values of the standard deviation of the space-tie satellite scenarios are for the case of EGM mismodelling in comparison to the reference solution with EGM mismodelling and in the case where the EGM is co-estimated in comparison to the reference solution where the EGM is co-estimated. For the computation of offset and trend the p-values are in all cases computed in relation to a priori.

	$\Delta X - Pole$						$\Delta Y - Pole$						ΔLOD					
	std. [mm]	p-value	mean ± std. [mm]	p-value	trend ± std. [mm/a]	p-value	std. [mm]	p-value	mean ± std. [mm]	p-value	trend ± std. [mm/a]	p-value	std. [mm]	p-value	mean ± std. [mm]	p-value	trend ± std. [mm/a]	p-value
Reference																		
- EGM mism.	0.133	0.000	1.308 ± 0.001	0.000	0.060 ± 0.001	0.000	0.062	0.001	-0.289 ± 0.001	0.000	-0.013 ± 0.001	0.000	0.477	0.923	-0.374 ± 0.009	0.000	-0.003 ± 0.005	0.583
- EGM mism. and co-est.	0.056	0.995	-0.008 ± 0.001	0.000	-0.000 ± 0.001	0.553	0.056	0.289	-0.071 ± 0.001	0.000	-0.004 ± 0.001	0.000	0.477	0.964	-0.214 ± 0.009	0.000	-0.003 ± 0.005	0.513
+ GRASP-like																		
- EGM mism.	0.172	0.000	2.064 ± 0.001	0.000	0.080 ± 0.001	0.000	0.055	0.000	0.004 ± 0.001	0.000	-0.003 ± 0.001	0.000	0.474	0.769	-0.339 ± 0.009	0.000	-0.007 ± 0.005	0.108
- EGM mism. and co-est.	0.057	0.544	-0.083 ± 0.001	0.000	-0.008 ± 0.001	0.000	0.055	0.201	0.001 ± 0.001	0.486	0.000 ± 0.001	0.437	0.467	0.352	-0.003 ± 0.009	0.721	-0.004 ± 0.005	0.403
+ E-GRASP-mod																		
- EGM mism.	0.153	0.000	1.566 ± 0.001	0.000	0.071 ± 0.001	0.000	0.063	0.293	-0.344 ± 0.001	0.000	-0.015 ± 0.001	0.000	0.463	0.202	-0.371 ± 0.009	0.000	-0.004 ± 0.005	0.420
- EGM mism. and co-est.	0.055	0.312	0.009 ± 0.001	0.000	-0.000 ± 0.001	0.818	0.056	0.999	-0.139 ± 0.001	0.000	-0.007 ± 0.001	0.000	0.462	0.188	-0.164 ± 0.009	0.000	-0.005 ± 0.005	0.281
+ E-GRASP-like																		
- EGM mism.	0.159	0.000	1.623 ± 0.001	0.000	0.074 ± 0.001	0.000	0.062	0.655	-0.340 ± 0.001	0.000	-0.015 ± 0.001	0.000	0.464	0.222	-0.370 ± 0.009	0.000	-0.003 ± 0.005	0.575
- EGM mism. and co-est.	0.055	0.154	0.016 ± 0.001	0.000	0.001 ± 0.001	0.152	0.055	0.147	-0.054 ± 0.001	0.000	-0.003 ± 0.001	0.000	0.463	0.219	-0.327 ± 0.009	0.000	-0.004 ± 0.005	0.415
+ Circular 30°																		
- EGM mism.	0.141	0.000	1.405 ± 0.001	0.000	0.064 ± 0.001	0.000	0.062	0.842	-0.325 ± 0.001	0.000	-0.015 ± 0.001	0.000	0.462	0.184	-0.374 ± 0.009	0.000	-0.002 ± 0.005	0.702
- EGM mism. and co-est.	0.055	0.093	-0.010 ± 0.001	0.000	-0.001 ± 0.001	0.121	0.055	0.329	-0.097 ± 0.001	0.000	-0.005 ± 0.001	0.000	0.462	0.170	-0.006 ± 0.009	0.523	-0.003 ± 0.005	0.543
+ Circular 60°																		
- EGM mism.	0.144	0.000	1.448 ± 0.001	0.000	0.066 ± 0.001	0.000	0.062	0.531	-0.339 ± 0.001	0.000	-0.015 ± 0.001	0.000	0.461	0.142	-0.374 ± 0.009	0.000	-0.002 ± 0.005	0.588
- EGM mism. and co-est.	0.055	0.183	-0.003 ± 0.001	0.014	-0.001 ± 0.001	0.306	0.055	0.207	-0.077 ± 0.001	0.000	-0.004 ± 0.001	0.000	0.460	0.125	0.137 ± 0.009	0.000	-0.004 ± 0.005	0.434
+ Circular 89°																		
- EGM mism.	0.139	0.014	1.391 ± 0.001	0.000	0.063 ± 0.001	0.000	0.061	0.392	-0.302 ± 0.001	0.000	-0.014 ± 0.001	0.000	0.458	0.097	-0.366 ± 0.009	0.000	-0.002 ± 0.004	0.648
- EGM mism. and co-est.	0.055	0.117	-0.006 ± 0.001	0.000	-0.001 ± 0.001	0.338	0.055	0.406	-0.131 ± 0.001	0.000	-0.006 ± 0.001	0.000	0.457	0.080	-0.055 ± 0.009	0.000	-0.002 ± 0.004	0.591

F.4 DORIS, GPS, SLR combination

F.4.1 Systematic error-free

Table F.54: Helmert parameters to a priori for the DORIS network in the multi-technique combination.

	T_x [mm] $\dot{T}_x$ [mm/a]	T_y [mm] $\dot{T}_y$ [mm/a]	T_z [mm] $\dot{T}_z$ [mm/a]	R_x [mm] $\dot{R}_x$ [mm/a]	R_y [mm] $\dot{R}_y$ [mm/a]	R_z [mm] $\dot{R}_z$ [mm/a]	sc [mm] $\dot{sc}$ [mm/a]	s_0 s_0
Reference								
+ GRASP-like w/o ST	0.04 ± 0.03	0.02 ± 0.03	0.17 ± 0.03	-0.11 ± 0.04	-0.06 ± 0.04	0.06 ± 0.04	-0.02 ± 0.03	0.24
	0.00 ± 0.01	-0.02 ± 0.01	0.01 ± 0.01	-0.02 ± 0.01	-0.01 ± 0.01	0.01 ± 0.01	0.00 ± 0.01	0.07
+ GRASP-like w/ ST	0.05 ± 0.03	0.02 ± 0.03	0.11 ± 0.03	-0.12 ± 0.04	-0.08 ± 0.04	0.09 ± 0.04	-0.02 ± 0.03	0.25
	0.00 ± 0.01	-0.02 ± 0.01	0.01 ± 0.01	-0.02 ± 0.01	-0.01 ± 0.01	0.02 ± 0.01	0.00 ± 0.01	0.07
+ E-GRASP-mod w/o ST	0.03 ± 0.03	0.05 ± 0.03	0.13 ± 0.03	-0.01 ± 0.04	0.02 ± 0.04	0.09 ± 0.04	-0.01 ± 0.03	0.23
	0.00 ± 0.00	0.00 ± 0.00	0.01 ± 0.00	-0.00 ± 0.00	0.00 ± 0.00	0.01 ± 0.00	-0.00 ± 0.00	0.02
+ E-GRASP-mod w/ ST	0.04 ± 0.03	0.07 ± 0.03	0.26 ± 0.03	-0.01 ± 0.04	0.03 ± 0.04	0.10 ± 0.04	-0.01 ± 0.03	0.23
	0.00 ± 0.00	0.01 ± 0.00	0.02 ± 0.00	-0.00 ± 0.00	0.00 ± 0.00	0.01 ± 0.00	-0.00 ± 0.00	0.02
+ E-GRASP-like w/o ST	0.02 ± 0.03	0.05 ± 0.03	0.08 ± 0.03	0.03 ± 0.03	-0.03 ± 0.04	0.06 ± 0.04	0.00 ± 0.03	0.22
	0.00 ± 0.00	0.01 ± 0.00	0.01 ± 0.00	0.00 ± 0.01	-0.00 ± 0.01	0.01 ± 0.01	-0.01 ± 0.00	0.03
+ E-GRASP-like w/ ST	0.05 ± 0.03	0.12 ± 0.03	0.46 ± 0.03	0.08 ± 0.04	-0.01 ± 0.04	0.08 ± 0.04	-0.00 ± 0.03	0.23
	0.00 ± 0.00	0.02 ± 0.00	0.04 ± 0.00	0.01 ± 0.01	-0.00 ± 0.01	0.01 ± 0.01	-0.01 ± 0.00	0.03
+ Circular 30 °w/o ST	0.06 ± 0.03	0.05 ± 0.03	0.12 ± 0.03	0.07 ± 0.04	-0.04 ± 0.04	-0.03 ± 0.04	-0.02 ± 0.03	0.22
	0.01 ± 0.00	0.00 ± 0.00	0.01 ± 0.00	0.01 ± 0.00	-0.00 ± 0.00	-0.00 ± 0.00	-0.00 ± 0.00	0.02
+ Circular 30 °w/ ST	0.06 ± 0.03	0.04 ± 0.03	0.09 ± 0.03	0.09 ± 0.03	-0.04 ± 0.03	-0.04 ± 0.04	-0.02 ± 0.03	0.22
	0.01 ± 0.00	0.00 ± 0.00	0.01 ± 0.00	0.01 ± 0.00	-0.00 ± 0.00	-0.00 ± 0.00	-0.00 ± 0.00	0.02
+ Circular 60 °w/o ST	0.05 ± 0.03	0.06 ± 0.03	0.09 ± 0.03	-0.07 ± 0.03	0.02 ± 0.03	0.06 ± 0.04	-0.03 ± 0.03	0.21
	0.00 ± 0.00	0.01 ± 0.00	0.01 ± 0.00	-0.00 ± 0.00	0.00 ± 0.00	0.01 ± 0.00	-0.00 ± 0.00	0.02
+ Circular 60 °w/ ST	0.05 ± 0.03	0.05 ± 0.03	0.06 ± 0.03	-0.06 ± 0.03	0.02 ± 0.03	0.06 ± 0.03	-0.02 ± 0.03	0.21
	0.00 ± 0.00	0.01 ± 0.00	0.00 ± 0.00	-0.00 ± 0.00	0.00 ± 0.00	0.00 ± 0.00	-0.00 ± 0.00	0.02
+ Circular 89 °w/o ST	0.02 ± 0.03	0.07 ± 0.03	0.06 ± 0.03	-0.07 ± 0.03	-0.05 ± 0.03	0.12 ± 0.04	-0.02 ± 0.03	0.21
	0.00 ± 0.00	0.01 ± 0.00	0.00 ± 0.00	-0.00 ± 0.00	-0.00 ± 0.00	0.01 ± 0.00	-0.00 ± 0.00	0.02
+ Circular 89 °w/ ST	0.01 ± 0.03	0.07 ± 0.03	0.04 ± 0.03	-0.06 ± 0.03	-0.05 ± 0.03	0.12 ± 0.04	-0.02 ± 0.03	0.21
	0.00 ± 0.00	0.01 ± 0.00	0.00 ± 0.00	-0.00 ± 0.00	-0.00 ± 0.00	0.01 ± 0.00	-0.00 ± 0.00	0.02

Table F.55: Helmert parameters to a priori for the GPS network in the multi-technique combination.

	T_x [mm] $T_{\dot{x}}$ [mm/a]	T_y [mm] $T_{\dot{y}}$ [mm/a]	T_z [mm] $T_{\dot{z}}$ [mm/a]	R_x [mm] $R_{\dot{x}}$ [mm/a]	R_y [mm] $R_{\dot{y}}$ [mm/a]	R_z [mm] $R_{\dot{z}}$ [mm/a]	sc [mm] $\dot{sc}$ [mm/a]	s_0 s_0
Reference								
+ GRASP-like w/o ST	0.00 ± 0.00	-0.00 ± 0.00	-0.00 ± 0.00	0.06 ± 0.00	-0.00 ± 0.00	0.01 ± 0.00	-0.00 ± 0.00	0.01
	0.00 ± 0.00	-0.00 ± 0.00	-0.00 ± 0.00	0.01 ± 0.00	0.00 ± 0.00	0.00 ± 0.00	-0.00 ± 0.00	0.01
+ GRASP-like w/ ST	0.00 ± 0.00	-0.00 ± 0.00	0.00 ± 0.00	0.07 ± 0.00	-0.00 ± 0.00	2.44 ± 0.00	-0.00 ± 0.00	0.01
	0.00 ± 0.00	-0.00 ± 0.00	-0.00 ± 0.00	0.02 ± 0.00	-0.00 ± 0.00	-0.20 ± 0.00	-0.00 ± 0.00	0.01
+ E-GRASP-mod w/o ST	-0.00 ± 0.00	-0.01 ± 0.00	-0.01 ± 0.00	-0.04 ± 0.00	-0.06 ± 0.00	0.01 ± 0.00	-0.00 ± 0.00	0.01
	0.00 ± 0.00	-0.00 ± 0.00	0.01 ± 0.00	0.00 ± 0.00	-0.01 ± 0.00	0.00 ± 0.00	-0.00 ± 0.00	0.01
+ E-GRASP-mod w/ ST	-0.00 ± 0.00	-0.01 ± 0.00	-0.02 ± 0.00	-0.04 ± 0.00	-0.06 ± 0.00	-1.47 ± 0.00	-0.00 ± 0.00	0.01
	-0.00 ± 0.00	-0.00 ± 0.00	0.01 ± 0.00	0.00 ± 0.00	-0.01 ± 0.00	0.14 ± 0.00	-0.00 ± 0.00	0.01
+ E-GRASP-like w/o ST	-0.00 ± 0.00	-0.01 ± 0.00	-0.00 ± 0.00	-0.08 ± 0.00	0.01 ± 0.00	0.01 ± 0.00	-0.00 ± 0.00	0.01
	-0.00 ± 0.00	-0.00 ± 0.00	0.00 ± 0.00	-0.01 ± 0.00	0.02 ± 0.00	0.00 ± 0.00	-0.00 ± 0.00	0.01
+ E-GRASP-like w/ ST	-0.00 ± 0.00	-0.01 ± 0.00	-0.02 ± 0.00	-0.13 ± 0.00	-0.00 ± 0.00	-1.51 ± 0.00	-0.00 ± 0.00	0.01
	0.00 ± 0.00	-0.00 ± 0.00	0.01 ± 0.00	-0.01 ± 0.00	0.01 ± 0.00	0.23 ± 0.00	-0.00 ± 0.00	0.01
+ Circular 30°w/o ST	-0.00 ± 0.00	-0.01 ± 0.00	-0.02 ± 0.00	-0.12 ± 0.00	0.01 ± 0.00	0.01 ± 0.00	-0.00 ± 0.00	0.01
	0.00 ± 0.00	-0.00 ± 0.00	-0.00 ± 0.00	-0.01 ± 0.00	0.01 ± 0.00	0.00 ± 0.00	-0.00 ± 0.00	0.01
+ Circular 30°w/ ST	-0.00 ± 0.00	-0.01 ± 0.00	-0.01 ± 0.00	-0.14 ± 0.00	0.02 ± 0.00	-0.62 ± 0.00	-0.00 ± 0.00	0.01
	0.00 ± 0.00	-0.00 ± 0.00	-0.00 ± 0.00	-0.01 ± 0.00	0.01 ± 0.00	0.04 ± 0.00	-0.00 ± 0.00	0.01
+ Circular 60°w/o ST	-0.00 ± 0.00	-0.01 ± 0.00	-0.02 ± 0.00	0.00 ± 0.00	-0.06 ± 0.00	0.01 ± 0.00	-0.00 ± 0.00	0.01
	0.00 ± 0.00	-0.00 ± 0.00	0.00 ± 0.00	0.00 ± 0.00	0.00 ± 0.00	0.00 ± 0.00	-0.00 ± 0.00	0.01
+ Circular 60°w/ ST	-0.00 ± 0.00	-0.01 ± 0.00	-0.02 ± 0.00	-0.00 ± 0.00	-0.06 ± 0.00	-0.63 ± 0.00	-0.00 ± 0.00	0.01
	-0.00 ± 0.00	-0.00 ± 0.00	0.00 ± 0.00	0.00 ± 0.00	0.00 ± 0.00	0.05 ± 0.00	-0.00 ± 0.00	0.01
+ Circular 89°w/o ST	-0.00 ± 0.00	-0.01 ± 0.00	-0.00 ± 0.00	0.04 ± 0.00	0.01 ± 0.00	0.01 ± 0.00	-0.00 ± 0.00	0.01
	0.00 ± 0.00	-0.00 ± 0.00	0.00 ± 0.00	0.00 ± 0.00	-0.00 ± 0.00	0.00 ± 0.00	-0.00 ± 0.00	0.01
+ Circular 89°w/ ST	-0.00 ± 0.00	-0.01 ± 0.00	0.01 ± 0.00	0.04 ± 0.00	0.01 ± 0.00	0.48 ± 0.00	-0.00 ± 0.00	0.01
	0.00 ± 0.00	-0.00 ± 0.00	0.00 ± 0.00	0.00 ± 0.00	-0.00 ± 0.00	0.03 ± 0.00	-0.00 ± 0.00	0.01

Table F.56: Helmert parameters to a priori for the SLR network in the multi-technique combination.

	T_x [mm] $T_{\dot{x}}$ [mm/a]	T_y [mm] $T_{\dot{y}}$ [mm/a]	T_z [mm] $T_{\dot{z}}$ [mm/a]	R_x [mm] $R_{\dot{x}}$ [mm/a]	R_y [mm] $R_{\dot{y}}$ [mm/a]	R_z [mm] $R_{\dot{z}}$ [mm/a]	sc [mm] $\dot{sc}$ [mm/a]	s_0 s_0
Reference								
+ GRASP-like w/o ST	-0.04 ± 0.16	0.01 ± 0.16	0.09 ± 0.16	-0.02 ± 0.20	0.05 ± 0.19	59.42 ± 0.19	-0.14 ± 0.15	0.82
	0.02 ± 0.06	0.01 ± 0.07	-0.08 ± 0.06	0.14 ± 0.08	-0.05 ± 0.08	8.87 ± 0.07	0.03 ± 0.06	0.33
+ GRASP-like	-0.04 ± 0.17	-0.01 ± 0.17	0.09 ± 0.16	-0.01 ± 0.20	0.03 ± 0.20	2.09 ± 0.19	-0.15 ± 0.16	0.84
	0.02 ± 0.07	0.01 ± 0.07	-0.06 ± 0.06	0.14 ± 0.08	-0.04 ± 0.08	-0.24 ± 0.07	0.02 ± 0.06	0.33
+ E-GRASP-mod w/o ST	-0.07 ± 0.22	0.09 ± 0.22	0.07 ± 0.21	-0.00 ± 0.27	0.13 ± 0.26	-39.24 ± 0.25	-0.13 ± 0.21	1.11
	-0.01 ± 0.10	0.02 ± 0.10	-0.05 ± 0.10	0.19 ± 0.12	-0.01 ± 0.12	7.96 ± 0.12	0.04 ± 0.10	0.51
+ E-GRASP-mod w/ ST	-0.07 ± 0.22	0.09 ± 0.22	-0.01 ± 0.21	0.00 ± 0.27	0.14 ± 0.26	-1.40 ± 0.25	-0.12 ± 0.21	1.12
	-0.01 ± 0.10	0.02 ± 0.10	-0.03 ± 0.10	0.20 ± 0.12	-0.02 ± 0.12	0.02 ± 0.12	0.03 ± 0.10	0.51
+ E-GRASP-like w/o ST	-0.02 ± 0.22	0.17 ± 0.22	-0.00 ± 0.21	0.11 ± 0.27	0.04 ± 0.26	3.22 ± 0.25	-0.05 ± 0.21	1.11
	0.04 ± 0.09	0.02 ± 0.09	-0.00 ± 0.09	0.12 ± 0.11	0.03 ± 0.11	4.53 ± 0.10	0.01 ± 0.09	0.46
+ E-GRASP-like w/ ST	-0.04 ± 0.22	0.18 ± 0.22	-0.22 ± 0.21	0.08 ± 0.27	0.02 ± 0.26	-1.56 ± 0.25	-0.04 ± 0.21	1.12
	0.04 ± 0.09	0.02 ± 0.09	0.06 ± 0.09	0.12 ± 0.11	0.03 ± 0.11	0.20 ± 0.11	0.01 ± 0.09	0.47
+ Circular 30°w/o ST	-0.02 ± 0.24	0.13 ± 0.25	0.05 ± 0.24	0.02 ± 0.30	0.13 ± 0.29	495.88 ± 0.28	-0.13 ± 0.23	1.23
	-0.05 ± 0.11	0.04 ± 0.11	-0.07 ± 0.10	0.19 ± 0.13	0.08 ± 0.13	7.88 ± 0.12	0.01 ± 0.10	0.54
+ Circular 30°w/ ST	-0.02 ± 0.24	0.13 ± 0.25	0.05 ± 0.24	0.01 ± 0.30	0.12 ± 0.29	-0.57 ± 0.28	-0.13 ± 0.23	1.23
	-0.05 ± 0.11	0.04 ± 0.11	-0.07 ± 0.10	0.19 ± 0.13	0.08 ± 0.13	-0.06 ± 0.12	0.01 ± 0.10	0.54
+ Circular 60°w/o ST	-0.04 ± 0.20	0.15 ± 0.20	0.13 ± 0.19	0.09 ± 0.24	0.14 ± 0.23	803.21 ± 0.23	-0.17 ± 0.19	0.99
	0.08 ± 0.10	0.01 ± 0.10	-0.09 ± 0.10	0.20 ± 0.12	-0.07 ± 0.12	8.46 ± 0.11	0.02 ± 0.10	0.50
+ Circular 60°w/ ST	-0.04 ± 0.20	0.15 ± 0.20	0.16 ± 0.19	0.08 ± 0.24	0.13 ± 0.23	-0.67 ± 0.22	-0.17 ± 0.19	0.99
	0.08 ± 0.10	0.01 ± 0.10	-0.10 ± 0.10	0.20 ± 0.12	-0.07 ± 0.12	0.12 ± 0.11	0.02 ± 0.09	0.50
+ Circular 89°w/o ST	-0.04 ± 0.22	0.23 ± 0.22	0.04 ± 0.21	0.30 ± 0.27	-0.02 ± 0.26	599.00 ± 0.25	-0.07 ± 0.21	1.09
	0.07 ± 0.10	0.04 ± 0.11	-0.10 ± 0.10	0.18 ± 0.13	-0.11 ± 0.12	8.61 ± 0.12	0.06 ± 0.10	0.53
+ Circular 89°w/ ST	-0.04 ± 0.22	0.23 ± 0.22	0.05 ± 0.21	0.30 ± 0.27	-0.01 ± 0.26	0.30 ± 0.25	-0.07 ± 0.21	1.10
	0.07 ± 0.11	0.04 ± 0.11	-0.09 ± 0.10	0.18 ± 0.13	-0.11 ± 0.13	0.09 ± 0.12	0.06 ± 0.10	0.54

Table F.57: Formal errors for the systematic error-free combination without ST for the DORIS stations.

	σ_x & p-value		σ_y & p-value		σ_z & p-value		$\sigma_{\dot{x}}$ & p-value		$\sigma_{\dot{y}}$ & p-value		$\sigma_{\dot{z}}$ & p-value		σ_{x_p} & p-value		σ_{y_p} & p-value		σ_{LOD} & p-value		exp. imp.
	[mm]		[mm]		[mm]		[mm/dec]		[mm/dec]		[mm/dec]		[cm]		[cm]		[μm]		[%]
GRASP-like	0.0000004	-0.000	0.0056070	-0.000	0.0184400	0.000	0.056	0.000	0.060	-0.000	0.048	-0.000	0.006	0.000	0.007	0.000	0.079	0.000	-92.46
E-GRASP-mod	0.0000004	0.000	0.0056280	0.000	0.0121800	-0.000	0.057	0.000	0.056	-0.000	0.048	-0.000	0.006	-0.000	0.006	-0.000	0.061	-0.000	-92.48
E-GRASP-like	0.0000004	0.000	0.0059080	0.000	0.0115900	-0.000	0.056	0.000	0.055	-0.000	0.048	-0.000	0.006	-0.000	0.006	-0.000	0.062	-0.000	-92.48
Circular 30°	0.0000004	0.000	0.0063870	0.000	0.0101300	-0.000	0.054	-0.000	0.055	-0.000	0.056	-0.000	0.006	-0.000	0.007	-0.000	0.062	-0.000	-92.49
Circular 60°	0.0000004	0.000	0.0056620	0.000	0.0111800	-0.000	0.060	-0.000	0.056	-0.000	0.049	-0.000	0.006	-0.000	0.006	-0.000	0.056	-0.000	-92.49
Circular 89°	0.0000003	0.000	0.0054440	0.000	0.0117700	-0.000	0.061	0.000	0.058	0.000	0.047	-0.000	0.006	-0.000	0.006	-0.000	0.054	-0.000	-92.49

	$\sigma_{Lat.}$ & p-value		$\sigma_{Lon.}$ & p-value		σ_{Height} & p-value		$\sigma_{Lat.}$ & p-value		$\sigma_{Lon.}$ & p-value		σ_{Height} & p-value	
	[mm]		[mm]		[mm]		[mm/dec]		[mm/dec]		[mm/dec]	
GRASP-like	0.0154795	-0.000	0.0027093	0.000	0.0106040	-0.000	0.048	-0.000	0.063	-0.000	0.056	-0.000
E-GRASP-mod	0.0117696	-0.000	0.0026801	0.000	0.0074416	-0.000	0.047	-0.000	0.058	-0.000	0.055	-0.000
E-GRASP-like	0.0111178	-0.000	0.0026720	0.000	0.0072155	-0.000	0.047	-0.000	0.057	-0.000	0.055	-0.000
Circular 30°	0.0093705	-0.000	0.0030149	0.000	0.0065554	-0.000	0.053	-0.000	0.056	-0.000	0.056	-0.000
Circular 60°	0.0107999	-0.000	0.0026952	0.000	0.0070659	-0.000	0.048	-0.000	0.060	-0.000	0.056	-0.000
Circular 89°	0.0113211	-0.000	0.0025902	0.000	0.0070103	-0.000	0.048	-0.000	0.062	-0.000	0.057	-0.000

Table F.58: Formal errors for the systematic error-free combination with ST for the DORIS stations.

	σ_x & p-value		σ_y & p-value		σ_z & p-value		$\sigma_{\dot{x}}$ & p-value		$\sigma_{\dot{y}}$ & p-value		$\sigma_{\dot{z}}$ & p-value		σ_{x_p} & p-value		σ_{y_p} & p-value		σ_{LOD} & p-value		exp. imp.
	[mm]						[mm/dec]						[cm]				[μm]		[%]
GRASP-like	0.0000004	-0.000	0.0055980	-0.000	0.0184300	0.000	0.056	0.000	0.060	-0.000	0.047	-0.000	0.006	0.000	0.007	0.000	0.079	0.000	-92.46
E-GRASP-mod	0.0000004	0.000	0.0056210	0.000	0.0121700	-0.000	0.057	0.000	0.056	-0.000	0.047	-0.000	0.006	-0.000	0.006	-0.000	0.061	-0.000	-92.48
E-GRASP-like	0.0000004	0.000	0.0058960	0.000	0.0115800	-0.000	0.056	0.000	0.055	-0.000	0.048	-0.000	0.006	-0.000	0.006	-0.000	0.062	-0.000	-92.48
Circular 30°	0.0000004	0.000	0.0063810	0.000	0.0101200	-0.000	0.054	-0.000	0.055	-0.000	0.056	-0.000	0.006	-0.000	0.007	-0.000	0.062	-0.000	-92.49
Circular 60°	0.0000004	0.000	0.0056600	0.000	0.0111800	-0.000	0.060	-0.000	0.056	-0.000	0.049	-0.000	0.006	-0.000	0.006	-0.000	0.056	-0.000	-92.49
Circular 89°	0.0000003	0.000	0.0054430	0.000	0.0117700	-0.000	0.061	0.000	0.058	0.000	0.047	-0.000	0.006	-0.000	0.006	-0.000	0.054	-0.000	-92.49

	$\sigma_{Lat.}$ & p-value		$\sigma_{Lon.}$ & p-value		σ_{Height}		$\sigma_{\dot{Lat.}}$ & p-value		$\sigma_{\dot{Lon.}}$ & p-value		$\sigma_{\dot{Height}}$ & p-value	
	[mm]						[mm/dec]					
GRASP-like	0.0154697	-0.000	0.0027059	0.000	0.0105709	-0.000	0.046	-0.000	0.063	-0.000	0.055	-0.000
E-GRASP-mod	0.0117605	-0.000	0.0026764	0.000	0.0074401	-0.000	0.047	-0.000	0.058	-0.000	0.054	-0.000
E-GRASP-like	0.0111090	-0.000	0.0026671	0.000	0.0072074	-0.000	0.046	-0.000	0.056	-0.000	0.054	-0.000
Circular 30°	0.0093685	-0.000	0.0030120	0.000	0.0065501	-0.000	0.053	-0.000	0.056	-0.000	0.056	-0.000
Circular 60°	0.0107942	-0.000	0.0026943	0.000	0.0070599	-0.000	0.048	-0.000	0.060	-0.000	0.056	-0.000
Circular 89°	0.0113210	-0.000	0.0025891	0.000	0.0070103	-0.000	0.047	-0.000	0.062	-0.000	0.057	-0.000

Table F.59: Formal errors for the systematic error-free combination without ST for the GPS stations.

,	σ_x & p-value	σ_y & p-value	σ_z & p-value	$\sigma_{\dot{x}}$ & p-value	$\sigma_{\dot{y}}$ & p-value	$\sigma_{\dot{z}}$ & p-value	σ_{x_p} & p-value	σ_{y_p} & p-value	σ_{LOD} & p-value	exp. imp.
	[mm]			[mm/dec]			[mm]		[mm]	[%]
GRASP-like	0.152 -0.000	0.160 -0.000	0.052 0.000	0.159 -0.000	0.167 -0.000	0.078 -0.000	0.057 0.000	0.065 0.000	0.000 0.000	-0.90
E-GRASP-mod	0.158 -0.000	0.166 -0.000	0.061 -0.000	0.166 -0.000	0.175 -0.000	0.090 -0.000	0.058 -0.000	0.063 -0.000	0.000 -0.000	-1.15
E-GRASP-like	0.158 -0.000	0.166 -0.000	0.059 -0.000	0.166 -0.000	0.175 -0.000	0.087 -0.000	0.058 -0.000	0.064 -0.000	0.000 -0.000	-1.14
Circular 30°	0.161 -0.000	0.169 -0.000	0.074 -0.000	0.169 -0.000	0.179 -0.000	0.110 -0.000	0.060 -0.000	0.069 -0.000	0.000 -0.000	-1.23
Circular 60°	0.161 -0.000	0.169 -0.000	0.067 -0.000	0.169 -0.000	0.178 -0.000	0.099 -0.000	0.059 -0.000	0.064 -0.000	0.000 -0.000	-1.26
Circular 89°	0.161 -0.000	0.169 -0.000	0.067 -0.000	0.169 -0.000	0.178 -0.000	0.099 -0.000	0.059 -0.000	0.062 -0.000	0.000 -0.000	-1.28

	$\sigma_{Lat.}$ & p-value	$\sigma_{Lon.}$ & p-value	σ_{Height}	$\sigma_{\dot{Lat.}}$ & p-value	$\sigma_{\dot{Lon.}}$ & p-value	$\sigma_{\dot{Height}}$ & p-value
	[mm]			[mm/dec]		
GRASP-like	0.074 0.000	0.215 -0.000	0.101 -0.000	0.092 0.000	0.218 -0.000	0.121 -0.000
E-GRASP-mod	0.081 0.000	0.223 -0.000	0.105 -0.000	0.101 0.000	0.227 -0.000	0.129 -0.000
E-GRASP-like	0.080 0.000	0.222 -0.000	0.105 -0.000	0.100 0.000	0.227 -0.000	0.129 -0.000
Circular 30°	0.088 0.000	0.227 -0.000	0.109 -0.000	0.114 0.000	0.232 -0.000	0.136 -0.000
Circular 60°	0.083 0.000	0.227 -0.000	0.108 -0.000	0.107 0.000	0.231 -0.000	0.133 -0.000
Circular 89°	0.083 0.000	0.226 -0.000	0.108 -0.000	0.106 0.000	0.231 -0.000	0.133 -0.000

Table F.60: Formal errors for the systematic error-free combination with ST for the GPS stations.

	σ_x & p-value		σ_y & p-value		σ_z & p-value		$\sigma_{\dot{x}}$ & p-value		$\sigma_{\dot{y}}$ & p-value		$\sigma_{\dot{z}}$ & p-value		σ_{x_p} & p-value		σ_{y_p} & p-value		σ_{LOD} & p-value		exp. imp.
’	[mm]						[mm/dec]						[mm]				[mm]		[%]
GRASP-like	0.077	-0.000	0.077	-0.000	0.052	0.000	0.112	-0.000	0.112	-0.000	0.077	-0.000	0.057	0.000	0.065	0.000	0.000	0.000	-0.90
E-GRASP-mod	0.076	-0.000	0.077	-0.000	0.060	-0.000	0.109	-0.000	0.112	-0.000	0.089	-0.000	0.058	-0.000	0.063	-0.000	0.000	-0.000	-1.15
E-GRASP-like	0.074	-0.000	0.076	-0.000	0.059	-0.000	0.108	-0.000	0.110	-0.000	0.087	-0.000	0.058	-0.000	0.064	-0.000	0.000	-0.000	-1.14
Circular 30°	0.075	-0.000	0.076	-0.000	0.072	-0.000	0.109	-0.000	0.111	-0.000	0.107	-0.000	0.060	-0.000	0.069	-0.000	0.000	-0.000	-1.23
Circular 60°	0.083	-0.000	0.083	-0.000	0.066	-0.000	0.120	-0.000	0.119	-0.000	0.098	-0.000	0.059	-0.000	0.064	-0.000	0.000	-0.000	-1.26
Circular 89°	0.088	-0.000	0.087	-0.000	0.066	-0.000	0.126	-0.000	0.125	-0.000	0.098	-0.000	0.059	-0.000	0.062	-0.000	0.000	-0.000	-1.28

	$\sigma_{Lat.}$ & p-value		$\sigma_{Lon.}$ & p-value		σ_{Height}		$\sigma_{\dot{Lat.}}$ & p-value		$\sigma_{\dot{Lon.}}$ & p-value		$\sigma_{\dot{Height}}$ & p-value	
	[mm]						[mm/dec]					
GRASP-like	0.054	-0.000	0.092	-0.000	0.067	0.000	0.080	-0.000	0.133	-0.000	0.099	0.000
E-GRASP-mod	0.060	-0.000	0.089	-0.000	0.072	-0.000	0.088	-0.000	0.128	-0.000	0.105	-0.000
E-GRASP-like	0.059	-0.000	0.087	-0.000	0.071	-0.000	0.086	-0.000	0.125	-0.000	0.104	-0.000
Circular 30°	0.067	-0.000	0.086	-0.000	0.076	-0.000	0.100	-0.000	0.123	-0.000	0.111	-0.000
Circular 60°	0.064	-0.000	0.098	-0.000	0.077	0.000	0.095	-0.000	0.140	-0.000	0.113	0.000
Circular 89°	0.065	-0.000	0.106	-0.000	0.079	0.000	0.095	-0.000	0.151	-0.000	0.115	0.000

Table F.61: Formal errors for the systematic error-free combination without ST for the SLR stations.

	σ_x & p-value	σ_y & p-value	σ_z & p-value	$\sigma_{\dot{x}}$ & p-value	$\sigma_{\dot{y}}$ & p-value	$\sigma_{\dot{z}}$ & p-value	σ_{x_p} & p-value	σ_{y_p} & p-value	σ_{LOD} & p-value	exp. imp.
	[mm]			[mm/dec]			[mm]		[mm]	[%]
GRASP-like	11.520 -0.000	13.319 -0.000	0.162 -0.000	5.759 -0.000	6.707 -0.000	0.231 -0.000	0.057 0.000	0.065 0.000	0.000 0.000	-99.11
E-GRASP-mod	7.772 -0.000	8.960 -0.000	0.163 -0.000	6.225 -0.000	7.262 -0.000	0.234 -0.000	0.058 -0.000	0.063 -0.000	0.000 -0.000	-99.12
E-GRASP-like	3.736 -0.002	4.324 -0.000	0.164 -0.000	5.107 -0.001	5.979 -0.000	0.236 -0.000	0.058 -0.000	0.064 -0.000	0.000 -0.000	-99.12
Circular 30°	63.315 -0.000	73.643 -0.000	0.181 -0.000	7.422 -0.000	8.601 -0.000	0.259 -0.000	0.060 -0.000	0.069 -0.000	0.000 -0.000	-99.12
Circular 60°	56.390 -0.000	65.584 -0.000	0.164 -0.000	6.777 -0.000	7.888 -0.000	0.236 -0.000	0.059 -0.000	0.064 -0.000	0.000 -0.000	-99.12
Circular 89°	52.750 -0.000	61.345 -0.000	0.165 -0.000	6.235 -0.000	7.299 -0.000	0.237 -0.000	0.059 -0.000	0.062 -0.000	0.000 -0.000	-99.12

	$\sigma_{Lat.}$ & p-value	$\sigma_{Lon.}$ & p-value	σ_{Height}	$\sigma_{\dot{Lat.}}$ & p-value	$\sigma_{\dot{Lon.}}$ & p-value	$\sigma_{\dot{Height}}$ & p-value
	[mm]			[mm/dec]		
GRASP-like	5.523 -0.000	15.088 0.000	7.308 -0.000	2.965 -0.031	7.496 0.000	3.978 -0.008
E-GRASP-mod	3.704 -0.000	10.171 0.000	4.913 -0.000	3.211 -0.013	8.122 0.000	4.304 -0.002
E-GRASP-like	1.978 -0.321	4.737 0.000	2.518 -0.035	2.572 -0.149	6.461 0.000	3.441 -0.020
Circular 30°	30.556 -0.000	83.477 0.000	40.391 -0.000	3.843 -0.002	9.698 0.000	5.087 -0.000
Circular 60°	27.212 -0.000	74.340 0.000	35.969 -0.000	3.496 -0.004	8.834 0.000	4.689 -0.001
Circular 89°	25.454 -0.000	69.538 0.000	33.645 -0.000	3.210 -0.013	8.135 0.000	4.312 -0.004

Table F.62: Formal errors for the systematic error-free combination with ST for the SLR stations.

	σ_x & p-value		σ_y & p-value		σ_z & p-value		$\sigma_{\dot{x}}$ & p-value		$\sigma_{\dot{y}}$ & p-value		$\sigma_{\dot{z}}$ & p-value		σ_{x_p} & p-value		σ_{y_p} & p-value		σ_{LOD} & p-value		exp. imp.
	[mm]						[mm/dec]						[mm]				[mm]		[%]
GRASP-like	0.170	-0.000	0.179	-0.000	0.157	-0.000	0.243	-0.000	0.259	-0.000	0.224	-0.000	0.057	0.000	0.065	0.000	0.000	0.000	-99.11
E-GRASP-mod	0.174	-0.000	0.184	-0.000	0.160	-0.000	0.250	-0.000	0.266	-0.000	0.229	-0.000	0.058	-0.000	0.063	-0.000	0.000	-0.000	-99.12
E-GRASP-like	0.170	-0.000	0.180	-0.000	0.161	-0.000	0.242	-0.000	0.260	-0.000	0.231	-0.000	0.058	-0.000	0.064	-0.000	0.000	-0.000	-99.12
Circular 30°	0.159	-0.000	0.170	-0.000	0.180	-0.000	0.236	-0.000	0.244	-0.000	0.258	-0.000	0.060	-0.000	0.069	-0.000	0.000	-0.000	-99.12
Circular 60°	0.182	-0.000	0.193	-0.000	0.162	-0.000	0.262	-0.000	0.280	-0.000	0.233	-0.000	0.059	-0.000	0.064	-0.000	0.000	-0.000	-99.12
Circular 89°	0.187	-0.000	0.200	-0.000	0.161	-0.000	0.277	-0.000	0.289	-0.000	0.231	-0.000	0.059	-0.000	0.062	-0.000	0.000	-0.000	-99.12

	$\sigma_{Lat.}$ & p-value		$\sigma_{Lon.}$ & p-value		σ_{Height}		$\sigma_{\dot{Lat.}}$ & p-value		$\sigma_{\dot{Lon.}}$ & p-value		$\sigma_{\dot{Height}}$ & p-value	
	[mm]						[mm/dec]					
GRASP-like	0.162	-0.000	0.177	-0.000	0.168	-0.000	0.233	-0.000	0.254	-0.000	0.241	-0.000
E-GRASP-mod	0.166	-0.000	0.183	-0.000	0.171	-0.000	0.239	-0.000	0.262	-0.000	0.246	-0.000
E-GRASP-like	0.166	-0.000	0.179	-0.000	0.168	-0.000	0.239	-0.000	0.256	-0.000	0.241	-0.000
Circular 30°	0.176	-0.000	0.173	-0.000	0.168	-0.000	0.253	-0.000	0.248	-0.000	0.241	-0.000
Circular 60°	0.168	-0.000	0.194	-0.000	0.179	-0.000	0.242	-0.000	0.278	-0.000	0.258	-0.000
Circular 89°	0.170	-0.000	0.206	-0.000	0.182	-0.000	0.245	-0.000	0.295	-0.000	0.262	-0.000

Table F.63: Statistics of estimated ERPs for the combination with GTs only and for the combination with GTs and ST. The p-values of the standard deviation are for the ST combination in comparison to the combination with GTs only. For the computation of offset and trend the p-values are in all cases computed in relation to a priori.

	$\Delta X - Pole$					$\Delta Y - Pole$					ΔLOD				
	std. [mm]	p-value	mean ± std. [mm]	p-value	trend ± std. [mm/a]	p-value	std. [mm]	p-value	mean ± std. [mm]	p-value	trend ± std. [mm/a]	p-value	std. [μm]	p-value	mean ± std. [μm]	p-value	trend ± std. [μm/a]	p-value
+ GRASP-like	0.069	NaN	0.001 ± 0.001	0.358	-0.001 ± 0.001	0.028	0.070	NaN	-0.060 ± 0.001	0.000	-0.012 ± 0.001	0.000	0.492	NaN	0.016 ± 0.010	0.116	0.010 ± 0.005	0.045
- w/o ST	0.068	0.361	0.001 ± 0.001	0.441	0.002 ± 0.001	0.019	0.077	0.000	-0.071 ± 0.001	0.000	-0.020 ± 0.001	0.000	0.449	0.859	0.028 ± 0.009	0.002	0.012 ± 0.005	0.009
- w/ ST																		
+ E-GRASP-mod	0.071	NaN	0.059 ± 0.001	0.000	0.010 ± 0.001	0.000	0.066	NaN	0.036 ± 0.001	0.000	-0.001 ± 0.001	0.069	0.269	NaN	0.003 ± 0.005	0.539	0.001 ± 0.003	0.675
- w/o ST	0.072	0.249	0.057 ± 0.001	0.000	0.013 ± 0.001	0.000	0.066	0.979	0.038 ± 0.001	0.000	-0.002 ± 0.001	0.003	0.279	0.858	-0.007 ± 0.006	0.217	0.002 ± 0.003	0.574
- w/ ST																		
+ E-GRASP-like	0.073	NaN	-0.007 ± 0.001	0.000	-0.014 ± 0.001	0.000	0.069	NaN	0.083 ± 0.001	0.000	0.011 ± 0.001	0.000	0.290	NaN	-0.024 ± 0.006	0.000	-0.004 ± 0.003	0.194
- w/o ST	0.069	0.032	0.000 ± 0.001	0.828	-0.010 ± 0.001	0.000	0.071	0.250	0.134 ± 0.001	0.000	0.013 ± 0.001	0.000	0.293	0.591	-0.042 ± 0.006	0.000	-0.005 ± 0.003	0.071
- w/ ST																		
+ Circular 30°	0.069	NaN	-0.015 ± 0.001	0.000	-0.008 ± 0.001	0.000	0.069	NaN	0.123 ± 0.001	0.000	0.010 ± 0.001	0.000	0.324	NaN	0.001 ± 0.006	0.876	-0.002 ± 0.003	0.476
- w/o ST	0.069	0.917	-0.015 ± 0.001	0.000	-0.008 ± 0.001	0.000	0.069	0.542	0.137 ± 0.001	0.000	0.012 ± 0.001	0.000	0.247	0.427	-0.003 ± 0.005	0.479	0.003 ± 0.002	0.256
- w/ ST																		
+ Circular 60°	0.067	NaN	0.063 ± 0.001	0.000	-0.002 ± 0.001	0.002	0.066	NaN	-0.004 ± 0.001	0.003	-0.002 ± 0.001	0.017	0.229	NaN	-0.037 ± 0.005	0.000	-0.001 ± 0.002	0.539
- w/o ST	0.067	0.943	0.064 ± 0.001	0.000	-0.002 ± 0.001	0.000	0.066	0.970	0.003 ± 0.001	0.028	-0.001 ± 0.001	0.339	0.299	0.468	-0.032 ± 0.006	0.000	-0.005 ± 0.003	0.120
- w/ ST																		
+ Circular 89°	0.069	NaN	-0.008 ± 0.001	0.000	0.003 ± 0.001	0.000	0.067	NaN	-0.043 ± 0.001	0.000	-0.002 ± 0.001	0.002	0.254	NaN	-0.053 ± 0.005	0.000	-0.007 ± 0.003	0.005
- w/o ST	0.069	0.996	-0.008 ± 0.001	0.000	0.004 ± 0.001	0.000	0.066	0.849	-0.039 ± 0.001	0.000	-0.001 ± 0.001	0.081	0.254	0.969	-0.053 ± 0.005	0.000	-0.007 ± 0.003	0.006
- w/ ST																		

G Supplementary illustrations of the analysis

G.1 DORIS

G.1.1 Reference solution

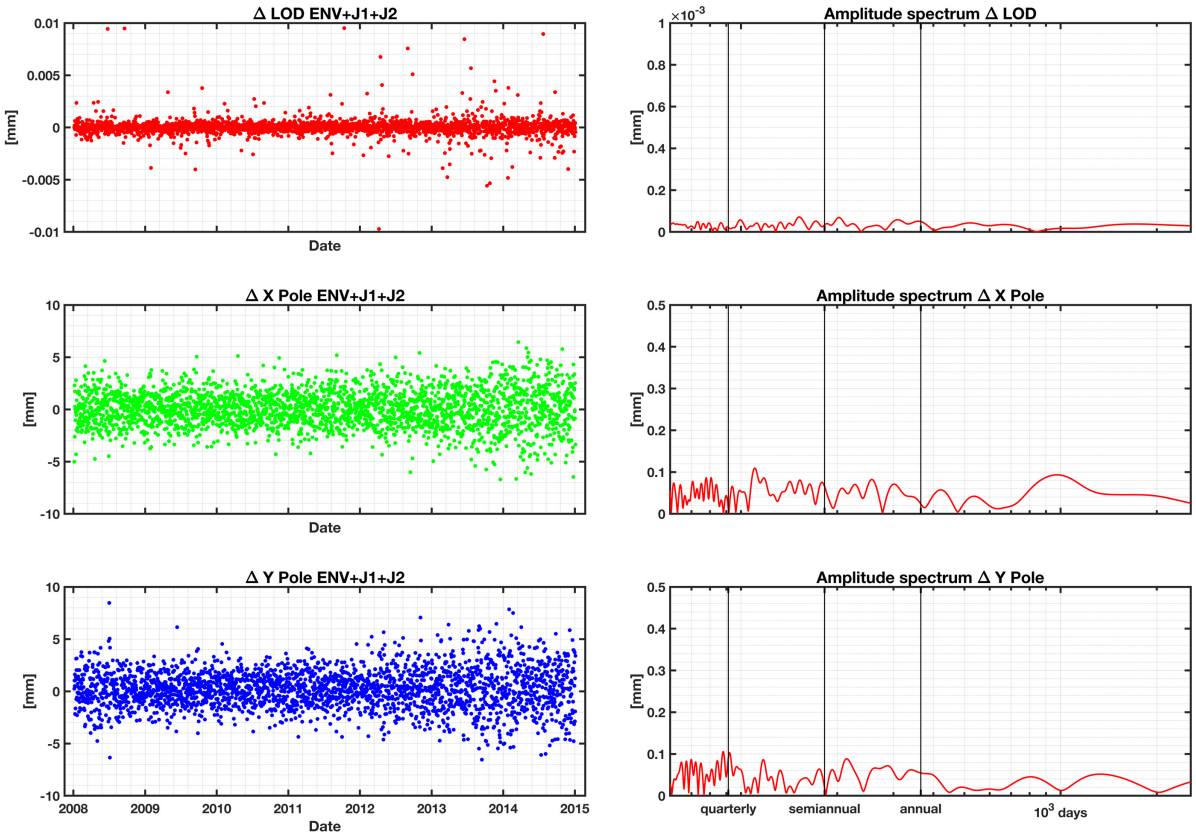

Figure G.1: Time series of the differences of the estimated LOD, X-pole, and Y-pole to a priori and their spectral analysis for the combined solution of ENVISAT, Jason-1, and Jason-2.

G.1.2 Systematic error-free

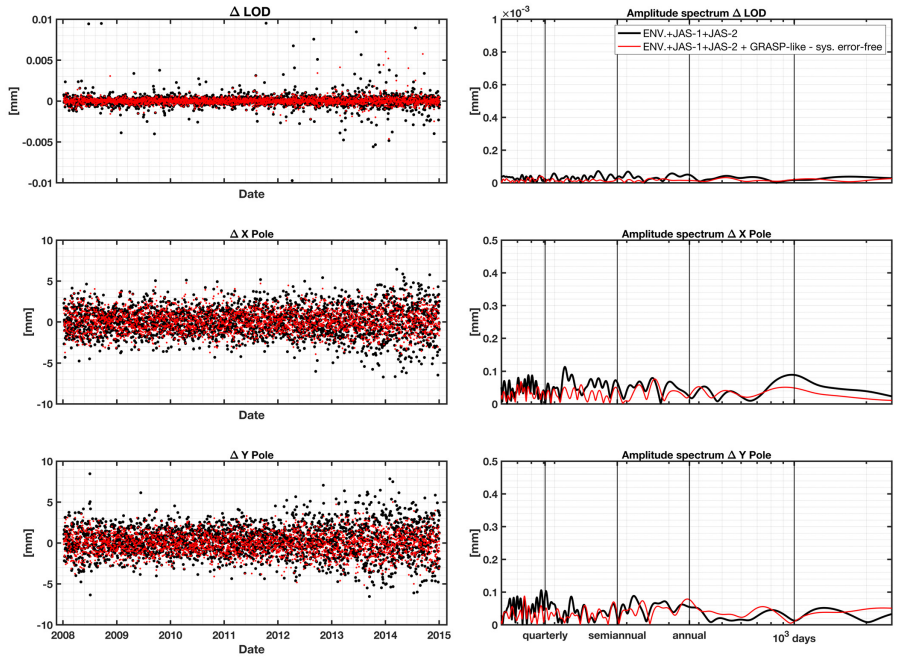

Figure G.2: Estimated differences of LOD, X-pole, and Y-pole over time and their spectral analysis for the combined solution in comparison to adding a GRASP-like scenario

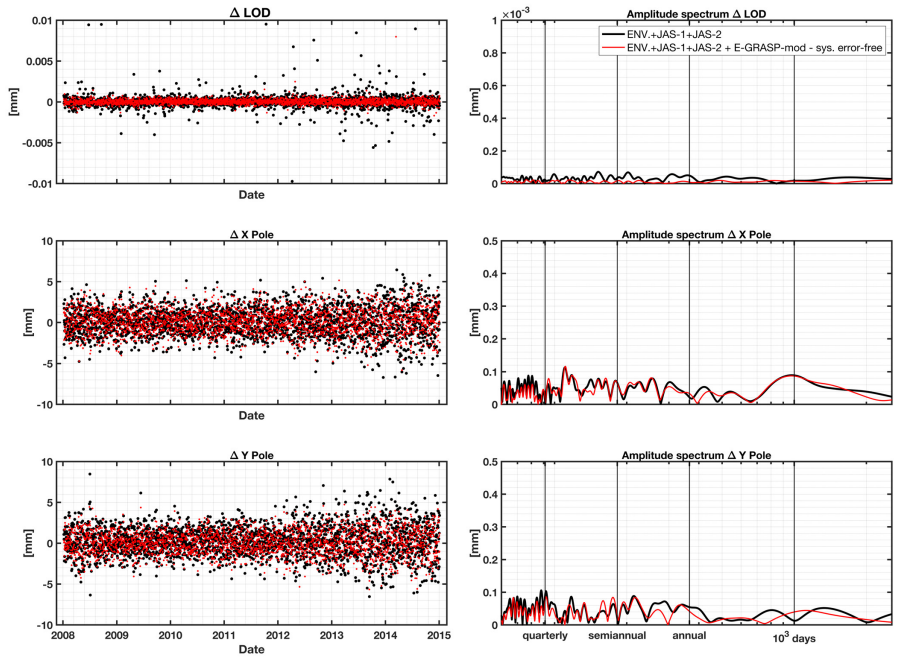

Figure G.3: Estimated differences of LOD, X-pole, and Y-pole over time and their spectral analysis for the combined solution in comparison to adding a E-GRASP-mod scenario

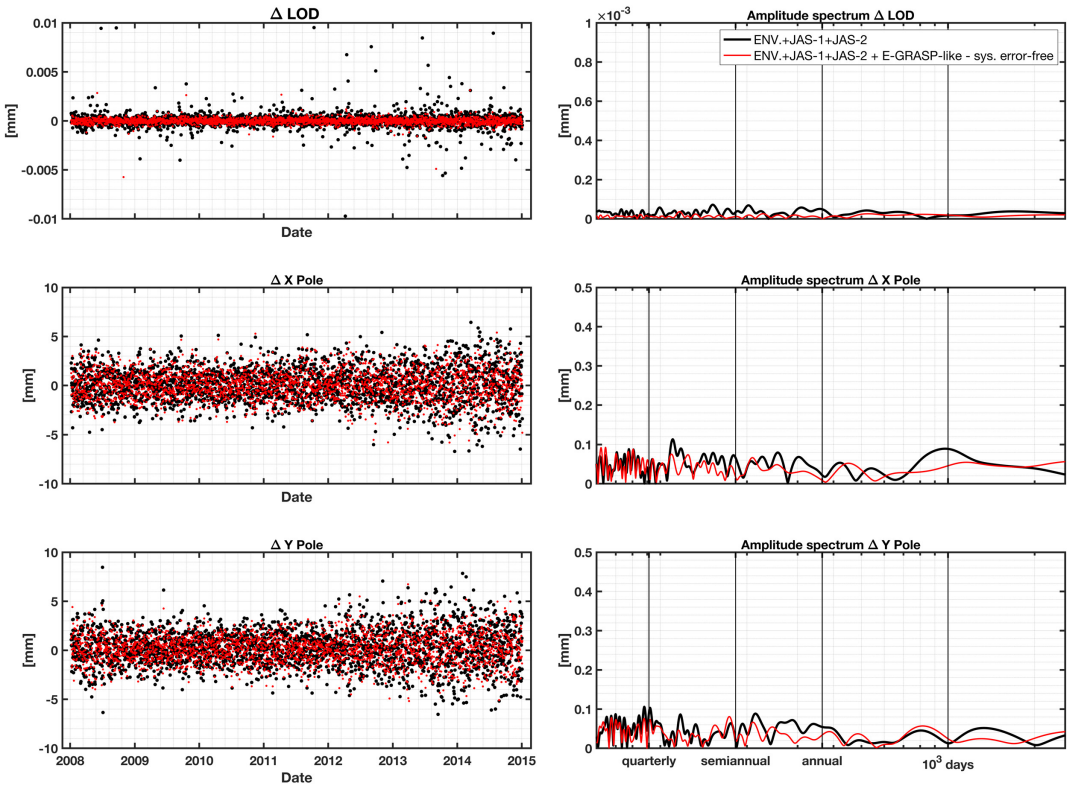

Figure G.4: Estimated differences of LOD, X-pole, and Y-pole over time and their spectral analysis for the combined solution in comparison to adding a E-GRASP-like scenario

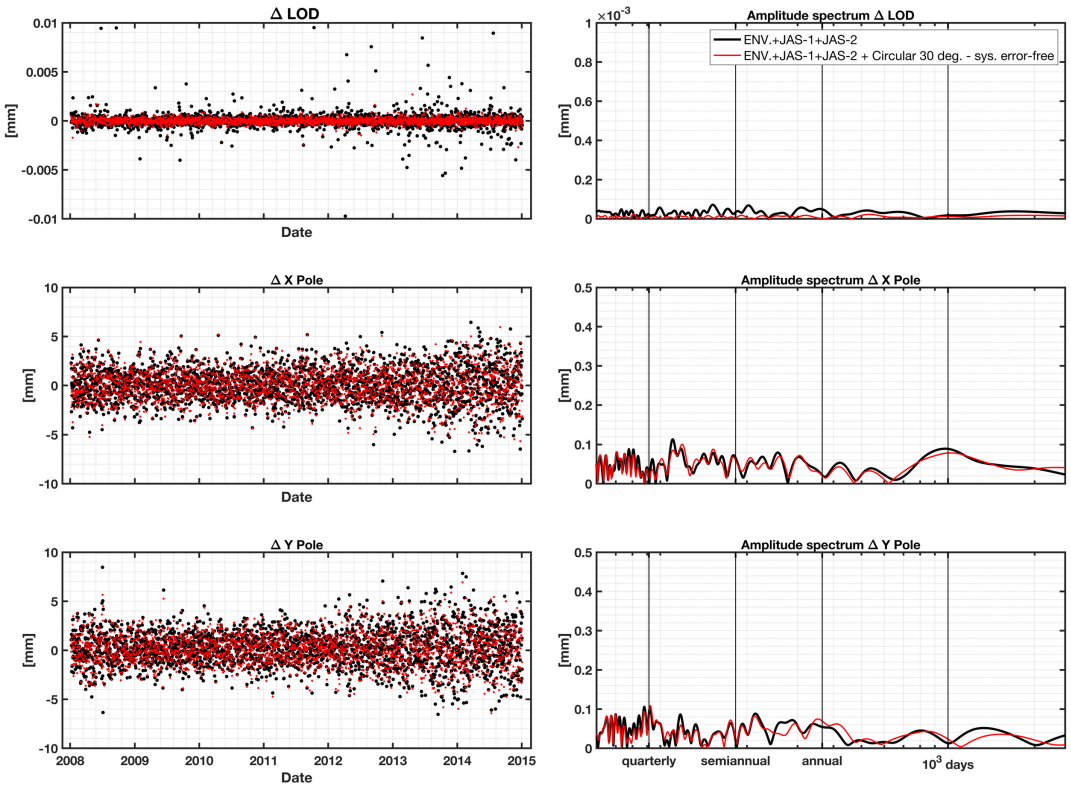

Figure G.5: Estimated differences of LOD, X-pole, and Y-pole over time and their spectral analysis for the combined solution in comparison to adding a Circular 30° scenario

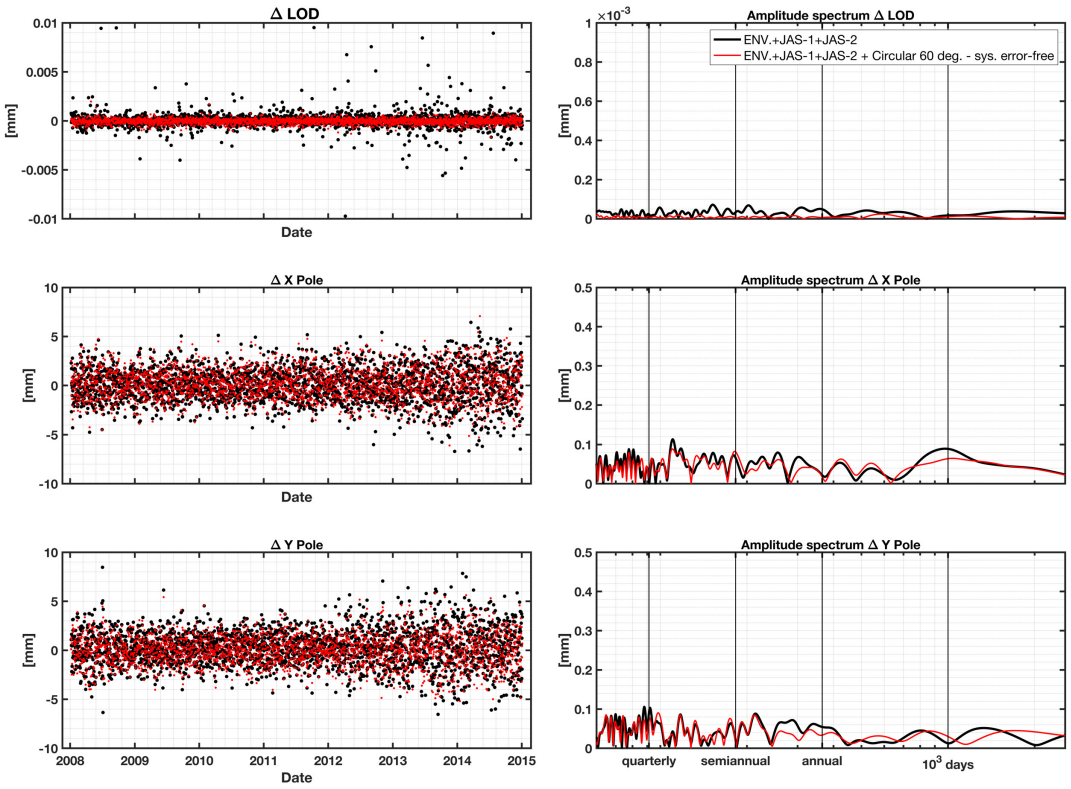

Figure G.6: Estimated differences of LOD, X-pole, and Y-pole over time and their spectral analysis for the combined solution in comparison to adding a Circular 60° scenario

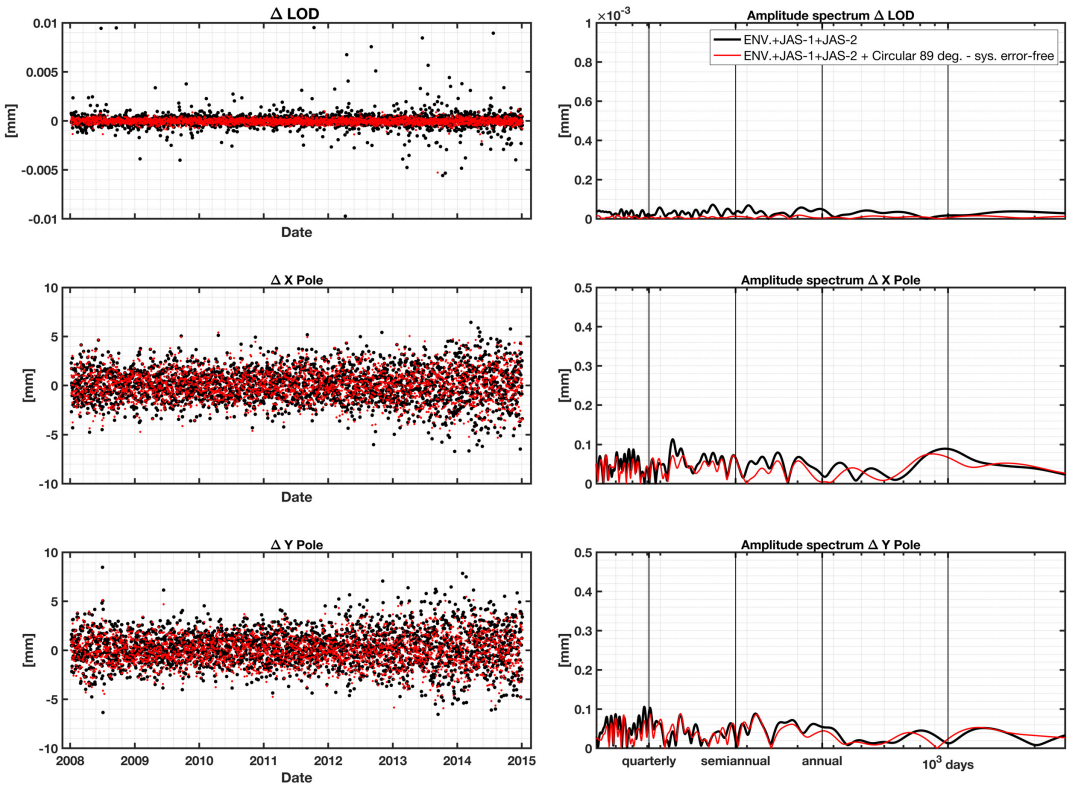

Figure G.7: Estimated differences of LOD, X-pole, and Y-pole over time and their spectral analysis for the combined solution in comparison to adding a Circular 89° scenario

G.1.3 Atmospheric drag mismodelling

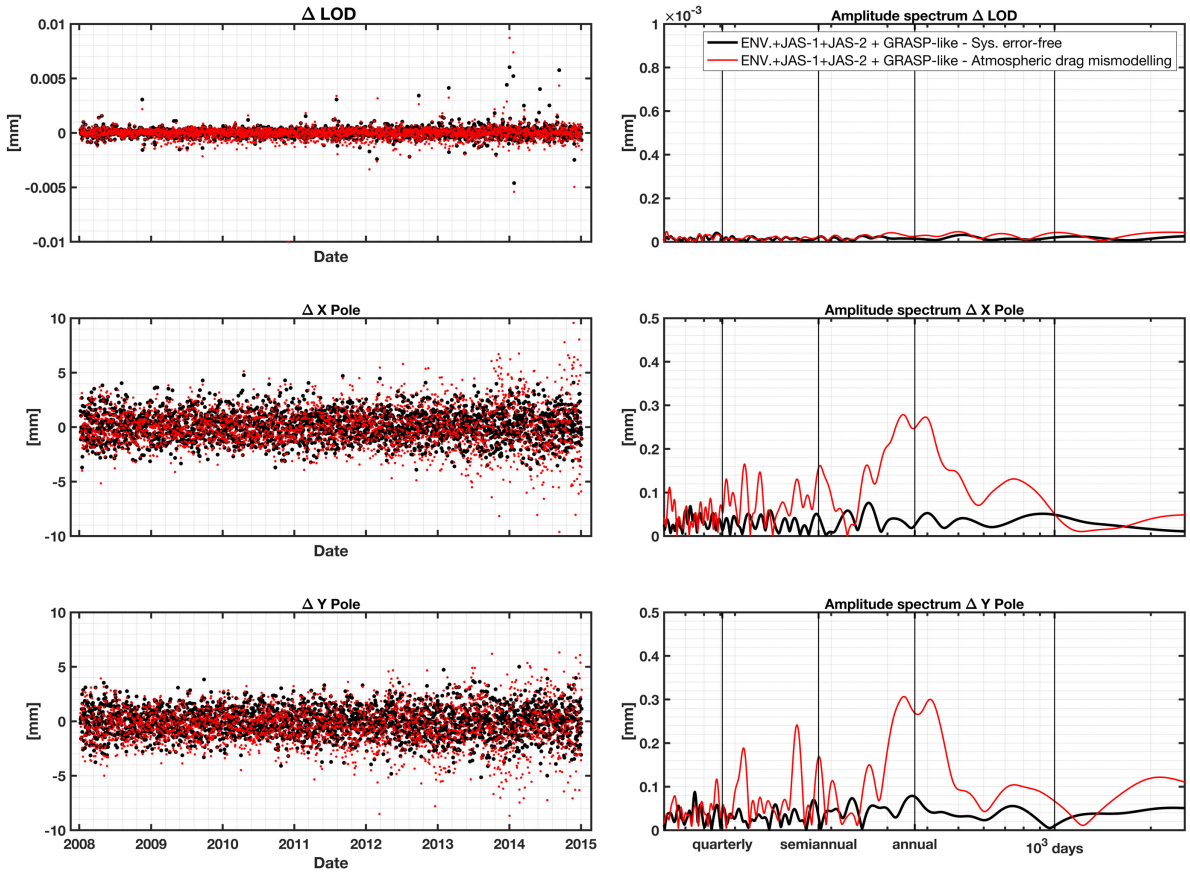

Figure G.8: Estimated differences of LOD, X-pole, and Y-pole over time and their spectral analysis for the reference combined with the GRASP-like scenario in the systematic error-free case in black, and combined with the drag mismodelled GRASP-like case in red.

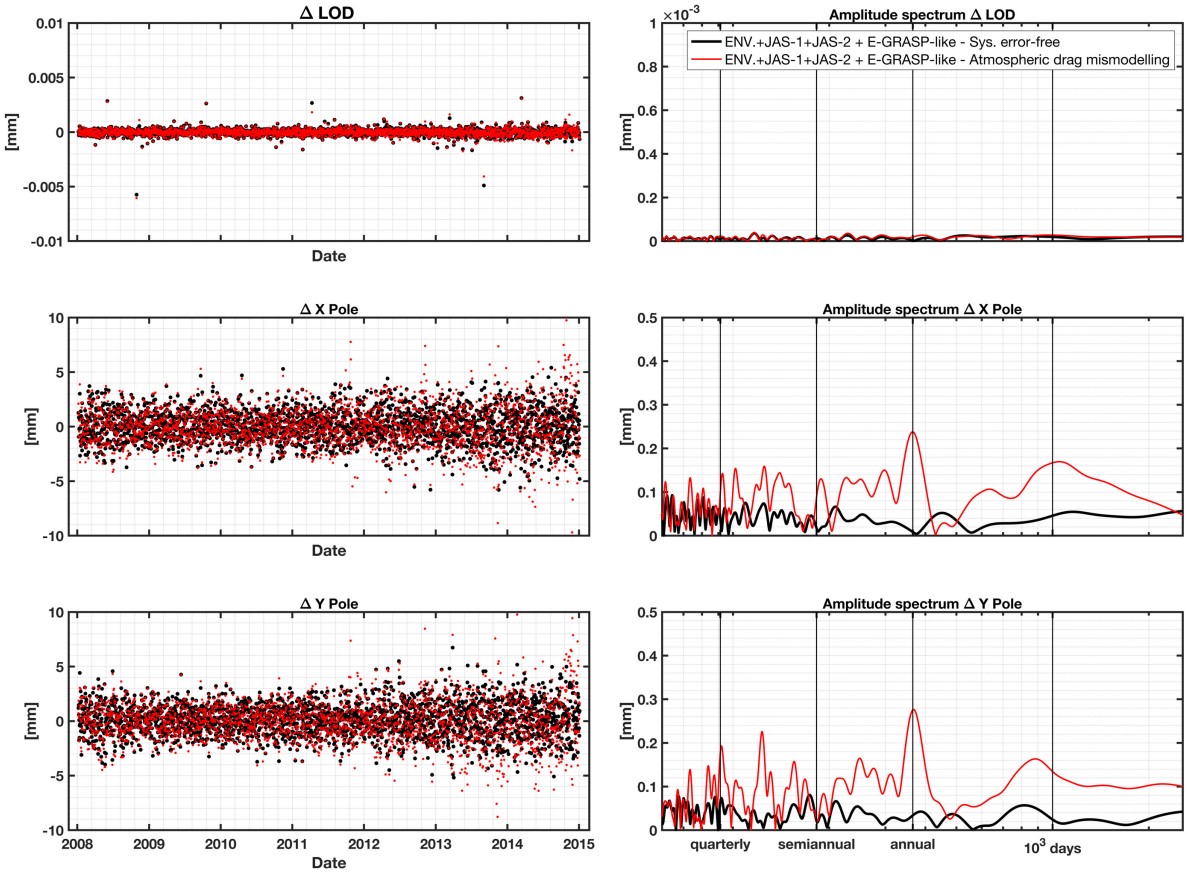

Figure G.9: Estimated differences of LOD, X-pole, and Y-pole over time and their spectral analysis for the reference combined with the E-GRASP-like scenario in the systematic error-free case in black, and combined with the drag mismodelled E-GRASP-like case in red.

G.1.4 Solar radiation pressure mismodelling

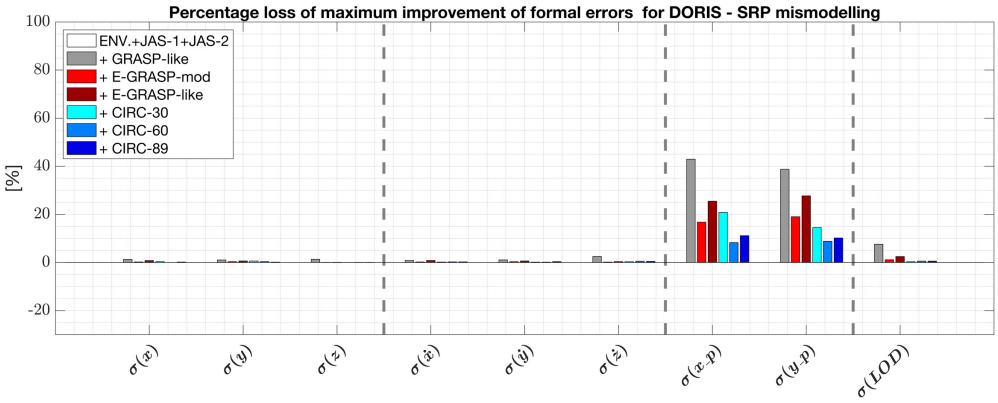

(a) Percentage loss of maximum improvement potential due to SRP mismodelling. Coordinates in X,Y, and Z

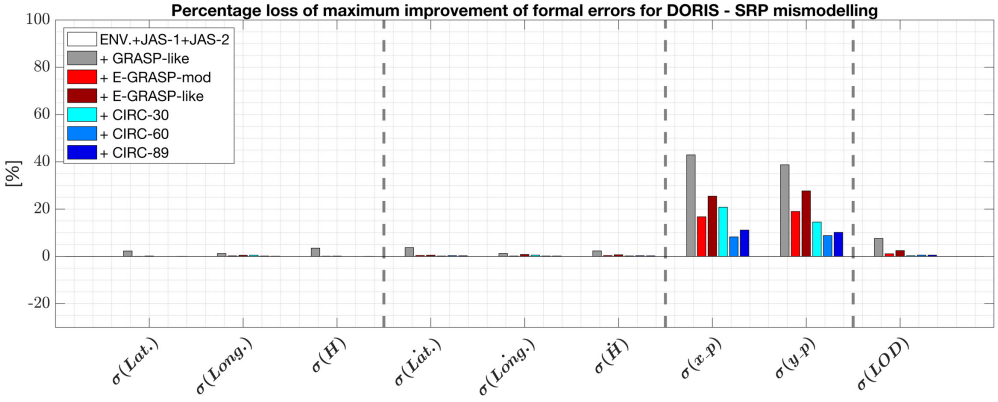

(b) Same as in Fig. a) but for coordinates in Latitude, Longitude, Height.

Figure G.10: Differences of the percentage improvements compared to the systematically error-free case. +10% means that from the full potential of improvement of the systematic error-free case 10% are lost. Figure a) shows the values for X,Y and Z, Figure b) the values for Latitude, Longitude, Height.

G.2 SLR

G.2.1 Systematic error-free

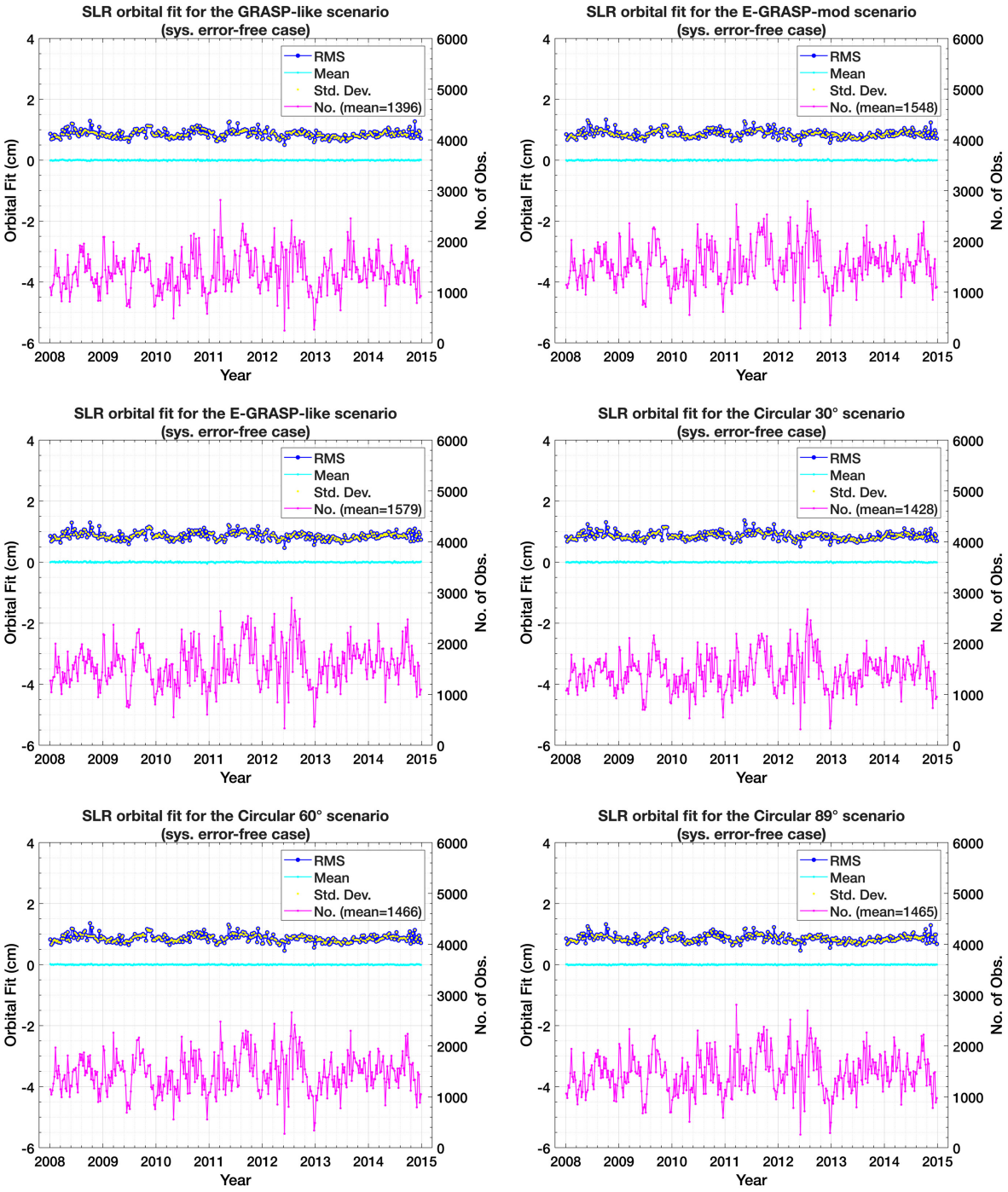

Figure G.11: Orbital fits for the SLR simulation scenarios in the systematic error-free case.

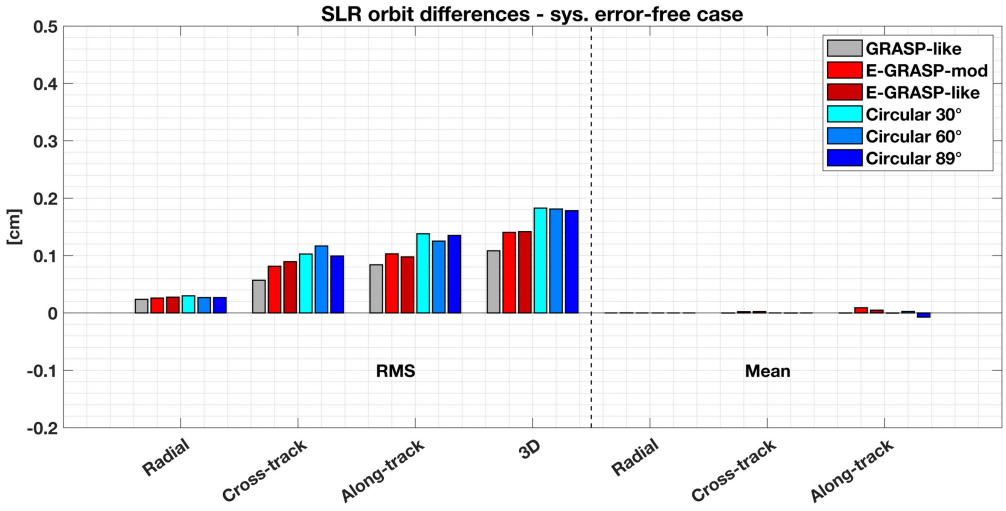

Figure G.12: Mean RMS value of the orbit comparison in radial, cross-track, along track and 3D directions, as well as the mean orbit deviation. True orbit of the simulation compared to the orbit recovered in the systematic error-free case.

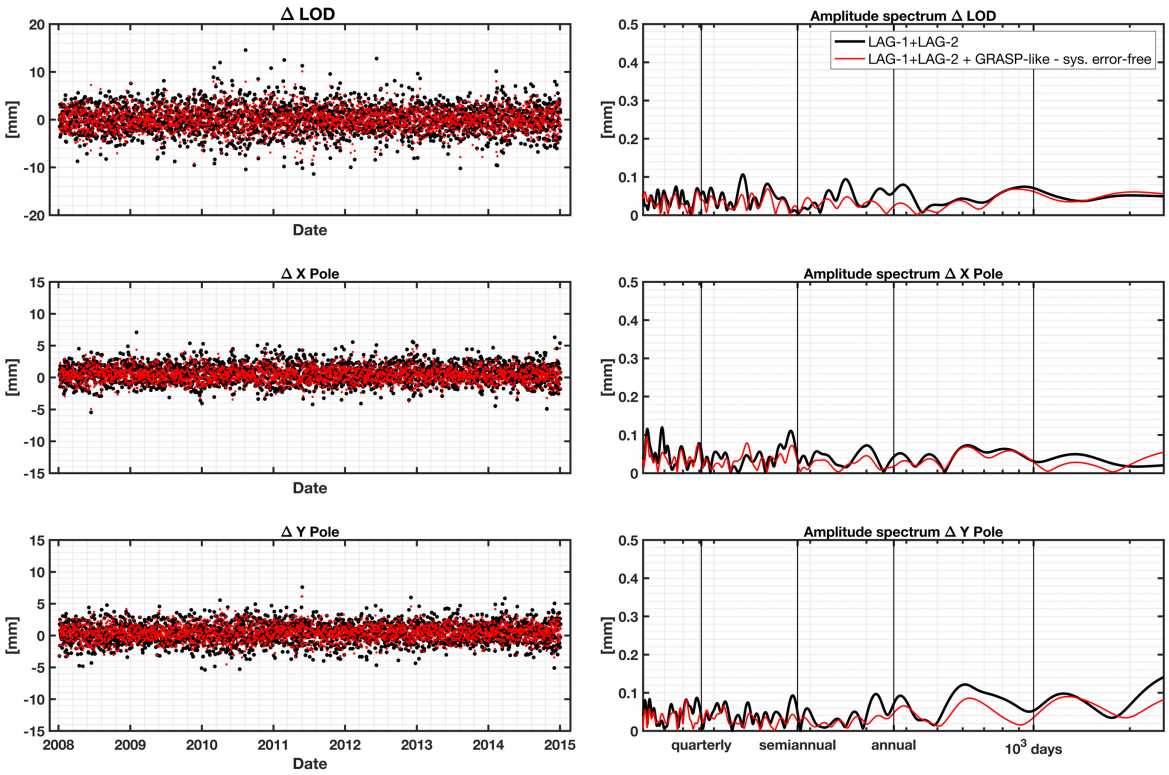

Figure G.13: Estimated differences of LOD, X-pole, and Y-pole over time and their spectral analysis for the combined solution in comparison to adding a GRASP-like scenario

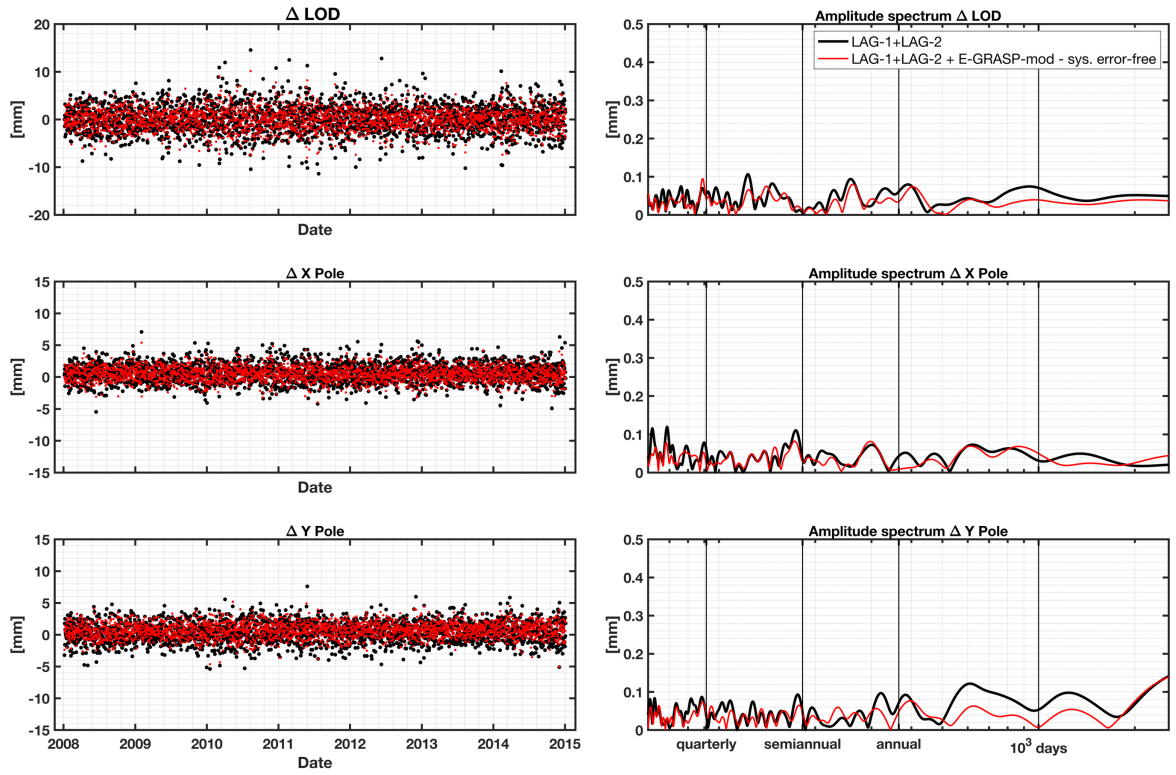

Figure G.14: Estimated differences of LOD, X-pole, and Y-pole over time and their spectral analysis for the combined solution in comparison to adding a E-GRASP-mod scenario

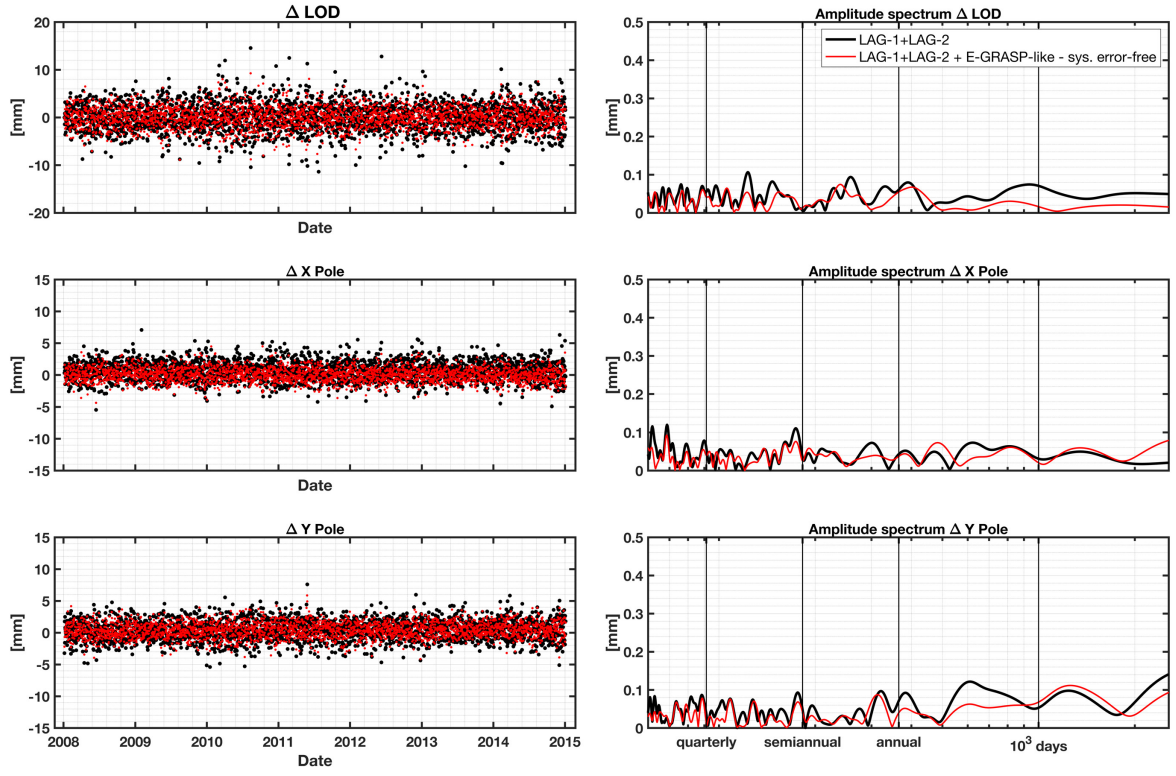

Figure G.15: Estimated differences of LOD, X-pole, and Y-pole over time and their spectral analysis for the combined solution in comparison to adding a E-GRASP-like scenario

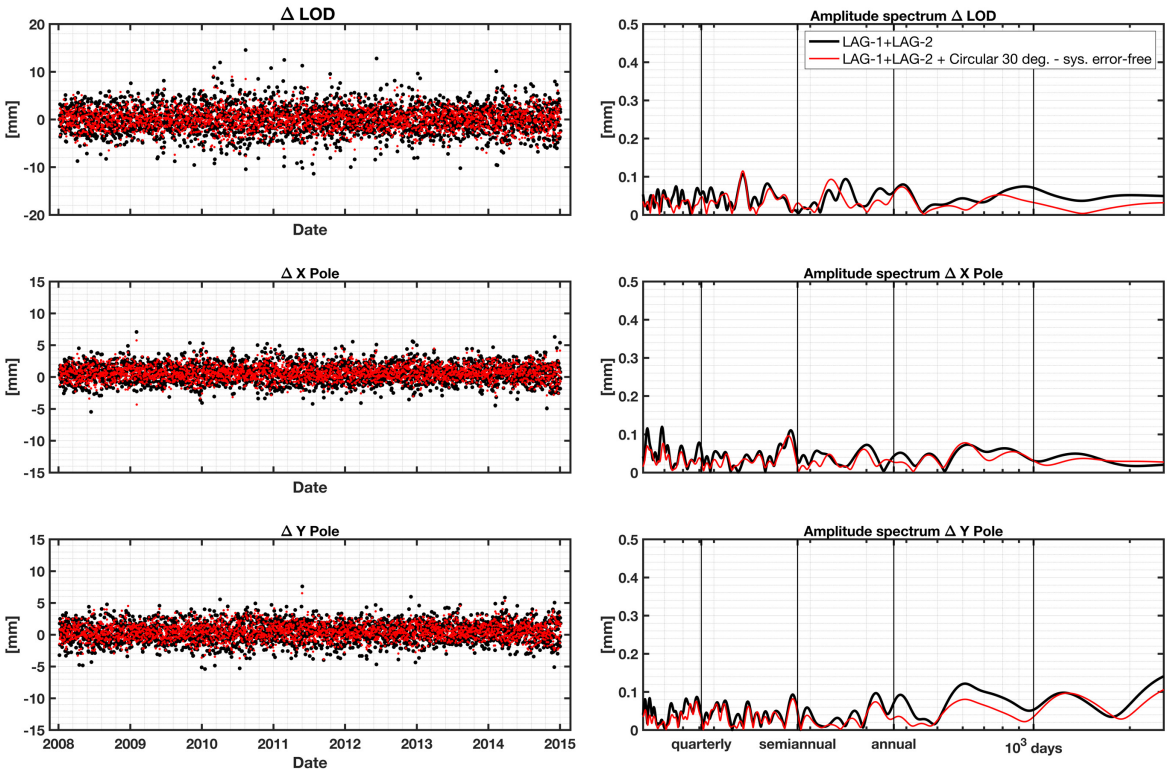

Figure G.16: Estimated differences of LOD, X-pole, and Y-pole over time and their spectral analysis for the combined solution in comparison to adding a Circular 30°scenario

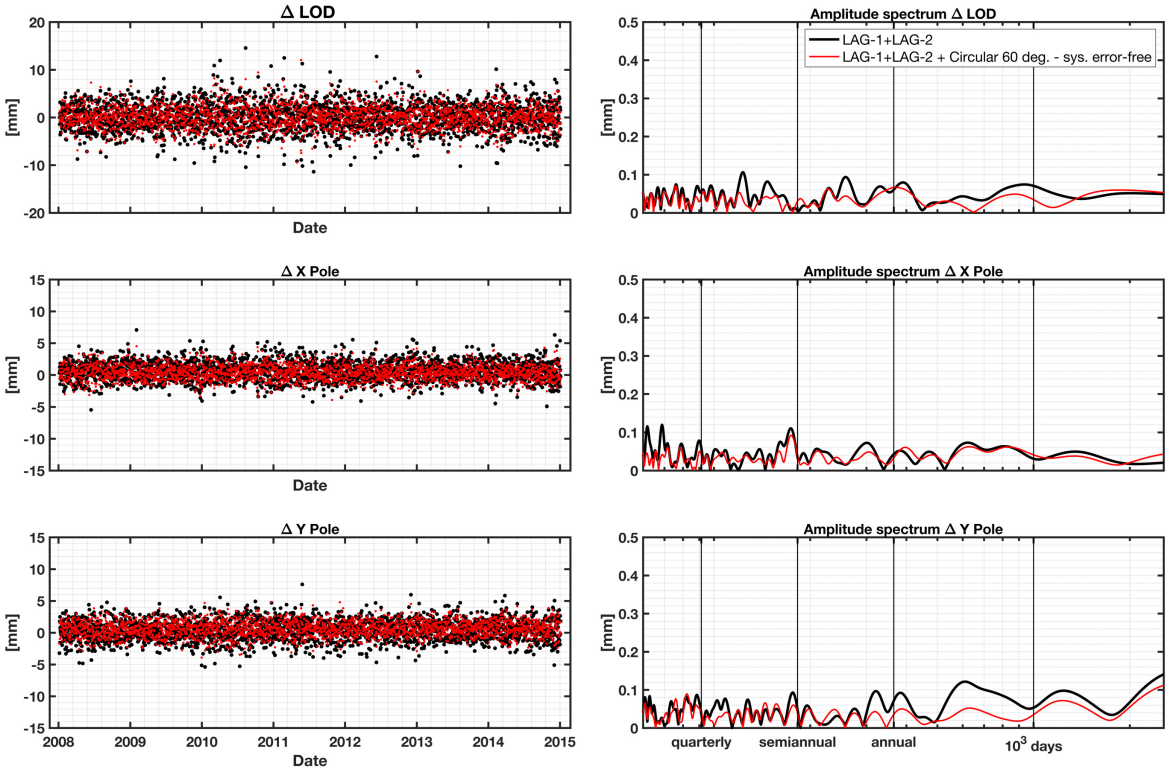

Figure G.17: Estimated differences of LOD, X-pole, and Y-pole over time and their spectral analysis for the combined solution in comparison to adding a Circular 60°scenario

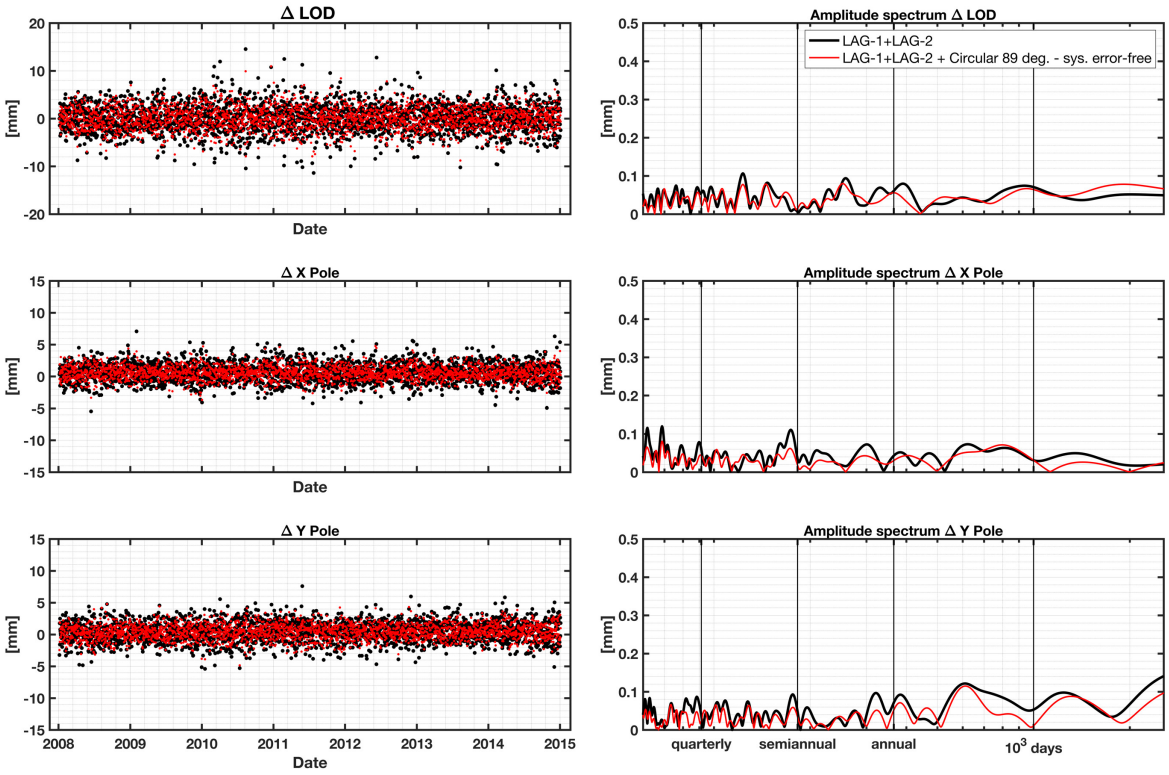

Figure G.18: Estimated differences of LOD, X-pole, and Y-pole over time and their spectral analysis for the combined solution in comparison to adding a Circular 89°scenario

G.2.2 Influence of systematic center-of-mass displacement

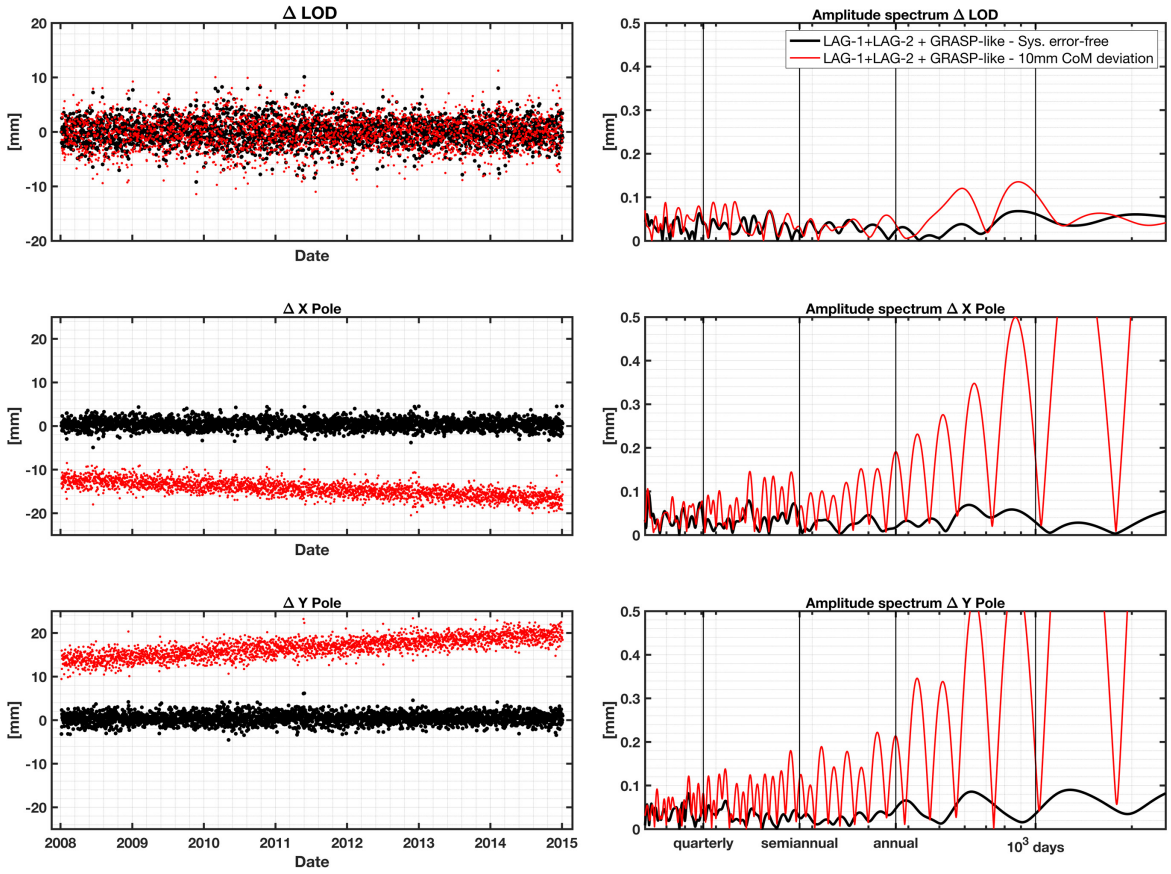

Figure G.19: Estimated differences of LOD, X-pole, and Y-pole over time and their spectral analysis for the GRASP-like combined solution. The systematic error-free case in black, the case with 10 mm CoM displacement for the GRASP-like satellite in red.

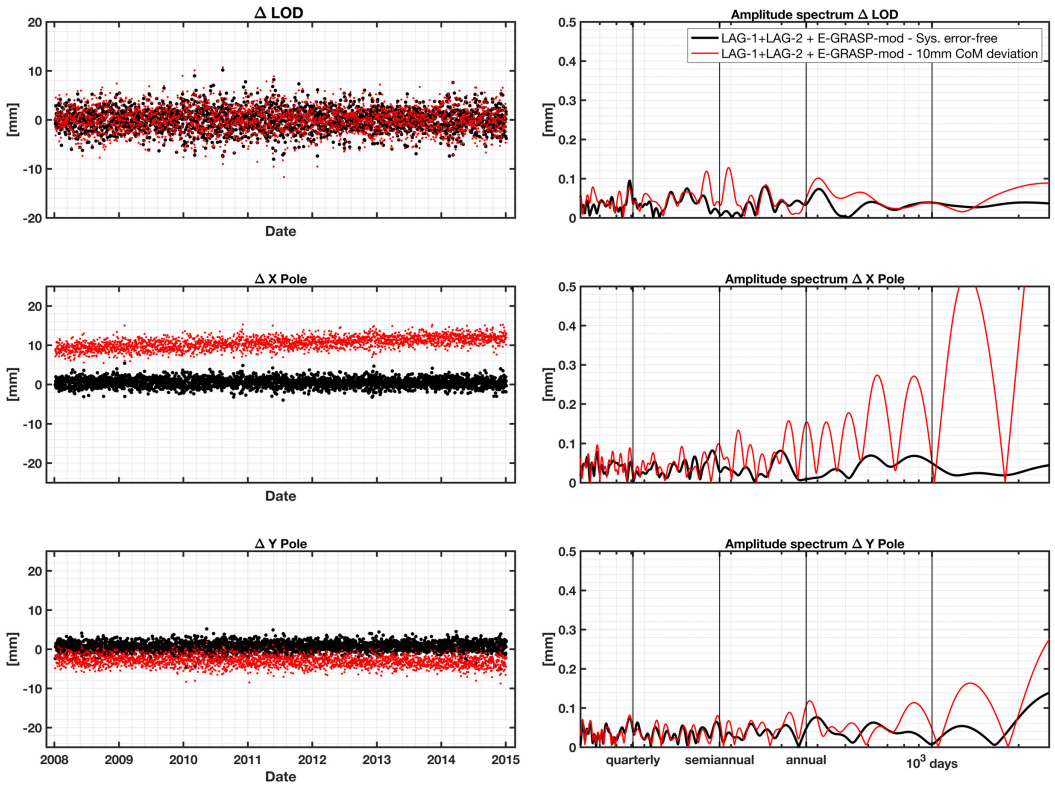

Figure G.20: Estimated differences of LOD, X-pole, and Y-pole over time and their spectral analysis for the E-GRASP-mod combined solution. The systematic error-free case in black, the case with 10 mm CoM displacement for the E-GRASP-mod satellite in red.

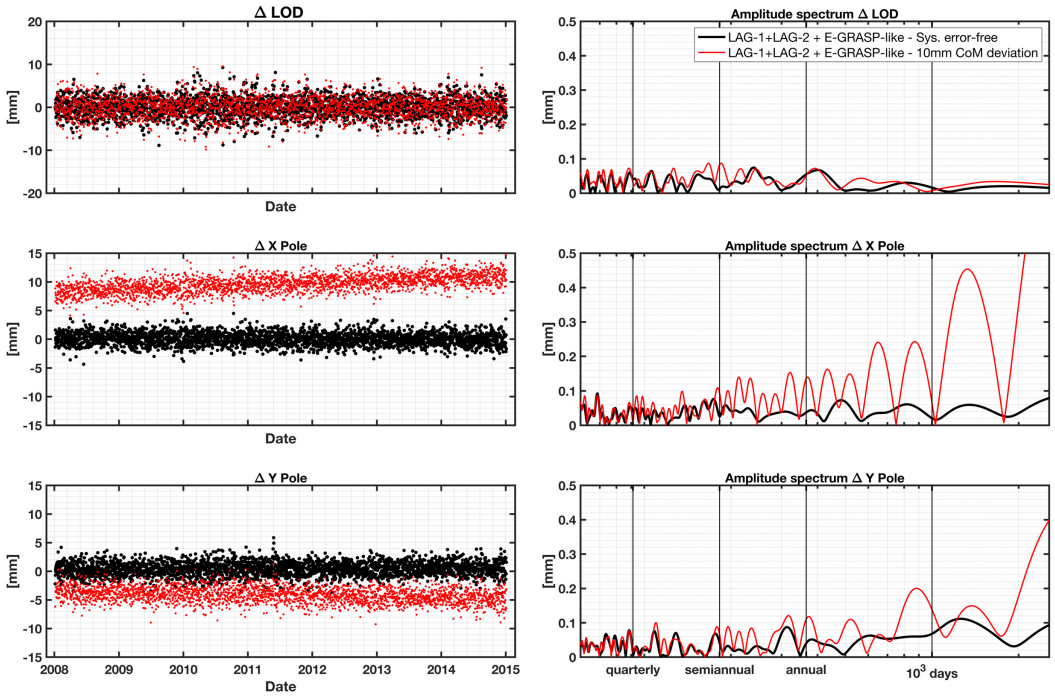

Figure G.21: Estimated differences of LOD, X-pole, and Y-pole over time and their spectral analysis for the E-GRASP-like combined solution. The systematic error-free case in black, the case with 10 mm CoM displacement for the E-GRASP-like satellite in red.

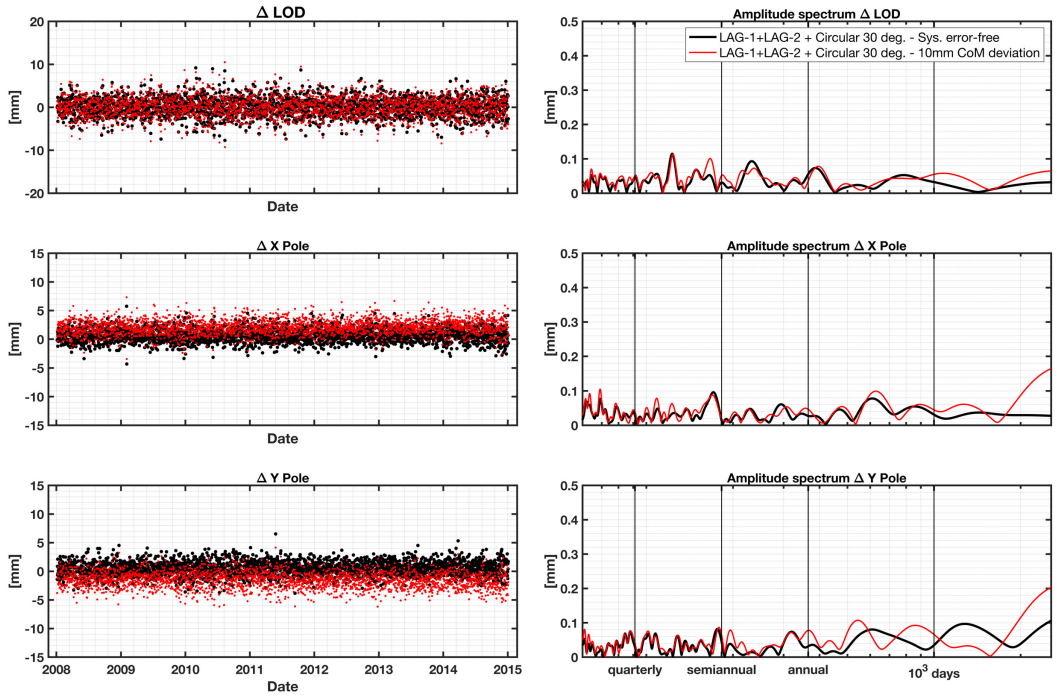

Figure G.22: Estimated differences of LOD, X-pole, and Y-pole over time and their spectral analysis for the Circular 30 °combined solution. The systematic error-free case in black, the case with 10 mm CoM displacement for the Circular 30 °satellite in red.

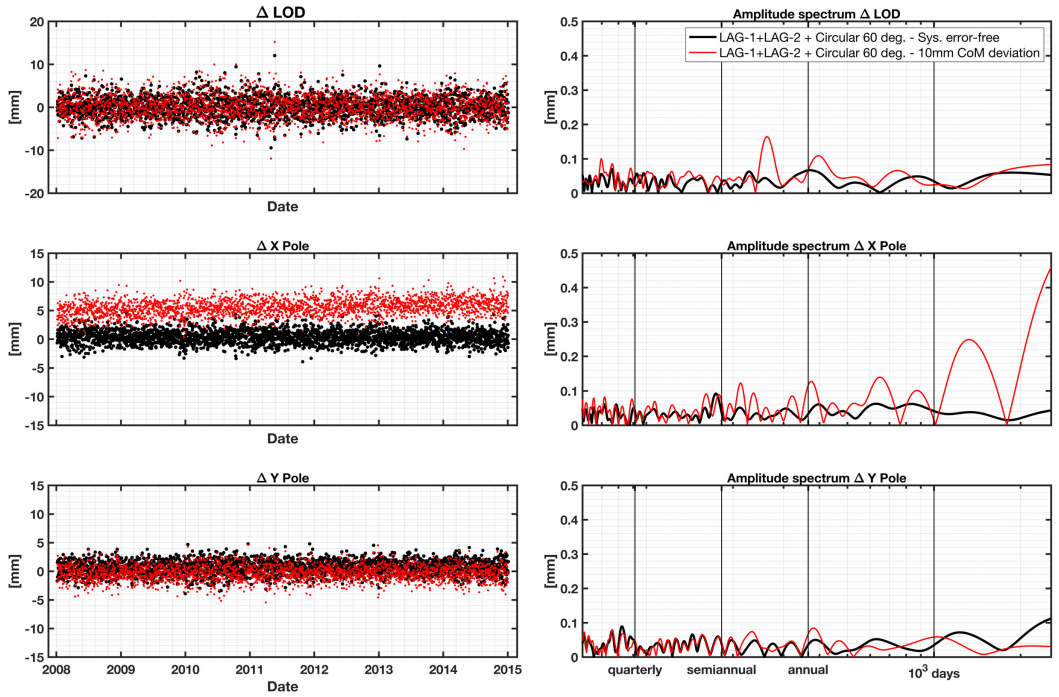

Figure G.23: Estimated differences of LOD, X-pole, and Y-pole over time and their spectral analysis for the Circular 60 °combined solution. The systematic error-free case in black, the case with 10 mm CoM displacement for the Circular 60 °satellite in red.

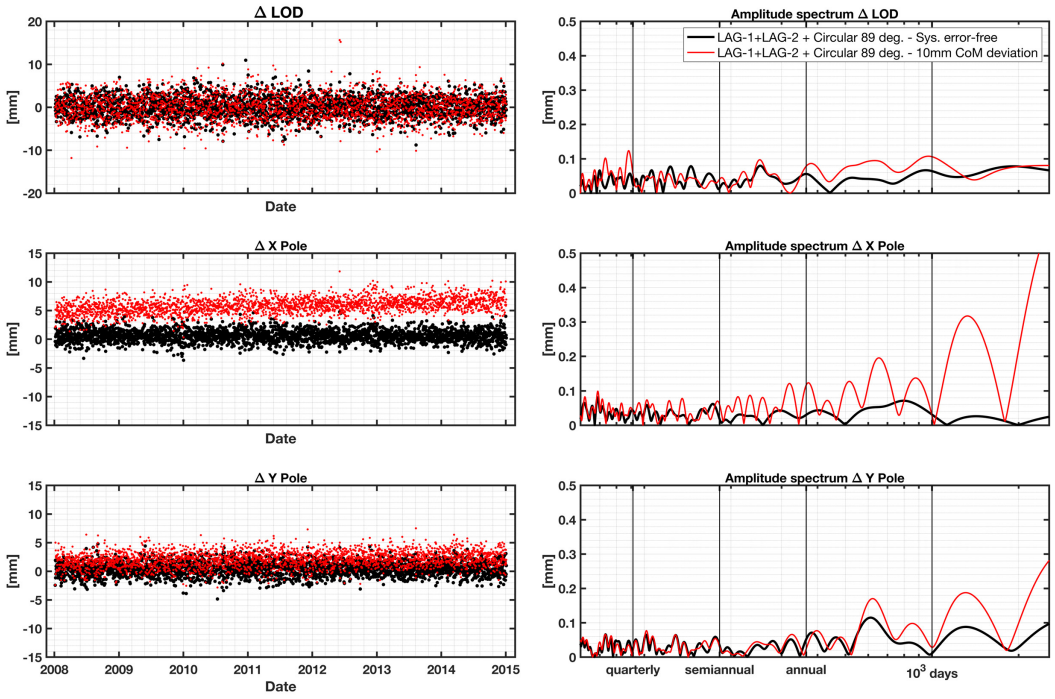

Figure G.24: Estimated differences of LOD, X-pole, and Y-pole over time and their spectral analysis for the Circular 89°combined solution. The systematic error-free case in black, the case with 10 mm CoM displacement for the Circular 89°satellite in red.

G.2.3 Atmospheric drag mismodelling

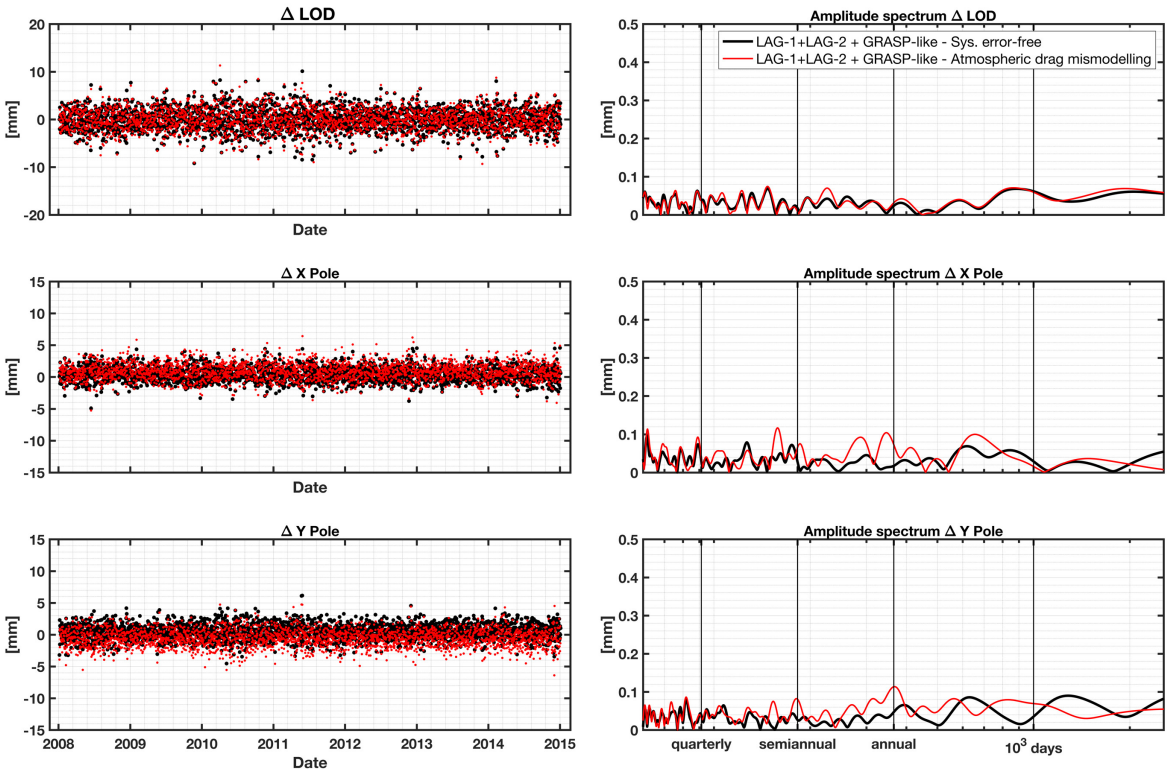

Figure G.25: Estimated differences of LOD, X-pole, and Y-pole over time and their spectral analysis for the reference combined with the GRASP-like scenario in the systematic error-free case in black, and combined with the drag mismodelled GRASP-like case in red.

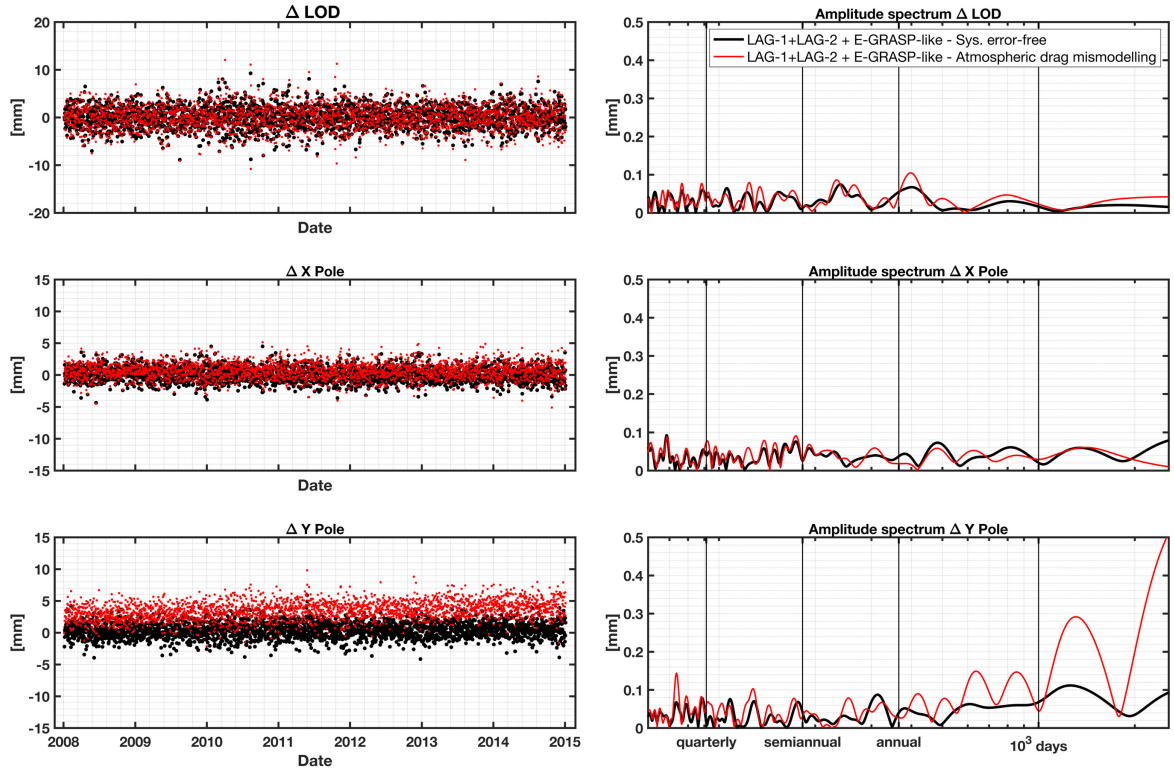

Figure G.26: Estimated differences of LOD, X-pole, and Y-pole over time and their spectral analysis for the reference combined with the E-GRASP-like scenario in the systematic error-free case in black, and combined with the drag mismodelled E-GRASP-like case in red.

G.3 GPS

G.3.1 Systematic error-free

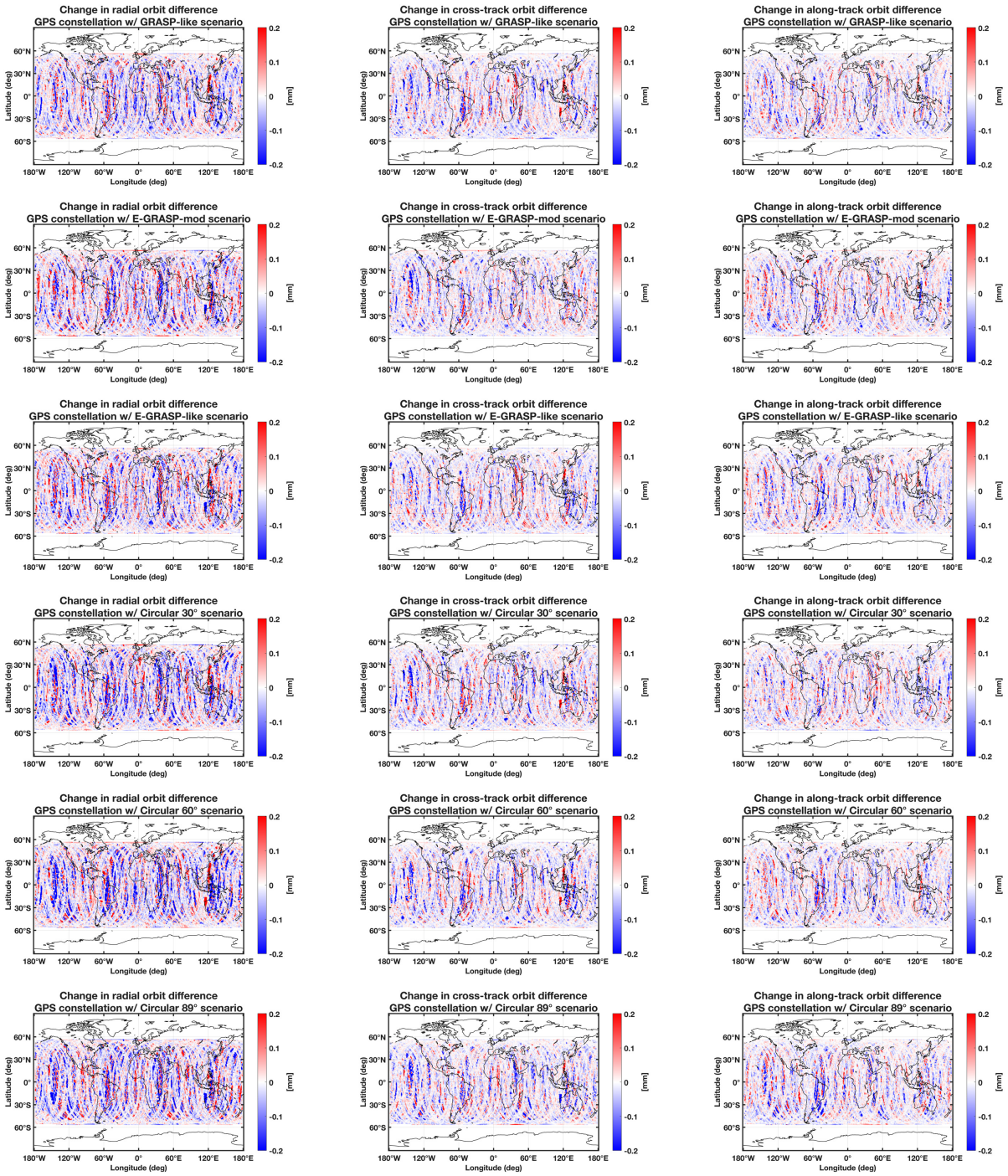

Figure G.27: Change in median orbit difference of the GPS constellation compared to the systematic error-free reference solution over a 1-year period. From top to bottom including the space-tie satellite: GRASP-like; E-GRASP-mod; E-GRASP-like; Circular 30°; Circular 60°; Circular 89°. From left to right in the radial, cross-track and along-track directions. Increases in orbital difference are shown in red, while reductions in orbit differences are shown in blue.

G.3.2 Solar radiation pressure mismodelling

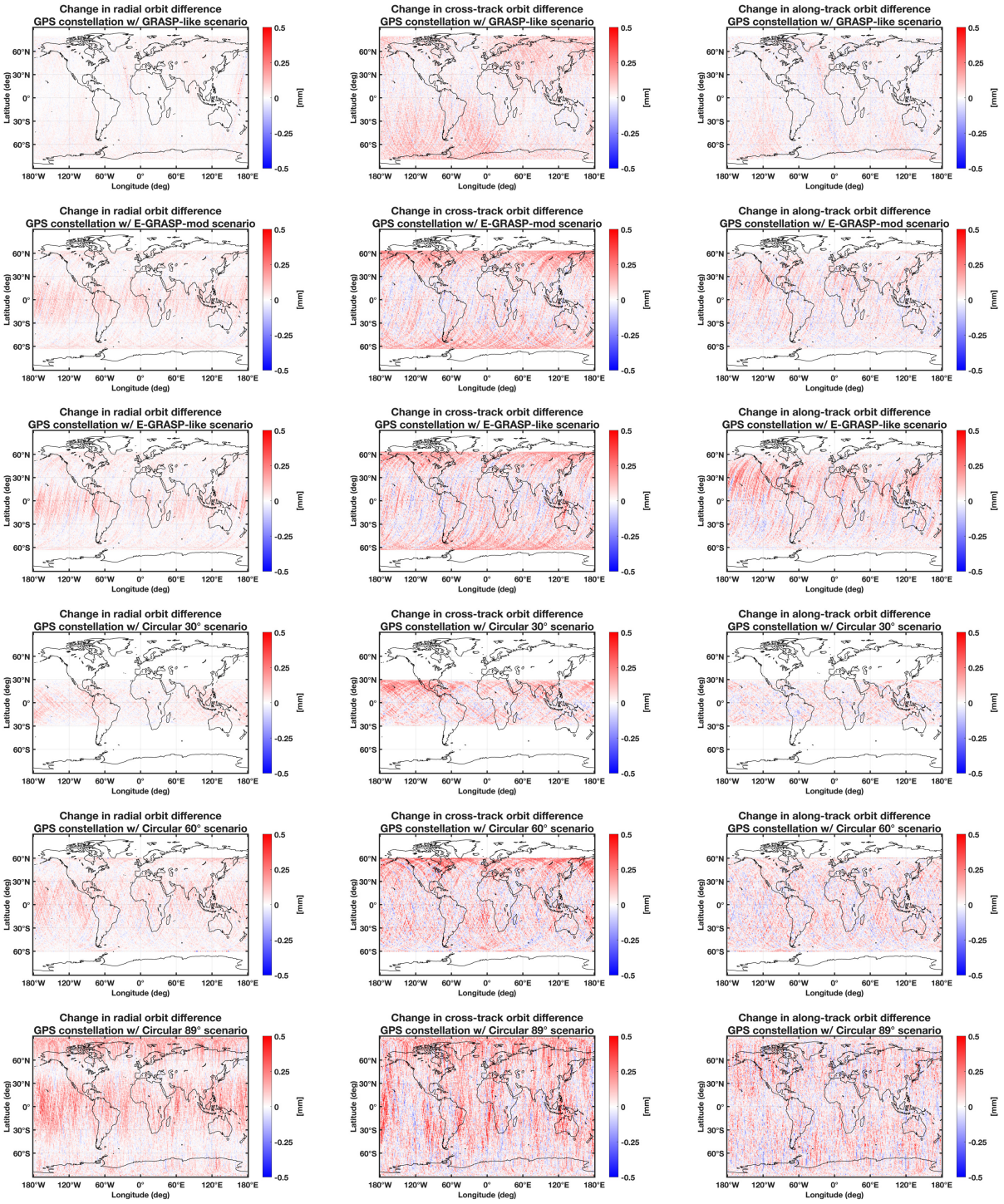

Figure G.28: Change in median orbit difference of the LEO satellites compared to the systematic error-free case over a 1-year period for GPS in the SRP mismodelling case. From top to bottom: GRASP-like; E-GRASP-mod; E-GRASP-like; Circular 30°; Circular 60°; Circular 89°. From left to right in the radial, cross-track and along-track directions. Increases in orbital difference are shown in red, while reductions in orbit differences are shown in blue.

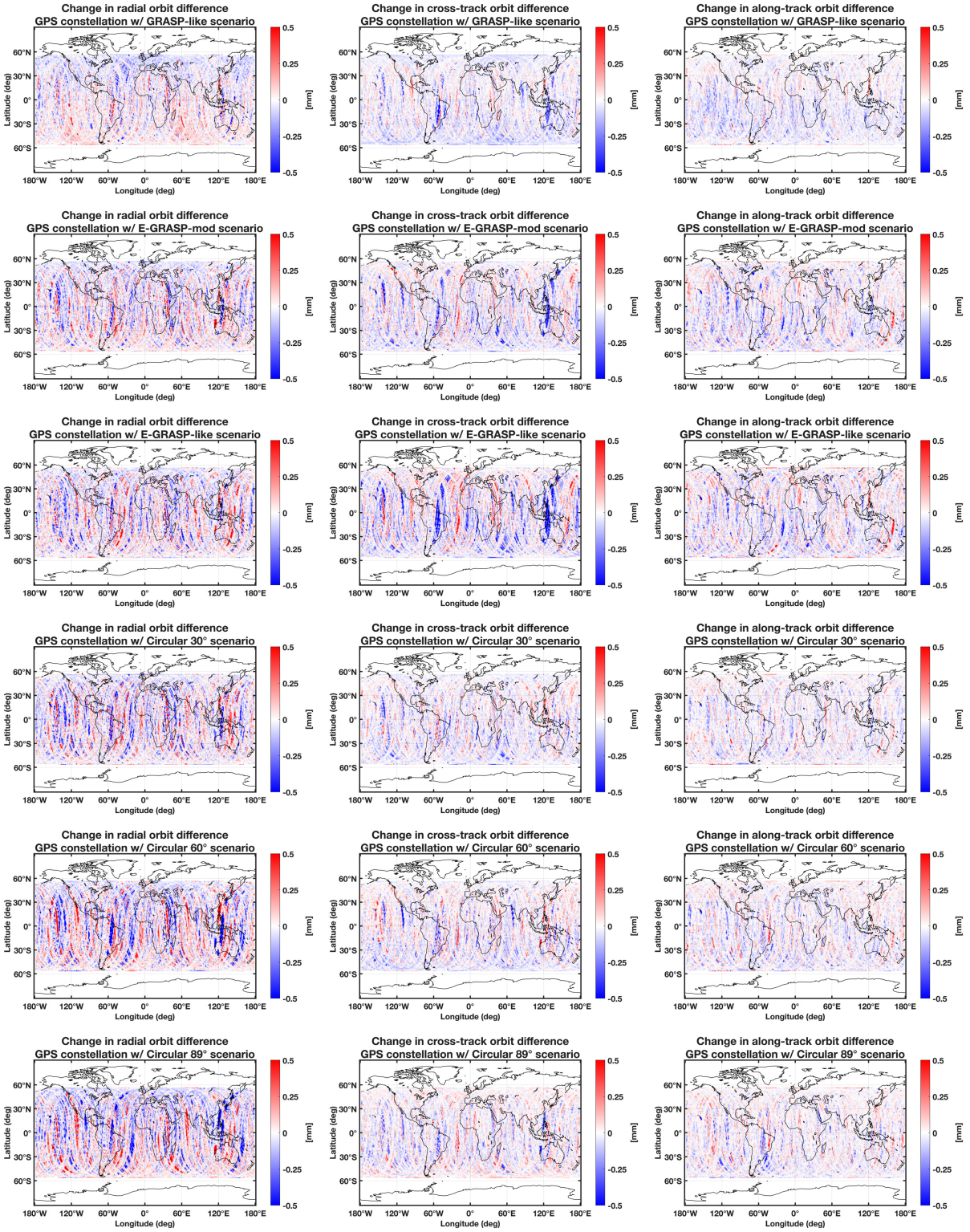

Figure G.29: Change in median orbit difference of the GPS constellation compared to the systematic error-free case over a 1-year period in the SRP mismodelling case. From top to bottom including the space-tie satellite: GRASP-like; E-GRASP-mod; E-GRASP-like; Circular 30°; Circular 60°; Circular 89°. From left to right in the radial, cross-track and along-track directions. Increases in orbital difference are shown in red, while reductions in orbit differences are shown in blue.

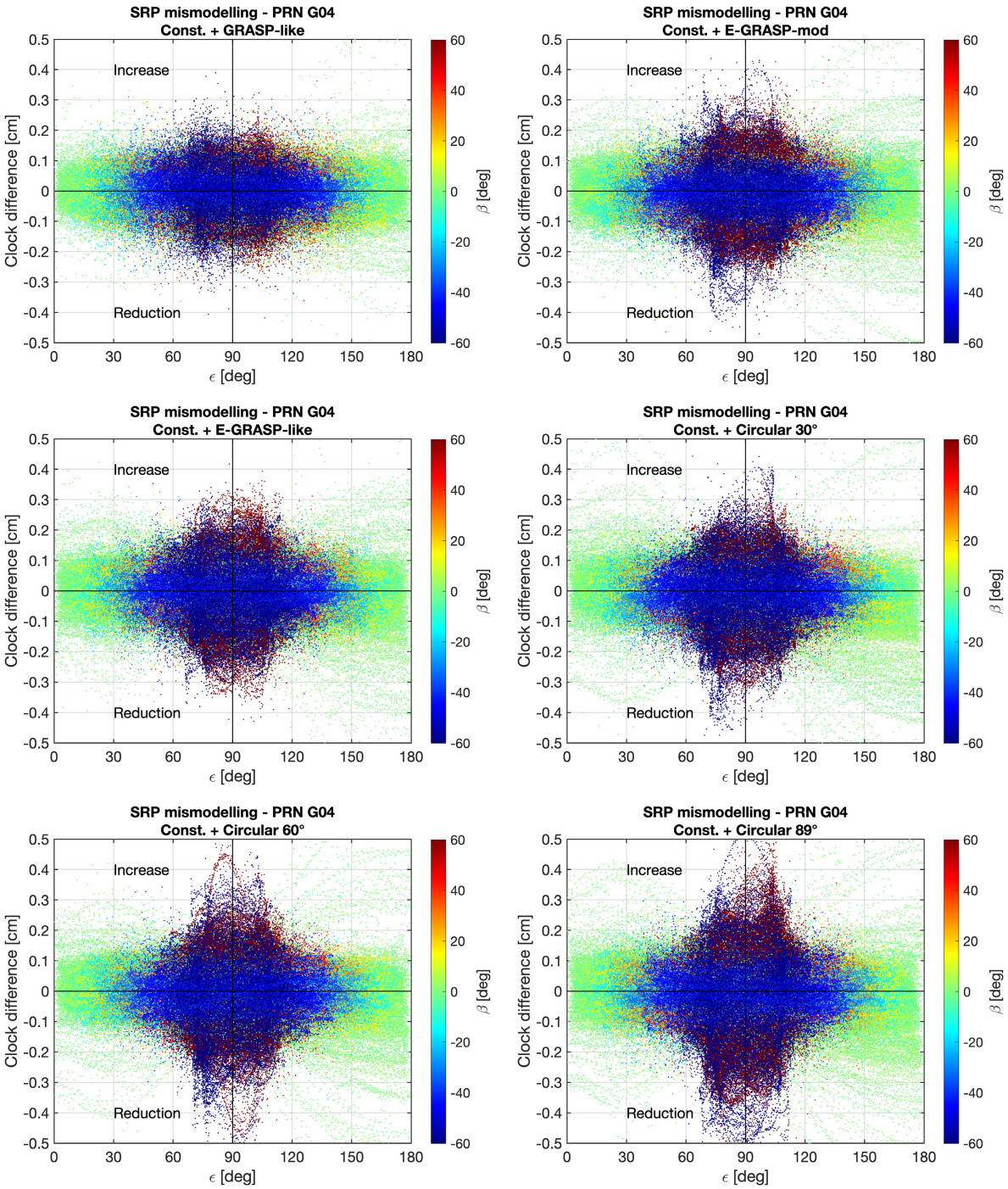

Figure G.30: Clock difference of absolute clock offset in comparison to GPS constellation alone in the SRP mismodelling case. Positive values indicate an increase in clock differences, negative values a reduction.

G.3.3 Earth gravity field mismodelling

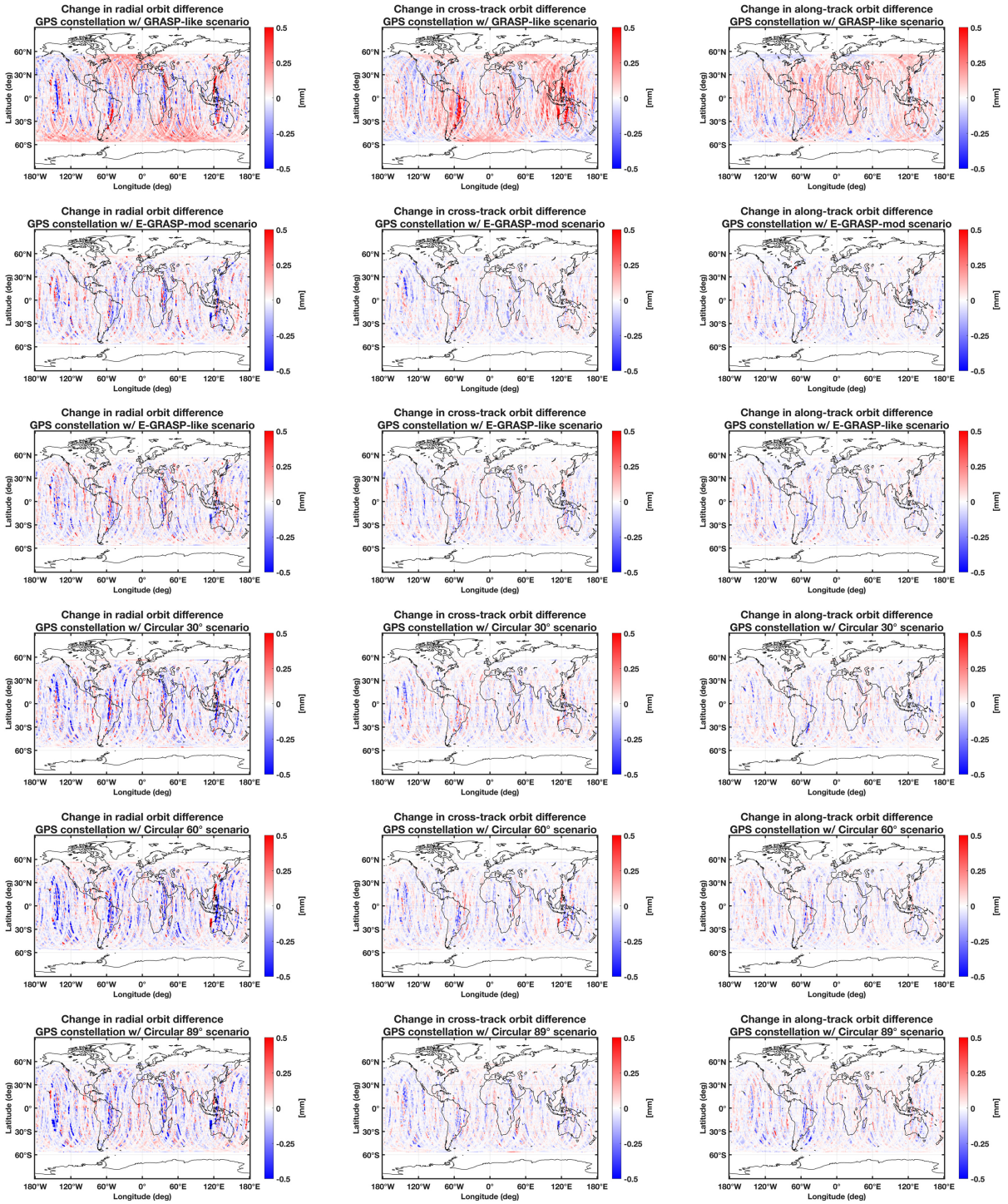

Figure G.31: Change in median orbit differences of the GPS constellation while including one of the space-tie satellite scenarios in the EGM mismodelling case over a time span one year. From the top to the bottom, GRASP-like, E-GRASP-mod, E-GRASP-like, Circular 30°, Circular 60°, Circular 89° scenario. From left to right in radial, cross-track, and along-track direction.

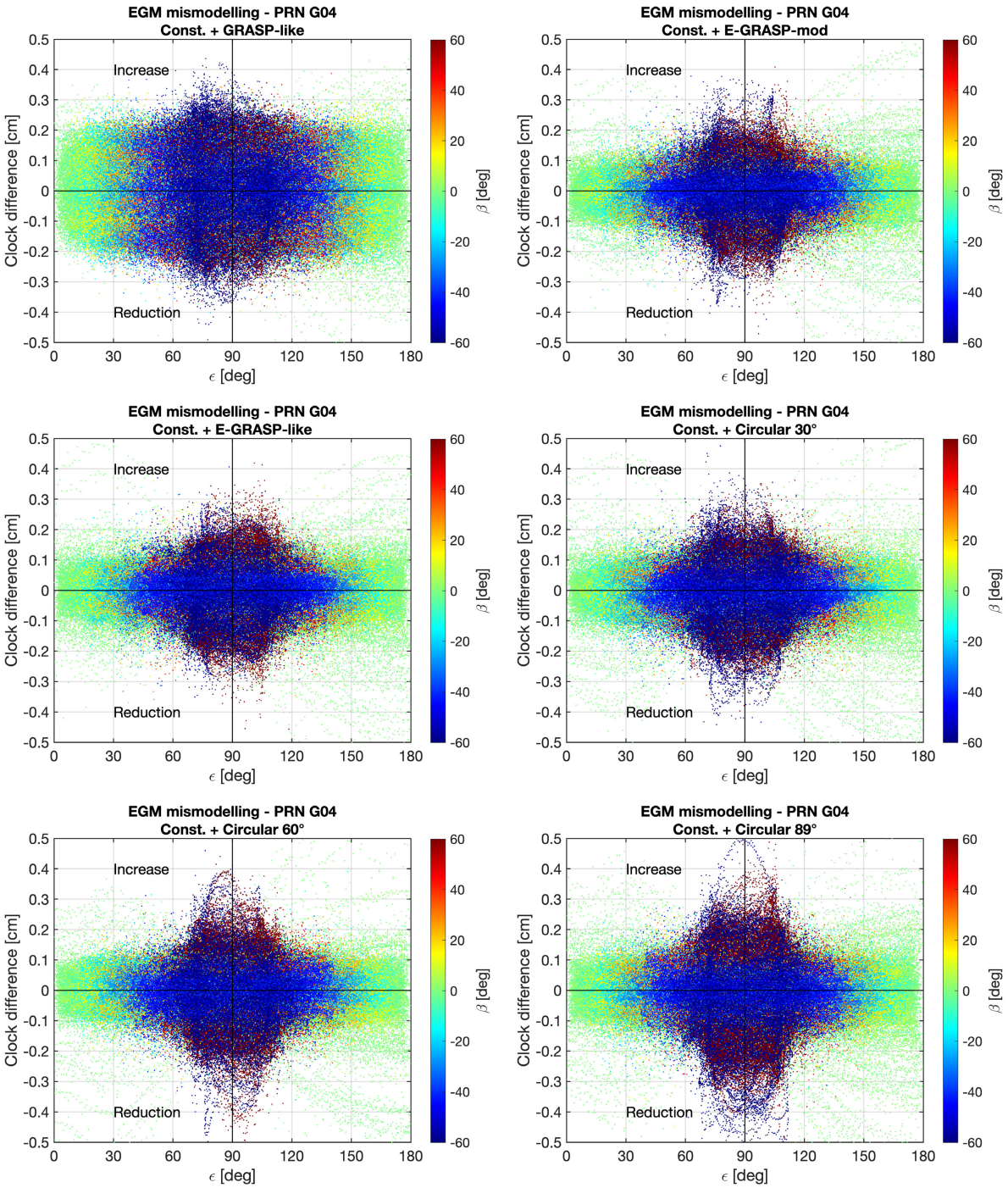

Figure G.32: Clock difference of absolute clock offset in comparison to GPS constellation alone in the EGM mismodelling case. Positive values indicate an increase in clock differences, negative values a reduction.

G.4 DORIS, GPS, SLR combination

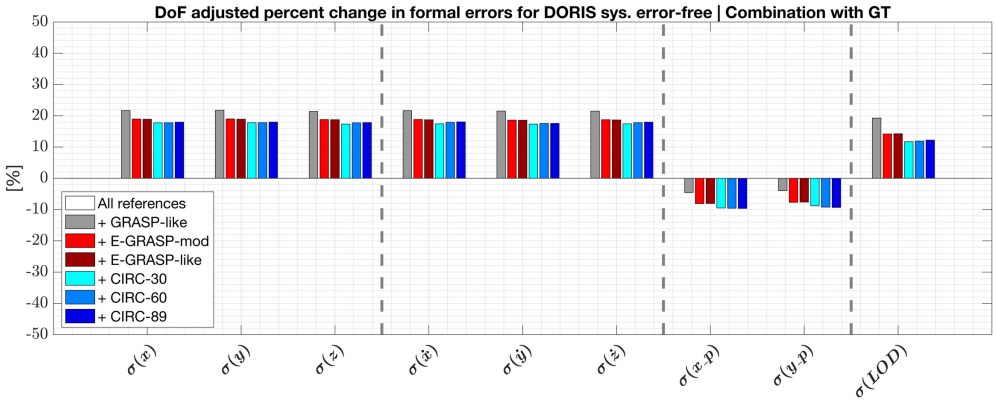

(a) DoF adjusted change in formal errors in comparison to single-technique solution. Coordinates in X,Y, and Z

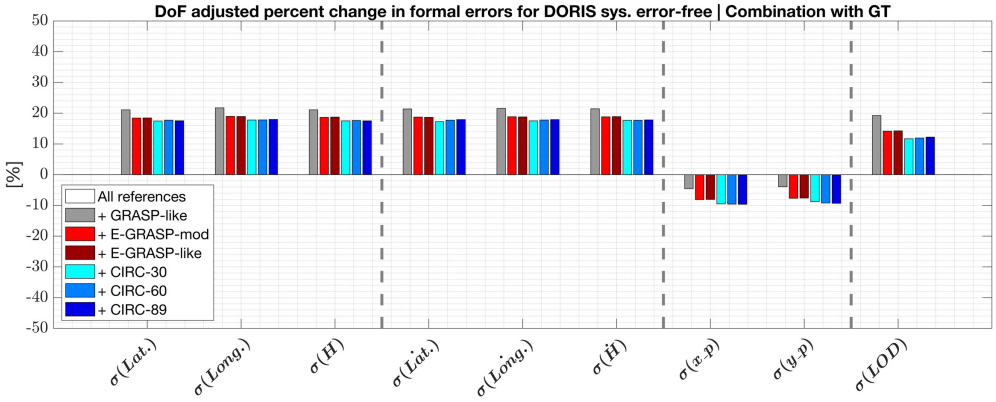

(b) Same as in Fig. a) but for coordinates in Latitude, Longitude, Height.

Figure G.33: DoF adjusted change in formal errors for the multi-technique combined solution using GTs in comparison to the systematic error-free single-technique case for DORIS. Figure a) shows the values for X,Y and Z, Figure b) the values for Latitude, Longitude, Height.

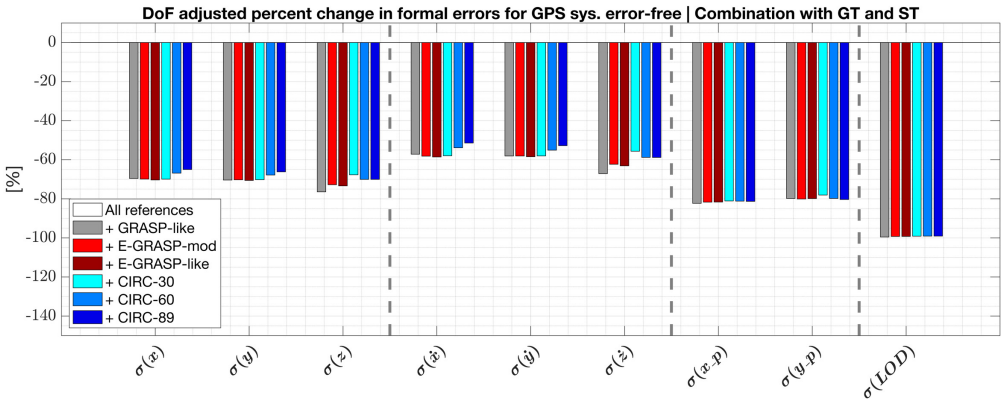

(a) DoF adjusted change in formal errors in comparison to single-technique solution. Coordinates in X,Y, and Z. Coordinates in X,Y, and Z

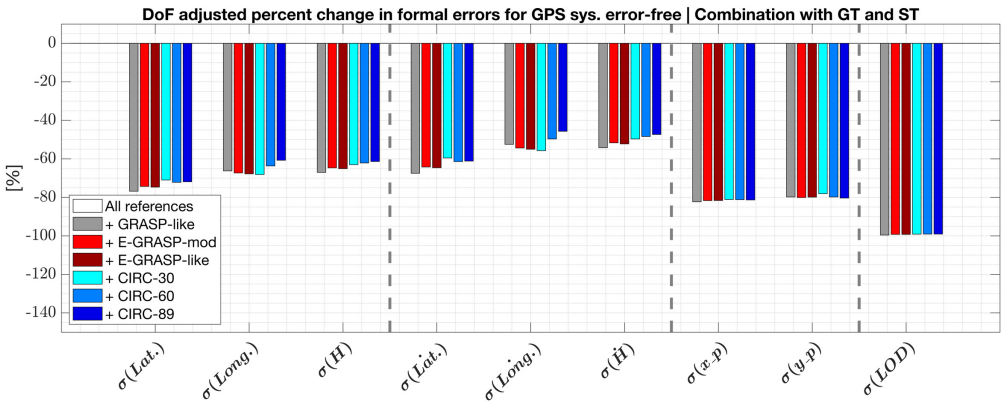

(b) Same as in Fig. a) but for coordinates in Latitude, Longitude, Height.

Figure G.34: DoF adjusted change in formal errors for the multi-technique combined solution using GTs and ST in comparison to the systematic error-free single-technique case for GPS. Figure a) shows the values for X,Y and Z, Figure b) the values for Latitude, Longitude, Height.

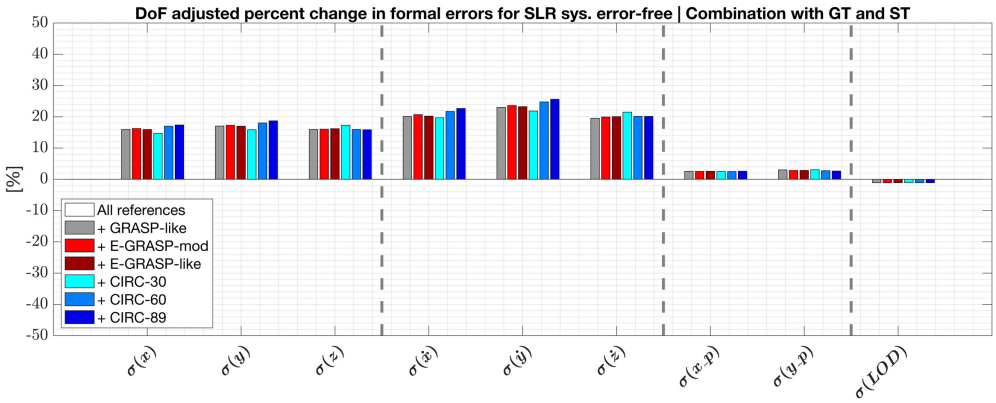

(a) DoF adjusted change in formal errors in comparison to single-technique solution. Coordinates in X,Y, and Z. Coordinates in X,Y, and Z

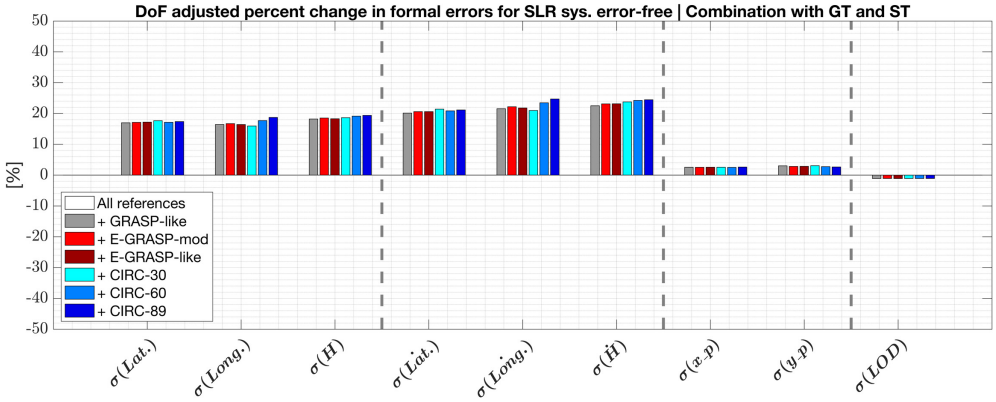

(b) Same as in Fig. a) but for coordinates in Latitude, Longitude, Height.

Figure G.35: DoF adjusted change in formal errors for the multi-technique combined solution using GTs and ST in comparison to the systematic error-free single-technique case for SLR. Figure a) shows the values for X,Y and Z, Figure b) the values for Latitude, Longitude, Height.

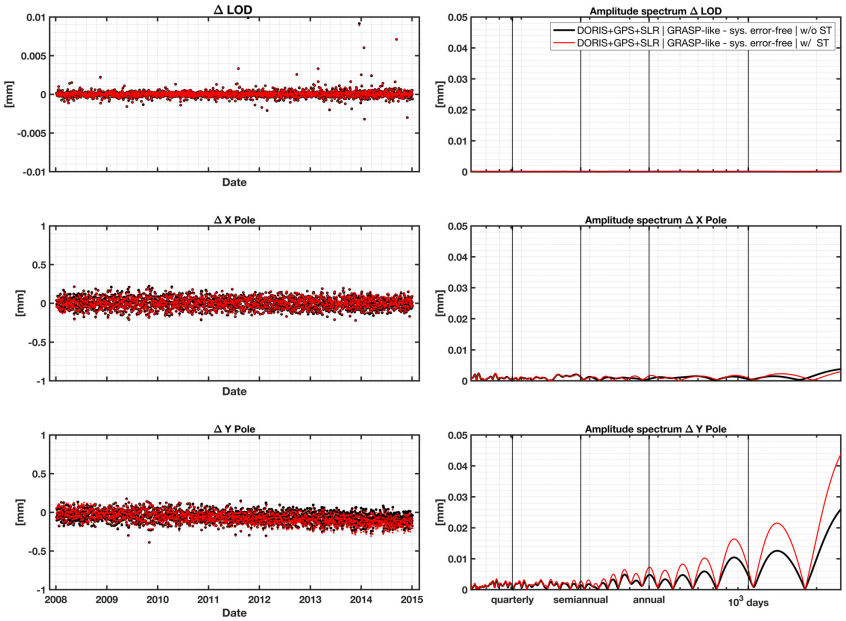

Figure G.36: Estimated differences of LOD, X-pole, and Y-pole over time and their spectral analysis for for the GRASP-like scenario in the systematic error-free multi-technique combination using GTs and GTs with STs.

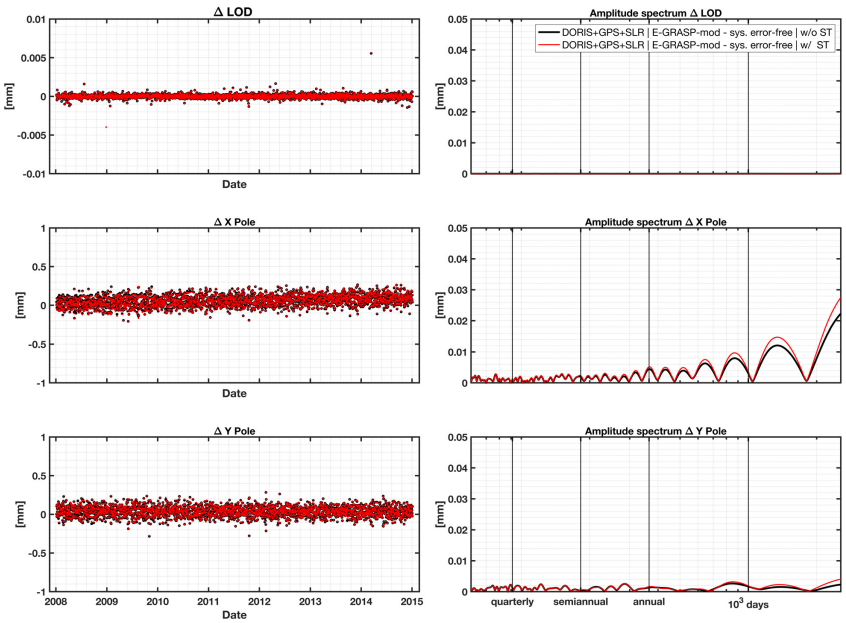

Figure G.37: Estimated differences of LOD, X-pole, and Y-pole over time and their spectral analysis for for the E-GRASP-mod scenario in the systematic error-free multi-technique combination using GTs and GTs with STs.

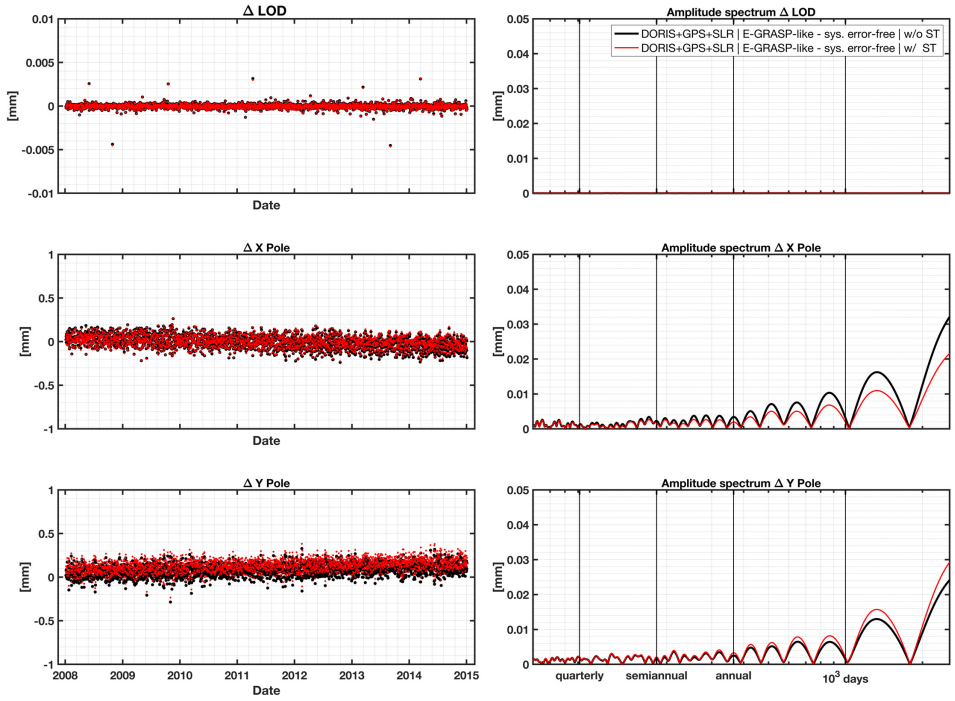

Figure G.38: Estimated differences of LOD, X-pole, and Y-pole over time and their spectral analysis for for the E-GRASP-like scenario in the systematic error-free multi-technique combination using GTs and GTs with STs.

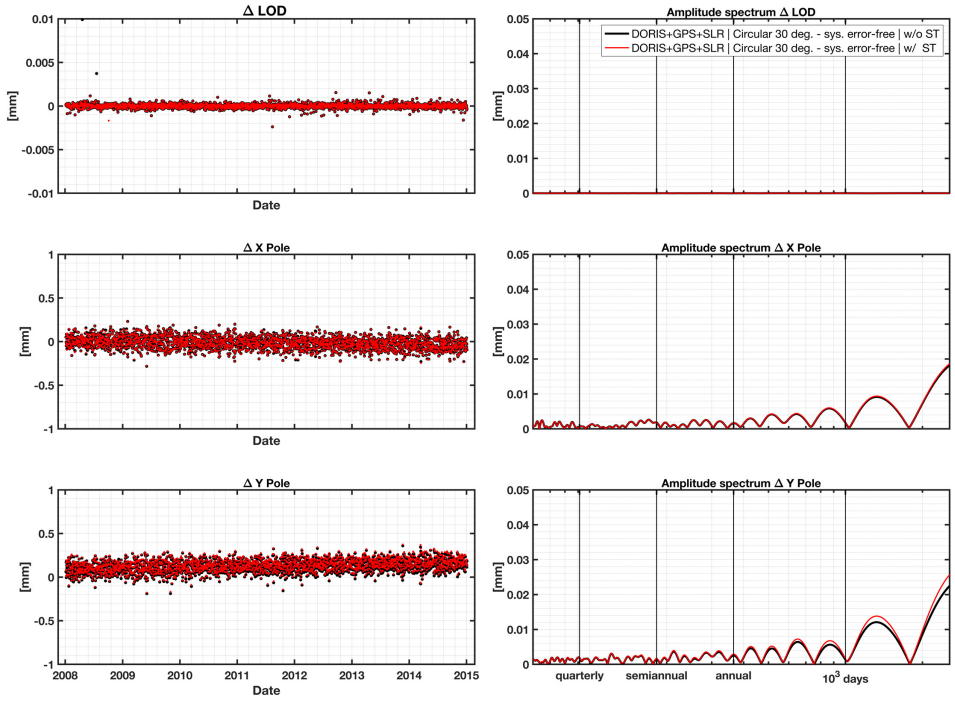

Figure G.39: Estimated differences of LOD, X-pole, and Y-pole over time and their spectral analysis for the Circular 30° scenario in the systematic error-free multi-technique combination using GTs and GTs with STs.

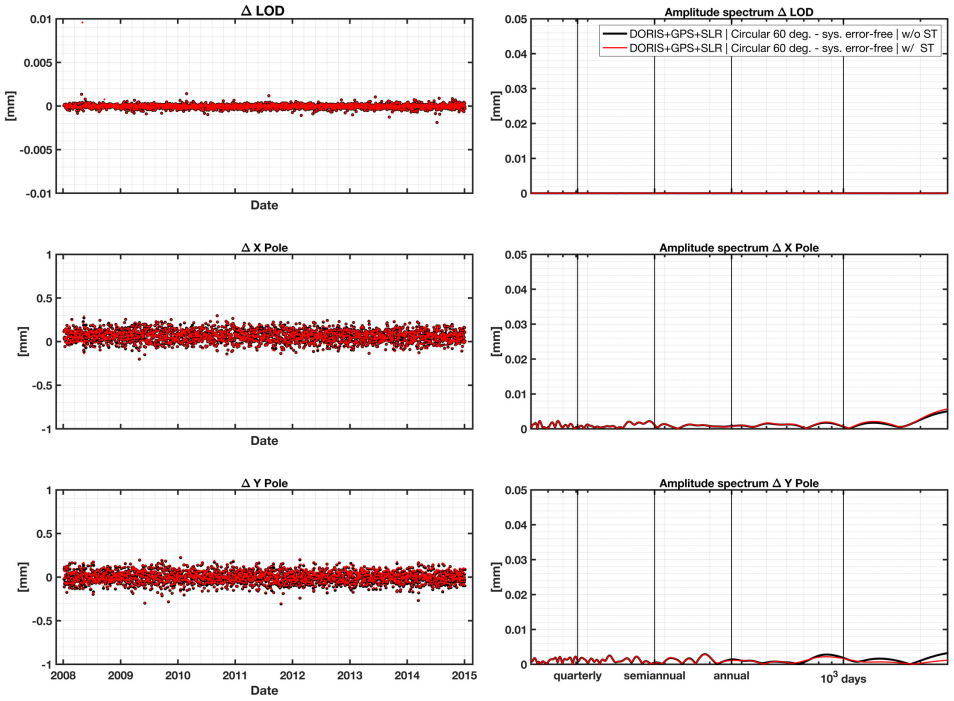

Figure G.40: Estimated differences of LOD, X-pole, and Y-pole over time and their spectral analysis for the Circular 60° scenario in the systematic error-free multi-technique combination using GTs and GTs with STs.

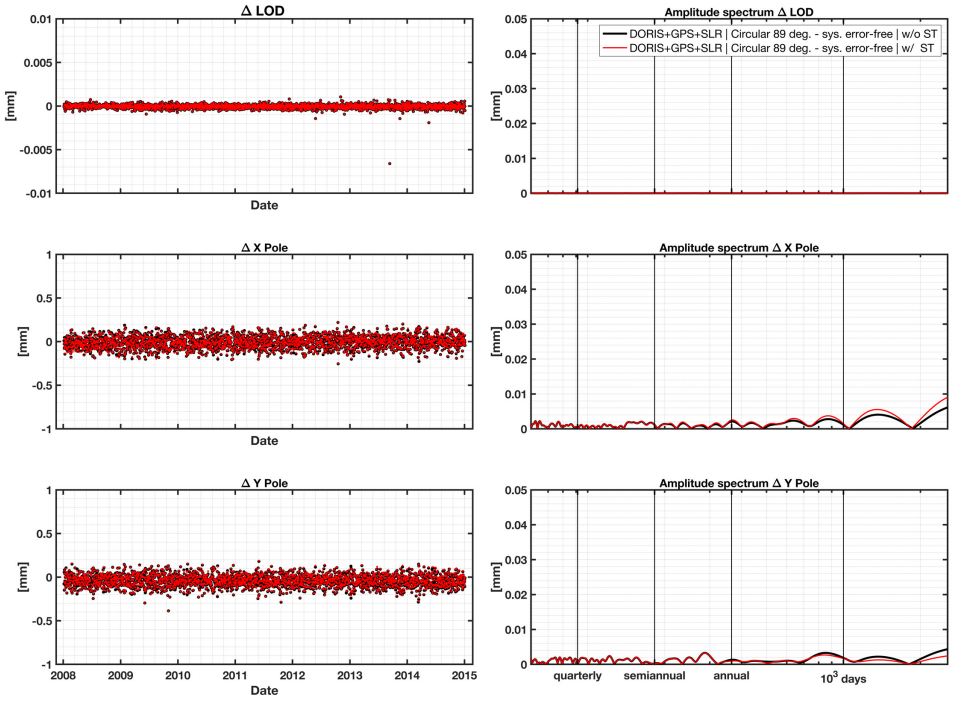

Figure G.41: Estimated differences of LOD, X-pole, and Y-pole over time and their spectral analysis for the Circular 89° scenario in the systematic error-free multi-technique combination using GTs and GTs with STs.

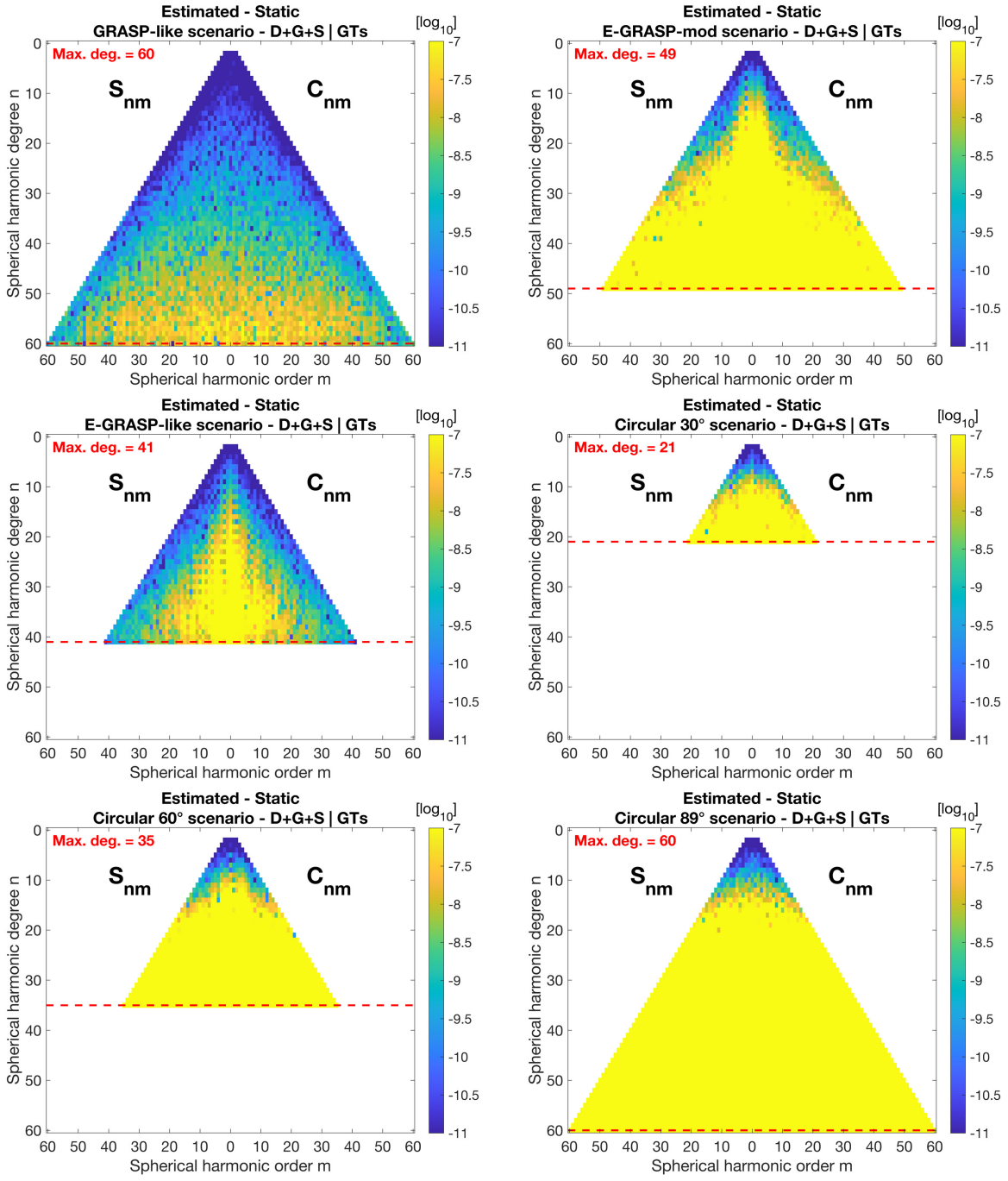

Figure G.42: Triangular plots showing the difference between estimated and simulated SH coefficient for the combination with GTs.

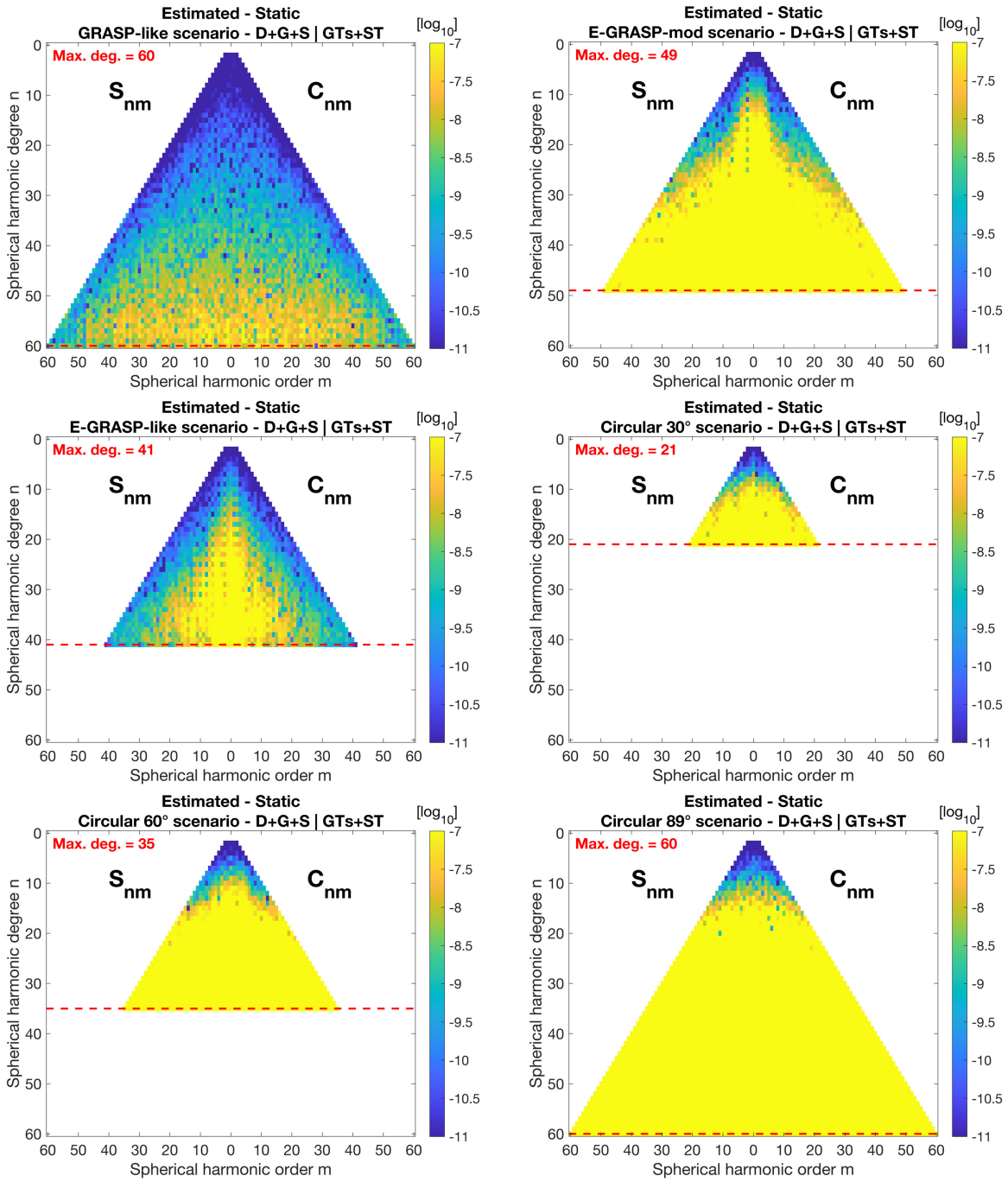

Figure G.43: Triangular plots showing the difference between estimated and simulated SH coefficient for the combination with GTs and ST.

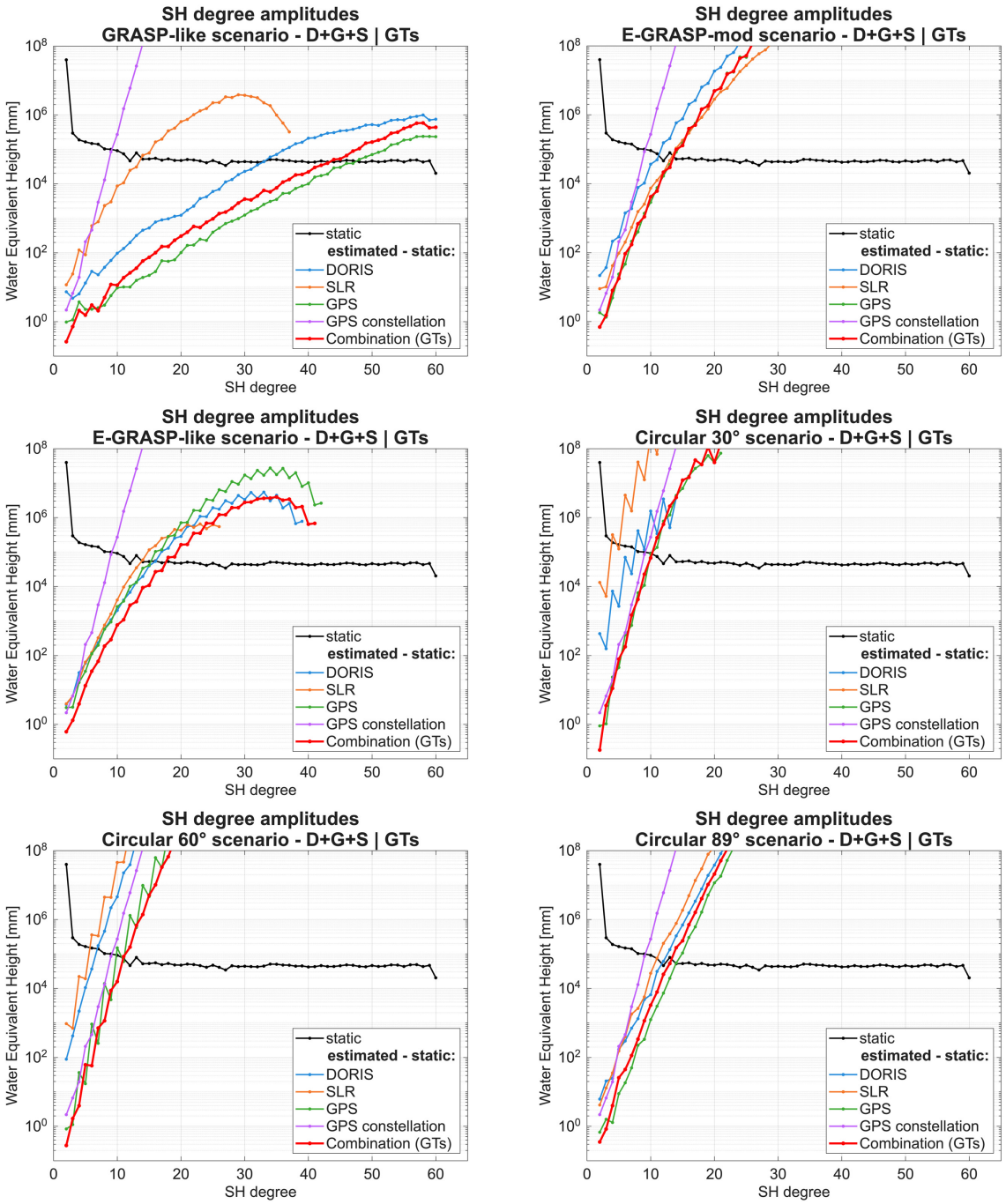

Figure G.44: SH degree amplitudes in equivalent water height for the combination with GTs.

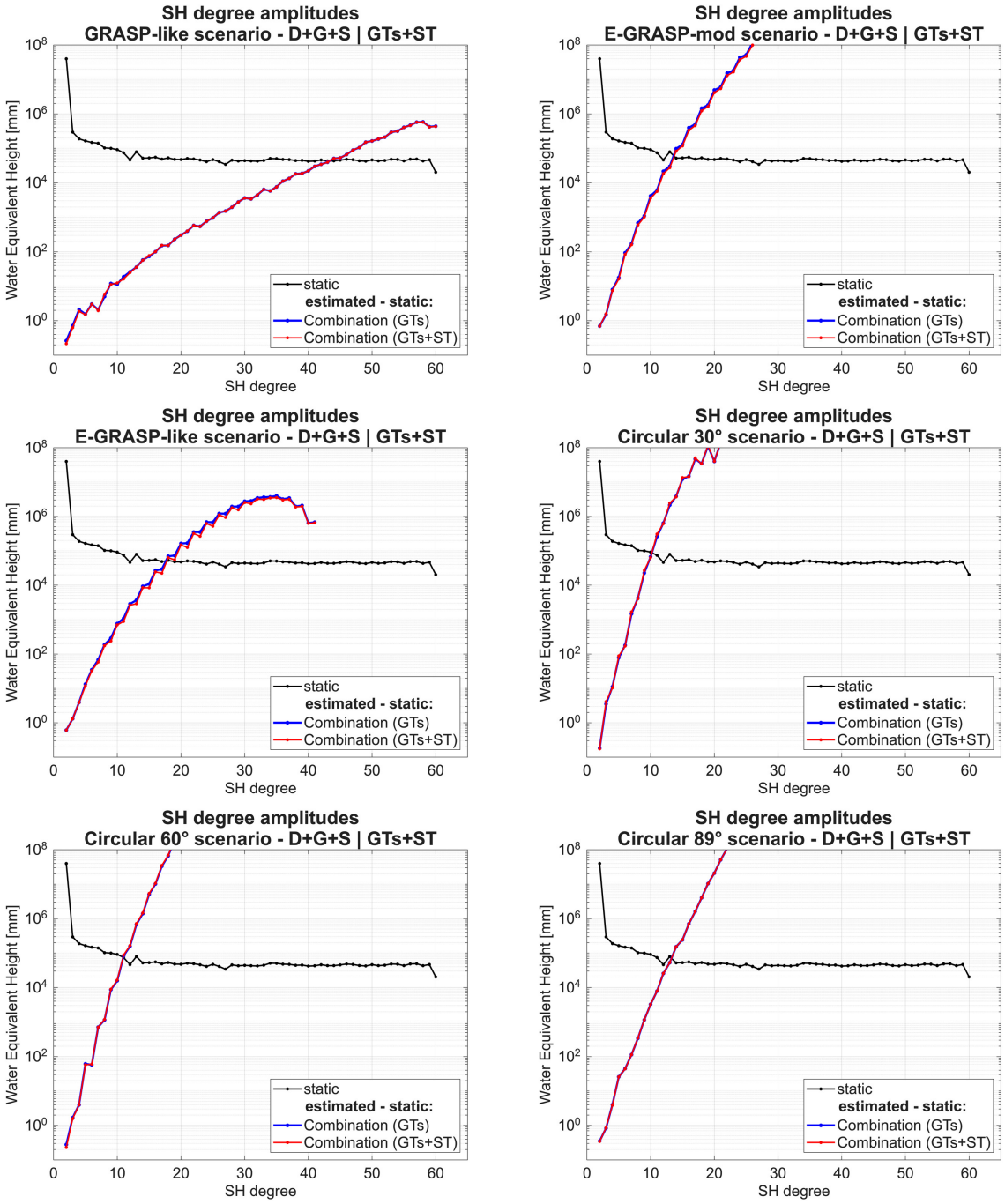

Figure G.45: SH degree amplitudes in equivalent water height for the combination with GTs and ST.

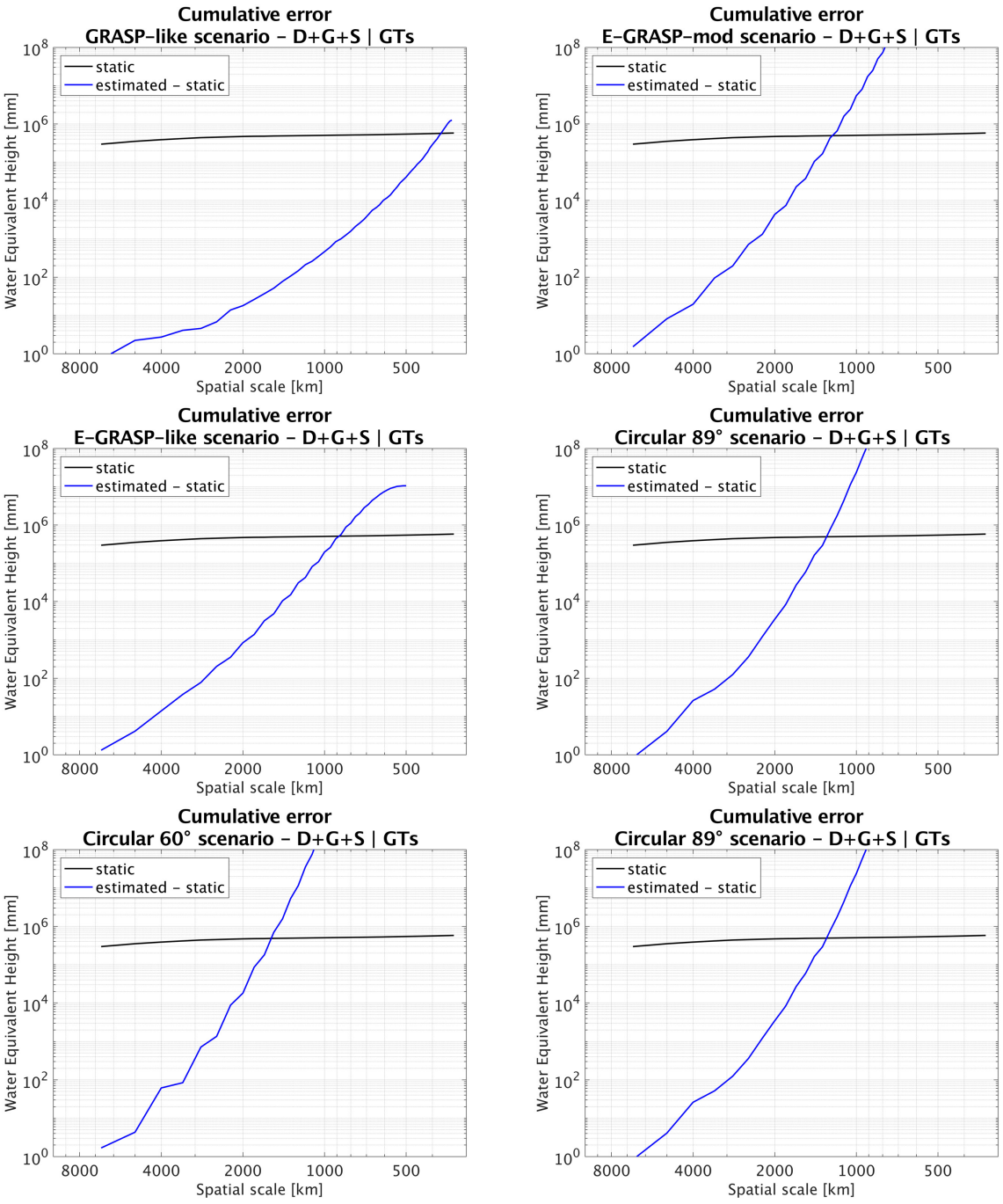

Figure G.46: Cumulative error in equivalent water height for the combination with GTs.

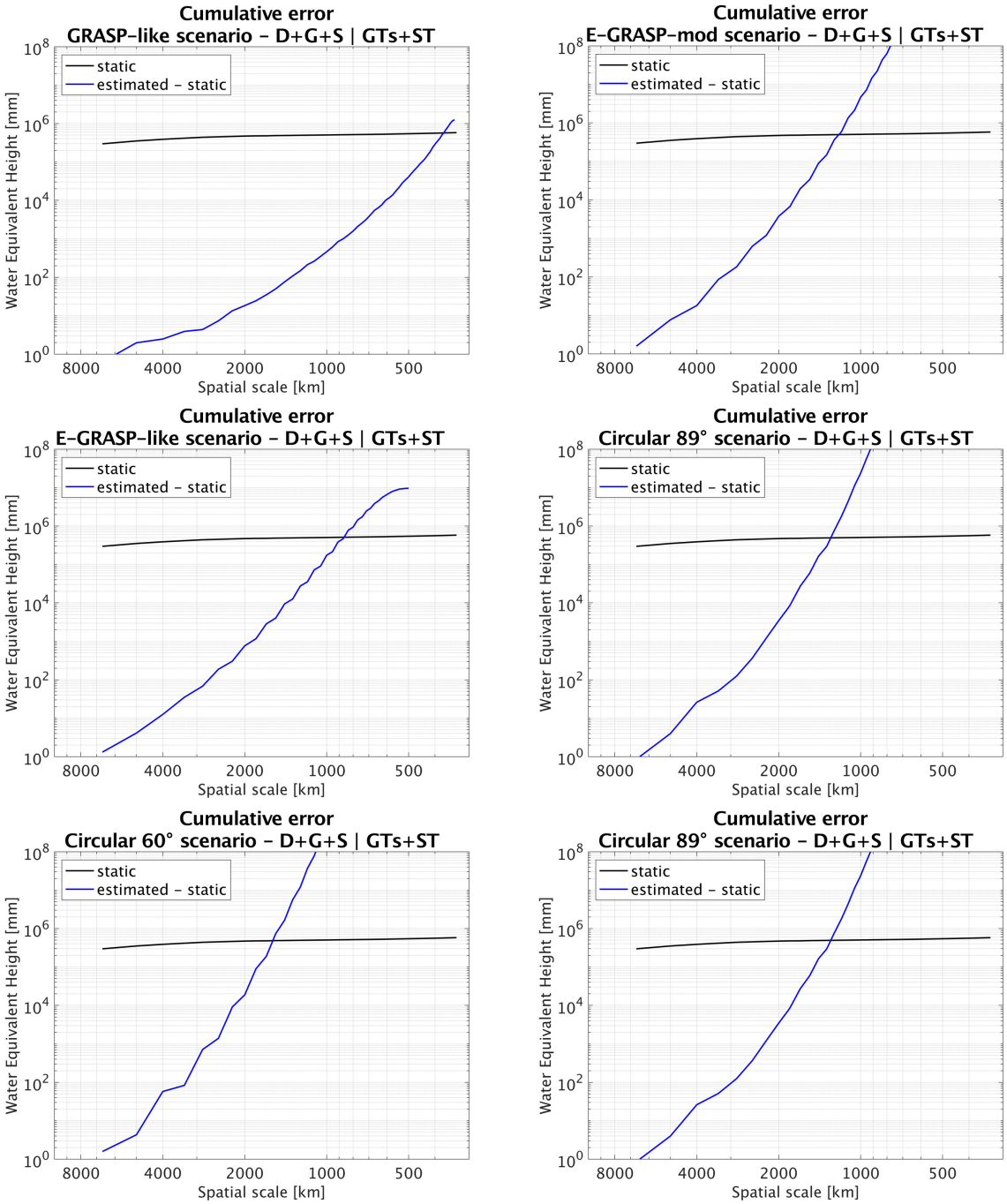

Figure G.47: Cumulative error in equivalent water height for the combination with GTs and ST.